

**BUILDING ICE-AGE ASKJA: PROCESSES, PRODUCTS AND PALEOCLIMATE**

by

Alison Hollomon Graettinger

BS, University of Puget Sound, 2005

MSc, University of Waikato, 2008

Submitted to the Graduate Faculty of  
Dietrich School of Arts and Sciences in partial fulfillment  
of the requirements for the degree of  
Doctor of Philosophy

University of Pittsburgh

2012

UNIVERSITY OF PITTSBURGH  
DIETRICH SCHOOL OF ARTS AND SCIENCES

This dissertation was presented

by

Alison Hollomon Graettinger

It was defended on

June 25, 2012

and approved by

Thomas Anderson, PhD, Professor Emeritus, University of Pittsburgh

Charles Jones, PhD, Lecturer, University of Pittsburgh

David McGarvie, PhD, Staff Tutor, The Open University, UK

Committee Co-Chair: Michael Ramsey, PhD, Professor, University of Pittsburgh

Dissertation Adviser: Ian P. Skilling, PhD, Senior Lecturer, University of Glamorgan, UK

Copyright © by Alison Hollomon Graettinger

2012

# **BUILDING ICE-AGE ASKJA: PROCESSES, PRODUCTS AND PALEOCLIMATE**

Alison Hollomon Graettinger, PhD

University of Pittsburgh, 2012

Austurfjöll is the largest glaciovolcanic construct at Askja Volcano, the best exposed and largest basaltic central volcano in Iceland. The massif records the repeated interaction of basaltic fissure-dominated eruptions with a 600-900 m thick Pleistocene ice sheet in Iceland. The Austurfjöll deposits serve as an important proxy record for ice presence and thickness, supplementing the limited terrestrial glacial record in Iceland.

The model of the construction of the 3.62 km<sup>3</sup> glaciovolcanic massif is the first to outline in detail and date the growth and evolution of a long-lived polygenetic ice-confined central volcano. The model is based on lithologic descriptions, petrologic investigations, textural studies, unspiked K-Ar dating, volatile saturation pressures based on FTIR analysis of water content in glass, and remote sensing-based mapping. The massif is composed of basal basaltic pillow lava sheets, dominantly subaqueously-deposited vitriclastic deposits erupted from overlapping fissure ridges, and accumulations of gravity-driven deposits in inter-ridge depositional centers. The ridges are locally capped by emergent to subaerial tephra and subaerial lava flows. Detailed textural studies of sequences of in-situ transitions from pillow lavas through breccias to overlying lapilli tuffs are interpreted as examples of phreatomagmatic explosions triggered by initial magmatic exsolution and fragmentation at water depths > 600 m.

A stratigraphy for Austurfjöll is established and consists of one interglacial unit, six glaciovolcanic units, and two glaciogenic sedimentary units established through chemostratigraphy and field mapping. Eruptive units are numbered chronologically, with glacial units designated Dm: Unit 1 (A and B), Dm1, Unit 2, Dm2, Unit 3, Unit 4, Unit 5, Unit 6 and Unit 7. Diamictite deposits and emergent facies are described for the first time at Austurfjöll. Two eruptive units were dated radiogenically by



unspiked K-Ar methods to 71 +/- 7 ka (Unit 2) and 29 +/- 8 ka (Unit 3). Ice presence is inferred from glacial, subaerial, and subglacial lithofacies including coherent margined volcanoclastic dikes (CMVDs) that are interpreted as the result of basaltic intrusions into ice-cemented sediments. The deposits described from Austurfjöll reflect a history of interglacial, ice-confined subaqueous, subglacial and emergent eruptions with a dynamic Pleistocene ice sheet over at least 40 ka.

## TABLE OF CONTENTS

<b>PREFACE.....</b>	<b>XXXVII</b>
<b>1.0 INTRODUCTION.....</b>	<b>1</b>
<b>1.1 INTRODUCTION TO THE GEOLOGIC SETTING AND HISTORY OF ERUPTIVE ACTIVITY OF ASKJA VOLCANO, ICELAND.....</b>	<b>2</b>
<b>1.2 REGIONAL SETTING.....</b>	<b>8</b>
<b>1.3 GLACIAL HISTORY .....</b>	<b>11</b>
<b>1.4 GEOLOGY OF ASKJA VOLCANO.....</b>	<b>12</b>
<b>1.5 STRUCTURE AND RELATIVE AGE OF ASKJA COMPONENTS .....</b>	<b>14</b>
<b>1.6 HOLOCENE ERUPTIVE HISTORY .....</b>	<b>17</b>
<b>1.7 HISTORIC ERUPTIONS FROM ASKJA.....</b>	<b>20</b>
<b>1.7.1 Eruption of 1875 .....</b>	<b>20</b>
<b>1.7.2 Eruptions of the 1920s.....</b>	<b>21</b>
<b>1.7.3 Eruption of 1961 .....</b>	<b>22</b>
<b>1.8 AREA OF INTEREST: AUSTURFJÖLL.....</b>	<b>22</b>
<b>1.9 DEFORMATION AND MONITORING OF ASKJA VOLCANO .....</b>	<b>23</b>
<b>2.0 ARCHITECTURE OF AUSTURFJÖLL MASSIF, ASKJA, ICELAND: LITHOLOGY, PETROGRAPHY.....</b>	<b>27</b>
<b>2.1 METHODOLOGY .....</b>	<b>29</b>

<b>2.2</b>	<b>LITHOLOGY .....</b>	<b>30</b>
<b>2.2.1</b>	<b>Lavas .....</b>	<b>32</b>
<b>2.2.2</b>	<b>Pillowed lavas.....</b>	<b>37</b>
<b>2.2.2.1</b>	<b>Geomorphology of pillowed units.....</b>	<b>38</b>
<b>2.2.2.2</b>	<b>Non-pillowed lavas .....</b>	<b>43</b>
<b>2.2.3</b>	<b>Rhyolite lava.....</b>	<b>46</b>
<b>2.2.4</b>	<b>Fragmental Units .....</b>	<b>48</b>
<b>2.2.4.1</b>	<b>Breccias .....</b>	<b>48</b>
<b>2.2.4.2</b>	<b>Diamictites .....</b>	<b>50</b>
<b>2.2.4.3</b>	<b>Tuffs.....</b>	<b>51</b>
<b>2.2.5</b>	<b>Intrusions.....</b>	<b>59</b>
<b>2.2.6</b>	<b>Xenoliths .....</b>	<b>61</b>
<b>2.3</b>	<b>PETROGRAPHY .....</b>	<b>62</b>
<b>2.4</b>	<b>STRUCTURE AND VENTS.....</b>	<b>68</b>
<b>2.5</b>	<b>INTERPRETATION OF LITHOFACIES.....</b>	<b>79</b>
<b>2.6</b>	<b>ARCHITECTURE.....</b>	<b>89</b>
<b>2.6.1</b>	<b>Fissure ridges .....</b>	<b>89</b>
<b>2.6.2</b>	<b>Lava dominated features.....</b>	<b>91</b>
<b>2.6.3</b>	<b>Depo-centers.....</b>	<b>92</b>
<b>2.6.4</b>	<b>Mantling deposits.....</b>	<b>94</b>
<b>2.7</b>	<b>SUMMARY .....</b>	<b>96</b>
<b>3.0</b>	<b>GEOCHEMISTRY AND RADIOMETRIC DATING OF AUSTURFJÖLL MASSIF, ASKJA, ICELAND.....</b>	<b>98</b>

3.1	METHODOLOGY .....	98
3.2	WHOLE ROCK GEOCHEMISTRY .....	104
3.3	PHENOCRYST COMPOSITION .....	114
3.4	RADIOGENIC DATING .....	117
3.5	DISCUSSION.....	118
3.5.1	Major and Minor element trends.....	119
3.5.1.1	Establishment of units .....	120
3.5.2	Mineralogy .....	122
3.5.3	Pearce element ratios.....	123
3.6	CONTEXT OF ASKJA .....	128
3.7	PETROGENESIS .....	132
3.8	CONCLUSIONS .....	137
4.0	ARCHITECTURE AND EVOLUTION OF AUSTURFJÖLL MASSIF: IMPLICATIONS FOR ASKJA VOLCANO, ICELAND.....	138
4.1	VOLUME CALCULATIONS .....	140
4.1.1	Construction of Austurfjöll.....	141
4.1.2	Eruptive units and chronology .....	144
4.2	ARCHITECTURE.....	152
4.3	PRE-CALDERA AUSTURFJÖLL.....	160
4.4	CONCLUSIONS .....	165
5.0	REMOTE SENSING AND GEOLOGIC MAPPING OF GLACIOVOLCANIC DEPOSITS IN THE REGION SURROUNDING ASKJA (DYNGJUFJÖLL) VOLCANO, ICELAND .....	166

<b>5.1</b>	<b>INTRODUCTION .....</b>	<b>166</b>
<b>5.1.1</b>	<b>Background .....</b>	<b>168</b>
<b>5.2</b>	<b>METHODOLOGY .....</b>	<b>169</b>
<b>5.2.1</b>	<b>Data collection.....</b>	<b>171</b>
<b>5.2.1.1</b>	<b>Field work .....</b>	<b>171</b>
<b>5.2.1.2</b>	<b>VNIR spectra .....</b>	<b>171</b>
<b>5.2.1.3</b>	<b>TIR spectra .....</b>	<b>172</b>
<b>5.2.1.4</b>	<b>ASTER Classification .....</b>	<b>173</b>
<b>5.2.1.5</b>	<b>VNIR reflectance spectra classification .....</b>	<b>175</b>
<b>5.2.1.6</b>	<b>Linear deconvolution of emissivity spectra (TIR).....</b>	<b>175</b>
<b>5.2.2</b>	<b>Compilation of the best-fit map.....</b>	<b>176</b>
<b>5.3</b>	<b>RESULTS .....</b>	<b>179</b>
<b>5.3.1</b>	<b>Best-Fit Map.....</b>	<b>179</b>
<b>5.4</b>	<b>DISCUSSION.....</b>	<b>186</b>
<b>5.5</b>	<b>CONCLUSIONS AND FURTHER RESEARCH.....</b>	<b>189</b>
<b>6.0</b>	<b>SUBAQUEOUS BASALTIC MAGMATIC EXPLOSIONS TRIGGER PHREATOMAGMATISM .....</b>	<b>190</b>
<b>6.1</b>	<b>BACKGROUND / MOTIVATION.....</b>	<b>192</b>
<b>6.1.1</b>	<b>Field area .....</b>	<b>193</b>
<b>6.2</b>	<b>METHOD .....</b>	<b>194</b>
<b>6.3</b>	<b>OVERVIEW OF DEPOSITS .....</b>	<b>195</b>
<b>6.3.1</b>	<b>Sequence Descriptions .....</b>	<b>196</b>
<b>6.3.2</b>	<b>Detailed description of lithofacies .....</b>	<b>200</b>

6.3.3	Interpretation of lithofacies .....	209
6.3.3.1	Pillow lava .....	209
6.3.3.2	Pillow fragments and fluidal bombs.....	210
6.3.3.3	Lapilli and coarse ash .....	213
6.3.3.4	Fine Ash .....	213
6.3.3.5	Deposit structure .....	215
6.3.3.6	Genetic relationship between the facies .....	216
6.4	A MODEL OF TRANSITION FROM EXPLOSION TO EFFUSION.....	218
6.4.1	Magma fragmentation at the onset of basaltic phreatomagmatic explosions .....	219
6.4.2	What triggers the transition from effusive eruptions to explosive activity in subaqueous eruptions? .....	224
6.4.3	Eruption Style .....	226
6.5	CONCLUSION .....	229
7.0	INTRUSION OF BASALT INTO FROZEN SEDIMENTS AND GENERATION OF COHERENT-MARGINED VOLCANICLASTIC DIKES (CMVDS).....	231
7.1	OBSERVATIONS.....	234
7.1.1	Dike Margins.....	235
7.2	DIKE INTERIORS.....	238
7.3	DISCUSSION.....	244
7.3.1	Fracture formation .....	244
7.3.2	Dike Margin Formation .....	245
7.3.3	Evidence for ice-cementation of the host.....	246

7.3.4	Melting of ice-cemented host .....	248
7.3.5	Dike Interior Formation .....	249
7.4	CONCLUSION .....	250
8.0	PALEO-ICE RECONSTRUCTIONS OF THE REGION AROUND ASKJA VOLCANO USING AUSTURFJÖLL MASSIF .....	253
8.1	METHODOLOGY .....	255
8.2	CLIMATE FACTORS INFLUENCING ICELAND .....	257
8.3	RECONSTRUCTION OF ICELAND'S GLACIAL HISTORY .....	258
8.3.1	First glaciation .....	259
8.3.2	Interstadials.....	259
8.3.3	Weichselian (Last Glacial Maximum) (100-70 ka to 11 ka).....	260
8.3.4	Deglaciation.....	261
8.3.5	Minor cooling periods .....	262
8.3.6	Modern ice coverage in Iceland.....	263
8.4	JUSTIFICATION OF ASKJA AS A RECORD OF PALEO-ICE THICKNESS.....	264
8.5	REGIONAL DATA .....	266
8.5.1	Offshore evidence .....	267
8.5.2	Onshore evidence.....	269
8.6	FORMER ICE-PRESENCE AT AUSTURFJÖLL.....	270
8.6.1	Ages .....	270
8.6.2	Deposits.....	271
8.6.2.1	Evidence of interaction with ice.....	272

8.6.2.2	Evidence of moving and ponding water .....	273
8.6.2.3	Emergent activity, paleo-water levels, and drainage events .....	275
8.6.2.4	Interpretation of deposits .....	277
8.6.3	Volatile saturation pressures .....	284
8.6.4	Interpretation of volatile content of glassy rinds .....	288
8.6.5	Tephra record .....	293
8.7	CONCLUSIONS .....	294
APPENDIX A .....		297
APPENDIX B .....		380
APPENDIX C .....		396
APPENDIX D .....		401
APPENDIX E .....		404
BIBLIOGRAPHY .....		406



## LIST OF TABLES

Table 2.1 Lithofacies codes .....	33
Table 2.2 Statistics pertaining to eruptive vents in Austurfjöll massif. ....	75
Table 3.1 Variability within and between datasets from the two XRF laboratories. ....	103
Table 3.2 Average crystal composition as determined semi-quantitatively by SEM EDS. ....	116
Table 3.3 K-Ar ages of subaqueous pillow lavas from Austurfjöll. Analysis conducted by H. Guillou, LSCE, CEA-CNRS, France. ....	118
Table 3.4 A comparison of y-intercept values for PER control lines with a slope of one, representative of each eruptive unit. Associated with Figure 3.13. ....	125
Table 4.1 Lithofacies present within each eruptive unit and major implications. ....	142
Table 4.2 Minimum and maximum aerial extent of eruptive units at Austurfjöll. Volume estimates are made for large eruptive units based on minimum extent. ....	150
Table 4.3 Production rates for Askja volcano including new data from Austurfjöll massif. ....	151
Table 4.4 Calculations of vent density based on the observed proportions of vents and depocenters (including channel fills) required to make up the volume of Austurfjöll. ....	153
Table 4.5 Regional estimates of production during glacial, early postglacial and recent eruptive periods. Austurfjöll values are reasonable in comparison to Krafla and the Reykjanes Peninsula. For locations see Figure 1.1. ....	155

Table 4.6 Estimates of potential volume of glaciovolcanic material lost to the calderas that intersect with Austurfjöll and Thorvaldstindur massifs.....	163
Table 5.1 Aerial extent of ground cover units in best fit map (Figure 5.6), with comparison to existing aerial extent from regional map (Figure 5.3). .....	180
Table 5.2 Techniques used to identify individual ground cover units.....	183
Table 6.1 Selection of quantified parameters of fluidal bombs from subaqueous effusive to explosive transitional deposits. Parameters were quantified using a combination of field, petrographic, and binocular microscope techniques. ....	205
Table 6.2 Occurrence of distinctive fine ash particle morphologies in DK and NG deposits....	214
Table 6.3 Dimensions and extent of subaqueous pillow lava, breccia and lapilli tuff sequences at Askja used to calculate the duration of the eruption based on a typical eruption rate of Strombolian and fissure eruptions (10-100 m <sup>3</sup> /s). ....	229
Table 7.1 Textural comparison of individual CMVDs with the associated host sediment, chill margins and when available, coherent interior domains of the same CMVD. Statistics were derived from petrographic image analysis. D= Coherent dike, coherent portion of a CMVD...	239
Table 7.2 Conditions of dike formation in Askja glaciovolcanic sediments and lavas. ....	247
Table 8.1 Summary of environmental indicators by eruptive unit. ....	280
Table 8.2 Summary of FTIR results and VolatileCalc computed volatile saturation pressures.	286
Table 8.3 Evidence for paleo-ice thicknesses based on volatile analyses and compared with geomorphic evidence. ....	289
Table 8.4 Summary of ice thickness values constructed for each eruption unit. Results indicate that an ice sheet of at least 400 m was present during all of the eruption units of Austurfjöll	

between 71 and after 29 ka. Ice thicknesses may have been as much at 900 m during largest eruption phases.....	291
Table A.1 Thin-section description.....	297
Table B.1 Complete XRF results split by eruptive unit.....	381
Table B.2 Microprobe results for selected samples of glassy pillow dike rind. Collected at the University of Wisconsin Madison, WI, USA. ....	390
Table B.3 Bulk rock geochemistry of greater Askja historic and Holocene lavas. ....	391
Table E.1 Complete FTIR results from the University of Wisconsin, Madison.....	404

## LIST OF FIGURES

Figure 1.1 Map of Iceland showing the active volcanic regions in Iceland: Reykjanes Peninsula (RP), Snæfellsnes Volcanic Zone (SVZ), Western Volcanic Zone (WVZ), Northern Volcanic Zone (NVZ), and Eastern Volcanic Zone (EVZ) (adapted from Sigvaldason 2002). .....	3
Figure 1.2 Location map showing Askja volcano and the surrounding region. Major geomorphologic features are labeled. SPOT image courtesy of Google Earth. ....	5
Figure 1.3 Simplified geology map of Askja with relevant features labeled. Base map is a hillshade produced from a 10 m resolution digital elevation model created by Landmælingar Íslands, Iceland. ....	7
Figure 1.4 Map of the fissure swarms that make up the North Volcanic Zone, Iceland (from Rymer and Tryggvason 1993). ....	10
Figure 1.5 Map of distribution and thickness of the 10 ka Askja pumice. Solid circles indicate sample locations and thin lines indicate estimated thickness contours. Dashed line indicates likely axis of distribution. The distribution of the 1875 pumice is included for comparison (from Sigvaldason 2002). ....	18
Figure 2.1 Study area Austurfjöll and reconnaissance areas nearby in shaded region. Stratigraphic logs collected in this study are indicated in yellow, and 1980s stratigraphic logs were collected by Strand (1987). ....	28

Figure 2.2 Lithofacies map produced through two field campaigns and augmented through comparison with aerial photographs and comparison with existing literature (Sigvaldason 1968). Lithofacies are extended to Thorvaldstindur speculatively using aerial photographs and reconnaissance visits.....	32
Figure 2.3 Field images of lava lithofacies at Austurfjöll. A) Pl1 regularly stacked pillows. B) Pl2 lavas with entablature jointing and irregular pillow dimensions and sizes. Porphyritic (>20% feldspar phenocrysts) examples of all lava lithofacies occur.....	37
Figure 2.4 Vertical pillows within a pillow lava sheet. A) Joint sets and pillow tube margins forming vertical pillows. B) Close up of internal structure of vertical pillows. C) Outcrop containing vertical pillows. D) Line sketch of C showing the transitions between Pl2 lavas, entablature jointed domains and vertical pillows. Pillows likely formed by flowing over a topographic barrier.....	40
Figure 2.5 Porphyritic pillow mounds are distributed in semi-radial patterns away from their source and mantle the underlying topography. A) View from top of pillowed ridge where yellow lines indicate upper exposed surfaces of pillow mound forms. B) Pillow breccia that commonly caps pillow lava mounds. C) Pillow lavas in pillow mounds and pillow breccias also commonly mantled by bedded ash tuff (At4). .....	41
Figure 2.6 Microcrystalline pillow lava mounds are much larger in scale than their porphyritic counterpart (100 m vs. 20 m across). A) Incised pillow mound reveal mantling units of At4, as denoted by yellow line, over pillow units. B) Pillow mound with two pillow units divided by yellow line, and overlying At4 units. C) Close up of B focusing on the top pillow unit of irregular pillows lavas. Yellow lines denote the contact between mantling At4 and pillow unit.	

D) Inset from C revealing the contrast between the upper irregular and lower regular pillow forms (for detailed explanation see text) Yellow line indicates contact. ....	42
Figure 2.7 Non-pillowed lavas A) Example of Lx1 subaqueous lava with radial cooling cracks and phenocryst content > 20%. B) L2 subaerial lava with glacial scour. Scale bar is 1 m. ....	44
Figure 2.8 Example fracture patterns in subaqueous lava flows (L1) with line matching line drawings. A) Tightly spaced entablature, blocky jointing in micro-porphyritic lava. B) Widely spaced predominantly vertical jointing in thin porphyritic flows. C) Radial cooling cracks in an over thickened porphyritic lava. ....	45
Figure 2.9 Rhyolite lava exposures in the southeastern caldera wall. A) Image of the freshest exposure of rhyolite, meter stick for scale. B) Regional view of image A location (images from D. McGarvie). C) Exposure of hydrothermally altered rhyolite on caldera rim. D) Sample location of rhyolite unit pictured in image C (Image courtesy of D. McGarvie). ....	47
Figure 2.10 Images of breccia lithofacies. A) Field image of a pillow-bearing B1 breccia with a pillow outlined in yellow. The scale bar has increments of 10 cm. B) Field image of an angular block-dominated B2 breccia. ....	49
Figure 2.11 Images of diamictite lithofacies. A) Dia1 is a coarse grained matrix supported diamictite. B) Dia2 is a finer grained matrix supported bedded diamictite. ....	51
Figure 2.12 Lt1 facies. A) Example of bombs clasts found in Lt1. Arrow in scale is 10 cm. B) Vesicular clasts of Lt, note the glassy quality of the clasts and lapilli. Small increments on scale are 1 cm each. C) Example of an exposure of Lt1, massive but weak grading occurs. ....	53
Figure 2.13 Other lapilli tuff lithofacies. A) Lt2 subrounded lapilli tuff with pillow fragments and bombs. Weak bedding may occur. B) Lt 4 heterolithic lapilli tuff containing a variety of clast types including porphyritic and micro-porphyritic clasts and red scoria. C) Lt3 Subaerial	

component lapilli tuff containing armored lapilli and red scoria. Large increments on scale are 10 cm, fine increments on scale are 1 cm. ....	54
Figure 2.14 Images of ash tuff lithofacies A) At1 massive coarse ash lapilli. Backpack for scale.	
B) At3 poorly sorted ash tuff with variable grain size concentrations. Loading structures are highlighted by the presence of lapilli. C) At2 laminated (mm scale) coarse and fine ash. D) At2 bedded (1-5 cm) coarse and fine ash.....	57
Figure 2.15 Images of the At4 facies in deformed domains. A) The bedding angle changes from near horizontal to near vertical. B) Acute fold angles with a variety of grain sizes. C) Tight fold angles and convoluted bedding composed of coarse ash. D) Localized thickening of layers in fold. E) Steep contact with underlying breccia. F) Complex sedimentary structures (cross-bedding and channels) in steeply dipping domain. G) Disruption of underlying lapilli tuff unit by At4 deposits. H) Multiple directions of deformation. Large black sections on scale are 10 cm, small divisions are 1 cm. Yellow lines highlight bedding and contacts. ....	
59	
Figure 2.16 Intrusion varieties documented at Austurfjöll. A) Tabular intrusions, D1, that cross-cut rock units with no interaction. Yellow lines indicate the outline of the dike. B) Pillowed intrusions that disrupt surrounding sediment D2 with notebook for scale. C) Intense deformation resulting from a pillowed intrusion with a meter stick for scale. D) CMVDs cross-cut rock units, but interact at the small scale of a 3 mm peperitic margin and internal peperite. Yellow lines indicate the margin of the dike and white lines outline pillows inside the dike. ....	
60	
Figure 2.17 Examples of gabbro nodules. Samples were cut open for thin section and geochemical analysis. Nodules occurred in fragmental hosts, such as lapilli or ash tuff. Size range of nodules is a few centimeters (pictured) up to 0.7 m. ....	
61	

Figure 2.18 Micro-porphyritic lava textures in thin section. A) Micro-phenocrysts of plagioclase dominate lavas and dikes in group one. Vesicles are typically irregular and coalescing. B) Cpx is common in the groundmass of these lavas, but typically does not exceed 30% by volume. C) Rapid quenching of crystals is evident in the spherulitic textures of the groundmass. D) Close up of quench crystals in tachylite glass groundmass. E) Skeletal growth structures in plagioclase feldspar. F) Swallow tail structure of plagioclase feldspar..... 63

Figure 2.19 Petrographic images of subaerial lava samples. A) Plane polarized light (PPL) reveals the abundance of opaque oxide minerals. Plagioclase micro-phenocrysts are common with a microcrystalline groundmass. B) Cross-polarized light reveals the Cpx crystals that typically occur in glomerocrysts with feldspar..... 65

Figure 2.20 Petrographic images showing the diversity of clast types in fragmental deposits. A) Tachylite glass may occur with or without visible crystals or with or without vesicles. B) Sideromelane glass dominates most fragmental deposits, but some tachylite may be present along the margins or within sideromelane fragments. C) Large free phenocrysts can occur with or without glass rims. C) Sideromelane glass can be crystal-free or crystal-rich. In some cases the presence of micro-phenocrysts is highlighted by radial alteration. .... 66

Figure 2.21 Petrographic images of phenocrysts present in porphyritic lithofacies and gabbro nodules. A) PPL image of clustered phenocrysts of plagioclase and Cpx. This clustering also increases the visibility of phenocrysts in porphyritic units. B) Cross-polarized image of the same crystals as in previous image, but better highlighting the interaction between phenocrysts and the groundmass. C) Glomerocrysts are common in porphyritic rocks, and typically have Cpx near their core. Plagioclase crystals may be radial, or large and blocky. D) Plagioclase phenocrysts are frequently twinned, and have complicated growth histories. Mechanically broken crystals are



common in many samples, but are not the norm. E) Large phenocrysts of Cpx are also common. Inclusions of plagioclase or Cpx may occur in either species. F) Plagioclase crystal cluster showing a seed crystal of plagioclase and disrupted twins. G) An example of the rare olivine that can occur as a phenocryst or groundmass constituent. H) Example of a gabbro nodule with large phenocrysts of plagioclase and Cpx. Glomerocrysts are common, and intersertal textures are also common..... 68

Figure 2.22 Hillshade of Austurfjöll showing dip measurements with arrows indicating the direction of dip. There is significant variation, but 35% of major bedded units dip away from the caldera at the rim indicating a potential missing source in what is now Öskjuvatn caldera. Background hillshade based on 10 m DEM produced by LoftMyndir..... 70

Figure 2.23 Summary of tectonic lineaments from Hjartardottir et al. (2009) and Annertz (1985). Background image is a hillshade created from 10 m DEM produced by LoftMyndir. .... 71

Figure 2.24 Example of incomplete dipping beds at the caldera rim. White lines highlight a package of sediments and the orientation of bedding ..... 73

Figure 2.25 Location of vents in Austurfjöll and Thorvaldstindur. Vents are divided into three categories based on method of identification. These categories also imply relative confidence: field relationships (well defined high confidence), vents topographic (moderately well defined, moderate confidence), speculative are implied through deposit distribution (not well constrained, low confidence). The image is overlain on a hillshade produced by LoftMyndir..... 74

Figure 2.26 Histogram showing relative abundance of vent length as measured from Figure 2.22. .... 75

Figure 2.27 Caldera outlines as they are currently proposed including evidence for the interaction with Austurfjöll massif. Black outlines focus on key locations that indicate the interaction of

Askja caldera and glaciovolcanic deposits. A) Location of glaciovolcanic deposits cut by Askja caldera. B) Location of glaciovolcanic beds dipping away from caldera cut by Askja caldera and not overprinted by Öskjuvatn. C) Potential continuation of Askja caldera fault within Öskjuop. This location requires further investigation to resolve this age relationship. ....	78
Figure 2.28 Map of Austurfjöll by Sigvaldason (1968) showing four units. Key for map and cross-section are the same. Unit 1 is non-porphyritic pillowed lavas. Unit 2 is non-porphyritic fragmental deposits. Unit 3 is porphyritic pillowed lava. Unit 4 is porphyritic fragmental deposits. ....	82
Figure 2.29 Map of Askja including Austurfjöll by Strand (1987) showing five lithofacies associations. The margins of Austurfjöll are not included, but porphyritic units and pillow lava sheet flows are notably absent. Mapped units along the caldera lake margin are currently covered by 1875 basaltic tuff cone, rhyolitic pumice and talus which may have been locally mistaken for glaciovolcanic deposits due to basaltic compositions.....	83
Figure 2.30 Schematic of the multiple mechanisms that can form breccias. This example is for a non-pillowed subaqueous lava flow. The processes would be similar, but the fragments produced unique for pillowed subaqueous or subaerial lava flows. Field relationships and componentry are necessary to interpret breccias. ....	86
Figure 2.31 Example of a fissure ridge with exposed feeder dike.....	90
Figure 2.32 Multiple fissure ridges overlapping pillow lava sheets. Steep sided gullies where stratigraphic logs were collected are visible. ....	90
Figure 2.33 Example of a single vent pillow mound. The orientation of the pillows enables identification of the vent. ....	92

Figure 2.34 Field image of a large channel eroded into lapilli tuff deposits and filled with bedded ash tuff deposits. The channel fill deposits are cross-cut by a younger basaltic dike.....	93
Figure 2.35 Field image and sketch of erosional channel in lapilli tuff deposits. The numbers indicate the relative order of each deposit or erosional surface. A pillow lava sheet composed of Pl1 and Pl2 lavas fills the erosional valley and is later covered by At4 deposits and porphyritic pillow mounds.....	94
Figure 2.36 Examples of At4 mantling deposits that fill paleotopography and mantle most lithofacies. The dip of mantling At4 can be used to determine the location of paleotopography.	96
Figure 3.1 Location map of all samples collected in Austurfjöll. The overlay shows which samples were collected for geochemical analysis. Samples that were analyzed for radiometric age dating are also indicated. ....	101
Figure 3.2 AFM diagram show the distribution of Austurfjöll samples. All samples plot neatly as tholeiites.....	104
Figure 3.3 The enrichment of the basaltic melt is highlighted by an incompatible element diagram and total alkali diagram. Symbols represent individual eruptive units of Austurfjöll. Gabbro nodules, Holocene spatter, and lava clasts from diamictons are included for comparison. Symbols will be used consistently throughout this document unless otherwise noted.....	105
Figure 3.4 Variation diagrams of major and trace elements against MgO. Plots along the left represent components of plagioclase and components on the right are incompatible elements. All oxides are in wt%.....	107
Figure 3.5 Variation diagram of CaO vs. TiO <sub>2</sub> and CaO vs. Al <sub>2</sub> O <sub>3</sub> . These comparisons highlight the linear trend of the Austurfjöll dataset. CaO/TiO <sub>2</sub> likely reflects the relative abundance of	

feldspars and oxides, where high CaO reflects high plagioclase content and high TiO <sub>2</sub> reflects high oxide content.....	109
Figure 3.6 Trace element variation diagrams contrasting incompatible and compatible elements. The linear trend of the data set is more pronounced than in the major elements. V/Y likely shows the influence of Cpx and oxide minerals and the overall enrichment of the samples. ....	110
Figure 3.7 Multi-element diagrams highlighting the relative enrichment of trace elements in the Austurfjöll samples. Samples are normalized to the primitive mantle (Lyubetskaya and Korenaga, 2007).....	112
Figure 3.8 REE plot of 15 samples including a sample of the rhyolite dome with a distinctive Eu anomaly, indicating the role of plagioclase in the evolution of the melt. Units 2 and 3 show very limited variability between samples. Unit 5 shows the lowest REE concentrations of all of the Austurfjöll lavas analyzed.....	112
Figure 3.9 Polished thin sections in PPL. The locations of EDS analysis are circled. Targets included phenocrysts and microlites in the groundmass. Blue epoxy indicates presence of vesicles.....	115
Figure 3.10 Example of EDS analysis locations and results. Sample AG 3, a porphyritic lava of eruptive unit 6 contains phenocrysts of plagioclase and Cpx with a microlite rich groundmass. Labels correspond to location within the slide image.....	116
Figure 3.11 Inclusions in macro-phenocrysts. ....	117
Figure 3.12 Pearce Element Ratio of all Austurfjöll samples indicating the control of the full range of plagioclase compositions and Cpx. That the slope of the resulting line is 1.126 suggests a reasonable cogenetic relationship, but indicates the need for further division of eruptive units to confirm this relationship, as a true relationship would have a slope of 1.0. ....	124

Figure 3.13 Control lines with a slope of one centered on characteristic samples for each eruptive unit. The overlap of Units 1, 2 and 3 is significant. Unit 5 and Unit 1B similarly overlap. Units 6, 4 and 7 are distinctive from all of the other slopes. The process that controls the evolution of all of the units, however; is consistent, being dependent on Cpx and Plagioclase. ....	126
Figure 3.14 Comparison of units 1, 2,3, and 5. The Unit 3 control line is included. An apparent relationship occurs between units 1, 2 and 3 (see text for discussion). ....	127
Figure 3.15 Locations of historic lava flows featured in geochemical analyses as they are distributed around Austurfjöll (hillshade). The locations of samples are approximate due to the absence of GPS data. Labels are of individual eruptive units from the 1920s. Eyja was not sampled. ....	129
Figure 3.16 Comparison of postglacial and historic lavas (McGarvie, pers. comm) with Austurfjöll suite. Values of Normal MAR basalts are from Jakobsson et al. (2008). ....	131
Figure 3.17 Austurfjöll samples with mixing lines between the most evolved units (2 and 3) to the least evolved gabbro sample. The Lever Law was applied to determine the approximate amount of fractional crystallization required to create the most evolved melts with different potential ‘parent’ melts. The melts more primitive than the ‘parent’ would be produced by the contamination of parent melt material with cumulate present in the magma chamber. ....	135
Figure 4.1 Chemostratigraphy map of the eruptive units of Austurfjöll. The distribution of waypoints and geochemical samples are included, as are glacio-sedimentary (diamictite) units Dm1 and Dm2 and other overlapping units. The black box shown on the main figure is the location of the insert map, which highlights the limited distribution of Unit 4 deposits.....	140
Figure 4.2 Generalized stratigraphic column of the evolution of Austurfjöll massif. The width of the column reflects the relative distribution of the unit and thickness represents relative thickness	

of units. The units that are cut by caldera faults are indicated. Holocene deposits are not assigned to eruptive units.....	144
Figure 4.3 Map showing the interaction of the Askja and Öskjuvatn calderas with Austurfjöll and related deposits. The inset, shown on the main map as a light grey box, focuses on a group of Unit 6 lavas identified in reconnaissance work that is clearly cross-cut by the younger Askja caldera. ....	148
Figure 4.4 Estimated production rates for Askja volcano using data from this study and Sigvaldason (1992). Interglacial production rate is extrapolated from modern low ice cover conditions.....	155
Figure 4.5 Map of Austurfjöll showing the lines of section used to create extrapolated cross-sections.....	158
Figure 4.6 Three extrapolated cross-sections through Austurfjöll massif. The stratigraphic position of the rhyolite dome is not well constrained. Its current position is controlled by exposures and the lack of deformation in over lying unit. The exposures of rhyolite in section 2 and 3 may represent one large deposit or two isolated deposits. Larger versions of these cross-sections can be found in Appendix C. ....	160
Figure 4.7 Map of Austurfjöll with projections of the potential original massif extent. The projections were used to calculate the volume of missing glaciovolcanic deposits. A) Loss of material based only on the Öskjuvatn caldera, representing a minimum volume of loss. B) More extensive area of potential volumetric loss. ....	162
Figure 4.8 Schematic model of the evolution of eruptive units involved in the construction of Austurfjöll massif and extended to include Thorvaldstindur and deposits just north of Öskjuop. The steps are labeled in order from A (oldest) to K (youngest). ....	165

Figure 5.1 Location map of Iceland with the volcanic zones highlighted (modified from Sigvaldason 2002). Note the location of Askja just north of Vatnajökull ice cap. The Northern Volcanic Zone stretches north from Vatnajökull icecap to the coast. Inset shows the Austurfjöll glaciovolcanic massif in relation to Öskjuvatn, the caldera lake of Askja. ....	167
Figure 5.2 Regional geologic map compiled from previously-published sources (Annertz et al., 1985; Sigvaldason, 2002; Hjartardottir, et al. 2009). Outlines indicate footprints of datasets used to compile the regional map and remote sensing datasets utilized in this study. Abbreviations reference features that are discussed in detail in the text: DY is Dyngjufjöll Ytri, HB is Herðubreið, AF is Austurfjöll, VA is Valðalða, KT is Kollóttadyngja. ....	170
Figure 5.3 Selected VNIR hyperspectral and ASTER resolution reflectance spectra of representative end-member samples. The limited spectral diversity of the compositional units (lapilli tuff, subaerial lava, ash tuff, pumice, subaqueous lava and rhyolite) is primarily from overall brightness levels of the samples. However, all units can be distinguished in the limited spectral resolution of ASTER. ....	173
Figure 5.4 Selected TIR hyperspectral and ASTER resampled emissivity spectra of representative lithology samples (subaerial lava, ash tuff, lapilli tuff, pumice, obsidian and porphyritic lava). There exists much more spectral diversity in the TIR due to the primary Si-O vibrational frequency in all silicate samples. ....	174
Figure 5.5 A) Best-fit map (BFM) of ground cover units in the region north of Askja Volcano. B) BFM with 1875 pumice removed. ....	178
Figure 5.6 Distribution of the 1875 pumice proximal to the Austurfjöll massif overlain on a grayscale hillshade (derived from 10 m Loftmyndir DEM). A) Complete distribution of the 1875 pumice overlapping the glaciovolcanic deposits. B) Outline of the 1875 pumice over colored	

hillshade to show relationship between eroded pumice and topography of the Austurfjöll massif.	
The pumice is mostly preserved in topographic lows. C) 1875 pumice cropped to extent over Austurfjöll to show the exposure of lithology-mapped field units under the pumice. D) Outline of cropped pumice distribution of TIR-based discrimination of glaciovolcanic units.....	182
Figure 6.1 Location of Askja, Iceland including locations of pillow lava, breccia, lapilli tuff sequences. The shaded area represents the field area, Austurfjöll. Sample sites are located in major gullies incised into the base of the glaciovolcanic sequence of Askja. Sample locations from north to south are Drekagil (DG), Nautagil (NG), and Rosagil (RG).....	191
Figure 6.2 Overview of Drekagil sequence including field image, annotated sketch of sampling sites and stratigraphic log.....	198
Figure 6.3 Overview of the Nautagil sequence including field image, annotated sketch of sampling sites, and stratigraphic log.....	199
Figure 6.4 Overview of the Rosagil sequence including field image, annotated sketch of sampling sites, and stratigraphic log.....	201
Figure 6.5 Comparison of pillow lava facies from a field location that presents both facies. Schematics of the pillow form outlines highlight the regularity of P11 and the irregularity of P12 lavas. ....	202
Figure 6.6 Schematic characterizations of outsized clasts found within the three sequences described at Askja. Outsized clasts include a pillow in cross-section, a fluidal bomb in cross-section and an angular block.....	203
Figure 6.7 Stratigraphic overview of a typical effusive to explosive transitional deposit from Askja. Three grain sizes (blocks / bombs, lapilli, and fine ash) were analyzed for size, morphology, and vesicularity as they trend up section. Maximum values are presented for	



abundance of fluidal bombs and fine ash textures. Average values for vesicularity are presented.

..... 206

Figure 6.8 Examples of clast morphologies and textures that reflect ductile fragmentation of the magma. Images on the right hand side are field images. Images on the left hand side are from a binocular microscope. A) Ductile structures in a lapillus quench crust. B) Large coalesced vesicles in a fluidal bomb. C) Fluidal crust structures preserved on a lapillus by surrounding matrix. D) Convolute bomb shape and vesicles. E) Large coalesced bubbles interacting with the clast surface. F) Fluidal bomb with intact quench rind (broken for sampling). G) Lapilli with stretched vesicles along glassy surface. H) Fluidal bomb with large randomly distributed vesicles. A brittle overprinting is present in images A, E and G, where the particle has been fractured by impact / transport. .... 207

Figure 6.9 SEM secondary electron images of example grain morphologies found in textural analysis of fine ash particles. Adhering particles and aggregate ash particles are common. Arrows are used to highlight features of interest. A) Fluidally deformed tube pumice. B) Tube pumice. C) Vesicles isolated within glassy ash particles. Vesicles may intersect fracture surfaces they do not control the fracture shape. D) Limu o Pele. E) A particle with vesicle-dominated fracture surfaces. F) Ash particles dominated by vesicles. G) Elongate needle-like dense particle shapes. Note the micron scale crust flaking off the particle. H) Needle and bladed shape particles. I) Flake and blocky shaped particles. Note the presence of conchoidal fracture. .... 208

Figure 6.10 Schematic diagram of subaqueous fragmentation mechanisms. 1) Explosive magmatic gas expansion, resulting in ductile deformation of magma. 2) Explosive interaction with external water including disruption of the magma from the surface, and bulk interactions where water becomes trapped in the magma. This results in the brittle deformation of the

quenching magma. 3) Non-explosive quench granulation. This results in the brittle deformation of cooled magma and can occur wherever magma is cooled rapidly, especially in conditions involving water. ....	222
Figure 6.11 Model of fragmentation mechanisms as they occur during the formation of the transitional sequences at Askja. Solid lines represent relative dominance of a fragmentation style. Dotted lines indicate continued, but diminished fragmentation. The textures used to construct the model are described. ....	223
Figure 7.1 Intrusion of Basalt into Frozen Sediments and Generation of Coherent-Margined Volcaniclastic Dikes (CMVDs). ....	233
Figure 7.2 Images of examples of CMVDs. Common features are the consistent glassy margins and complex volcaniclastic interiors. A) Example from main area of CMVD distribution, the segments on the scale are 10 cm. Note the lack of mechanical or thermal alteration of the host sediment by the dike. B) Example of CMVD from western massif of Askja (17 km from main cluster), backpack for scale. ....	235
Figure 7.3 Dike margins in hand sample and thin section. Field scale increments are 1 cm. A) CMVD chill margin hand sample and sketch showing textures. B) Petrographic image of the outer margin of the dike. Note the relict clast, a product of shear. C) Petrographic image of interior of dike margin. D) Hand sample of dike margin revealing multiple chills. E) Hand sample of interior portion of margin displaying complex ropey structures. F) Hand sample of CMVD margin in cross-section the reveals the variations in vesicularity within the margin. ...	237
Figure 7.4 Dike interiors in outcrop and thin section. Yellow lines indicate dike margins; white lines indicate pillows. A) CMVD with pillows and vitric ash interior. B) CMVD with pillow and pillow breccia interior. C) Ash-rich CMVD with deformation of ash banding (parallel to strike)	

around larger clasts. D) Detailed sketch of the interior of a pillow-dominated CMVD with strike-parallel bands of ash-sized particles between the pillows and the chill margin, as detailed in the inset. ....	240
Figure 7.5 C MVD with ash and lapilli dominated interior. Sketch indicates zones of clast concentration with white lines to indicate the weak structure present within the domains. The sedimentary structure of the host sediment is not disrupted by the dike. Complex margins indicate multiple magma pulses that resulted in the trapping of intact host sediment between an earlier chill margin and a later, final margin which truncates it. ....	241
Figure 7.6 Petrographic image of CMVD ash interior matrix with variable grain shapes and intact vesicular clasts mixed with blocky grain shapes. B) Petrographic image of typical CMVD ash tuff host matrix. Grains are well-sorted and shapes reflect fewer vesicles than CMVD interiors. Free crystals of pyroxene and feldspar, similar in size to the average grain size, are visible in cross-polarized light (xpl) in dike host sediments only. ....	242
Figure 7.7 Example of a CMVD transition from coherent basaltic to volcanioclastic dike interior with coherent glassy margins (double lines). Radial cooling cracks are found within the dense dike below the transition. The correlation of a stratigraphic boundary between a massive lapilli tuff and ash tuff with the transition (horizontal line) is limited to this CMVD. ....	243
Figure 7.8 Field image and B) sketch of the Rosa structure, a cylindrical void (outlined) in a 90 cm wide tabular coherent basaltic dike that transitions to a CMVD up dip. View is perpendicular to strike. The void is symmetrical with thick (3 cm) glassy margins and does not disrupt the dike width or the host. This is interpreted as the result of a cryolith (ice-block) that fell into a drained dike after margin formation. Subsequent dike pulses chilled around and thermally eroded the cryolith and associated vapor, creating a round void. ....	244

Figure 7.9 Model of CMVD formation in ice-cemented host (ash / lapilli). A-1) Chill margins form along a rising basaltic dike. The ice-cemented host and overlying ice fracture. The gas driven pulses of magma depressurize near the host / ice / meltwater interface. A-2) Dike drainage creates space, allowing downward flooding of the dike. A-3) Meltwater and magma interact non-explosively, forming a slurry. A-4) Later pulses interact with the slurry; mingling continues. B) Motion of magmatic gas, steam and clasts develop near-vertical flow banding. A final pulse is chilled against the interior, resulting in radial cooling cracks. Evidence of the preceding steps may be preserved in the CMVD (labels). C) Formation of a very thin peperite between chill margin and ice-cemented host. D) Dike behavior when cryolith becomes trapped in the drained dike, forming a Rosa structure. ....	252
Figure 8.1 Oceanographic climactic influences on Iceland, adapted from Knudsen and Eriksson, 2002.....	258
Figure 8.2 Modeled extent of the Last Glacial Maximum ice sheet in Iceland adapted from Hubbard et al. (2006). Numbers indicate feature ages in thousands of years, and references are noted. The location of offshore end-moraines is illustrated. The position of Askja was fairly central to this large ice sheet. ....	261
Figure 8.3 Modeled ice flow models for the LGM ice sheet from Bourgeois et al. (2000). ....	265
Figure 8.4 Location of paleoenvironmental indicators overlain on a chronostratigraphy map of Austurfjöll. The largest paleo-water level is at 1290 m asl. Arrows indicate the orientation of drainage channels and proposed direction of flow. ....	271
Figure 8.5 Example of ice confined lava in Unit 6 at an elevation of 850 m asl. The orientation of the radial cooling cracks can be used to estimate a cooling surface that likely reflects the position of ice around the flow. The cooling surface may be a thin water film, or direct ice contact.....	274

Figure 8.6 Exposure of subaerial lavas buried by subaqueous pillow lavas at 800 m elevation in eruptive Unit 2. White lines indicate outlines of pillows in the outcrop. The angle of the image does not show the thin (20 cm) of bedded ash between the two deposits. ....	276
Figure 8.7 Coated lapilli in subaerial lapilli tuff (Lt3). Divisions on black and white scale are 1 cm.....	277
Figure 8.8 Cartoon of ice thickness and relative position at Austurfjöll massif during construction for each eruptive unit. Elements of greatest speculation are denoted with a question mark in the color or arrow appropriate to the features in question. Lake size is intended to suggest order of magnitude scale only.....	279
Figure 8.9 Location of samples for volatile analysis. Samples either occur in Unit 2 or Unit 5. Samples AG 94 and AG 108 both occur in gullies where Unit 2 is exposed beneath Unit 3. Compositions of the samples were confirmed with microprobe analyses (See Chapter 3). .....	285
Figure 8.10 Dissolved water content measured by FTIR compared with elevation of the sample. Compositional unit and morphology of the samples is indicated. ....	287
Figure 8.11 Idealized cross-section of Austurfjöll at two time windows with estimated water levels and confining ice. ....	292
Figure A.1 Log 1 .....	334
Figure A.2 Log 2.....	335
Figure A.3 Log 3.....	336
Figure A.4 Log 4.....	337
Figure A.5 Log 5.....	338
Figure A.6 Log 6.....	339
Figure A.7 Log 7.....	340

Figure A.8 Log 8.....	341
Figure A.9 Log 9.....	342
Figure A.10 Log 10.....	343
Figure A.11 Log 11.....	344
Figure A.12 Log 12.....	345
Figure A.13 Log 13.....	346
Figure A.14 Log 14.....	347
Figure A.15 Log 15.....	348
Figure A.16 Log 16.....	349
Figure A.17 Log 17.....	350
Figure A.19 Field image and mosaic accompanying Log 17 .....	351
Figure A.20 Log 18.....	352
Figure A.21 Field image and mosaic for log 18 .....	353
Figure A.22 Log 19.....	354
Figure A.23 Log 20.....	355
Figure A.24 Log 21.....	356
Figure A.25 Log 22.....	357
Figure A.26 Log 23.....	358
Figure A.27 Log 24.....	359
Figure A.28 Log 25.....	360
Figure A.29 Log 26.....	361
Figure A.30 Log 27.....	362
Figure A.31 Log AH1-2.....	363

Figure A.32 Log KS1.....	364
Figure A.33 Log KS2.....	365
Figure A.34 Log KS3.....	366
Figure A.35 Log KS4.....	367
Figure A.36 KS5 .....	368
Figure A.37 KS6 .....	369
Figure A.38 KS7 .....	370
Figure A.39 KS9 .....	371
Figure A.40 KS10 .....	372
Figure A.41 KS11 .....	373
Figure A.42 KS12 .....	374
Figure A.43 KS13 .....	375
Figure A.44 KS14 .....	376
Figure A.45 KS19 .....	377
Figure A.46 KS20 .....	378
Figure A.47 KS21 .....	379
Figure B.1 Key for cross-sections For locations see Chapter 4 Figure 4.5 .....	397
Figure B.2 Cross-section 1 .....	398
Figure B.3 Cross-section 2.....	399
Figure B.4 Cross-section 3.....	400
Figure D.1 Location of deposits in Chapter 6 and including Gully 6 (G6). ....	401
Figure D.2 Image of sample locations and stratigraphic column for Gully 6.....	403

## LIST OF EQUATIONS

Equation 7.1 .....	248
Equation 7.2 .....	248
Equation 7.3 .....	248
Equation 7.4 .....	248
Equation 7.5 .....	249



## PREFACE

*“Science, in its most fundamental definition, is a fruitful mode of enquiry, not a list of enticing conclusions. The conclusions are the consequence, not the essence.”* From The Flamingo’s Smile by S. J. Gould 1985.

This project is the culmination of research conducted over three years to fulfill an NSF grant awarded to Ian Skilling, Dave McGarvie, and Ármann Höskuldsson. This project had lofty goals of applying volcanology of Askja volcano to the paleoclimate of Iceland. I am pleased to say that through their guidance and the fortuitous chemistry of my field area, we were capable of satisfying my personal goals, and, I believe theirs. I cannot say how grateful I am to have been a part of this project. I have learned more and experienced more than I could have imagined back when I stalked Ian at a conference in Iceland to convince him to take me on as a student.

First let me acknowledge the monetary obligations that have made this research possible. I have been supported financially by TA/TF awards from the University of Pittsburgh (2009-2011), the above mentioned NSF grant (summer 2011), a Mellon Pre-Doctoral Fellowship from the University of Pittsburgh (2011-2012), and one GSA research grant (2010). I always dreamed of getting paid to play with rocks, now to only keep it up!

None of this would be possible without the fabulous field seasons I spent in Iceland with encouragement and helping hands from all of the Dreki/ Herðubreið rangers in 2010 and 2011. With particular hats off to Hrönn, Hildur and Ragga for making Dyngja and Dreki my home away from home. Who could forget Jólin? The great pilot who flew the over flight in 2011 Siggi, and the logistical support of Ármann and the NORVOLK institute helped me get where I needed to go. Our trusty Land Rovers

Útsula and Fatty Puff get credit for getting me there and back again. I give much credit to the Helluhraun, and Dyngjagil huts for keeping the rain, wind, snow and summer sun off of me and my brave companions. Without a doubt excessive thanks must go to all of my field assistants: Kevin Reath, Mary Kate Ellis, Robin Wham, Rachel Lee, Antonia Lema, the McGarvie boys, and The Duck. I'm glad you got more than injuries from your experiences.

I must thank my advisers, for I've collected a few first-class advisers these past few years, for putting up with my ambition and attachment to volcanoes. Ian has always been a source of fabulous food-related analogies, wild ideas, tillite finding skills, and level-headed advice. Dave McGarvie has always known when to question my work (and work load), when to give my ego a shake, or a boost, and when to bring out the scotch (and guitar). I must thank Mike Ramsey for welcoming me into his lab group, long before he ever had to. And thanks also go to Ben Edwards for always being available for discussion, debates, and advice.

At home I've been supported within the department by the rest of my committee including Dr. Tom Anderson, Dr. Charlie Jones, and Dr. Mark Abbot, who have all been willing to sit through long conversations and presentations that have nothing to do with their own specialties. Our administrative staff: Shannon Granahan, Dolly Chavez, and Lorrie Robbins, too have always helped me out with all the ins and outs of university red tape. Jóna Hammer, ég þurf að þaka þig fyrir hjálpa mig að læra íslensku. Fyrirgefðu mér fyrir að gleyma eins mikið og ég hef. I must also thank Robert Dean at Dickinson College for putting up with me for a whole week of abusing their SEM.

Of course I must thank all of my fellow graduate students of days past and present including Dr. Rachel Lee, Dr. Emily Mercurio, Dr. Shellie Rose, Masters Lindsay Williams, Sarah Morealli, Kevin Reath, and Holly Kagy. You showed me what to do, what not to do, and made sure I still had fun. Emily and Rach get extra props for helping keep me running when it seemed too much, and nerded out when I needed someone to understand just how cool volcanoes are. Mary Kate Ellis gets a special nod for helping be the most organized rock hoarder this department has ever seen. Roommate fantastic Bobby Karimi cannot possibly be thanked enough in these few lines. And Dr. Topher Hughes for anytime I get mad at

you for talking me out of crazy things, or talk me into other crazy things, know that I appreciate every ounce of advice, support, and humor. You know I'd be obstinate and have done this all alone, but I am grateful that you never let me.

My family gets full credit for letting me know that I can, and should go for my dreams, even if they have to worry about me playing on volcanoes in foreign countries. And I must say thank you for the patience they have already stored up for dealing with me as I take another step to being the absent minded professor I feel I am to be. I am very grateful they let me play, and tolerate need to derail perfectly normal conversations to include rocks, travel, languages, and (with extra credit to my father for teaching me how) puns. Heather Crawford I've always appreciated that I can tell you anything without need of explanation, unless it's more amusing that way. Loise Yates gets credit for being excited about each of my next adventures. Natalie Huls-Simpson is appreciated for always making room and time for me and my whole family! I appreciate you all for letting me teach you more than you ever wanted to know about rocks, volcanoes and the earth.

## 1.0 INTRODUCTION

The evolution of large volume, polygenetic, glaciovolcanic centers is currently poorly understood, in part due to the lack of detailed investigations of such complexes. The only detailed description of a central volcano in Iceland, that includes glaciovolcanic deposits, was conducted on the partially ice-covered Eyjafjallajökull volcano (Loughlin, 2002). To expand our understanding of the growth and evolution of a polygenetic glaciovolcanic system a study was conducted on Askja volcano, north central Iceland. Askja volcano is one of the largest and best exposed formerly ice-confined basaltic volcanoes on earth. Askja, also known as Dyngjufjöll (65 N° and 17 W°), is a central volcano within the Northern Volcanic Zone (NVZ), Iceland (Figure 1.1).

Glaciovolcanic deposits represent a currently untapped paleoclimate proxy for ice-thickness reconstructions in Iceland. The resolution of these proxies is limited to the ability to date deposits, making poly-genetic systems, with repeated eruptions interacting with glacial ice of great value to augmenting the limited terrestrial record. This record is limited in part due to increased volcanic activity throughout Iceland immediately following deglaciation that is associated with depressurization of the mantle through isostatic rebound (Jull and McKenzie, 1996; Larsen and Eriksson, 2008; Sigvaldason et al., 1992). The large volume of postglacial lavas buried most of the previous land surface that may have had glacial signatures. Marine cores of the Icelandic shelf and Greenland ice cores are the basis of current reconstructions of ice presence in Iceland (Abbott et al., 2012; Brendryen et al., 2010; Haflidason et al., 2000; Larsen and Eriksson, 2008), but they cannot provide ice thickness data.

The purpose of this study is to reconstruct the ice-confined, glaciovulcanic, eruptive history of Askja volcano based on analysis of the largest thickness of exposed glaciovulcanic rocks within the complex at Austurfjöll massif. This reconstruction is based on lithofacies analyses, remote sensing-based mapping, stratigraphy, petrology, geochemistry, quench glass rind volatile analysis, unspiked K/Ar age dating, and textural studies of individual deposits. The results of this study are then used as a proxy to infer the paleo-ice presence and thickness in a region lacking more traditional methods of paleoclimate reconstructions.

## **1.1 INTRODUCTION TO THE GEOLOGIC SETTING AND HISTORY OF ERUPTIVE ACTIVITY OF ASKJA VOLCANO, ICELAND**

Askja is composed of a cluster of basaltic glaciovulcanic mountains and ridges, three calderas, postglacial basaltic lavas and minor rhyolitic lavas and tephra. Askja volcano is named after its largest caldera, Askja that has a floor that sits 1100 m above sea level. The area around the complex is surrounded by numerous postglacial lavas, large pumice / sand plains, and fluvially reworked deposits (Figure 1.2); creating a local level typically 650 m asl, part of the Icelandic Highlands. The highest elevations of Askja occur along Thorvaldstindur (1475 m), along the southern edge of the main caldera, followed closely by Austurfjöll (1375 m), the eastern mountains, forming the eastern margin of caldera lake Öskjuvatn (Figure 1.2).

The volcano sits 40 km north of the Vatnajökull icecap in the central highlands, near the proposed center of the Last Glacial Maximum (LGM) ice sheet (Bourgeois et al., 1998; Hubbard et al., 2006). The position of Askja is also close to the proposed location of the Icelandic Hot Spot (Allen et al., 2002; Breddam, 2002; Sigvaldason et al., 1974; Tryggvason, 1989), and the highest geothermal flux in Iceland occurs along the NVZ (Bourgeois et al., 2000).

The vast plain of postglacial basaltic lavas that surround Askja is known as Ódádahraun. The 150 km long, 30 km wide region, covering 4000 km<sup>2</sup>, represents the Mid-Atlantic Rift (MAR) through northern Iceland (Annertz et al., 1985; Sigvaldason, 1968). The young volcanic zones of Iceland lack significant glacial features due to the dominance of postglacial lava flows. The glaciovolcanic deposits of Askja, therefore, provides a unique opportunity to reconstruct the ice conditions during the Pleistocene near the former LGM over an area of high heat flux where traditional methods of identifying ice presence are limited.

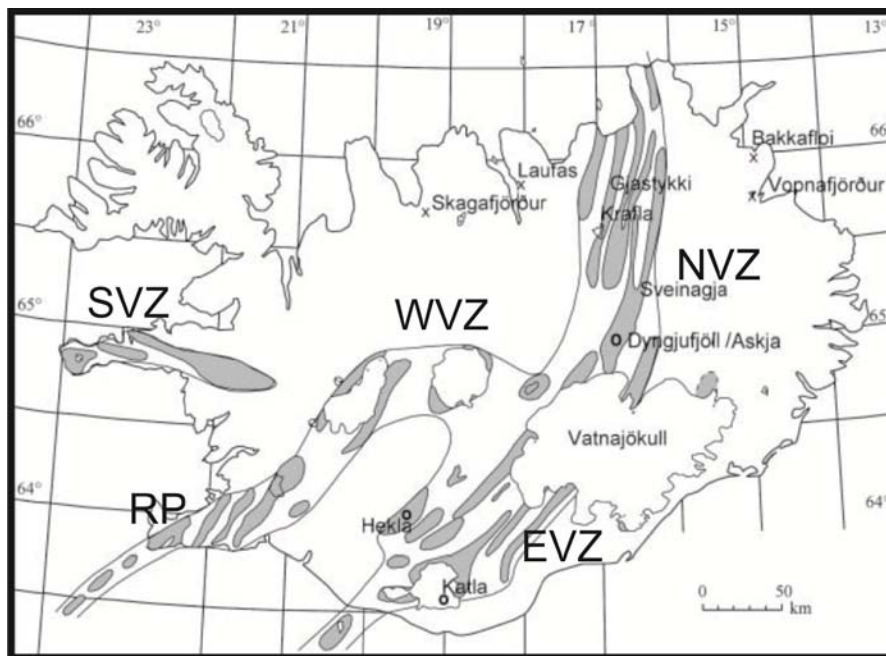


**Figure 1.1 Map of Iceland showing the active volcanic regions in Iceland: Reykjanes Peninsula (RP), Snæfellsnes Volcanic Zone (SVZ), Western Volcanic Zone (WVZ), Northern Volcanic Zone (NVZ), and Eastern Volcanic Zone (EVZ) (adapted from Sigvaldason 2002).**

Askja, the largest of the five NVZ volcanoes is predominantly constructed of basaltic vitriclastic tuffs and pillow lavas erupted in subglacial and ice-confined conditions (Sigurdsson and Sparks, 1978). These deposits occur within a complex that includes three calderas, multiple episodes of postglacial effusive lavas, historic basaltic lavas, and silicic explosive tephras. Descriptions of the historic eruptions, postglacial lavas, and deformation of the caldera complexes dominate the body of literature on Askja (Annertz et al., 1985; Bemmelen and Rutten, 1955; Brown et al., 1991; de Zeeuw-van Dalfsen et al., 2005; Hartley and Thordarson, 2012; Hjartardóttir et al., 2009; Kuritani et al., 2011; Sigurdsson and Sparks, 1978; Sigvaldason, 1964; Soosalu et al., 2010; Sturkell et al., 2006; Thorarinsson, 1968; Thorarinsson and Sigvaldason, 1962). The goal of this study is to address the greatest preserved volume of glaciovulcanic deposits within the center, Austurfjöll, and to reconstruct the interaction of a large long-lived poly-genetic central volcano and the confining ice at the time of eruption.

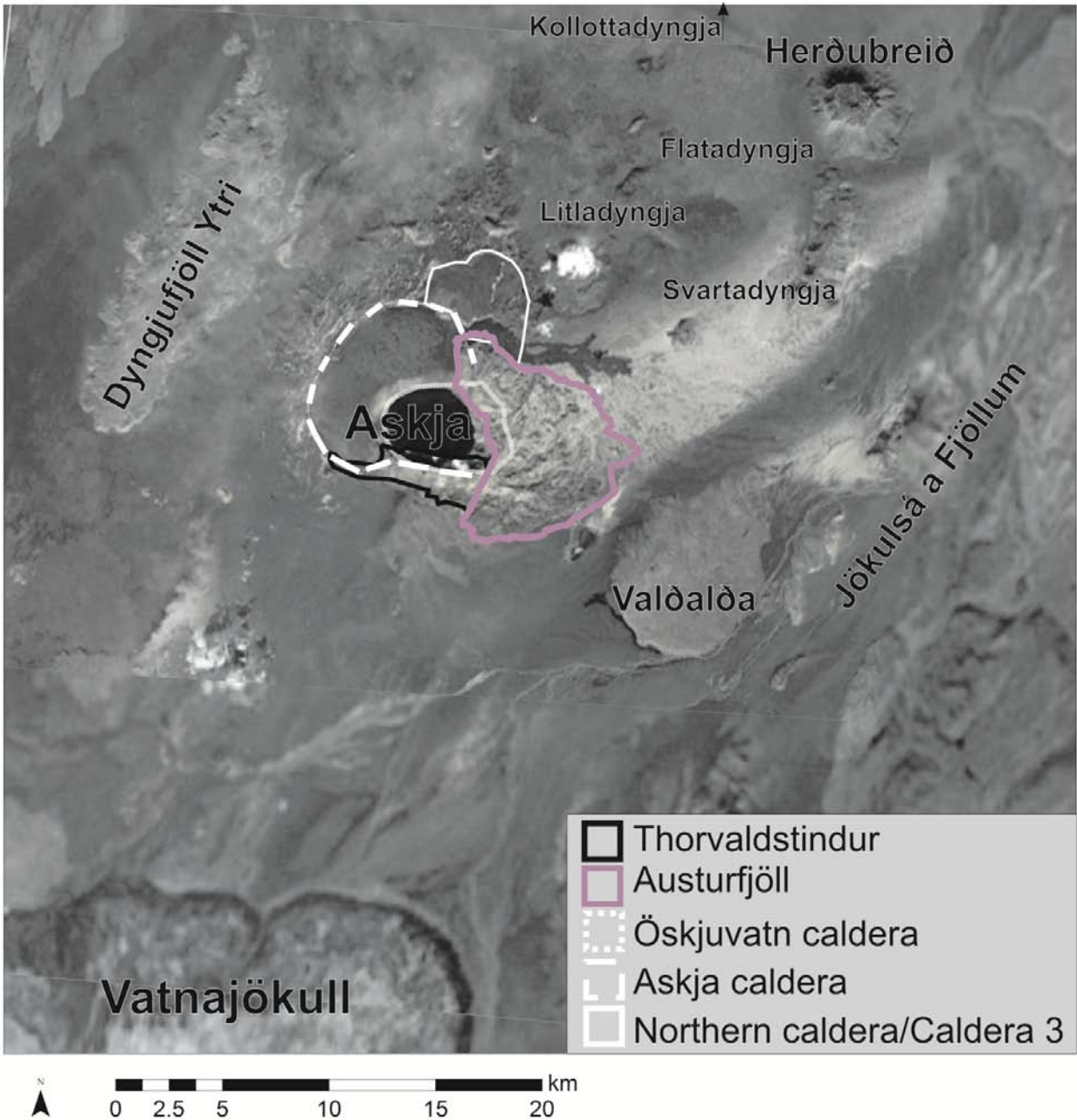


**Figure 1.2** Location map showing Askja volcano and the surrounding region. Major geomorphologic features are labeled. SPOT image courtesy of Google Earth.



The study area is a crescent shaped massif known as Austurfjöll (Figure 1.2) composed of 800 m of glaciovolcanic basaltic lavas and tuffs, which previous studies (Sigvaldason, 1968) revealed were erupted and deposited predominantly under water. Austurfjöll is the largest volume of glaciovolcanic deposits within the region.

Austurfjöll intersects a west-east running ridge along the southern edge of the Askja and Öskjuvatn calderas called Thorvaldstindur, named for Thorvald Thordenssen. Tindur simply means ‘peak,’ but the term is typically reserved for fissure-fed mountains of glacially confined origin. Due to the active rock falls along the caldera wall, and the challenge of accessing the southern wall, Thorvaldstindur was surveyed at a reconnaissance level only. Additionally, glaciovolcanic deposits occur along the western and northern edge of Askja, but are separated from Austurfjöll by two postglacial lava-filled topographic lows Öskjuop (NE) and Suðurskarð (SW) (Figure 1.3). Further to the west of the complex lies Dyngjufjöll-Yitri or ‘outer Dyngjufjöll.’ Brief descriptions of Dyngjufjöll Ytri appear in Bemmelen and Rutten (1995) and Sigvaldason (1992).

Askja volcano is cut by three calderas. The youngest and most central of the calderas is now filled by Öskjuvatn, or simply Lake of Askja. The largest depression of the system is Askja caldera, which has been partially filled with postglacial lavas. The northern caldera is predominantly buried by postglacial lavas, and consequently less well defined.

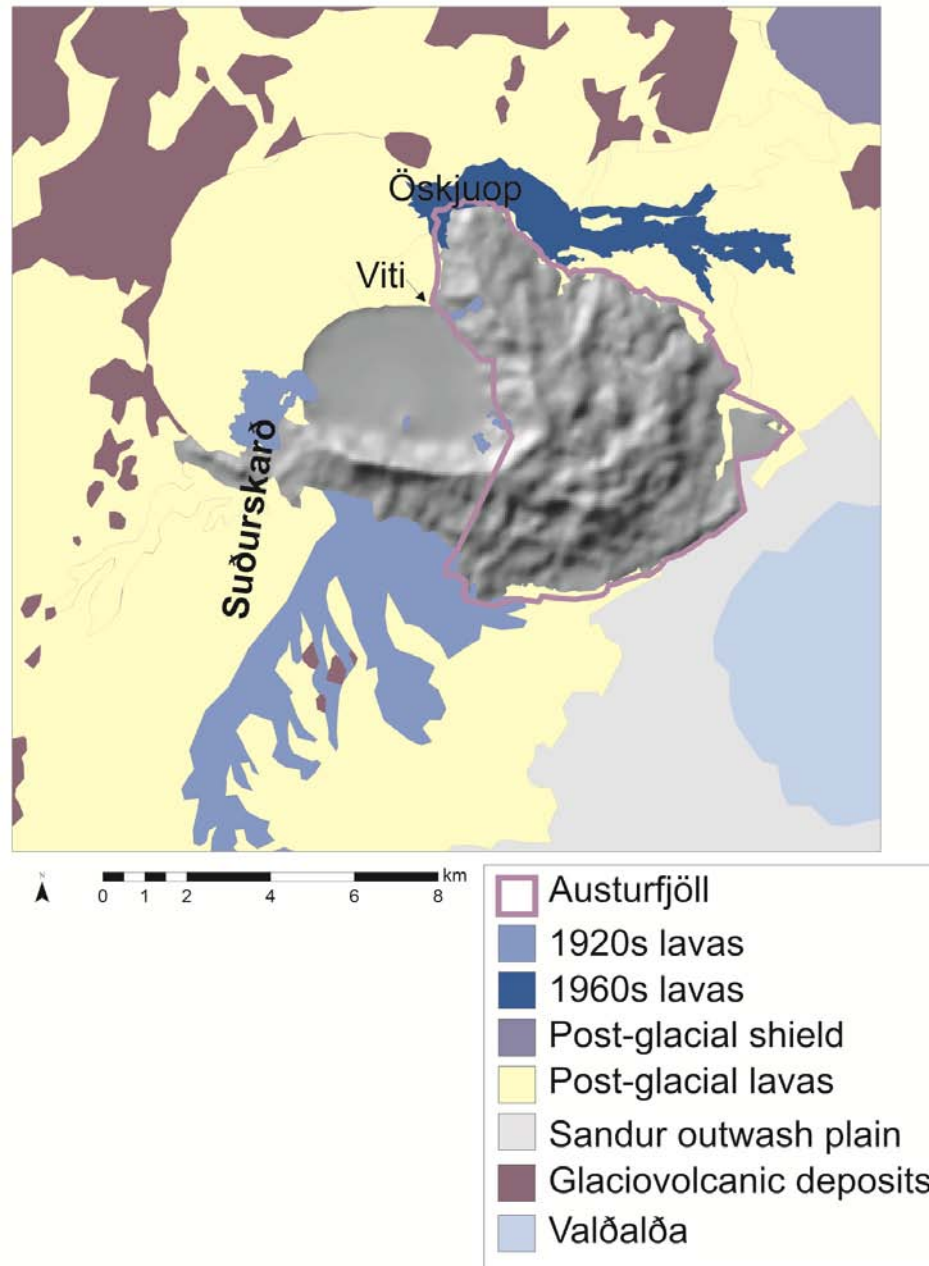


**Figure 1.3 Simplified geology map of Askja with relevant features labeled. Base map is a hillshade produced from a 10 m resolution digital elevation model created by Landmælingar Íslands, Iceland.**

## 1.2 REGIONAL SETTING

Askja sits in the Northern Volcanic Zone (NVZ) of Iceland and resides above the Icelandic hot spot and Mid-Atlantic Ridge (MAR). The MAR intersects Iceland along its western coast, creating the Reykjanes Ridge. The rift then jumps to the east in central Iceland, which results in the Eastern Volcanic Zone to the south and the Northern Volcanic Zone. The MAR steps to the west slightly just off the northern coast of Iceland and continues north beneath the Arctic Ocean.

The NVZ contains five central volcanoes spaced approximately 30 to 40 km apart, including from south to north Kverkfjöll, Askja, Fremrinámur, Krafla, and Theistareykir (Figure 1.4). The plate boundary spreading rate in this region is 1.8-2 cm/yr (Annertz et al., 1985; Árnadóttir et al., 2009; Einarsson, 2008; Pedersen et al., 2009). Each central volcano is associated with northerly trending fissure fields and significant volumes of predominantly basaltic lava. These centers are all basalt dominated, but have displayed minor rhyolitic activity (Rymer and Tryggvason, 1993; Saemundsson, 1991). High temperature geothermal fields are dotted throughout the NVZ (Sigurdsson and Sparks, 1978).

The southernmost volcano of the NVZ, Kverkfjöll, is partially buried under the Vatnajökull ice sheet its fissure system extends 150 km to the north. The complex is predominantly composed of basaltic pillow lavas and breccias with 300 m high ridges of vitriclastic tuff parallel to the dominant rift direction (NE-SW) (Carrivick et al., 2004; Höskuldsson et al., 2006; Óladóttir et al., 2011). Askja lies to the north and west of Kverkfjöll. The middlemost central volcano of the NVZ is Fremrinámur. This complex contains a rhyolite intrusion and a well developed geothermal field. The recent activity dissects a shield volcano which last erupted 4000 years ago (Sigurdsson and Sparks, 1978).

The northern three central volcanoes, including Fremrinámur, are more closely spaced with minor overlapping of the fissure swarms of Fremrinámur, Krafla, and Theistareykir. Krafla is one of the best studied northern Icelandic volcanoes, is a built on an interglacial shield volcano. The volcano is known for a large eruption of icelandite and formation of a 10 km caldera filled with significant welded air-fall tuff (Allen et al., 2002; Saemundsson, 1991; Sigurdsson and Sparks, 1978; Tuffen and Castro, 2009).

Later subglacial extrusions of rhyolite have been studied at the southern end of the caldera (Tuffen and Castro, 2009). Postglacial activity includes widespread fissure-fed basalt flows. The most recent historic activity occurred between 1724 and 1729 AD, in an eruption known as the Krafla Fires. A significant rifting event was recorded at Krafla in the 1970s (Sigurdsson and Sparks, 1978). The northernmost NVZ volcano Theistareykir intersects a postglacial shield volcano with a well developed geothermal field and historic fissure eruptions in 1618-1885 (Sigurdsson and Sparks, 1978) but is poorly studied.

The fissure swarms of the NVZ are both eruptive and tectonic in origin. Individual fissure swarms are 5-10 km wide and dominated by parallel normal faulting, creating local basins / graben structures (Sigurdsson and Sparks, 1978). The fissure swarms dissect the central volcano and surrounding lava flows equally, but remain focused (laterally) around the central volcano. There is an en echelon overlap of the fissure swarms (Sigurdsson and Sparks, 1978). The Askja fissure swarms are 100 km long and disappear to the south under the Vatnajökull ice cap.

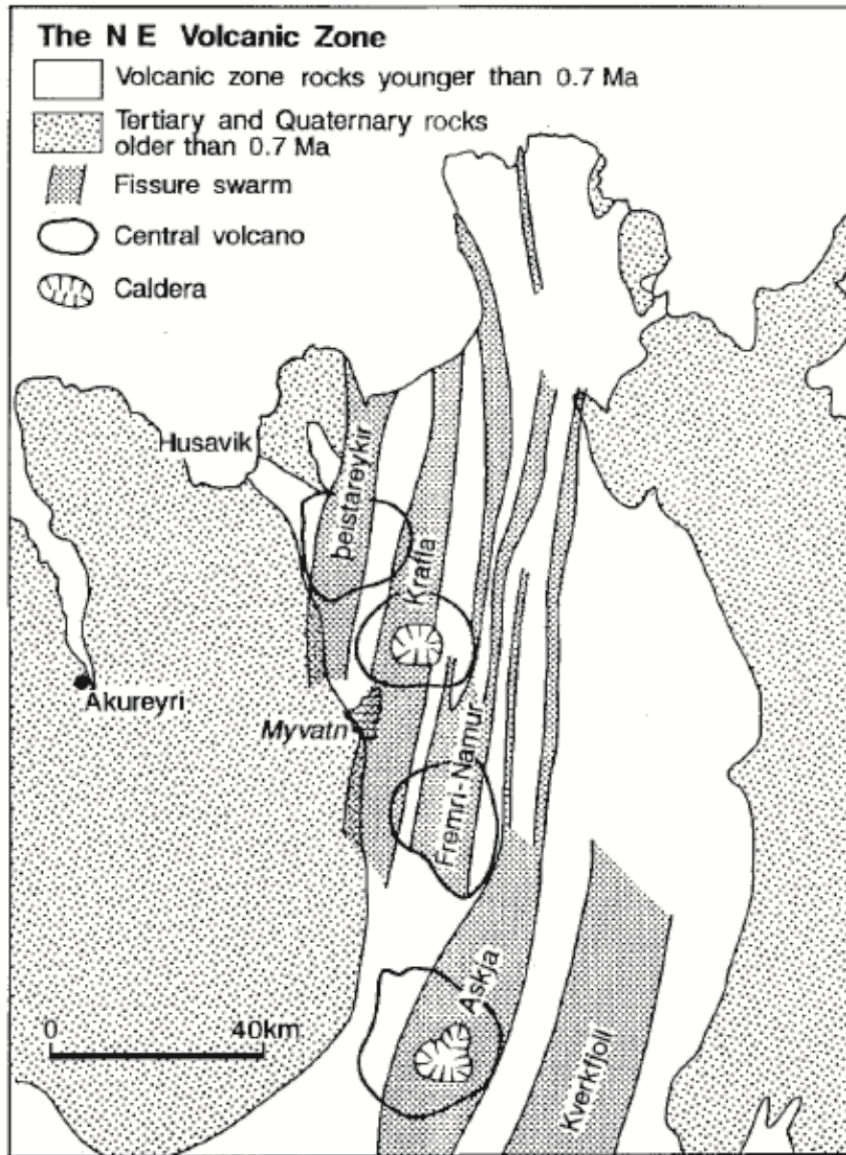


Figure 1.4 Map of the fissure swarms that make up the North Volcanic Zone, Iceland (from Rymer and Tryggvason 1993).

### 1.3 GLACIAL HISTORY

There are estimated to have been as many as 15 to 23 glacial periods that impacted Iceland over the last four million years (Bourgeois et al., 2000; Geirsdóttir and Eiriksson, 1994). The first major glaciation is dated to 3.8 mya, but this and most of the subsequent glacial periods are difficult to constrain onshore due to overprinting of glacial evidence by later glaciations, and high volumes of lava during interglacial periods (Geirsdóttir and Eiriksson, 1994). The most recent interglacial period is dated to 70-90 ka (Norðdahl and Petursson, 2005) based on marine shelf sediments. The Last Glacial Maximum, known as the Weichslian, in the North Atlantic is estimated to have initiated around 70 ka (Bourgeois et al., 2000; Norðdahl and Petursson, 2005; Slater et al., 1998). Although not well documented, regional evidence indicates that Askja would have been at the center of a very large ice sheet that covered most of Iceland during the LGM. Central ice sheet thicknesses are estimated to be about 1,500-2,000 m thick (Sigmundsson, 1991). The last temperature minimum during the LGM was 10,500 BP according to Sigmundsson (1991; and references within). Evidence of the continued ice presence from 70 ka to 10 ka, the LGM in Iceland, has been detected in pollen records, marine shelf cores, and Greenland ice cores, but these records do not preserve the thickness of ice present. Several minor cooling periods were observed after 10 ka in pollen records and marine cores (Eiriksson et al., 2000; Norðdahl and Petursson, 2005) including the Little Ice Age (LIA) that started around 1200 AD and reached its maximum around 1800 AD (Árnadóttir et al., 2009).

The use of volcanic deposits to constrain ice position and thicknesses is dependent on the ability to date the deposits in question. The most prevalent method for dating recent volcanic and interbedded sedimentary rocks in Iceland has been tephrochronology of predominantly rhyolite tephra. Datable tephra at and surrounding Askja are predominantly from Hekla, a highly active stratovolcano located in south central Iceland (Figure 1.1). Hekla has been the site of the most explosive eruptions during the Holocene, producing nearly 50 identified silicic tephra (Larsen and Eiriksson, 2008). The tephra layer known as H5 was produced 7000 BP, which corresponds to a regional temperature maximum. However,

this tephra was not found in the Askja area, suggesting that the highlands were ice covered, or that high erosion prevented the preservation of the ash (Annertz et al., 1985; Bemmelen and Rutten, 1955; Thorarinsson, 1968). The only confirmed locations of the H5 ash in northern Iceland are all 600 m asl and below. Because most of the region around Askja is above 600-700 m asl, it can be argued that ice was still persistent around 7 ka at these elevations (Annertz et al., 1985). Similarly the Plinian rhyolitic pumice traced back to Askja, dated by Sigvaldason (2002) as 10000 BP, occurred when ice had receded from coastal areas, but still remained in higher elevations at the start of the Holocene (Sigvaldason, 2002).

Regional glacial evidence can be useful to constrain the presence and thickness of former ice. However, throughout the highlands, evidence of past ice is surprisingly limited, largely due to postglacial cover. The valley between Dyngjufjöll Ytri and the western mountain of Askja contains some evidence of glacial scour. To the east the nearby interglacial Valðalða shield volcano has scour marks that reflect a glacial thickness of 300 m (Bemmelen and Rutten, 1955). To the south Kverkfjöll is the only alpine area in north central Iceland to have moraines that contain local glaciovolcanic deposits and are thus stratigraphically related to subglacial volcanic edifices (Carrivick et al., 2009). The lack of direct glacial evidence requires the use of glaciovolcanic deposits as a paleoclimate proxy for ice reconstructions.

## **1.4 GEOLOGY OF ASKJA VOLCANO**

The geology of the Askja complex has been previously described in brief based on field work, tephrochronology, and remote sensing-based structural investigations (Annertz et al., 1985; Hjartardóttir et al., 2009; Sigvaldason, 1968; Sigvaldason et al., 1992). These descriptions reveal some basic relationships, such as relative age and distinguish glaciovolcanic units from postglacial units and the identification of two major petrologic textures. More detailed lithologic (presented in Chapter 2) and geochemical (Chapter 3 and 4) detail resolved in this project help to resolve the timing of the past distribution of ice and water in the region (Chapter 8).

The volume of postglacial lavas and tephtras interpreted as originating from Askja indicate that it is the most active center within the NVZ (Brown et al., 1991; Larsen and Eriksson, 2008). Volume estimates of the complex are based on a gravity survey conducted between 1980 and 2000 and distribution / thickness of exposed lava. Exposures within the calderas suggest a minimum estimate of a 140 m thick lava pile consisting of lavas mainly older than 4500 years. Of this 140 m thick pile only 40 m of lavas are younger than 2900 BP (Annertz et al., 1985; Brown et al., 1991). However, the glaciovolcanic deposits were not included in these estimates due to a lack of a reliable method for dating the vitric tuffs and pillow lavas at the time (Brown et al., 1991).

The composition of eruptive products in the NVZ including Askja is typically tholeiitic basalts. The volume of silicic products preserved in the area represent only 1% of the total volume (Brown et al., 1991), with three silicic tephtras attributed to Askja in the Holocene (Larsen and Eriksson, 2008; Sigmundsson, 1991). However, this figure likely under-represents the volume of silicic products as they are not well preserved near source.

Askja and Krafla are the only centers in the NVZ that have unequivocal calderas at the present day (Pedersen et al., 2009). A 15 km<sup>2</sup> caldera at the center of Askja formed in 1875 (Tryggvason, 1989), and is currently filled with the 11 km<sup>2</sup> Öskjuvatn caldera lake. The lake is the deepest in Iceland at 230 m (Porarinsson, 1963). The historic caldera sits within the larger Askja caldera (45 km<sup>2</sup>) (Sigvaldason, 1964) which both cuts, and is filled by, postglacial lavas. An older caldera sits to the north east of Askja and is almost completely filled with postglacial lavas (Annertz et al., 1985) (Figure 1.2) and whose age is not constrained.

Caldera-related ring fractures have served as conduits for postglacial and historic eruptions, as indicated by the superposition of fissures over caldera faults (Sigvaldason, 1979). There has been some debate as to whether the glaciovolcanic activity may have also utilized the ring fractures (Brown et al., 1991; Sigurdsson and Sparks, 1978; Sigvaldason, 2002), if they in fact were present prior to the eruption of the glaciovolcanic deposits. It has been proposed by Brown et al (1991) and Sigurdsson and Sparks



(1978) that subsidence may then be minor in comparison to the amount of extrusion. They argued that the distribution of the glaciovolcanic deposits around the Askja caldera was an artifice of construction, not subsidence. This debate will be addressed in Chapter 2.

## **1.5 STRUCTURE AND RELATIVE AGE OF ASKJA COMPONENTS**

The typical model of a central volcano in a rift zone displays a single, or nested, caldera(s) with a complex interplay of concentric ring faulting, radial faulting, shadow zones and regional parallel-to-rift faulting (Kinvig et al., 2009). Numerous maps of faults, fissure, and lineaments have been produced for the Askja region. These maps display reasonable agreement, but have inconsistent nomenclature and classifications. Nevertheless, the system of lineaments at Askja volcano can be simplified into MAR tectonic components and local caldera components (Annertz et al., 1985; Bemmelen and Rutten, 1955; Hjartardóttir et al., 2009; Sigvaldason, 2002; Thoroddsen, 1925).

Volcanic edifices that include layers of contrasting mechanical properties are more likely to develop the critical stress conditions required for ring fault initiation at the ground surface (Kinvig et al., 2009). In a simple structural system, caldera ring faults form where the minimum compressive stress occurs at the earth's surface. Maximum shear stress and tension are present at the lateral margins of a magma chamber (Kinvig et al., 2009) and propagate to the surface to form ring faults. The very prominent structure of the MAR also creates pre-existing weaknesses that were and are exploited by calderas and eruptive fissures (Pedersen et al., 2009). Once initiated, the ring faults can be reactivated by continued activity or sealed by eruptive activity. The modern hydrothermal system at Askja exploits caldera faults, and occurs along the south eastern margins of Öskjuvatn.

Tephra found within the Askja complex can be used to constrain the ages of various eruptive phases. The youngest significant tephra layer “a” has been dated to 1477 AD which is correlated to a source under the NW portion of the modern Vatnajökull. Other layers include the well documented

Öræfajökull (1362 AD), Hekla 1 (1104); Hekla 3 (2820 $\pm$ 70 bp); Hekla 4 (4030  $\pm$ 120 BP) (Larsen and Eriksson, 2008). What is notably absent is the Hekla 5 (6185 $\pm$  100) tephra. As mentioned earlier, the absence of the tephra suggests wide spread erosion and / or deposition on ice (Annertz et al., 1985).

More recently a 10 ka rhyolitic tephra from Askja has been recognized and dated in distal coastal locations (Sigvaldason, 2002). The tephra has since been identified in seven sites within the complex providing important information regarding the timing of younger structural events (Sigvaldason, 2002). Larsen Erikson (2008) recognized the 10 ka Askja tephra, but also mentions another tephra that pre-dates the 1875 silicic eruption. However, they provide no details on the eruption itself or volume of tephra (Larsen and Eriksson, 2008).

The structure of the Askja fissure swarm is complicated by the extended glacial history. Estimates of the LGM ice sheet indicate that the region was covered by ice up to 1500 m thick that retreated rapidly throughout Iceland in the last 7,000 years. The rebound likely reactivated numerous faults and fractures, especially near Askja volcano. The rate of isostatic rebound associated with Holocene deglaciation may have been as high as 30 cm/year, reaching equilibrium in less than 1000 years (Brown et al., 1991).

At least three calderas have been identified at Askja, with a relatively accepted progression of age. Proposed vent locations for rhyolitic eruptions (Sigvaldason, 2002) and the distribution of fractures (Hjartardóttir et al., 2009) may suggest intermediate calderas, which have been obscured by postglacial activity. The oldest caldera (Caldera 3) sits to the north, forming the southern boundary of Norðurfjöll. Caldera 3 has been cut by the larger Askja caldera to the south (Sigvaldason 1979), within which occurs the youngest caldera Öskjuvatn. Caldera age constraints are important to our understanding the overall development of the complex but precise data remains limited. The age of formation of Caldera 3 is difficult to constrain because the boundaries of the caldera are mantled by several tens of meters of postglacial lavas. Cross-cutting relationships between Caldera 3 and Austurfjöll are not identified in the literature (Annertz et al., 1985).

The volume of silicic eruptions at Askja low and only the 1875 eruption is correlated with the formation of a caldera, Öskjuvatn. Based on the historic observations of the formation of Öskjuvatn, and the absence of older large rhyolitic pumice deposits suggests that the formation of each caldera was likely not a discreet singular collapse and rather each caldera formed through a more progressive collapse process (Pedersen et al., 2009).

The Askja caldera is clearly older than the Öskjuvatn caldera, and younger than Caldera 3, however, its age relationship with Austurfjöll is less clear. On its western margin the caldera wall cuts a thick section of subaerial lavas that are likely post glacial in origin (Annertz et al. 1985). Based on the presence of a 10 ka rhyolitic tephra in the Askja caldera wall the caldera is suggested to be younger than 10 ka (Annertz et al., 1985; Sigvaldason et al., 1992). The relationship between postglacial lavas along the north and western boundaries of Askja caldera indicates a minimum age of 5000 years (Annertz et al., 1985; Brown et al., 1994; Sigvaldason, 2002).

Gravity surveys of Askja reveal a large density contrast between the vitriclastic ridges and the caldera floor (Brown et al., 1991; De Zeeuw-van Dalssen et al., 2012; de Zeeuw-van Dalssen et al., 2005). Sharp peaks in density coincide with the margin of the Öskjuvatn caldera, especially along its eastern margin, likely reflecting the presence of vertical mafic dikes emplaced in conjunction with the historic eruptive activity (Brown et al., 1991). However, along the western margin there is no equivalent anomaly along the caldera rim near similar historic activity. This is possibly related to the scale and concentration of the intrusions, or perhaps the contrast in density between the dikes and glaciovolcanic deposits is less along this margin (Brown et al., 1991). Models of caldera infill from gravity surveys suggest that the collapse was minimal, rather growth of the massif is responsible for the topographic relief (Brown et al., 1991; Sigvaldason, 2002).

The fissure swarms associated with Askja are approximately 100 km long and 20 km wide (Brown et al., 1991) (Figure 1.4). To the north the fissures are characterized by well developed graben structures of Sveinagjá, Hafrangjá, and Fjallagjá (Sigurdsson and Sparks, 1978). There is some debate in the literature of exactly how long the fissure swarm extends to the north (Pedersen et al., 2009;

Sigurdsson and Sparks, 1978; Thorarinsson and Sigvaldason, 1962). The eruption of Sveinagjá in 1875 represents the most recent tectonic rifting event of Askja. Lateral subsurface transport of lava has been proposed up to 100 km away from a central vent by (Pedersen et al., 2009; Sigurdsson and Sparks, 1978). Sigvaldason (1992) describes the Askja caldera as having formed through minor subsidence associated with more significant uplift resulting from deglaciation. However, this theory involving dramatic uplift (300 m) within an extensional regime requires evidence for why uplift was so concentrated along the northern block of the massif, and that must account for the deposits on either side of the fault were cut as a result of rebound.

## **1.6 HOLOCENE ERUPTIVE HISTORY**

The following is a summary of the current knowledge of the Holocene constructional history of the complex. No basaltic tephra associated with Askja from the Holocene are yet recognized beyond the immediate NVZ (Larsen and Eriksen, 2008).

The earliest Holocene deposit within the Askja complex is a limited distribution highly silicic tephra (ca. 74 wt. % SiO<sub>2</sub>) (Sigvaldason, 2002) with an estimated age of 10 ka. This age is based on the relative position of this tephra to other analytically dated tephra layers within coastal sections (Saemundsson, 1991) (Figure 1.5). Within more proximal sections the pumice occurs between numerous thick layers of poorly studied phreatomagmatic basaltic ash indicating a wet environment (Sigvaldason, 2002). The limited distribution of undisturbed tephra may suggest the continued presence of ice in the region, with only patchy ice-free areas (Sigvaldason, 2002), or highly erosive conditions following emplacement.

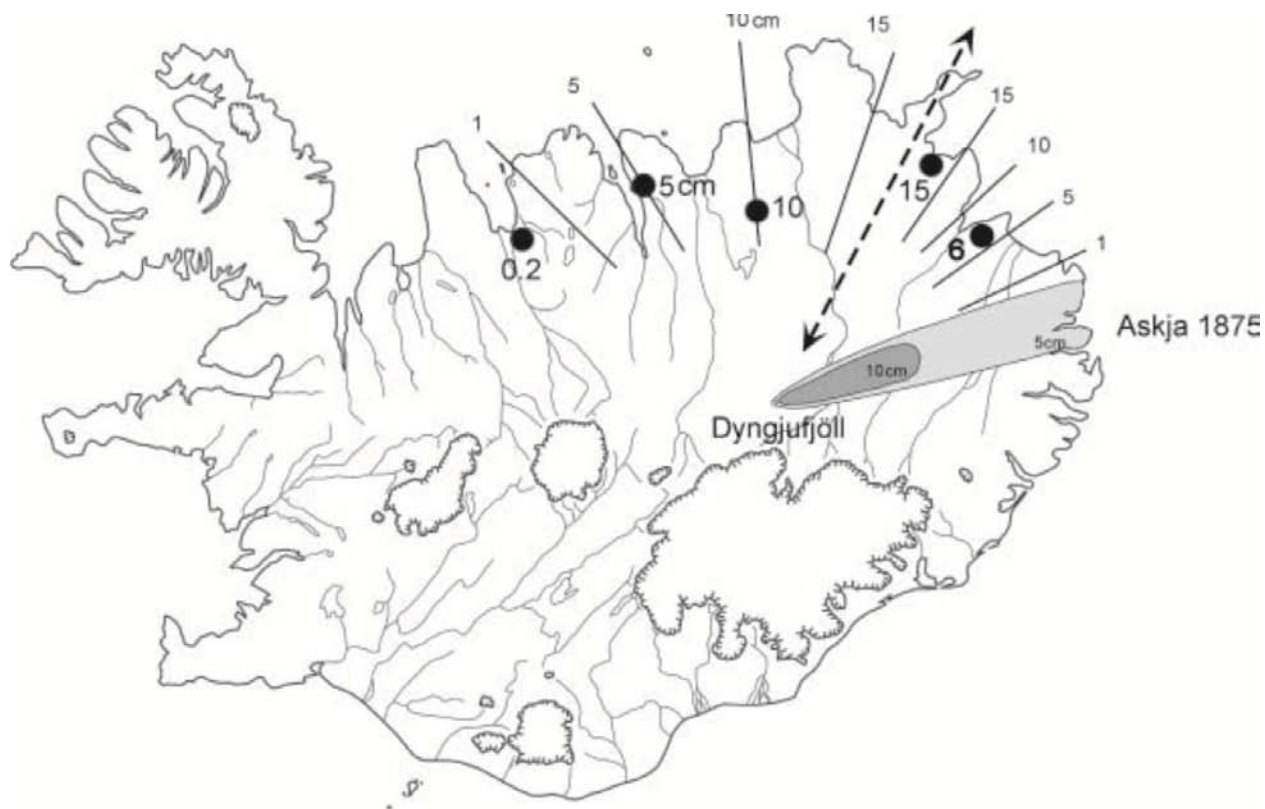


**Figure 1.5 Map of distribution and thickness of the 10 ka Askja pumice. Solid circles indicate sample locations and thin lines indicate estimated thickness contours. Dashed line indicates likely axis of distribution.**

**The distribution of the 1875 pumice is included for comparison (from Sigvaldason 2002).**

Holocene activity in the NVZ is dominated by unconfined subaerial basaltic lava flows. The postglacial lavas in the Askja region area predominantly younger than 7000 years based on the distribution of regional tephras within the lava stratigraphy (Annertz et al., 1985). Postglacial eruptions included considerable production of basaltic lava flows forming two shield volcanoes north of Askja called Kollóttadyngja and Svartadyngja (Figure 1.2) and large plains of unconfined lavas. The oldest identified postglacial lava flows originated from fissures along the western portion of the Askja complex and were erupted before tephra H4 (4500 BP), and they are clearly truncated by the Askja caldera boundary faults. The flows both travelled to the west, extending northwest beyond Dyngjufjöll Ytri, and to the east, filling Caldera 3 (Annertz et al., 1985). There may have also been lava production at this time along the northern extension of the Askja fissure system (Annertz et al., 1985). The vitriclastic ridge just northeast (Norðurfjöll) of Caldera 3 is covered in poorly described ‘explosion craters’, which may be associated with this eruptive phase (Annertz et al., 1985). A large field of pre-H4 lavas extends from Öskjuop and extends as far as Jökulsá a Fjöllum, a distance of 30 km (Annertz et al., 1985). Annertz et al. (1985) suggest that the subsidence of Askja caldera may have been accompanied by lava production along the ring faults and fractures.

The next package of tephrochronologically constrained lavas erupted between the emplacement of tephra layers H4 and an undated but stratigraphically confined tephra ‘x’ (3-4 ka). These lavas are found predominantly between Kollóttadyngja and Askja, northeast of the main Askja complex. This period also corresponds with the formation of the shield volcano Flatadyngja (Annertz et al., 1985). Litladyngja and Flatadyngja two monogenic shield volcanoes with volumes estimated to be between 3-20 km<sup>3</sup> (Sigvaldason, 2002) are all older than 2900 BP (Annertz et al., 1985). In particular Litladyngja has been proposed as the youngest shield volcano in Iceland (3500 BP) (Annertz et al., 1985). Since that time most of the activity has originated from within the Askja and Öskjuvatn calderas. Correlations with the extensive fissure system are limited, but historic activity, and the large volume of fractures and eruptive vents suggests that there was postglacial activity throughout the system away from the central caldera (Hjartardóttir et al., 2009).

Following the tephra layer x, and before tephra H3 (2900 BP; Annertz et al. 1985), lava production returned to the Askja caldera following a similar path to the H4 covered lavas through Öskjuop. Lava flows that erupted between 2900 BP and 1000 B P occur predominantly north of the complex along the ‘western’ fissure (Annertz et al., 1985). There may have been contemporaneous activity within the caldera; however, no deposits have been identified.

A package of lavas constrained by a tephra produced by Öräfajökull (Ö1362) are clustered within the Askja caldera, but their exact distribution is unknown due to the extensive cover of these flows by a subsequent group of lavas that were erupted prior to the next dated tephra layer ‘a’. The very thick basaltic tephra ‘a’ was produced in 1497 AD from an unconfirmed source under the northwestern margin of Vatnajökull. The lavas constrained by tephra ‘a’ also extend east through Öskjuop (Annertz et al., 1985). Younger postglacial, but pre-1875, lavas were focused in the western portion of the massif (Annertz et al., 1985; Brown et al., 1991).

## **1.7 HISTORIC ERUPTIONS FROM ASKJA**

Three major Icelandic historic eruptive periods have been documented. The historic annals (from 900 AD) contain little information about eruptions of Askja before 1875 (Þorarinsson, 1963). There has been no activity identified along the fissure system between 1497 and the 1875 (Annertz et al., 1985).

### **1.7.1 Eruption of 1875**

The earliest historic eruption occurred in 1875, produced significant subaerial basaltic lava flows along the northern fissure swarms and a collapse caldera following a plinian eruption of Askja. The silicic eruption that occurred on March 29, 1875 is one of the largest explosive historic eruptions in Icelandic history. The ash fall from this eruption led to the abandonment of at least 17 farms and increased

immigration to the US from eastern Iceland (Sigurdsson and Sparks, 1978). The eruption consisted of a basaltic fissure eruption in the northern Sveinagjá graben (Figure 1.1) and contemporaneous plinian rhyolite explosion, and minor basaltic activity at the Askja central volcano (Sigurdsson and Sparks, 1978). This dual composition eruption is one of the best indications of the proposed lateral plumbing system of the NVZ (de Zeeuw-van Dalfsen et al., 2005; Pagli et al., 2006; Sigurdsson and Sparks, 1978; Sturkell et al., 2008).

There are detailed descriptions of the eruption both phases of the eruption, with a greater number of accounts of the basaltic fissure eruptions to the north, due to greater accessibility and proximity to local farms (Sigurdsson and Sparks, 1978). Descriptions of the activity at Askja include early observations of the collapse of the Öskjuvatn caldera. The progression of the collapse and the formation of the lake Öskjuvatn was described over several visits by later travelers and geologists (Bemmelen and Rutten, 1955). Descriptions of this eruption have been summarized in Hartley and Thordarson (2012) with products and processes of the eruption outlined in Carey et al. (2009 and 2010), Lupi et al (2011), and Sigvaldason (1979).

### **1.7.2 Eruptions of the 1920s**

Small eruptions of basaltic lava also occurred between 1921 and 1929 (Tryggvason, 1989). Seismic activity recorded in 1921 was followed closely by observations of small lava flows emerging through the wall of the Austurfjöll massif just east of Víti (Þorarinsson, 1963) (Figure 1.3). Further eruptions were produced from vents located in the Austurfjöll massif along the southeastern margin of Öskjuvatn in 1922 and 1923. A larger vent was formed on the westernmost edge of the massif flowing into the lake in 1922 and 1923. A larger vent was formed on the westernmost edge of the massif flowing into the lake in 1922 (Annertz et al., 1985). Although the actual date is unconfirmed, lavas erupted along the fissure system that extends south of Askja in 1924 and 1929. A small (30–40 m) scoria cone was formed around 1926 in the middle of lake Öskjuvatn, known as Eyja (Annertz et al., 1985; Bemmelen and Rutten, 1955; Þorarinsson, 1963).



### **1.7.3 Eruption of 1961**

After a three decade hiatus, a large increase in geothermal activity (Sigvaldason, 1964), just south of the Öskjuop, marked the location that would later become the eruptive fissure. The activity initiated as very wet basaltic explosions (Sigvaldason, 1964). Lavas first appeared from the 800 m long fissure (Annertz et al., 1985) on the 26<sup>th</sup> of October, 1961 and lasted until November 7<sup>th</sup> 1961 (Þorarinsson, 1963). The composition of the basaltic lavas was chemically very similar to those from 1921 (Þorarinsson, 1963). Average rates of lava production were near 600 m<sup>3</sup>/s, producing flows 3 m thick over a area of 5.8 km<sup>2</sup> (Þorarinsson, 1963).

Significant deformation (inflation and deflation) of up to 20 cm/yr occurred during the late 1960s and 1970s, but no eruption occurred at this time. Leakage of water from Oskjuvatn through fresh fractures immediately following the 1961 eruption (most likely through Austurfjöll or caldera faults) were estimated on the order of  $2 \times 10^7$  m<sup>3</sup> (Sigvaldason, 1964).

## **1.8 AREA OF INTEREST: AUSTURFJÖLL**

The most recent geologic map of the Askja area by Landmælingar Íslands (1998) identifies Austurfjöll and surrounding ridges of Askja as basic to intermediate ‘hyaloclastites’, pillow lavas and associated breccias dated as younger than 0.8 m y, upper Pleistocene as based on paleomagnetic techniques (Jóhnnesson and Sæmundsson, 1998). In depth descriptions of Austurfjöll itself are limited to two studies (Bemmelen and Rutten, 1955; Sigvaldason, 1968). According to Bemmelen and Rutten (1955) the degree of incision of the edifice indicates that Austurfjöll is the oldest portion of the Askja complex exposed. The density of the vitriclastic ridges is estimated between 1.7 and 2.0 g/cm<sup>3</sup> in contrast to the surrounding subaerial basalts 2.6-3.0 g/cm<sup>3</sup> (Brown et al., 1991). Bemmelen and Rutten (1955) explored the base of

the easternmost portion of the massif as part of a greater survey of the entire complex, and incorporated the observations of Olafur Jonsson (1942). The most recent description of Austurfjöll by Sigvaldson (1968) was based on a single transect of the massif, and identified two major textural groups of micro- and macro-porphyritic lavas. In order to more accurately map and describe the deposits of Austurfjöll a detailed stratigraphic investigation in conjunction with textural analyses and geochemical analyses was undertaken in this project.

## **1.9 DEFORMATION AND MONITORING OF ASKJA VOLCANO**

Askja caldera has been actively monitored for deformation over the last 50 years. The NVZ has been the main center of rifting in northern Iceland for the last 6-7 mya (Pedersen et al., 2009). Spreading rates of 1.97 cm/yr have been measured using remote sensing techniques such as InSAR and GPS surveys for the MAR (de Zeeuw-van Dalfsen et al., 2005). Localized rift related spreading is estimated to be 1.9 cm/yr distributed over a 100 km wide zone (Sturkell et al., 2006). Deformation surveys starting in the 1960s have revealed alternating episodes of inflation and deflation in the Askja caldera, with near constant subsidence since the early 1970s (De Zeeuw-van Dalfsen et al., 2012; de Zeeuw-van Dalfsen et al., 2005; Rymer and Tryggvason, 1993; Tryggvason, 1989). Between 1960 and 1968, 5 m of deflation was observed on the northeastern shore of the lake, likely under the margin of Austurfjöll, possibly as a result of the 1961 eruption (Tryggvason, 1989). However, the rate of subsidence over the last 20 years has decreased (Sturkell et al., 2006). InSAR images over Askja reflect deformation up to 25 km from the center (Pagli et al., 2006; Pedersen et al., 2009). The resulting interferograms reveal a recent (since 1992) average of deflation of 5 cm/yr (Pagli et al., 2006).

Gravity surveys of the complex indicate a large negative anomaly in the center of the Askja caldera and a positive anomaly associated with the fissure swarm that runs through the eastern side of the caldera (some of which erupted in 1920 and 1960) (Brown et al., 1991; Rymer and Tryggvason, 1993). A

north-south positive Bourguer anomaly is interpreted to represent a ‘corridor’ some 0.5-1.0 km wide of basaltic dikes (Rymer and Tryggvason, 1993). This corridor occurs along the north eastern margin of the lake, a location of frequent historic activity (Rymer and Tryggvason, 1993). Sigvaldason (2002) suggests this positive anomaly represents the source of the 10,000 BP plinian eruption.

Modeling of gravity data and surface tilt have revealed a point source at approximately 3 km depth for the source of the subsidence (de Zeeuw-van Dalfsen et al., 2005; Rymer and Tryggvason, 1993; Tryggvason, 1989). The source is located north west of the lake, within the main Askja caldera. Up to 80% of the tilt is attributed to this point source. The residual subsidence measured may be associated the subsidence of the eastern caldera boundary (Brown et al., 1991). Other models distributed 80% of the deformation to a shallow point source, and 20% from a deeper source (Sturkell et al., 2006) occurring at 3 km and 16.2 km respectively (De Zeeuw-van Dalfsen et al., 2012; de Zeeuw-van Dalfsen et al., 2005; Sturkell et al., 2006). The location of the second source is predicted to be immediately below the shallow one (Pagli et al., 2006; Sturkell et al., 2006). The depth of the second source must be below 15 km otherwise there would be greater surface deformation (Pagli et al., 2006). Unusually deep (14-26 km) earthquakes recorded between 2006 and 2007 support the presence of this lower source (Soosalu, 2009). Draining from the upper source to the lower source may be accommodating spreading of the plate boundary within the ductile lower crust (Pagli et al., 2006).

Progressive subsidence of the complex may be attributed to three possible mechanisms of deformation: cooling and contraction of magma in a shallow chamber, void compaction of underlying material; and magma drainage from a shallow chamber (de Zeeuw-van Dalfsen et al., 2005). Glacial rebound in most of Iceland was completed by 9000 BP (Sigmundsson, 1991). Askja’s central location and higher elevation means that ice was present at least until 7 ka, but the crust likely rebounded quickly due to the low viscosity of the mantle under the MAR (Bourgeois et al., 2000; Sigmundsson, 1991).

The location of this deformation is notably in areas free of glaciovolcanic deposits (Pagli et al., 2006) which suggests the location of the boundaries of the calderas. The greatest deformation has occurred within the Askja caldera (Pagli et al., 2006). The location of the center of deformation within the

Askja caldera may indicate a fairly recent formation of the caldera relative to Austurfjöll, as the massif has experienced significantly less deformation than the caldera (De Zeeuw-van Dalssen et al., 2012; Rymer and Tryggvason, 1993). Gravity surveys in the late 1980s and early 1990s included one station on the southeastern portion of Austurfjöll. The resulting tilt over the three year survey revealed that any deformation occurring within the massif is independent of the larger trends of subsidence throughout the Askja and Öskjuvatn calderas (Rymer and Tryggvason, 1993). The most recent earthquake data reflects activity along the eastern part of the caldera, the eastern shore of Öskjuvatn along Austurfjöll, possibly connected with current geothermal activity (Hjartardóttir et al., 2009; Pagli et al., 2006; Sturkell et al., 2006).

The lack of significant earthquake activity post-1961 suggests a lack of magma movement, which might indicate the caldera system was emptied during the eruption (de Zeeuw-van Dalssen et al., 2005). The crust is estimated to be 30 km thick beneath Askja, with a brittle-ductile transition at 7 km (de Zeeuw-van Dalssen et al., 2005). Seismicity is typically limited to the upper 8 km of crust in Iceland (Soosalu, 2009). It is important to differentiate between a mass change and volume change. Microgravity surveys by de Zeeuw-van Dalssen et al. (2005) and Sturkell et al. (2006) reflect a new mass change, that they argue is not the result of delayed response to previous mass loss.

Postglacial and historic lavas are predominantly aphyric in nature, suggesting the lack of a large volume of partially crystallized magma in a chamber beneath the complex producing phenocrysts large enough to produce porphyritic textures common in the NVZ (Hansen and Gronvöld, 2000). The predominantly aphyric texture of historic Askja products suggests that there is no large volume of magma during the Holocene residing under the complex cooling, crystallizing, and contracting (de Zeeuw-van Dalssen et al., 2005; Sturkell et al., 2006). The basaltic Sveinagjá lavas of 1875 are proposed to have come from a deeper source than the evolved magma of the caldera focused plinian eruption (de Zeeuw-van Dalssen et al., 2005).

The long, lateral plumbing system proposed to connect Askja to its fissure swarm was potentially exploited during the 1875 eruption when lavas from the same magma batch were erupted at two locations (Pedersen et al., 2009; Sigurdsson and Sparks, 1978), and remote sensing (InSAR) deformation surveys suggest a possible connection between Krafla and Askja (de Zeeuw-van Dalfsen et al., 2005). While subsidence at Askja is an order of magnitude greater than observed at Krafla (Sturkell et al., 2008), the systems share a similar two magma chamber plumbing system, as Magnetotelluric, InSAR, and microgravity studies of nearby Krafla indicate a shallow magma chamber between 3 and 7 km depth (Brown et al., 1991; de Zeeuw-van Dalfsen et al., 2005; Sturkell et al., 2008; Sturkell et al., 2006).

In order to fully understand the evolution of the Askja volcanic center a more complete history of the volcano must be outlined, requiring detailed investigation of the glaciovolcanic deposits of Austurfjöll that represent the Pleistocene growth of this complex central volcano. This project is a detailed reconstruction of the history of Askja as recorded by Austurfjöll, and the interaction of the basaltic eruptions and the confining glacial ice. The study is multi-disciplinary and focuses on the timing, chemical variation, eruption frequency, structure, and environment of the construction of this large glaciovolcanic edifice.

## **2.0 ARCHITECTURE OF AUSTURFJÖLL MASSIF, ASKJA, ICELAND: LITHOLOGY, PETROGRAPHY**

The framework of the project to reconstruct the eruptive history and paleoclimate of the Austurfjöll massif is the physical volcanology and sedimentology of the massif as described in two field seasons. The 49 km<sup>2</sup> massif represents only a portion of the overall Askja volcano, but its central position and high relief (800 m) make it critical to the understanding of the evolution of the volcanic center (Figure 1.2). Austurfjöll also represents the greatest intact volume of glaciovolcanic material currently attributed to the volcano. The Austurfjöll massif contains representative deposits of a wide variety of basaltic subaqueous glaciovolcanic deposits. Because it is composed of over 80% subaqueously emplaced lavas and clastic deposits, Austurfjöll has significant implications for the interpretation of ponded water and therefore paleo-ice reconstructions in the region (see Chapter 8).

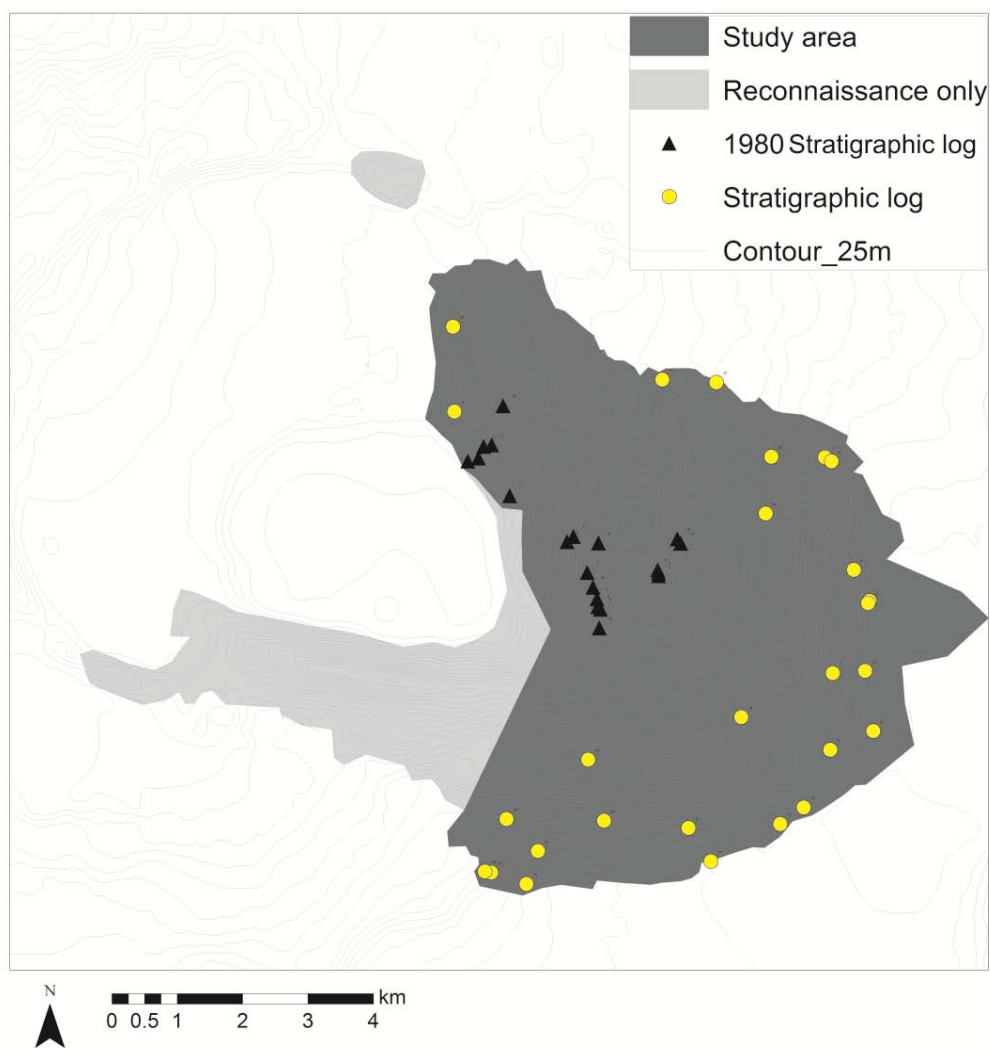


**Figure 2.1** Study area Austurfjöll and reconnaissance areas nearby in shaded region. Stratigraphic logs collected in this study are indicated in yellow, and 1980s stratigraphic logs were collected by Strand (1987).

## 2.1 METHODOLOGY

The geologic mapping of Austurfjöll was completed during two successive field seasons of four weeks each. Field work included lithofacies descriptions, structural measurements, sample collection, and photographic documentation of the entire massif including one over flight to collect aerial photographs. Glaciovolcanic samples were collected for textural and geochemical analysis, radiogenic dating, and volatile analyses (results to be discussed in Chapter 3).

Structural data included strike and dip measurements and field relationships to determine the role of tectonic and caldera faulting on the massif, and to aid in the identification of vents. Twenty three stratigraphic logs were collected around the massif (Figure 2.1). These logs were used to reconstruct the relationships between lithofacies and to document major erosional boundaries within the massif. Most logs were collected in steep-sided gullies, but others were collected over gentler terrain with thicknesses estimated using GPS and topographic maps. The lithofacies, sedimentary structures, unit boundaries, and nature of unit contacts were documented. Samples of representative units, where accessible, were collected for every log. The logs were digitized using SedLog (Zervas et al., 2009) and include unit thickness, grain size, type of contact, sample number, and lithofacies information (Appendix A). Some logs are accompanied by a photo mosaic of the outcrop, annotated to reveal the lateral variation of the deposits. An additional 19 logs collected by K. Strand and A. Höskuldsson in 1980 for NORVOLK (Strand, 1987) were digitized in the same format as the more recent logs (Appendix A).

Lithofacies codes were assigned to common deposit types observed, with a focus on key features that enabled field identification. Textural studies included the description of materials in the field, hand sample, thin section, and using the scanning electron microscope (SEM). Binocular microscope and SEM based textural studies were limited to individual fragmental deposits of interest (Chapter 6). A total of 245 hand samples were selected for thin section preparation. A blue epoxy was used both to provide strength to friable samples, particularly the tuffs, and to facilitate image analysis of pore space and vesicularity.



Petrographic descriptions were used to support lithofacies divisions and interpretation of geochemical data (Chapter 3). The lithofacies were interpreted in terms of the generation, transport, and emplacement of the deposits.

## **2.2 LITHOLOGY**

Two field seasons, in 2010 and 2011, were devoted to the collection of data on Austurffjöll. The objectives of the campaigns were to identify the dominant lithofacies, their distribution, and to use this information, coupled with structural data, to identify eruptive centers, i.e. vents. The distribution of lithofacies was mapped from observed outcrops, and then extrapolated in covered or difficult to access areas using wider-scale field observations such as field photos, aerial photos, and topographic constraints (Figure 2.2). Approximately 80% of the surface area of the massif, reflected by satellite imagery and aerial photography, is covered by a rhyolitic pumice erupted in 1875 (Chapter 5). Vertical exposures in the field reveal complicated internal structures and stratigraphic relationships. Lithofacies codes were defined for five groups: lavas, breccias, lapilli tuffs, ash tuffs, and intrusions. These five groups were then further subdivided based on componentry, grain size, petrology and in the case of the lavas, gross flow morphology and surface textures (Table 2.1).

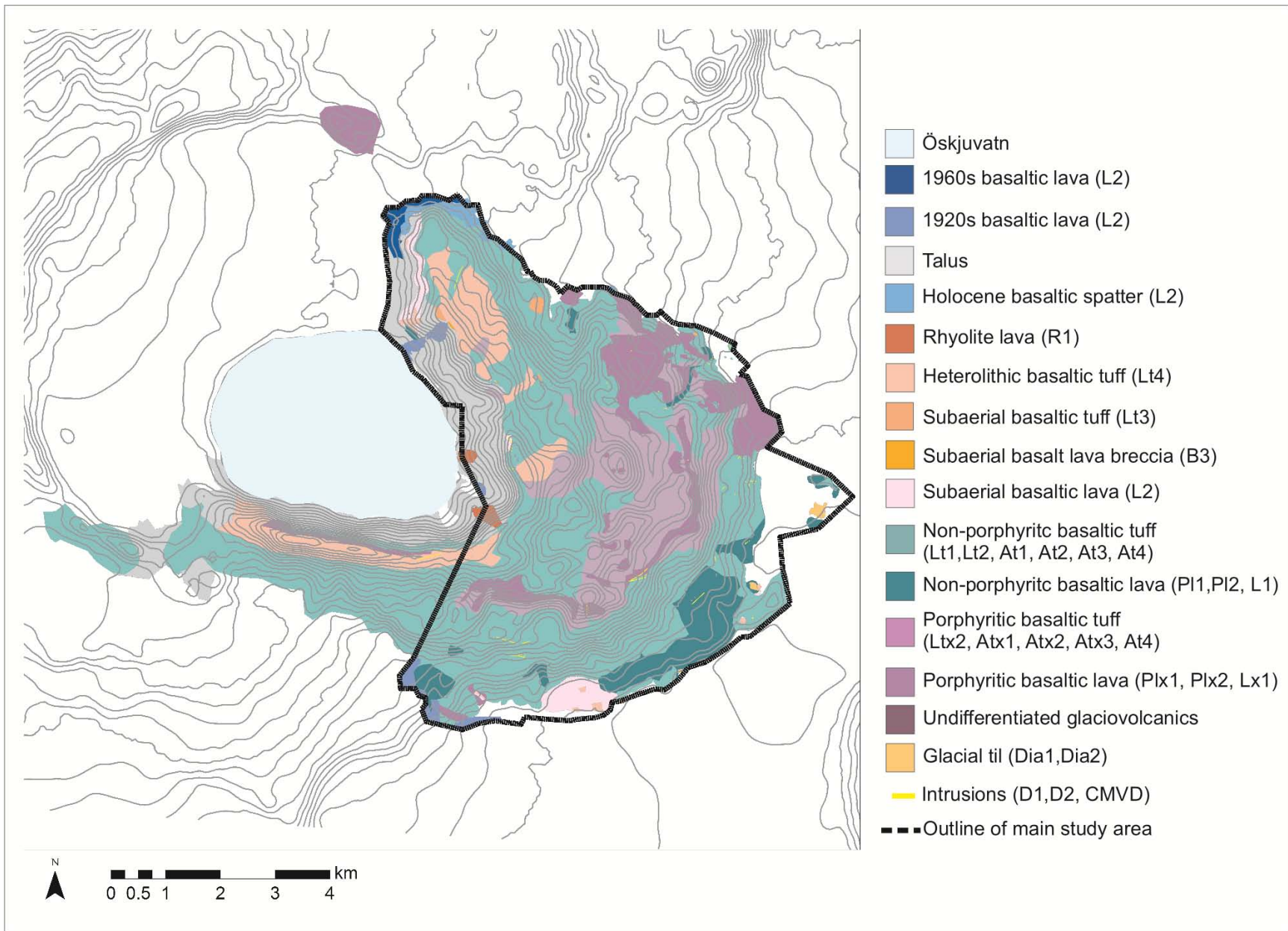


**Figure 2.2 Lithofacies map produced through two field campaigns and augmented through comparison with aerial photographs and comparison with existing literature (Sigvaldason 1968). Lithofacies are extended to Thorvaldstindur speculatively using aerial photographs and reconnaissance visits.**

### **2.2.1 Lavas**

Coherent lithofacies (lavas) were divided into pillowed and non-pillowed units, with further subdivisions to indicate porphyritic textures (indicated with an x in the lithofacies code) and an interpretation of subaqueous or subaerial depositional environment based on internal and surface textures. The phenocryst content of the porphyritic lavas is on the order of 20-40% by volume. Some porphyritic pillows have concentrations of crystals at the base of pillows.

**Table 2.1 Lithofacies codes**

<b>Code</b>	<b>General</b>	<b>Description</b>
<i>x= porphyritic</i>		
<b>L</b>	<b>Lavas</b>	
<b>PL<sub>1</sub></b>	Microcrystalline pillows	Regularly stacked pillow forms, extrusive. Wide range in vesicularity. Typically dark black in color.
<b>PL<sub>2</sub></b>	Microcrystalline pillows	Irregular pillow forms, may have columnar flow cores. Wide range in vesicularity of pillow cores. Typically black to dark grey in color.
<b>PL<sub>x1</sub></b>	Porphyritic pillows	Regular pillow forms, extrusive. Displays radial and vertical pipe vesicles. Wide range in pillow core vesicularity. Display a distinctive medium grey color. Crystal population dominated by plagioclase (Bytownite), with minor Cpx.
<b>PL<sub>x2</sub></b>	Porphyritic pillows	Irregular pillow forms, may have columnar flow lobes Wide range in pillow core vesicularity. Display a distinctive medium grey coloration. Phenocryst population dominated by plagioclase (Bytownite), with minor Cpx.
<b>L1</b>	Subaqueous sheet lava	Microcrystalline lava, vesicularity is low, ranges from 0 to only a few %, can display columnar joints, and cooled margins. Dark grey to black in color.
<b>Lx</b>	Porphyritic subaqueous sheet lava	Porphyritic lava flow, vesicularity is low. Can display columnar jointing, and cooled margins. Phenocryst population dominated by plagioclase (Bytownite), with minor Cpx. Displays a distinctive medium grey coloration.
<b>L2</b>	Subaerial lava	Maybe a'a or pahoehoe. Obvious subaerial textures including oxidation, scoriaceous tops etc.
<b>Lx2</b>	Porphyritic subaerial lava	Maybe a'a or pahoehoe. Obvious subaerial textures including oxidation, scoriaceous tops etc Contains visible phenocrysts of plagioclase feldspar. Phenocryst population dominated by plagioclase (Bytownite), with minor Cpx. Light grey to pink in color.
<b>R1</b>	Rhyolite dome	Highly altered rhyolitic lava. Exposed in the caldera wall with a roughly dome like morphology. Less altered portions of the lava are light grey in color and altered portions of the lava are yellow to brownish orange in color.

<b>B</b>	<b>Breccias</b>	
<b>B1</b>	Microcrystalline pillow breccia	Contains intact pillows and fragments of pillows. Typically angular to subangular. May contain fluidal bombs. Clast to variable clast / matrix support, Ac matrix. Ac matrix varies in color from dark grey to brown to orange.
<b>Bx1</b>	Porphyritic pillow breccia	Porphyritic pillows and pillow fragments. Phenocryst population dominated by plagioclase (Bytownite), with minor Cpx. Clast to variable clast / matrix support, Ac matrix. Ac matrix varies in color from dark grey to brown to orange. Overall deposit has distinctive light grey hue.
<b>B2</b>	Microcrystalline angular block breccia	Contains angular blocks. Clast to variable clast / matrix support, Ac matrix. Ac matrix varies in color from dark grey to brown to orange.
<b>Bx2</b>	Porphyritic angular block breccia	Porphyritic angular blocks. Phenocryst population dominated by plagioclase (Bytownite and Labradorite), with minor Cpx. Clast to variable clast / matrix support, Ac matrix. Ac matrix varies in color from dark grey to brown to orange. Overall deposit has distinctive light grey hue.
<b>B3</b>	Subaerial lava fragment breccia	Fragments of dense subaerial lava. Matrix or clast supported breccia containing Ac and lapilli. Ac matrix varies in color from dark grey to brown to red. May include red scoria or porphyritic lithics.
<b>Dm</b>	<b>Diamictite</b>	
<b>Dm1</b>	Matrix supported conglomerate, contains glacial clasts	Subrounded to rounded clasts supported in a fine ash matrix. Distinctive striated cobbles and outsized clasts (glacial erratics). Typically on the order of 1 m thick, but not laterally continuous.
<b>Dm2</b>	Matrix supported conglomerate	Subrounded to rounded clasts supported in a fine ash matrix. Glacial characteristics like striated clasts may be lacking. Thin units that are well bedded, dominated by ash sized particles. Typical deposit thickness is on the order of 50 cm and occurs on glacially scoured surfaces.
<b>Lt</b>	<b>Lapilli tuffs</b>	
<b>Lt1</b>	Angular glassy lapilli tuff with pillows and fluidal bombs	Dominated by 2-4 cm diameter angular glass fragments , clast or matrix supported with Ac matrix Outsized clasts include pillow fragments and pillow Ac matrix varies in color from dark grey to brown to orange. Massive, normal grading common. Bedding, if present, is weak.
<b>Lt2</b>	Subrounded lapilli tuff with subangular blocks / bombs no visible phenocrysts	Dominated by subrounded lapilli, clast or matrix supported with outsized clasts of subangular to rounded blocks Ac matrix varies in color from dark grey to brown to orange. Bedding is inconsistent and weak.

<b>Lt2x</b>	Porphyritic subrounded lapilli tuff with subangular blocks / bombs	Dominated by subrounded lapilli of porphyritic lava and occasional independent crystals up to 1 cm in diameter May be clast- or matrix-supported Outsized clasts include subangular to rounded blocks Ac matrix varies in color from dark grey to brown to orange. Overall deposit has distinctive light grey hue. Phenocryst population dominated by plagioclase (Bytownite and Labradorite), with minor Cpx.
<b>Lt3</b>	Subaerial component lapilli tuff	Dominated by subrounded lapilli, clast or matrix supported with outsized clasts of bombs / bomb fragments. Ac matrix varies in color from dark grey to brown to orange. Contains armored lapilli, in addition to other subaerial pyroclasts.
<b>Lt3x</b>	Subaerial porphyritic lapilli tuff	Dominated by subrounded lapilli of porphyritic lapilli sized clasts of lava and independent crystals up to 1 cm in diameter May be clast or matrix supported Outsized clasts include lava blocks and bombs Ac matrix varies in color from dark grey to brown to orange. Overall deposit has distinctive light grey hue. Phenocryst population dominated by plagioclase (Bytownite and Labradorite), with minor Cpx.
<b>Lt4</b>	Heterolithic lapilli tuff	Dominated by 2-4 cm diameter angular lapilli of porphyritic and Microcrystalline vesiculated clasts. May include red scoria and / or clasts of ash tuff or subaerial lava. Ac matrix supported with outsized clasts of 2-15 cm Ac matrix varies in color from dark brown to orange.

<b>At</b>	<b>Ash Tuffs</b>	
<b>At1</b>	Massive coarse ash	Massive unit of coarse ash, varies in color from dark brown to light tan
<b>At2</b>	Bedded coarse and fine ash, Laminated ash units	Bedded units to laminated unit of coarse ash, fine ash, and occasional silt. Laminations consist of beds 2 cm and below. Dark brown to orange in color, Dark brown to orange in color.
<b>At3</b>	Alternating beds of variable grain sizes dominated by ash	Beds of ash, lapilli and block bearing tuffs Individual beds range between 2 and 15 cm. Weak sedimentary structures on cm scale, such as ripples and scours may occur.
<b>At4</b>	Deformed domains of vitric ash	Discrete packets of bedded ash dominated tuffs that have steep dips and convoluted folding that does not match the surrounding bedding. Outsized clasts may range from lapilli to block size.

<b>D &amp; G</b>	<b>Intrusions (dikes)</b>	
<b>D1</b>	Dense intrusion	Coherent dike with no clear interaction with their host 5-100 cm in diameter Typically low vesicularity and tabular.
<b>D1x</b>	Dense porphyritic intrusion	Porphyritic coherent dike with no clear interaction with their host 5-100 cm in diameter Typically low vesicularity and tabular.
<b>D2</b>	Pillowed intrusion	Coherent dikes with irregular morphologies and pillowed margins in 2-4 m wide domains of fluidal and blocky peperite
<b>D2x</b>	Porphyritic pillowed intrusion	Coherent dikes with irregular morphologies and pillowed margins in 2-4 m wide domains of fluidal and blocky peperite
<b>CMVD</b>	Coherent margined volcanoclastic dike	Dikes that display multiple continuous basaltic glassy coherent 6 cm chill margins, very thin (< 3 mm) marginal peperite and a variety of vitriclastic interiors.
<b>G1</b>	Gabbro	Occurs as nodules in fragmental units. Phenocryst populations include plagioclase with intersertal Cpx and rare Olivine.

### 2.2.2 Pillowed lavas

Pillow lavas represent the bulk of lava facies at Austurfjöll, and occur as two major morphologies. Regular pillow lavas (P11) have self-similar cross-sectional pillow dimensions, with widest diameters that range between 20 and 100 cm for different outcrops. The stacking of pillow tubes is also highly regular throughout the exposure (Figure 2.3A). P11 lavas contain only pillow tubes. Irregular pillow lavas (PL2) contain highly asymmetrical pillow forms. They range in diameter from 50 to 200 cm, with distended shapes and heterogeneous stacking. Lobes of columnar jointed lava appear periodically at the base of P12 lavas and are interspersed with pillow tubes; the contacts between lobate and P12 lavas are gradational (Figure 2.3B).

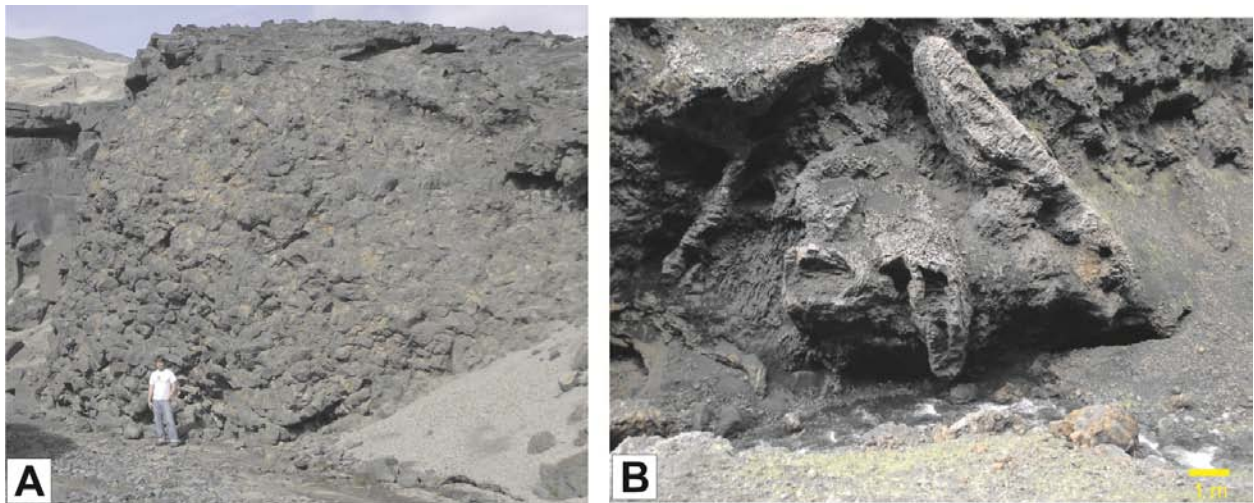


**Figure 2.3 Field images of lava lithofacies at Austurfjöll. A) P11 regularly stacked pillows. B) P12 lavas with entablature jointing and irregular pillow dimensions and sizes. Porphyritic (>20% feldspar phenocrysts) examples of all lava lithofacies occur.**



Irregular pillows commonly occur directly above a regular pillow unit or pillow breccia. Most pillow lavas occur in thick tabular flows between 20 m and 60 m thick. Of the 200 measured pillow dimensions and gross vesicularities within different pillow constructions (sheets, mounds, sills) the average maximum cross-sectional dimension is 50 cm. The associated core vesicularity averages 60%. Rim vesicularities were less abundant, but averaged 60% where preserved. These averages, however, do not accurately describe the variation inherent in these features and the overall range of values found within a given sheet, and across the massif. There is no significant variation vesicularity between porphyritic and micro-porphyritic counterparts of either pillow facies.

#### **2.2.2.1 Geomorphology of pillowed units**

Pillowed lavas form in sheets or mounds. Pillow lava sheets are large in scale, and can extend up to 1 km in length and have thicknesses up to 60 m. Compound pillow sheets eroded by modern gullies form steep cliffs up to 100 m high. The sheets are internally complex being made up of multiple individual pillowed lava flows, but produce a regular geomorphologic bench with sub-horizontal tops. Individual flows can be made up of P11 or P12 lavas and local lobate lava flows (L1). The three facies can transition gradationally or have sharp contacts. Locally vertical pillows may occur in both micro-and macro-porphyritic units. Vertical pillows have an elongate pillow shape dipping between 80 and 90° (Figure 2.4). The easternmost margin of Austurfjöll is predominantly composed of micro-porphyritic pillow sheet units (Figure 2.2). The large sheet flows (up to 60 m thick) are associated with clast-rich breccias between lavas. Porphyritic pillow lava sheets are less common and have a limited distribution.

Pillow mounds have more limited distributions and are smaller in scale. The eastern slopes of the massif have at least two areas of obvious pillow mounds (Figure 2.2), with slightly different scales and morphologies that correlate to feldspar phenocryst content. Both of these mound morphologies display steep dips, 40-50°, and appear to have formed on paleo-slopes between 10 and 20°. Pillow mounds and sheets regularly display bedded, sometimes convolute, ash tuffs (At4) 20-100 cm thick mantling the uppermost surface of the mound. These tuffs are dominated by coarse ash with angular vesiculated micro-

porphyritic 2-8 cm lapilli-sized lithics including some pillow fragments. Both pillow mound types occur stratigraphically above the more laterally continuous, tabular, 10 to 30 m thick, pillow lava sheet flows.

Porphyritic pillow mounds occur in random to radiating suites of small (20 to 100 m in diameter) lobate mounds typically displaying slope angles between 40 and 60°. The bases of the mounds are covered by pillow-derived detritus and pumice from the 1875 rhyolitic Askja eruption. Exposed heights range from 15 to 25 m. The mounds are cored by coherent pillow lavas, but grade vertically into pillow-fragment breccia, with increasing fragmental (coarse ash) matrix. However, coherent pillowed lavas PL1 are still present at the top of the fairly flat mounds. All mounds in this area radiate toward the east, away from an elongate ridge (500 m by 150 m) of pillows and pillow breccia (Figure 2.5). Fresh porphyritic units have a distinctive light grey coloration in contrast to the dark grey-black micro-porphyritic units.

Microcrystalline pillow lava mounds are larger (100 m in diameter, 15-30 m thick) and occur at the top of gullies, providing exposure of their internal structure. These pillow mounds are similar to their porphyritic counterparts, except scale. The larger mounds are also mantled by the bedded ash tuff. Besides the obvious textural distinction, microcrystalline pillow mounds display rounder tops, a larger minimum dimension, and far greater occurrence of mound overlap (Figure 2.6). The pillow mounds are predominantly P11 lavas, but these pillow mounds also contain some mega-pillows and P12 pillow forms (>1 m across). At the margins of the mound, individual pillow tubes can display dips up to 40° potentially highlighting the paleotopography.

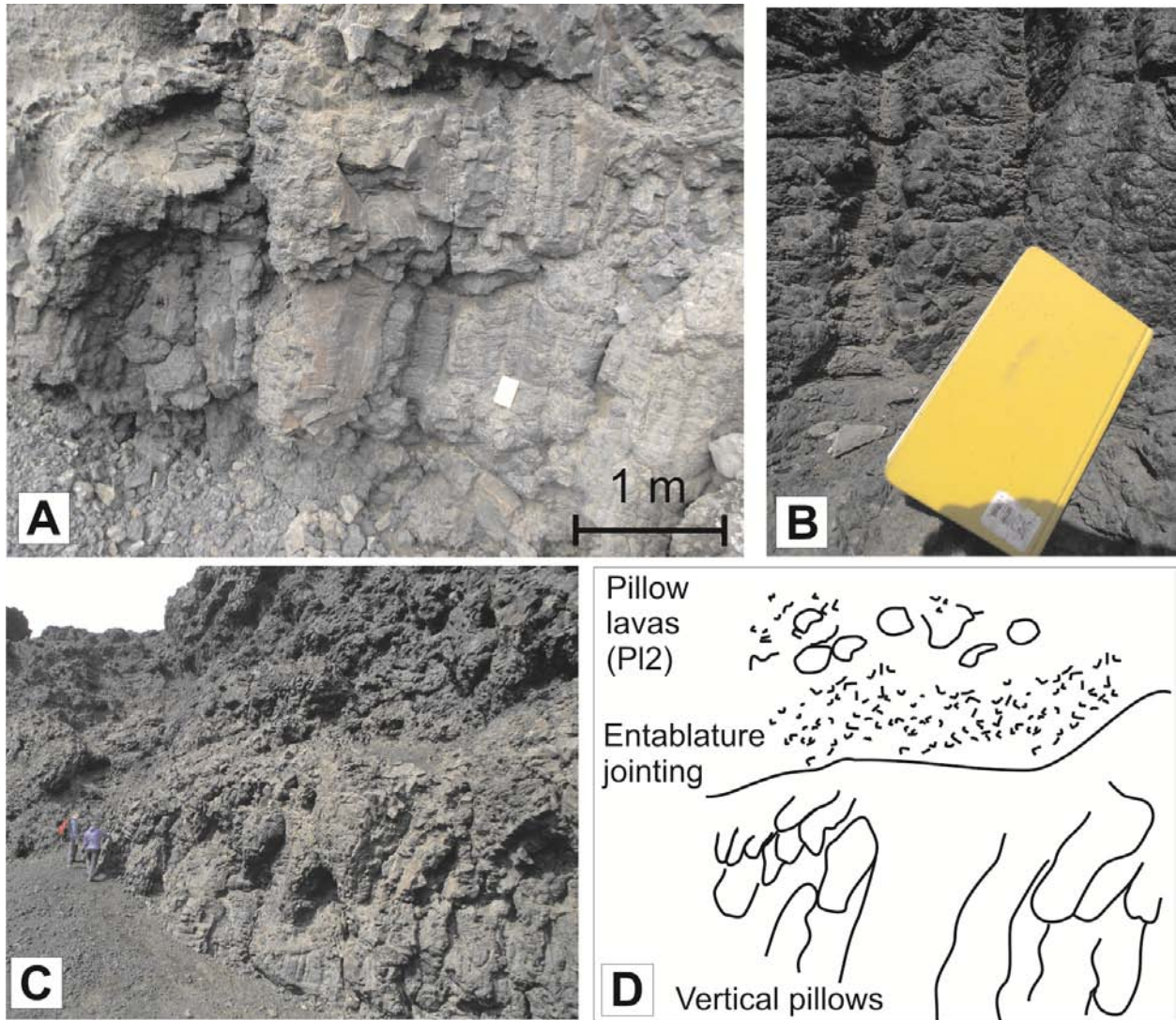


**Figure 2.4 Vertical pillows within a pillow lava sheet. A) Joint sets and pillow tube margins forming vertical pillows. B) Close up of internal structure of vertical pillows. C) Outcrop containing vertical pillows. D) Line sketch of C showing the transitions between PI2 lavas, entablature jointed domains and vertical pillows. Pillows likely formed by flowing over a topographic barrier.**

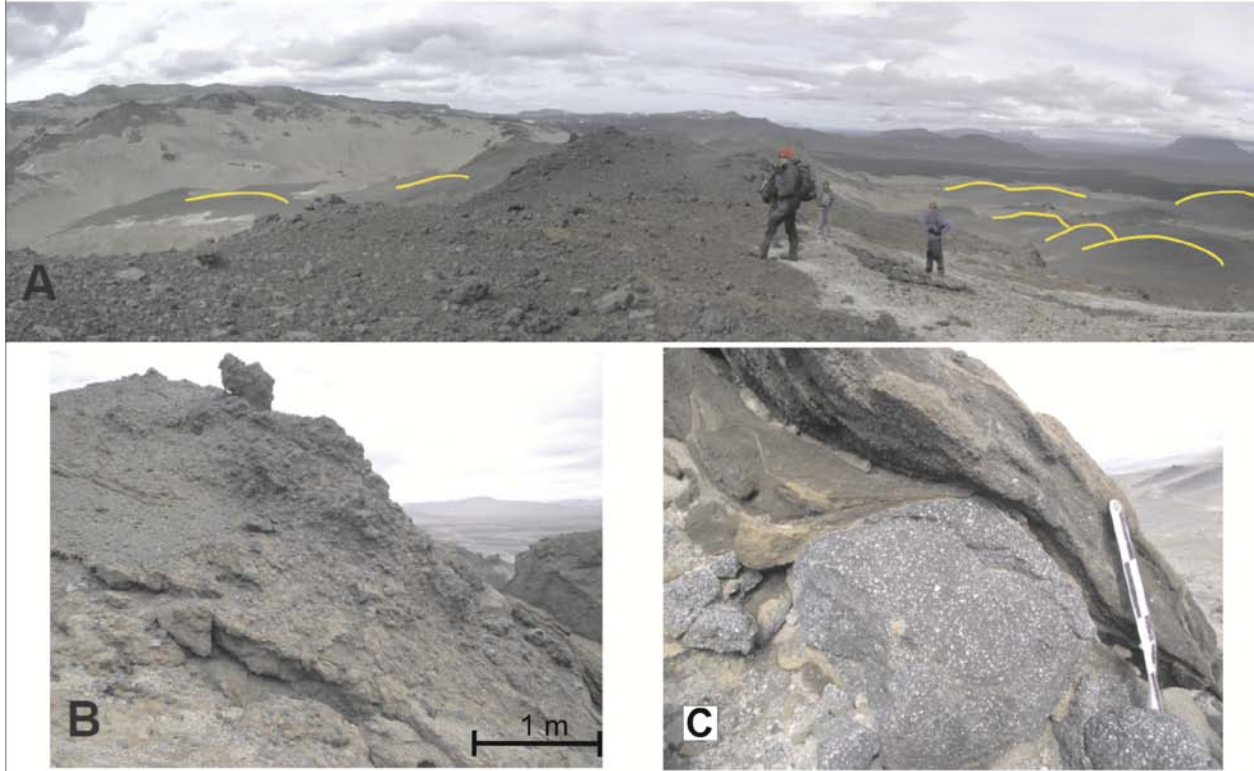


**Figure 2.5** Porphyritic pillow mounds are distributed in semi-radial patterns away from their source and mantle the underlying topography. A) View from top of pillowed ridge where yellow lines indicate upper exposed surfaces of pillow mound forms. B) Pillow breccia that commonly caps pillow lava mounds. C) Pillow lavas in pillow mounds and pillow breccias also commonly mantled by bedded ash tuff (At4).



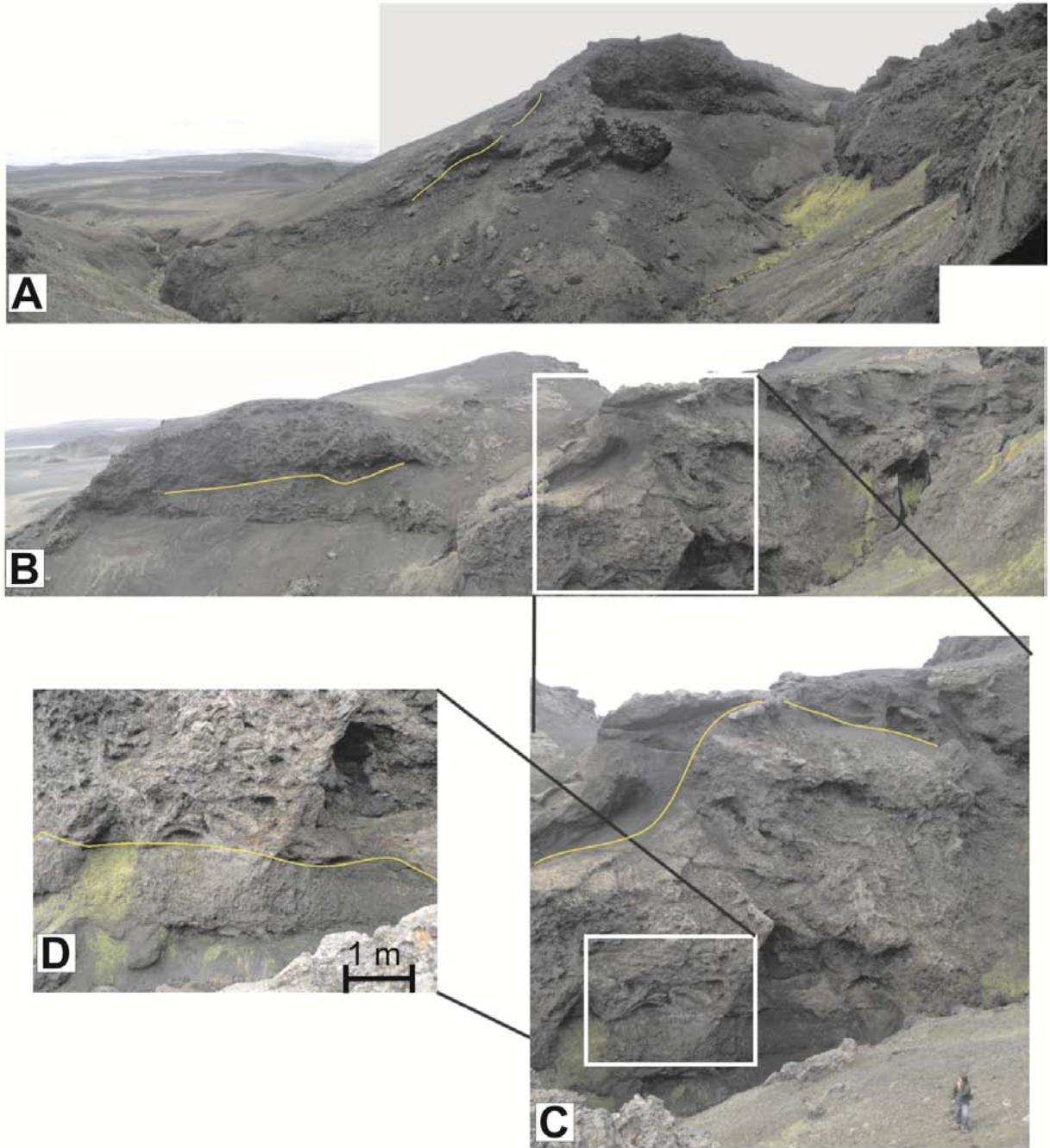


**Figure 2.6** Microcrystalline pillow lava mounds are much larger in scale than their porphyritic counterpart (100 m vs. 20 m across). A) Incised pillow mound reveal mantling units of At4, as denoted by yellow line, over pillow units. B) Pillow mound with two pillow units divided by yellow line, and overlying At4 units. C) Close

**up of B focusing on the top pillow unit of irregular pillows lavas. Yellow lines denote the contact between mantling At4 and pillow unit. D) Inset from C revealing the contrast between the upper irregular and lower regular pillow forms (for detailed explanation see text) Yellow line indicates contact.**

#### **2.2.2.2 Non-pillowed lavas**

Subaqueous sheet lavas (L1), lavas with no pillow forms, are smaller than pillowed lavas, being 1 to 10 m wide, and typically 0.5 to 3 m thick. Small lobes appear as resistant ridges and are surrounded by angular block-bearing breccias and lapilli tuffs. The non-pillowed lavas are either micro-porphyritic or porphyritic with a wide range of feldspar phenocryst populations. Like the pillow lavas, porphyritic units have a distinctive light grey coloration in contrast to the dark grey to black micro-porphyritic units (Figure 2.7A). L1 lavas display vertical widely spaced joints to dense networks of entablature fractures or radial columns (Figure 2.8). Most L1 lavas have widely spaced near vertical fractures without regular spacing or length and may extend through the flow. Entablature jointed flows display blocky tightly spaced (10 cm) joints that are perpendicular to the flow surfaces. Radial cooling cracks, the least common fracture pattern observed, are oriented radially from the interior of the flow display an increase in width of the columns towards the center of the flow. In the field, subaerial lavas (L2) are distinguished by the presence of a scoriaceous a'a carapace, lower glass content and red oxidation (Figure 2.7B). Identification of subaqueous lavas is confirmed through distinctive microscopic textures including a uniformity of microlite sizes in the groundmass and a high concentration of well formed oxide microlites (See section 2.3).

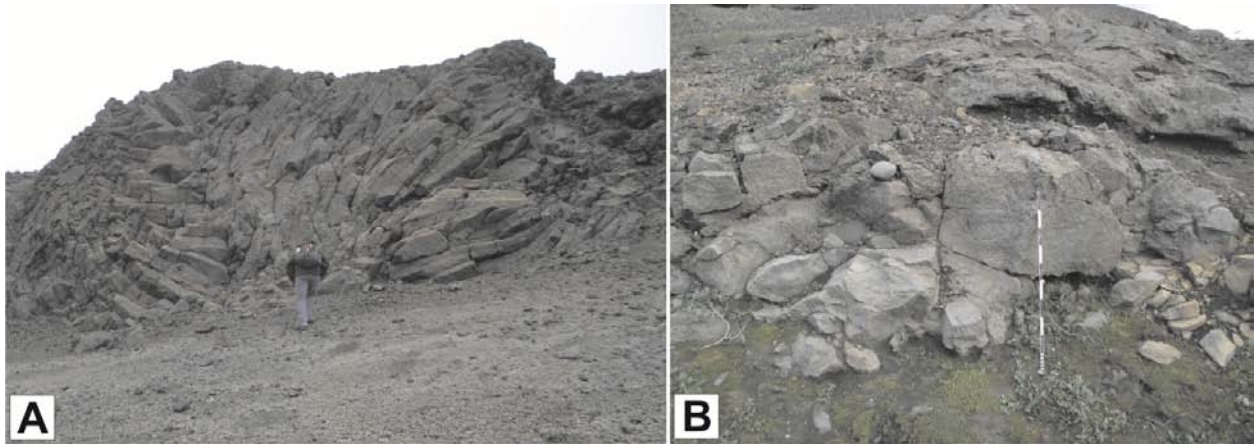


**Figure 2.7 Non-pillowed lavas A) Example of Lx1 subaqueous lava with radial cooling cracks and phenocryst content > 20%. B) L2 subaerial lava with glacial scour. Scale bar is 1 m.**

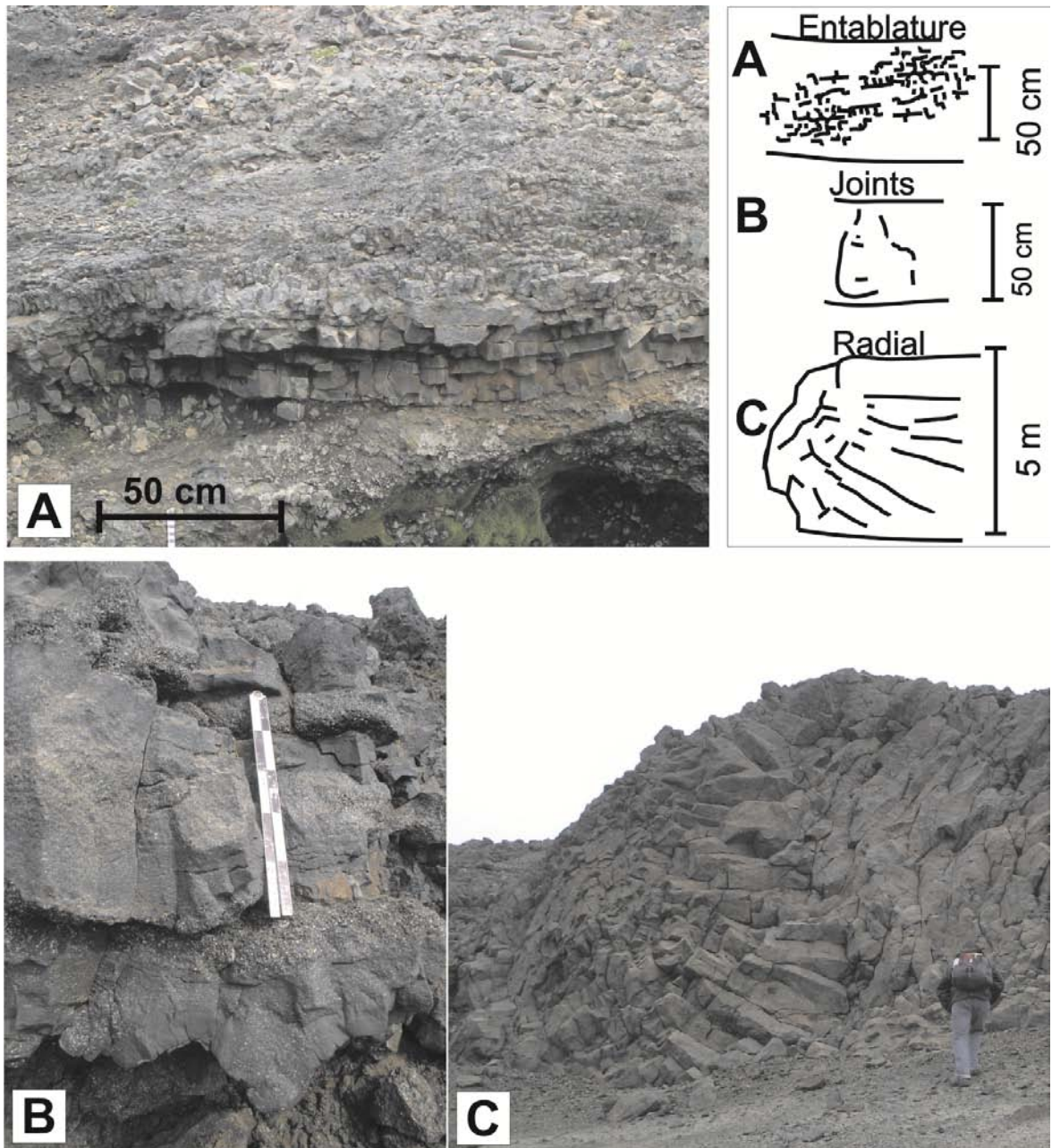


**Figure 2.8 Example fracture patterns in subaqueous lava flows (L1) with line matching line drawings. A) Tightly spaced entablature, blocky jointing in micro-porphyritic lava. B) Widely spaced predominantly vertical jointing in thin porphyritic flows. C) Radial cooling cracks in an over thickened porphyritic lava.**



### **2.2.3 Rhyolite lava**

Hydrothermally altered rhyolite lava (R1) occurs in two exposures within the dissected caldera wall of the eastern mountains (Figure 2.2). Near the lake at low elevations the exposures are the freshest (Figure 2.7). The second, and more altered exposure continues from 1175 m asl to the top of the caldera rim. The exposures are difficult to access, and the original morphology is obscured by deep erosion and talus. The deposits display some fresh grey surfaces, but are predominantly white to yellow orange or dark brown depending on the degree of hydrothermal alteration. Active hydrothermal activity continues through the higher exposure. Local, poorly constrained pockets of rhyolitic ash are associated with the lava. The high degree of alteration can make distinguishing the ash and lava difficult. Mapped distribution of the rhyolite is a minimum estimate due to burial by basaltic glaciovolcanic lavas and tuffs. Basaltic bombs cored with rhyolitic lava occur at high elevations of Austurfjöll; these bombs were mentioned in brief by Sigvaldason (2002).

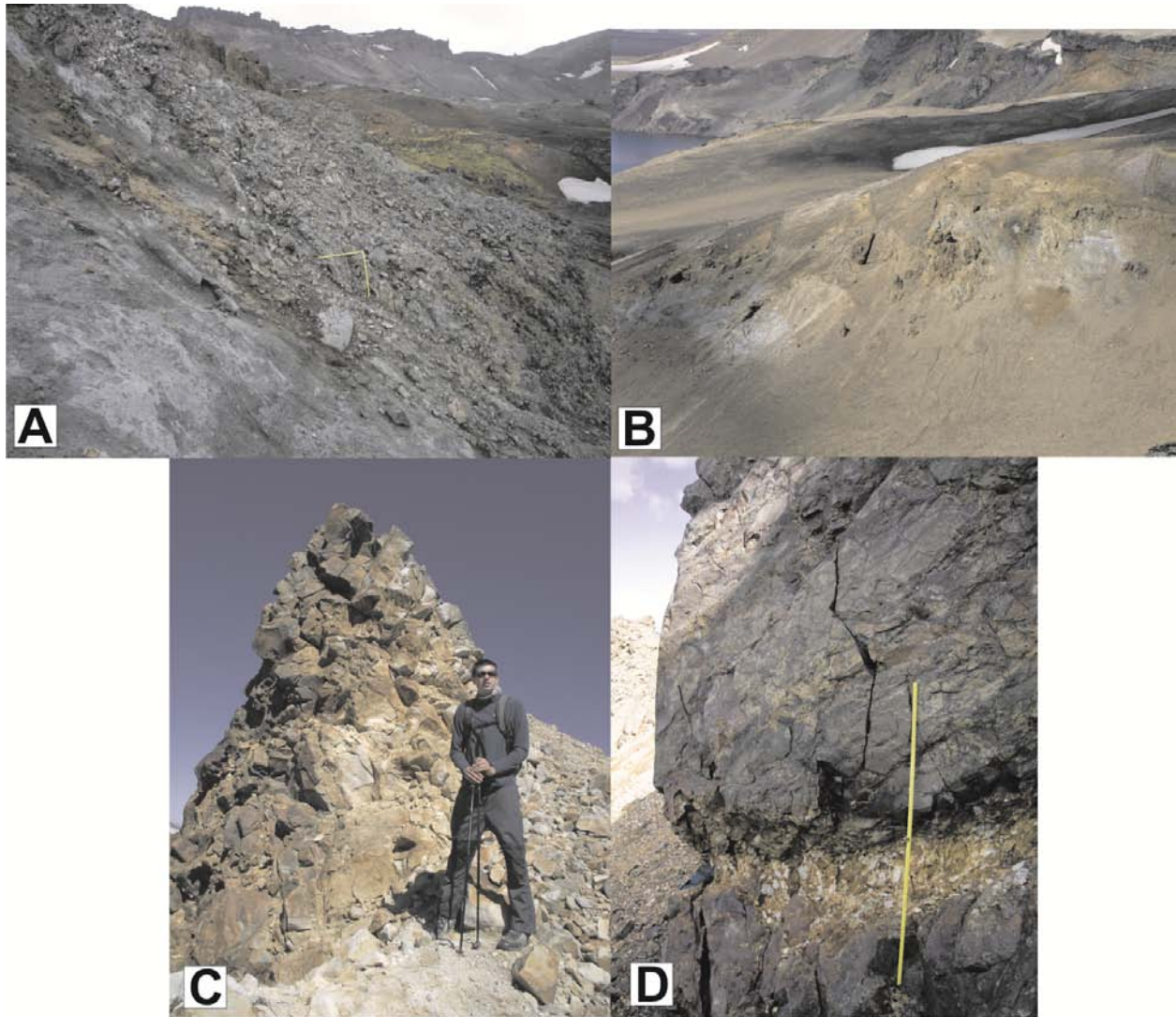


**Figure 2.9 Rhyolite lava exposures in the southeastern caldera wall. A) Image of the freshest exposure of rhyolite, meter stick for scale. B) Regional view of image A location (images from D. McGarvie). C) Exposure of hydrothermally altered rhyolite on caldera rim. D) Sample location of rhyolite unit pictured in image C (Image courtesy of D. McGarvie).**

#### **2.2.4 Fragmental Units**

The bulk of deposits exposed on Austurfjöll are fragmental in nature, with clast sizes ranging from millimeter to meter scale. These lithofacies are subdivided by the dominant grain size, and then by the nature of the dominant outsized clasts (Table 2.1). Outsized clasts are the clasts of the largest dimensions within any given deposit that significantly exceeds the median grain size. Many deposits contain outsized clasts of isolated pillows, pillow fragments and / or bombs / blocks, or some combination of the above. Pillows and pillow fragments are distinguishable by their thick glassy rinds (mm to cm), frothy cores, and radial pipe vesicles. Bombs shape ranges from aerodynamic, ribbon, and fluidal morphologies. They display a wide range of glassy rind thicknesses and may have extensive bread crust-like tensional cracks. Vesicle distribution is typically random in bombs. Large angular blocks may have some similarities in appearance to bombs and pillows, but they have sharp broken margins. Further discussion of fluidal bombs is found in Chapter 6. Fragmental deposits occur as both micro-porphyritic and porphyritic varieties (as indicated by an x in the lithofacies code).

##### **2.2.4.1 Breccias**

Pillow breccias (B1) contain pillows and pillow fragments and are clast- or variably matrix-supported, with zones of clast concentration. Typically no distinguishable fabric is present (Figure 2.10A). Clasts are between 7 and 70 cm with recognizable pillow forms, pillow fragments, and may include fluidal bombs. Clasts may have significant preserved glass rims 2-10 mm thick. The matrix is dominated by lapilli-sized angular vitric particles. Vesicularity of the lapilli is variable, but is typically between 10-30%. These units are either micro-porphyritic or porphyritic with wide range of feldspar phenocryst populations. The color varies from dark grey to orange depending on the degree of palagonitization. Fresh porphyritic units have a distinctive light grey coloration in contrast to the dark grey to black micro-porphyritic units. Pillow breccias may be intruded by any one of the intrusion varieties described.

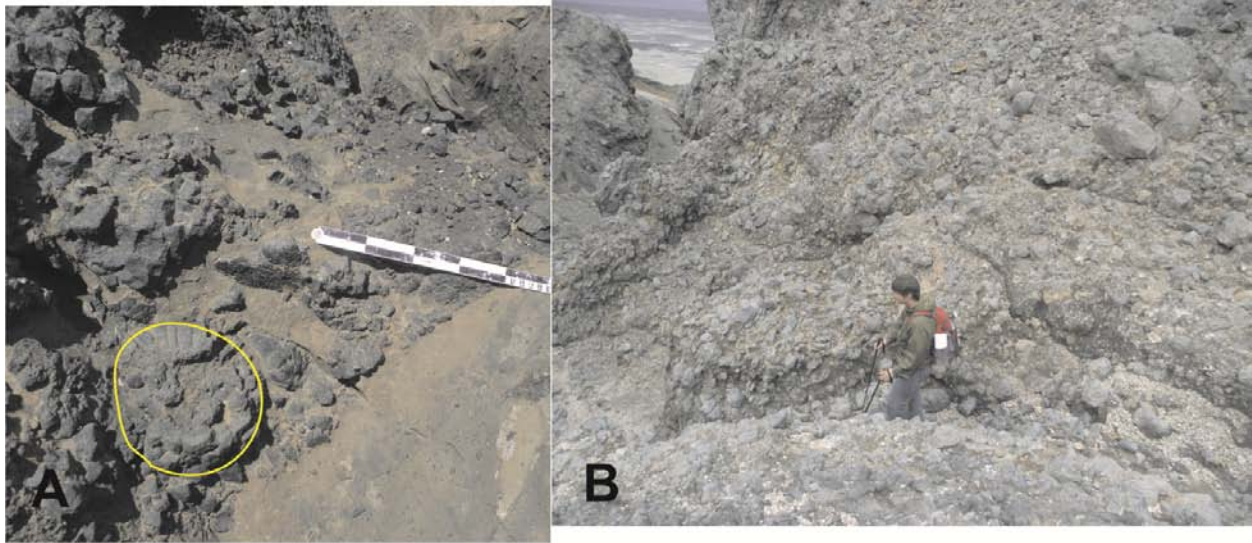


**Figure 2.10 Images of breccia lithofacies. A) Field image of a pillow-bearing B1 breccia with a pillow outlined in yellow. The scale bar has increments of 10 cm. B) Field image of an angular block-dominated B2 breccia.**

Angular block-bearing breccia (B2) is clast- to variably matrix-supported. This breccia displays clast concentration zones, but displays no regular fabric (Figure 2.10B). Clast size and internal variation in angular breccias is similar to B1 breccias, but the clast types are notably distinct. B2 breccias display the same variability of color and crystal content as B1.

Subaerial lava fragment breccia (B3) occurs typically in thin (<1 m) lenses between lapilli tuffs and subaerial lavas along the caldera rim. B3 contains distinctive pieces of dense subaerial lava and other subaerially derived clasts including red scoria. Other clasts include microcrystalline lava, porphyritic lava and lithified ash tuff. The deposit is clast- or matrix- supported. Matrix-supported deposits exhibit a matrix of coarse ash and lapilli, with a wide range of vesicularities and particle shapes. The matrix varies in color from dark grey to red.

#### **2.2.4.2 Diamictites**

Diamictite comprises matrix-supported conglomerate (Dia1) that contains clasts that are well-rounded and with scoured and polished surfaces. The clasts are subrounded to rounded and occur in a grey-brown fine ash matrix (Figure 2.11 A). The facies is very poorly-sorted with heterolithic componentry. Outsized clasts and matrix components may include dense or vesicular clasts of porphyritic and micro-porphyritic lava. Clasts of palagonitized tuff are rare, and such clasts are pebble-sized or smaller if present. Deposits of Dia 1 are typically on the order of one meter thick, but do not occur in neat beds or have consistent contacts. The facies is not laterally continuous beyond a few meters. This facies locally mantles vertical exposures or is disrupted by pillowed intrusions.

Matrix-supported pebble conglomerate (Dia2) contains subrounded to rounded clasts supported in a grey-brown fine ash matrix. Clasts are typically small cobble to pebble sized and may display glacial polish or striations. Outsized clasts are diverse in lithology, but dominant clast types include dense and vesicular micro-porphyritic lava. The unit is typically on the order 50 cm or less in thickness, and has a sub-horizontal upper surface. The Dia2 lithofacies may overlie lava units exhibiting glacial scour (Figure 2.11 B).



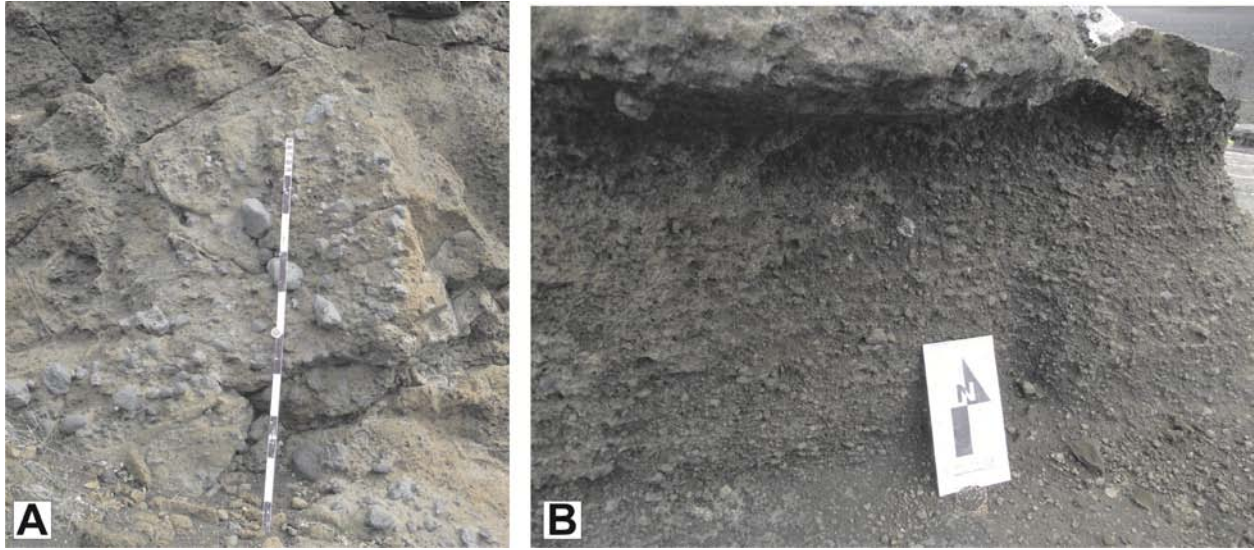


**Figure 2.11 Images of diamictite lithofacies. A) Dia1 is a coarse grained matrix supported diamictite. B) Dia2 is a finer grained matrix supported bedded diamictite.**

#### **2.2.4.3 Tuffs**

Lithofacies Lt1 is a highly glassy and angular lapilli dominated tuff. Clast shapes are predominantly angular, but larger outsized clasts are highly glassy and commonly fluidal in shape. Lt1 is clast- or matrix-supported, with varying quantities of coarse ash matrix. The deposit is poorly sorted, but typically displays a subtle upward fining. Lt1 is commonly fresh and distinctly black, but lightens to grey as the matrix to clast ratio increases. The matrix of Lt1 may alter to a bright orange, but clasts remain fairly black. No porphyritic version of this lithofacies has been observed. The facies is massive, but weak bedding is present in some deposits only in the upper few meters.

The clasts within Lt1 deposits are distinctly vitreous, but some also have intact glass rinds 1-2 mm thick. The unit is lapilli (2-20 mm) supported, vesicular, micro-porphyritic and highly angular. In outcrop and hand sample, there is limited apparent finer matrix. Exposures of this facies range between 15 to 50 m thick, with grain size variations occurring over tens of meters. Outsized clasts average 5 cm with

pillow fragments that reach 10 cm. Fluidal bombs occur between 10 and 60 cm in diameter, but decrease in frequency higher in Lt1 sequences. The glassy rims on fluidal bombs and pillow fragments are surprisingly well preserved. As units of Lt1 increase in thickness outsized clast dimensions and quantity decrease (Figure 2.12). No bomb sags were observed. Some exposures have stark differences in alteration that is in fact typical of all fragmental deposits within the field area, with fairly sharp, non-systematic transitions between zones of alteration. Accessibility to the full extent of any one exposure is limited by debris, 1875 pumice, and steep cliffs. The distinct angular glassy texture is rapidly muted by alteration. In some examples the clast supported fabric resembles a matrix of clay, with remnant glassy angular clasts. This facies is described and interpreted further in Chapter 6.

The subrounded lapilli tuff, with sub-angular blocks (Lt2) facies is a glassy to dull lapilli dominated tuff with distinctly subrounded clasts. Lapilli are typically 1 to 6 cm in diameter. Small (10-20 cm) isolated pillows may also occur. Outsized clasts of large lapilli-sized vesicular to non-vesicular lava, occur in zones of concentration, but with no regular fabric. The facies is otherwise poorly sorted. Lt2 is typically dark grey to tan and orange in color. Blocks are typically sub-angular to rounded and up to 30 cm in diameter. These units are either micro-porphyritic or have a wide range of feldspar phenocryst populations in the clasts. In porphyritic units isolated crystals of feldspar may contribute up to 20% of the matrix portion of the deposit (Figure 2.13). No bomb sags were observed.

Subaerial lapilli tuff (Lt 3) contains subrounded lapilli with distinctive subaerial clasts including red scoria and armored lapilli (Figure 2.13). The deposit is clast- or matrix-supported with outsized clasts of bombs / bomb fragments. The coarse ash matrix varies in color from dark grey brown to orange. Rare bomb sags were observed. Porphyritic deposits can have free crystals of plagioclase up to 1 cm in diameter in the matrix.



**Figure 2.12 Lt1 facies. A) Example of bombs clasts found in Lt1. Arrow in scale is 10 cm. B) Vesicular clasts of Lt, note the glassy quality of the clasts and lapilli. Small increments on scale are 1 cm each. C) Example of an exposure of Lt1, massive but weak grading occurs.**



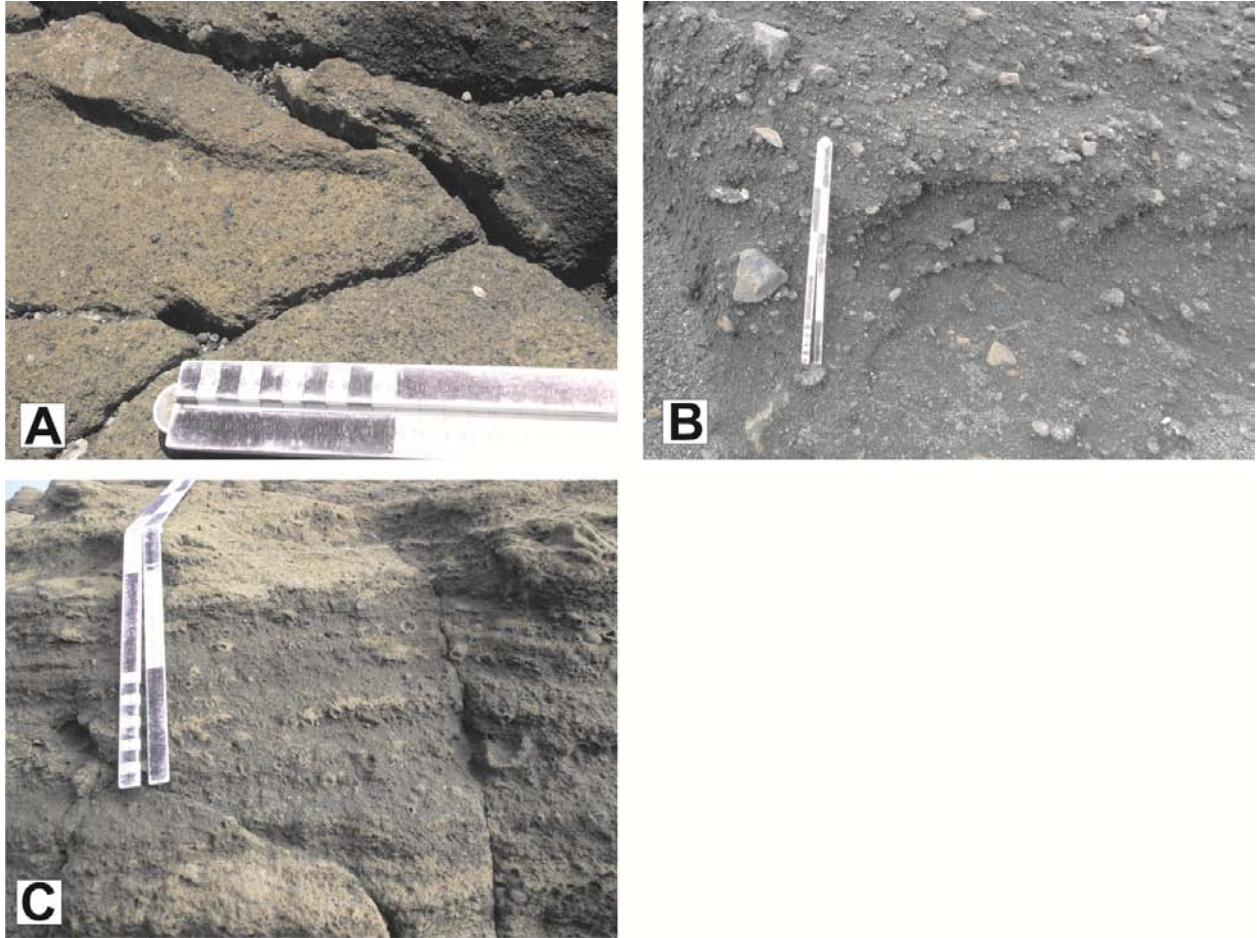


**Figure 2.13 Other lapilli tuff lithofacies. A) Lt2 subrounded lapilli tuff with pillow fragments and bombs. Weak bedding may occur. B) Lt 4 heterolithic lapilli tuff containing a variety of clast types including porphyritic and micro-porphyritic clasts and red scoria. C) Lt3 Subaerial component lapilli tuff containing armored lapilli and red scoria. Large increments on scale are 10 cm, fine increments on scale are 1 cm.**

The heterolithic lapilli tuff (Lt4) facies is a lapilli tuff that contains little to no fresh glass in a highly heterolithic subrounded to rounded lapilli dominated tuff. Clast composition ranges from porphyritic to micro-porphyritic dense and vesicular lavas, red scoria, and consolidated blocks of ash tuff. The deposit is supported by a coarse ash matrix. Outsized clasts (blocks) are up to 20 cm. The color is typically light grey to tan to orange. Isolated crystals of feldspar may contribute to the matrix (Figure 2.13).

Massive coarse ash tuff (At1) facies is composed of predominantly coarse ash, massive in nature, and forms units that are frequently thick (> 5-50 m) and display occasional outsized clasts of micro-porphyritic and porphyritic (At1x) pillow and non-pillowed lava fragments (blocks). Thin localized zones of weakly bedded material are uncommon. Porphyritic units may contain individual feldspar subhedral crystals up to 2 cm in diameter (Figure 2.14A).

Bedded well-sorted ash tuff and laminated tuff (At2) contains coarse ash, fine ash, and occasional very fine ash. Laminations occur on the scale of <2 cm with units having a maximum thickness of 2 m. Occasional millimeter thick very fine ash layers occur up to a few cm in thickness. The color varies from medium grey to orange depending on the degree of palagonitization (Figure 2.14B, D).

Alternating bedded ash tuff of variable grain sizes (At3) consists of well-sorted coarse ash beds of between 5 and 50 cm, that are inter-bedded with fine ash beds between 3 and 15 cm. Weak centimeter-scale sedimentary structures such as cross-bedding, ripple marks, and normal grading may also occur. Overall unit thickness can vary from a few centimeters to >15 m thick (Figure 2.14C).

Highly deformed domains of vitric ash tuff (At4) are an interesting and common feature in the field area. These domains occur at all elevations, and overlap all other lithologies. The At4 deposits are domains of coarse, ash-dominated, bedded sediment, that display both meter scale folding, and centimeter-scale convolutions (Figure 2.15). These deformed sediment domains display preserved internal bedding, lamination, and sedimentary structures (including scours, cross-bedding, and ripples), but the packets of sediment in most cases displays a modern steeply dipping orientation and is folded at high angles (tilted bedding is as high as 85°). Within the sediment domains individual beds are centimeters in

thickness (5 to 10 cm average) with varying clast sizes from fine ash, to coarse ash, and lapilli up to 4 cm. Clasts can vary from subrounded to rounded, to outsized clasts of angular blocks of dense to vesicular, micro-porphyritic to porphyritic lava.

The domains range from 20 to 200 cm thick. Contacts with surrounding beds are typically very sharp, but transitional boundaries were observed towards the edges of some of the domains. Some domains are the lateral extension of apparently undeformed At2/At3 units. There are also several instances of deformed domains of non- porphyritic clastic deposits occurring on top of and apparently surrounded by a porphyritic lapilli tuff. Although initial observations suggested that these domains were mostly associated with pillow breccias, further investigation revealed deformed sediment domains contacting lithofacies of every grain size.

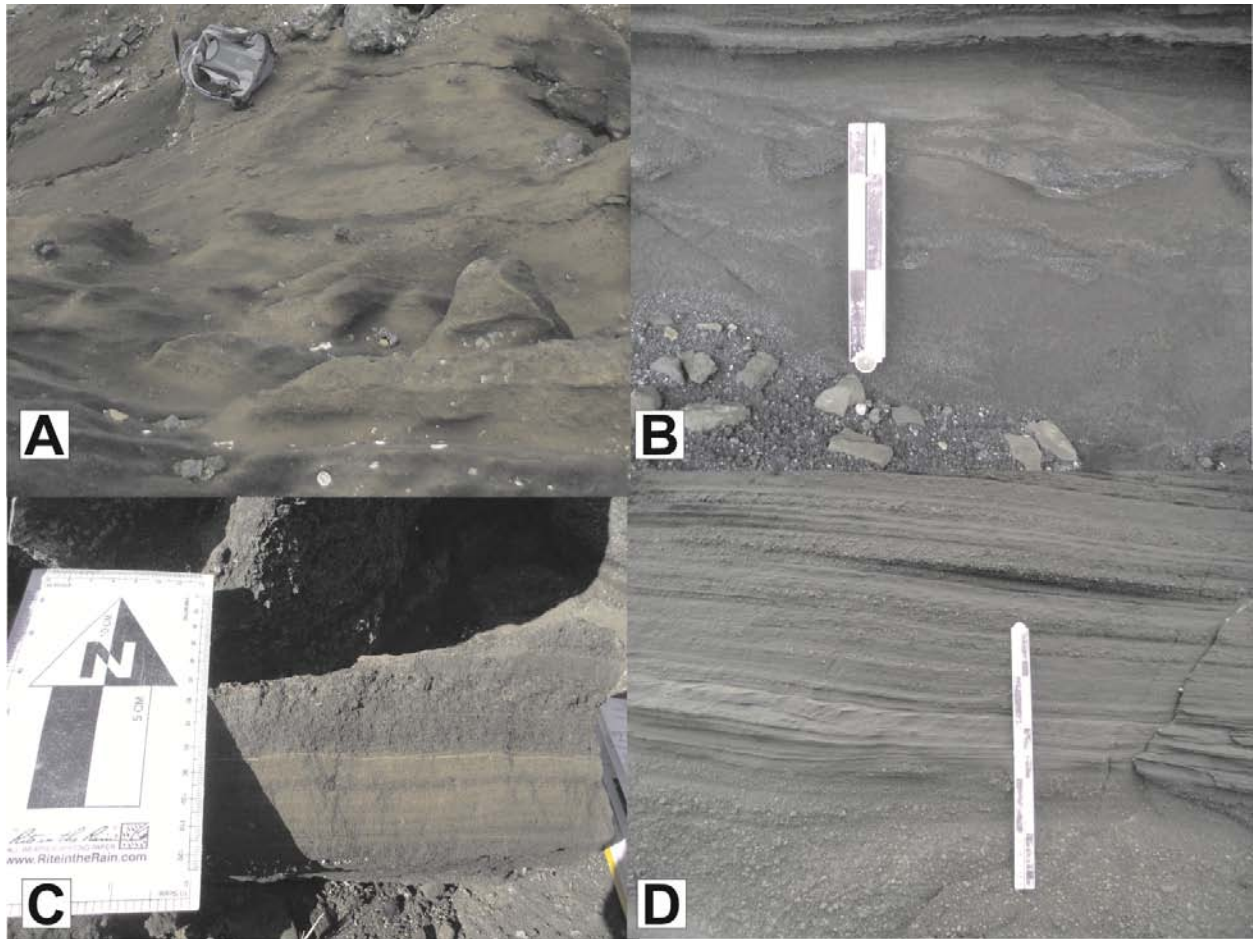


**Figure 2.14 Images of ash tuff lithofacies A) At1 massive coarse ash lapilli. Backpack for scale. B) At3 poorly sorted ash tuff with variable grain size concentrations. Loading structures are highlighted by the presence of lapilli. C) At2 laminated (mm scale) coarse and fine ash. D) At2 bedded (1-5 cm) coarse and fine ash.**



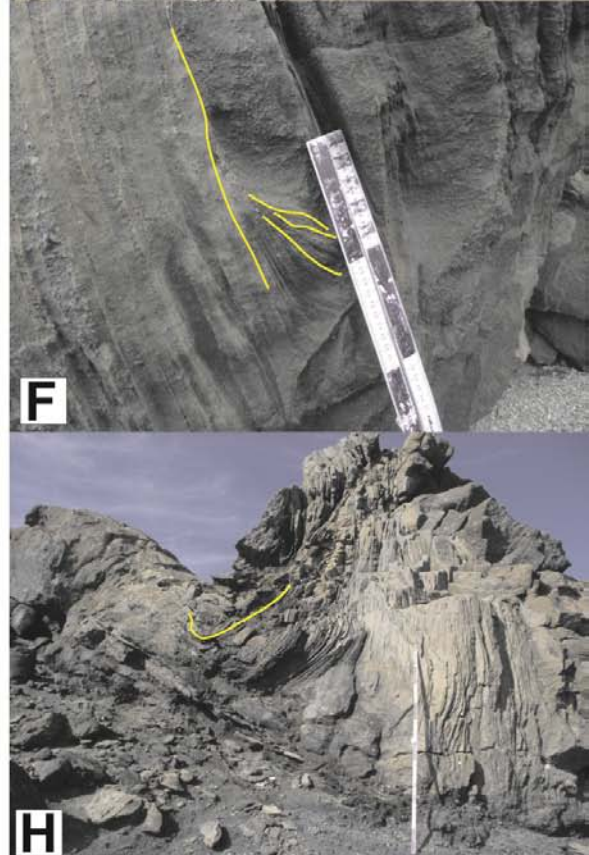
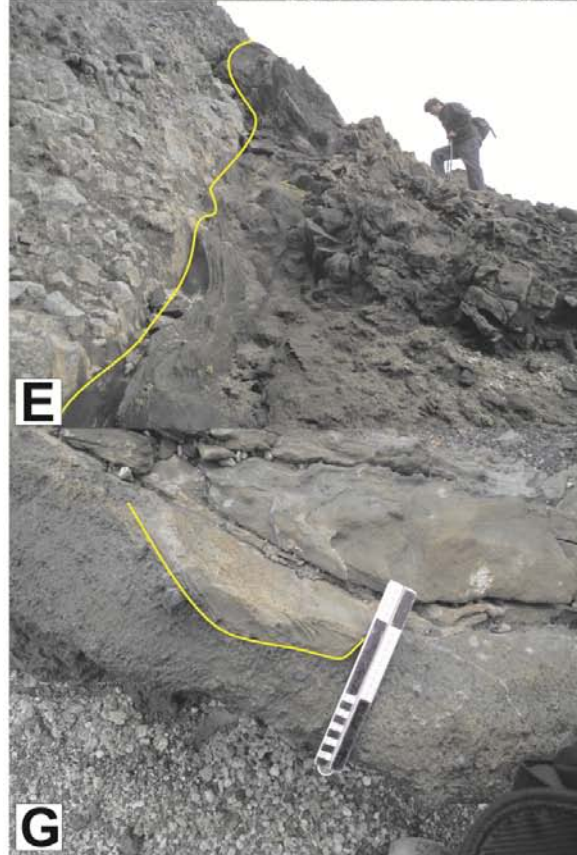


**Figure 2.15 Images of the At4 facies in deformed domains. A) The bedding angle changes from near horizontal to near vertical. B) Acute fold angles with a variety of grain sizes. C) Tight fold angles and convoluted bedding composed of coarse ash. D) Localized thickening of layers in fold. E) Steep contact with underlying breccia. F) Complex sedimentary structures (cross-bedding and channels) in steeply dipping domain. G) Disruption of underlying lapilli tuff unit by At4 deposits. H) Multiple directions of deformation. Large black sections on scale are 10 cm, small divisions are 1 cm. Yellow lines highlight bedding and contacts.**

### 2.2.5 Intrusions

Intrusions are a common, but a rarely-described feature at glaciovolcanic edifices (Edwards et al., 2009; Schopka et al., 2006). Three major types of basaltic intrusions were recognized at Austurfjöll including never-before described coherent-margined volcanoclastic dikes (CMVDs) (see Chapter 7) (Graettinger et al., 2012).

Typical tabular dikes (D1) are coherent and show no clear interaction with their host. The dikes are 5-100 cm across (Figure 2.16 A). Tabular dikes display a low vesicularity and may have centimeter-thick glassy chill margins. Macro-phenocryst populations range from 0-50%. A few porphyritic dikes have macrophenocrysts concentrations at the center of the dike. Pillowed intrusions (D2) are coherent dikes with irregular morphologies and pillowed margins. These intrusions are narrow and constrained, or occur in 2-4 m wide domains of fluidal and blocky peperite (Figure 2.16 B, C). Peperitic examples are less common, but have been described at Askja. CMVDs are dikes that display multiple continuous basaltic glassy coherent chill margins with very thin ( $< 3\text{mm}$ ) marginal peperite and a variety of vitriclastic interiors (Figure 2.16 D). Dike interiors can contain pillow chains, individual pillows, bomb and lapilli size fragments and coarse ash. No porphyritic equivalent of a CMVD has been observed. CMVDs occur clustered in a  $1\text{ km}^2$  area on Austurfjöll, but additional examples were documented over 17 km away in the western mountains of Askja (Chapter 7).



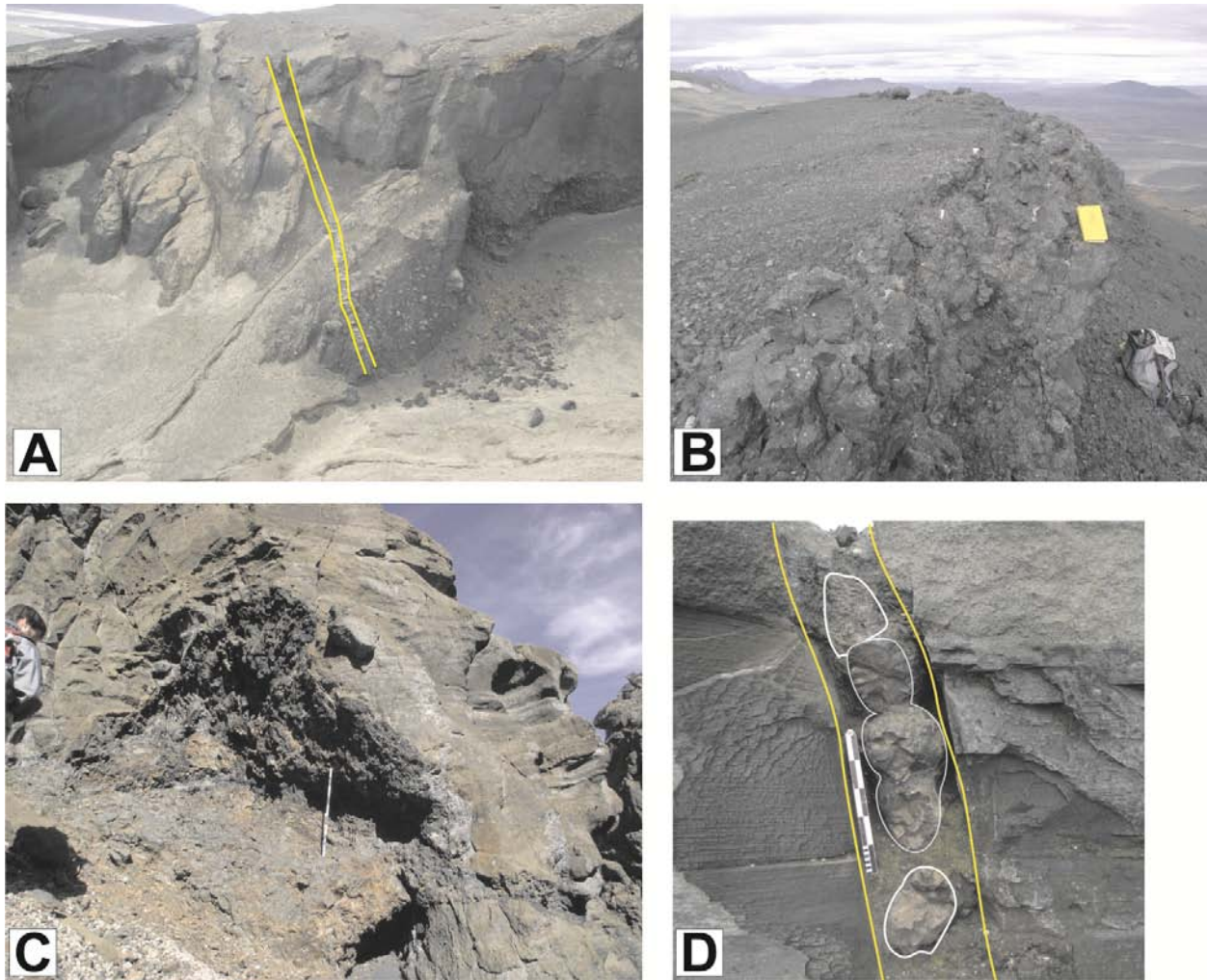


**Figure 2.16 Intrusion varieties documented at Austurfjöll. A) Tabular intrusions, D1, that cross-cut rock units with no interaction. Yellow lines indicate the outline of the dike. B) Pillowed intrusions that disrupt surrounding sediment D2 with notebook for scale. C) Intense deformation resulting from a pillowed intrusion with a meter stick for scale. D) CMVDs cross-cut rock units, but interact at the small scale of a 3 mm peperitic margin and internal peperite. Yellow lines indicate the margin of the dike and white lines outline pillows inside the dike.**

### 2.2.6 Xenoliths

Gabbro nodules occur as rounded blocks in lapilli tuffs and breccias at Austurfjöll above 1,000 m above sea level. These blocks are between 5 cm and 50 cm in diameter. They are holocrystalline phaneritic rocks dominated by clinopyroxene and plagioclase (Figure 2.17). They make up <1% of any given deposit, but are common at multiple elevations. Phenocrysts reach up to 2 cm in diameter. Individual nodules have variable concentrations of the two major minerals, which influences the relative color of the sample. Further discussion of the distribution of gabbro nodules occurs in Chapter 3.



**Figure 2.17** Examples of gabbro nodules. Samples were cut open for thin section and geochemical analysis. Nodules occurred in fragmental hosts, such as lapilli or ash tuff. Size range of nodules is a few centimeters (pictured) up to 0.7 m.



## 2.3 PETROGRAPHY

Thin sections were prepared from 245 samples of representative lithologies. 40% of the samples were of coherent materials. Petrographically the coherent (lava) samples can be divided into two groups to correspond with the observed lithofacies divisions, particularly subaerial and subaqueous divisions. Group one lavas occur in lithofacies groups L1 (subaqueous lavas), Pl1, Pl2 (pillowed lavas), D1 and D2 (intrusions). These lavas are all subaqueous, are fine-grained, vesicular, and display a microcrystalline groundmass dominated by plagioclase, clinopyroxene, and tachylite glass. This group also contains porphyritic samples with megacrysts (5-10 mm) of plagioclase and phenocrysts (0.1-2.0 mm) of clinopyroxene in the same microcrystalline groundmass as seen in the micro-porphyritic samples. Group two lavas occur in lithofacies L2 and are all subaerial fine-grained and dense lavas, dominated by < 0.1 mm microlites of oxides and plagioclase crystals. Porphyritic lavas in this group are less common, but still contain the distinctive quantities of opaque oxide minerals in addition to macrophenocrysts of plagioclase up to 2 cm. Approximately 7% of coherent lava samples contain olivine as minor (<5%) phenocrysts or macrophenocrysts.

Group one lavas and intrusions display rapid quench textures including spherulites, quench microlites, and skeletal crystals (Figure 2.18). The vesicle volume percent is on the order of 30%, and vesicles are typically irregular and show signs of coalescence and interaction with microlites. The vesicles are typically bimodal, with fine vesicles (ca. 0.1 mm) and large convoluted vesicles (ca. 1 mm). Dikes in this group have variable vesicularities (0-50%), but the crystalline groundmass is similar throughout (plagioclase and Cpx dominated) and phenocrysts are rare.

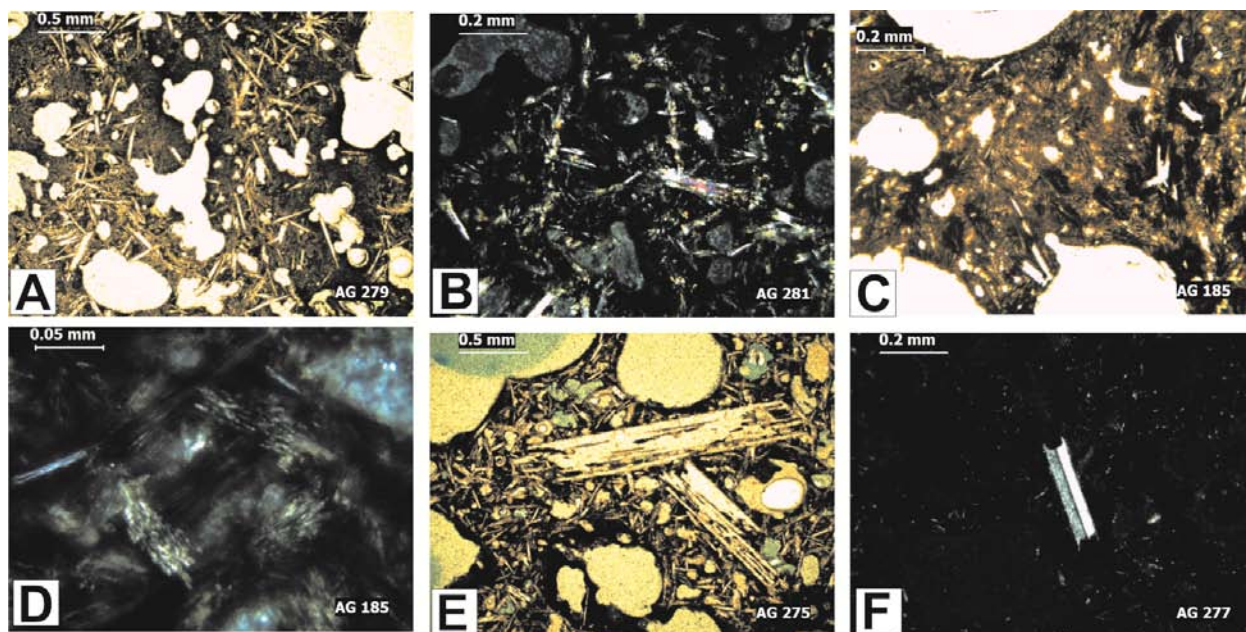


**Figure 2.18 Micro-porphyritic lava textures in thin section. A) Micro-phenocrysts of plagioclase dominate lavas and dikes in group one. Vesicles are typically irregular and coalescing. B) Cpx is common in the groundmass of these lavas, but typically does not exceed 30% by volume. C) Rapid quenching of crystals is evident in the spherulitic textures of the groundmass. D) Close up of quench crystals in tachylite glass groundmass. E) Skeletal growth structures in plagioclase feldspar. F) Swallow tail structure of plagioclase feldspar.**

L2 lavas are characterized by a nearly equant microlite groundmass with rare, if present isolated phenocrysts of plagioclase (Figure 2.19). Microphenocrysts of oxides and plagioclase dominate the texture of the groundmass. The phenocrysts typically have broken margins or anhedral shapes and compose less than 5% of the sample. Vesicles are rare (<15%) and where present less than 1 mm in diameter. Alteration of oxide minerals and Cpx can result in red staining of the hand sample or may be only visible in thin section. Rare examples of zeolites were observed in samples collected from the caldera wall.

Fragmental deposits have a far greater range in textures and can contain a greater diversity of components. These deposits include all of the breccia (B), lapilli tuff (Lt) and ash tuff (At) samples. The mineralogy remains limited to Cpx, plagioclase, and olivine. Oxide minerals occur in subaerially derived clasts, but not as independent grains. The fragmental deposits, including breccias, lapilli, and ash tuffs can contain components of coherent units, such as free crystals, sideromelane glass, tachylite glass, lithic fragments and altered glass (Figure 2.20). Breccia samples contain clasts that are indistinguishable from the lava units described above. Glass particles in thin sections are typically coarse to fine ash sized, and can have a range of morphologies and vesicularities. Characteristics such as sorting and particle size distribution vary widely between and within lithofacies. Lt1 is dominated by sideromelane glass, Lt2, At1, At2 and At3 contain up to 5% of tachylite glass and lithic components (distinguishable microcrystalline lava, porphyritic lava and free crystals in porphyritic examples). The diversity of components significantly increases in Lt3, Lt4, and At4 and includes a greater proportion of lithic fragments, and diversity of glass types. The degree of glass alteration also increases in these three facies. Detailed descriptions of glass particle morphology are presented in Chapter 6.

Diamictite deposits (Dia1 and Dia2) bear some similarities to the subaqueous fragmental tuff deposits. They are distinguished in thin section by the dominance of crystals with mechanically broken faces, the diversity of componentry, and the occurrence of rounded ash particles. Without field and hand sample-scale evidence, these samples could be confused with heterolithic tuff (Lt4) samples.

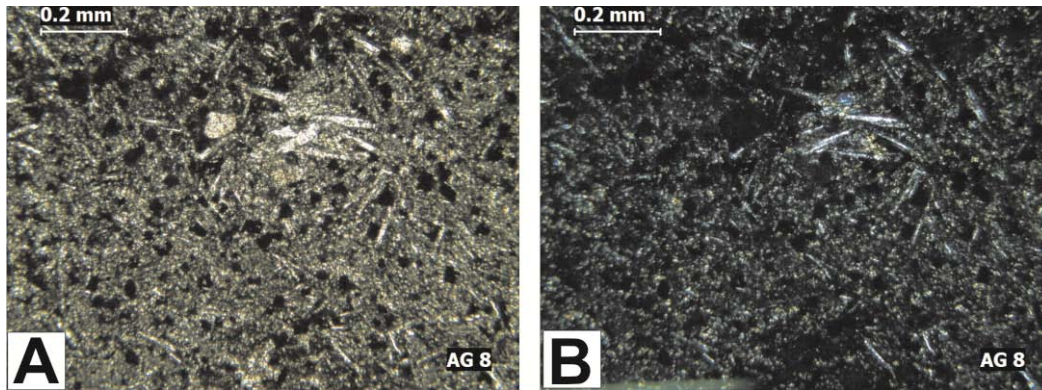


**Figure 2.19 Petrographic images of subaerial lava samples. A) Plane polarized light (PPL) reveals the abundance of opaque oxide minerals. Plagioclase micro-phenocrysts are common with a microcrystalline groundmass. B) Cross-polarized light reveals the Cpx crystals that typically occur in glomerocrysts with feldspar.**

Macro-phenocrysts of all lithofacies are complex crystals that may be isolated or occur in glomerocrysts. Zoning and multiple growth histories dominate the structure of plagioclase crystals (Figure 2.21). Inclusions of plagioclase and Cpx also occur within the largest plagioclase crystals. Gabbro samples contain large convoluted crystals of plagioclase with intersertal Cpx, and rare (<5%) olivine. Full detailed descriptions of all of the samples occur in Appendix A (Table A.1). The crystals observed in porphyritic lava and lapilli samples share many of the textural characteristics with those found in the gabbros.



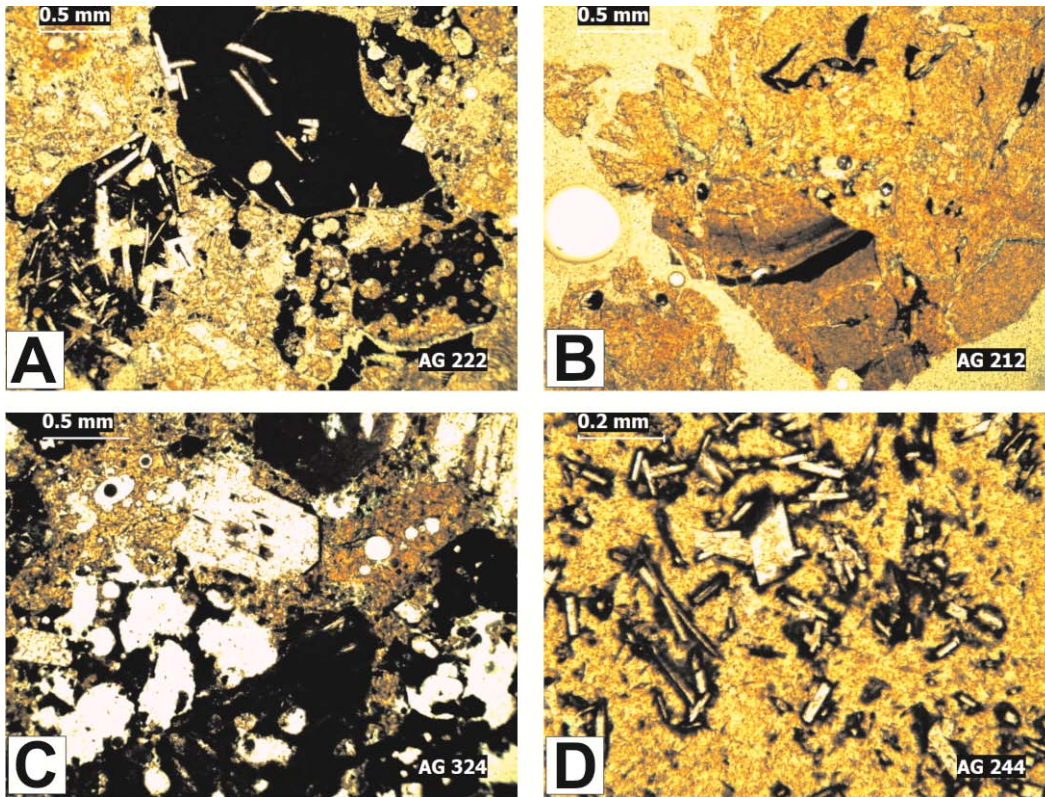


**Figure 2.20 Petrographic images showing the diversity of clast types in fragmental deposits. A) Tachylite glass may occur with or without visible crystals or with or without vesicles. B) Sideromelane glass dominates most fragmental deposits, but some tachylite may be present along the margins or within sideromelane fragments. C) Large free phenocrysts can occur with or without glass rims. C) Sideromelane glass can be crystal-free or crystal-rich. In some cases the presence of micro-phenocrysts is highlighted by radial alteration.**



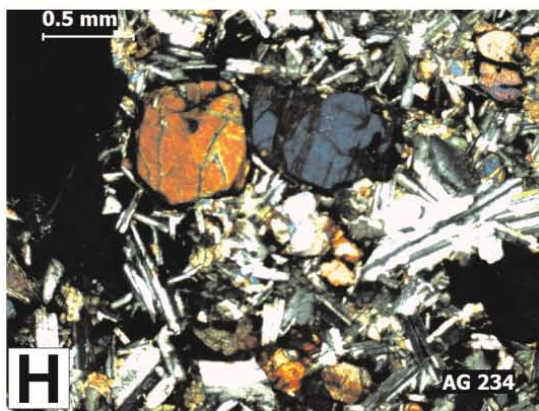
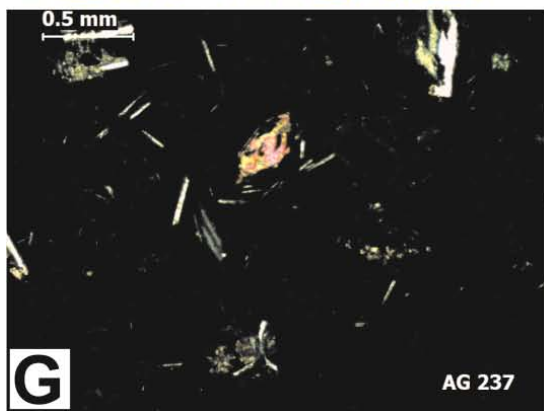
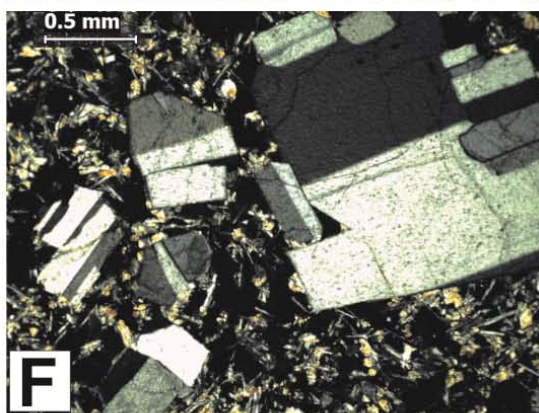
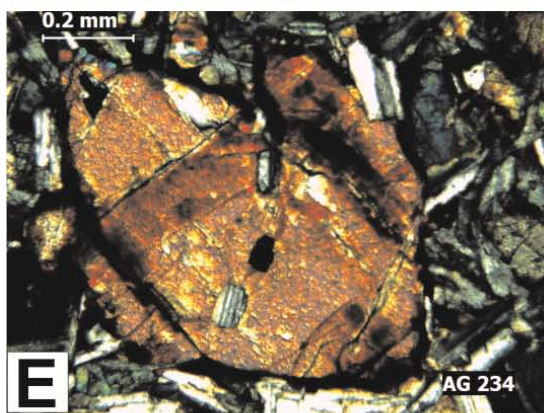
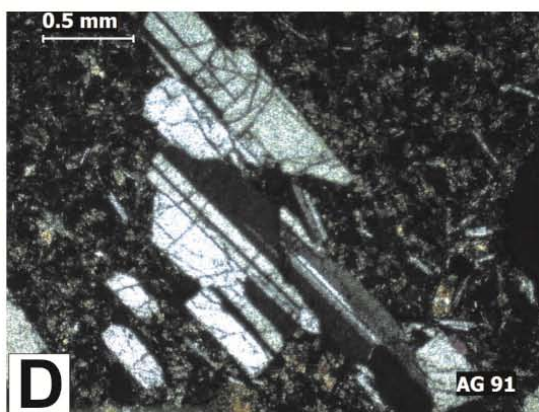
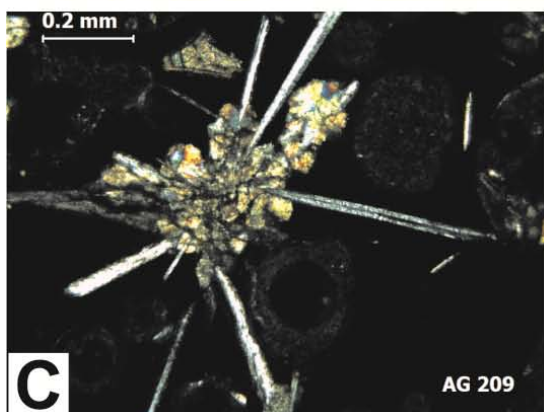
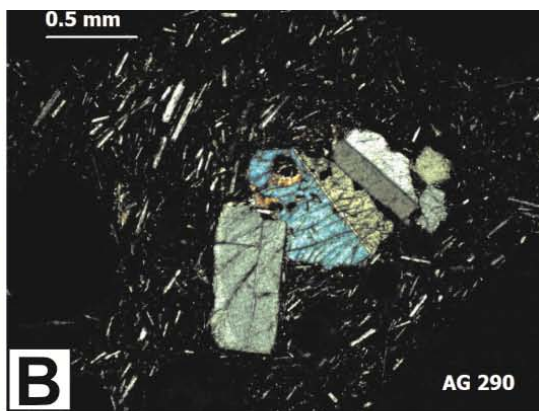
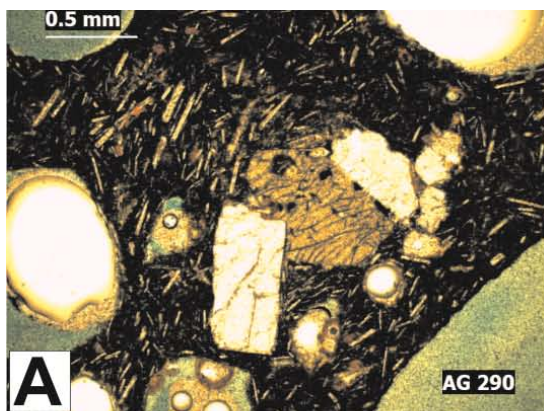


**Figure 2.21 Petrographic images of phenocrysts present in porphyritic lithofacies and gabbro nodules. A) PPL image of clustered phenocrysts of plagioclase and Cpx. This clustering also increases the visibility of phenocrysts in porphyritic units. B) Cross-polarized image of the same crystals as in previous image, but better highlighting the interaction between phenocrysts and the groundmass. C) Glomerocrysts are common in porphyritic rocks, and typically have Cpx near their core. Plagioclase crystals may be radial, or large and blocky. D) Plagioclase phenocrysts are frequently twinned, and have complicated growth histories. Mechanically broken crystals are common in many samples, but are not the norm. E) Large phenocrysts of Cpx are also common. Inclusions of plagioclase or Cpx may occur in either species. F) Plagioclase crystal cluster showing a seed crystal of plagioclase and disrupted twins. G) An example of the rare olivine that can occur as a phenocryst or groundmass constituent. H) Example of a gabbro nodule with large phenocrysts of plagioclase and Cpx. Glomerocrysts are common, and intersertal textures are also common.**

## **2.4 STRUCTURE AND VENTS**

Where bedding was present the orientation was measured and the distribution of these measurements plotted (Figure 2.22). Bedding typically can be traced for tens of meters and was observed predominantly in At2, At3, At4 and Lt2 deposits and their porphyritic counterparts. The orientation of the beds are strongly controlled by local features, but near the caldera rim most of the beds dip away radially from the caldera. The regional structure as identified through lineament presence (Figure 2.23) is based on aerial photos and previous studies of the region (Annertz et al., 1985; Hjartardóttir et al., 2009). A study of the tectonic lineaments within the Askja region conducted by Hjartardóttir et al. (2009) revealed that the dominant strike of lineaments was between 0-40° with longer features being more constrained to 10-30°. Their study area included Askja's 1929 lava flows at the southern most mapped unit and extended north towards Herdubreidarfjöll. The trend of tectonic lineaments becomes more northerly in orientation in the northeastern portion of the study area (Einarsson, 2008). The region around Askja area represents a

reorientation of the MAR north of the oblique Eastern Volcanic Zone, where it becomes covered by the Vatnajökull glacier. Portions of the Askja caldera show a strong tectonic influence, displaying a straight rather than curved morphology (Hjartardóttir et al., 2009). The number of lineaments that can be mapped significantly decreases within the Askja volcanic complex, but the influence of the tectonic regime is still evident. The most prominent faults, which interact with Austurfjöll and Thorvaldstindur, are the young caldera faults of Öskjuvatn that occur as steep cliffs along the modern lake.

Vent positions were determined using a combination of structural data, aerial photographs, a 10 m DEM, and field relationships. Three classes of vents were identified based on the confidence of the identification from highest to lowest: field relationships, topography, and speculative. The number and dimensions of the vents were measured to determine what, if any, trends in vent formation were present and the potential impact of erosion on the preservation of such features. Vents are described using a combination of field evidence, topographic evidence, and speculation based on the distribution of deposits. Due to limited exposure, burial by younger deposits, and erosion, this is likely an underestimation of the total presence of vents within the field area, and should be treated as a minimum (Figure 2.24). The orientation of the vents is semi-concentric relative to the position of the Askja caldera. Vent orientations show some correlation with fault and lineament maps compiled from the literature and aerial photos. Vents are predominantly oriented with a strike of  $50^{\circ}$ .



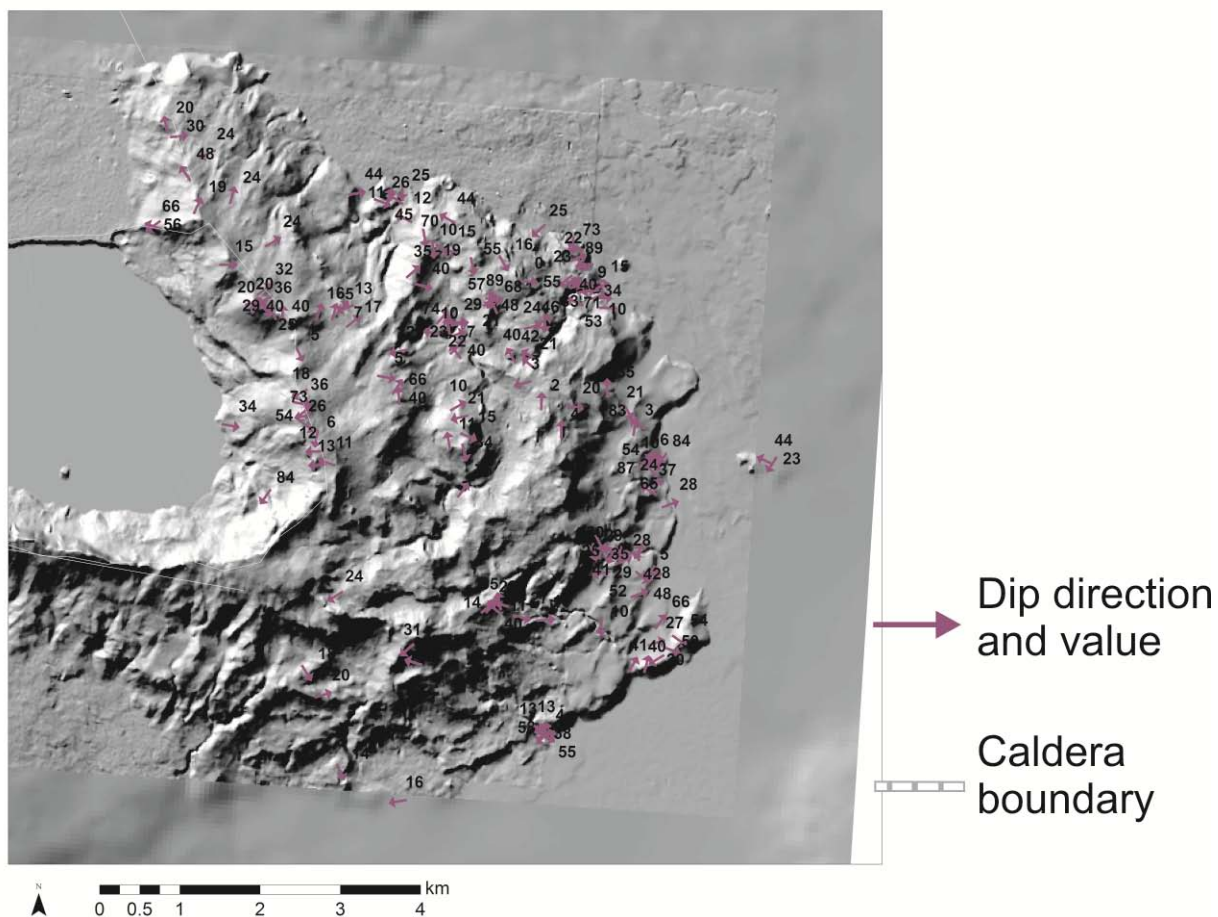


**Figure 2.22 Hillshade of Austurfjöll showing dip measurements with arrows indicating the direction of dip. There is significant variation, but 35% of major bedded units dip away from the caldera at the rim indicating a potential missing source in what is now Öskjuvatn caldera. Background hillshade based on 10 m DEM produced by LoftMyndir.**

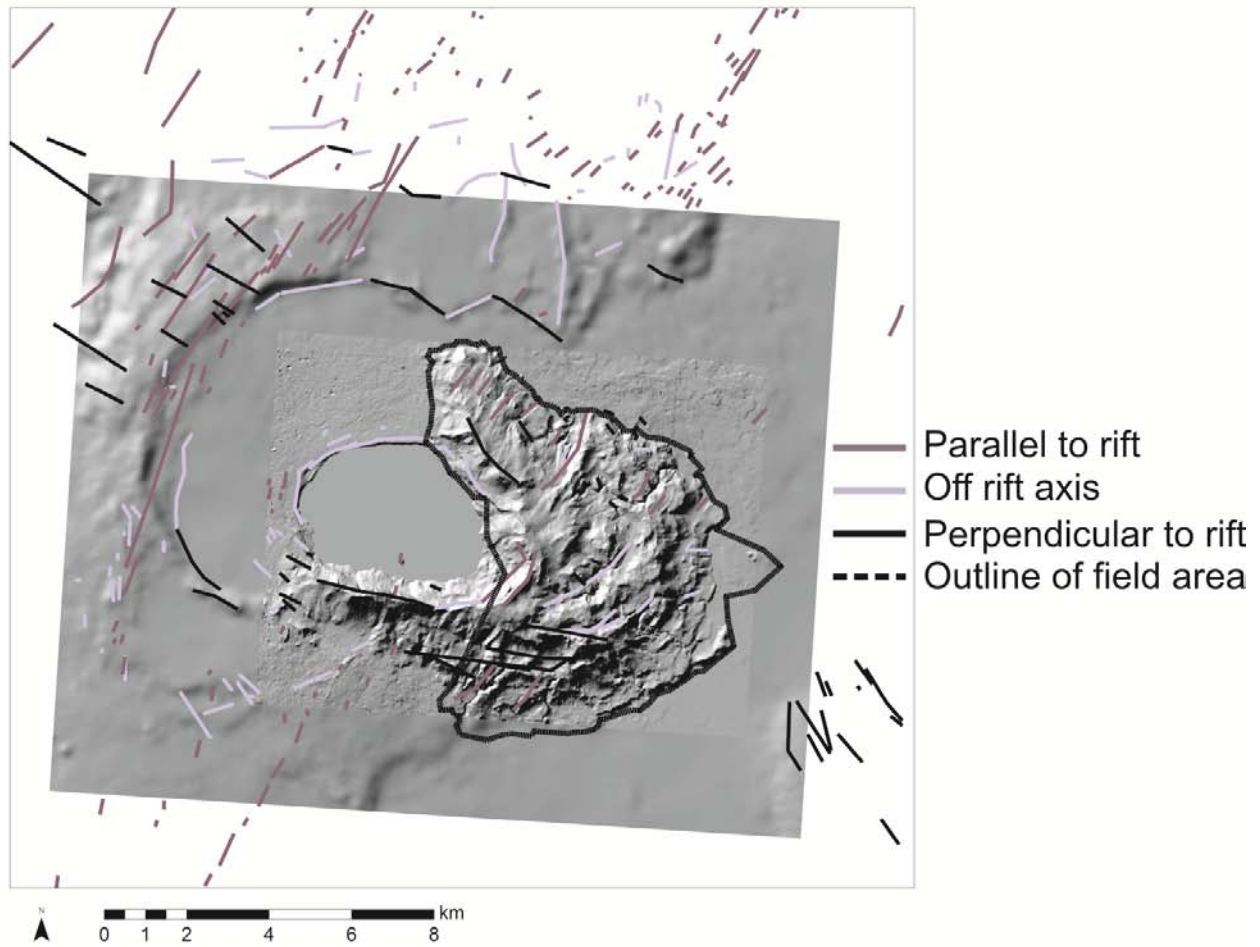


**Figure 2.23 Summary of tectonic lineaments from Hjartardottir et al. (2009) and Annertz (1985). Background image is a hillshade created from 10 m DEM produced by LoftMyndir.**

Field described vents are well constrained and may include a feeder dike and strong correlation with dipping beds away from the vent location. Of the vents that occur in Figure 2.24, 45% are defined based on field relationships. Topographic vents are resistant ridges that likely are reinforced by a feeder dike and have a relative elevation higher than surrounding deposits. Topographic vents make up 18% of the vents identified. Speculative vents were identified through a variety of methods, including extrapolation from incomplete beds and fragmental deposits dipping away from the caldera (Figure 2.25), and significant volumes of effusive deposits with no obvious vent (due to poor exposure erosion etc.). Some speculative vents are associated with lineations identified in this study and (Hjartardóttir et al., 2009). Speculative vents represent 37% of the vents identified.

Average vent size is on the order of 300 m long and up to 50 m tall. There are two vents identified through field relationships as up to 600 m in length representing the maximum vent size for the massif (Figure 2.26). Erosion is potentially a contributor to the variety of vent size, but the variability is diverse enough to suggest that vents were fissures, but were subject to processes that constrained the eruption to more limited vent areas. Each preserved vent likely represents a portion of a fissure, and is dominated by the final morphology of the vent (Table 2.2).



**Figure 2.24 Example of incomplete dipping beds at the caldera rim. White lines highlight a package of sediments and the orientation of bedding.**

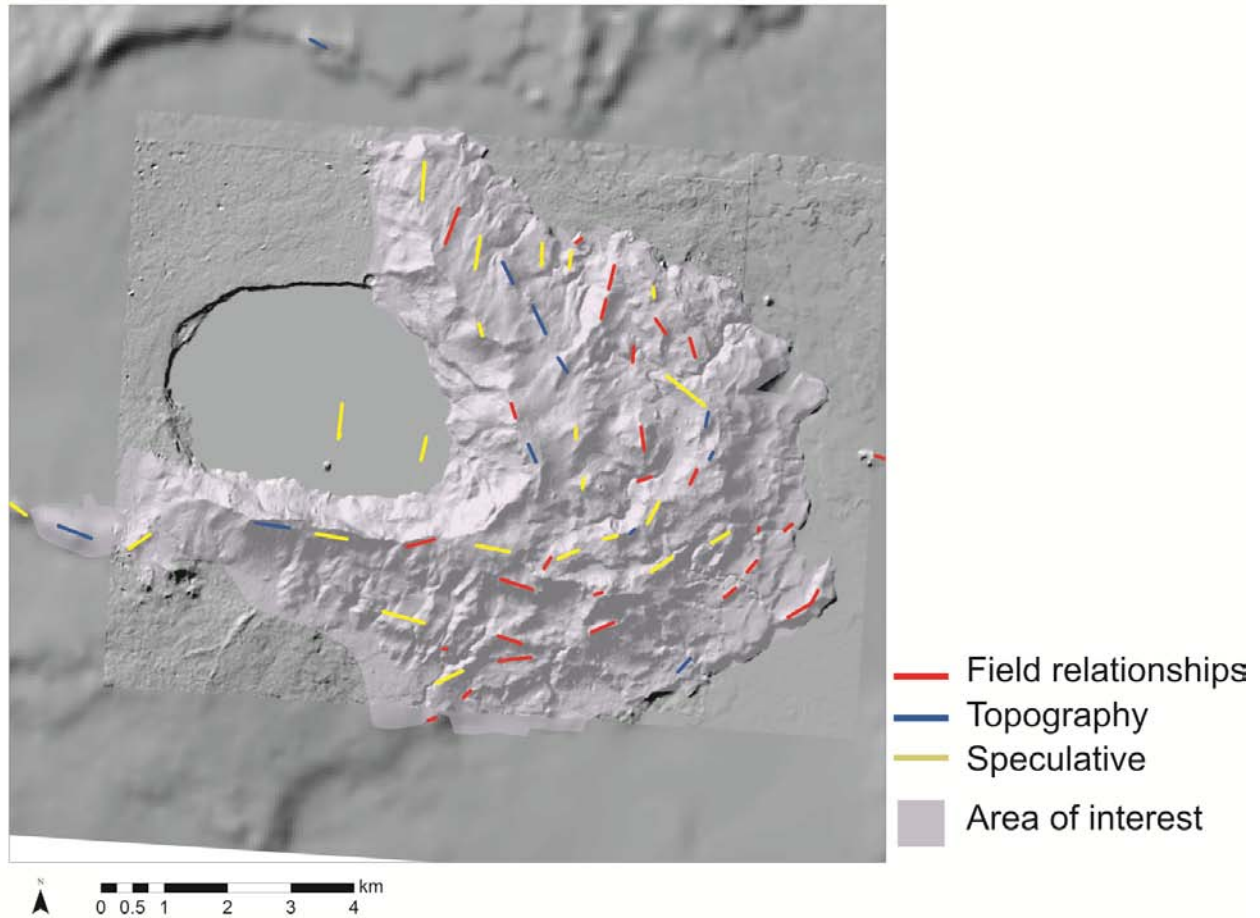


**Figure 2.25 Location of vents in Austurfjöll and Thorvaldstindur. Vents are divided into three categories based on method of identification. These categories also imply relative confidence: field relationships (well defined high confidence), vents topographic (moderately well defined, moderate confidence), speculative are implied through deposit distribution (not well constrained, low confidence). The image is overlain on a hillshade produced by LoftMyndir.**

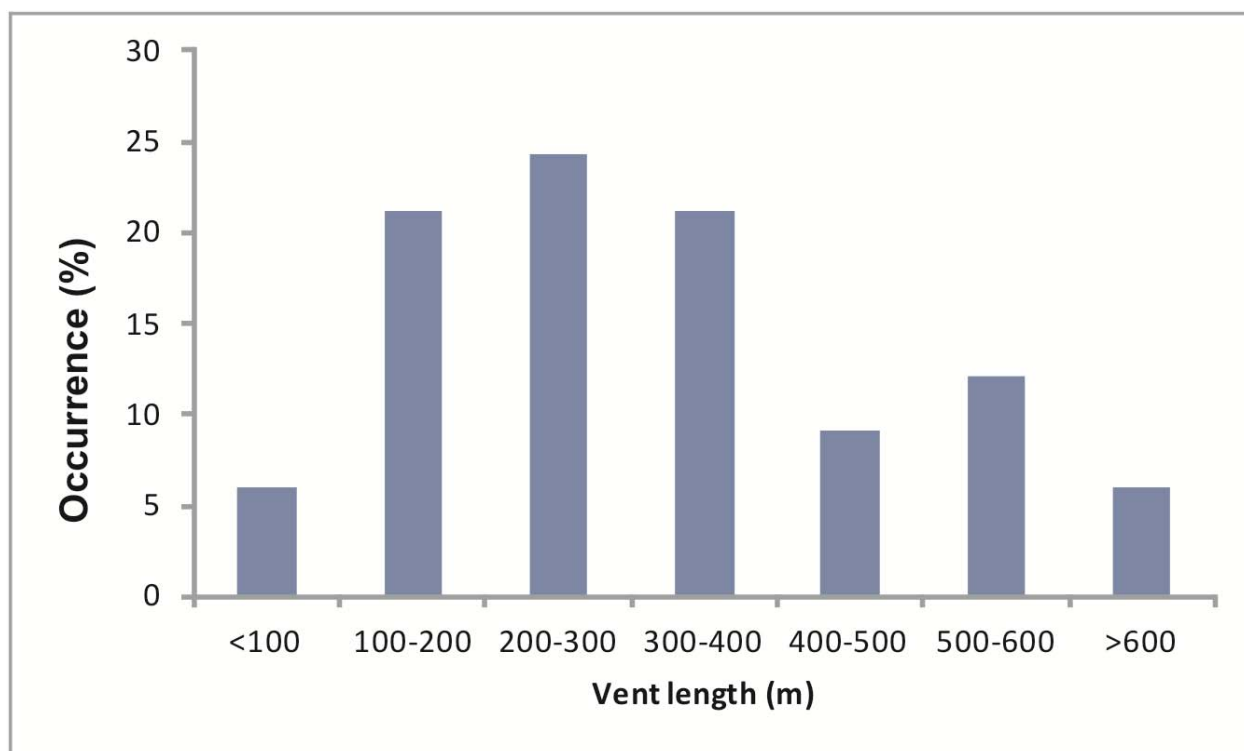


Figure 2.26 Histogram showing relative abundance of vent length as measured from Figure 2.22.

Table 2.2 Statistics pertaining to eruptive vents in Austurfjöll massif.

	Field relationships	Topography	Speculative	Average
<b>Length (m)</b>	264	131	434	300
<b>Orientation (°)</b>	63	47	57	50
<b>Number</b>	27	11	22	n/a
<b>Percent of total (%)</b>	45	18	37	n/a
Regional orientation of fissures is between 40 (Hjartardottir et al. 2009).				

The orientation and structure of the calderas themselves are influenced by the local tectonic influence of the MAR. Askja caldera is dominated by unusually straight fault segments (Hjartardóttir et al., 2009), and the direction of elongation in the Askja caldera is consistent with the direction of rifting. The northern caldera, not well defined or studied has an apparent NE elongation, parallel to the rift. As the elongation of the oldest described caldera is not the result of actual spreading it can then be concluded that Askja, a younger caldera, is merely exploiting the presence of long parallel to rifting transform faults, rather than being deformed by extension. The Öskjuvatn caldera outline mimics that of the Askja caldera, again supporting the opportunistic orientations of the caldera and not deformation of the calderas due to plate motions. Additionally, if the spreading rate of 18-20 mm/year (Einarsson, 2008; Pedersen et al., 2009) were extended over the period since the formation of Askja caldera (<10 ka) the feature would have expanded at most 200 m, which is only 1/10 of the apparent distortion of the caldera. As such the caldera faults are exploiting existing tectonics.

The Austurfjöll fissures are also considered to be the product of local tectonics, complicated locally by the presence of earlier deposits related to the growth of the massif. The distribution of these vents is not consistent across the massif. Along the southern extension of Thorvaldstindur into Austurfjöll, there is a distinctive west-east trend that is perpendicular to the regional rift. This is the same orientation as numerous transform faults that occur along the NVZ portion of the rift (Sigvaldason, 2002). Vent through the central portion of the Austurfjöll massif are oriented in a more north-south orientation, with some fissures orientated parallel to the rift orientation, and others as much as 20-30° towards the west. The northernmost segment of the massif is dominated by rift parallel oriented vents.

The combined lineament identification, new structural data, and field evidence are useful tools to constrain the relative ages of the caldera and the development of Askja volcano, including the Pleistocene glaciovolcanic deposits. Öskjuvatn caldera has dominant steep sided boundary faults, which exhibits modern mass wasting of glaciovolcanic material into the lake. In comparison, steep caldera boundary faults of Askja caldera can easily identified only in the western portion of the caldera where it clearly cuts some subaerial unconfined postglacial lavas, and is locally overtopped by others (Figure 2.27). Just north

of Öskjuop a pile of isolated glaciovolcanic deposits are cross-cut by the Askja caldera boundary fault and now dips away from the caldera center. Along the main Austurfjöll massif most of the western boundary is disrupted by Öskjuvatn caldera or covered by historic 1960's lavas and Holocene spatter. Between the northernmost 1920's lava flow known as Båtshraun and the 1960's eruptive fissure there are local outcrops of subaerial and subaqueous lava flows that have dips on the order of 10-20° that are directed east-northeast, away from the Askja caldera. This is the only location where there is no influence of Öskjuvatn faulting within the Askja caldera along the Austurfjöll massif. This suggests then that the beds were cut by the Askja caldera, not emplaced into an existing depression that would result in bedding orientations that dip into the caldera. This helps support a young Holocene age for the Askja caldera. There are, however, some evidences that the Askja caldera extends further to the east, than the line proposed here, mainly as a result of the apparent continuation of steep faults along the northern boundary of Öskjuop. If the margin of the caldera were to then follow from this furthest extension of the potential caldera it would have to intersect with a larger portion of the Austurfjöll massif. However, no significant areas of faulting can be identified in the field area. This would then suggest that if this fault is part of a caldera this feature would likely predate Askja due to the lack of morphological expression. Caldera 3 to the north is defined by a curvilinear feature of glaciovolcanic deposits (Norðurfjöll) and is predominantly covered by postglacial lavas. There is no obvious feature of this caldera within the Austurfjöll massif, which may suggest that the Norðurfjöll caldera predates the eruption of the Austurfjöll glaciovolcanics. Further investigation of the glaciovolcanic deposits along the caldera rim, briefly studied by Strand (1987) would be necessary to further constrain the time of the formation of the northernmost caldera.



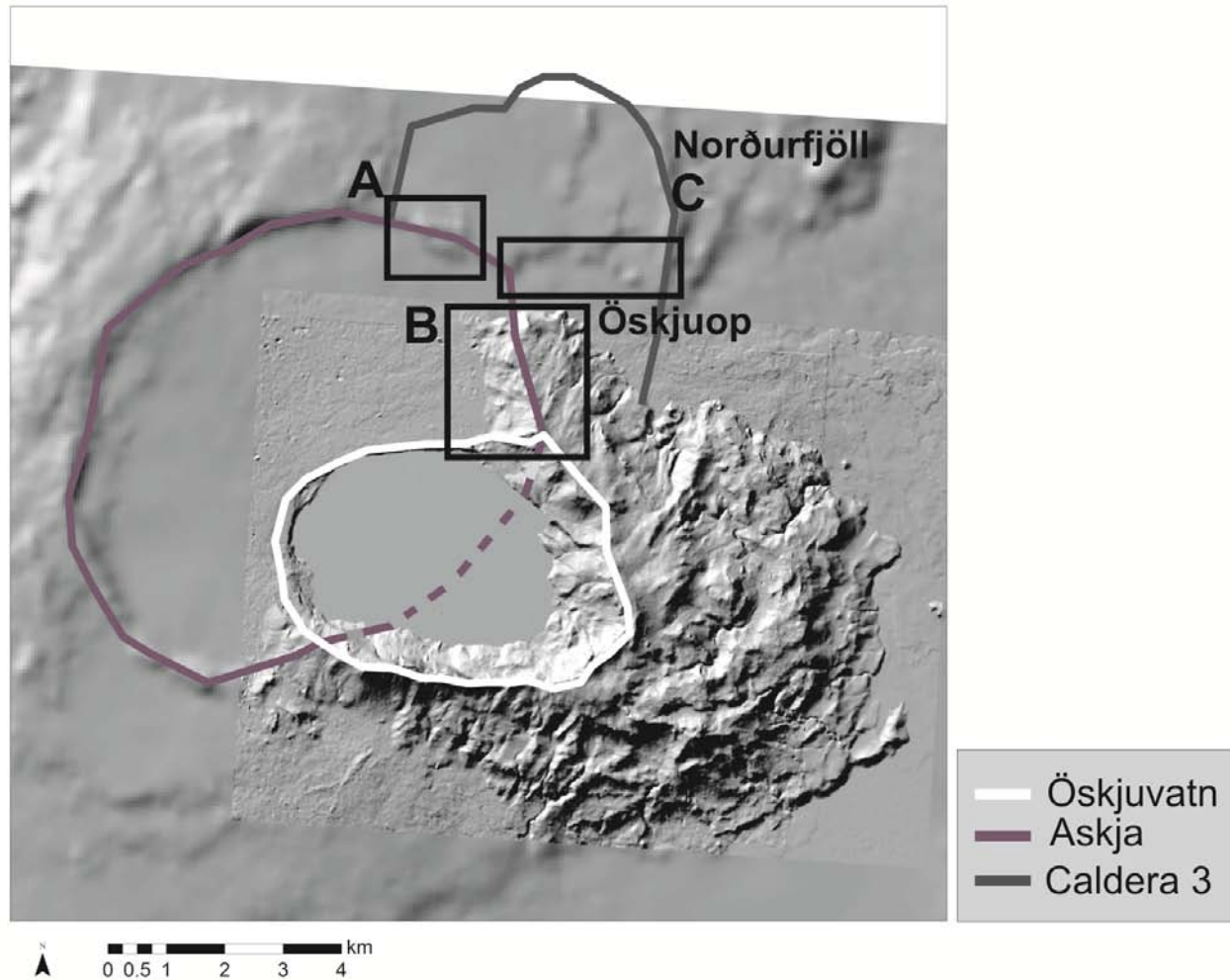


**Figure 2.27** Caldera outlines as they are currently proposed including evidence for the interaction with Austurfjöll massif. Black outlines focus on key locations that indicate the interaction of Askja caldera and glaciovolcanic deposits. A) Location of glaciovolcanic deposits cut by Askja caldera. B) Location of glaciovolcanic beds dipping away from caldera cut by Askja caldera and not overprinted by Öskjuvatn. C) Potential continuation of Askja caldera fault within Öskjuop. This location requires further investigation to resolve this age relationship.

## 2.5 INTERPRETATION OF LITHOFACIES

The lithofacies map presented here (Figure 2.2) contains more complexity than the original maps by Sigvaldason (1968) and Strand (1987) (Figure 2.28 and 2.29). In particular the previous maps do not include any facies with subaerially derived or emplaced components, and while intrusions were noted, they were not included in the earlier maps. The map by Sigvaldason has major outcrops of porphyritic units in similar, but smaller distributions than presented here. The Strand (1987) map includes crystal bearing units, which correspond to Lt4, heterolithic tuff facies along the caldera rim of the map presented here, but does not include the porphyritic units further to the east. Additionally, the Strand (1987) map assigns glaciovolcanic lithofacies to historic basaltic tuff cone deposits along Öskjuvatn caldera (Carey et al., 2010). What is most important about the Strand (1987) map is the mapping of basaltic glaciovolcanic units in Norðurfjöll and the western mountains.

The lithofacies in this study are interpreted based on the textural and petrographic characteristics and stratigraphic positions. The bulk of lavas described are subaqueous in nature (P11, P12 and L1) and displayed pillow morphologies, entablature fracturing, and/or thick chill rinds typical of subaqueous lavas (Dimroth et al., 1978; Goto and McPhie, 2004; Gregg and Fink, 1995; Kennish and Lutz, 1998; Smellie and Hole, 1997; Tucker and Scott, 2009). Pillow lavas represent a low effusion rate (P11 and P12) and sheet lavas (L1) represent higher effusion rate subaqueous lavas (Gregg and Fink, 1995; Gregg and Smith, 2003; Parfitt et al., 2002). The P12 lavas are interpreted to represent an end-member of pillow style effusion, where a minor increase in eruption rate results in the development of transitional textures such as localized lobe formation and entablature jointing. Pillow lavas are a convenient indicator of subaqueous conditions and form a significant portion of the massif up to 1300 m above sea level.

The two pillow lithofacies groups P11 and P12 can occur in two types of morphology, namely pillow mounds and pillow sheets, and both lithofacies can occur in both morphologies. P12 lavas are interpreted to form where the eruption rate, as influenced by flux rate or topography, exceeds that of the average P11 range and results in local transitions to lobate flow characteristics including large irregular

pillows and blocky jointing. Large pillow sheets containing both P11 and P12 lavas form the base of the southeastern massif. Pillow sheets contain pillow lavas and breccias in localized laterally discontinuous packets. The pillow lavas are subject to significant auto-brecciation and collapse during eruption from a fissure or point source (Carlisle, 1963; Edwards et al., 2009; Walker, 1992). As the eruption continues more pillow flows are formed and interact with existing and developing pillow flows. The presence of vertical pillows within some pillow sheet flows indicates the interaction of moving pillowed lavas with steep topography such as previous flow fronts. This aggregation of individual flows an extended period of effusive fissure activity develops a broad sheet morphology with complex internal structures. These sheets are interpreted to represent long eruptions from fissures that contributed significantly to edifice growth.

Pillow lava mounds represent smaller discrete eruptions of pillow lavas from fissures that are not confined and may exploit paleo-slopes to spread out. The smaller pillow mounds mantle topography and create local hillocks, but do not significantly alter the topography of the construct. Both pillow lava sheets and pillow mounds may be mantled by At4 deformed sediment packets. This indicates that pillow lavas are frequently buried by later ash deposits that are likely not related to the eruption that formed the pillow lavas. The dominance of ash, rather than lapilli, within these mantling deposits may be indicative of the distance of emplacement from the source vent, supporting an interpretation of long transport and remobilization of deposits from eruptions from different vents than the mounds. In the case of pillow sheets, the sheet-like geomorphology is enhanced by infill by At4 and local deposits of other ash and lapilli tuff deposits. At4 deposits frequently dip away from the margins of P11 and P12 lavas within the pillow sheet unit, highlighting former flow boundaries.

Pillow size has been attributed to lava viscosity, where larger pillows form as viscosity increases (Walker, 1992). On average the Austurfjöll porphyritic pillows have a larger cross-sectional diameter than micro-porphyritic pillows. Specifically, the minimum porphyritic pillow size measured is 30 cm in diameter, but only 4.5 cm for micro-porphyritic pillow lavas. There is, however, no correlation between phenocryst abundance and the morphology of the overall flow or the lithofacies assignment (P11, P12),

and vesicularity remains similar for both facies. This then suggests that while pillow size may be controlled by viscosity and crystal content, the changes in morphology are dependent on the volume and lava-supply rate, rather than rheological limitations (Walker, 1992).

The subaerial L2 lavas predominantly occur below the subaqueous sequence and are locally covered by Dia2 displaying an a'a morphology. A'a lavas are common in Icelandic fissure fields, but are not typical of shield building eruptions (Andrew and Gudmundsson, 2007). L2 lavas below 800 m asl are thus interpreted as the result of localized unconfined fissure eruptions that preceded the onset of glacial activity. Localized L2 lavas were observed at higher elevations (200-650 m above local base level) on the caldera rim, with lateral extents of less than 10 m. These lavas also have a'a morphologies and the isolated distribution of the deposits suggest that they are the product of fissure eruptions, from a vent which was located in what is now Öskjuvatn caldera. One example of L2 lavas was observed just above 800 m asl that transition laterally and are overtopped by pillow lavas. These two outcrops will be discussed further for their environmental indicators in Chapter 8.

The rhyolite domes (R1) noted in the caldera wall are poorly exposed and their origin remains uncertain (McGarvie, 2009). The important features of the rhyolite dome is that it does not disrupt the overlying basaltic subaqueous and emergent deposits indicating that it is not intrusive in origin. This also indicates they are older than the uppermost Austurfjöll deposits, but the relationship to deposits lower in the sequence remains unknown due to significant cover by slumps and talus. Rhyolite-cored bombs found in upper Austurfjöll deposits suggest that some basaltic glaciovolcanic vents occurred in the region of the rhyolite dome to enable the incorporation of accidental lithics of rhyolite in basaltic bombs during eruption.

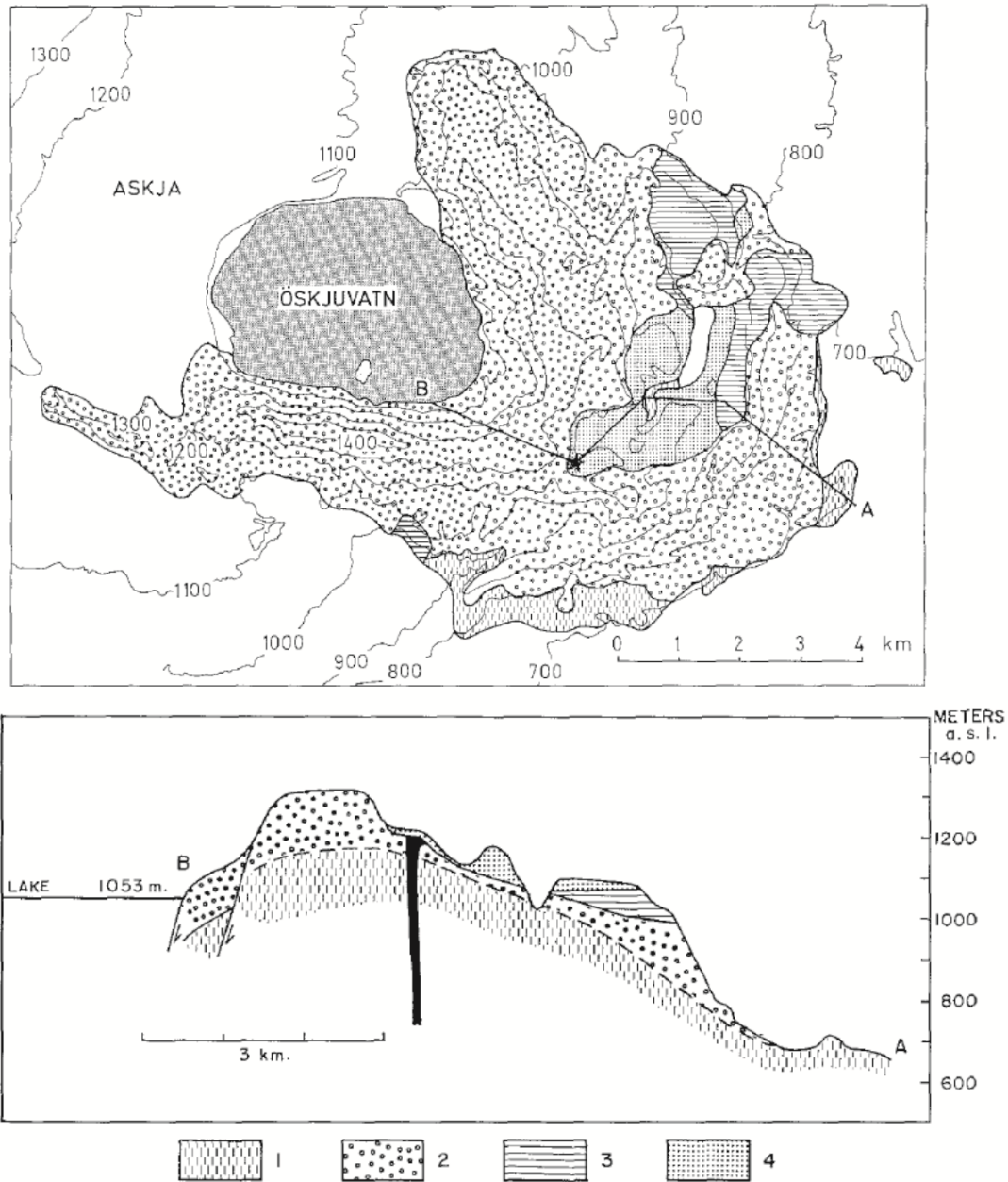


**Figure 2.28 Map of Austurfjöll by Sigvaldason (1968) showing four units. Key for map and cross-section are the same. Unit 1 is non-porphyritic pillowed lavas. Unit 2 is non-porphyritic fragmental deposits. Unit 3 is porphyritic pillowed lava. Unit 4 is porphyritic fragmental deposits.**

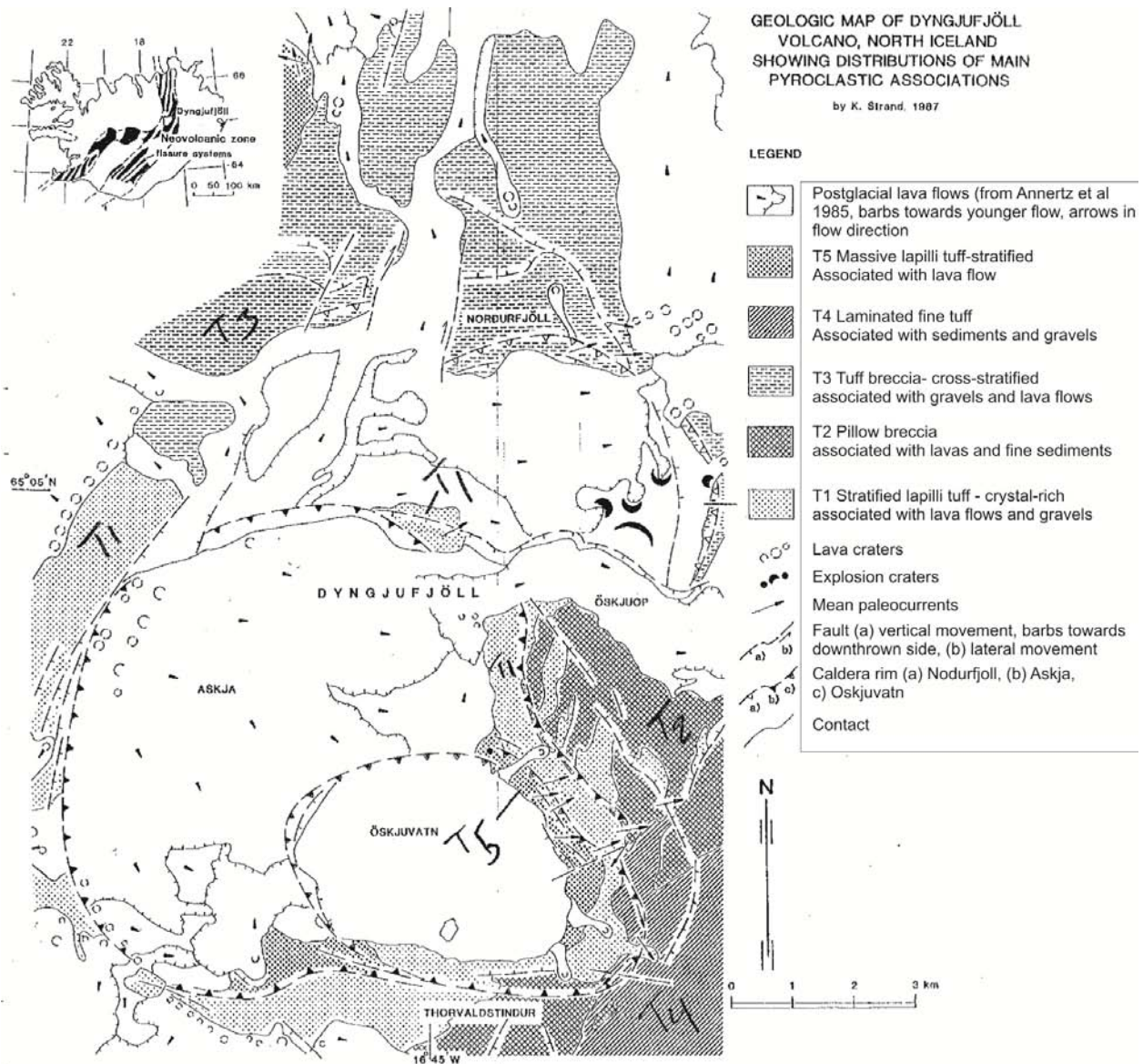


**Figure 2.29 Map of Askja including Austurfjöll by Strand (1987) showing five lithofacies associations. The margins of Austurfjöll are not included, but porphyritic units and pillow lava sheet flows are notably absent.**

**Mapped units along the caldera lake margin are currently covered by 1875 basaltic tuff cone, rhyolitic pumice and talus which may have been locally mistaken for glaciovolcanic deposits due to basaltic compositions.**

Breccias are a common feature in and around subaqueous lava flows in a variety of eruptive conditions. There are many mechanisms of producing clast-supported breccias including (Figure 2.30): collapse, flow-generated breccias, explosion, and disruption by intrusions (peperite formation or destabilization) (Carlisle, 1963; Dimroth et al., 1978; Edwards et al., 2009; Loughlin, 2002; Mercurio, 2011; Sansone and Smith, 2006; Skilling, 2009; Tucker and Scott, 2009; Vezzoli et al., 2008). The nature of the clasts in conjunction with field relationships helps divide explosive, intrusive and gravitationally-derived breccias. In Austurfjöll breccias were texturally similar in terms of clast-support, diversity of clasts, and deposit thickness. The greatest difference between the breccias (B1, B2 and B3) is the morphology and therefore origin of the clasts within the breccia. B1 breccias contain unequivocal clasts of intact and fractured pillows and in some cases fluidal bombs. In contrast B2 and B3 are associated with angular blocks that may be of ballistic or gravitational origin. Blocks in B3 are distinguished as pieces of broken subaerial lava, with oxidation staining and occasional scoriaceous textures.

To interpret the three groups of breccias identified at Austurfjöll the field relationships of the deposit are of vital importance. B1 breccias containing pillow fragments and fluidal bombs occur in two settings. Of the B1 breccias there is a small subset that contains fluidal bombs and displays gradational transitions into lapilli tuffs. These deposits, described in Chapter 6, are interpreted as transitions from effusive to explosive activity at a single vent, incorporating pillow fragments as lithics in a juvenile fluidal bomb bearing deposit. The bulk of B1 breccias, however, are associated with a series of discontinuous pillowed lava sheets. The breccias occur as lenses at the margins and between lava flows. Both the flows and breccias are laterally discontinuous, and in some cases have gradational contacts. These breccias are interpreted as the result of flow related brecciation at the base and margins of flows.

B2 lavas contain blocks of non-pillowed lava and are associated with the margins of L1 lavas or occur within packets of bedded lapilli tuffs. These are interpreted as the results of collapse of lava flow margins due to emplacement on unstable fragmental deposits. Porphyritic varieties of B1 and B2 are interpreted to have formed through the same mechanisms as their micro-porphyritic counterparts.

B3 lavas are present near the caldera rim steeply dipping away from the caldera towards the east. These breccias are interpreted to be collapse breccias from emergent deposits that were formed uphill of the B3 deposits before caldera collapse removed the source area. Peperites are distinguished from the three breccia types identified at Austurfjöll by their proximity to a pillowed intrusion and occur frequently in pillow lava sheets and near feeder dikes in fissure ridges.

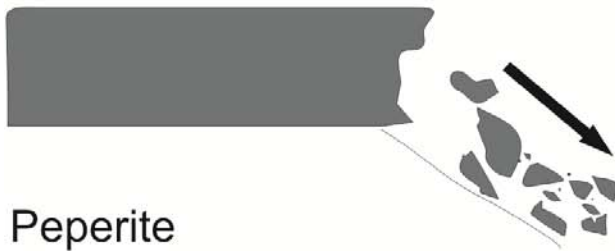
Diamictites (Dia1 and Dia2) are matrix-supported conglomerates. Dia1 is a thick massive deposit that contains clasts with distinctive glacial signatures such as a high degree of rounding and scour. The concentration of glacially altered clasts indicates that the deposit is either glacial in origin or reworked from a glacial deposit. Glacial deposits are not commonly described from glaciovolcanic centers (Bennett et al., 2006; Bergh and Sigvaldason, 1991; Carrivick et al., 2009; Loughlin, 2002; Smellie, 2008) and are difficult to identify in such monolithologic terrains such as Iceland. The lack of lateral continuity of the deposits described at Austurfjöll suggests that these deposits were likely not wide-scale regional glacial till deposits, but more likely localized lodgment tills, or moraine material that was later eroded during the incision of the modern gullies. Some of the Dia1 deposits are also disrupted by intrusions and/or loading from overburden. Intrusions help constrain the timing of the emplacement of the diamictites before subsequent glaciovolcanic basaltic activity. Dia2 deposits are significantly thinner and have broader more continuous distributions over several hundreds of meters than Dia1. The deposits are bedded and display better sorting than Dia1, being dominated by coarse ash and pebbles. They are therefore interpreted as localized glacial outwash deposits, where the glacially deposited material was fluvially remobilized by meltwater at the base or front of the glacier.



### Autobrecciation






### Gravitational collapse



### Peperite



-  Active lava
-  Cooled lava
-  Unconsolidated fragmental deposit

### Explosive disruption of previous deposits

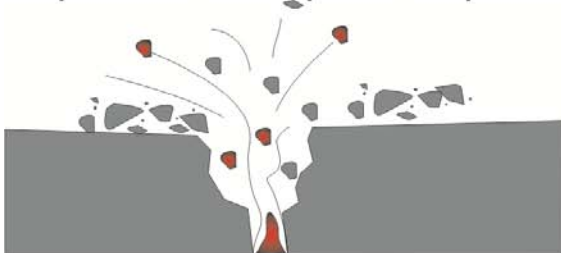


**Figure 2.30 Schematic of the multiple mechanisms that can form breccias. This example is for a non-pillowed subaqueous lava flow. The processes would be similar, but the fragments produced unique for pillowed subaqueous or subaerial lava flows. Field relationships and componentry are necessary to interpret breccias.**

The bulk of ash and lapilli tuff deposits belong to the Lt2 or At1 facies, dominated by subrounded to subangular, poor to moderately sorted particles that may be weakly bedded or massive. The rounding of clasts and, more importantly, the development of local sedimentary structures is indicative of transport in water following eruption. Bedding, cross-stratification, ripple marks, and loading structures are most common in ash dominated facies. The poor sorting and lack of sedimentary structures of most lapilli tuffs at Austurfjöll, suggests fairly rapid deposition of large volumes of material (Maicher et al., 2000). The development of traction current structures in more distal deposits, in this case ash tuffs, is consistent with sediment gravity flows at other subaqueous eruptive centers (White, 2000). Grading is not a common feature in Austurfjöll deposits, but where present normal grading is typical. Submarine density currents dominate at other glaciovolcanic and submarine volcanic eruptions (Maicher et al., 2000; Schopka et al., 2006; White, 2000) and are considered the likely mechanism of emplacement for these facies. Thick (20 m), massive deposits such as At1 may represent deposits that were rapidly emplaced without remobilization. However, palagonitization, a common process in submerged basaltic vitric depocenters, can mask evidence of bedding or other fine structures (Stroncik and Schmincke, 2002). Partially palagonitized deposits at Austurfjöll revealed that structures were most effectively disguised in deposits dominated by ash size particles. This may result in an overestimate in the volume of primary material at Austurfjöll. The thick sequences of Lt2 and At1 deposits are interpreted as eruption-fed density currents that form during the rapid deposition of large volumes of material in a subaqueous environment. The Lt1 facies is the only example of subaqueous fallout of coarse material identified at Austurfjöll. These deposits are distinguished by a high degree of angularity of all grain sizes, preserved fragile glassy particles, a gradational upward fining, and fluidal bombs (further discussion occurs in Chapter 6).

The steep slopes of subaqueous volcanic piles are conducive to mass wasting of unconsolidated deposits, which can produce deposits with similar characteristics to eruption-fed density currents (Sansone and Smith, 2006). The regular bedding and frequent presence of sedimentary structures such as ripples and loading structures within At2 and At3 is indicative of low energy density currents (distal flows of eruption-fed currents) or the gravitational remobilization of previous deposits. The

differentiation of these deposits is dependent on field relationships including slope and stratigraphic relationships. Measured slopes of these At2 and At3 units are typically between 10 and 25°. Deposits at steeper angles (ca. 20°) likely indicate distal deposits of eruption-fed density currents that were not remobilized. At2 deposits on shallower slopes most commonly occur in large packets up to 40 m thick and fill large (100 m wide) channel forms, suggesting a remobilized history.

Lt4 and Lt3 facies contain more diverse components than Lt1-2 and At1-3. These deposits are limited to the margin of the caldera at high elevations (Figure 2.2). Both lithofacies are typically bedded and the beds are oriented with dips that radiate away from the caldera (Figure 2.22, 2.23). These units may contain subaerially derived clasts such as red scoria and blocks of subaerial lava. Lt3 contains armored lapilli, which formed above the water level, but likely were not subject to significant remobilization underwater. It is important to note that armored lapilli have been preserved in subaqueous environments (McPhie et al., 1993; White, 1996b). The presence of preserved bomb sags suggests it was within a few meters of the surface of the water, or emergent. The Lt3 facies is, therefore, an indicator of shallow or subaerially emplaced emergent deposits. Lt4 contains a combination of subaerially and subaqueously derived clasts, suggesting the remobilization of subaerial deposits in an erosive traction current or through collapse underwater to incorporate both clast types.

The variety of intrusions in the Austurfjöll complex is similar to intrusions described in other glaciovolcanic massifs (Edwards et al., 2009; Schopka et al., 2006; Stevenson et al., 2009). Tabular dikes (D1) are typical of basaltic volcanic centers where magma interacts with competent rock and lithified deposits (Baer, 1995; Gudmundsson, 2002; Rivalta and Dahm, 2006). These dikes can serve as feeders for eruptions, or they may be arrested on the way to the surface providing internal stability to the massif. Pillowed dikes (D2) and peperites associated with intrusions are an indicator of unconsolidated, and typically saturated, sediments (Doyle, 2000; Kagy, 2011; Mercurio, 2011; Walker, 1992; White et al., 2000). Pillowed dikes may feed eruptions, but no good field relationships were present in Askja to confirm this connection. The third variety of dike, CMVDs, are interpreted as the result of magma interacting with ice-cemented sediments (Graettinger et al., 2012) and are discussed further in Chapter 7.

## **2.6 ARCHITECTURE**

The distribution and stratigraphic relationships of lithofacies were both documented during field work. Stratigraphic columns along 3D exposures enabled the documentation of the internal structure of common constructs of the Austurfjöll massif. These logs reveal several basic constructional elements of the massif: fissure ridges, lava dominated features, and depo-centers.

### **2.6.1 Fissure ridges**

The most common primary eruptive features preserved on Austurfjöll are fissure ridges. These ridges are composed predominantly of ash and lapilli tuffs and are in most cases probably cored with a feeder dike and in some locations are associated with basal pillow lavas and pillow breccias (Figure 2.31). The linear feature produced by the resistant core of the feeder dike and dipping slopes of the tuffs is typical of tindars described all over Iceland and British Columbia (Edwards et al., 2009; Jakobsson and Gudmundsson, 2008; Schopka et al., 2006; Smellie, 2007). In Austurfjöll, fissure ridges overlap each other and pillow lava sheets (Figure 2.32). The expected morphology of fissure ridges is a length of twice the width of the ridge (Jakobsson and Gudmundsson, 2008), which is maintained for most Austurfjöll examples. Fissure ridges that do not preserve this proportion may reflect erosion or burial of the ridge altering the original proportions. Fissure ridges described at Austurfjöll are typically 300 m in length and 50 m high relative to surrounding terrain. The presence of these ridges contributes greatly to the stepped ridge and valley appearance of the massif.

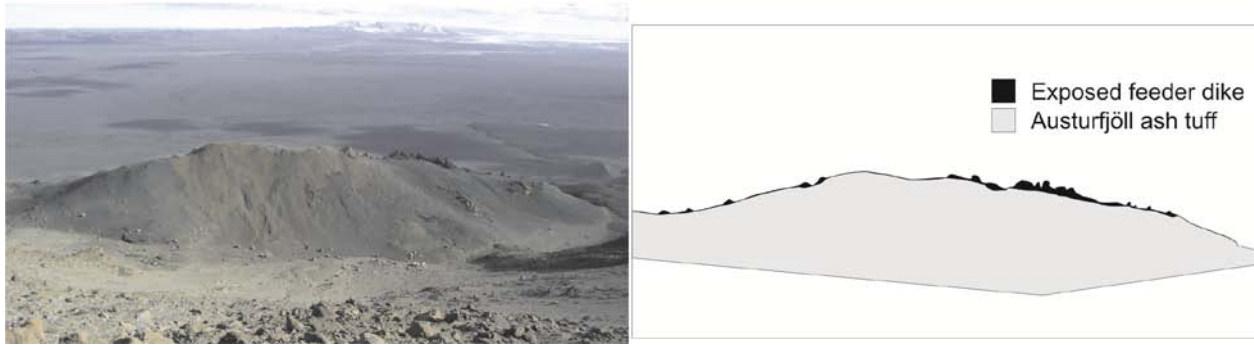


**Figure 2.31** Example of a fissure ridge with exposed feeder dike.

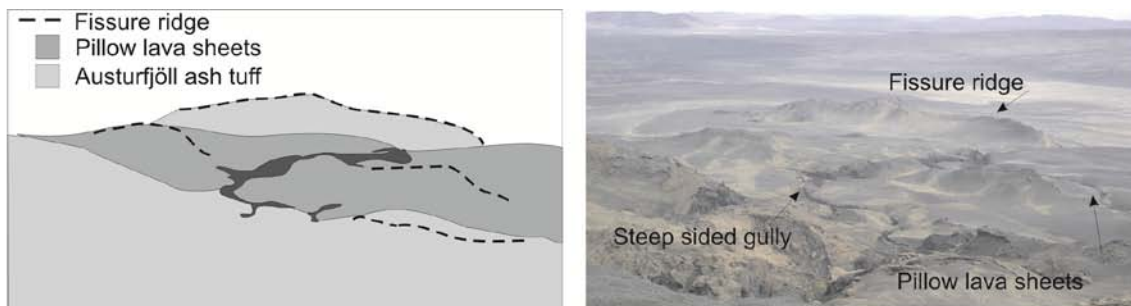


**Figure 2.32** Multiple fissure ridges overlapping pillow lava sheets. Steep sided gullies where stratigraphic logs were collected are visible.

### **2.6.2 Lava dominated features**

As detailed in section 2.2.1.2 pillow lavas have produced pillow lava sheets and pillow lava mounds. There are a few examples at Austurfjöll of concentrated vents that produce large volumes of pillows built up at the vent site to produce a pillow mound with preserved flow directions (Figure 2.33). These focused vent eruptions result in distinct morphological features that are partially overlapped and surrounded by fissure ridge deposits. Pillow lava sheets are the single largest morphologic feature in the field area. The pillow lava sheets are typically only exposed in the lowest elevations and make up the bulk of the southeastern edge of Austurfjöll. Fissure ridges and pillow mounds overlie the pillow sheets and locally overlap each other. There are limited exposures of pillow sheets overlapping thick sequences of lapilli and ash tuff that also occur within the lower portion of the massif. The stratigraphic relationships between these constructional features indicate the relative trend in eruption styles at Austurfjöll. The earliest eruptions documented by the massif were subaerial unconfined fissure eruptions, dominated by a'a lava flows. Following glaciation, including erosion and advancement of an ice sheet over the Askja volcano, long lived ice-confined subaqueous effusive fissure eruptions produced large pillowed lava sheets, which are now mainly exposed along the southeastern margin of the massif. As fissure activity continued it became locally explosive, producing fissure ridges and locally centralized to produce point source vents and pillow mounds. The architecture of the massif then continued to develop as a series of overlapping fissure ridges with local topographic convolutions produced by pillow lava mounds.

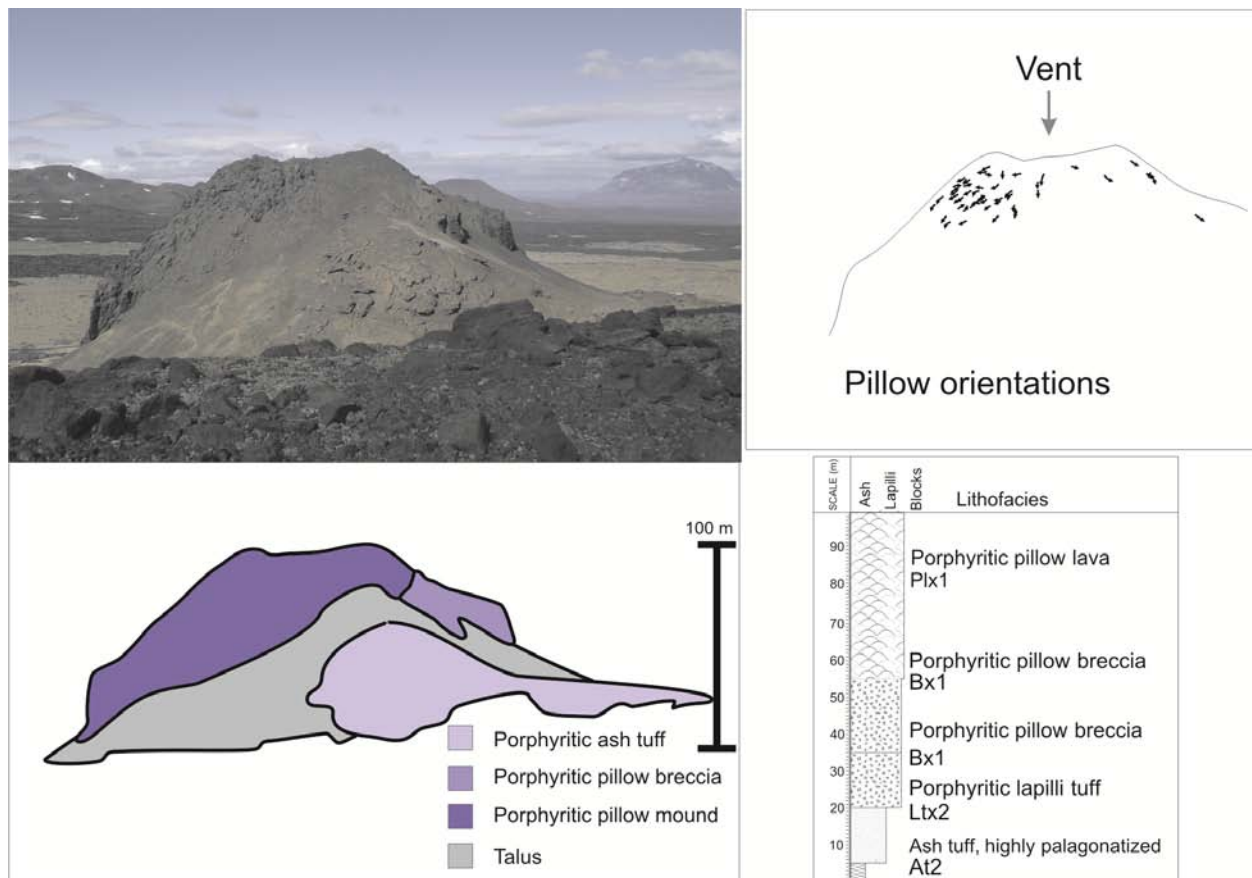


**Figure 2.33 Example of a single vent pillow mound. The orientation of the pillows enables identification of the vent.**

### 2.6.3 Depo-centers

In at least two locations larger (>100 m wide) erosional surfaces cutting large Lt1 and Lt2 deposits have been mapped and their younger infill documented. In most instances the infill is well bedded ash and lapilli tuffs (At2, At3 and Lt2) with shallow ( $\sim 10\text{-}20^\circ$ ) dips that suggest the valley was reused as a regular drainage and depositional channel for the re-mobilization and re-deposition of fragmental deposits (Figure 2.34). In one example the valley fill deposits were later cut by a basaltic dike, while the sediments

were still wet and unconsolidated, indicating that eruptive activity continued after the erosion event. In at least one example the valley was filled with thick pillow lava sheets, which deformed and backed up against the external boundary of the channel (Figure 2.35). The pillow units filled and eventually overflowed the valley. Due to a later erosional period following the cessation of activity, locally the topography is now partially reversed, where the valley fill presents a resistant ridge. At Eyjafjallajökull in southern Iceland, glacial U-shaped valleys were recognized (Loughlin, 2002) and were associated with polygenetic growth of the volcanic edifice through several glacial advances. The valleys at Austurfjöll are fairly large, and some examples are moderately U-shaped. The orientation of the valleys is north-south, parallel to the trend of local trend of the rift zone and many of the fissure ridges identified at Austurfjöll. The continuation of eruptive activity as recorded by the presence of dikes and thick lava sheets may indicate that meltwater floods are a more likely mechanism for the formation of the valleys rather than glacial ice. The orientation of the valleys is typically oriented perpendicular to the apparent paleo-slope, suggestive of a subglacial hydrology, rather than a gravitationally driven movement of ice or water. The potential for glacial erosion of the massif is discussed in Chapter 8.

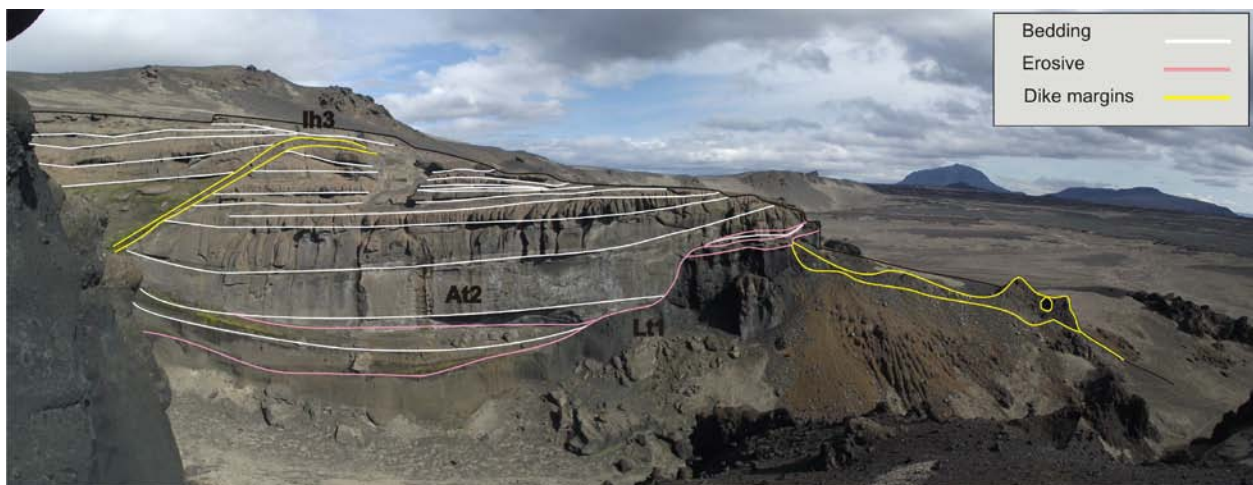


**Figure 2.34 Field image of a large channel eroded into lapilli tuff deposits and filled with bedded ash tuff deposits. The channel fill deposits are cross-cut by a younger basaltic dike.**



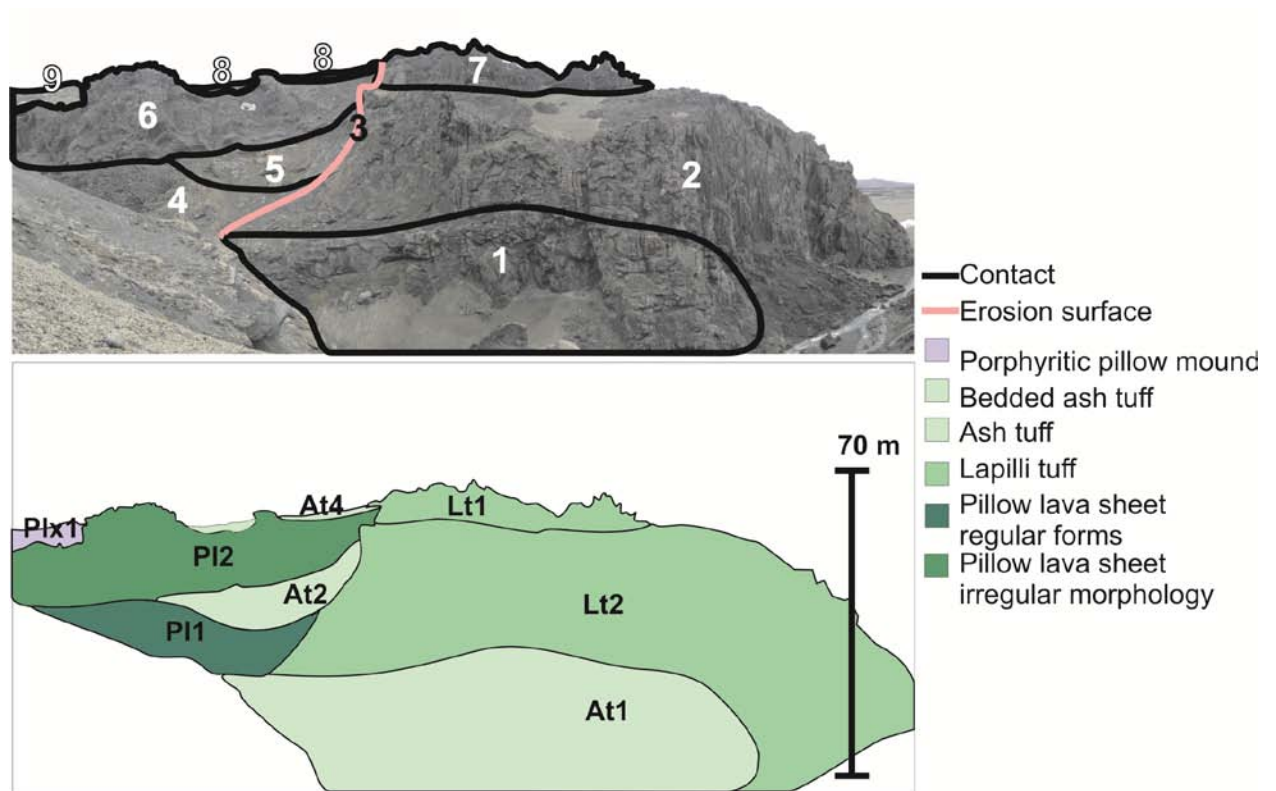


**Figure 2.35** Field image and sketch of erosional channel in lapilli tuff deposits. The numbers indicate the relative order of each deposit or erosional surface. A pillow lava sheet composed of PI1 and PI2 lavas fills the erosional valley and is later covered by At4 deposits and porphyritic pillow mounds.

#### 2.6.4 Mantling deposits

The surface of pillow lava sheets and pillow mounds are frequently mantled by thin bedded deposits of ash and lapilli. These deposits are exposed by the modern steep-walled gullies. These features provided excellent three-dimensional opportunities that enable relatively easy access to describe the internal stratigraphy of the lower deposits of the massif. The rims of the gullies frequently are lined with dipping packages of At4 deposits less than one meter thick. These units typically are found on the margins of

large pillow sheets, and fill in topographic lows. They can also be found perched atop partially eroded ash and lapilli tuff deposits and mantling pillow mounds. The orientation of bedding of these At4 units, dipping into the modern-day gully along the upper wall of several of these gullies, suggests that the gully may be exploiting pre-existing topographic lows that coincide with the margins of adjacent large pillow lava sheets (Figure 2.36). These topographic lows would encourage meltwater to continue to exploit existing drainage features, and progressively create the modern steep walled gullies. Similar gullies are described at Eyjafjallajökull (Loughlin, 2002). The position of the pillow sheet flow margins may have in turn been influenced by confining ice. Less resistant deposits, such as ash and lapilli tuff, can also be incised to form steep walled gullies, but the At4 mantling deposits do not have the same trend of dipping into the gully, suggesting some gullies were merely exploiting more readily eroded deposits such as partially consolidated ash and lapilli tuffs.

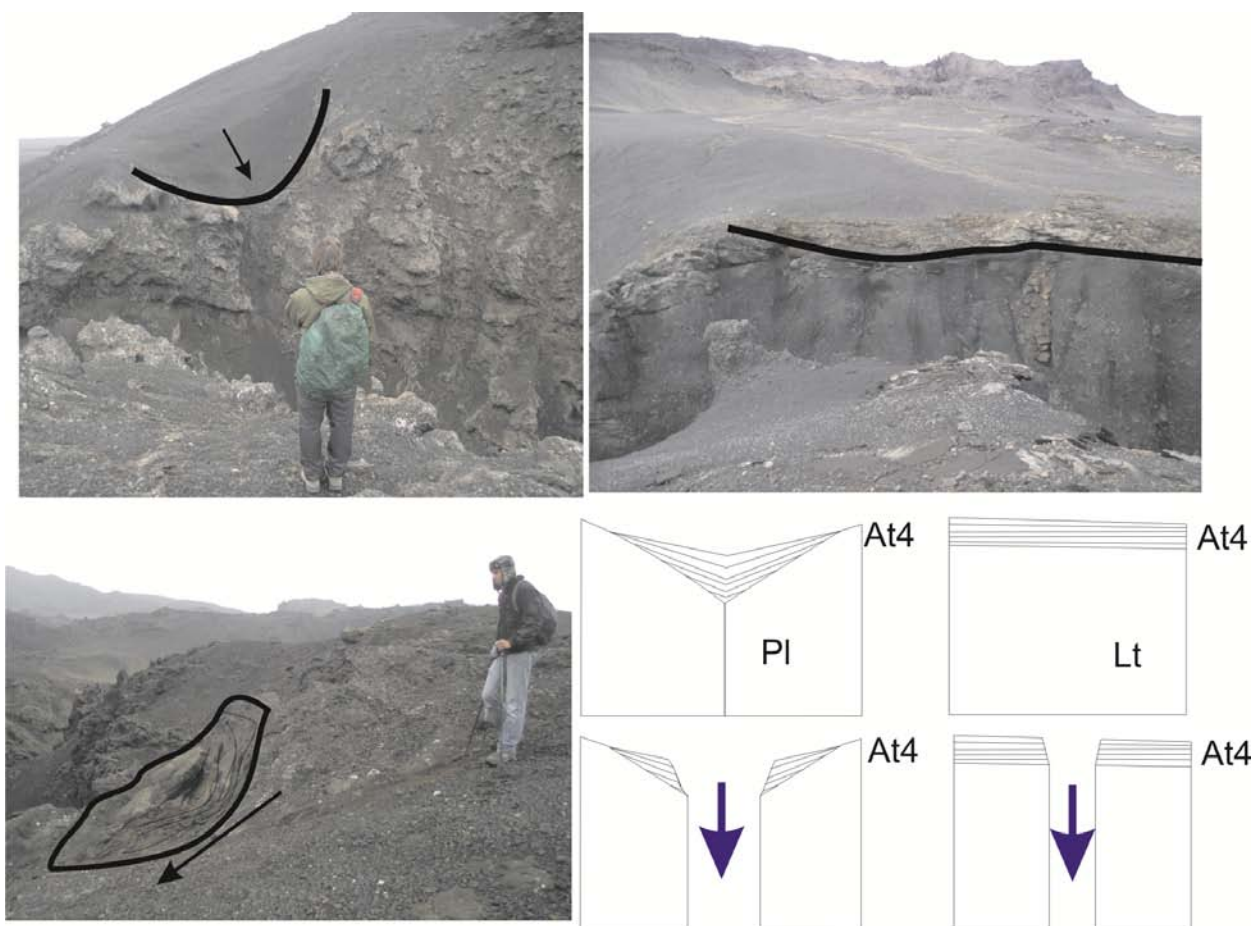


**Figure 2.36 Examples of At4 mantling deposits that fill paleotopography and mantle most lithofacies. The dip of mantling At4 can be used to determine the location of paleotopography.**

## 2.7 SUMMARY

The Austurfjöll massif is a crescent shaped edifice that reaches 750 m above the local elevation and forms the eastern margin of the Öskjuvatn caldera. The Austurfjöll massif is constructed of large pillow lava sheets overlain by overlapping fissure ridges and pillow mounds. The topography of the massif steps down in a series of ridges and valleys towards the east away from the caldera rim. The steps are irregular

and made up of small ridges that are typically 300 m long, but can reach 600 m in length, with moderate infill along the uphill side of the ridge by fragmental deposits. The ridges may be up to 50 m taller than surrounding deposits, and typically more so on the down slope side. The bulk of the massif is made up of subaqueous coherent and fragmental units. Up to 650 m of the massif is made up of subaqueous sequences with only three minor locations of subaerial lavas that cover less than 1 km<sup>2</sup> each (Figure 2.2). The massif is underlain by subaerial lavas (L2) and local diamictites (Dia1 and Dia2). The subaqueous lithofacies are typically ordered into localized sequences of pillow lava and pillow breccia (Pl1, Pl2, B1) or subaqueous lavas and related breccias (L1, B2), overlain by fragmental deposits of ash and lapilli tuffs (Lt1, Lt2, At1). Deposits of remobilized fragmental material accumulate in topographic lows and as channel fills between eruptive fissure ridges (At2, At3, At4). Many of the depo-centers are cross-cut by later dikes indicating that the erosional and depositional events occurred before the construction of the massif was complete. Deposits intruded before consolidation contain pillowed or CMVD intrusions (D2, CMVD). Those deposits that are intruded after consolidation are cut by tabular dikes (D1). Above 600 m higher than local base level emergent deposits were first emplaced and were locally re-deposited down slope as remobilized tuffs and breccias (B3, Lt4, At3). Locally subaerial deposits were preserved in situ at the highest preserved modern elevations (L2) 1250- 1450 m asl representing a putative paleo-water level. The basic architecture and distribution of deposit types within the Austurfjöll massif are important for the reconstruction of the eruptive history of the volcano and understanding subaqueous eruptions of a polygenetic central volcano (stratovolcano) such as Askja.

### **3.0 GEOCHEMISTRY AND RADIOMETRIC DATING OF AUSTURFJÖLL MASSIF, ASKJA, ICELAND**

The investigation of Austurfjöll massif was accomplished through a combination of techniques with a focus on field-based mapping and description. The stratigraphic relationships and petrographic descriptions were supported by geochemical analysis for the purpose of defining discrete eruptive units, chemostratigraphic relationships, and relative and absolute dating of coherent lithofacies. These geochemical analyses enabled the identification of seven eruptive units that correlate with the lithostratigraphic divisions identified in the field mapping (Figure 2.2). The geochemical data also revealed the major and trace elements that enable the differentiation of such similar sets of lavas. The ages of the Austurfjöll lavas presented here are the first for the glaciovolcanic sequence at Askja and represent the successful use of unspiked K/Ar dating method, which is critical to expanding the paleoclimate applications of glaciovolcanic deposits in Iceland. The discrimination of discrete eruptive units, and their relative and absolute ages, reflect the diversity of magma batches at a long lived polygenetic ice-confined volcano such as Askja.

#### **3.1 METHODOLOGY**

Bulk rock geochemical analyses of 57 coherent rock samples were conducted using X-Ray Fluorescence spectroscopy (XRF). Samples selected for analysis included pillow and sheet lavas, intrusion margins and cores, and lava blocks from breccias and lapilli tuffs. These samples were representative of lithofacies,

unit contacts, and units selected for radiogenic dating as established through lithostratigraphic mapping (Figure 3.1). Major element and selected trace element analyses were conducted using XRF spectroscopy conducted at University of McGill (Montreal) using a Philips PW2440 4KW X-ray Fluorescence spectrometer and the GeoAnalytical lab at Washington State University, using a ThermoARL XRF instrument. Multiple samples from the same intrusion were selected for repeat analysis within and between the two data sets to enable comparison of the results. As the bulk of analyses were conducted at WSU, these samples are used in preference. However, the similarity in the two data sets is sufficient to enable comparison without any calibration (Table 3.1). The McGill samples, fifteen in total, were analyzed for Rare Earth Element (REE) concentrations. Additional analyses include SEM analysis of six porphyritic samples (2 gabbro, 2 lava, and 2 lapilli tuff) using the Energy Dispersive Spectrometer (EDS) at Dickinson College for semi-quantitative mineral compositions of phenocrysts and the groundmass. Compositional data were also collected from pillow glass rinds using an electron microprobe in conjunction with Fourier Transform Infrared (FTIR) analyses conducted at the University of Wisconsin-Milwaukee. These analyses provided major element and volatile contents of the glassy pillow lava quench rinds.

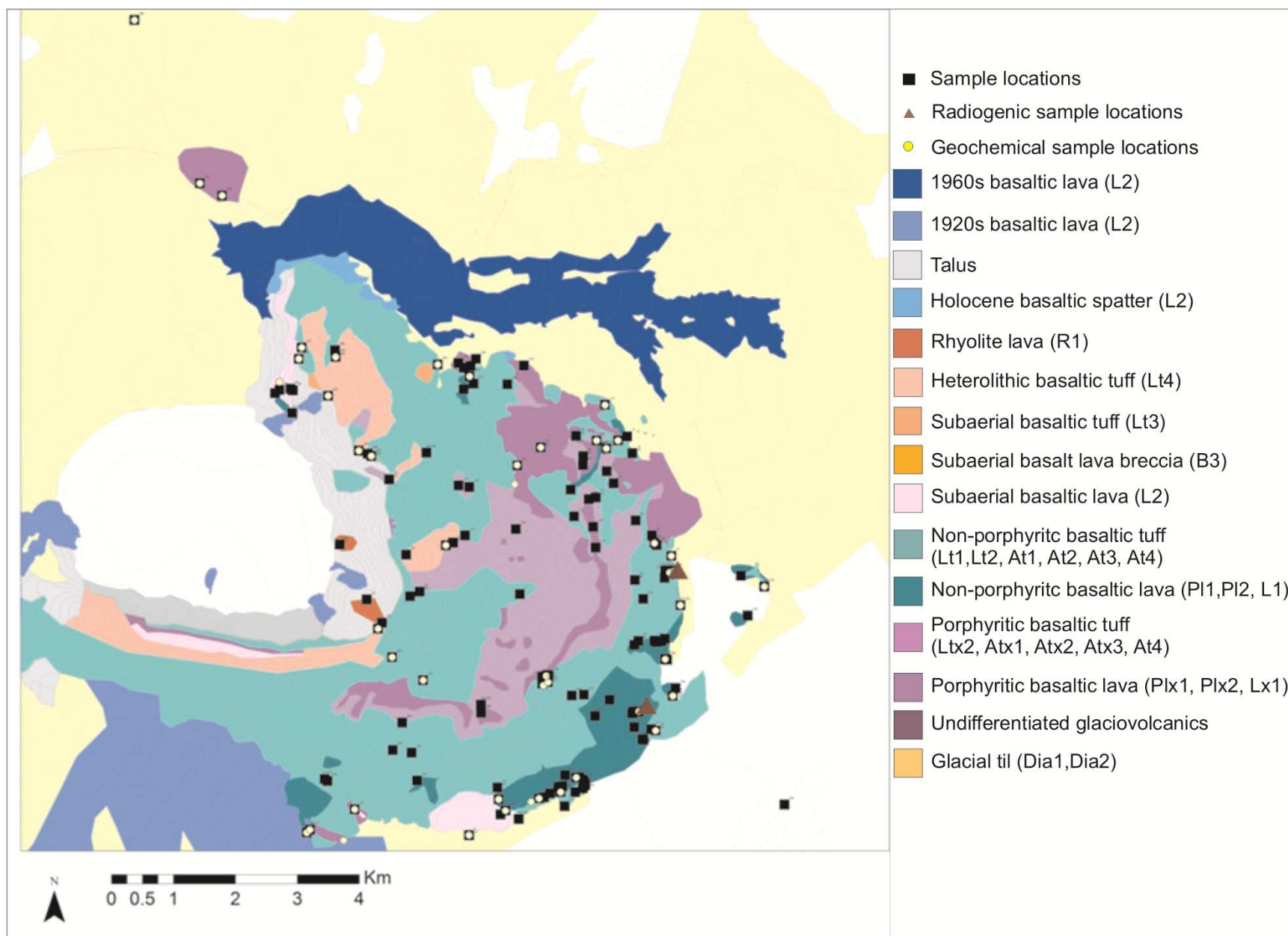


**Figure 3.1 Location map of all samples collected in Austurfjöll. The overlay shows which samples were collected for geochemical analysis. Samples that were analyzed for radiometric age dating are also indicated.**

Major and minor element trends were highlighted using single element and element ratio variation diagrams. The data were initially divided by groups of duplicate samples from the same morphologic unit (multiple samples from a single dike or pillow lava sheet). The general trends of these initial groups were used to divide the remainder of the samples into compositionally similar units. Variation diagrams were used to check the success of the manual division. Divisions were compared with lithostratigraphic boundaries for correlation. Outliers were studied for anomalous trends against element enrichment. If an outlier displayed consistent enrichment similar to a single chemical group it was considered part of that chemical group. However, if the enrichment trends were inconsistent and the sample trended toward multiple groups it was considered an independent chemical group. All samples were assigned a confidence rating to indicate the confidence of their assignment to a given chemical unit. The rating ranges from one star to three stars, where one is the lowest confidence and three stars represent a strong fit. Samples that have a low confidence rating of one star indicate that the sample is most closely related to its present group, but exceeds the range of values of the unit for approximately half of the elements analyzed. Samples with a confidence rating of three exceed the expected range of values of the unit for less than three elements analyzed. These geochemical groups were also tested using Pearce Element Ratios (Russell et al., 1990; Stenly and Russel, 1989). Corroborative discrimination diagrams were produced to highlight the relationships between each eruptive unit. These geochemical units were then superimposed on lithostratigraphic boundaries established in Chapter 2 to create a chemostratigraphic map presented in Chapter 4.

Six samples were collected for radiogenic dating using unspiked K/Ar ratios (Guillou et al., 2010). Each sample was 1 kg of fresh rock chips from the interior of a significant lithostratigraphic unit. The samples were selected for their position within the massif and lack of alteration. Due to the low potassium content of typical Icelandic basalts, samples for K/Ar dating require large sample volume. Two



samples were successfully prepared for unspiked K/Ar analysis at the Laboratoire des Sciences du Climat & de l'Environnement, Unité Mixte de Recherche CEA-CNRS, France. The four other samples were determined to have insufficient detectable argon isotope concentrations. This method involved three independent determinations of potassium and two determinations of argon to resolve the radiogenic  $^{40}\text{Ar}$  concentrations and enable dating (Charbit et al., 1998; Guillou et al., 2010). Age calculations are based on decay constants of Steiger and Jaeger (1997) (Steiger and Jaeger, 1977). The Ra/Th dating required plagioclase and magnetite mineral separates and thus also used 1 kg samples.

**Table 3.1 Variability within and between datasets from the two XRF laboratories.**

Lab	McGill internal	WSU internal	Inter-lab	Inter-lab exceeds internal variability	Percent in excess of internal variability
# of samples	3	4	3		
Wt % difference between samples					% excess variability
SiO <sub>2</sub>	0.19	0.19	0.56	0.37	1.94
TiO <sub>2</sub>	0.04	0.01	0.04	0.02	0.68
Al <sub>2</sub> O <sub>3</sub>	0.04	0.06	0.09	0.04	0.78
FeO/Fe <sub>2</sub> O <sub>3</sub> * *	0.10	0.21	1.61**	1.46**	9.64 **
MnO	0.00	0.00	0.00		0
MgO	0.10	0.03	0.03		0
CaO	0.09	0.04	0.04		0
Na <sub>2</sub> O	0.05	0.01	0.01		0
K <sub>2</sub> O	0.03	0.00	0.03	0.02	1.23
P <sub>2</sub> O <sub>5</sub>	0.00	0.00	0.00		0
Totals *	0.99	0.95	1.52	0.55	55.0
ppm difference between samples					
Nb	0.15	0.45	0.63	0.33	1.11
Rb	0.40	0.45	0.37		0
Sr	2.70	0.75	5.43	3.71	2.15
Y	0.45	0.40	3.03	2.61	6.14
Zr	0.55	0.70	3.97	3.34	5.35
Ce	13.50	1.35	13.90	6.48	0.87
Cu	8.00	2.75	83.27	77.89	14.49
Ni	8.50	0.30	5.30	0.90	0.20
Sc	2.00	0.75	1.50	0.13	0.09
V	4.20	0.55	5.97	3.59	1.51
Zn	3.00	2.00	29.90	27.40	10.96
*All values are normalized by the labs.					
**McGill recalculated Fe totals as Fe <sub>2</sub> O <sub>3</sub> resulting in higher totals.					

### 3.2 WHOLE ROCK GEOCHEMISTRY

A manual comparison of major and trace elements and variation diagrams reveals distinct eruptive units that correlate with lithofacies boundaries that were established by textural, stratigraphic, and geomorphological evidence. The narrow suite of basaltic samples neatly falls within the range of tholeiitic lava (Figure 3.2). The alkali content of the samples is low and displays no definitive trend. Total alkalis versus silica therefore does not aid in the initial discrimination of lava groups. Instead, incompatible elements reveal strongly linear trends of enrichment and reveal discrete chemical clusters (Figure 3.3). The linear trend is particularly strong for CaO, TiO<sub>2</sub>, Al<sub>2</sub>O<sub>3</sub>, and Sr (Figure 3.4).

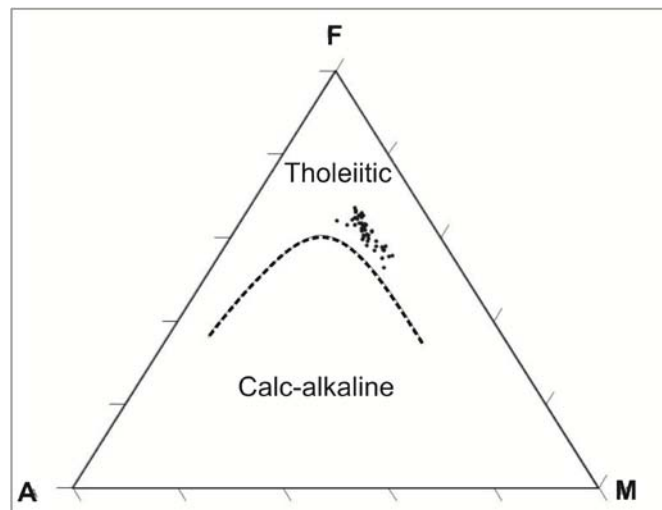
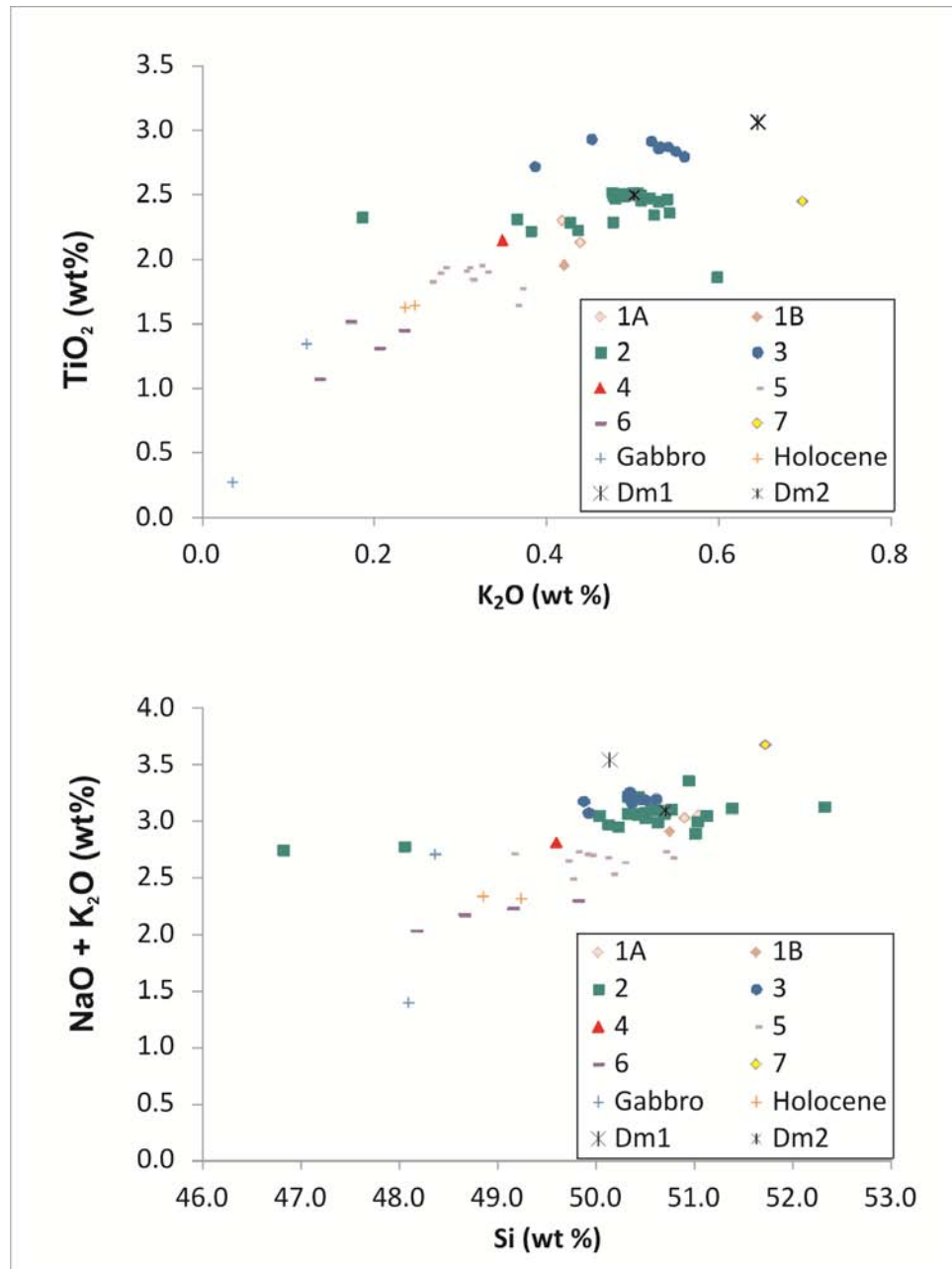
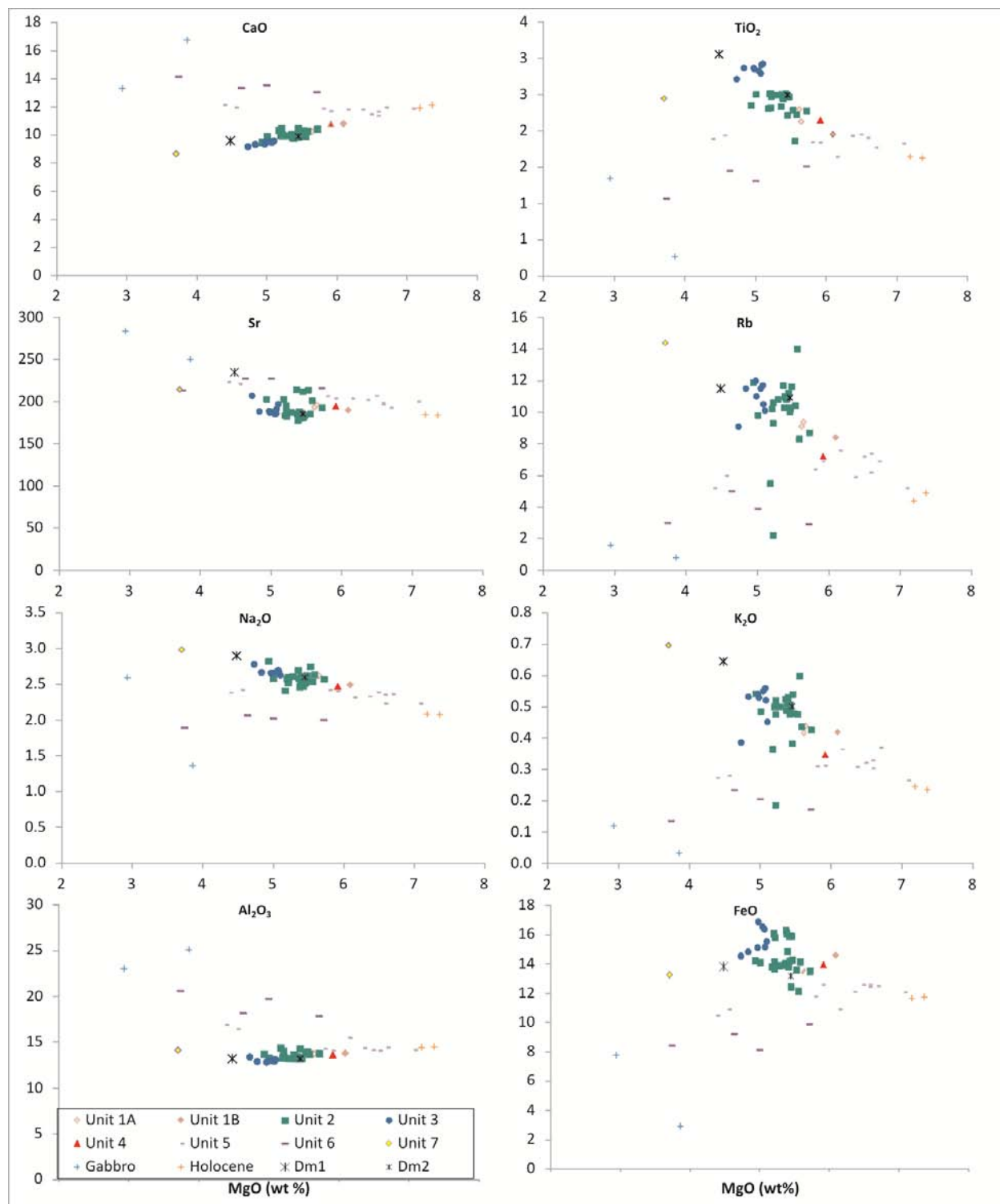


Figure 3.2 AFM diagram show the distribution of Austurfjöll samples. All samples plot neatly as tholeiites.



**Figure 3.3** The enrichment of the basaltic melt is highlighted by an incompatible element diagram and total alkali diagram. Symbols represent individual eruptive units of Austurfjöll. Gabbro nodules, Holocene spatter, and lava clasts from diamictons are included for comparison. Symbols will be used consistently throughout this document unless otherwise noted.



**Figure 3.4 Variation diagrams of major and trace elements against MgO. Plots along the left represent components of plagioclase and components on the right are incompatible elements. All oxides are in wt%.**

The Austurfjöll sample suite was divided into seven eruptive units associated with the construction of Austurfjöll massif, two additional sedimentary units, one post-Austurfjöll eruptive unit, and one unit of gabbro nodules. Tables of the complete results appear in Appendix B (Table B-1 and B-3). The units identified include gabbro nodules, Unit 1 (A, B), Unit 2, Unit 3, Unit 4, Unit 5, Unit 6, Unit 7, Dm1, Dm2 and Holocene spatter / lava. Units 1-7 are stratigraphically and chronologically defined units containing samples of similar geochemistry. Unit 1 is divided into A and B as they are stratigraphically equivalent, but have unique geochemical signatures. Units Dm1 and Dm2 are defined from samples of lava contained within diamicton units, the geochemistry of which helps establish the relationship between the eruptive units and the diamictons. Variation diagrams comparing elements relevant to the phenocryst species identified in petrographic investigations (plagioclase and clinopyroxene) provided the most useful visual distribution of the chemical units. Of particular interest is CaO/TiO<sub>2</sub>, CaO, Al<sub>2</sub>O<sub>3</sub> (Figure 3.5) and trace element diagrams comparing V/Y or two incompatible elements Zr/Ti (Figure 3.6). All four diagrams display a strong linearity in the distribution of the data, with well defined consistent clusters of data points representing each eruptive unit.

Microprobe analysis of ten samples produced highly similar results to the XRF whole rock geochemistry, and provided additional information about the volatile species present in the samples to support FTIR results (See Chapter 8). The samples analyzed by microprobe confidently fell within the Unit 2 and Unit 5 eruptive units both stratigraphically and chemically, supporting the divisions defined above (See Table A-4).

Normalized trace element trends of samples using primitive mantle (Lyubetskaya and Korenaga, 2007) reveal that the samples are enriched in incompatible elements relative to Mid-Ocean Ridge Basalt (MORB) lavas (Figure 3.7). This trend in enrichment spans from Unit 3 as the most enriched and the gabbro as the least. The trends are fairly similar for most of the eruptive units, with some of trends

accentuated between the least enriched group, Unit 6, and most enriched Unit 3. The signature of the trace elements is dominated by the behavior of Sr, which correlates with enrichment of CaO in major element plots.

Rare earth element analyses were conducted on only 15 samples at McGill University. The REE trends produced through the normalization with chondrites (Anders and Grevesse, 1989) reveal the same relative enrichment of eruptive units that was observed in the major and trace elements. One sample of rhyolite dome that pre-dates the basaltic subaqueous sequence shows similar trends in REE, but has notably higher values and a strong negative Eu anomaly (Figure 3.8). All samples are enriched in incompatible elements relative to compatibles of the REE series. Unit 5 is notably less enriched than Units 1, 2, and 3. Analyses of Units 1, 4, 6, and 7 were not conducted.

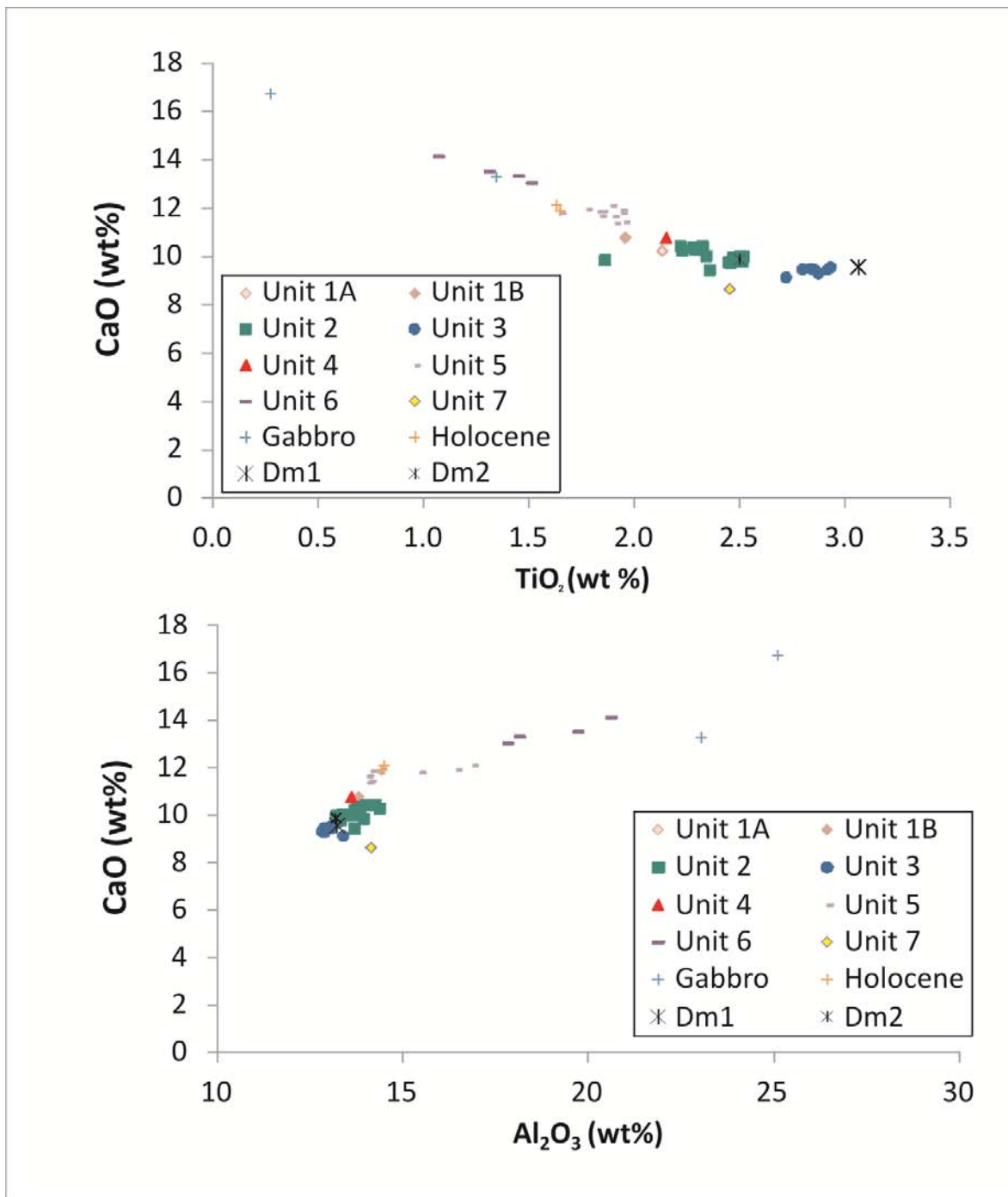


**Figure 3.5** Variation diagram of CaO vs. TiO<sub>2</sub> and CaO vs. Al<sub>2</sub>O<sub>3</sub>. These comparisons highlight the linear trend of the Austurfjöll dataset. CaO/TiO<sub>2</sub> likely reflects the relative abundance of feldspars and oxides, where high CaO reflects high plagioclase content and high TiO<sub>2</sub> reflects high oxide content.



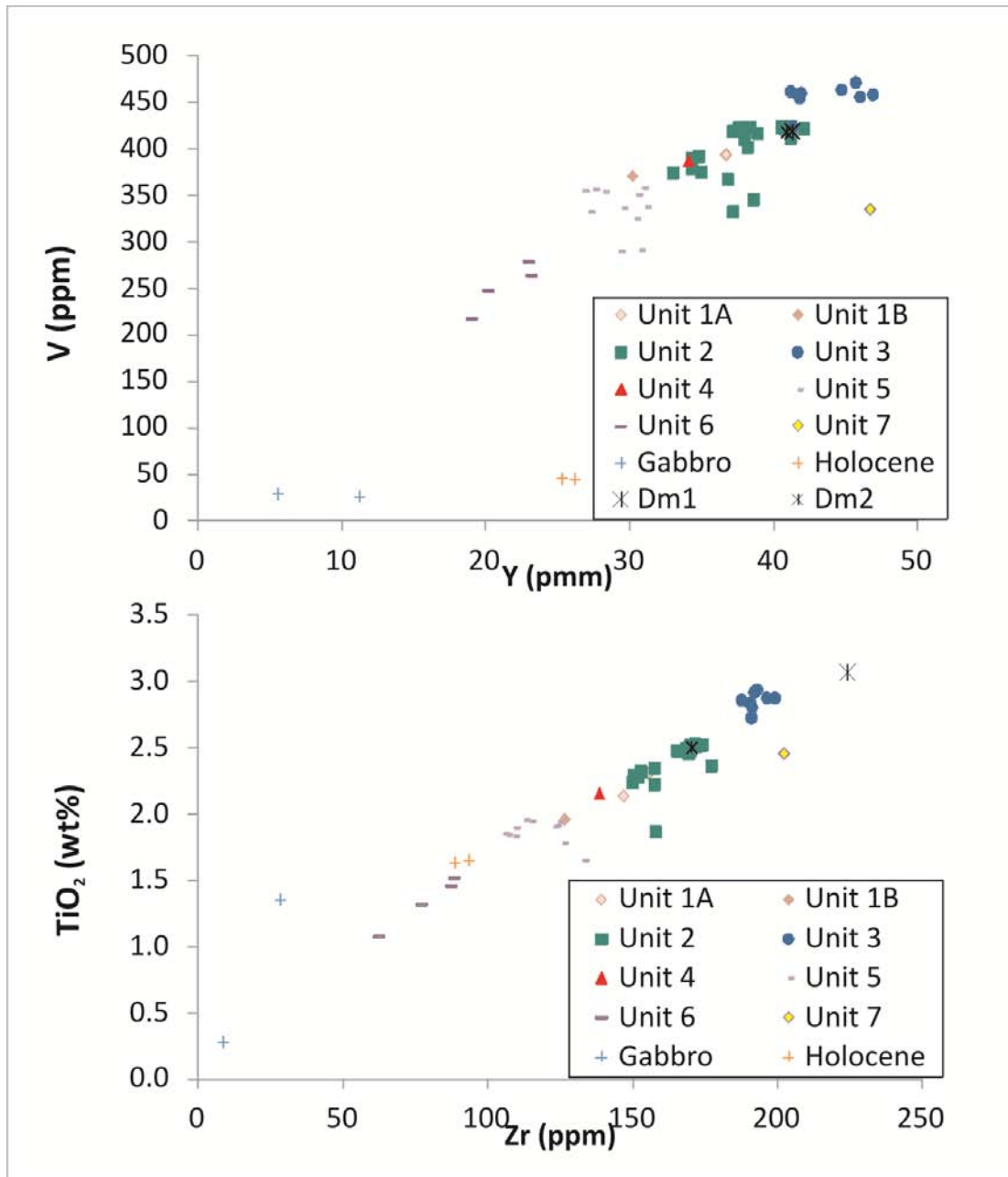


**Figure 3.6 Trace element variation diagrams contrasting incompatible and compatible elements. The linear trend of the data set is more pronounced than in the major elements. V/Y likely shows the influence of Cpx and oxide minerals and the overall enrichment of the samples.**

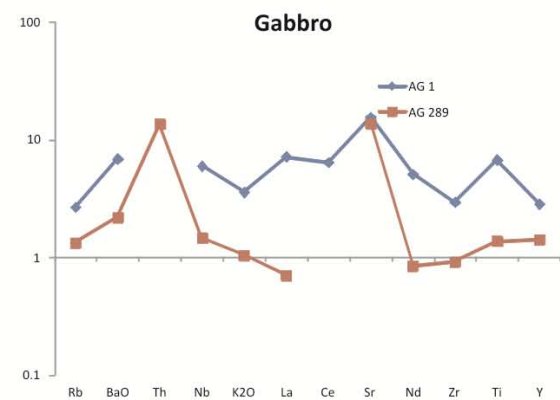
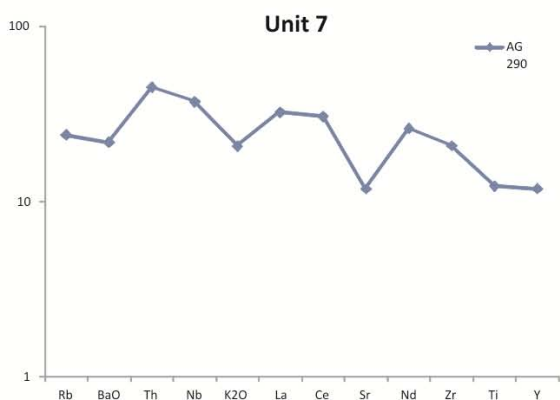
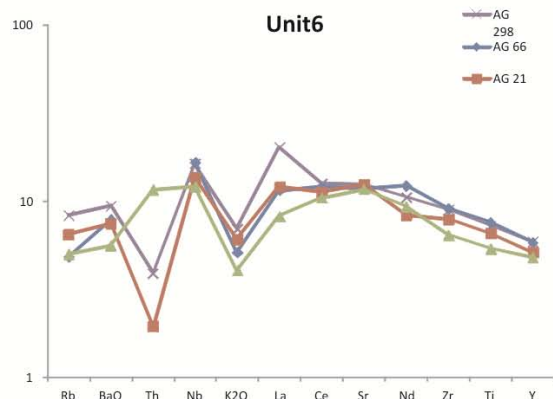
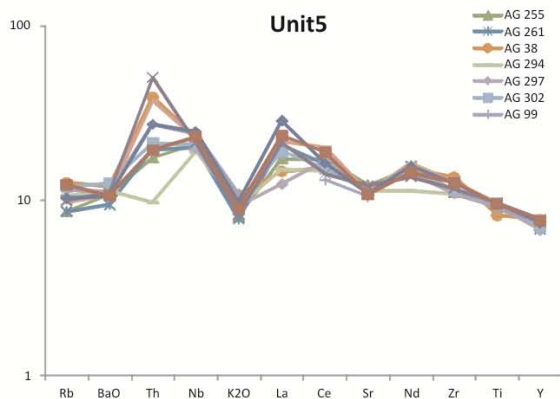
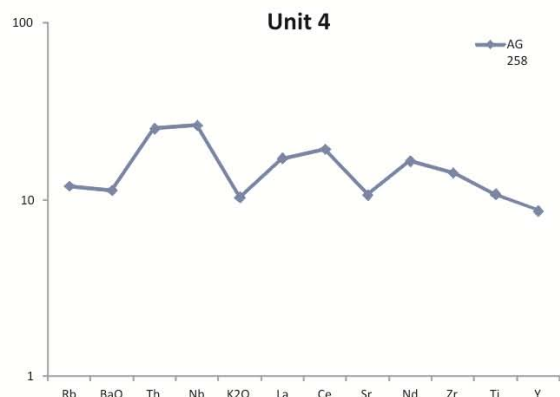
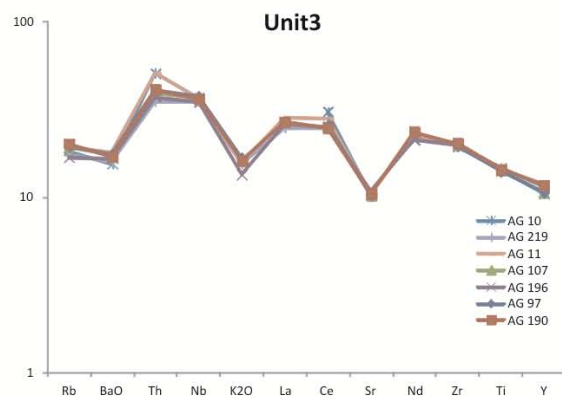
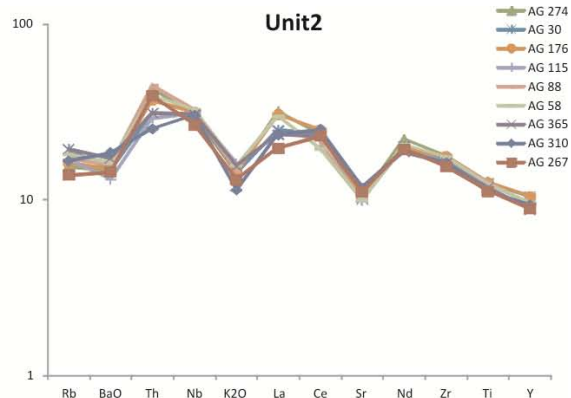
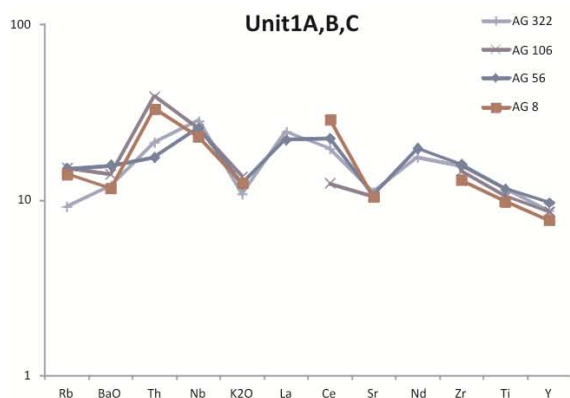


**Figure 3.7 Multi-element diagrams highlighting the relative enrichment of trace elements in the Austurfjöll samples. Samples are normalized to the primitive mantle (Lyubetskaya and Korenaga, 2007).**

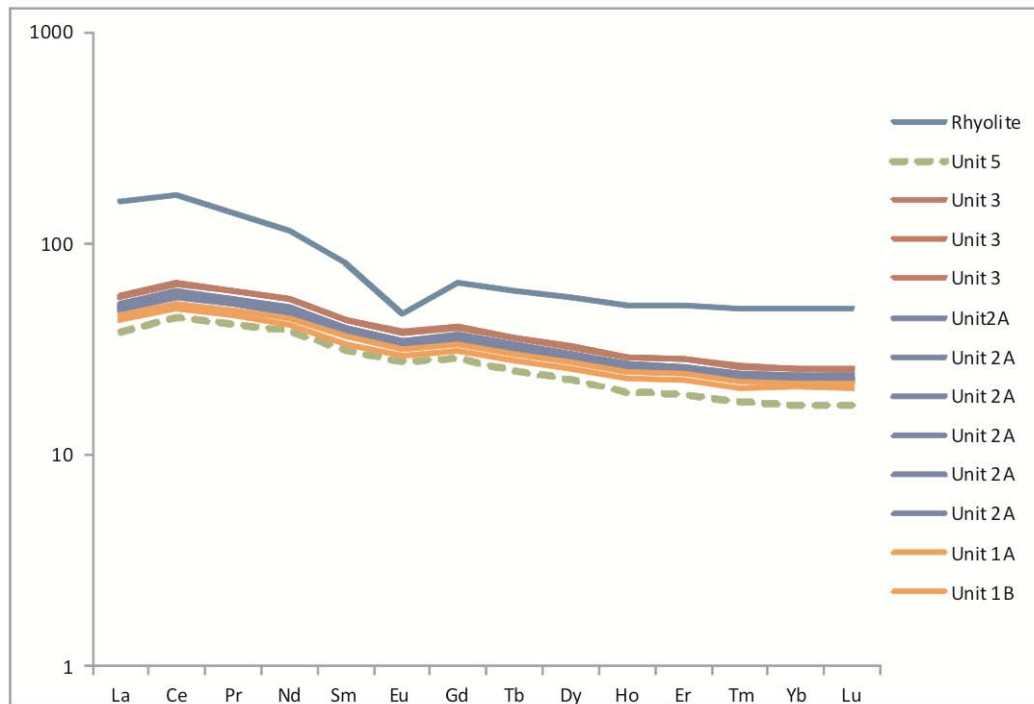


**Figure 3.8 REE plot of 15 samples including a sample of the rhyolite dome with a distinctive Eu anomaly, indicating the role of plagioclase in the evolution of the melt. Units 2 and 3 show very limited variability between samples. Unit 5 shows the lowest REE concentrations of all of the Austurfjöll lavas analyzed.**

Unit 1 is the lowest exposed unit of the sequence and precedes the glaciovolcanic eruptive activity. The unit is divided into two sub-units that differentiate two chemical suites of subaerial lavas that are stratigraphically equivalent. Overlying the lavas are diamictite (facies Dia1) deposits that contain clasts of basaltic lava with a chemical composition unique to the Austurfjöll suit that are assigned to unit Dm1. The lavas display subaerial textures and glacial scour (facies L2). The subaqueous eruptive sequence includes units 2 through 7 and Dm2. Within units that contain both porphyritic and microcrystalline lithofacies, there is no significant trend in the results of porphyritic samples relative to those of micro-porphyritic samples. However, the linear trend of eruptive units 2, 3, 5 and 6 of increasing concentration of incompatible elements and plagioclase cations correlates to the abundance of porphyritic samples within the unit, rather than chronology. Of the subaqueous eruptive sequences, Unit 3 is the most evolved (Figure. 3.3, 3.6) and displays no porphyritic samples. Unit 6 is the least evolved unit and is the only exclusively porphyritic unit. Units 4 and 7 are both defined by small outcrops and a single geochemical sample. As such it is hard to evaluate the consistency of this trend through these units, which plot reasonably well along this trend. The Holocene samples are subaerial and occur on the margins of the massif, locally overlying glaciovolcanic units and plot toward the less evolved end of the spectrum of Austurfjöll compositions.

### 3.3 PHENOCRYST COMPOSITION

The coherent lava samples collected for geochemical analysis contain up to five mineral species as described in Chapter 2, but are dominated by plagioclase feldspar and clinopyroxene, with abundant opaque minerals in subaerial samples. Secondary crystals of olivine and orthopyroxene were observed in 5% of the samples comprising typically less than 5 vol. % of the sample. SEM based EDS provided semi-quantitative data on the composition of the major phenocrysts and microlites (Figure 3.9). The composition of microlites in the groundmass and larger phenocryst mineral species were compared for similarities (Table 3.2).

EDS mineralogical composition data revealed that the composition of large phenocrysts of plagioclase crystals fall into two major groups of Bytownite (An 80) and Labradorite (An 60), with groundmass microlites having compositions of Labradorite (An 70) and less commonly as Andesine (An 40) (Figure 3.10). The clinopyroxene phenocrysts covered a range of compositions of Mg #50-70 and groundmass microlites occurred in two groups of Mg# 40 and Mg# 70. Gabbro and lava samples frequently contained two compositions of both plagioclase and clinopyroxene phenocryst species and one or two groundmass crystal compositions of each mineral (Table 3.2).

Some megacrysts of plagioclase display poikilitic textures, containing inclusions of clinopyroxene, earlier plagioclase crystals, or glass (Figure 3.11). One of the gabbro nodules (AG 1) also contains glass in voids between crystals near the sample margins. The composition of the inclusions is highly variable. In the lapilli tuff some of the apparent glass inclusions are similar to the host glass. Oxides identified in thin section were determined to have significant titanium content, suggesting the presence of ilmenite and titanomagnetite (Höskuldsson, 1987).

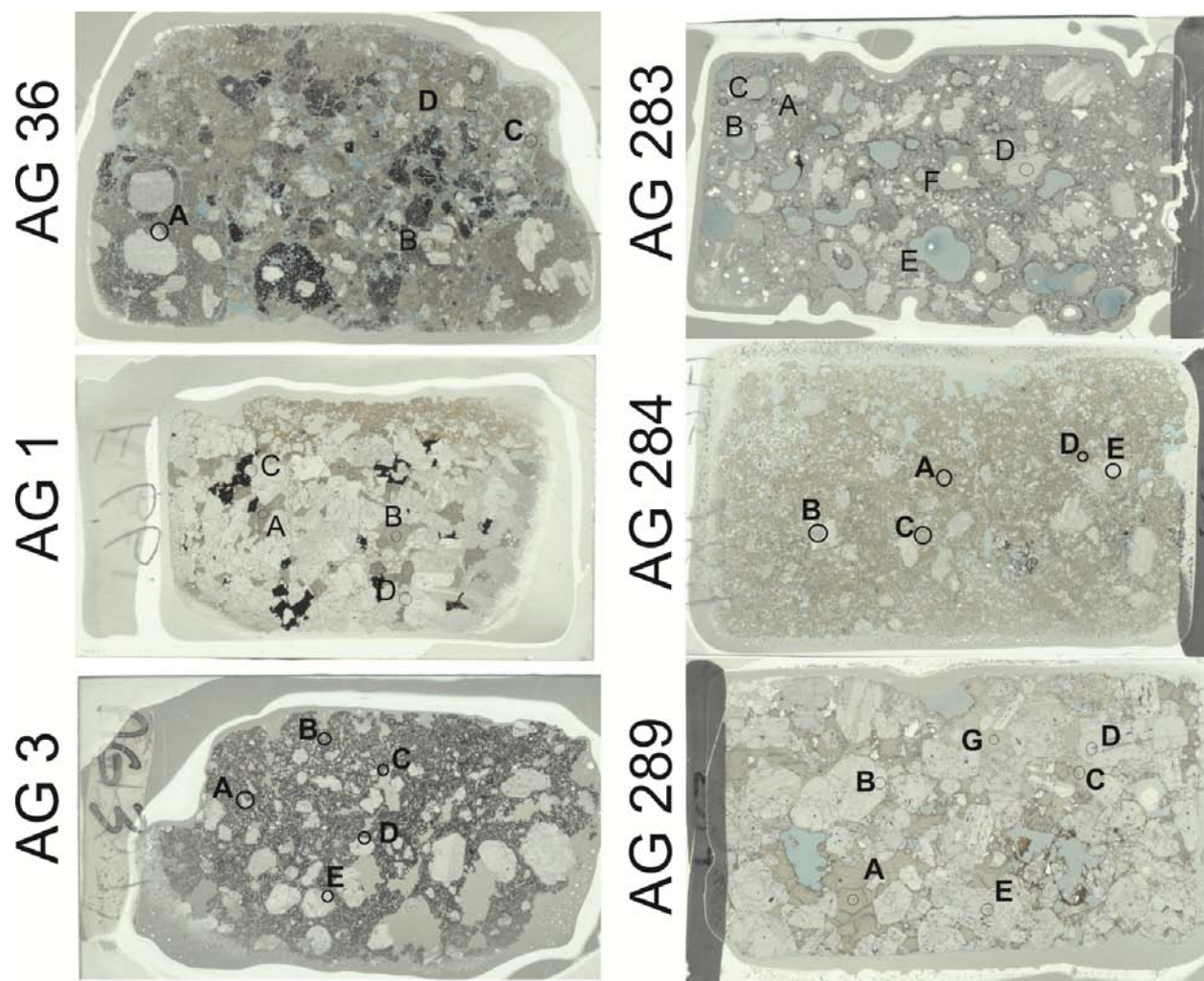


**Figure 3.9** Polished thin sections in PPL. The locations of EDS analysis are circled. Targets included phenocrysts and microlites in the groundmass. Blue epoxy indicates presence of vesicles.



**Table 3.2 Average crystal composition as determined semi-quantitatively by SEM EDS.**

	Plagioclase		Clinopyroxene	
	Phenocryst	Groundmass	Phenocryst	Groundmass
Gabbro	An 60, An 80		Mg # 60-70	
Lava	An 50, An 85	An 45, An 70	Mg # 75	Mg # 75

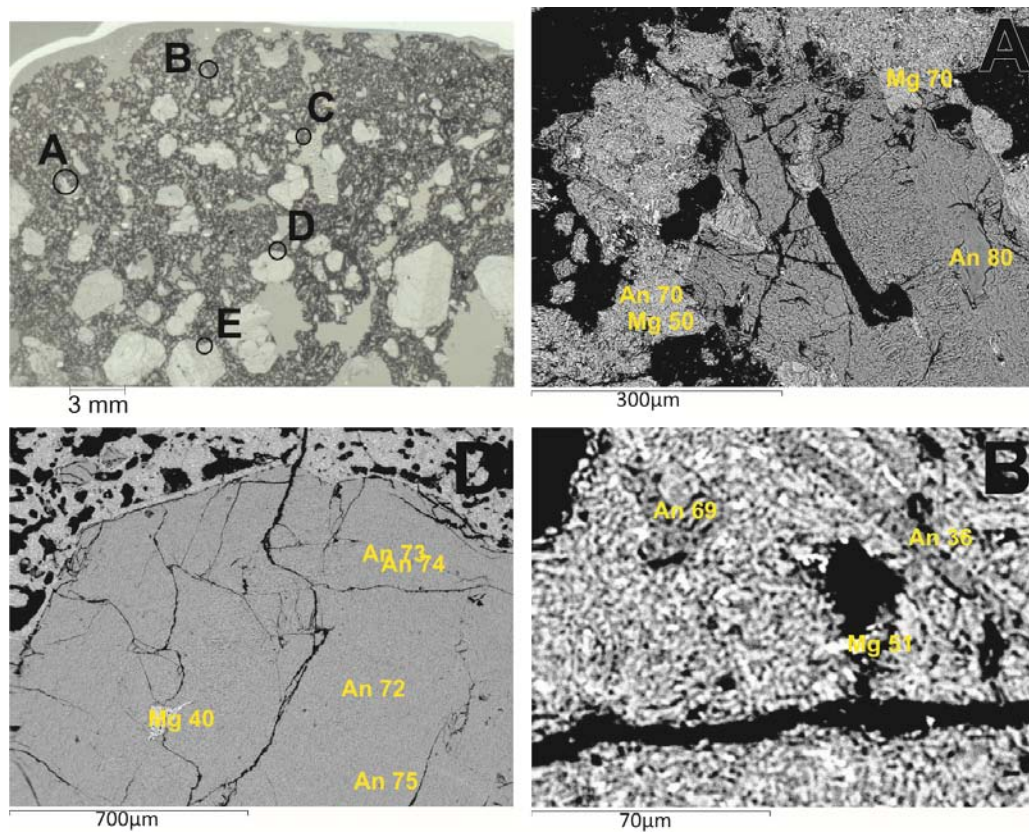


**Figure 3.10** Example of EDS analysis locations and results. Sample AG 3, a porphyritic lava of eruptive unit 6 contains phenocrysts of plagioclase and Cpx with a microlite rich groundmass. Labels correspond to location within the slide image.

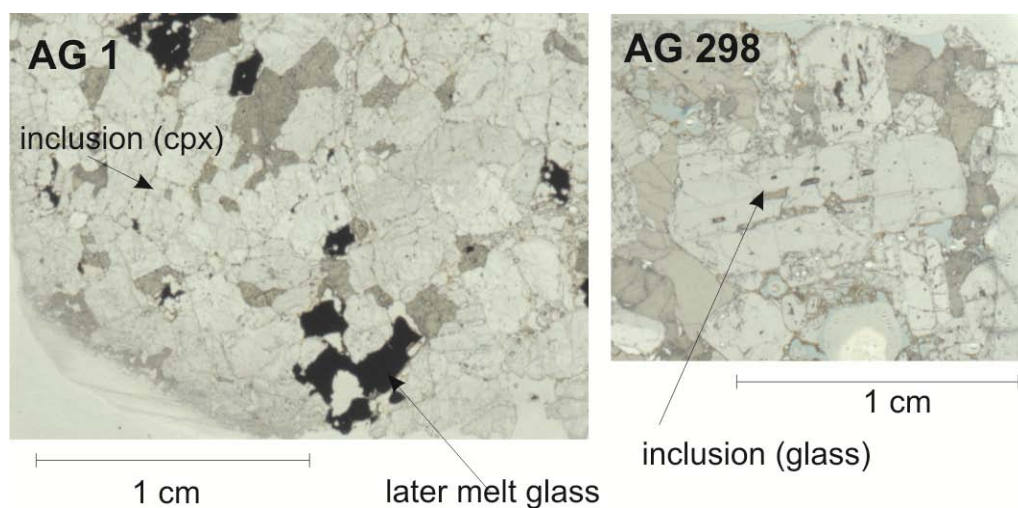


**Figure 3.11 Inclusions in macro-phenocrysts.**

### **3.4 RADIOGENIC DATING**

Two samples of glaciovolcanic basaltic lava were successfully dated using unspiked K/Ar methods of Guillou et al. (2010) (Table 3.3). Prior to this study many Icelandic basalts with low potassium contents were considered undatable (Guillou et al., 2010). This study presents the first age calculations for the glaciovolcanic deposits of Askja. Unspiked K/Ar dating of such basalts opens new possibilities for paleoclimate studies in Iceland. The ages derived were  $71 \pm 7$  ka (AG 131) for Unit 2 and  $29 \pm 8$  ka (AG 137) Unit 3. The two units are texturally similar and both occur near the base of the massif, but were distinguished through morphological and geochemical characteristics. In several locations Unit 3 directly overlies Unit 2.



**Table 3.3 K-Ar ages of subaqueous pillow lavas from Austurfjöll. Analysis conducted by H. Guillou, LSCE, CEA-CNRS, France.**

Sample	Eruptive Unit	Lithofacies	Age
AG 130	Unit 2	Pl2	71+/-7 ka
AG 137	Unit 3	Pl1	29+/- 8 ka
Error is a calculated by 2 $\sigma$ where 1 $\sigma$ consists of analytical uncertainties as propagated and quadratically averaged of the Ar and K determinations.			

### 3.5 DISCUSSION

Despite the narrow compositional range of the tholeiitic basalts at Austurfjöll, bulk rock geochemistry was successfully used to discriminate seven eruption units corresponding to lithofacies divisions, two sedimentary units, gabbros, and Holocene basaltic cover. Two of the eruptive units were dated at 71 ka and 29 ka. The linear trend of all of the Austurfjöll lavas and similarity in major and minor element chemistry indicates consistent mechanisms for melt evolution at the Askja volcano. The large window of time represented by the lavas suggests that multiple magma batches must be involved, but the process which forms each batch is similar. It is interesting to note that the two eruptive units that are absolutely dated with a 40 ka gap have some of the most similar compositional trends and represent the most evolved eruptive units within the massif (Figure 3.3). This data set reveals significantly more compositional diversity than was initially described in early mapping efforts (Höskuldsson, 1987; Sigvaldason, 1968; Strand, 1987).

Within units that contain both porphyritic and microcrystalline lithofacies, there is no significant trend in porphyritic samples relative to those of micro-porphyritic samples. However, there is a trend of decreasing proportion of porphyritic lavas within an eruptive unit as the samples become more evolved, where the least evolved sample is exclusively porphyritic and the most evolved is macrophenocrysts-free.

### **3.5.1 Major and Minor element trends**

The whole rock geochemistry of the Austurfjöll lavas reveals tholeiitic compositions similar to what is observed elsewhere in the NVZ (Jakobsson et al., 2008; Meyer et al., 1985). The near absence of olivine in Austurfjöll samples is distinctive for an Icelandic tholeiite, and likely influences the lower MgO values detected. The Austurfjöll samples are otherwise fairly typical for Icelandic olivine tholeiites and are slightly enriched in REE and incompatible elements than typical mid-Atlantic ridge basalts (Jakobsson et al., 2008; Schilling et al., 1983). Incompatible element variation diagrams reveal strong linear trends in the sample suite revealing and increasing enrichment of the units with decreasing macro-phenocryst presence. The REE trends of the Austurfjöll lavas share similarities to Bárðarbunga and Grímsvötn volcanoes that occur under the north eastern portion of the Vatnajökull icecap (Meyer et al., 1985). Austurfjöll samples are similar in bulk rock chemistry, but has higher K than other NVZ, eastern volcanic zone, or Reykjanes Peninsula lavas (Meyer et al., 1985; Óladóttir et al., 2011).

A normative mineral classification (CIPW) was used to test whether the eruptive units were evolved enough to classify as quartz tholeiites (Jakobsson et al., 2008; Kelsey, 1965). The norm is typically applied to porphyritic and aphanitic samples, where mineral phases are not detectable in typical petrographic techniques (Kelsey, 1965). The norm utilizes major elements to predict the mineral phases that would occur in equilibrium within an anhydrous system. CIPW norm calculations highlighted an apparent silica saturation of a 35% of the samples, particularly those that contain the brown glass typical of a quartz tholeiite in thin section (AG 290 and AG 277). However, there is no consistent trend of silica

saturation among eruptive units, with no unit being more than 50% silica saturated, indicating that the lavas are not silica saturated. By acknowledging the subjective location of the saturation threshold, the Austurfjöll lava suite is therefore more appropriately described as olivine normalized tholeiite.

### **3.5.1.1 Establishment of units**

Eruptive units were defined through the establishment of clusters of similar geochemistry that corresponded with established lithostratigraphic boundaries mapped in the field. Of the seven eruptive units, the confidence rating indicates which units are well defined and which are limited due to either distribution or sampling bias. Typically the units with fewer than three samples have lower ratings. Unit 1A contains 2 samples whereas Unit 1B only contains one. This division into two subunits is a result of their unique compositions, their stratigraphic position, and glacially scoured / eroded morphology. The stratigraphic position indicates that they both predate the glaciovolcanic sequence of Austurfjöll. As there is no exposed contact between 1A and 1B they are considered equivalent stratigraphically. They both display textures characteristic of subaerial lavas, including an abundance of opaque oxide minerals.

Unit 2 has the greatest number of samples (23) and likely as a consequence, the greatest internal chemical diversity, but it retains an average confidence rating of 2.56, having a standard deviation of less than 10% of the total range in values. Unit 3 has a reasonable number of samples to define the chemical unit (8), and has the greatest internal consistency and narrowest range of major and trace element values, with an average confidence rating of 2.75 and a standard deviation less than 5% of the total abundance of a given element. This unit is also the most evolved of all of the eruptive units, having the greatest abundance of incompatible elements. Unit 5 has the second highest number of samples (11), but greatest textural variability as it contains subaqueous microcrystalline, subaqueous porphyritic, and subaerial emergent lavas. The confidence rating of all of the samples within the group is high at 2.63 with a standard deviation less than 10% of the total abundance of a given element. Unit 6 was established from four samples, defining the only all porphyritic chemical group, but with a high confidence rating of 3 and a standard deviation of no more than 10% of the abundance of a given element.

Units 4 and 7 both are represented by only one sample and have small geographic distributions. However, their major and trace element abundances are distinctive, but still fit within the established linear trend of the better defined eruptive units, indicating they are likely genuine groups and not significantly altered. The two gabbro samples have distinctive compositions from each other and the rest of the Austurfjöll suite. They were both collected as xenoliths within Unit 5. The most primitive sample of gabbro plots along a linear trend with all other samples, but has much lower concentrations of incompatible elements and plagioclase cations. The second gabbro sample is more evolved, and fits on the same linear trend as the rest of the sample suite and plotting within the cluster of Unit 6 (Figure 3.5, 3.6). This sample contains glass in the void spaces between crystals (Figure 3.11). The glass may represent more evolved melt that coated the xenolith during eruption and would benefit from more precise microprobe analyses.

Two samples of subaerial spatter that were collected from the northeastern margin of Austurfjöll, near Öskjuop were analyzed to confirm that they were not associated with glaciovolcanic sequence. They have the highest MgO contents of all the samples and are typically less enriched in all other major and trace elements relative to the Austurfjöll suite, and can be confidently assigned to a unique chemical group. The Holocene spatter samples do fall roughly within the linear trend of Austurfjöll lavas (Figure 3.5, 3.6).

Unit Dm1 was defined from a basaltic lithic clast in a diamictite that locally overlies Unit 1A. The composition of the clast is unique to any in the Austurfjöll sequence, which supports the interpretation of Dm1 as a glacial erratic. Dm2 corresponds geochemically to Unit 2; however, it is a basaltic lithic clast within a diamictite that sits directly on top of an exposure of Unit 2. This indicates that it is a glacially derived diamictite that was produced after the formation of Unit 2 and incorporated eroded clasts of Unit 2.

### 3.5.2 Mineralogy

The most distinctive linear trends observed in the Austurfjöll chemical suites involve elements that are critical components to plagioclase phenocryst formation (i.e. CaO, Al<sub>2</sub>O<sub>3</sub>, and Sr). TiO<sub>2</sub> is also important tool for eruptive unit discrimination. This suggests that the formation of mineral phases, particularly plagioclase feldspar, clinopyroxene, and titanium bearing oxides, play a role in the evolution of the melt. The linearity of the trend of CaO/TiO<sub>2</sub> indicates the importance of opaques (metallic oxides) and the V/Y ratios indicate the importance of clinopyroxene and the opaques. These trends match well with the petrography described in Chapter 2.

Typical macro-phenocryst tholeiitic lavas observed in Iceland, sometimes called Plagioclase Ultraphyric Basalts (PUBs) contain plagioclase crystals with compositions between An 80 and An 90 (Hansen and Gronvöld, 2000; Meyer et al., 1985). Some of the macrophenocrysts present rims of compositions as low as An 70. PUB groundmass phenocrysts are typically on the order of An 60, with some examples as high as An 75 (Hansen and Gronvöld, 2000; Meyer et al., 1985). These compositions show a trend with decreasing MgO content as the An value decreases. The Austurfjöll lavas have an average MgO value of 5.5 wt % and have lower An numbers than the values presented in previous studies. Askja Holocene basalts contain An 80-90 plagioclase phenocrysts (Kuritani et al., 2011). The lowest MgO values and correspondingly lowest An values presented by Hansen and Gronvöld (2000) occur at NVZ volcanoes. If the phenocryst-rich lavas of Austurfjöll were expected to follow the trend presented along the Eastern and Northern Volcanic zones of Iceland based on low MgO values, they would be expected to have An values on the order of An 80, the high end-member of Austurfjöll values. What makes the Austurfjöll samples unique relative to these other PUBs is the low abundance of olivine, and consequently lower MgO. The greatest similarity between the Austurfjöll porphyritic lavas and other Icelandic PUB is the MgO content of the glass inclusions in the plagioclase crystals, where Hansen and Gronvöld (2000) reported 4-9 wt% MgO to the Austurfjöll 7.5 wt% MgO. The potential genetic relationship between the gabbros and the Austurfjöll lavas will be discussed further in section 3.8.

### 3.5.3 Pearce element ratios

Pearce element ratios were used to investigate the potential for closed-system evolution of magma batches through crystallization of an individual or multiple crystal species. The presence of plagioclase and clinopyroxene crystals in Austurfjöll lavas suggests that these minerals may have influenced melt evolution. Olivine makes up less than 5% of any sample suite and therefore was not considered to have contributed significantly to the overall melt evolution. Pearce element ratios are based on the principle of plotting a hypothesized variable (mineral species) normalized to an element not involved in the formation of the mineral (i.e. K), against a conserved element (i.e. Si), also normalized to the same non-participating element. Detailed explanations of the technique can be found in Russell et al (1990) and Stanley and Russell (1989). Pearce element ratio diagrams were used to rule out melt evolution histories that only involved one mineral, such as plagioclase or Cpx, and led to the hypothesis that plagioclase and clinopyroxene were both responsible for the evolution of the melts. These initial tests revealed a strong correlation for the whole dataset (Figure 3.12). Cogenetic relationships are indicated by a slope of one for the trend of the data (Russell et al., 1990; Stanley and Russell, 1989). The next step was to plot individual eruptive units with a control line where slope = 1 through the sample that represents that melt (lowest phenocryst population) and compare the y-intercepts of the resulting line (Table 3.4). According to the PER diagrams all of the units can be explained by the same process, where plagioclase crystals of a range of compositions and clinopyroxene are crystallized and removed from the melt (Figure 3.13). There is significant overlap between the control line of units 1A, 2, and 3. Unit 5 plots closely to Unit 1B, but Unit 4, 6, and 7 display clear independent groupings where the y-intercept of the control line for the unit is unique. However, stratigraphic evidence and radiogenic dating support the eruptive unit divisions (Figure 3.14). Units 1A, 2, and 3 are well established within the Austurfjöll chronology. Particularly Unit 2 and Unit 3 have a known age difference of 42 ka  $\pm$  8. This age gap suggests that it is therefore unlikely that the two units tap the same magma body, despite the overlap of their control lines in PER diagrams. This apparent cogenetic relationship between eruptive units occurring over a 40 ka period implies a

consistency of processes that contribute to magma batch evolution in this long-standing rift system. Unit 1A and Unit 2 are stratigraphically separated by the presence of Dm1 and erosional surfaces. The control line of Unit 1B has a very similar y-intercept to Unit 5, but again the stratigraphic relationships, here multiple eruptive units spanning a minimum of 40 ka, preclude a shared melt. In addition to any closed system magma differentiation process, eruptive unit chemical variability may be the result of a variety of path effects, recharge, contamination by crust, or interaction with cumulates. The similarity of all of the Austurfjöll lavas, however, indicates a consistency in melt generation mechanisms and evolution beneath Askja over this time period.

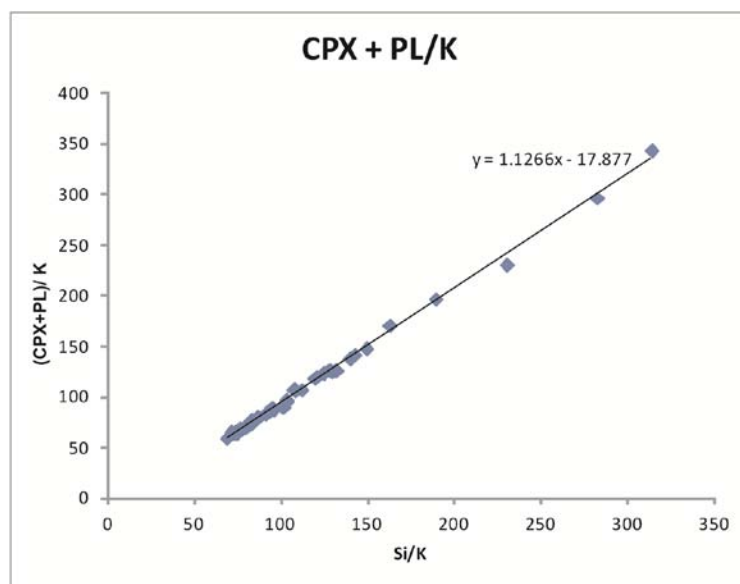


**Figure 3.12** Pearce Element Ratio of all Austurfjöll samples indicating the control of the full range of plagioclase compositions and Cpx. That the slope of the resulting line is 1.126 suggests a reasonable cogenetic relationship, but indicates the need for further division of eruptive units to confirm this relationship, as a true relationship would have a slope of 1.0.

**Table 3.4 A comparison of y-intercept values for PER control lines with a slope of one, representative of each eruptive unit. Associated with Figure 3.13.**

Unit	Y –intercept	
1A	-7.0614	*
1B	-5.0818	**
2	-8.5008	*
3	-8.5003	*
4	+4.1672	
5	-4.5336	**
6	-0.9863	
7	-30.061	
*Apparent cogenetic relationship between these units.		
**Apparent cogenetic relationship between these units.		



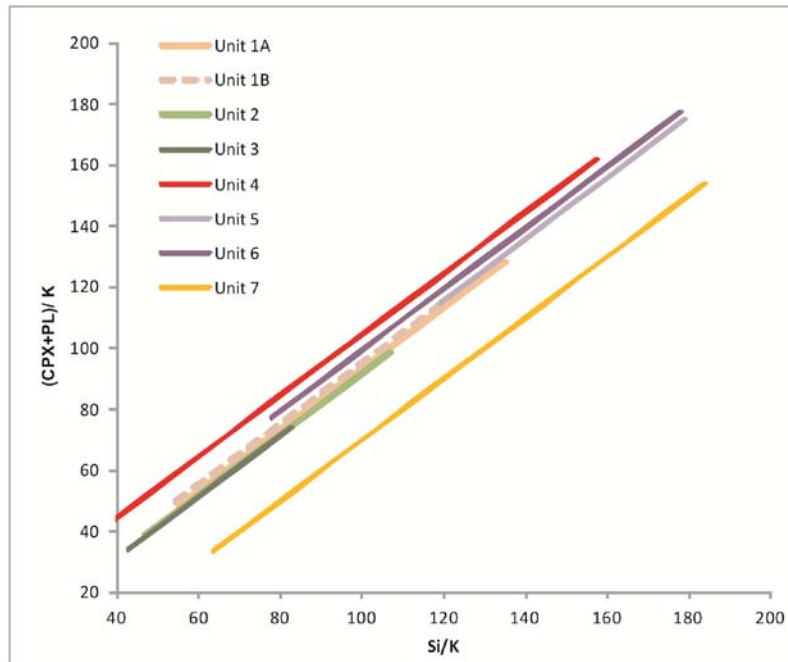


**Figure 3.13 Control lines with a slope of one centered on characteristic samples for each eruptive unit. The overlap of Units 1, 2 and 3 is significant. Unit 5 and Unit 1B similarly overlap. Units 6, 4 and 7 are distinctive from all of the other slopes. The process that controls the evolution of all of the units, however, is consistent, being dependent on Cpx and Plagioclase.**

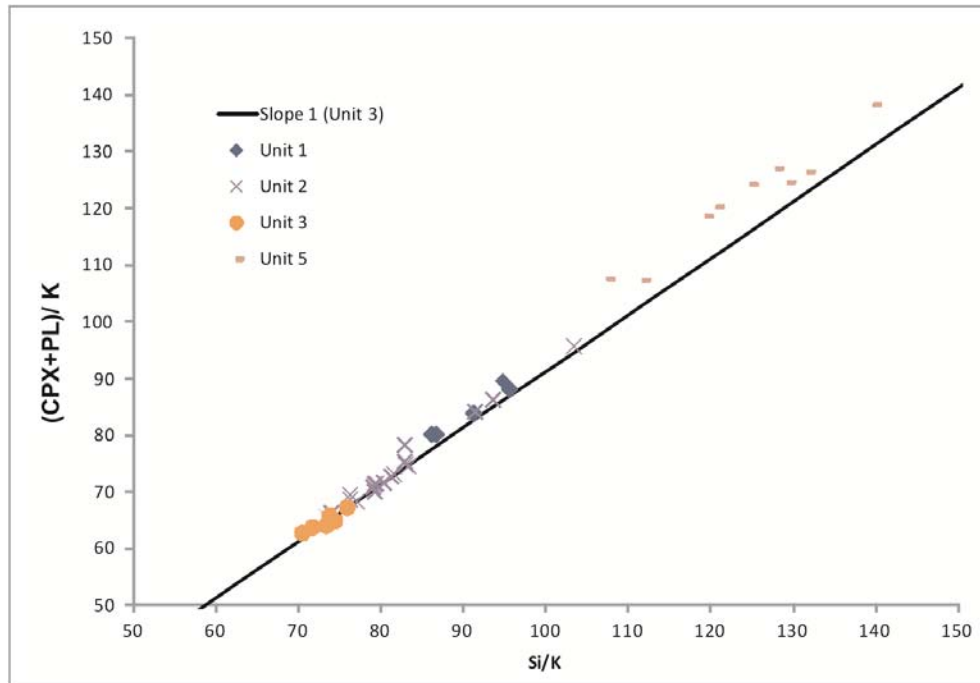


**Figure 3.14 Comparison of units 1, 2, 3, and 5. The Unit 3 control line is included. An apparent relationship occurs between units 1, 2 and 3 (see text for discussion).**

### 3.6 CONTEXT OF ASKJA

Studies of postglacial and historic lava flows around Askja have included some scattered bulk rock compositional data (Kuritani et al., 2011; Thorarinsson and Sigvaldason, 1962). However, the largest dataset of XRF geochemical data on lavas in the Askja area was collected by D. McGarvie in the 1980s. These data include Holocene basaltic lava flows, interglacial shield volcanoes, rhyolite domes, dacite lavas, and historic basaltic lava flows (McGarvie pers. comm.). The bulk rock major and trace element results from these previous studies of Holocene and historic basaltic lavas are presented here in Appendix B.4. Major element and trace element trends were investigated in the same manner as the Austurfjöll lavas to compare the range of melt variation of Austurfjöll massif relative to the longer history of Askja volcano.

The historic effusive activity proximal to Austurfjöll occurred in two main periods during the 1920s and in 1961 (Figure 3.15). The events of the 1920s are more disperse, with multiple small vents and resulting lava flows. Samples in the collection include samples from Bátshraun (1921), Mývatnsveitahraun (1922), Kvíslahraun and Suðurbotnahraun (1922/23), and lavas fed from the western corner of Thorvaldstinudur that extend south and east are here referred to as the Southeastern Flank (1924 and 1929). A scoria cone constructed in 1926 in southern Öskjuvatn produced the island Eyja. This island was not sampled for this study. Samples of the 1961 a'a lava flows are also included in the analyses that are comparable to previously published values (Thorarinsson and Sigvaldason, 1962). Samples of postglacial lavas were collected in the region around Askja from various locations. Samples of historic basaltic lava from the Sveinagjá fissure located 60 km north of Askja that were erupted in conjunction with the 1875 rhyolitic eruption of Askja (Sigurdsson and Sparks, 1978) are included in the comparison.

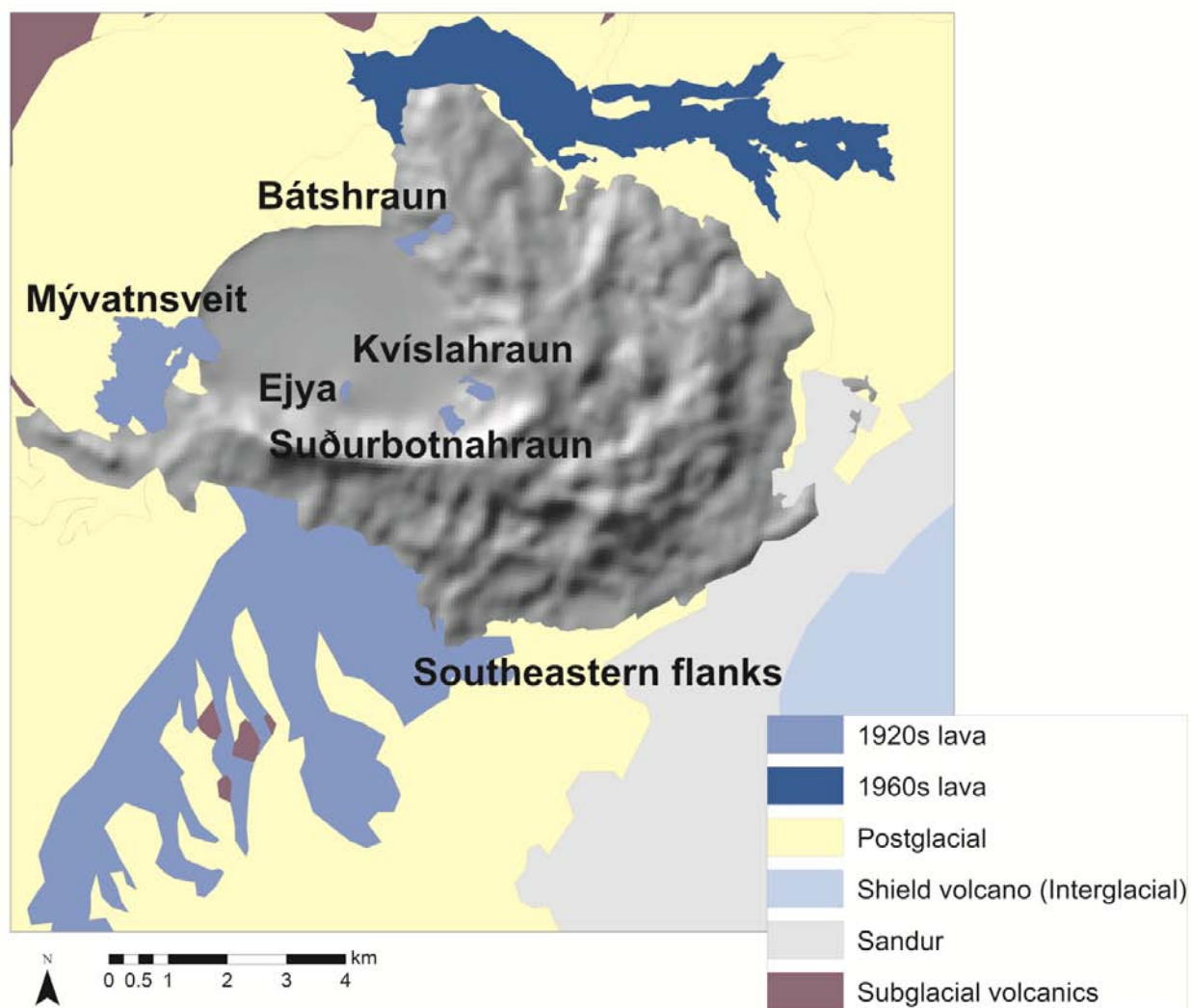


**Figure 3.15** Locations of historic lava flows featured in geochemical analyses as they are distributed around Austurfjöll (hillshade). The locations of samples are approximate due to the absence of GPS data. Labels are of individual eruptive units from the 1920s. Eyja was not sampled.

The total range of compositions of historic basalts and postglacial lavas is comparable to that of the Austurfjöll suite (Figure 3.16), with a similar linear trend of plagioclase cations and incompatible elements and overall enrichment relative to MAR basalts. Only Mývatnsveitahraun (MYV) and a subgroup of the Southeastern Flank lavas plot outside of the range of the Austurfjöll lavas. These two sets of samples are enriched in alkalis relative to the rest of the samples. The postglacial lava suite alone has as much diversity as the Austurfjöll suite. With the exception of MYV, the 1920s lavas and 1961 lavas have a fairly constricted range of compositions, and plot at the more enriched end of the spectrum of Askja compositions. The Sveinagjá lavas also plot well with the enriched Austurfjöll lava range, but the sample number is limited. The lavas of the southeastern flank have by far the greatest diversity of any Askja sample set, falling into three apparent subgroups. As the sample locations are not well constrained geographical trends for this set of lavas are not yet feasible. One of the southeastern flank sub-groups plots with the other enriched historic lavas. A second southeastern flank lava sub-group is uniquely enriched in  $K_2O$ , but not other incompatibles. The final subgroup plots with the least enriched Austurfjöll and postglacial lavas and glass-bearing gabbro sample (AG 1). The Holocene spatter samples collected during this study from the margins of Austurfjöll do not match chemically with the historic 1961 lavas, which they are proximal to in the field. They do, however, fall into the envelope of postglacial lavas collected by McGarvie, which suggests that they predate the historic activity, confirming their identification as Holocene spatter.

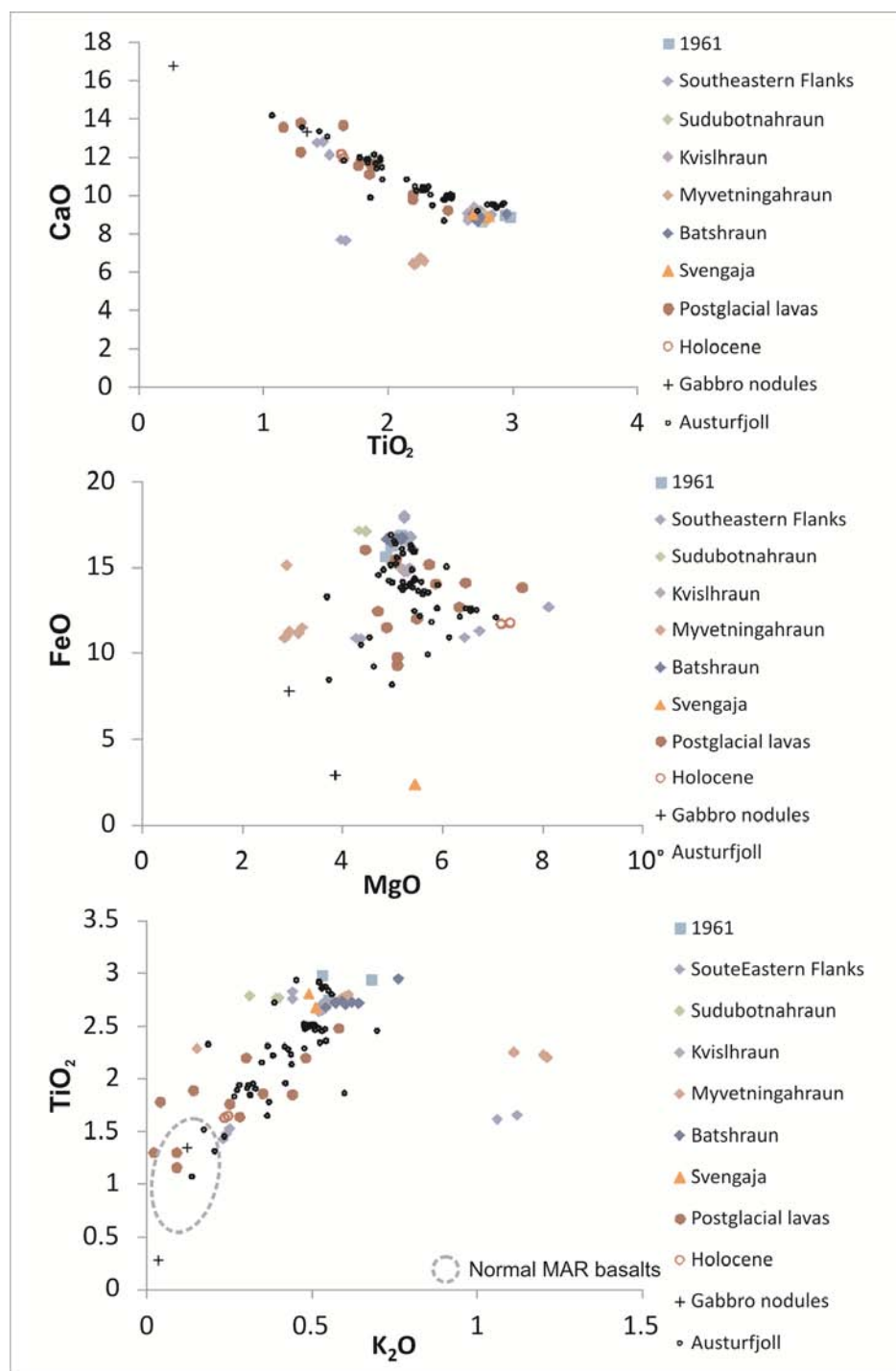


Figure 3.16 Comparison of postglacial and historic lavas (McGarvie, pers. comm) with Austurfjöll suite. Values of Normal MAR basalts are from Jakobsson et al. (2008).

### 3.7 PETROGENESIS

The geochemical analyses of two gabbro nodules revealed distinct compositions for each sample despite similar crystal populations. In thin section, however, the interaction of the nodule AG 1 with a basaltic melt during transport during eruption is preserved in the form of tachylite glass in void spaces between the outermost crystals of the nodule. The geochemistry of this sample is evolved relative to the uncontaminated gabbro sample AG 289. The presence of the nodules also suggests that Austurfjöll units interacted with a crystal-rich zone before eruption. This may indicate that the gabbro represents crystals that were removed from the evolving tholeiitic melt and accumulated in a magma chamber beneath Askja. The nodules would be formed where moving melt batches dislodge and capture part of the cumulate. There are multiple sources of evidence to indicate the relationship between melt evolution and macro-phenocrysts of plagioclase and clinopyroxene including: petrology of porphyritic samples, enrichment of Sr, gabbro nodule xenoliths, semi-quantitative mineral compositions of macro-phenocrysts matching gabbro crystals to lava phenocrysts, PER test diagrams of plagioclase and clinopyroxene genetic relationship, and similarities to other macro-phenocryst-rich tholeiites at Icelandic central volcanoes (Furman et al., 1992; Hansen and Gronvöld, 2000). Despite the apparent similarities in magma evolution processes of Austurfjöll lavas, there is still sufficient diversity of the resulting lavas to enable the discrimination of eruptive units. This then suggests that there are likely other controls to this melt evolution, including path effects, recharge, contamination by crust, or interaction with cumulates.

Unit 6 and 3 represent the most extreme compositions of the spectrum of the Austurfjöll compositions. Unit 3 is the most evolved melt, with low MgO concentrations, enrichment in alkali and incompatible elements, and low phenocryst populations. Unit 6, in contrast, is the least evolved of the eruptive units, with lower incompatible element compositions, and exclusively porphyritic textures. The Unit 6 samples are enriched in CaO and Al<sub>2</sub>O<sub>3</sub> and are lower in TiO<sub>2</sub>, Na<sub>2</sub>O, FeO, and K<sub>2</sub>O relative to Unit 3. This supports the enrichment in calcium-rich plagioclase in the less evolved samples as indicated by the presence of macro-phenocrysts of plagioclase.

The PER analysis and gabbro nodules reflect the likely crystallization and removal of plagioclase and clinopyroxene from the melt in order to produce the Austurfjöll lavas. As a further test of this hypothesis, a model was created where the most primitive gabbro (AG 298) was added to Unit 3 until compositions of Unit 6 were reproduced. This test was repeated using Unit 2 as the evolved melt. The test was accomplished by adding a percent of gabbro to the average composition of Unit 3 and renormalized to produce a modeled melt with increasing concentrations of plagioclase and clinopyroxene. The process was repeated for Unit 2 (Figure 3.17). The linear trend of the lava was easily reproduced through the progressive mixing of gabbro with the evolved Unit 3 and Unit 2 melts. There is a slight variation in the slope of the mixing lines produced for Unit 2 and Unit 3, but they define a narrow window, which represents the bulk of Austurfjöll compositions. The Unit 6 lavas represent an interim melt composition that was reproduced through the modeled incorporation of a greater percentage of plagioclase and clinopyroxene. However, if the gabbro represents the cumulate of solid removed from a parental melt with a composition similar to Unit 6, the melt would have to experience over 66% crystallization, according to the Lever Law (Figure 3.17). If instead Unit 5 were to be used as the parent, and Unit 6 were the product of contamination by crystals from the cumulate, the resulting crystallization is on the order of 33%. If the parent were Unit 4 only 10 % fractional crystallization would be required to produce the most evolved melts (Unit 2 and Unit 3). Unit 6 lavas are exclusively porphyritic in texture, and Unit 5 has numerous porphyritic units which supports the idea of contamination by phenocrysts. However, porphyritic lavas with a Unit 2 composition were analyzed, and they fit well in the variability expected of the group on the more evolved end of the compositional range. This exercise remains interesting, but cannot advance beyond speculation without further data including melt inclusions and radiogenic isotopes (e.g. Kuritani et al., 2011) in order to fingerprint the parental melt and the dominance of contamination vs. crystallization. The accumulation of a cumulate that could produce the observed gabbros would require a significant residence time in the lower crust. Deformation studies (InSar, GPS, Tilt, gravity) over the last three decades have led to models of two discrete sources in the crust below Askja at 3 km and 15 km (de Zeeuw-van Dalen et al., 2005; Pagli et al., 2006; Soosalu et al., 2010; Sturkell et al., 2006). These are



potential locations for cumulate accumulation. Evolution of a central volcano including a gabbro accumulation stage and replenishment has been proposed based on dissected massifs on the eastern coast of Iceland (Furman et al., 1992). Crustal reservoirs have been also been suggested for EVZ and NVZ volcanoes from geochemical evidence (Hansen and Gronvöld, 2000). The formation of the cumulate, through the fractional crystallization of plagioclase and clinopyroxene would occasionally be disrupted by recharge and eruptions. Under the right conditions the rising lava would potentially carry macro-phenocrysts derived from a disrupted cumulate dispersed within the melt to produce macro-porphyritic lavas. Alternatively, the cumulates are left undisturbed until later injections of magma disrupt them and carry portions of the cumulate to the surface in the form of gabbro nodule (Furman et al., 1992; Hansen and Gronvöld, 2000). To further elucidate the mechanisms and time scales of this process more must be known about the composition of the melts in the form of radiogenic isotopes, melt inclusions, and more precise crystal compositional data (i.e. microprobe).

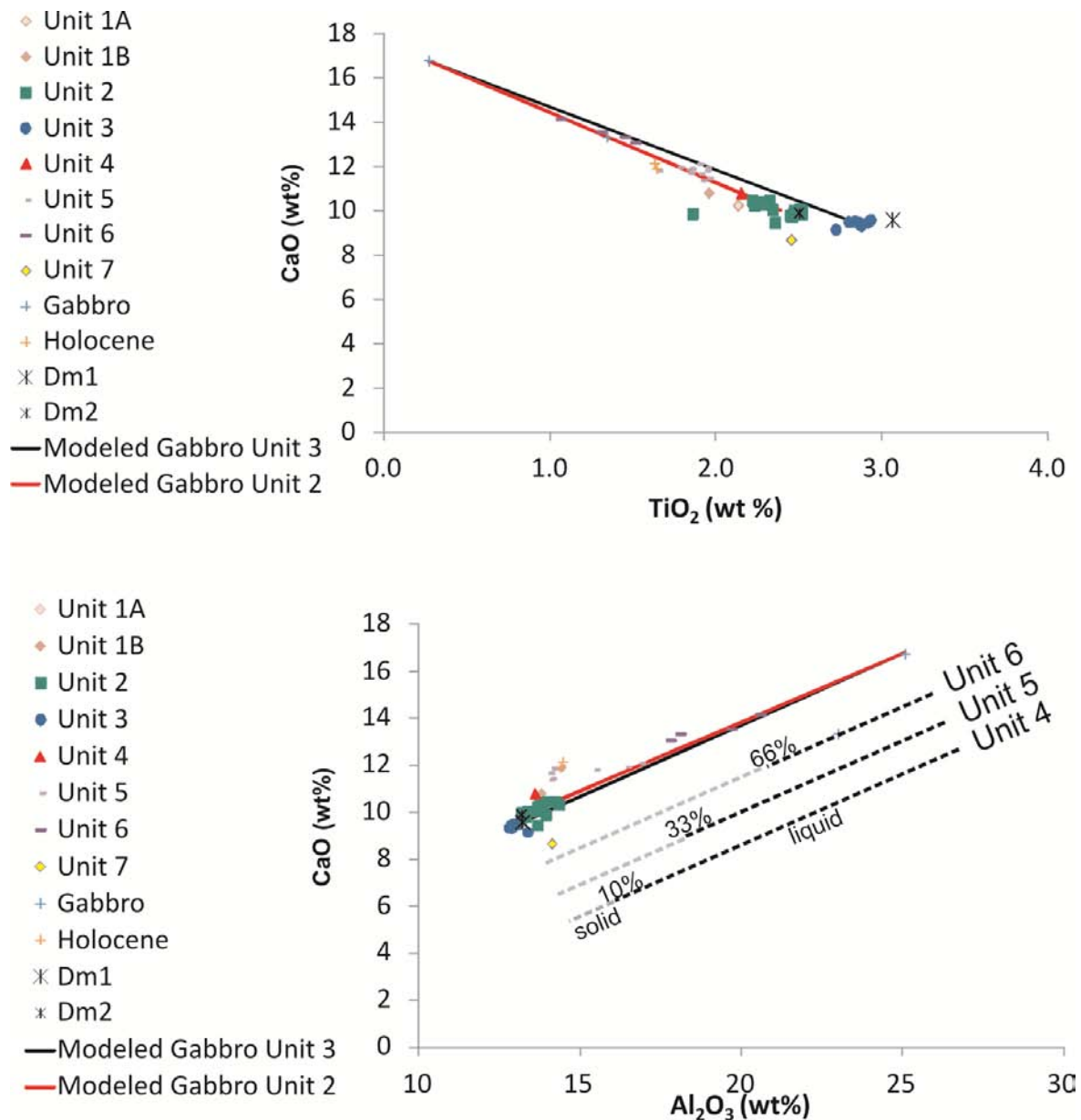


**Figure 3.17** Austurfjöll samples with mixing lines between the most evolved units (2 and 3) to the least evolved gabbro sample. The Lever Law was applied to determine the approximate amount of fractional crystallization required to create the most evolved melts with different potential ‘parent’ melts. The melts more primitive than the ‘parent’ would be produced by the contamination of parent melt material with cumulate present in the magma chamber.

The chemistry of the Austurfjöll and Holocene lavas are all enriched in incompatible elements relative to the MAR (Jakobsson et al., 2008; Sigmarsson et al., 2008) as seen in Figure 3.13. Iceland sits along the Mid-Atlantic Ridge, but is 3000 m higher in elevation than the neighboring ridges. The Icelandic crust is 15-35 km thicker than normal oceanic crust and has an enriched chemistry relative to N-MORB lavas (Allen et al., 2002; Gee et al., 1998). The enrichment of both the Austurfjöll and greater Askja lavas matches the expected enrichment of Icelandic tholeiites as a result of the interaction between the MAR and the Icelandic hotspot (Allen et al., 2002; Gee et al., 1998; Jakobsson et al., 2008; Sigmarsson et al., 2008). The center of the hotspot is typically proposed, through geochemical and geophysical techniques, to be around Bárðarbunga or Kverkfjöll (Schilling et al., 1983; Sigmarsson et al., 2008; Sigvaldason et al., 1974) at the margins of Vatnajökull icecap to the southeast of Askja. The most primitive composition in Iceland, reflecting the greatest influence of the hot spot, occurs at Kistufell (Breddam, 2002), just south of Askja near the location of the estimated thickest Icelandic crust (Allen et al., 2002). Discrimination between mantle sources and residence times of magma batches cannot be resolved without radiogenic isotope data, particularly Sr, Pb and He (Sigmarsson and Steinthórsson, 2007).

The low MgO contents, REE, and abundance of incompatible elements even in the gabbros indicate that the melts that produced these eruptive units were evolved relative to the regional mantle (N-MORB of the MAR). From this knowledge a few qualitative observations can be made. The evolution of the melt is similar to expected compositions of MAR melts that have interacted with the Icelandic Hot Spot. The range in compositions, linear trend, and consistency in mineralogy indicates that the melts are generated using the same repeating process. Further exploration of the petrogenesis of the Austurfjöll lavas requires a new sampling campaign focusing on the identified eruptive units for the purpose of radiogenic isotopic fingerprinting. Further sampling of gabbro nodules and detailed microprobe analysis of phenocryst populations are necessary to reveal the processes which have repeated in generating, storing, and erupting magmas at Askja, and what produces the distinctive characteristics of individual magma batches.

### 3.8 CONCLUSIONS

The establishment of seven eruptive units, two diamictite units, and two gabbro chemical groups indicates a complexity within the Austurfjöll massif not previously detected (Höskuldsson, 1987; Sigvaldason, 1968; Strand, 1987). A similar trend in compositional diversity is observed in the postglacial lavas that are exposed around the Austurfjöll massif (McGarvie pers. comm.). As some eruptive units were defined using only one geochemical sample, these eruptive units may actually under represent the diversity of the Austurfjöll lavas. Nevertheless, the chemical similarity of eruptive units, such as Unit 2 and Unit 3, which have numerous samples and wide geographic distribution, suggest that the major massif building eruptive phases are well characterized.

The dates presented here are the first for the glaciovolcanic deposits of Askja and indicate a complicated history with ample time for the interaction with multiple glacial advances within the last glacial period (to be discussed further in Chapter 8). The linear trend and PER analysis indicate repeating mechanisms of melt generation dependent on plagioclase and clinopyroxene phenocrysts. However, the range of compositions also suggests there is more than closed-system melt evolution, potentially reflecting path effects, recharge, and / or contamination. To fully reconstruct the petrogenesis of Austurfjöll lavas further investigation is required, using such tools as radiogenic isotopes and melt inclusions in order to fingerprint mantle sources and differentiate between mixing and differentiation.

The seven eruptive units of Austurfjöll reveal that Askja is a long lived poly-genetic basaltic central volcano with over 40 ka of glaciovolcanic activity and significant Holocene activity (Annertz et al., 1985; Carey et al., 2009; Hartley and Thordarson, 2012; Sigurdsson and Sparks, 1978; Þorarinsson, 1963; Þorarinsson and Sigvaldason, 1962). The chemical variability of the subaqueous Austurfjöll lavas is similar to the range of lavas produced during the Holocene in subaerial environments. This is clearly a well established system built up of multiple small to moderate volume eruptions.

#### **4.0 ARCHITECTURE AND EVOLUTION OF AUSTURFJÖLL MASSIF: IMPLICATIONS FOR ASKJA VOLCANO, ICELAND**

The reconstruction of the eruptive history of the Austurfjöll massif is based on a combination of physical volcanology, geochemistry, and radiogenic age dating. The 48 km<sup>2</sup> massif was described and mapped in detail with representative sampling of coherent and fragmental glaciovolcanic deposits, and related subaerial lavas. Two maps were produced of the massif, one based solely on lithology (Chapter 2) and a second based on chemostratigraphy presented here. The eruptive units defined through geochemical and lithostratigraphic evidence were used to establish the chronology of the eruptive units and their relative contributions to the growth of the massif. The chemostratigraphic map shows the seven lithostratigraphic and geochemically-identified eruptive units, the location of coherent facies, porphyritic deposits, and glacio-sedimentary deposits (Figure 4.1). The chemostratigraphy map is restricted to the Austurfjöll massif due to a low sample density in reconnaissance areas such as Thorvaldstindur and the area north of Öskjuop. These additional data points imply a likely relationship between Austurfjöll and the northern glaciovolcanic deposits of Askja, but further field work and analyses would be required to properly establish this connection. Extrapolated cross-sections through Austurfjöll (Section 4.2) are based on the simplified stratigraphy and the morphology of constructional features such as fissure ridges, pillow sheets, and inter-ridge depositional centers.

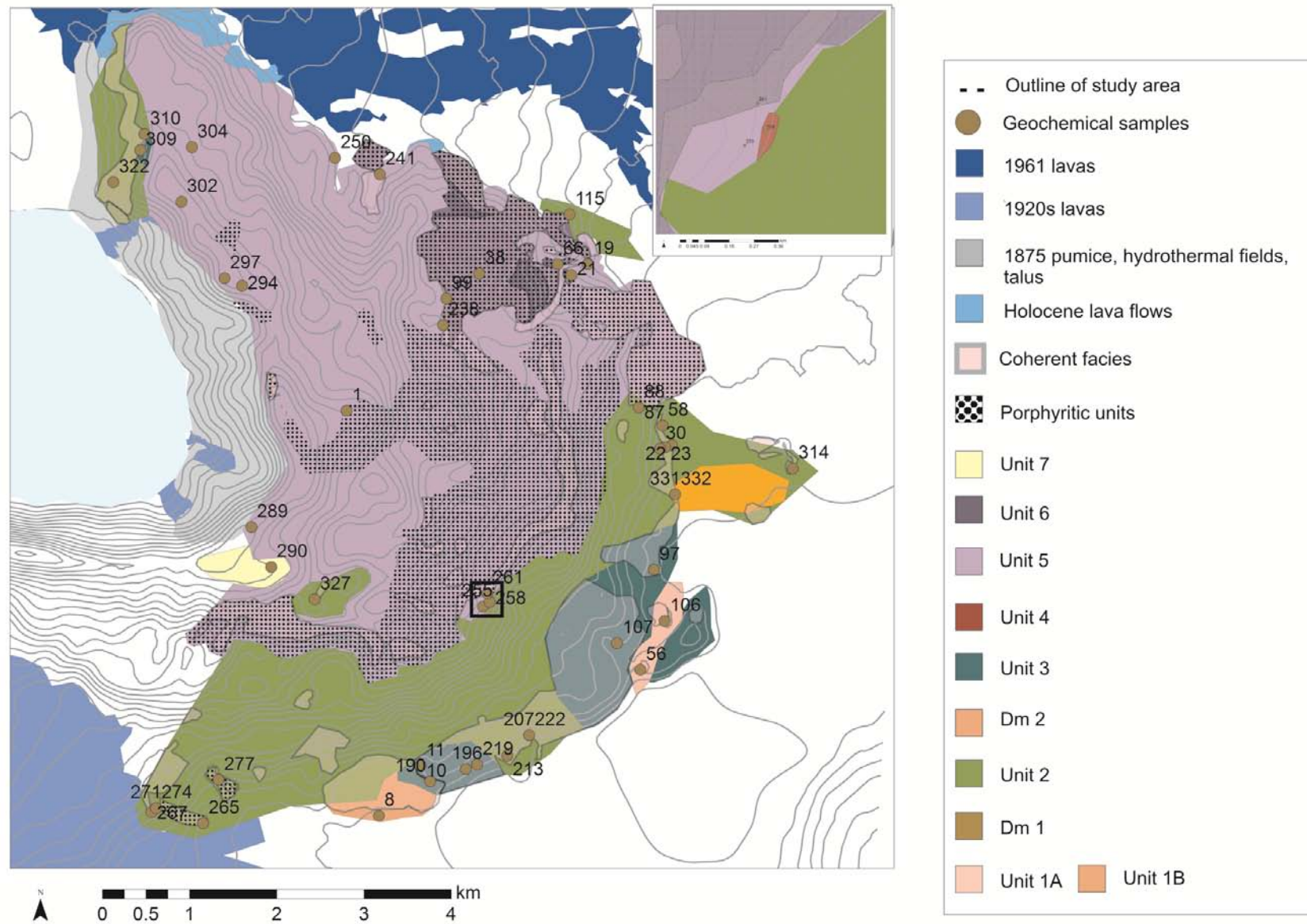


**Figure 4.1 Chemostratigraphy map of the eruptive units of Austurfjöll. The distribution of waypoints and geochemical samples are included, as are glacio-sedimentary (diamictite) units Dm1 and Dm2 and other overlapping units. The black box shown on the main figure is the location of the insert map, which highlights the limited distribution of Unit 4 deposits.**

## **4.1 VOLUME CALCULATIONS**

The techniques used to reconstruct the chronology and architecture of Austurfjöll massif and its role in the construction of the Askja volcano are multidisciplinary. These reconstructions are dependent on the physical volcanology (Chapter 2) and geochemistry (Chapter 3) of the Austurfjöll massif. The integration of these datasets in conjunction with topographic data in the form of a Digital Elevation Model (DEM) produced by Landmælingar Íslands (LMI) enables the extrapolation of the original distribution of glaciovolcanic deposits and the volume of the central Askja massif composed of Austurfjöll and Thorvaldstindur.

The LMI DEM has a 10 m resolution, enabling an accuracy of volume estimates on the order of 0.001 km<sup>3</sup>. Eruptive unit volumes were calculated using deposit distribution areas computed within ArcGIS and average thicknesses observed in the field with support from ArcGIS. The volume of constructional features, including fissure ridges, pillow lava sheets, single vents, and inter-ridge depositional centers, were calculated using areas derived from ArcGIS and thicknesses observed in the field. Volumes were simplified to ideal geometries such as triangular or rectangular prisms. The volumes were then used to estimate the contribution of eruptive units to the overall construction of Austurfjöll. Reconstructions of the central massif of Askja volcano were calculated using estimated geometries of material missing as a result of caldera formation between Austurfjöll and Thorvaldstindur. No additional height was added.

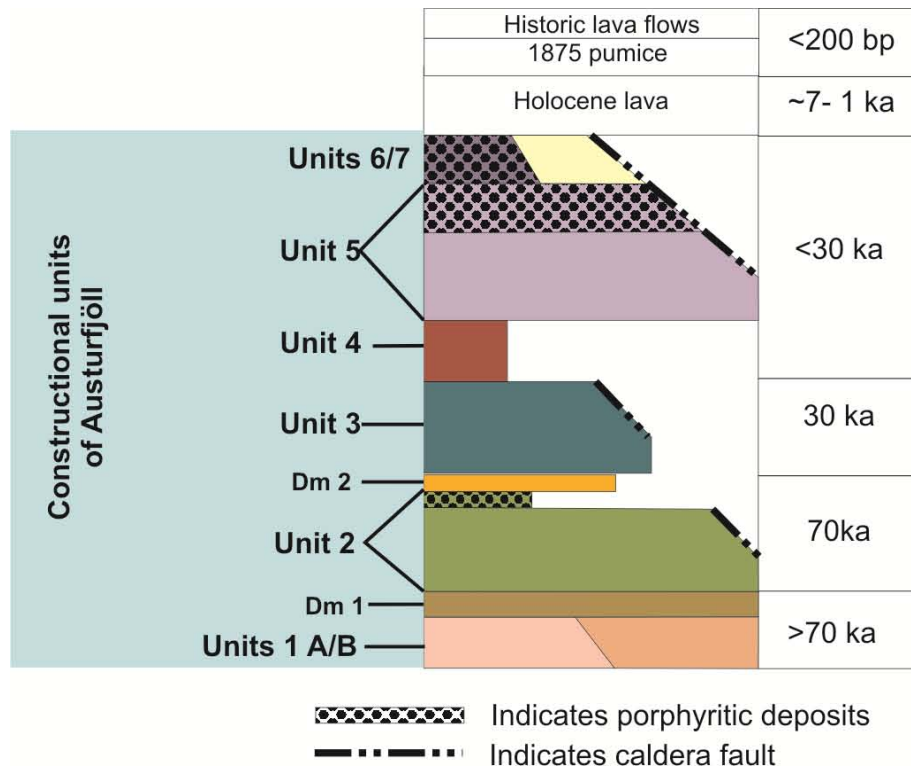
#### **4.1.1 Construction of Austurfjöll**

Each eruptive unit is composed of deposits of multiple lithologies (Table 4.1), and the boundaries of the eruptive units are defined by lithofacies contacts. The combination of the geochemistry and lithology enables the reconstruction of the general evolution of Austurfjöll massif, including a simplified stratigraphy and chronology (Figure 4.2). The eruptive units are numbered chronologically, and sedimentary units are assigned an independent nomenclature of Dm. Holocene and historical deposits are discussed by relative age, but not assigned unit numbers. The massif was dissected by two calderas >10 ka and 137 years ago, and eruptive units that are clearly cut by the calderas are indicated. There is no exposed contact relationship between Units 1 A and B or Units 6 and 7, but the pairs are stratigraphically equivalent. The original volume of erupted material is estimated based on the distribution, thickness, and orientation of the units (Section 4.4).



**Table 4.1 Lithofacies present within each eruptive unit and major implications.**

<b>Eruptive unit</b>	<b>Facies</b>	<b>Unique properties</b>	<b>Implications</b>
<b>7</b>	B3	Isolated with no obvious source, subaqueous and subaerial components	Vent was located in area of modern calderas
<b>6</b>	Plx1, Plx2, Ltx2, Atx2, Dx1, Dx2	Exclusively porphyritic and subaqueous	Subaqueous activity continued after emergence
<b>5</b>	Pl1, Pl2, Plx1, Plx2, L1, L2, Lx1, B1-3, B1x, Lt1-4, At1-4, G1, D1-2, Dx1-2	Contains diverse componentry, including xenoliths, red scoria, and coated lapilli. G1, B3, Lt4	Records both subaqueous and emergent activity
<b>4</b>	Pl2	Mega pillows, isolated	Possible burial of deposits, or limited eruption
<b>3</b>	Pl1, Pl2, L1, L2, B1-2, Lt1-2, At1- 4, D1, D2	Limited distribution	Mantling paleotopography
<b>2</b>	Pl1, Plx1, Pl2, L2, B1, Lt1-2, At1-3, D1, D2, CMVD, Dia1	Voluminous pillow sheets, CMVD	First subaqueous Austurfjöll unit
<b>1 (A, B)</b>	L2, Dia1 , Dia2	Subaerial lava only Glacial scour	Pre-glacial advance



#### Brief description of Austurfjöll units:

Unit 7: Localized subaqueous lava breccia

Unit 6: Subaqueous porphyritic lavas

Unit 5: Subaqueous porphyritic and non-porphyritic lavas, subaqueous porphyritic and non-porphyritic tuffs, and emergent lavas and tuffs

Unit 4: Subaqueous lavas

Unit 3: Subaqueous lavas, subaerial lavas, and localized subaerial lava breccias

Dm 2: Diamictite containing clasts of Unit 2A

Unit 2: Subaqueous lavas and tuff with localized subaqueous porphyritic lava and non-porphyritic subaerial lavas

Dm 1: Diamictite

Unit 1 A and B: Subaerial lavas with local glacial scour

**Figure 4.2 Generalized stratigraphic column of the evolution of Austurfjöll massif. The width of the column reflects the relative distribution of the unit and thickness represents relative thickness of units. The units that are cut by caldera faults are indicated. Holocene deposits are not assigned to eruptive units.**

#### **4.1.2 Eruptive units and chronology**

Unit 1 (A and B): Multiple interglacial basaltic lavas dating to >71 ka were erupted into unconfined, predominantly dry, conditions. The paleo-topography was likely fairly simple, with a large plains region between shield volcanoes, such as Valðalða southeast of Askja (Figure 1-2). The highlands have a gradual slope away from the region currently covered by Vatnajökull glacier and away from the axis of the ridge through the Northern Volcanic Zone (Bourgeois et al., 2000; Bourgeois et al., 1998; Harðarson et al., 2008). The Unit 1 lava flows all exhibit a'a textures, which are typically associated with fissure eruptions, whereas shield-building eruptions in Iceland are dominated by pahoehoe morphologies (Andrew and Gudmundsson, 2007; Thorarinsson and Sigvaldason, 1962). This suggests the distribution of the lavas was likely no larger than the postglacial lavas mapped by Annertz et al. (1985) that average  $4.0 \times 10^7 \text{ km}^2$ . The flows were then subject to glaciation as evident from the significant glacial scour and the deposition of local overlying till, outwash deposits (Dia2), and erratics.

Dm1: Following the scour of the Unit 1A and 1B lavas, diamictites (Dia1) were locally deposited, including well polished clasts of basalt and significant coarse ash-sized matrix. Clasts within the tillites are varied and sourced from multiple locations, as indicated by the unique chemistry of the sampled clasts. Unit 1B is predominantly covered by Dia2 outwash deposits.

Unit 2: The first subaqueous deposits of the sequence consist of large volumes of basaltic pillow lavas and associated pillow breccias forming pillow lava sheets along the base of the massif are dated to 71 +/- 7 ka. Intrusions of Unit 2 pillowed dikes into Dm 1 are locally exposed in gullies. Several sequences of deposits within Unit 2 show a transition from effusive to explosive behavior (see Chapter 6). Porphyritic deposits of Unit 2 are limited to the southeast corner of the growing massif, and contain

pillow lavas interacting with previous topography (vertical pillows), intrusions, and fragmental deposits. The unit is dominated by fissure ridges, large sheet flows, and moderately common intrusive deposits. The fissures produced a new more convoluted topography overtopping the plateau-like pillow lava sheets. There was local erosion of the massif by large volumes of meltwater that created channel systems through ash and lapilli tuffs up to 100 m in diameter and 30 m deep (Figure 2.27). The channels are filled with well bedded ash and lapilli tuffs. The channel fills are also cross-cut by intrusions of Unit 2 composition, indicating the erosion was occurring contemporaneously with the volcanic growth of the massif. Some of these intrusions are CMVDs, indicating that there was confined meltwater and potentially ice contact with the massif during this intrusive activity. Localized exposures of subaerial lavas occur within the Unit 2 deposits (to be discussed further in Chapter 8).

Dm2: Local deposits of diamictite occur over 10s of meters, up to 2 m thick, on top of Unit 2 lavas. Dm2 deposits contain clasts of lava of Unit 2 composition. They mantle the sides of Unit 2 deposits and may have filled in topography between units. The valleys between Unit 2 lava sheets have been reused by modern drainage, and resulted in significant erosion of the diamictites.

Unit 3: The next glaciovolcanic eruptive unit is dominated by basaltic subaqueous deposits of predominantly pillowed lavas and breccias dated to 29 +/- 8 ka. The constructional features of this unit are a combination of thin pillowed sheets and fissure ridges. Local tuff deposits occur, particularly on small fissure ridges on the order of 100s of m long and 50 m high. Unit 3 deposits are less aerially extensive than Unit 2 lavas. The deposits mantle and fill in the topography of the Unit 2 deposits. No porphyritic deposits were associated with this unit.

Unit 4: This eruptive unit is composed of basaltic weakly porphyritic mega-pillows with limited outcrop and apparently limited distribution. The chemistry of the deposits is unique relative to the other Austurfjöll deposits, but occurs stratigraphically on top of Unit 2 lapilli tuffs and below Unit 5 pillow breccias and lavas. The only known exposure is on the order of 200 m wide by 20 m high.

Unit 5: This eruptive unit contains the greatest diversity of lithofacies, including subaqueous and emergent basaltic lavas and fragmental deposits. It lays stratigraphically above all previous eruptive units

and has a significant presence over northwestern Austurfjöll. At low elevations, the sequence contains micro-porphyritic pillow lavas and associated breccias. The lower sequences are similar to the Unit 2 basal deposits, containing local sequences of effusive to explosive transition deposits. At higher elevations, lapilli tuffs and other fragmental deposits dominate. By 1100 m elevation (ca. 450 m above local base level), subaerially influenced deposits are common, particularly breccias containing subaerial lavas and red scoria, and rare primary subaerial deposits including subaerial lavas and lapilli tuffs containing red scoria and bomb sags. Many of these deposits are clearly mass flow deposits (Lt4) that may create the appearance of subaerial activity at lower elevations. The first Unit 5 in situ lava flows occur along the caldera rim at 1250 m (600 m above local base level). Subaerial lavas are typically microcrystalline with abundant oxide minerals. Porphyritic deposits are common throughout the sequence, but are locally overtopped by micro-porphyritic units. Gabbro nodules are found frequently within this eruptive unit. The constructional features of this unit are predominantly fissure ridges, with some inter-ridge depositional centers. Within the caldera wall, this unit lies conformably on top of hydrothermally altered rhyolite deposits. The contact of the rhyolite with Unit 5 is difficult to follow, but may represent up to two rhyolitic domes with local ash deposits. The local occurrence of rhyolite-cored bombs in Unit 5 deposits and stratigraphic relationships between the rhyolite and Unit 5 clearly indicate that the rhyolite pre-dates Unit 5. These bombs were previously misidentified as part of the 10 ka rhyolitic eruption (Sigvaldason, 2002). However, the relationship between the rhyolite and deposits older than Unit 5 is unknown due to a lack of stratigraphic relationships.

Unit 6: A locally confined unit of exclusively porphyritic subaqueous basaltic lavas mantles the topography of the Unit 5 deposits. Consequently, Unit 6 occurs at a range of elevations in the northeastern corner of the massif. Pillow lava mounds dominate the morphology, but local sheet flows also occur. Based on reconnaissance and geochemical evidence, Unit 6 may continue north of Öskjuop as porphyritic pillows and subaerial lavas (Samples AG 298, AG 299).

Unit 7: This unit is a localized breccia deposit along the caldera rim containing subaqueous basaltic pillow lava clasts of unique composition. The source material of the breccia is likely inside the

area that is now Öskjuvatn caldera. The stratigraphic position and elevation of this unit is used to justify its designation as the youngest glaciovulcanic unit described at Austurfjöll. Unit 7 has stratigraphic relationships with Unit 5, there is no contact with Unit 6, leaving the precise position of Unit 7 uncertain.

Caldera formation: The Askja volcano is bisected by at least three calderas: Öskjuvatn (1875), Askja (< 10 ka), and the Northern Caldera (>71 ka). The older two calderas are not well dated; however, the interaction of the Askja caldera with the Austurfjöll massif suggests that it post-dates the glaciovulcanic deposits. Structural evidence in tuffaceous material is muted by the friable nature of the deposit, one particularly striking example of cross-cutting relationships is a small exposure just north of Öskjuop, a gap in the Askja caldera wall (Figure 2.27). This group of porphyritic lavas and tuffs is clearly dissected by the main Askja caldera fault. As these deposits have chemistry matching that of Unit 6 and are dissected by the caldera fault, the caldera clearly formed after the bulk of the Austurfjöll massif (Figure 4.3). The lack of clear interaction between Austurfjöll and the Northern Caldera suggests that the caldera predates the Austurfjöll deposits. However, chemostratigraphy work on Norðurfjöll would be more suited to answer this question. The orientation of fissures identified in the Austurfjöll massif are predominantly in line with the regional tectonic setting and do not display patterns that are convincingly the result of exploitation of caldera ring faults (Figure 2.21, 2.22).

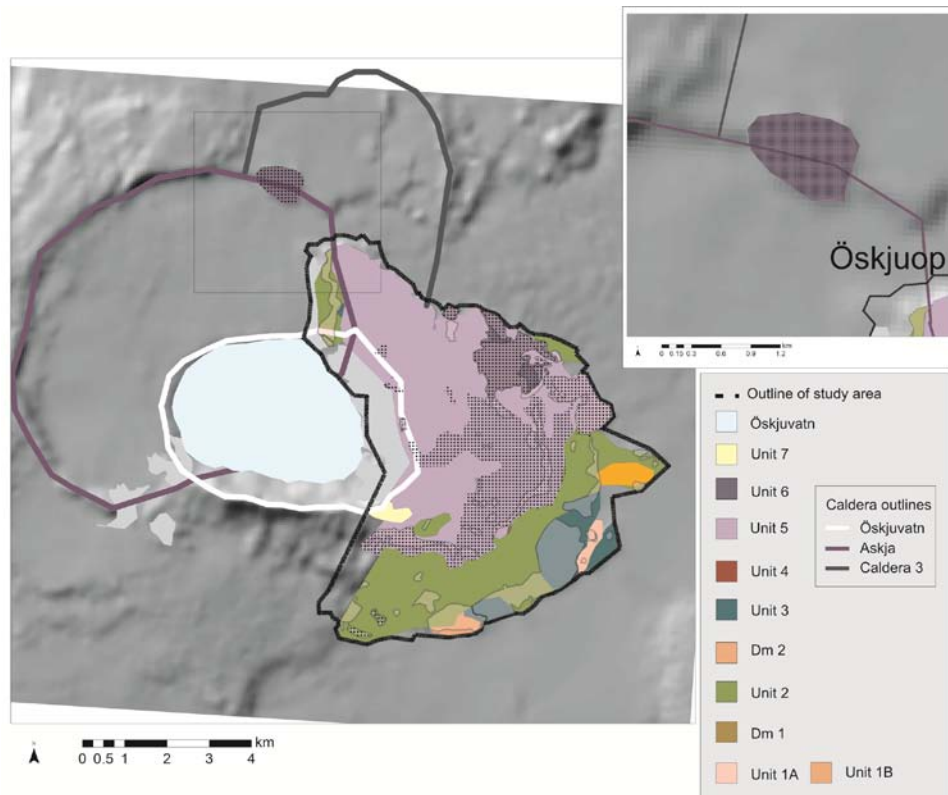


**Figure 4.3 Map showing the interaction of the Askja and Öskjuvatn calderas with Austurfjöll and related deposits. The inset, shown on the main map as a light grey box, focuses on a group of Unit 6 lavas identified in reconnaissance work that is clearly cross-cut by the younger Askja caldera.**

Holocene: The Austurfjöll region was subject to significant postglacial volcanic activity, with large volumes of basaltic lava flows erupted within the Askja caldera and to the north of Askja (Annertz et al., 1985; Brown et al., 1991). Along the northwestern margins of the Austurfjöll massif, near Öskjuop, the glaciovolcanic deposits are mantled by Holocene a'a lava flows and spatter deposits. The spatter deposits extend up to 200 m into the gullies of the northern part of the massif. Holocene spatter and a'a lava flows erupted from vents near Austurfjöll and Thorvaldstindur have the same range of chemical compositions observed within the Austurfjöll massif itself, but have some internal clustering (See section 3.7).

Historical deposits: The 1875 caldera-forming eruption was the first historically documented eruption at Askja. This eruption produced significant rhyolitic pumice, minor basaltic lava, and scoria (Carey et al., 2009; Carey et al., 2010). The pyroclastic deposits of the 1875 eruption cover significant portions of the Austurfjöll massif. In the 1920s and the 1960s, basaltic fissure eruptions produced predominantly a'a lava flows that interacted with the Austurfjöll massif's northern, southern, and caldera boundaries (Annertz et al., 1985; Þorarinsson, 1963; Thorarinsson and Sigvaldason, 1962).

Volumetrically, Austurfjöll massif is dominated by Unit 2 and Unit 5 (Table 4.2). These two major phases of construction are dated to 71 ka and some time following 29 ka. The range of deposits on and within the Austurfjöll massif represent a history of over 71 ka of interglacial, subglacial, postglacial, and historical activity. Relative production rates over this period are on the order of  $0.059 \text{ km}^3/1000 \text{ yr}$ . Production rates for Askja during deglacial periods reached as high as  $9.39 \text{ km}^3/1000 \text{ yr}$  and are currently on the order of  $0.32 \text{ km}^3/1000 \text{ yr}$  (Table 4.3) (Sigvaldason et al., 1992). The significant decrease in production rate during glacial periods, and rapid increase immediately following the rapid deglaciation around 10 ka, are consistent with the changes in confining pressure resulting for the presence and absence of a thick ice sheet (MacLennan et al., 2002; Sigvaldason et al., 1992).



**Table 4.2 Minimum and maximum aerial extent of eruptive units at Austurfjöll. Volume estimates are made for large eruptive units based on minimum extent.**

<b>Unit</b>	<b>Minimum extent (km<sup>2</sup>)*</b>	<b>Maximum extent (km<sup>2</sup>)**</b>	<b>Volume estimate (km<sup>3</sup>) ***</b>
<b>1A</b>	3x10 <sup>5</sup>	4x10 <sup>7</sup>	0.023
<b>1B</b>	3.5x10 <sup>5</sup>	4x10 <sup>7</sup>	0.024
<b>2</b>	1x10 <sup>7</sup>	5.5x10 <sup>7</sup>	2.313
<b>3</b>	2.5x10 <sup>6</sup>	2x10 <sup>7</sup>	0.14
<b>4</b>	7x10 <sup>3</sup>	2x10 <sup>5</sup>	<0.0001
<b>5</b>	2x10 <sup>7</sup>	4x10 <sup>7</sup>	0.99
<b>6</b>	2x10 <sup>6</sup>	5.5x10 <sup>6</sup>	0.10
<b>7</b>	3x10 <sup>5</sup>	3x10 <sup>6</sup>	0.0008
<b>Total</b>	4.8x10 <sup>7</sup>	2.0x10 <sup>8</sup>	3.59
<p>*Minimum extents are based on modern exposures of eruptive units.</p> <p>**Maximum extents are estimates based on the distribution of exposures and topography, and comparison with similar deposits in Iceland (Annertz et al. 1985). Where necessary conservative estimates of material lost to the calderas is incorporated.</p> <p>***Volume estimates use minimum areas. Totals do not add up to the volume estimated for all of AF due to rounding, thickness and extent estimates.</p>			

**Table 4.3 Production rates for Askja volcano including new data from Austurfjöll massif.**

Time period			Duration	Average production rate (km <sup>3</sup> / ka)
Pleistocene	Interglacial		100 yr *	0.32
	Last Glacial Maximum		60 ka	0.058**
		Unit 2	40 ka	0.058
		Unit 3-7	20 ka	0.061
This Study				
Holocene	10000-4500 ka		5.5 ka	5.98
		8000-4500	3.5 ka	9.39
	4500-2900 ka		1.8 ka	3.88
	2900 ka-present		2.9 ka	0.32
Sigvaldason, 1992				
* Estimate of eruption duration based on modern production rates as representative of interglacial conditions (Sigvaldason, 1992)				
** Austurfjöll only.				

## 4.2 ARCHITECTURE

The massif is constructed of a series of smaller volcanic and sedimentary features, predominantly fissure ridges, a few point sources, pillow lava sheets, and local depo-centers, that form between ridges or in channels eroded into previous deposits. Terminology in glaciovolcanic literature referring to fissure ridges is variable; with interchangeable terms such as tindar, hyaloclastite ridge, and fissure ridge being prevalent. In this study the term fissure ridge refers to individual fissure segments composed predominantly of vitirclastic deposits and cored with minor coherent deposits (feeder dikes and pillow lavas), not to be confused with fissure complexes (tindars) such as Sveifluhals (Reykjanes Ridge) and Lakagigar (Eastern Volcanic Zone).

The volumes of eruptive units and constructional features at Austurfjöll were estimated using a digital elevation model (DEM) produced by LMI. The volume of the features calculated here is likely an underestimate due to erosion, overlapping deposits, and remobilization. The volume of fissure ridges was assumed to be an elongate triangular prism. Point sources were modeled as conical features, and pillow sheets were modeled as rectangular prisms. The inter-ridge depo-centers were modeled as half cylinders to match the channel fills that were observed in cross-section in large gullies. The depth of depo-centers was estimated to be typically between 30 and 50 m deep based on the observed thick channel fills locally observed in cross-section.

The total volume of the horseshoe-shaped massif is  $3.6 \text{ km}^3$  as it is currently preserved (Table 4.4). The number of identified vents (Chapter 2) is 63, with 10 recognized depositional centers. Based on the average volume of fissure ridges, point sources, pillow lava sheets, and inter-ridge depositional centers, this vent identification represents less than 62% of the volume of the massif. Assuming the relative proportions of features is representative of the total massif, the number of vents would need to increase from 63 to 103, and include additional inter-ridge depo-centers. The low number of vents

observed in the field may be the result of alteration or erosion, however, it is more likely that the overlapping of constructional features and vents during the growth of the massif prevents the observation of earlier vents. This calculation does not take into account any material lost to the formation of the youngest calderas.

The volume estimates for individual vents on Austurfjöll can be compared to typical Icelandic eruptions from the Pleistocene to historical eruptions (Table 4.5) (Andrew and Gudmundsson, 2007; Bergh and Sigvaldason, 1991; Brown et al., 1991; Mercurio, 2011; Schopka et al., 2006; Sigvaldason, 2002; Sinton et al., 2005; Smellie et al., 2008; Werner and Schmincke, 1999). While some of these estimates represent eruptive centers that are complexes of individual vents, they nevertheless suggest that the Austurfjöll estimates are low. Therefore the total number of vents suggested by the calculations above would be an overestimate.

**Table 4.4 Calculations of vent density based on the observed proportions of vents and depo-centers (including channel fills) required to make up the volume of Austurfjöll.**

	Single vents	Fissure ridges	Pillow lava sheets	Inter-ridge depo-centers	Volume calculated	Underestimate	
					km <sup>3</sup>	km <sup>3</sup>	% of total
<b>Number of features</b>	10	50	3	10			
<b>Volume (km<sup>3</sup>)</b>	0.0025	0.0209	0.1806	0.0086	<b>3.62</b>		
<b>Volume of features identified (km<sup>3</sup>)</b>	0.025	1.045	1.083	0.086	2.24	1.38	38.12
<b>Volume required to maintain ratio observed (km<sup>3</sup>)</b>	0.040	1.673	1.734	0.138	3.58	0.04	0.99
<b>Difference (km<sup>3</sup>)</b>	0.015	0.627	0.650	0.052	1.34		
<b>Additional features needed</b>	6	30	4	6			
<b>Total features</b>	16	80	7	16			
<b>Total Vents</b>	103			<b>Vent density (vents/km<sup>2</sup>)</b>	2.15		

However, an interesting discussion in the literature focuses of the substantial volume of material produced during the Holocene as a result of deglaciation, which then trails off as ice volumes stabilize and rebound slows (Andrew and Gudmundsson, 2007; Annertz et al., 1985; Brown et al., 1991; Jull and McKenzie, 1996; MacLennan et al., 2002; Óladóttir et al., 2011; Sigmundsson, 1991; Sigvaldason, 2002; Sigvaldason et al., 1992; Sinton et al., 2005). There has been no comprehensive discussion on the scale of vent sizes for glaciovolcanic deposits throughout the Pleistocene. Production rate estimates for the NVZ, Western Volcanic Zone, and Reykjanes Peninsula (Figure 1.1) indicate that the LGM production at Austurfjöll is reasonable. The Norðurfjöll and Vesturfjöll regions require further study to determine the connection to Askja volcano and the age of the eruptions, but these regions may increase these estimates. Nevertheless the expected trend of decreased eruption rates during glacial periods is upheld (Figure 4.4).

**Table 4.5** Regional estimates of production during glacial, early postglacial and recent eruptive periods. Austurfjöll values are reasonable in comparison to Krafla and the Reykjanes Peninsula. For locations see Figure 1.1.

Location	Glacial	Early postglacial	Recent
Theistareykir (NVZ)	0.13*	12.12*	0.26*
Krafla (NVZ)	0.03*	1.32*	0.03*
Askja (NVZ)	0.058**	9.39***	0.32***
Western Rift Zone	0.5*	11.25*	0.34*
Reykjanes	0.05*	3.76*	0.15*
Average	0.1536	7.568	0.22
Range ****	0.03-0.13	1.32-12.12	0.03-0.34
*MacLennan et al. 2002 ** This study *** Sigvaldason 1992 **** MacLennan et al. 2002, This Study, Sigvaldason, 1992, and Jull and McKenzie 1999			

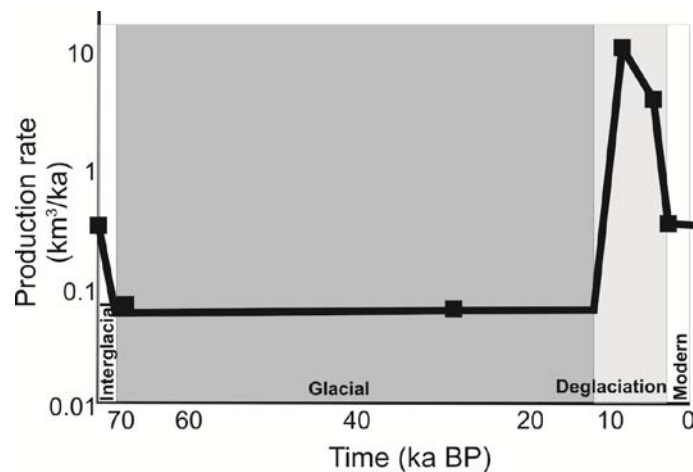


**Figure 4.4** Estimated production rates for Askja volcano using data from this study and Sigvaldason (1992).

Interglacial production rate is extrapolated from modern low ice cover conditions.

Based on field evidence, the lithology map, the chemostratigraphy map and topography, extrapolated cross-sections through the Austurfjöll massif were developed (Figure 4.5). These cross-sections reflect the piecemeal construction of the massif by a series of fissure eruptions and pillow lava sheets in six major eruptive units on top of inter-glacial lavas of Unit 1 (Figure 4.6). The interaction of the massif with rhyolitic domes exposed in the caldera, and the interaction of the calderas with Austurfjöll are hypothesized from the limited preserved structures and lithofacies contacts. The overlapping of fissures was deduced by the interaction of vents and their deposits at the surface, and the volume calculations. The locations of these potential vents in cross-section are based on topography, and locations of intrusions, but are grossly over-simplified for the purpose of illustration.

The rhyolite exposed in the caldera rim is not well constrained within the chronology. It is possible that the rhyolite domes observed in the caldera wall were emplaced between the 71 and 29 ka dated lava groups as portrayed in the cross-sections, but more sampling and an age of the domes would be required to confirm the relative age of the rhyolite.

**Table 4.5 Volume measurements for fissures and shields throughout Iceland. Holocene shield volcanoes are typically larger than fissure eruptions. Austurfjöll fissure segments are likely underestimated due to erosion and cover. Most values reported to fissure eruptions total all deposits.**

<b>Volcano type</b>	<b>Volume</b>	<b>DRE</b>	<b>Age</b>	<b>Source</b>
<b>Fissure</b>				
1920's fissures Askja combined	0.0275		Historic	<b>This study</b>
1960's fissure Askja	0.015		Historic	<b>This study</b>
Laki	12.8-14.7		Historic	Brown et al. 1991; Sinton et al. 2005
Reykjanes fissures	0.11		Holocene	Andrew and Gudmundsson, 2007
Western Volcanic Zone	0.4		Holocene	Sinton et al. 2005
Fissure segments Austurfjöll	0.02		Pleistocene	<b>This study</b>
<b>Shield</b>				
Skjaldbreiður	25		Holocene	Andrew and Gudmundsson, 2007
Skjaldbreiður	13.5		Holocene	Sinton et al. 2005
Reykjanes shields	1.11		Holocene	Andrew and Gudmundsson, 2007
WVZ shields	0.63		Holocene	Sinton et al. 2005
Postglacial Askja	3-20		Holocene	Sigvaldason 2002
Valðalða	9.22		Interglacial	<b>This study</b>
<b>Glaciovolcanic complexes and components</b>				
Herðubreið	4.01		Pleistocene	<b>This study</b> / Werner and Schminke, 1999
Pillow sheet flows Askja	0.18		Pleistocene	<b>This study</b>
Austurfjöll (central volcano)	3.62		Pleistocene	<b>This study</b>
Hyaloclastite slumps	most 0.1-5; max. 30	1.7	Pleistocene	Bergh and Sigvaldason 1991
Inter-ridge deposits (remobilized)	0.015		Pleistocene	Mercurio 2011
Sveifluhals (tindar complex)	2.73		Pleistocene	Mercurio 2011
Helgafell (tindar)	0.17	0.2	Pleistocene	Schopka et al. 2006
Typical Iceland/Antarctica/BC	0.6		Pleistocene	Smellie 2008
Siða-Fjotshveði (tindar)	13		Pleistocene	Smellie 2008



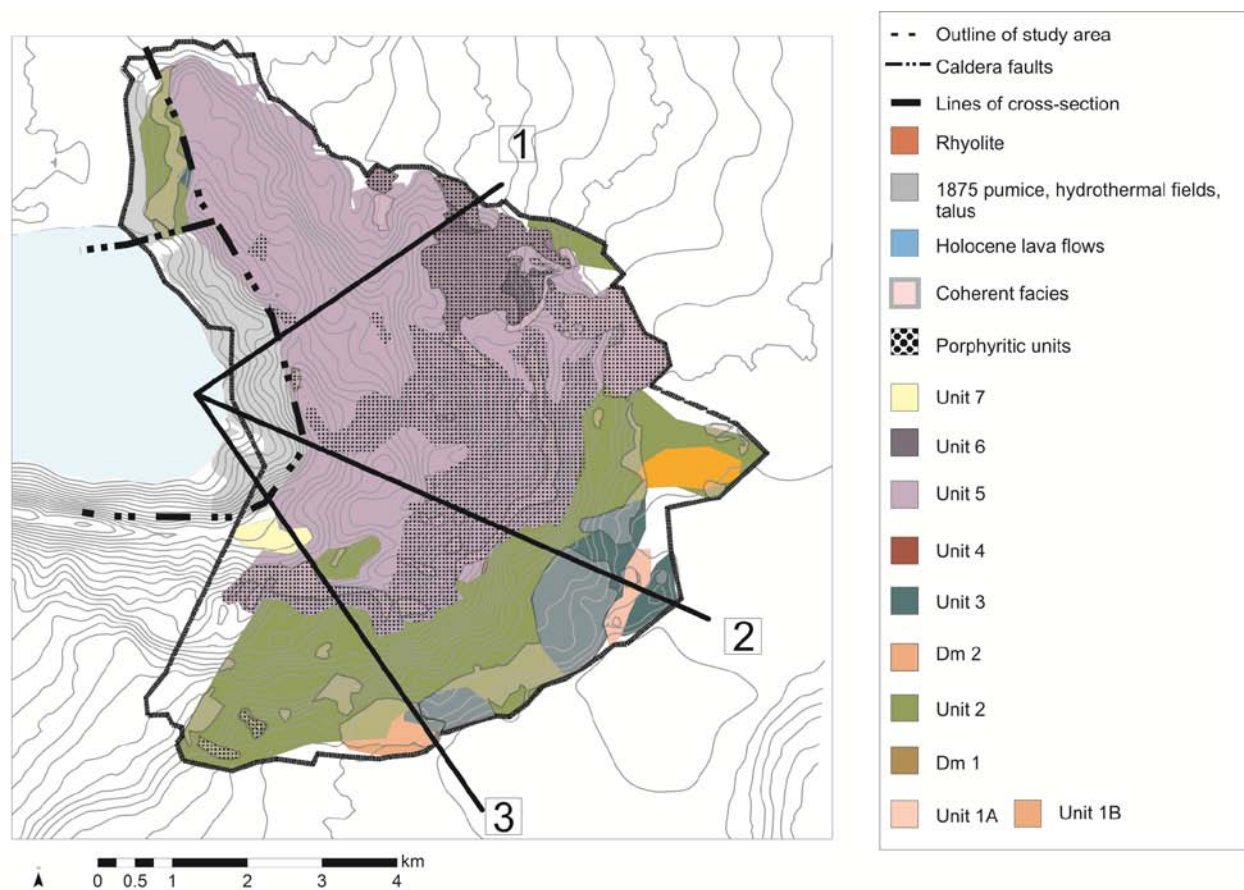


**Figure 4.5 Map of Austurfjöll showing the lines of section used to create extrapolated cross-sections.**

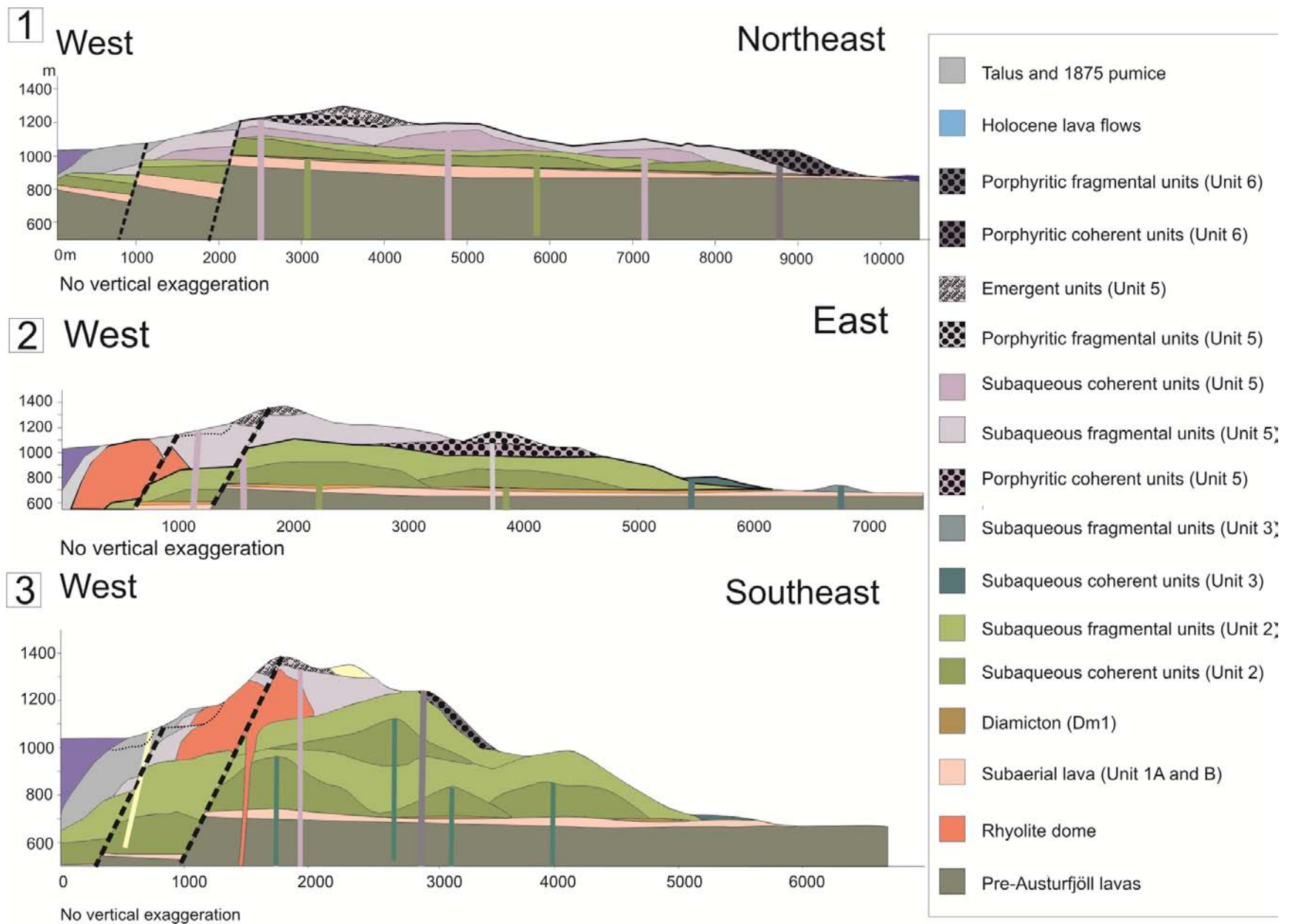


**Figure 4.6 Three extrapolated cross-sections through Austurfjöll massif. The stratigraphic position of the rhyolite dome is not well constrained. Its current position is controlled by exposures and the lack of deformation in over lying unit. The exposures of rhyolite in section 2 and 3 may represent one large deposit or two isolated deposits. Larger versions of these cross-sections can be found in Appendix C.**

### **4.3 PRE-CALDERA AUSTURFJÖLL**

The Austurfjöll massif has been disrupted by the formation of the Öskjuvatn and Askja calderas, consequently, the initial extent of the eruptive units can only be estimated. Previous studies have noted the likely loss of material to the calderas, and give fairly conservative estimates for the volume missing (Bemmelen and Rutten, 1955; Brown et al., 1991; Hartley and Thordarson, 2012; Sigvaldason et al., 1992). Based on the orientation of deposits within the caldera wall, and some observational evidence from 1875 of the evolution of the Öskjuvatn caldera (Hartley and Thordarson, 2012), the glaciovolcanic deposits of Austurfjöll likely extended further to the west (Figure 4.7). ArcGIS was used to create two estimates of the initial volume of the glaciovolcanic massif including Thorvaldstindur. The first is more conservative, and limited to volumes related to the formation of the Öskjuvatn caldera. The second more extensive estimate extends the current range of Austurfjöll and Thorvaldstindur to create a more typical tuya-like morphology (Table 4.6). In the largest end-member volume estimate, the massif may have been up to 69 km<sup>2</sup> and composed of 9 km<sup>3</sup> of basaltic glaciovolcanic material. These estimates have not taken into account any additional height as there are no field constraints on the order of magnitude of the previous elevation of the massif. Estimates made based on gravity surveys proposed ridges up to 1000 m tall, an additional 150 m taller than the modern massif (Brown et al., 1991).

The distribution of the eruptive units has been modeled using these massif reconstructions, and used to make a map-view model of the evolution of the central portion of Askja Volcano (Figure 4.8).

The orientation of vents suggests that the distribution of eruptive units was controlled in part by the regional tectonic setting, unlike historic deposits that are frequently constrained by the Askja caldera. In at least two instances there are deposits with multiple exposures isolated from the main exposure of the eruptive unit. These isolated deposits may indicate that there was contemporaneous eruption of the same eruptive units at separate and distal locations within the massif. This type of eruption can also be deduced from the geochemistry of the eruptive units from the 1920s, which show independent vents with highly similar chemistry distributed over several years and several kilometers. The alternative model would suggest that the original extent of the eruptive unit connects all of the deposits of the same chemical unit that were later buried by younger deposits. The former model has been used to maintain conservative volumes and distributions, rather than extending deposit areas and volumes beyond what is exposed, or indicated by structural evidence (bedding).

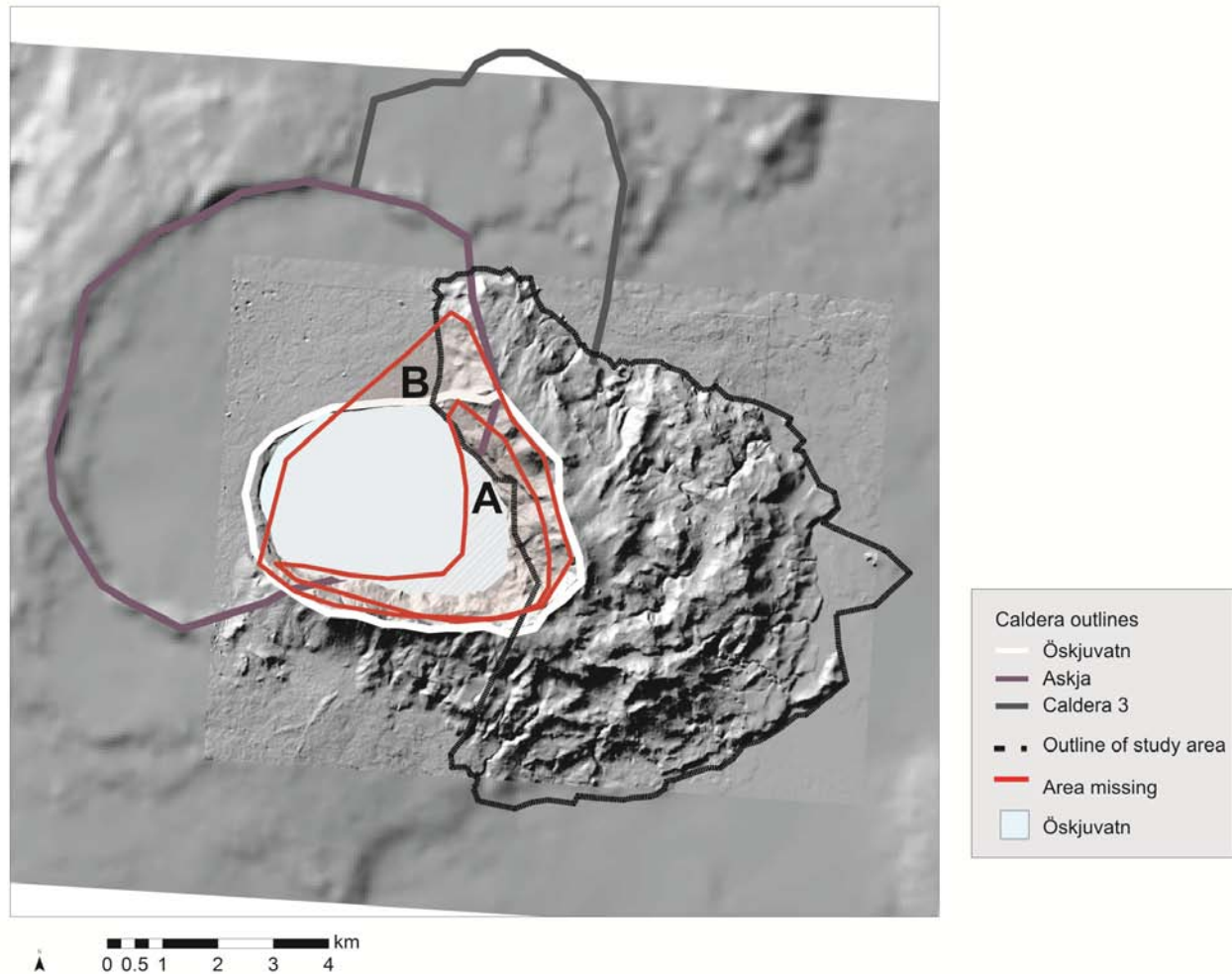


**Figure 4.7** Map of Austurfjöll with projections of the potential original massif extent. The projections were used to calculate the volume of missing glaciovolcanic deposits. A) Loss of material based only on the Öskjuvatn caldera, representing a minimum volume of loss. B) More extensive area of potential volumetric loss.

**Table 4.6 Estimates of potential volume of glaciovolcanic material lost to the calderas that intersect with Austurfjöll and Thorvaldstindur massifs.**

	<b>Area (km<sup>2</sup>)</b>	<b>Volume (km<sup>3</sup>)</b>
Austurfjöll	48	3.62
Loss observed since 1875 (Hartley et al. 2012)		0.856
Conservative estimate of loss (Area A)	6.25	2.03
Loss to Askja Caldera (Area B)	20.01	5.00
Thorvaldstindur	1.05	0.54
<b>Total</b>	55.30	6.19
Maximum potential volume of central Askja glaciovolcanic deposits	69.06	9.16
See Figure 4.6 for the outline of the areas calculated.		

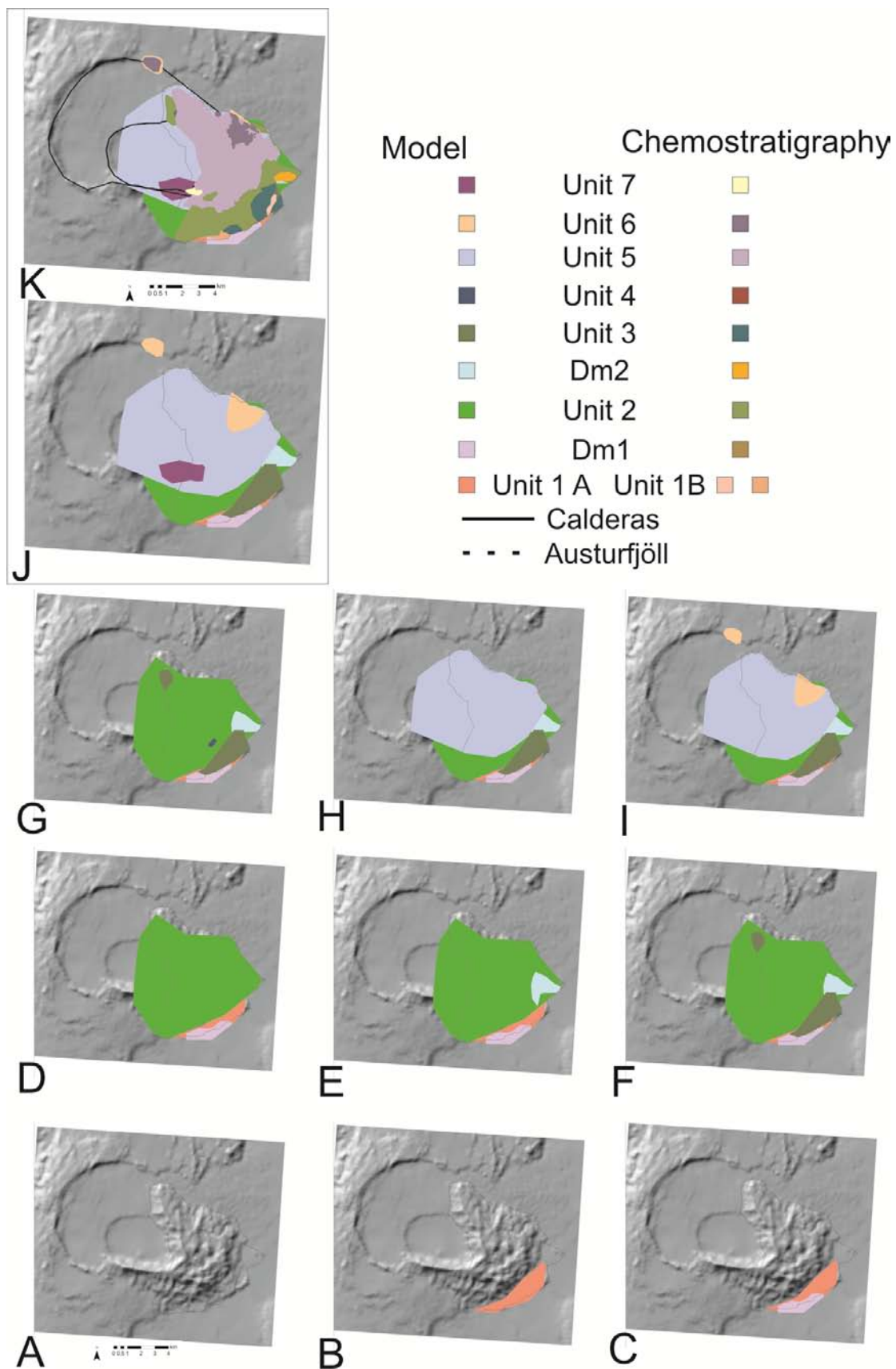




**Figure 4.8 Schematic model of the evolution of eruptive units involved in the construction of Austurfjöll massif and extended to include Thorvaldstindur and deposits just north of Öskjuop. The steps are labeled in order from A (oldest) to K (youngest).**

#### **4.4 CONCLUSIONS**

The glaciovolcanic constructional history of Austurfjöll represents 40-60 ka of the history of Askja volcano, central Iceland. The massif represents one of the largest constructs of basaltic glaciovolcanic deposits in Iceland. This study of Austurfjöll can serve as an important starting point for investigations of Norðurfjöll, Vesturfjöll, and Thorvaldstindur constructs. Reconnaissance work indicates a likely chemical relationship between Austurfjöll and deposits north of the Askja caldera and Thorvaldstindur. However, the eruptive units described here likely do not fully portray the chemical variability within the entire Pleistocene history of Askja or the internal structure of these other constructs.

Nevertheless, this study represents the first comprehensive lithostratigraphic and geochemical investigation of a large polygenetic basaltic centralized glaciovolcanic massif in Iceland. The chemical variability and the multiple periods of activity appear to have continued into the postglacial eruption of subaerial lavas (Annertz et al., 1985) revealing extensive volcanism associated with a central construct at Askja from 71 ka to present. The evolution of the glaciovolcanic deposits also represents 40 ka of predominantly subaqueous activity, with brief periods of local glacial sediment deposition. Such a long-standing and active volcanic feature would have a large impact on the confining ice-sheet, the evidence of which is discussed in detail in Chapter 8.



## **5.0 REMOTE SENSING AND GEOLOGIC MAPPING OF GLACIOVOLCANIC DEPOSITS IN THE REGION SURROUNDING ASKJA (DYNGJUFJÖLL) VOLCANO, ICELAND**

### **5.1 INTRODUCTION**

The Icelandic landscape is dominated by basaltic glaciovolcanic and Holocene landforms. Simplified geologic maps exist for the entire country, with detailed studies of individual locations of interest. One area that has received considerable attention in the last century is Askja (Dyngjufjöll) a glaciovolcanic central volcano in the Northern Volcanic Zone (NVZ) (Figure 5.1). Central volcanoes are shield volcanoes with intermittent caldera-forming rhyolitic activity, and are polygenetic. The massif is bisected by at least three calderas and is the site of recent eruptions (1875, 1920-1929, and 1961) (Annertz et al., 1985). This area is of great interest to volcanologists and paleoclimate researchers due to its range in basaltic to rhyolitic products and its polygenetic glaciovolcanic history. The bulk of the research conducted on this volcano, however, has focused on its historic activity. Maps of the region group all of the local glaciovolcanic features into one generalized unit (Sigvaldason, 2002).

A field-based mapping project of the glaciovolcanic sequences of Askja's 48 km<sup>2</sup> eastern mountains (Austurfjöll) was conducted in 2010 and 2011 (Figure 5.2). The results presented here are a parallel project to map the Askja volcano and surrounding region using a variety of remotely acquired data. The primary input is an ASTER scene acquired in August 2010 and ASTER global DEM (GDEM). The results derived from these data are validated through previous datasets and the 2010/2011 lithofacies map. The remote sensing-based geologic map enabled the discrimination of wide-spread rhyolitic pyroclastic deposits which locally obscure older deposits, and identify the variation within previously

unmapped glaciovolcanic massifs near Askja. This project serves as a practical assessment of the use of remote sensing-based geologic mapping of typically difficult to access glaciovolcanic terrains such as Iceland, British Columbia, and Antarctica.

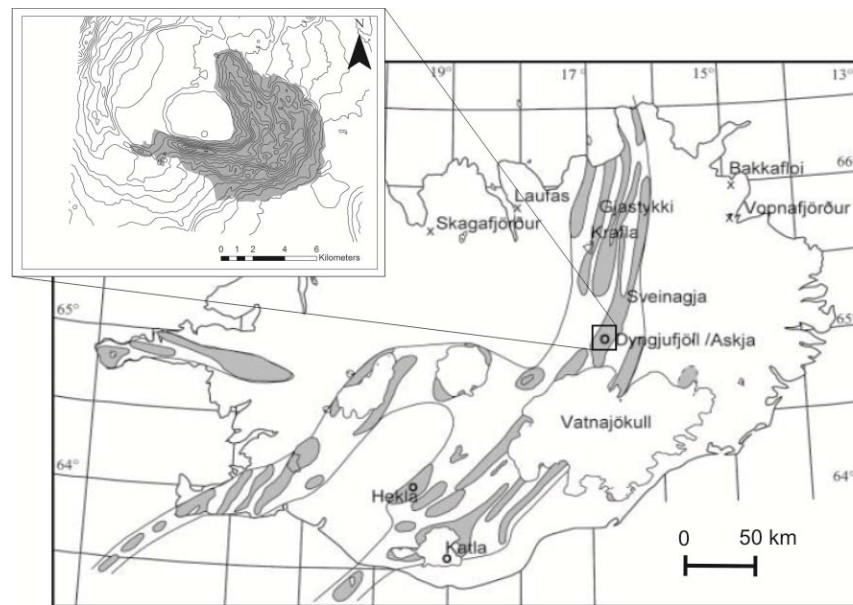


**Figure 5.1 Location map of Iceland with the volcanic zones highlighted (modified from Sigvaldason 2002). Note the location of Askja just north of Vatnajökull ice cap. The Northern Volcanic Zone stretches north from Vatnajökull icecap to the coast. Inset shows the Austurfjöll glaciovolcanic massif in relation to Öskjuvatn, the caldera lake of Askja.**

### 5.1.1 Background

Askja is a large basalt-dominated central volcano ca. 40 km north of the modern Vatnajökull icecap. A major topographic feature of the volcano is a glaciovolcanic massif, Austurfjöll, whose deposits consists of three major textural groups: micro-porphyrific glaciovolcanic effusive and explosive deposits; porphyritic glaciovolcanic effusive and explosive products; and the later-stage micro-porphyrific eruptive activity with subaqueous to emergent fissure activity (Figure 2.2).

Maps of historical deposits and regional geologic features of Askja and its immediate surroundings have been published in the last century (Annertz et al., 1985; Bemmelen and Rutten, 1955; Carey et al., 2009; Carey et al., 2010; Hjartardóttir et al., 2009; Sigvaldason, 1968, 2002; Þorarinsson, 1963; Thorarinsson and Sigvaldason, 1962; Thoroddsen, 1925). Additional information on the nature of the historic volcanic activity has been collected since 1875 following a 0.321 km<sup>3</sup> rhyolitic caldera forming eruption from Askja (Carey et al., 2009; Carey et al., 2010; Höskuldsson, 1987; Kuritani et al., 2011; Sigurdsson and Sparks, 1978; Sigvaldason, 1964, 2002). The nearby iconic edifice Herðubreið has also been mapped (Werner and Schmincke, 1999; Werner et al., 1996). These data, in conjunction with new field evidence from Askja, provide excellent opportunities to validate remotely collected data (Figure 2.2). Other predominant features in this portion of the highlands include the glacial river Jökulsá á Fjöllum, that flows roughly south - north along the eastern edge of the ASTER scene; Dyngjuvatn, a shallow periglacial lake between Askja and Valðalða (interglacial shield volcano); Öskjuvatn a lake filling the youngest caldera of Askja; and extensive sandur (glacial outwash) plains derived from Vatnajökull.

Remote sensing data include: aerial photographs collected by LoftMyndir Iceland comprising a grayscale mosaic from 2003 (850 km<sup>2</sup>), an orthorectified color image from 2008 (50 km<sup>2</sup>), and a digital elevation model (DEM) created by LoftMyndir Iceland from stereopairs of orthophotos (280 km<sup>2</sup>). Previously published maps used in this study include a lineament and simplified geology map (2,400 km<sup>2</sup>) (Hjartardóttir et al., 2009) and a map of the Holocene lavas surrounding Askja (1,400 km<sup>2</sup>) with some

simplified units of glaciovolcanic and interglacial origin (Annertz et al., 1985). A daytime ASTER scene acquired on August 8, 2010 (AST\_L1A.003:2080525361) allowed the mapped area to be extended to approximately 4,000 km<sup>2</sup>. ASTER level 2 data used for this study include the atmospherically corrected surface radiance product (15 m/pixel for the VNIR and 90 m/pixel for TIR), the VNIR surface reflectance product (15 m/pixel) and the TIR surface emissivity product (90 m/pixel) (Figure 5.3). These data were integrated with the 25 m resolution ASTER GDEM, which encompasses all of the previously listed datasets.

## **5.2 METHODOLOGY**

The creation of a 4,000 km<sup>2</sup> ground surface map of Askja and its surroundings involved the use of VNIR and TIR laboratory hyperspectral data of rock samples, VNIR and TIR multispectral data extracted from the ASTER data, topographic data (ASTER GDEM, Austurfjöll DEM), detailed (Figure 2.2) and simplified (Figure 5.2) geologic maps, as well as and several different image processing approaches using the Environment for Visualizing Images (ENVI) software. It was through the comparison and correlation of these varying spatial and spectral resolution datasets that the best-fit map (BFM) was produced.

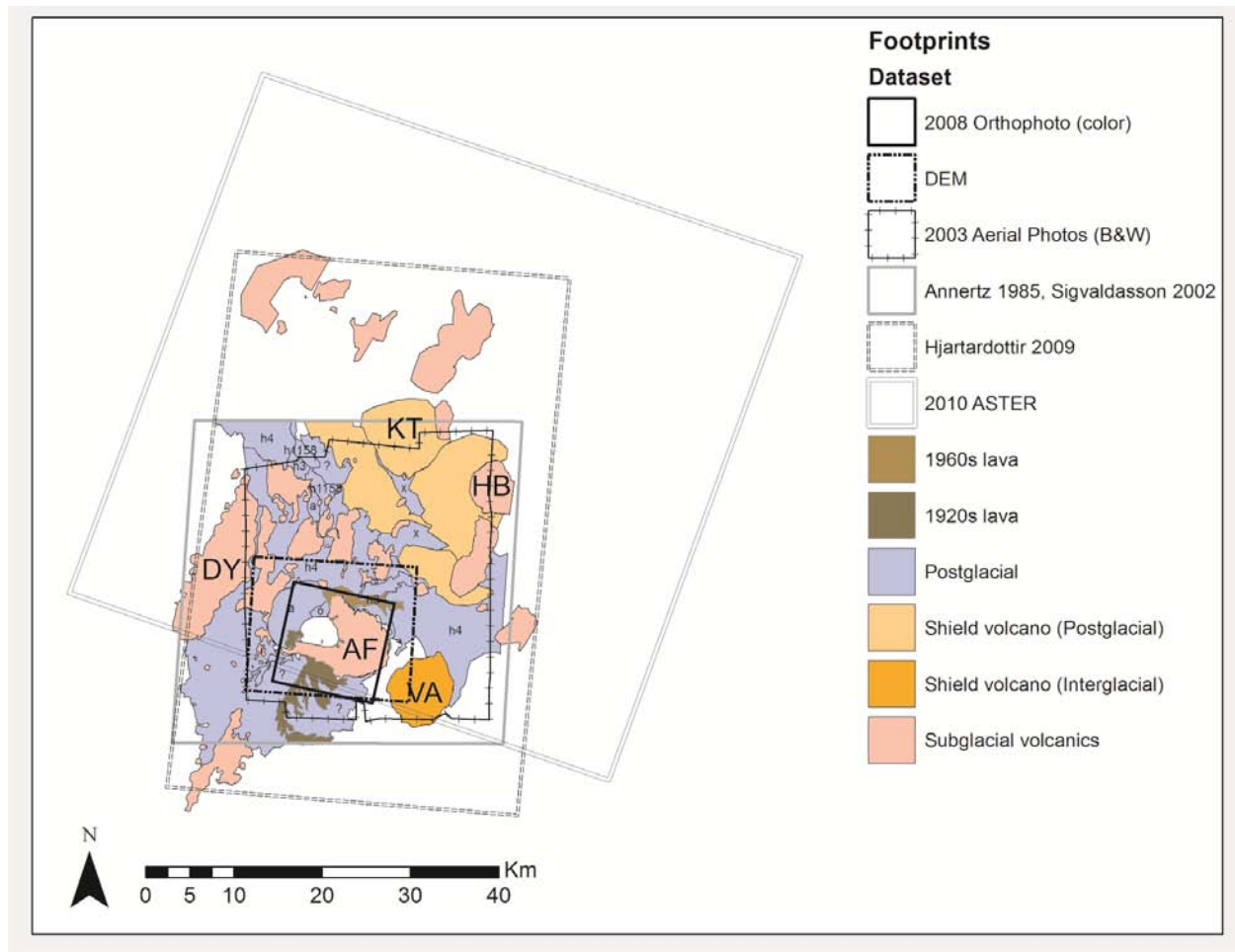


Figure 5.2 Regional geologic map compiled from previously-published sources (Annertz et al., 1985; Sigvaldason, 2002; Hjartardottir, et al. 2009). Outlines indicate footprints of datasets used to compile the regional map and remote sensing datasets utilized in this study. Abbreviations reference features that are discussed in detail in the text: DY is Dyngjufjöll Ytri, HB is Herðubreið, AF is Austurfjöll, VA is Valðalöa, KT is Kollóttadyngja.

### **5.2.1 Data collection**

Remote sensing data sets were augmented by the collection of data from the field site. Field investigations resulted in the production of a lithofacies map of Austurfjöll massif and sample collection of representative surface units.

#### **5.2.1.1 Field work**

The surface volcanic geology was studied in detail through two field expeditions augmented by chemostratigraphy and analysis of aerial photographs. Representative samples of the dominant lithologies were identified on and around Austurfjöll in order to create a spectral end-member library. End-members were selected and sampled based on several criteria including: 1) their compositional relevance to the evolution of Askja massif, 2) their dominance in the surrounding landscape, and 3) previous documentation. End-members included: glaciovolcanic subaqueously emplaced basaltic lavas (micro- and macro-porphyritic), subaqueous basaltic lapilli and ash tuff, Askja subaerial basaltic lava, Valðalða basaltic subaerial lava, Askja historic basalt (1920's), Askja historic pumice components (1875 pumice, obsidian, and lithics), Askja hydrothermally altered rhyolite, diamictite, and basaltic glass (intrusive chill margin). Preexisting regional maps indicate the presence of the majority of the spectral-end members within the region surrounding Askja (Figure 5.2).

#### **5.2.1.2 VNIR spectra**

Directional VNIR reflectance spectra of the end-member lithology samples were collected at the Image Visualization and Infrared Spectroscopy (IVIS) laboratory at the University of Pittsburgh using an Analytical Spectral Devices (ASD) FieldSpec HH spectrometer (0.35-1.1 $\mu$ m spectral range). Spectra were collected using a full-spectrum lamp for illumination and calibrated against a Spectralon plate. Whole rock samples with intact natural surfaces were used and no atmospheric control was made due to the short path length ( $\sim 0.5$  m) and limited atmospheric contamination in this wavelength region. These spectra

were used to create a hyperspectral end-member VNIR (H-VNIR) spectral library of the selected lithologies. The spectra were also resampled by convolving them with the ASTER spectral response function to produce an ASTER spectral resolution end-member (A-VNIR) library (Figure 5.3).

### **5.2.1.3 TIR spectra**

Hemispherical TIR emissivity spectra of the natural rock surfaces were also collected in the IVIS laboratory using a Nicolet Nexus 670 FTIR spectrometer with a KBr beam splitter and a DTGS detector (allowing data from 5-25  $\mu\text{m}$ ) (Carter et al., 2008; King et al., 2004). To derive the instrument response function, a two temperature approach was used (Ruff et al., 1997). The instrument response function derived from the measurement of two highly-accurate blackbodies is used to produce a calibrated emissivity spectrum. This approach requires that only one sample measurement at one temperature be made and has a cumulative error of  $\sim 2\%$  (Ruff et al., 1997). Samples were heated to  $75^\circ\text{C}$  and spectra were collected within an environment purged of  $\text{CO}_2$  and  $\text{H}_2\text{O}$  to reduce atmospheric interference in this wavelength region. These spectra were used to create a hyperspectral end-member TIR (H-TIR) spectral library. The spectra were also resampled by convolving them with the ASTER spectral response function to produce an ASTER spectral resolution end-member (A-TIR) library (Figure 5.4). The A-TIR end-member spectra were later used for linear deconvolution (Byrnes et al., 2004; Ramsey and Christensen, 1998).

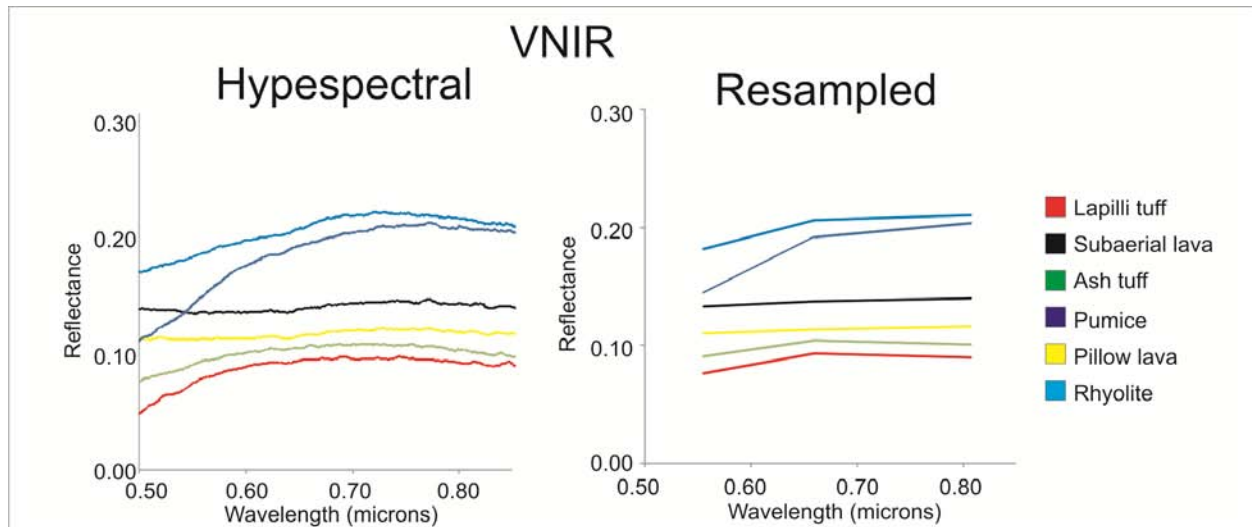


**Figure 5.3 Selected VNIR hyperspectral and ASTER resolution reflectance spectra of representative end-member samples. The limited spectral diversity of the compositional units (lapilli tuff, subaerial lava, ash tuff, pumice, subaqueous lava and rhyolite) is primarily from overall brightness levels of the samples. However, all units can be distinguished in the limited spectral resolution of ASTER.**

#### 5.2.1.4 ASTER Classification

VNIR, TIR, and combined VNIR / TIR ASTER registered radiance data were classified using ISODATA (Ball and Hall, 1965) and k-means (Lloyd, 1982) algorithms. ISODATA differs from k-means in that the number of clusters is permitted to vary during classification. Classifications were set to use five initial classes, ten maximum classes, and ten iterations. These unsupervised classifications are useful to highlight spectral variability within the scene.

Regions of Interest (ROIs), selected from the field data, aerial photos, and from the k-means classification results were then defined. Based on the compiled maps (lithofacies and regional), areas of known lithology were utilized for the creation of nine ROIs: pumice, subaqueous ash and lapilli tuff,



glaciovolcanic coherent lava, rhyolite, historical lava, Valðalða, water, snow and vegetation. Supervised minimum-distance classifications were conducted using these ROIs on the ASTER VNIR reflectance data.

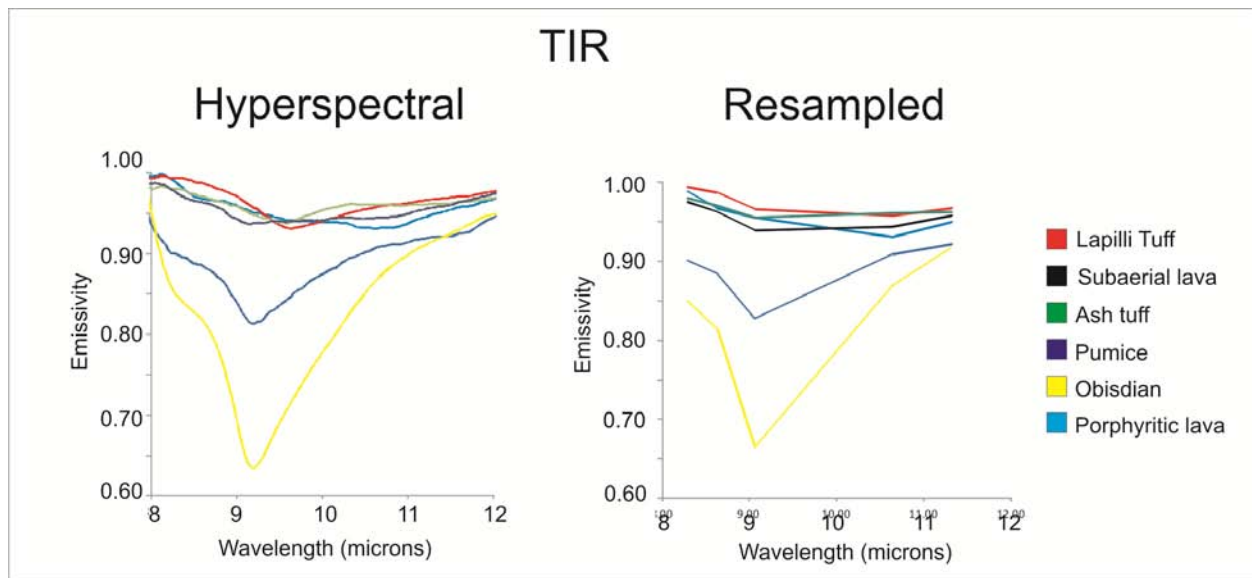


**Figure 5.4 Selected TIR hyperspectral and ASTER resampled emissivity spectra of representative lithology samples (subaerial lava, ash tuff, lapilli tuff, pumice, obsidian and porphyritic lava). There exists much more spectral diversity in the TIR due to the primary Si-O vibrational frequency in all silicate samples.**

A similar process was used for the TIR emissivity data. End-members to be used in the TIR data were selected using the highest resolution data sets, including the ASTER VNIR data, field data, and aerial photographs. Classes whose members exhibited spatial distributions smaller than a single TIR pixel, such as vegetation and snow, were excluded, due to a lack of pure end-member spectra within the ASTER data. The image-based end-members were used to create another spectral library (R-TIR). These end-members were used to further refine the minimum-distance classification.

#### **5.2.1.5 VNIR reflectance spectra classification**

The A-VNIR spectral library was used for supervised minimum-distance classification of the reflectance data. The 12 sample spectral library was further refined by creating ROI-based spectra from a targeted region of the known 1875 pumice that was highlighted by the initial classification to produce the A-VNIR + spectral library. The classification was rerun to produce the best-fit VNIR classification of the pumice ground cover unit.

#### **5.2.1.6 Linear deconvolution of emissivity spectra (TIR)**

Spectral deconvolution, or linear unmixing, is based on the principal that the TIR energy emitted or reflected from a surface containing multiple components (minerals, lithologies) is a linear combination of the energy emitted from each individual component in proportion to the end-member's surface abundance (Ramsey and Christensen, 1998). Because this mixing is linear, it can be modeled using an end-member library and a least squares linear fit of the data in order to extract the surface composition percentages of each end-member for every pixel (Adams et al., 1989; Byrnes et al., 2004; Ramsey and Dehn, 2004 ). Linear deconvolution was conducted using the two broadband TIR spectral libraries (R-TIR and A-TIR).

Spectral deconvolution of ASTER TIR data using the image end-members was performed using combinations of end-member spectra from the R-TIR spectral library. The TIR ROIs were defined initially with VNIR data and the spectra extracted from the ASTER emissivity data resampled to the same pixel size (15 m) as the VNIR data to ensure accurate ROI perimeters. The deconvolution process was then run on the atmospherically corrected surface emissivity data. The process was repeated using the laboratory-based A-TIR spectral library.

The deconvolution process involved using four spectral end-members plus a blackbody spectrum for all iterations. Multiple iterations were performed for each spectral library with end-members selected to target deposits of interest: 1875 pumice, historical lava, Holocene lava, fragmental glaciovolcanic deposits (ash tuff and lapilli tuff) and coherent glaciovolcanic deposits (subaqueous lava flows). Results were evaluated by examining the end-member images as well as the root-mean-squared (RMS) error image that maps the success of fit of those end-members. This comparison allowed each spectral subset to be assessed and to isolate false identifications of ground cover units in outlying areas, particularly glaciovolcanic and pumice ground cover units.

### **5.2.2 Compilation of the best-fit map**

Dominant ground cover units were identified from the ROI, VNIR, and TIR classifications as well as the linear deconvolution results. The ground cover units were then divided into sub-units based on the success and agreement of classifications and deconvolution results. Individual landforms were assessed independently with the results from each methodology compared for consistency and extent of the units. The ground cover units were also compared with the GDEM to better define the boundaries of the lithologic units and morphological features. The end-member map was refined and further validated by comparing it with the regional (Figure 5.2) and Askja lithologic (Figure 2.2) maps. Individual ground cover units were compared with existing literature discussing the regional features and deposit distributions. For example, the 1875 pumice extent was constrained by the work of Carey et al. (2010),

which documented 233 km<sup>2</sup> of pumice coverage. The final map derived from the remote sensing data is described as the best-fit map (BFM) (Figure 5.5). The 1875 pumice unit was subtracted from the ground surface to produce a “pumice-free” best-fit map to highlight glaciovolcanic lithologic variations.

The construction of a best-fit map from multiple techniques was intended to reduce the error associated with any of the individual remote sensing based mapping techniques described here. By utilizing the lower spatial resolution but more lithologically diverse TIR data, and the high spatial resolution, but limited spectral resolution VNIR data, the drawbacks of the individual techniques can be reduced. The results are further supported by the inclusion of the 25 m resolution ASTER GDEM, which provides critical morphological data for interpreting unit boundaries and the distribution of topographically influenced fragmental deposits (e.g. sandur and pumice).

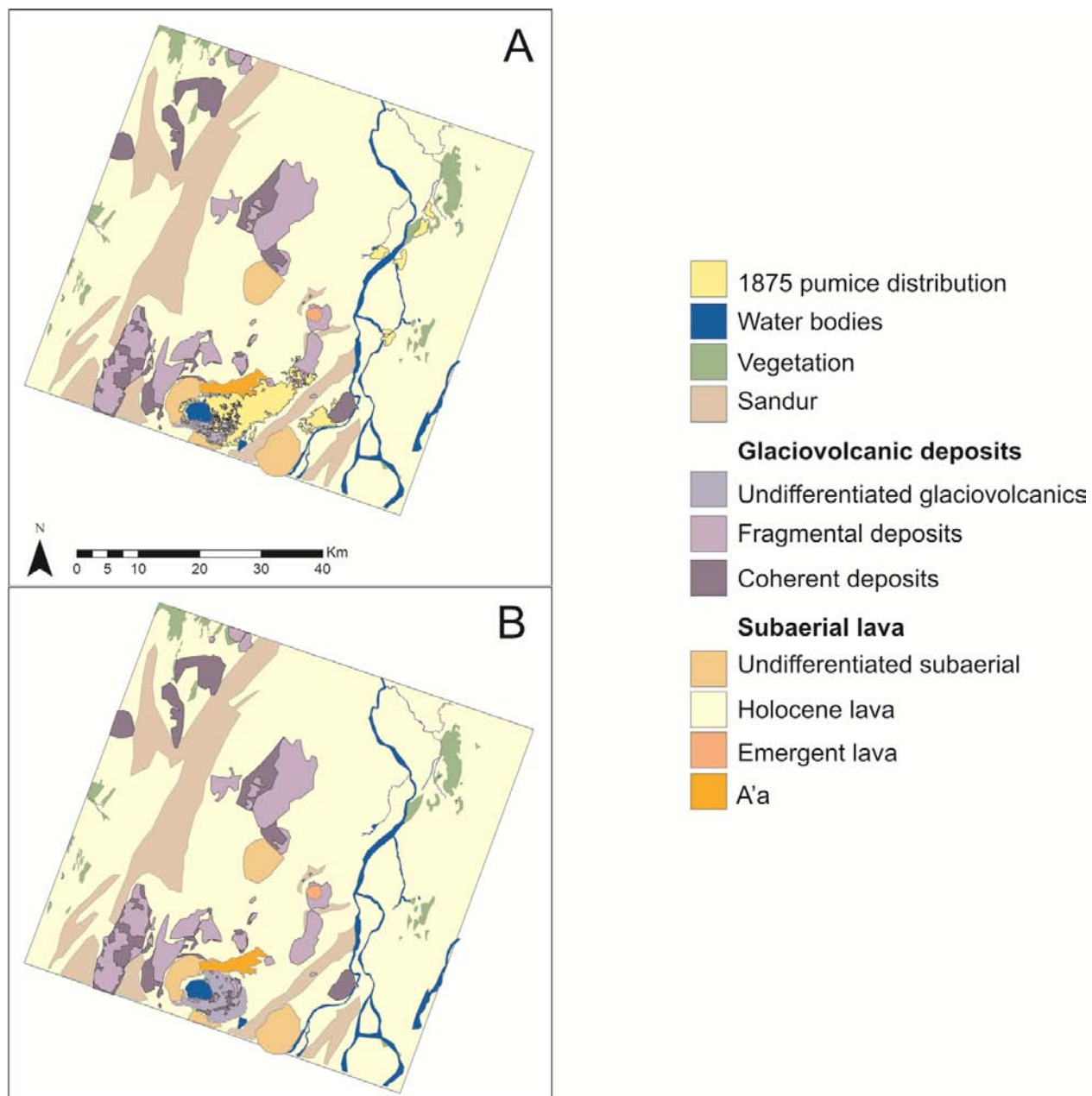


**Figure 5.5 A) Best-fit map (BFM) of ground cover units in the region north of Askja Volcano. B) BFM with 1875 pumice removed.**

## 5.3 RESULTS

### 5.3.1 Best-Fit Map

The BFM map based on the ASTER data contains six primary ground cover units: subaerial lava (31%), glaciovolcanic deposits (21%), sandur deposits (25%), 1875 pumice (5%), water bodies (5%), and vegetation (4%). Two primary ground cover units, subaerial lava and glaciovolcanic deposits, were further divided into textural, or geomorphologically distinguished sub-units. Subaerial lava was divided into a'a lava, shield volcano, undifferentiated Holocene lava, and emergent glaciovolcanic lava subgroups. The a'a subgroup was defined by a high blackbody anomaly on lava flows from 1960 and 2.9 ka just north of Öskjuvatn (Annertz et al., 1985), a result of the high surface roughness of the flows (Ramsey and Fink, 1997). This does not preclude the presence of other a'a flows, rather this blackbody anomaly represents the distinctive nature of these particular deposits. Shield volcanoes, Holocene lava, and emergent lava were distinguished from one another by their geomorphic expression and relative elevation to the regional base elevation. Shield volcanoes had distinctive low-angle relief and near circular morphologies, but cannot be assigned any age relationships using the remote techniques alone. The Holocene lavas that infill the large Askja caldera were grouped with the shield volcano ground cover sub-unit due to their association with a single geomorphologic feature, and distinctive quality relative to the Holocene lavas of the surrounding area. This assignment is intended to reflect morphology, not imply a genetic origin of the lavas. Emergent lavas are identified due to their topographic position as subaerial lavas perched atop subaqueous dominated features, in this case Herðubreið glaciovolcanic volcano (Figure 5.5). The general base topography identified by TIR techniques as subaerial lava was mapped as undifferentiated Holocene lava, which is supported by regional mapping by Annertz et al. (1985) (Figure 5.2).

**Table 5.1 Aerial extent of ground cover units in best fit map (Figure 5.6), with comparison to existing aerial extent from regional map (Figure 5.3).**

<b>Feature</b>	<b>BFM</b>		<b>Regional Map</b>
	m <sup>2</sup>	% of total	m <sup>2</sup>
<b>Water</b>	1.03 x 10 <sup>8</sup>	5	
<b>Vegetation</b>	8.41 x 10 <sup>7</sup>	4	
<b>Pumice</b>	1.11 x 10 <sup>8</sup>	5	2.33 x 10 <sup>8</sup>
<b>Valðalða</b>	5.99 x 10 <sup>7</sup>	3	4.53 x 10 <sup>7</sup>
<b>Subaerial lava</b>	1.18 x 10 <sup>8</sup>	6	
A'a lava	2.25 x 10 <sup>7</sup>	1	9.86 x 10 <sup>6</sup>
Shield volcanoes	3.18 x 10 <sup>7</sup>	1.5	2.40 x 10 <sup>8</sup>
Emergent lava	4.55 x 10 <sup>6</sup>	0.2	
Holocene lava (undifferentiated)	7.90 x 10 <sup>8</sup>	39	4.90 x 10 <sup>8</sup>
<b>Sandur</b>	5.06 x 10 <sup>8</sup>	25	
<b>Glaciovolcanic</b>	4.31 x 10 <sup>8</sup>	21	3.57 x 10 <sup>8</sup>
Fragmental	2.66 x 10 <sup>8</sup>	13	
Subaqueous lavas	2.89 x 10 <sup>8</sup>	14	

The glaciovolcanic deposits unit was divided into fragmental and coherent-dominated subgroups. A third subgroup, porphyritic units, was attempted. Porphyritic deposits cover >1% of the field map, but the TIR spectral mapping identified only 3% of the mapped porphyritic units from the lithofacies map. As such, the distribution of the training areas and potential distribution have much lower confidence than the two major glaciovolcanic subgroups, and will be discussed separately. Fragmental glaciovolcanic deposits were distinguished by their frequent misclassification as other clastic deposits (sandur and pumice) and correlation with laboratory VNIR and TIR spectra of the known fragmental deposits from Askja (dominantly ash tuff) (Table 5.1). Coherent glaciovolcanic deposits include subaqueous lavas of pillowed, lobate and sheet morphologies and likely include clast-rich breccias associated with the lavas. Based on the deposits mapped at Austurfjöll, the deposits are assumed to be dominated by pillowed lava flows.

Due to a combination of pumice cover, 1920s lava flow cover, and steep slopes, approximately 19% of the 49 km<sup>2</sup> glaciovolcanic deposits of Austurfjöll massif are exposed for satellite based ground-cover mapping (Figure 5.6A). The corridors of exposed glaciovolcanic deposits within the pumice unit are on the order of <1 km in width and up to 4 km long. A comparison of the DEM and pumice-free areas of Austurfjöll reveal a correlation of topographic highs with pumice-free regions of Austurfjöll (Figure 5.6B). An overlay of 1875 pumice on the lithofacies map shows the diversity of lithologic units exposed in areas not obscured by the pumice (Figure 5.6C). However, not all of the pumice-free areas were successfully discriminated between fragmental and coherent-dominated glaciovolcanic units using remote sensing techniques (Figure 5.6D), and instead are classified as undifferentiated glaciovolcanic deposits (Figure 5.8). Of the viable surfaces on Austurfjöll massif 66 % of those surfaces are identified as coherent glaciovolcanic units.



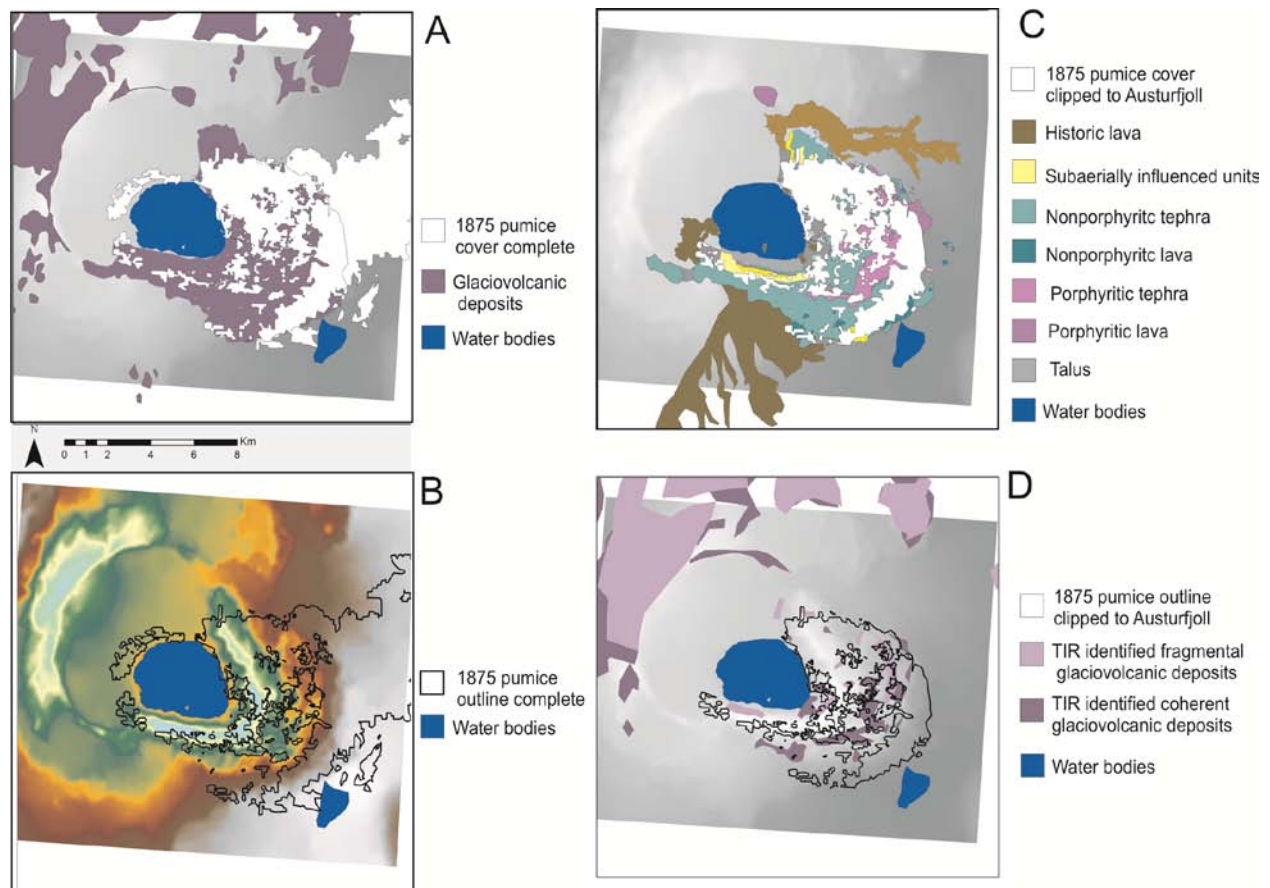


**Figure 5.6 Distribution of the 1875 pumice proximal to the Austurfjöll massif overlain on a grayscale hillshade (derived from 10 m Loftmyndir DEM). A) Complete distribution of the 1875 pumice overlapping the glaciovolcanic deposits. B) Outline of the 1875 pumice over colored hillshade to show relationship between eroded pumice and topography of the Austurfjöll massif. The pumice is mostly preserved in topographic lows. C) 1875 pumice cropped to extent over Austurfjöll to show the exposure of lithology-mapped field units under the pumice. D) Outline of cropped pumice distribution of TIR-based discrimination of glaciovolcanic units.**

**Table 5.2 Techniques used to identify individual ground cover units.**

Feature	VIS			AVNIR Class.	TIR				Topography
	False color	ISO	ROI Class.		ROI Class.	ROI Unmix	ATIR Unmix	Black- body	
Water		X	X	X		X	X	X	
Vegetation	X		X						
Pumice	X	X	X	X		X	X		
Valðalöða									X
Subaerial lava		X	X	X		X	X		
A'a lava								X	
Shield volcanoes									X
Emergent lava									X
Sandur	X	X	X	X		X	X		
Glacio- volcanic			X						X
Fragmental Dominated		X					X		
Subaqueous lavas						X	X		
Holocene lava (undifferent- iated)		X	X	X	X	X			X

A comparison of the various mapping techniques used to create each layer and the areal extent of the final units and any interim steps necessary is presented in Table 5.2. The overall distribution of glaciovolcanic units is larger in the BFM (17%), and the placement and extent of features farther from Askja have been improved by topographic data (Figure 5.7). However, small-scale features in the vicinity of the calderas were not consistently recognized by either the VNIR or TIR techniques, and thus do not appear on the BFM (Figure 5.7). The BFM also incorporates additional groundcover units that were not previously discriminated (e.g. fragmental from coherent glaciovolcanic units, sandur, and vegetation).

Non-lithologic units (water and vegetation) compose 9% of the scene. The water bodies are well-correlated to recent maps of the major water features (Öskjuvatn, Jökulsá á Fjöllum, and Dyngjuvatn). Minor tributaries and ponding near the river likely are ephemeral, or intermittent, and thus the BFM is only representative of their condition in August 2010. The snow groundcover unit was dropped from the final map due to its low spatial distribution. Snow has a high degree of variability temporally and, for this particular scene, did not have sufficient training areas to create an accurate ROI.

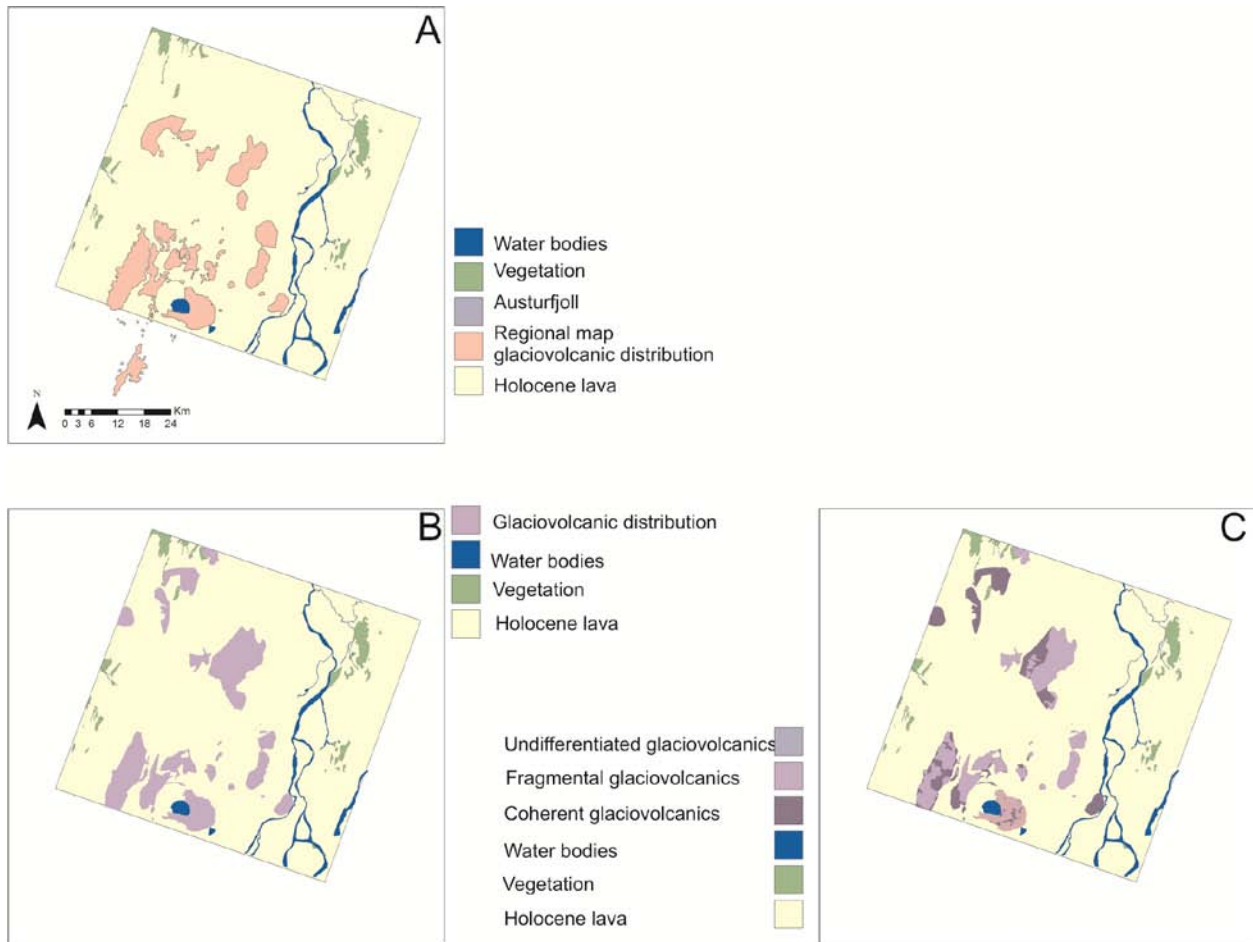


**Figure 5.7 Comparison of glaciovolcanic unit distributions between existing maps (regional map Figure 5.2) and remote sensing based BFM with 1875 pumice and other groundcover units removed. A) Glaciovolcanic units as compiled from the previous literature on Askja and surroundings (Hjartadottir et al. 2009; Annertz et al. 1985). B) Undifferentiated glaciovolcanic deposit distribution in BFM, results with constraints from ASTER GDEM topographic data. C) Differentiated glaciovolcanic deposits in BFM including fragmental, coherent, and undifferentiated glaciovolcanic deposits.**

## 5.4 DISCUSSION

The BFM improved existing regional maps through a combination of 1) increased aerial extent of the map of the portion of the Northern Volcanic Zone around Askja, 2) the discrimination of two lithologic subgroups of glaciovolcanic massifs, 3) a detailed outline of the distribution of the remobilized 1875 pumice deposit, and 4) the introduction of the new ground cover units: sandur and vegetation. The production of the map also served as an important test for remote sensing-based techniques for the mapping of glaciovolcanic terrains in Iceland, which has a very limited application in the past.

VNIR based methodologies were successful at identifying vegetation, pumice, and sandur ground cover units. The VNIR also served as support for the identification of subaerial lava (and sub-units), and fragmental glaciovolcanic deposits. The high spatial resolution (15 m/pixel) of the VNIR data was necessary to discriminate detailed aspects of the vegetation and pumice. These units display high contrast in the visible wavelengths producing well-defined units from supervised and unsupervised classifications. The sandur groundcover unit only represents the thickest areas of glacial outwash, having a uniform coloration and texture, distinguishing it from lava flow surfaces. However, this map does not distinguish thin deposits of outwash-derived eolian sands that are easily observed in the field.

Supervised VNIR classifications produced highly variable results, with the least consistent results produced using the laboratory-based hyperspectral end-member classification. The VNIR classifications were limited by the low brightness variability of the end-member samples. The glaciovolcanic deposits were all dark basaltic samples with high vesicularity and / or porosity. However, the unsupervised classifications were highly consistent and had a high correlation of external unit boundaries with TIR results. Consequently, the unsupervised VNIR classifications were given the highest preference in map creation, followed by ROI based end-member classifications and A-VNIR classification.

The remaining groundcover units were mapped based on variations in micron-scale roughness and composition identified in the TIR classifications and linear deconvolutions, with support from VNIR and topographic data. The glaciovolcanic deposits were most successfully identified using A-TIR and

ROI spectral deconvolution (in that order). Thermal wavelength characteristics are primarily produced by the abundance of micron-scale roughness elements such as vesicles and macro-phenocrysts (Byrnes et al., 2004; Ramsey and Fink, 1999). The textural qualities of the glaciovolcanic fragmental deposits and pillow lavas are distinctive from the surrounding subaerial lava flows, but display large internal variability. The bulk of the fragmental deposits were identified using the linear deconvolution approach. Some deposits were more easily distinguished from coherent glaciovolcanic deposits with support from the VNIR, particularly Dyngjufjöll Ytri, where fragmental glaciovolcanics were identified by TIR spectral deconvolution as 1875 pumice (Sigvaldason, 1992). This misclassification is the direct result of the textural similarity between the fragmental deposits of Dyngjufjöll Ytri and the 1875 pumice. Consequently the two deposits are better distinguished by the unsupervised VNIR classification which identifies the compositionally influenced color variation between the basaltic glaciovolcanics and the rhyolitic pumice.

The glaciovolcanic deposits of Askja have the most complicated spectral signature of the edifices in the region as the Austurfjöll massif has the greatest variability of all landforms in the map area. This variability is a result of the steeper slopes of the caldera walls and gullies, and the abundance of more recent pumiceous deposits on the older (glacial age) deposits. Steep slopes on table mountains, like Herðubreið, and caldera walls, are not ideal targets for remote sensing as their steep slopes prevent the collection of spectra from glaciovolcanic units. In the case of Herðubreið, only the emergent subaerial lava cap is recognized. The lithofacies map (Figure 2.2) reveals the textural variability of Austurfjöll massif, including micro- and macro-porphyritic lavas and tuffs. The macro-porphyritic lavas should have a distinct TIR spectral signature (Byrnes et al., 2004) (Figure 5.4). However, A-TIR linear deconvolution did not produce confident results. The identification of units under the pumice by TIR remote sensing techniques are less accurate due to the interference of 1875 pumice with thicknesses from 0.05 to 2 m thick (Carey et al., 2010). Nevertheless, interesting trends were produced on Austurfjöll; the areas identified successfully beneath the fringes of pumice deposits as coherent, do have a high correlation, though limited direct overlap, with porphyritic units of the lithofacies map (Figure 5.7). The interference

of the pumice may have led to the misidentification of porphyritic tephra and lava as coherent micro-porphyritic glaciovolcanic deposits. Therefore, distinction between coherent glaciovolcanic lavas that are micro- and macro-porphyritic requires further investigation, whether remotely or in the field.

Subaerial lavas as a group were spectrally unique, with consistent results between classification and deconvolution techniques. The establishment of the subgroups was enabled by incorporating the topographic data. This was of particular importance for distinguishing between shield volcanoes and background Holocene lava. These two subgroups do not have significant compositional, textural, or visible color variations as revealed in the TIR and VNIR spectra. This lack of spectral variation is unexpected, as the shield volcano Valðalða is interglacial in age and has significant glacial scour, but remains indistinguishable compositionally from the background Holocene lava. The similarity of the scoured Valðalða and Holocene lava is likely due to the dominance of pahoehoe flows in both subgroups and thin eolian cover (derived from the sandur) over both features, muting surface textures. The DEM was utilized to identify the discrete morphologies of Valðalða and Kollóttadyngja shield volcanoes, which enabled the separation of these features from the Holocene lava subgroup. The remaining shields indicated in the regional map (Figure 5.2) have much less topographic relief, and were not identified through this mapping process; they are instead included in the Holocene lava subgroup.

Unconsolidated fragmental ground cover units (such as pumice and sandur) should also be easily resolved using thermophysical techniques such as apparent thermal inertia (Scheidt et al., 2010). However, the high latitude, commonly cloudy weather, and long snowy season in the Icelandic Highlands has, to date, precluded the acquisition of an ASTER day-night pair of temperature images over Askja. It would be worthwhile to consider testing apparent thermal inertia to detect unconsolidated fragmental ground cover units using other instruments with higher temporal resolution or ASTER data of regions with a higher abundance of useful scenes. The addition of higher spectral and spatial resolution data sets would also improve the discrimination of smaller or more compositionally mixed features.

## 5.5 CONCLUSIONS AND FURTHER RESEARCH

The best-fit groundcover map produced by this research was refined by supplemental field work and the introduction of additional remote sensing data. However, the success of the best-fit map based on only one ASTER data scene, in a studied, but not well-detailed area, reveals the potential for regional mapping of glaciovolcanic terrains remotely. The variability observed within the surrounding glaciovolcanic massifs warrants further field investigation in order to understand the volcanic and depositional processes, as well as the regional volcanic evolution and glacial history of the NVZ. In particular, macro-porphyritic lithologies may be more common than currently documented. The discrimination of fragmental from coherent glaciovolcanic units serves as an important starting point for reconnaissance-based mapping and the identification of critical field areas in Iceland and other difficult terrains such as British Columbia and Antarctica (Figure 5.7). The glaciovolcanic deposits of these regions are becoming increasingly important due to the lack of preservation of other terrestrial paleoclimate indicators, particularly of pre-last glacial maximum ice positions (Bourgeois et al., 2000; Edwards et al., 2009; Edwards et al., 2011). This project was intended to validate remote sensing data through the use of existing and recently collected data, but it also revealed the potential for supplementing field-based mapping. The new outline of the remobilized 1875 pumice distribution over the Austurfjöll massif adds a highly visible, but previously poorly constrained unit to the lithologic map (Figure 5.7C). With over one decade of global ASTER data, this study provides an important constraint on the use of ASTER VNIR and TIR data for complex compositional reconnaissance mapping of volcanic terrains around the world.



## **6.0 SUBAQUEOUS BASALTIC MAGMATIC EXPLOSIONS TRIGGER PHREATOMAGMATISM**

The question of what initiates and drives subaqueous basaltic explosions has been a matter of debate over the last 20 years. As the submarine exploration technology advances, and our ability to describe surficial subaqueous explosive volcanic deposits in detail have increased. Glaciovolcanic deposits in Iceland, British Columbia, and Antarctica provide the opportunity to examine subaqueous explosive deposits in three dimensions. In highly dissected volcanic edifices it is possible to describe the entire eruptive sequence, from the onset of explosive activity through the evolution of fragmentation as the eruption continues. Three sequences that transition from pillow lavas to breccias to lapilli tuffs from Askja volcano, Iceland are interpreted as subaqueously emplaced sequences of basaltic pillow lavas transitioning to explosively-generated vitric tuffs erupted from the same vent in the same temporally continuous eruption. The study is based on the textural analysis of the fragments produced at the onset of the eruption through the height of the deposit, which ranged between 15 and 35 m vertically.

The major relief of Askja is the basaltic glaciovolcanic Austurfjöll massif that is dissected by the lake-filled caldera Öskjuvatn (Figure 6.1). The Austurfjöll massif at Askja contains several well-exposed sequences composed of pillow lava, overlain by pillow fragments and fluidal bomb-bearing breccias that are capped by vitric lapilli tuffs. Such sequences contain textural evidence of the fragmentation mechanisms that occur during the transition from effusion of lavas to explosions from the same vent. The focus of this study is three massive, ca. 30 m thick, glassy subaqueous pyroclastic deposits that directly overlie pillow lavas. They are dominated by a systematic and continuous fining upward from pillow-fragment breccia to fluidly-shaped bomb-bearing breccia and ultimately to lapilli tuff.

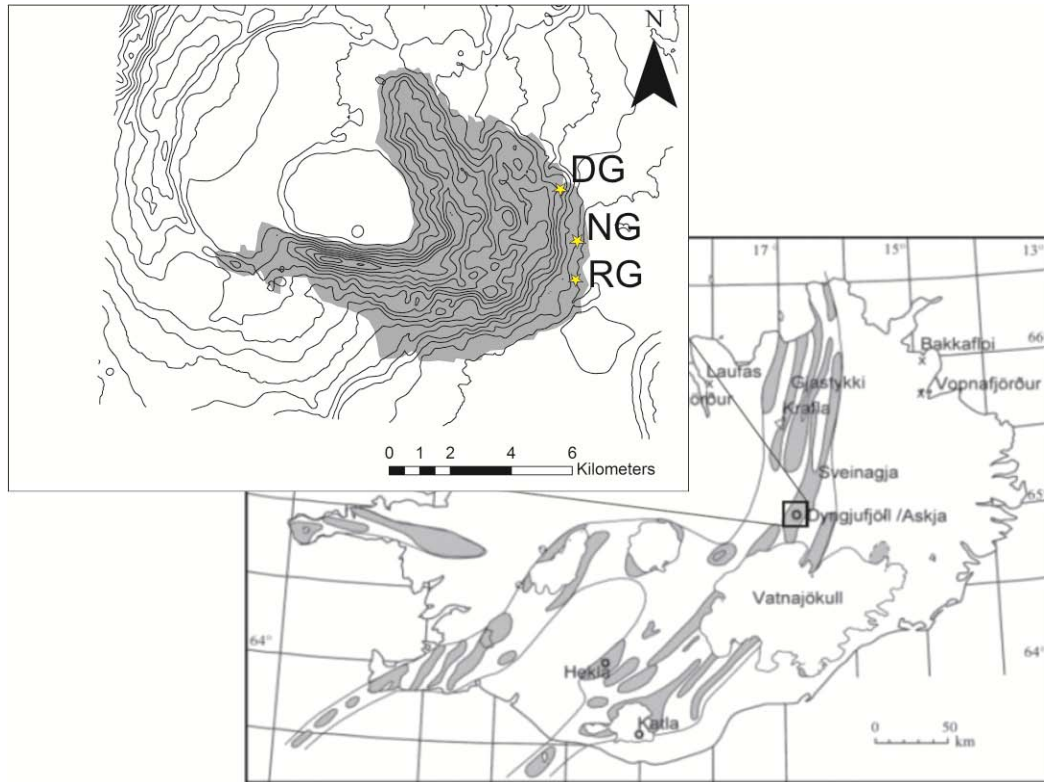


**Figure 6.1 Location of Askja, Iceland including locations of pillow lava, breccia, lapilli tuff sequences. The shaded area represents the field area, Austurfjöll. Sample sites are located in major gullies incised into the base of the glaciovolcanic sequence of Askja. Sample locations from north to south are Drekagil (DG), Nautagil (NG), and Rosagil (RG).**

Ostensibly similar sequences of pillow lavas overlain by breccias, containing pillow fragments and blocks, capped by vitric lapilli tuffs have been described in ophiolite sequences (Carlisle, 1963), Archean basalt provinces (Dimroth et al., 1978), ocean island settings (Fujibayashi and Sakai, 2003), and several glaciovolcanic sequences (Jones, 1970; Skilling, 2009; Werner and Schmincke, 1999). Breccias overlying subaqueously emplaced lava flows could be derived through many processes, such as lava flow emplacement (autoclastic breccias), post-emplacement collapse, invasive lavas (peperitic breccias), or through explosive disruption of the erupting lava. Explosive disruption of such lavas may have several possible origins, including a continuous transition from effusive emplacement to magmatic and / or phreatomagmatic explosions of the same lava, or it could be due to later explosions of either type, that occurred beneath earlier solidified lava flows. The sequences from Askja described here are interpreted as near-vent sequences generated during a continuous transition from effusion to explosion. The aim of this research is to distinguish the textural signatures of fragmentation from a co genetic explosively derived pillow, breccia, and lapilli sequence from other mechanisms of fragmentation.

## **6.1 BACKGROUND / MOTIVATION**

Basaltic glaciovolcanic systems under thick-ice (>300 m) typically evolve into ice-confined lacustrine eruptive centers (Allen et al., 1982; Gudmundsson, 2003; Gudmundsson et al., 1997; Werner and Schmincke, 1999). Within the ice-confined lake the water level may change rapidly and repeatedly through time (Bjornsson, 2002; Gudmundsson et al., 1997; Höskuldsson et al., 2006; Smellie et al., 2008). Simplified models of deep water basaltic glaciovolcanic center evolution include initial subaqueously emplaced effusive products, dominated by pillowed lavas, followed by a shift towards more explosive activity and deposition of fragmental deposits (Allen, 1980; Jones, 1970; Moore et al., 1995; Werner et al., 1996). Within this model it is assumed that there is a decreasing violence of subaqueous eruptions as

water depth increases, particularly above 300 m (Allen, 1980; Clague et al., 2003; Zimanowski and Büttner, 2003). However, investigations of submarine basaltic deposits are revealing the presence of explosively derived deposits at depths up to 3 km (Clague and Davis, 2003; Fujibayashi and Sakai, 2003; Helo et al., 2011; Portner et al., 2010; Schipper and White, 2010; Schipper et al., 2010a; Schipper et al., 2011a; Sohn et al., 2008; Wohletz, 2003). This uncertainty over the control of confining pressure, and the role of other possible controls (Mastin et al., 2009; Schipper et al., 2011b; White, 1996a) in natural settings on the triggering of subaqueous explosions emphasizes the importance for detailed studies of deposits that may record the onset of basaltic explosions in water. The signature of the mechanisms of fragmentation, transportation, and deposition are preserved at multiple scales in the textures of subaqueous pyroclasts, over the full range of grain sizes, including bombs, lapilli and fine ash. These textures within the overall deposit structure and glaciovolcanic stratigraphy are important tools to understand basaltic subaqueous explosions in deep water environments and the construction of thick ice glaciovolcanic centers.

### **6.1.1 Field area**

Askja is one of the largest and best-exposed formerly ice-confined volcanoes on Earth. Most research to date has been on its Holocene (ice-free) evolution. It comprises a complex of basaltic glaciovolcanic massifs that are dominated by pillow lavas and subaqueously emplaced vitric lapilli tuff deposits, cut by several calderas, and surrounded by Holocene subaerial lava flows (Figure 6.1). The greatest volume of glaciovolcanic deposits at Askja is the eastern mountain massif, Austurfjöll, which is truncated by younger calderas. Austurfjöll has been described briefly by Brown et al. (1991), Sigvaldason, (1968 and 2002) and more recently in detail by Graettinger et al. (2012).

Austurfjöll is incised by large gullies that extend up to 3 km into the massif. The vertical exposure within the gullies is between 10 and 100 m. The vertical exposures are dominated by pillow lava sheets, breccias, and vitric lapilli tuff. Three of these gullies contain well-exposed sequences that display

gradual transitions up section between effusive pillow lavas at their base, to an upward fining pillow fragment and bomb-bearing breccia vitric lapilli tuff sequence. The sequences have lateral continuity of tens of meters, and can be traced in multiple directions. The three gullies from north to south are named: Drekgil, Nautagil, and Rosagil (Figure 6.1).

## **6.2 METHOD**

This study is based mostly on field work conducted over two seasons at Austurfjöll. The three sequences of glassy pillow lava, breccia, lapilli tuffs were identified in 2010 and revisited in 2011 for more detailed sampling and study. Samples were collected from the top of the basal pillow units, the lowermost breccia at the contact with the pillow lavas, and then progressively up through the section of overlying breccias and vitric lapilli tuffs, with an average sample interval of 2 m. At each point a sample of matrix and an outsized clast was taken. Outsized clasts are defined here as the largest clasts that exceed the visually estimated median grain size at a stratigraphic level. Measurements were taken of the average clast size and the outsized clasts. Measurements were limited to the largest outsized clasts with intact glassy chill rinds, in order to sample the largest intact fluidal bombs. Measurements of vesicularity percentages of the core, and glassy rim of outsized clasts were supported by photographs. A minimum of five measurements of such clasts were taken at each site. If a secondary size mode of outsized clast was present, the largest clasts representative of both modes were studied.

Samples were prepared for thin-section after impregnation with blue epoxy and polished for scanning electron microscope (SEM) analysis. A binocular microscope with mounted digital camera was used to document and estimate the vesicularity of partially disaggregated clast and matrix samples. Additional observations of vesicle shape, distribution, and coalescence were recorded. Matrix samples were used to estimate the range of grain sizes. The partial consolidation, high friability, and fragile clast morphologies precluded full granulometric analyses. Digital images of thin sections were used to quantify

2D vesicularity through image analysis using ImageJ software. The presence of vesicles, crystals, tachylite fragments, mixed tachylite-sideromelane fragments, sideromelane fragments, and vesicle dimensions were all documented. SEM analysis, using secondary electron images collected on a JEOL JSM-5900, of the fine ash fraction included study of grain mounts of loose grains, coated in carbon. Samples were sieved to isolate particles  $<50\text{ }\mu\text{m}$  to target potential ‘active’ particles ( $<130\text{ }\mu\text{m}$ ) of fuel coolant interaction (FCI) experiments, described by Büttner (2002). SEM images aided the description of the ash morphology, vesicularity and vesicle textures. Statistics were produced from SEM images based on the number of grains that displayed a target feature (e.g. blocky shape, conchoidal fracture, vesicles). Consequently, these values represent the abundance of a given texture, not volumetric presence of vesicles within the ash particles.

The results of this textural study were compiled to calculate average, minimum, maximum, and the range of values for grain size and vesicularity for each sample site. As outcrop estimates of vesicularity were routinely higher than digital analyses using ImageJ in this study, field photographs were used to help calibrate outcrop and digital estimates of vesicularity.

### **6.3 OVERVIEW OF DEPOSITS**

All three sequences are exposed in steep walled gullies incised into the base of the 750 m Austurfjöll massif. The sequences have basal pillow lavas overlain by pillow- to bomb-bearing breccia, and then lapilli tuff with a decreasing occurrence of fluidal bombs up-section. The deposits range from 15-35 m in thickness and display gradational transitions between each lithofacies. Here the transition from breccia to lapilli tuff is defined as the point where the fluidal bomb presence is less than 30 vol. % of the total deposit. Geomorphologic evidence, particularly the thickness of subaqueous sequences at Austurfjöll (700

m), and volatile saturation pressure data indicate the eruption of these sequences occurred in water ca. 700 m deep, or beneath some combination of water, ice, and sediment with a confining pressure of ca. 7.7 MPa (Chapter 8). There is no structural or textural evidence that the sequence became emergent.

The stratigraphically lowest pillow breccias, within the first meter of the contact with the underlying coherent pillows, are dominated by clast-supported pillows forms and pillow fragments, up to 30 cm across. Fluidly-shaped bombs (referred to here as fluidal bombs) up to 40 cm occur within the breccia, replacing the pillows and pillow fragments within the lowest 2 m of the clastic sequences. The breccia matrix comprises coarse, glassy and angular vitric lapilli. As the breccia transitions into lapilli tuff, the proportion of matrix to blocks, outsized clasts namely fluidal bombs, increases. The mean vesicularity of bombs and lapilli remains similar throughout the sequences (ca. 25%). The proportion of ash-sized vitric matrix increases systematically upwards from the breccia (0-5%) to the lapilli tuff (30%), and is accompanied by a decrease in fluidal bomb size and a minor decrease in mean lapilli size. All vitric clasts within the breccias and lapilli tuffs are highly angular with fragile shapes, including glassy spines, and display no rounding, traction current structures, slump structures or other evidence of remobilization or lateral transport. All three of the sequences are dominated by fluidal bomb-bearing lapilli tuff and represent the transition from effusion to phreatomagmatic explosion.

### **6.3.1 Sequence Descriptions**

The three sequences studied are called Drekagil, Nautagil, and Rosagil (Figure 6.1). The sequence in Drekagil (DG) is exposed in a near vertical cliff within a 50 m deep east-west trending gully. Laterally, the sequence overlies a sharp erosional contact with well-bedded lapilli and ash tuff units (Figure 6.2). The pillow lavas occur in a thick pillow lava sheet that abuts and overtops a paleotopographic wall of ash and lapilli tuff. The pillow unit is thinnest at the top of the paleotopographic high, which occurs 30 m laterally from the main vertical sequence. Sampling of this sequence was limited to a diagonal transect from this thin lateral pillow outcrop to the top of the more centrally located lapilli tuff. The maximum

thickness of the pillows (30 m) occurs directly below the sampled lapilli tuff. The pillow unit is well exposed in the vertical wall and contains several intrusions and irregular pillow forms, with a local tabular base. The breccia that overlies the pillow lavas is ca. 5 m thick, with intact and fragmented pillow forms preserved in the bottom 1 m, and fluidal bombs occurring in the upper 4 m. The lapilli tuff has a thickness of 14 m and displays an upward fining upward of the fluidal bombs and a coincident increase in fine vitric ash content. The lapilli are typically 1-3 cm sized and do not change dramatically in size up-section. Lapilli are typically equant or partially fluidal in shape. The sequence is capped by a genetically unrelated convolute bedded ash that is overlain by a porphyritic subaqueous non-pillowed sheet lava. The contact between the lapilli tuff and the ash tuff is sharp, but there is no evidence of erosion. The transitional sequences at Drekgil is the only deposit to contain accidental lithics in the lapilli tuff, namely subangular porphyritic tholeiite lava lapilli, which comprise <1% of the deposit.



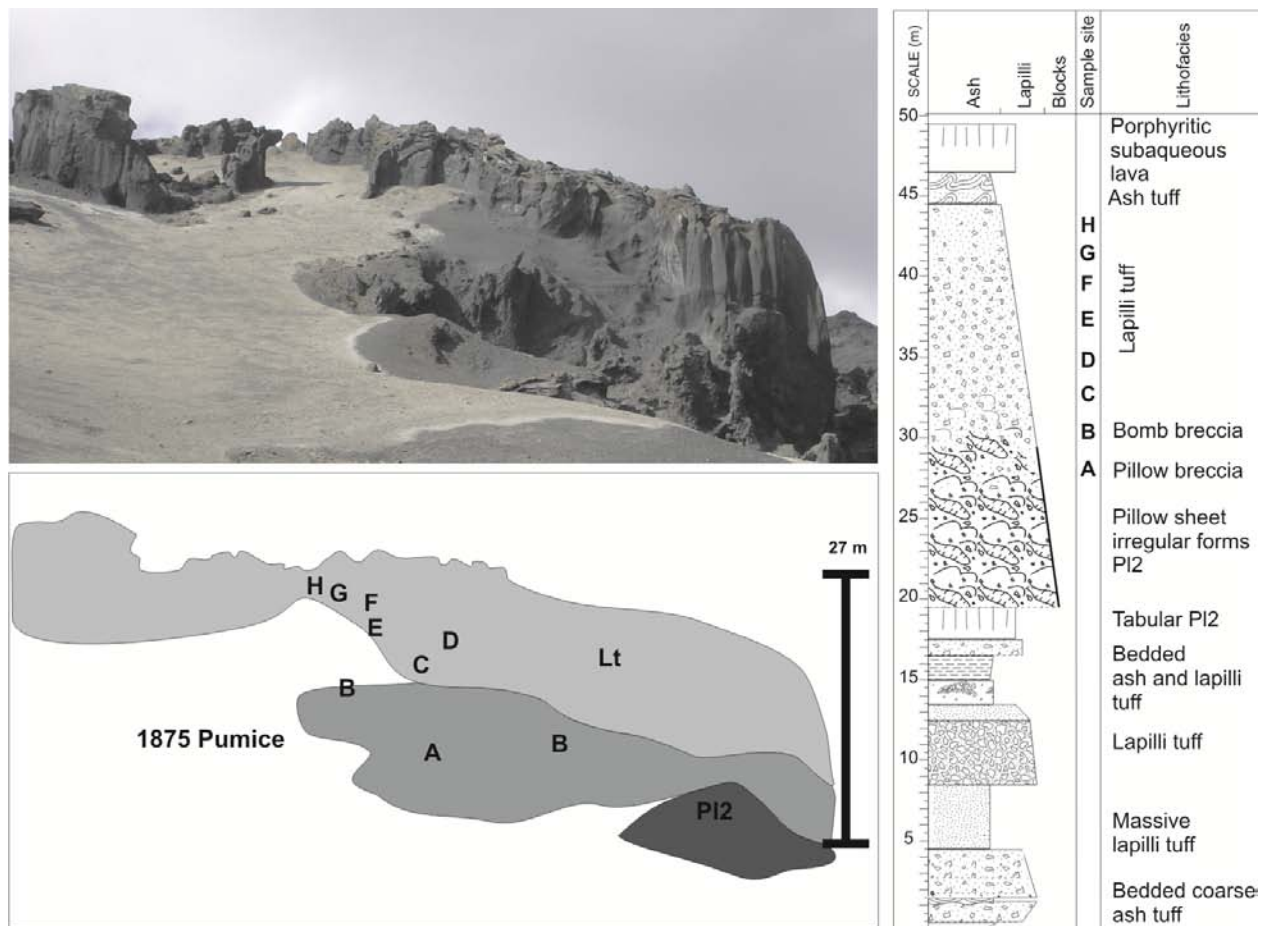


**Figure 6.2 Overview of Drekagil sequence including field image, annotated sketch of sampling sites and stratigraphic log.**

Nautagil (NG) contains the thickest of the transitional sequences (35 meters) where it forms the entire southern wall of the gully (Figure 6.3). The thickness of the basal pillow lava unit is unclear as the pillows are mostly covered by thick unconsolidated deposits of pumice from the 1875 eruption of Askja and local talus, but the pillow lavas are at least 2 m thick. The overlying breccia is 7 m thick with pillow forms and fragments dominating the lowest 2 m, and fluidal bombs dominating the upper 5 m. This breccia is then overlain by 24 meters of fluidal bomb-bearing vitric lapilli tuff. The lapilli tuff has a progressive upward fining that is due to a decrease in size and occurrence of fluidal bombs. The lapilli

tuff matrix is predominantly 1 cm sized throughout. An upwards increase in the presence of fine ash (1-10%) also contributes to the overall fining of the deposit. In the upper three meters of the lapilli tuff a weak parallel bedding at shallow angles (ca.  $10^0$ ) develops. Laterally, the deposit displays some obvious palagonitization, but typically appears fresh along the sampled southern wall of the valley. This sequence is cut by a younger basaltic dike that is one of the type examples of coherent margined volcanoclastic dikes (CMVDs) described from Askja (Graettinger et al., 2012).

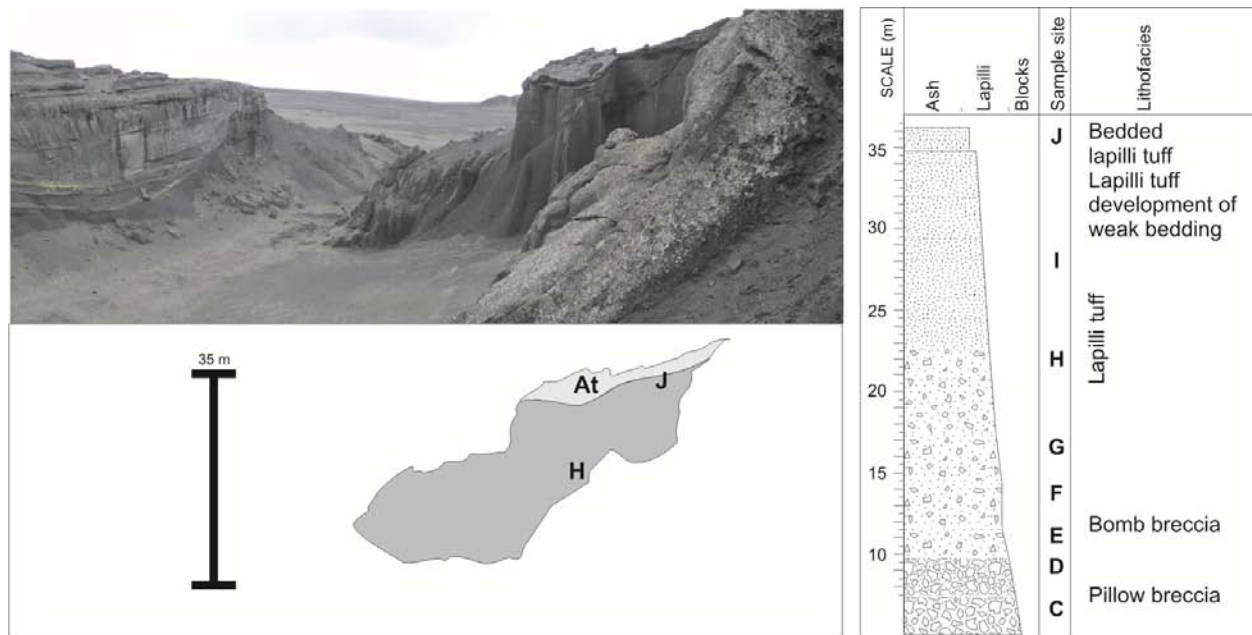


**Figure 6.3 Overview of the Nautagil sequence including field image, annotated sketch of sampling sites, and stratigraphic log.**

The exposure in Rosagil (RG) makes up a large portion of the southern wall of the gully, with a total thickness of 16 m. The basal pillow lava exposure is limited due to talus, but has a minimum thickness of 2 m (Figure 6.4). The breccia is 4 m thick with pillow fragments dominating the lower 1 m and fluidal bombs occurring in the upper 3 m. The breccia is overlain by ten meters of fluidal bomb-bearing vitric lapilli tuff. A weak parallel and shallow ( $10^0$ ) stratification develops in the upper meter of the tuff. The lapilli tuff fines upward expressed in the decrease in the size and abundance of fluidal bombs and an increase in the proportion of fine vitric ash. The lapilli display no systematic trend in particle size. The upper 1 m of the deposit is also locally more intensely palagonitized than the rest of the deposit. Laterally this sequence is intruded by pillowed intrusions with meter-wide peperitic margins.

### **6.3.2 Detailed description of lithofacies**

Measurement of 200 pillow forms within pillow lava sheets at the base of Austurfjöll massif yield an average cross-sectional diameter of 60 cm, and average core vesicularities of 65 vol. %. Due to poor preservation, rim vesicularities were measured less frequently, but averaged 60 vol. %. Pillow lava flows at Askja can be subdivided into two main lithofacies, named P11 and P12. The distinction between the two lithofacies is the variability in the dimensions of the pillow tubes and the frequency of transitions into non-pillowed lavas. P11 lavas are comprised of highly regular tubes, both in shape and cross-sectional dimension with average diameters of 50 cm, and a range of <20 cm in diameter per lava flow lobe. P12 lavas contain much greater diversity of pillow dimensions, with cross-sectional diameters ranging from 50–200 cm. They also commonly display transitions to columnar, curvi-columnar and blocky-jointed subaqueous lava flows without pillow forms. P12 lavas have more distended pillow shapes with less regular stacking (Figure 6.5). Pillows measured in the basal lava of the transitional sequences and apparently intact pillows in the lowermost pillow breccia, fall within the statistical norm of the massif, where cross-sectional diameters are typically 60 cm and core vesicularities around 65 vol. %. The basal lavas of all three sequences described here are P12 facies.

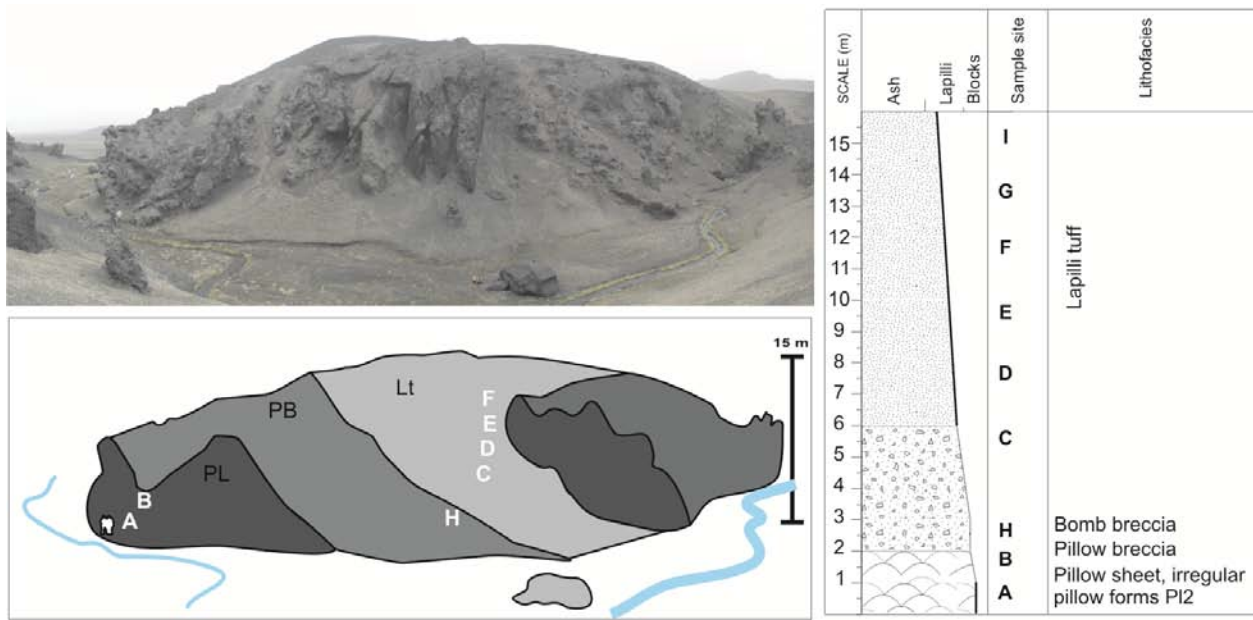
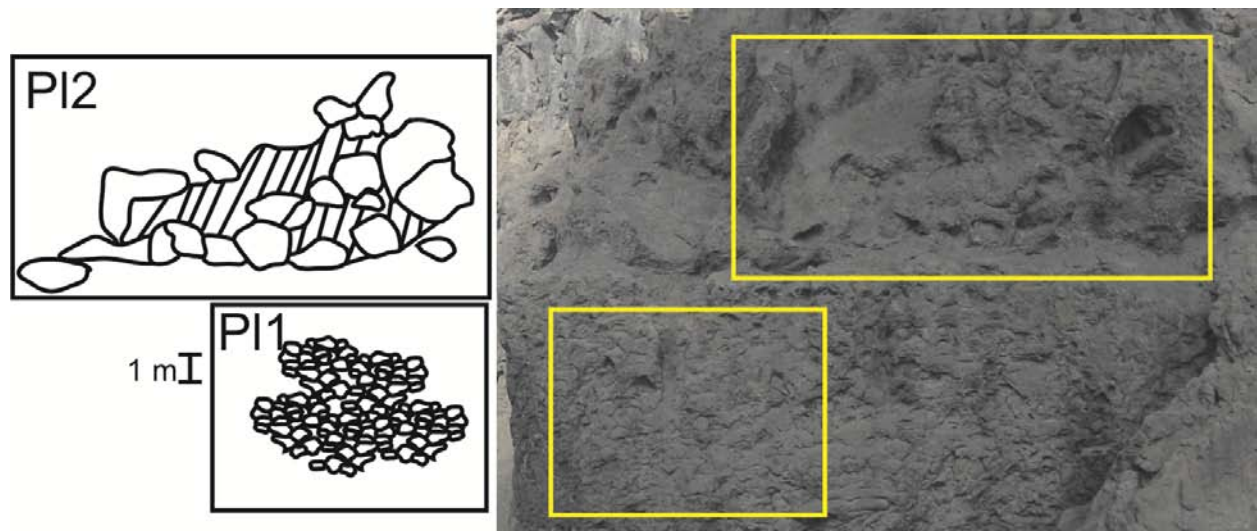


Figure 6.4 Overview of the Rosagil sequence including field image, annotated sketch of sampling sites, and stratigraphic log.



**Figure 6.5 Comparison of pillow lava facies from a field location that presents both facies. Schematics of the pillow form outlines highlight the regularity of PI1 and the irregularity of PI2 lavas.**

The breccia that immediately overlies the pillow lavas in all three sections is initially entirely clast-supported, composed of apparently intact pillows and pillow fragments, with decreasing occurrence of pillow forms within 1-2 meters of the contact. The fragments become progressively more isolated as the vitric lapilli matrix increases in proportion and fluidal bombs appear. Typically, pillow fragments are replaced by fluidal bombs within one meter of the pillow lava to breccia contact. The fluidal bombs are intact or display jig-saw fit fractures, and have preserved glassy rinds around most of their circumference. Fluidal bombs are distinguished from pillow forms based on morphology and vesicle distribution. Pillows are distinguished by their typically more regular, ellipsoidal shape in cross-section and occasional presence of keels. Typical pillows also exhibit vesicle bands and pipe vesicles (Figure 6.6). Pillows typically have regular glassy rinds centimeters thick with some example of millimeter thick rinds. Vesicles are typically round and undeformed in the pillow rinds with more convoluted vesicle morphologies in the pillow interior (Edwards et al., 2009; Fujibayashi and Sakai, 2003; Höskuldsson et

al., 2006). Fluidal bombs on the other hand display a wider range of cross-sectional morphologies, with convolute shapes particularly common and no regular distribution or pattern of vesicles. When not intact, bombs display a jig-saw fit fracture pattern. The average fluidal bomb vesicularity is on the order of 25% but can be as much as 60% vol. Fluidal bombs have glassy rinds that may reach two centimeters in diameter, but the thickness may vary around the margin of the bomb. Vesicles are also typically coalesced and polylobate, with an abundance of elongate vesicles near the rim. Glassy rinds are typically on the order of centimeters thick.

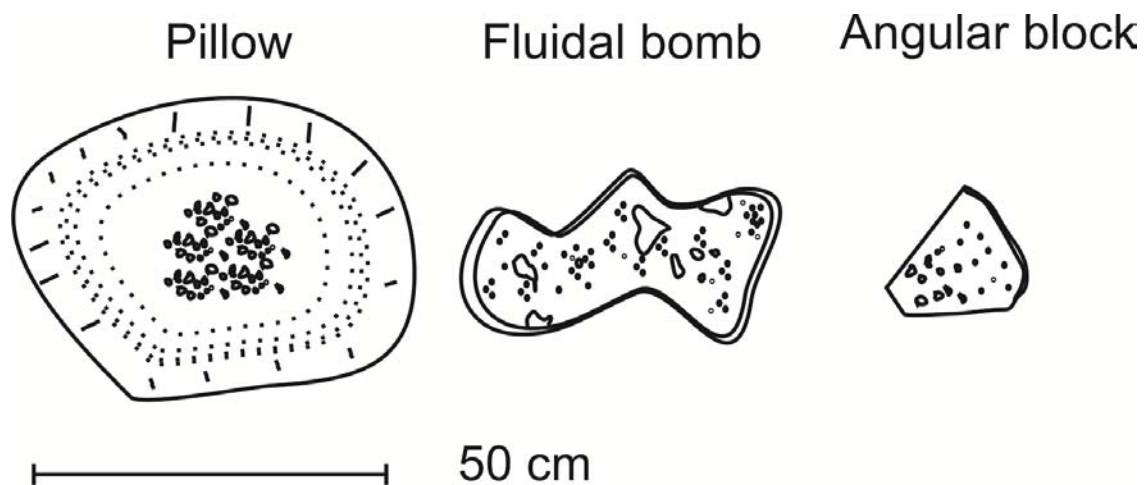


**Figure 6.6 Schematic characterizations of outsized clasts found within the three sequences described at Askja. Outsized clasts include a pillow in cross-section, a fluidal bomb in cross-section and an angular block.**

The vitric lapilli tuff makes up the bulk of the transitional sequence. The lithofacies change from breccia into overlying vitric lapilli tuff is characterized by a gradual decrease in the abundance of fluidal bombs with height in all three sequences, from 30% in the top of the breccia unit to 5% at the top of lapilli tuff (Table 6.1). Weak sub-parallel bedding develops only in the upper 3 m of the lapilli tuff in two of the sequences, NG and RG. The diameter of the bombs peaks in the lower portion of the lapilli tuff, frequently within 5-10 m of the facies transition (Figure 6.7), and then decreases rapidly up section. Vesicle morphology within the bombs displays an increase in coalescence up section (Figure 6.7). Vesicles in both the bombs and the vitric lapilli display a wide range of morphologies that include isolated vesicles, high degrees of interconnectedness, and tube pumice morphologies (Figure 6.8). Peak vesicularity values of all grain sizes in DK, NG, and RG occur higher in the sequence than the largest bomb dimension. The microlite content of bombs increases up-section from 2% up to nearly 10%. The microlite content of lapilli however, peaks in the breccia, and remains low in the lapilli tuff, less than half the peak value. Fluidal bombs and blocks greater than 2 cm have sideromelane rims up to 2 cm thick and microlite-bearing tachylite cores. Lapilli are ubiquitously glassy, and fragments below 2 cm in diameter are dominated by sideromelane. Ash and lapilli particles in the sequences are very angular, with delicate spine structures and cusped forms preserved (Figure 6.9). The vesicularity of the largest bombs is on average greater than that of the associated lapilli and ash within a given deposit at a stratigraphic level (Table 6.1).

Fourteen fine ash samples were selected for SEM microtextural analysis from the uppermost breccias and through the lapilli tuff unit of the DG and NG. Less than 25 vol. % of the fine ash particles had any detectable vesicle presence. Of the vesicles present, only about 3% had any clear influence on particle margin fracture formation. The bulk of vesicles observed were small and isolated within significantly larger grains and dissected by planar or obviously stepped conchoidal fracture surfaces. Vesicles sizes recorded in the fine ash were mostly between 5 and 100 microns in diameter (Figure 6.9). A significant portion of fine ash grain shapes (35-40%) were chips, blade, or needle-like. Approximately 45% of grains were blocky and roughly equant or prismatic in shape. The fine ash samples also include

minor occurrences of tube pumice (<10 %) and limu o Pele (<5 %). Limu o Pele are broken stretched bubble walls of a diameter greater than the typical vesicles observed (> 60  $\mu\text{m}$ ). There are no crystals in the fine ash component of any of the sequences. The peak limu o Pele abundance occurs stratigraphically above the maximum bomb size of both sequences.

**Table 6.1 Selection of quantified parameters of fluidal bombs from subaqueous effusive to explosive transitional deposits. Parameters were quantified using a combination of field, petrographic, and binocular microscope techniques.**

		Vesicularity (%)			Crystallinity (%)			Bomb diameter (cm)		
		DG	NG	RG	DG	NG	RG	DG	NG	RG
Lapilli tuff	I		45			2			15	5
	H	22	61	31	3	10	0	7	10	8
	G	24	61	25	5	10	3	9	50	13
	F	20	60	32		5	8	6	20	10
	E	20	60	40	4	6	15	20	23	10
	D	24	20	19	6	3	8	19	20	24
	C	21	55	40	8	1	20	8	10	32
Brecci	B	17	53	40	4	1	15	14	33	45
	A	30	40	37	2	4		9	55	63



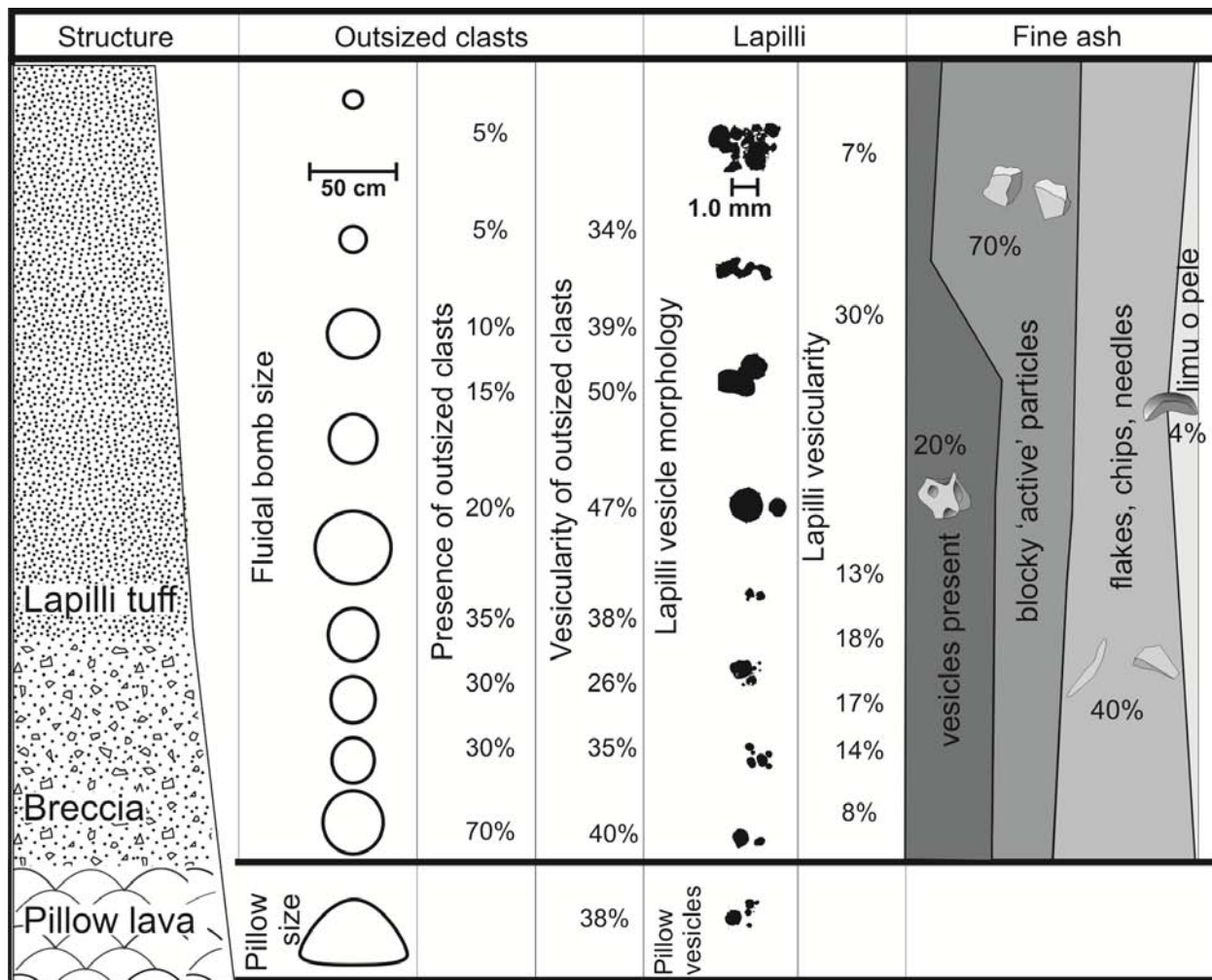
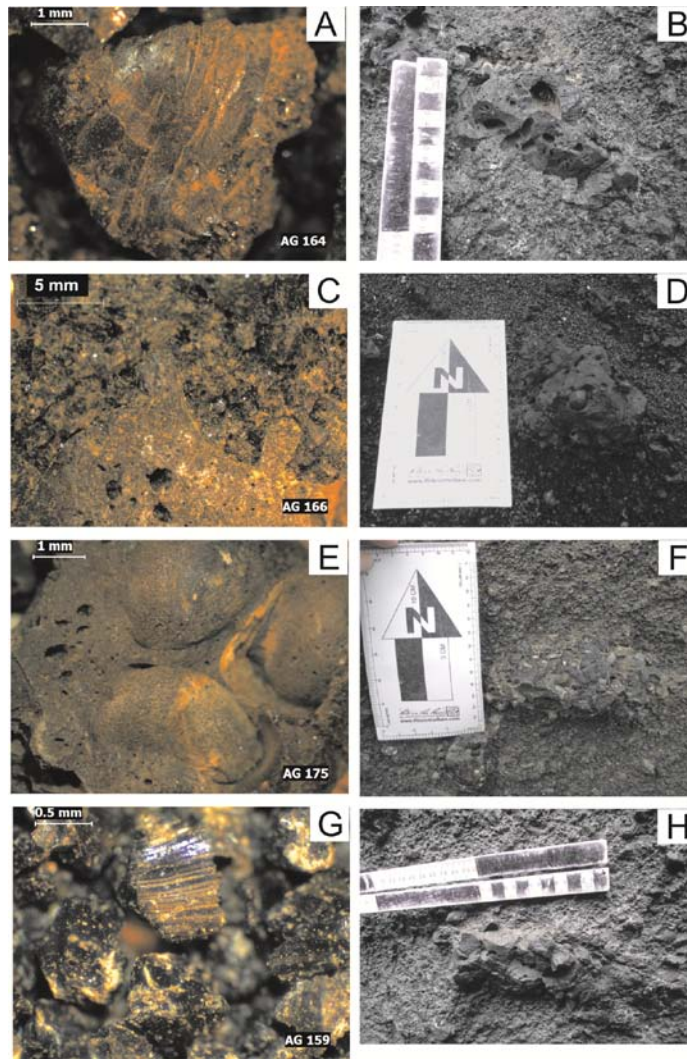


Figure 6.7 Stratigraphic overview of a typical effusive to explosive transitional deposit from Askja. Three grain sizes (blocks / bombs, lapilli, and fine ash) were analyzed for size, morphology, and vesicularity as they trend up section. Maximum values are presented for abundance of fluidal bombs and fine ash textures.

Average values for vesicularity are presented.



**Figure 6.8 Examples of clast morphologies and textures that reflect ductile fragmentation of the magma.**

Images on the right hand side are field images. Images on the left hand side are from a binocular microscope.

**A) Ductile structures in a lapillus quench crust. B) Large coalesced vesicles in a fluidal bomb. C) Fluidal crust structures preserved on a lapillus by surrounding matrix. D) Convoluted bomb shape and vesicles. E) Large coalesced bubbles interacting with the clast surface. F) Fluidal bomb with intact quench rind (broken for sampling). G) Lapilli with stretched vesicles along glassy surface. H) Fluidal bomb with large randomly distributed vesicles. A brittle overprinting is present in images A, E and G, where the particle has been fractured by impact / transport.**

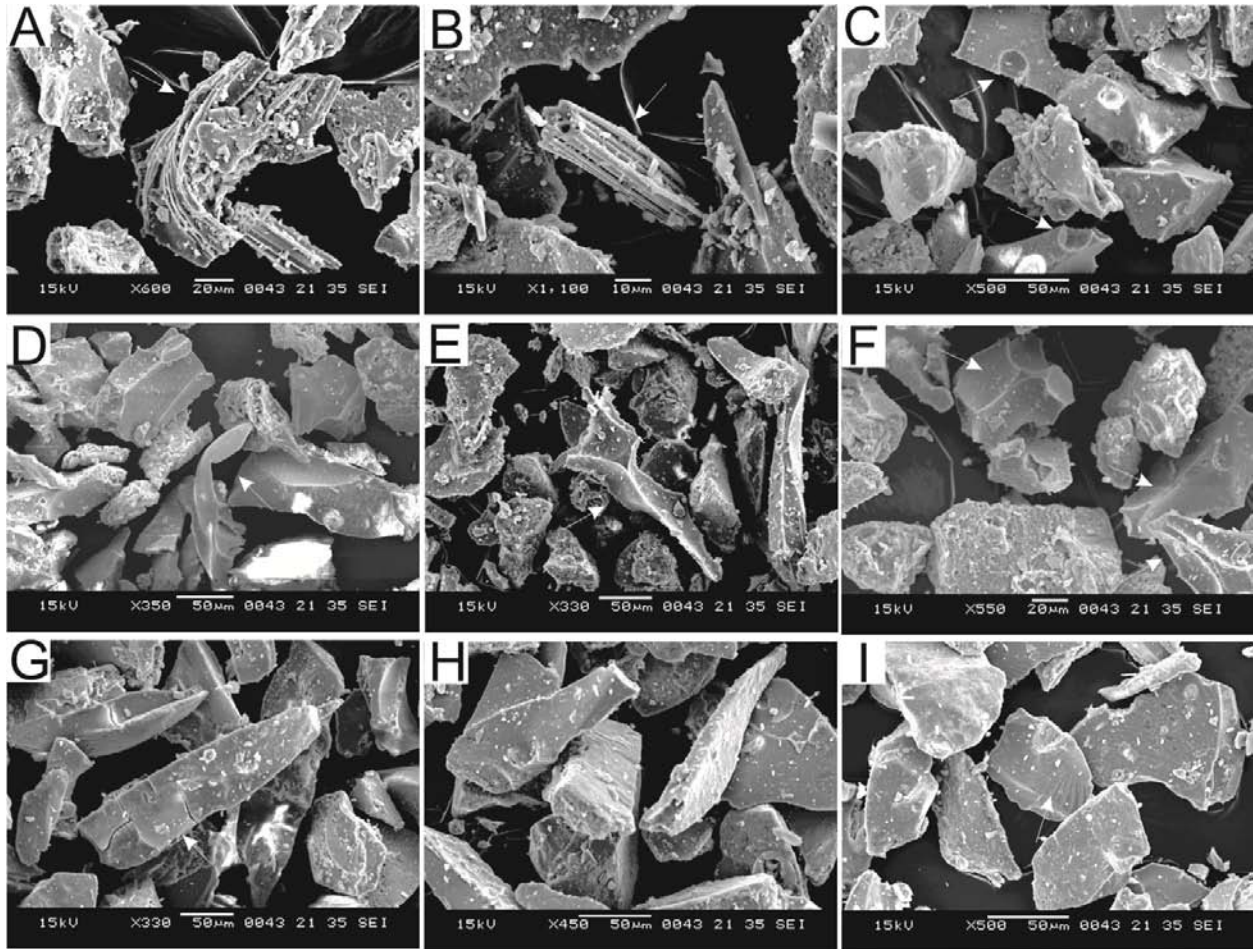


**Figure 6.9 SEM secondary electron images of example grain morphologies found in textural analysis of fine ash particles. Adhering particles and aggregate ash particles are common. Arrows are used to highlight features of interest. A) Fluidally deformed tube pumice. B) Tube pumice. C) Vesicles isolated within glassy ash particles. Vesicles may intersect fracture surfaces they do not control the fracture shape. D) Limu o Pele. E) A particle with vesicle-dominated fracture surfaces. F) Ash particles dominated by vesicles. G) Elongate needle-like dense particle shapes. Note the micron scale crust flaking off the particle. H) Needle and bladed shape particles. I) Flake and blocky shaped particles. Note the presence of conchoidal fracture.**

Fine ash particles with sharp edges showed evidence of minor abrasion, including rounding and scalloping, on less than 10% of all grains. Additionally, convolute and fragile shapes, including thin spines of glass, were present on an average 12% of the ash grains. The fine ash fraction of NG and DG displays some minor discoloration from a grey brown to yellow brown. Other evidence for chemical alteration of the fine ash fraction includes pitting of fracture surfaces, and flakey and irregular coatings. Adhering particles are common on 50% of the grains, but rarely obscure the complete grain. Some particles have thin (micron) skins or coatings that are cracked and flaking away from the grain.

### **6.3.3 Interpretation of lithofacies**

#### **6.3.3.1 Pillow lava**

Pillow lava sheets made up of both P11 and P12 lavas are the dominant morphology of subaqueous lavas at Askja. Subaqueous lava morphology has been used to infer the effusion rate of the flow (Gregg and Fink, 1995; Gregg and Smith, 2003; Griffiths and Fink, 1992). The relationship between subaqueous lava flow morphology and effusion rate is established based on three major groups: pillow lavas (lowest effusion rate), lobate (intermediate effusion rate), and sheet flows (highest effusion rate) (Gregg and Fink, 1995). Lava flow morphology can also be a factor of slope angle, however, as the large pillow sheet flows at Askja occur on shallow slopes, slope effects can be ignored here. P11 lavas, displaying regular pillow forms and stacking, represent the lowest effusion rate end-member of subaqueous lava flows. P12 lavas have a more complex internal structure and locally display textures of lobate subaqueous lava flows, including blocky and columnar jointing zones comingled with large irregular pillow lava tubes. These internal structures suggest that P12 lavas represent an intermediate step between slow pillow lavas, such as P11, and moderate effusion rate lobate flows (Bear and Cas, 2007; Dimroth et al., 1978; Griffiths and Fink, 1992; Walker, 1992). All three sequences described here have P12 lavas at their base.

### **6.3.3.2 Pillow fragments and fluidal bombs**

The breccias that immediately overlie the pillow lavas are dominated by three main types of block-sized components: isolated pillow forms, pillow fragments, and fluidal bombs. Pillows can become isolated in the breccia through an influx of fragmental material during effusion, intrusive eruption through the breccia matrix, or separation from the main flow and deposition (Bevins and Roach, 1979; Carlisle, 1963; Dimroth et al., 1978; Edwards et al., 2009; Gorny et al., 2012; Jones, 1970; Moore, 1975; Schipper et al., 2011a; Staudigel and Schmincke, 1984). It is important to note that where the pillows are fractured perpendicular to the pillow tube the fragments may appear as intact pillow forms in outcrop. Differentiation of these processes requires three dimensional exposures to determine if the pillows are truly isolated, or if they can be traced to an intrusion or pillow lava tube. In the Askja deposits, isolated pillows are the least common block-sized component, and while intrusions are present, sampling was preferentially collected away from exposed intrusions. The matrix of the breccia in the Austurfjöll sequence is consistently lacking any apparent bedding or foliation, which is observed in the more continuous pillow sheets at Askja and described by Carlisle (1963) in isolated pillow breccias formed by an increase in sedimentation during the advance of pillow tubes. Isolated pillows are interpreted as pillow fragments that are incompletely exposed in the outcrop, although occasional intrusive pillows are likely also present.

Pillow fragments are produced through the mechanical disruption of partially or fully cooled pillow lavas (Dimroth et al., 1978). Fragmented pillow breccias can form through gravitational collapse of flow margins during effusion (Dimroth et al., 1978; Jones, 1970; Moore, 1975), slumping of the deposit (Cas et al., 2003; Jones, 1970), or explosive disruption by a new or existing vent in the vicinity of the flow. The deposits described here have significant lateral continuity and do not display any slump structures. Flow-generated breccias are frequently observed within large pillow sheets at the Askja complex, these breccias, however, occur as lenses between multiple lava flows and have both lateral and vertical gradational contacts with coherent pillowed lavas. Pillow fragments and angular blocks can be incorporated in breccias as a result of collapse of nearby areas (including talus) or by lateral entrainment



within a debris flow, but the abundance of fragile glass features, including glassy rinds, complex fluidal shapes, spines on fine ash and the lack of sedimentary structures indicating lateral transport suggest that they deposits are not reworked. In the sequences described here pillow fragments are rapidly replaced by fluidal bombs. Significant collapse or transport of the deposit would result in a greater presence of purely angular blocks, i.e. those without recognizable features of pillows or fluidal bombs rather than the dominance of fluidal shapes that is observed within these three sequences. The structure-less upward fining of the transitional sequences of DG, NG, and RG from pillow lavas, through breccias, into lapilli tuffs is suggestive of an explosive origin for the breccia. Smellie and Hole (1997) have alluded to an explosive origin for pillow lava breccias associated with lapilli tuffs, but no detailed description of the textures resulting from this process have yet been described in the literature.

Fluidal bombs display convolute shapes reflecting ductile fragmentation of liquid magma (Houghton and Gonnermann, 2008; Houghton and Nairn, 1991; Houghton and Schmincke, 1989; Walker and Croasdale, 1971). Similar bombs have been described in submarine sequences and frequently have been misnamed pillows (Portner et al., 2010; Staudigel and Schmincke, 1984). Fluidal bombs have been identified as juvenile products in similar subaqueous environments (Simpson and McPhie, 2001; Sorrentino et al., 2011; Staudigel and Schmincke, 1984). The fluidal bombs from Austurfjöll share significant similarities in morphology, vesicularity, and coalescence of vesicles to the examples attributed to subaqueous fire fountaining (Cas et al., 2003; Simpson and McPhie, 2001; Staudigel and Schmincke, 1984). Bombs in subaerial Strombolian and Hawaiian and Surtseyan deposits can have fluidal shapes including fusiform, ribbon, or cowpie morphologies that also result from the ductile disruption of liquid magma (Houghton and Gonnermann, 2008; Houghton and Schmincke, 1989; Murtagh et al., 2011; Sorrentino et al., 2011; Walker and Croasdale, 1971). Fluidal shapes in subaerial environments are most commonly associated with Hawaiian style deposits (Cas et al., 2003; Houghton and Gonnermann, 2008; Houghton and Schmincke, 1989). Fluidal bombs are distinct from more common Surtseyan angular blocks, which are derived from solidified lava potentially derived from cooled lava flows, larger fragmented bombs, vent material, or dikes. Additionally, juvenile bombs are frequently subordinate in

abundance to accidental lithics in Surtseyan eruption deposits (Murtagh et al., 2011; Sohn, 1995; Walker and Croasdale, 1971). Descriptions of bombs are notably absent in numerous characterizations of deep submarine explosive eruptions and may be exacerbated in part due to sampling logistics (Clague et al., 2003; Clague and Davis, 2003). The fluidal bombs within the Austurfjöll sequences are interpreted as juvenile, being the product of subaqueous explosive magmatic fragmentation, based on their morphology, intact glass rinds, and poly-lobate vesicles.

Subaerial Strombolian and Hawaiian bombs typically display a range of vesicularity 30-60% and 60-90 % vol. respectively. These values are higher than what is observed at Askja (20-60% vol.) or Surtseyan typical eruptions (5-40% vol.) (Brown et al., 1994; Cas et al., 2003; Head and Wilson, 2003; Houghton and Schmincke, 1989; Murtagh et al., 2011; Sorrentino et al., 2011). Head and Wilson (2003) suggest that the vesicularity required for deep subaqueous explosive eruptions is 75%, but values are commonly reported significantly lower at mid-ocean ridges (Clague and Davis, 2003). The boundaries between Surtseyan eruptions and Strombolian eruptions are frequently crossed and can be difficult to distinguish without textures revealing interaction with air (oxidization) vs. water (thick glassy rinds) (Brown et al., 1994; Sorrentino et al., 2011). Consequently, bomb vesicularity is currently one of the few characteristics used to differentiate between Strombolian and Surtseyan eruptions, where Surtseyan bombs have lower average vesicularities than Strombolian bombs (Houghton and Gonnermann, 2008). Fluidal bombs from Askja have low vesicularities, thick glassy rinds, and no apparent oxidization showing the greatest similarity to Surtseyan bombs. The size of basaltic bombs indicates the relative driving energy of the magmatic gas expansion within the eruption, but represents a low efficiency of fragmentation of the magma. The deposits indicate the greatest magmatic volatile expansion occurs low in the lapilli tuff, coincident with maximum bomb diameter and vesicle coalescence (Figure 6.7).

#### **6.3.3.3 Lapilli and coarse ash**

Lapilli dominate the bulk of the deposit from the matrix of the breccia to the top of the lapilli tuff. The dominant lapilli size range is from 1 to 3 cm with vesicle morphologies and shapes similar to vesicles found in the fluidal bombs. The lapilli may display partial quench rims or be entirely glassy. The bulk of lapilli are equant in size and serve as matrix for the larger blocks and bombs in the upper breccia and lapilli tuff. The lapilli are interpreted as the products of magmatic fragmentation and mechanical breakage of larger particles. Fragmentation of the lapilli reflects a combination of magmatic degassing, quench granulation, and interaction with other particles and deposition.

#### **6.3.3.4 Fine Ash**

Fine ash first occurs within the lapilli tuff and progressively increases in abundance up section. In order to use fine ash textures to infer primary fragmentation mechanisms, it must be assumed that they are primary, the result of molten magma break up, not post-explosive mechanical fragmentation (Mattox and Mangan, 1997). The fine ash component of the DG and NG tuffs are dominated by chips, blades and needle shapes that are associated with quench granulation, from mechanical stress and spalling in experimental magma-water interactions (Büttner et al., 1999) (Table 6.2). Particles produced through quench fragmentation are abundant (up to 40%) in the fine ash fraction of the breccia and lapilli sequence. Evidence of bulk water interaction is preserved in the presence of a small percentage (5%) of limu o Pele, where external water becomes trapped within the melt and results in local ductile deformation in the formation of a large bubble wall fragment (Maicher et al., 2000; Schipper and White, 2010; Schipper et al., 2011b).



**Table 6.2 Occurrence of distinctive fine ash particle morphologies in DK and NG deposits.**

		Quench granulation Blades, needles, chips  %		SMWI  Equant blocky  %		Magmatic  Frothy (including tube pumice) %		BMW  Limbo Pele  %	
		DG	NG	DG	NG	DG	NG	DG	NG
Lapilli tuff	H	30	43	21	38	5	4		
	G	22		57		1			
	F	9	48	70	36	20	2		
	E	30		55		9		4	
	D	36	60	60	37	3	0		2
	C	25	41	73	32	4	2		
Breccia	B	45	46	55	23	5	1		1
	A	30		51		0			
SMWI= surface magma water interaction (FCI)  BMW = bulk magma-water interaction(Wohletz, 2003; Zimanowski and Büttner, 2003; Zimanowski and Wohletz, 2000)									

Blocky, equant grains are frequently called ‘active particles’ (<130 microns) of FCI surface magma / water explosions (Büttner et al., 2002). Also known as molten fuel coolant interactions (MFCI), these are the explosive interaction of mingled magma and a coolant (water, wet sediment etc.) (Büttner et al., 2002; Wohletz, 2003; Zimanowski and Wohletz, 2000). Blocky grains have also been produced in non-explosive interactions of magma water or sediment-rich water (Mastin et al., 2009; Schipper et al., 2011b). These particles are all the product of the thermal transfer from the particles to a coolant, resulting in the brittle fragmentation of the magma. However, in the non-explosive cases the particle sizes

produced were on the order of several millimeters in diameter representing the fine lapilli grain size, rather than the fine ash of the explosive FCI of Büttner et al. (1999) and Kokelaar (1986). Blocky / equant particles make up on average 45% of the fine ash fraction of the Austurfjöll sequences. Lapilli within the breccias and tuffs of the sequence between 2 -20 mm can also have blocky equant shapes, but have vesicularities up to 25% vol. and crystal contents up to 10% vol. The blocky particles of the fine ash fraction are both vesicle and crystal free and less than 50  $\mu\text{m}$  in diameter. FCI explosions represent the most effective fragmentation of a melt through interaction with an external coolant, and the blocky ‘active’ particles are constrained to those particles below 130  $\mu\text{m}$  (Büttner et al., 1999). It is nevertheless important to acknowledge the similarity in morphology of the fine ash particles with coarser grain fractions at Askja as well as in non-explosive thermal granulation experiments. This similarity highlights the importance of investigating multiple grain size fractions to reconstruct the mechanisms of fragmentation.

Scalloped edges and rounding of fine ash particles are indicative of physical alteration of fine ash particles (Solgevik et al., 2007), but were only found on 10% of all grains studied at Austurfjöll. Fragile shapes, including thin spines of glass, were present on an average 12% of the grains, such delicate features would be difficult to preserve in the event of any remobilization of the deposit. Flakey coatings probably indicate minor alteration post-fragmentation (Büttner et al., 2002; Büttner et al., 1999; Harpel et al., 2008; Nemeth and Cronin, 2011), rather than a coating of secondary minerals (Figure 6.9). Fine ash particles remain a critical grain size for unraveling the fragmentation mechanisms of an eruption, but this grain size only records the most effective and last stage fragmentation mechanisms and must be used in context of a complete deposit.

#### **6.3.3.5 Deposit structure**

The dominant feature of the three sequences is the massive nature of the lithofacies with a progressive upward fining from pillow breccia, through fluidal bomb breccia, to lapilli tuff. This gradational upward fining, associated poor sorting, and random clast orientations is likely the result of high sediment fallout

rates possibly from direct deposition from subaqueous convective plumes (Maicher et al., 2000). Grading of outsized clasts may result from Stokes settling of larger particles before smaller particles; however, the lack of sorting present in the lapilli and ash sized particles, and initial increase in bomb size, does not support this as the mechanism for bomb distribution in these deposits. There are no bomb sags, channel forms, loading structures, or other typical structures of a tuff cone, which is dominated by lateral transport of deposits in density current (Maicher et al., 2000; White, 2000). The lack of remobilization is confirmed by the presence of jig-saw fit bombs, a lack of alteration of sharp grain edges (Solgevik et al., 2007) and the preservation of fragile glassy spines and limu o Pele (Figure 6.9) that would be easily damaged if mobilized (Sohn, 1995). The consistency of the deposit supports fairly continuous deposition of pyroclasts, indicating that the eruption itself was reasonably constant and the deposits are vent proximal. A weak parallel bedding is present in the upper few meters of two of the three deposits. This bedding implies some degree of sorting develops in the later stage of the eruption, and may be a result of a decrease in flux rate, or delayed gravitational sorting of the finer deposits. If the deposits are primary and vent proximal, as is suggested by the lack of transportation and limited distribution of deposits, it would imply that the deposits approximately represent the inverse of what was expelled from the vent. This then suggests that the eruption initially produced large and abundant blocks and bombs, and pyroclasts progressively decreased in size through the eruption, until a fairly consistent lapilli dominated deposit was formed. The lack of associated feeder dikes for these vent proximal deposits is likely due to lack of exposure.

#### **6.3.3.6 Genetic relationship between the facies**

The pillow lavas, pillow breccia, fluidal bombs, lapilli and fine ash of these deposits can be texturally, chemically, and stratigraphically linked. The absence of dominant pillowed intrusions and the gradational transition (no obvious contacts) of the pillow into pillow breccia, into fluidal bomb-bearing breccia into fluidal bomb-bearing lapilli tuff support the genetic relationship between the pillows and fragmental units. The cogenetic relationship between the fluidal bomb and lapilli components of the breccia and lapilli tuff

can be traced through vesicle morphology. Vesicles textures are the product of a combination of up to six processes: nucleation, diffusive growth, decompressive expansion, coalescence, collapse and escape (Schipper et al., 2010a). Larger vesicles rise faster, but have greater drag, and thus greater deformation (Parfitt and Wilson, 2009). The overall vesicularity of the deposits described here (25-60% vol.) is comparable to subaqueous and emergent basaltic deposits (10-60% vol.) (Houghton and Gonnermann, 2008; Houghton and Schmincke, 1989; Murtagh et al., 2011; Schipper et al., 2011a; Simpson and McPhie, 2001). The dominance of coalescence and vesicle growth in the lapilli and fluidal bombs is suggestive of decoupled gas within the magma (Schipper et al., 2011a), rather than continuous nucleation and exsolution.

The differences observed in vesicularity between the three grain size groups (ash, lapilli and blocks / bombs) are clearly influenced by the size of vesicles that can be observed, and the method of calculating vesicularity. The vesicularity of bombs and lapilli were calculated both in the field and with image analysis using ImageJ, both methods are two dimensional, and converted to three dimensions based on the assumption of representative distribution. The vesicularity of fine ash was not calculated as a vesicle percent, but rather a binary value of presence of vesicles. Vesicles present in bombs can be the result of post-fragmentation growth, or pre-fragmentation growth. The deformed vesicles along fluidal bomb margins indicate that ductile deformation of the bomb occurred after vesiculation. Large irregular vesicles may indicate that vesicle growth and coalescence may have continued after fragmentation of large fluidal bombs, but there is no evidence of continued nucleation of vesicles. Due to the size and partial glassy rinds of lapilli, the vesicles present in these particles likely formed in a bomb, or were in existence in the conduit, and thus present before fragmentation. Lapilli vesicle morphology and distribution is nearly identical to that of the fluidal bombs suggesting the vesicles of both grain sizes have the same pre-fragmentation origin. In very fine ash, those vesicles observed isolated within a particle and smaller than the fracture planes formed prior to fragmentation. The <50  $\mu\text{m}$  size of fine ash particles measured precludes the preservation of vesicles larger than 100  $\mu\text{m}$ . Those vesicles present, however, are indicative of pre-fragmentation vesiculation.

The similarity of vesicle coalescence and other textures between bomb and lapilli clasts suggests that similar processes were controlling vesicle formation in all grain sizes and likely that the smaller particles were derived from the larger clasts and the partially degassed melt. This supports the uniform origin of vesicles across the grain sizes. The presence of a significant number of coalesced vesicles in the magma prior to fragmentation, reveal the magmatic degassing prior to eruption. The vesicles in fluidal bombs display increased coalescence relative to the basal pillow lava flows indicating an increase in gas exsolution within the melt, and point to a magmatic gas driver for the onset of explosive activity. The fluidal morphology of the bombs indicates ductile deformation during transport through the vent and the water column, in agreement with a magmatic, rather than phreatomagmatic origin for the bombs. The textures of the lapilli and ash indicate multiple fragmentation mechanisms were contributing to the formation of finer particles.

#### **6.4 A MODEL OF TRANSITION FROM EXPLOSION TO EFFUSION**

Mechanisms of magma fragmentation clearly impart textural characteristics to glass particles at all scales. Vesicle size, shape, and interconnectedness reflect magmatic volatile exsolution, fragmentation, and quenching with implications for the relative timing of all of these processes (Murtagh et al., 2011; Stovall et al., 2011). Quench rinds, sideromelane vs. tachylite glass, and crystal presence indicate the relative rate of cooling and the effectiveness of fragmentation (Schipper et al., 2011a). However, the signatures of initial fragmentation can be easily altered during transport, deposition, and chemical alteration. The final deposition of subaqueous volcanoclastic material is commonly the result of lateral transport mechanisms such as density currents (Maicher et al., 2000; Smellie and Hole, 1997; White, 2000), the collapse of over-steepened deposits (Jones, 1970; Sohn, 1995), or suspension settling (Eissen et al., 2003; Maicher et al., 2000). Remobilization can cause additional fragmentation and / or impart textures such as the chipping of edges or rounding through abrasion (Solgevik et al., 2007), muting or destroying textural

signatures of initial fragmentation. The introduction of accidental clasts during transport also complicates interpretations. A full interpretation should include fragmentation, eruption mechanism, transport, deposition and environment (Harpel et al., 2008).

A comprehensive model of the transition from effusion to explosion at Austurfjöll is based on the interpretation of the structure of the three deposits and four major components (pillows, bombs, lapilli to coarse ash, and fine ash) of the fragmental deposits of these sequences. The deposits of DK, NG, and RG are interpreted as the result of explosive disruption of an active pillow lava flow involving magmatic expulsion of fluidal bombs that enabled the surface magma FCI, increasing the effective fragmentation and dominating behavior in the later part of the eruption. The breccia represents the deposits of initial subaqueous fragmentation, the pillow fragments disrupted by the onset of subaqueous explosive activity, followed shortly thereafter by juvenile fluidal bombs and secondary lapilli fragments. The deposits are of primary explosive origin without any transport after initial deposition or textural modification during such transport. The sequences are interpreted as the products of continuous transitions from effusion to explosion during a single eruption from a single vent. This origin was determined from their gradational transition, consistency of vesicularity, bomb and lapilli morphology, the lack of sedimentary structures, and the lack of evidence of any mobilization of the deposit. The sequences described here would be insufficiently characterized by only one grain size fraction due to the limitations of each particle type to record the interplay of fragmentation mechanisms observed through this more comprehensive textural study.

#### **6.4.1 Magma fragmentation at the onset of basaltic phreatomagmatic explosions**

The kinetic disruption of a magma is accomplished in two main ways: ductile deformation of the melt, and brittle deformation of the cooling glass / lava. Ductile, or inertial fragmentation, is the breakup of magma during decompression in the form of inertial stretching and breakup of the liquid magma (Houghton and Gonnermann, 2008; and references within). Magmatic explosions involve the ductile

disruption of the melt through the nucleation and growth of vesicles (Parfitt and Wilson, 2009; Zimanowski et al., 2003). The fluidal texture of bombs, with elongate vesicles in the glassy rim, and convolute vesicle morphologies is a result of the ductile deformation of magma driven by the expansion and coalescence of juvenile water in magma (Büttner et al., 1999; Eissen et al., 2003; Kokelaar, 1986; Mastin et al., 2009; Zimanowski and Büttner, 2003; Zimanowski and Wohletz, 2000). Vesicle morphologies and distributions are distinct in the fragmental deposits relative to pillow lavas and pillow lava fragments, suggesting a buildup of magmatic gas that could lead to the formation of fluidal bombs. This ductile disruption is also mirrored in the lapilli, where complicated vesicle morphologies including polylobate bubbles occur throughout the deposit (Figures 6.7 & 6.8). Within the deposits of DG, NG, and RG there is deformation of juvenile particles during vesiculation and contemporaneously with quenching (tube vesicles and deformed vesicles on clast margins).

Brittle fragmentation is typically the disruption of cooled magma or glass. In order for liquid magma to deform in a brittle fashion the strain rate must be high enough to prevent liquid relaxation of the melt (Büttner et al., 2002; Büttner et al., 1999). Fragmentation of the magma by brittle processes include: FCI, quench granulation, and mechanical fracture through impact upon landing or transportation (Maicher et al., 2000). Most studies of subaqueous fragmentation focus on the fine ash grain size fraction ( $<64\ \mu\text{m}$ ) as it records the most efficient fragmentation mechanism involved in the creation of the deposit, i.e. the mechanism that requires the greatest energy to produce (Büttner et al., 1999; Zimanowski et al., 2003). Surface water interactions, frequently referred to as FCI, occur where vapor is produced through the rapid heating of the water interacting with melt. This vapor film must be disrupted to bring the melt in direct contact with the water. This disruption of the vapor film can be an internal or external process, where changes in the system, including other mechanisms of fragmentation, can initiate FCI explosions (Kokelaar, 1986; Wohletz, 1986, 2003; Zimanowski and Büttner, 2003; Zimanowski and Wohletz, 2000). The resulting explosion can then create pressure variations and fragment country rock or cooling crusts and result in the exposure of fresh magma to the system. This consequently can produce a feedback loop where any one of the three major fragmentation mechanisms can enable fragmentation by the other

processes (Kokelaar, 1986). The influence of surface water interactions on Austurfjöll deposits is recorded in the presence of blocky fine ash particles that increase in abundance up section.

Quench granulation accompanies any interaction of magma and water due to contraction during cooling and the brittle failure of the outer contracted layers (Cas et al., 2003; Schipper et al., 2010a; Wohletz, 1986, 2003). Textural indications of this secondary fragmentation include jig-saw fit bombs, angular blocks, and some flakey and needle-shaped fine ash particles. Lapilli that have partial sideromelane or tachylite rims reflect the mechanical fragmentation of cooled magma, but the dominance of sideromelane only clasts suggests that there was quench fragmentation of liquid magma in contact with water, in addition to the production of lapilli through the fragmentation of larger cooled particles. Quench granulation only releases 10% of the thermal energy available (Schmid et al., 2010) and creates larger particles than FCI.

A subordinate process in the Austurfjöll deposits is the ductile deformation of melt as a result of trapping external volatiles within the melt. The texture that is most commonly associated with this process is *limu o Pele*. These structures are fluidal in origin, but are the result of the entrapment of external water by magma. The trapped water rapidly expands as vapor creating a thin film of melt, in a processes documented in littoral, submarine, and subglacial environments (Clague et al., 2009; Maicher et al., 2000; Schipper and White, 2010). *Limu o Pele* are not a dominant feature within the Askja deposits, but are frequent enough (Figure 6.9) to indicate that trapping of external volatiles by molten magma did occur in this fully subaqueous environment.

These fragmentation processes are not isolated, as each individual mechanism disrupts the magma and may enable the decompression of internal volatiles, increase the surface area for interaction with external volatiles, and disrupt insulating vapor films (Maicher et al., 2000) triggering other mechanisms of fragmentation. Quench granulation, in particular, can occur in any wet eruptive environment and contributes to all subaqueous eruptions (Cas et al., 2003; Mastin et al., 2009; Schipper et al., 2010c; Wohletz, 1986, 2003) (Figure 6.10).



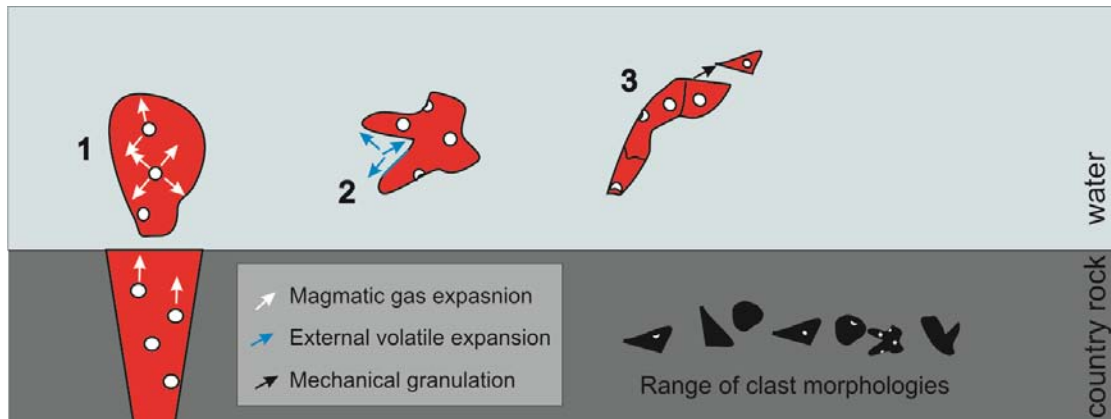


**Figure 6.10 Schematic diagram of subaqueous fragmentation mechanisms. 1) Explosive magmatic gas expansion, resulting in ductile deformation of magma. 2) Explosive interaction with external water including disruption of the magma from the surface, and bulk interactions where water becomes trapped in the magma. This results in the brittle deformation of the quenching magma. 3) Non-explosive quench granulation. This results in the brittle deformation of cooled magma and can occur wherever magma is cooled rapidly, especially in conditions involving water.**

The interpretation of pillow, fluidal bomb, lapilli and fine ash particle textures from the three transitional sequences at Askja reflect a complex interplay of fragmentation mechanisms that evolve throughout the eruption sequence. The shape of clasts and fine particles reflect the ductile or brittle nature of the fragmentation. The interrelated nature of the mechanisms of fragmentation, and therefore, their textural signatures results in the overprinting, alteration and even destruction of textural signatures of the fragmentation mechanisms that may be occurring simultaneously or progressively. It is therefore, critical to use multiple parameters, such as vesicularity, grain size, grain shape at multiple scales to reconstruct the mechanisms of fragmentation of a pyroclastic subaqueous deposit. In this example magmatic fragmentation likely initiated explosive activity enabling the more efficient FCI explosion with accompanying minor entrapment of external water by ductile melt (bulk magma water interaction) and persistent, but inconsistent quench granulation (Figure 6.11).

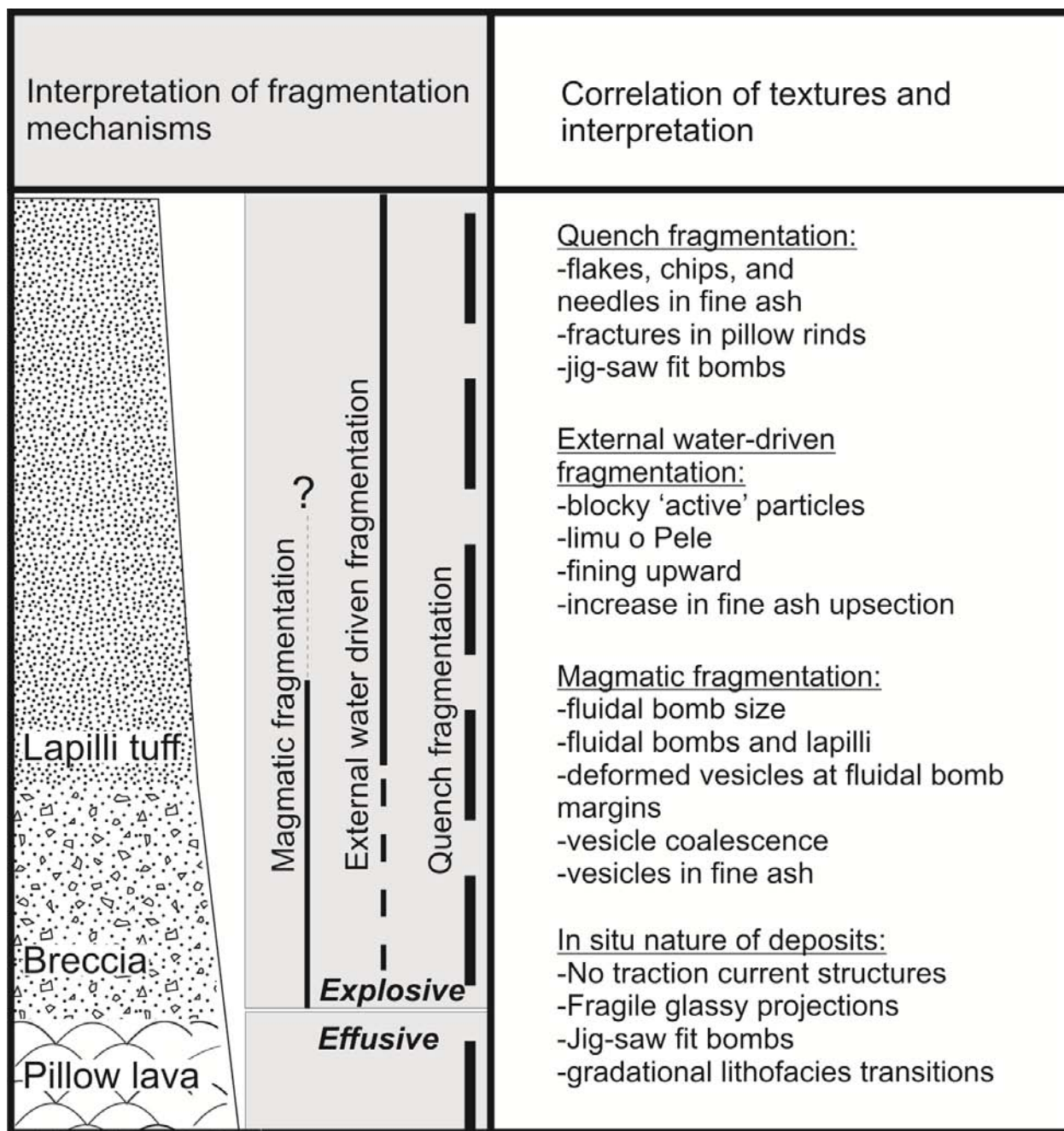


**Figure 6.11** Model of fragmentation mechanisms as they occur during the formation of the transitional sequences at Askja. Solid lines represent relative dominance of a fragmentation style. Dotted lines indicate continued, but diminished fragmentation. The textures used to construct the model are described.

#### **6.4.2 What triggers the transition from effusive eruptions to explosive activity in subaqueous eruptions?**

Potential triggers for a transition from effusive to explosive activity in a subaqueous environment include: depressurization by a decrease in confining pressure, access / infiltration of water to the rising magma, and internal dynamics of the magma due to changes in the magma flux or composition. In a glaciovolcanic setting a reduction of confining pressure can result from a decrease in the overburden, such as water or ice, due to the temporally dynamic nature of the environment. Englacial lake water levels are highly dynamic and can drain slowly or rapidly during and after an eruption (Bjornsson, 1985; Höskuldsson et al., 2006; Skilling et al., 2009; Smellie, 2001; Smellie and Hole, 1997). Decompression would also occur as a result of increasing the elevation of a vent relative to the water level through the construction of a massif (Edwards et al., 2009; Moore and Calk, 1991; Zimanowski and Büttner, 2003). A sudden collapse of the growing massif, or collapse of the vent itself would also result in rapid decompression over the vent area (Fujibayashi and Sakai, 2003; Scott et al., 2003; Wohletz, 2003).

The initiation of external water-magma interaction may further instigate decompression, or destabilization of the eruption and initiate explosive activity (White, 1996b; Wohletz, 1986, 2002). This may be accomplished through the trapping of external water under an advancing flow over wet sediments, or between pillows, or the infiltration of water into the vent, or fractured lava flow crusts (Brown et al., 1994; Clague et al., 2009; Eissen et al., 2003; Maicher et al., 2000; Schipper and White, 2010; White, 1996a; Zimanowski and Büttner, 2002). In the case of the completely subaqueous sequence at Askja, ample volumes of water are available for interaction with erupting magma. The presence of effusive pillow lavas during the early phase of the eruption indicates that water was available for magma water interaction, but conditions were not conducive for the sufficient mixing of the fluids to initiate explosivity during pillow formation. The pillow fragment breccia indicates that the pillow lava was mechanically disrupted, likely through the onset of explosive magmatic activity which formed juvenile fluidal bombs that progressively dominate the breccia. Vesicle morphologies and distribution in fluidal bombs points to

an increase in magmatic volatile expansion and accumulation of vesicles through coalescence between pillow formation and bomb formation. During the initial explosive phase lapilli were also produced in small quantities to form the matrix of the breccia. As the eruption continued lapilli became the dominant pyroclast size, producing a massive lapilli tuff. This upward fining of the deposit and increasing abundance of very fine blocky ash particles indicates that eruption conditions became favorable for surface / FCI magma-water interaction. The initial shift to explosive magmatic behavior (the production of fluidal bombs and brecciation of existing pillow lavas) enabled the dynamic mingling of magma and water to enable FCI and increased quench granulation. The identification of triggering mechanisms of natural subaqueous phreatomagmatic eruptions remains a challenge. The deposits described here suggest that magmatic fragmentation enable surface magma / water interaction and water infiltration to facilitate phreatomagmatic explosions that subsequently drive themselves, and dominate the remainder of the eruption. If this model is valid, one question still remains, what then initiated the increase in magmatic gas expansion required to drive the explosive chain of events?

Variations of internal eruption dynamics could initiate explosive activity through an increase in eruption rate (Clague et al., 2009; Fujibayashi and Sakai, 2003), changes in volatile content, or viscosity (composition or crystallization) (Fowler et al., 2002; Wohletz, 2003). The presence of textures reflecting magmatic gas expansion and coalescence in the DK, NG, and RG deposits indicates that internal volatiles play a critical role in the first stages of fragmentation, and thus it is reasonable to consider internal drivers for the initiation of explosivity, such as eruption rate. The presence of Pl2 morphology lavas at the base of the Austurfjöll sequences indicates that the effusion of pillow lavas occurred at a higher eruption rate than would form typical pillow lava forms. Deformed sideromelane glass quenched particles, and elongated vesicles on clast rims suggest a high strain rate that is also associated with a high eruption rate.

However, the increase in internal volatile expansion and coalescence recorded in the fluidal bombs can also be the result of decompression from a reduction of confining pressure over the vent. Investigations of glaciovolcanic deposits have sought geologic textures that preserve the evidence of syn-eruptive decompression through environmental changes, and suggest that bulk vesicularity may be a key

to identifying this process (Höskuldsson et al., 2006). The vesicularity of the pillows and the fluidal bombs differs in the morphology of the vesicles, reflecting coalescence, which does not reflect an increase in nucleation as was suggested in the study of Kverkfjöll. However, there is geologic evidence within the Austurfjöll massif of drainage of the ice-confined lake, reducing the water level. The timing and duration of such an event is not well constrained, however, at least one drainage event can be stratigraphically associated within the same eruptive unit as the NG transitional sequence. Evidence for this drainage is preserved in large channels that have been eroded into lapilli tuff deposits stratigraphically equivalent to the transitional sequence. Large ice sheets are less susceptible to rapid drainage events than thinner, more localized ice bodies; however, the volume of water drained may not need to be significant to influence eruptive conditions of a vesiculating magma. There is no evidence that the transitional sequences at Austurfjöll became emergent. Nevertheless drainage events are frequent at glaciovolcanic centers (Bennett et al., 2006; Carrivick et al., 2004; Gudmundsson et al., 1997; Höskuldsson et al., 2006), and are strong candidate for decompression events that would enable the transition to explosive activity during an ongoing effusive eruption.

### **6.4.3 Eruption Style**

The discussion of basaltic magma fragmentation in subaqueous environments is complicated by the comparisons made with named subaerial explosive eruption styles of basaltic magma. Comparisons have included Strombolian, Hawaiian, phreatic, and phreatomagmatic eruptions (Cas et al., 2003; Clague et al., 2003; Clague et al., 2009; Head and Wilson, 2003; Schipper et al., 2011a). Deep (ca. 1 km), gas-coupled submarine eruptions have been given the term Poseidic (Schipper et al., 2010c).

Fluidal bombs have been used to suggest the occurrence of submarine fire fountaining (Simpson and McPhie, 2001), but the nature of vesicles in the Austurfjöll deposits is more suggestive of decoupled gas as is characteristic of Strombolian eruptions (Clague and Davis, 2003; Clague et al., 2009; Schipper et

al., 2011a; Schipper et al., 2010b). The vesicularity of Hawaiian eruption deposits is typically high, and pyroclasts are dominated by uniformly distributed vesicles. Strombolian eruptions of basaltic magma, however, are contrasted with Hawaiian eruptions in that it is not a continuous ‘steady’ eruption with sustained discharge, due to the fluid mechanics of the decoupled gas. Instead the eruptions are discrete explosions caused by plugs of accumulated gas (Houghton and Gonnermann, 2008). The transitional sequences at Austurfjöll are predominantly massive with a gradual upward fining, and weak bedding only in the upper meters of the larger deposits. This indicates a more continuous eruptive behavior, and resulting continuous deposition. Surtseyan deposits also do not neatly match the Austurfjöll sequence as the deposits are typically more heterogeneous in composition, vesicularity, and display sedimentary structures indicative of a pulsing eruption style. This complexity of deposit characteristics and eruption styles is a common challenge in subaqueous eruption deposits. It is likely in subaqueous eruptions that the occurrence of multiple fragmentation mechanisms will produce deposit structures inconsistent with the initial eruption style. In the case of the Austurfjöll deposits it is likely that secondary fragmentation by FCI explosions imparts a more uniform character to the deposits of what was initially a pulsatory Strombolian / Surtseyan style eruption by.

The first formation of dislocated globules of magma, fluidal bombs, where the magma flux rate exceeds the threshold for explosive activity, is the result of rapid extrusion of magma driven by internal volatiles, propelling the magma into the water column. The shear stress imparted on the surface of the magma exceeds the surface tension causing a separation of magma globules, and forming the fluidal bombs (Cas et al., 2003; Head and Wilson, 2003; Wohletz, 2003). The ejection of this first globule then exposes a greater surface area of magma to interact with external water. Concurrently, the formation of pillows and existing pillow lava is disrupted by the initiation of explosive activity. Large fluidal bombs represent the initial globules formed through rapid ejection of magma driven by magmatic gasses, and the smaller particles represent material that was subject to disruption by surface and bulk magma-water interactions (FCI) and quench granulation. The increased efficiency of the fragmentation is recorded in the overall decreasing grain size of the deposits through the increase in the proportion of lapilli and ash.

The peak magmatic gas energy is recorded by the largest bomb, which coincides with the peak in vesicle coalescence within a few meters of the breccia / lapilli contact (Figure 6.11). The coalescence of vesicles and vesicle size indicate decoupled volatile behavior similar to Strombolian-like gas slugs (Clague and Davis, 2003; Head and Wilson, 2003; Schipper et al., 2011a). The interaction of phreatomagmatic fragmentation (FCI) with magmatic fragmentation is not unique to fully submerged eruptions (Houghton and Schmincke, 1989; Skilling, 2009; Solgevik et al., 2007; White, 1996b). However, the initiation of a phreatomagmatic eruption by a decoupled gas magmatic eruption has not yet been described in a completely subaqueous environment. The appearance of an apparently continuous eruption triggered by decoupled magmatic gas expansion is attributed to the increasing contribution, and eventual dominance of phreatomagmatic fragmentation mechanisms, rather than a more magmatic gas dominated Hawaiian fountaining event.

The erosional history and complex overlapping facies of adjacent fissure eruptions at Askja make the identification of exact vent locations for each sequence very difficult. Without sufficient exposure vent position is estimated to be roughly located within the deposit itself, and therefore within 10-50 m of sample location based on the scope of the deposit and the lack of evidence for remobilization. Deposit volume is calculated from lateral extent, estimated by observation of the three-dimensional dissection of the deposit and from lithofacies mapping of DK, NG, and RG. Original volume estimates are clearly approximate due to the degree of deposit overlap and erosion. The estimated volume of the individual deposits is between 0.0004-0.003 km<sup>3</sup>. Typical Strombolian eruptions and Icelandic fissure eruptions have extrusion rates between 10 and 100 m<sup>3</sup>/s (Parfitt and Wilson, 2009). These explosive eruptive rates are also similar in range to the values estimated for subaqueous lobate lava flows (Griffiths and Fink, 1992). Estimates for eruption duration can be established from these values to be minutes to a few hours for each sequence (Table 6.3).

**Table 6.3 Dimensions and extent of subaqueous pillow lava, breccia and lapilli tuff sequences at Askja used to calculate the duration of the eruption based on a typical eruption rate of Strombolian and fissure eruptions (10-100 m<sup>3</sup>/s).**

	Thickness	Areal extent m <sup>2</sup>	Volume m <sup>3</sup>	Time range
Drekagil	20	8000	8.0 x 10 <sup>4</sup>	13–120 min
Nautagil	35	7000	1.2 x 10 <sup>5</sup>	20-180 min
Rosagil	14	3000	2.4 x 10 <sup>4</sup>	4-40 min

## 6.5 CONCLUSION

The investigation of transitional sequences of subaqueous basaltic pillow lavas, breccia, and fluidal-bomb bearing lapilli tuff from Austurfjöll, Askja revealed the pyroclast textures that record the transition from effusive to explosive subaqueous eruptive behavior. The textures of fluidal bombs, lapilli, and fine ash revealed the interaction of multiple fragmentation mechanisms across the range of particle sizes. The deposits of these three sequences were produced through the initial disruption of the effusively erupting magma by decoupled magmatic volatile expansion associated with decompression resulting from a change in ice-confined lake level. This explosive behavior subsequently enabled surface magma-water interaction (FCI), and to a lesser degree bulk magma-water interaction with the partially fragmented magma. At any time when magma is exposed to liquid water it can be expected that quench granulation will occur. The prevalence of granulation in the sequences described here is supported by the presence of flakey and elongate needles of fine ash from the breccia and lapilli tuff units. Quench granulation contributes to the production of ash sized particles during the eruption. The initial disruption of the



magma is preserved in the form of the intact fluidal bombs up to 40 cm in diameter, and the large polylobate vesicles of the lapilli and bombs. Minor evidence of magmatic fragmentation can be observed at the fine ash scale, but independently these particles would not be sufficient to determine the role of this fragmentation in the transition to explosive activity. The role of phreatomagmatic, surface magma / external water interaction, is recorded predominantly in the fine ash fraction of the deposit in the form of blocky, vesicle free grains, and the overall decrease in grain size of the deposits. The combination of sideromelane dominated, effectively quenched fine ash, and large clasts with intact quench rims indicates the simultaneous interplay of multiple fragmentation mechanisms, in a moderately energetic subaqueous basaltic decoupled gas slug triggered phreatomagmatic eruption of a few minutes to a few hours in duration.

## **7.0     INTRUSION OF BASALT INTO FROZEN SEDIMENTS AND GENERATION OF COHERENT-MARGINED VOLCANICLASTIC DIKES (CMVDS)**

Askja is one of the largest and best-exposed, formerly ice-confined, volcanoes on Earth. Most research has been on its Holocene (ice-free) evolution. The complex of basaltic glaciovolcanic massifs is dominated by volcaniclastic deposits that are cut by several calderas, and surrounded by Holocene subaerial lava flows (Figure 7.1).

Monogenetic basaltic eruptions under thick ice initially form a subglacial cavity filled with a temporally variable meltwater volume, subaqueous lavas and a variety of clastic deposits (Edwards et al., 2009; Höskuldsson et al., 2006; Skilling, 2009; White, 1996b). Eruptions may become explosive and emerge through the ice to generate an edifice of ice-confined phreatomagmatic tephra (Gudmundsson et al., 1997; Smellie and Hole, 1997). However, models of the evolution of basaltic glaciovolcanic centers have largely neglected intrusive processes. There are detailed discussions of the interactions of intrusions with the Martian cryosphere (Head and Wilson, 2002; Wilson and Head, 2002); however, there is a current lack of the three-dimensional exposure required to explore these interactions further (Head and Wilson, 2002).

Basaltic glaciovolcanic centers on Earth demonstrate the common presence of intrusions emplaced into wet and unconsolidated, or partially cemented, volcaniclastic deposits (Edwards et al., 2009; Mercurio, 2011; Schopka et al., 2006). Dike formation can be simplified into three steps: 1) fracture of the host, 2) propagation of magmatic gases at the dike tip (Carrigan et al., 1992) and 3) emplacement of magma and chill margin formation (Baer, 1995; Platten, 1995). This process is often repeated, as evidence of multiple magmatic pulses is preserved in vesicle bands and multiple chill margins (Baer,

1995; Huppert and Sparks, 1989; Liss et al., 2002; Platten, 1995; Taisne and Jaupart, 2010). Dike emplacement may be punctuated by volumetric contraction, or drainage of the dike (Agnon and Lyakhovsky, 1995).

Clastic dikes are common in sedimentary settings such as deep marine, lacustrine and glacial environments (Jolly and Lonergan, 2002). Volcaniclastic dikes have been described in various volcanic terrains (Heiken et al., 1988; Ross and White, 2005). Examples of clastic dikes formed in unconsolidated sediment clearly demonstrate that the host sediment need not be lithified to fracture in a brittle manner (Jolly and Lonergan, 2002; Rijdsdijk et al., 1999; Ross and White, 2005). The dominant mechanism responsible for the formation of clastic dikes is the fluidization of saturated sediments under excess pore fluid pressures (Jolly and Lonergan, 2002; Rijdsdijk et al., 1999; Ross and White, 2005). These fluidized sediments fill fractures in the host that formed when the tensile strength of the host was exceeded by the fluid pressure. This process, referred to as hydrofracturing, is common in environments with high sedimentation rates (e.g. deep marine shelf) and under rapid loading (e.g. glacial) (Boulton and Caban, 1995; Jolly and Lonergan, 2002). The interior fills of such dikes are sourced from deposits stratigraphically below the host sediment, with the exception of some glacial clastic dikes (Jolly and Lonergan, 2002; Rijdsdijk et al., 1999). CMVDs differ from clastic dikes as the dikes are lined with coherent glassy chill margins, and we also interpret the dike interiors as volcaniclastic material derived in situ in the dike fracture.

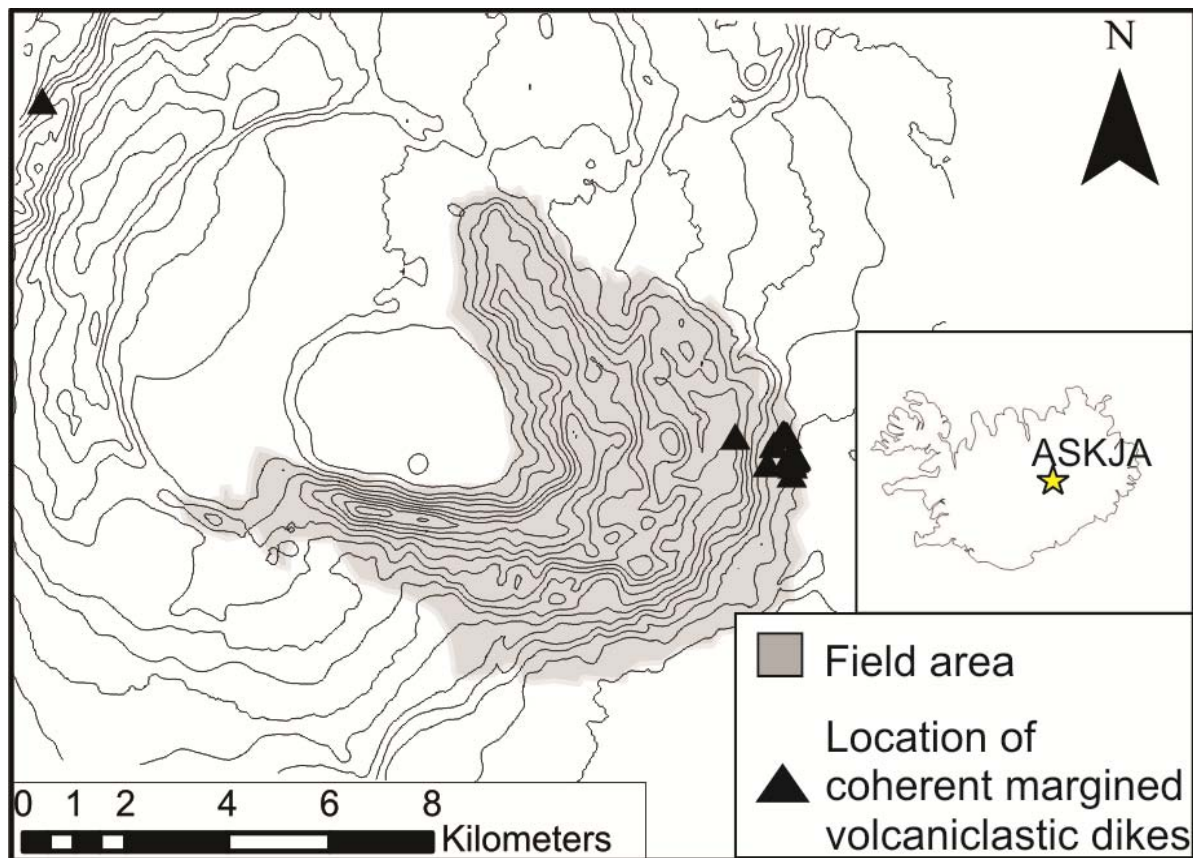


**Figure 7.1 Intrusion of Basalt into Frozen Sediments and Generation of Coherent-Margined Volcaniclastic Dikes (CMVDs).**

## 7.1 OBSERVATIONS

Ninety-four intrusions were described within the tholeiitic ca. 800 m Austurfjöll massif (Figure 7.1). They are subdivided into three types: 1) coherent dikes with no clear interaction with their host, 2) coherent dikes with irregular morphologies and pillowed margins in 2-4 m wide domains of fluidal and blocky peperite and 3) dikes we term CMVDs, that display multiple continuous basaltic glassy coherent chill margins, very thin (<3 mm) marginal peperite and a variety of vitriclastic interiors. The first two types of dike have been observed and described at other glaciovolcanic (Edwards et al., 2009; Mercurio, 2011) and submarine settings (Befus et al., 2009; Kano, 1989).

Sixteen CMVDs were documented, dominantly within a 1 km<sup>2</sup> area 10-300 m above the massif base (Figure 7.1). At least two additional examples have been investigated, at a reconnaissance level, in the western massif, 17 km away from the main cluster, and within 300 m of the local base elevation (Figure 7.2). The CMVDs were emplaced into a variety of bedded and massive ash and lapilli tuffs. The dikes are 0.5-2 m in diameter and are exposed in three dimensions over 10-100s of meters in length. They dip steeply (~60°) with fairly constant strikes, but have minor variations in orientation over 10s of meters and can display minor offshoots. In the western massif the CMVDs have less tabular morphologies but retain similarities to the main dike cluster in margin, fill type, scale and interaction with the surrounding host.



**Figure 7.2 Images of examples of CMVDs. Common features are the consistent glassy margins and complex volcanoclastic interiors. A) Example from main area of CMVD distribution, the segments on the scale are 10 cm. Note the lack of mechanical or thermal alteration of the host sediment by the dike. B) Example of CMVD from western massif of Askja (17 km from main cluster), backpack for scale.**

### **7.1.1 Dike Margins**

CMVDs display continuous margins of coherent unvesiculated basaltic glass up to 2 cm thick, with an additional 1-3 cm of coherent vesiculated (up to 40 vol.%, 0.1-1 mm vesicles) glass on the margin interior (Figure 7.3). The margins retain consistent thicknesses on both sides of a dike. Some have slickenline-like textures between the vesiculated and unvesiculated zones (Baer, 1991). Localized margin variations include mini-pillows (< 7 cm long) (Figure 7.3) and rare segments of absent glassy margin. The clasts of absent margin (up to 6 cm long) can be found within 5 m of their origin, in the interior of the dike. The bulk of the margin (2-3 cm) contains occasional (ca. 5 vol.%) faint, rounded, irregular, outlines of darker glass (0.5 mm), which are possible relict clasts (Figure 7.3 B). The inner portion of the margin has slight

variations in glass color, suggesting possible relict glassy clasts or mixing of glass domains (Figure 7.3C). The interior margins locally reveal ropey and bulbous textures in contact with the volcanoclastic interior (Figure 7.3E). There was no evidence of deformation of bedding in the host material at the dike contact (Figure 7.2A) (Kano, 1989; Ross and White, 2006). Typical dike wet sediment interactions obscures and / or destroys bedding and fabric of the host sediment (Skilling et al., 2002). Host materials display no apparent thermal or chemical alteration along the dike, and only a very thin (<3 mm) marginal peperite (Figure 7.3A). Dike-derived fragments in the peperite are angular, blocky, vesicle-free sideromelane.



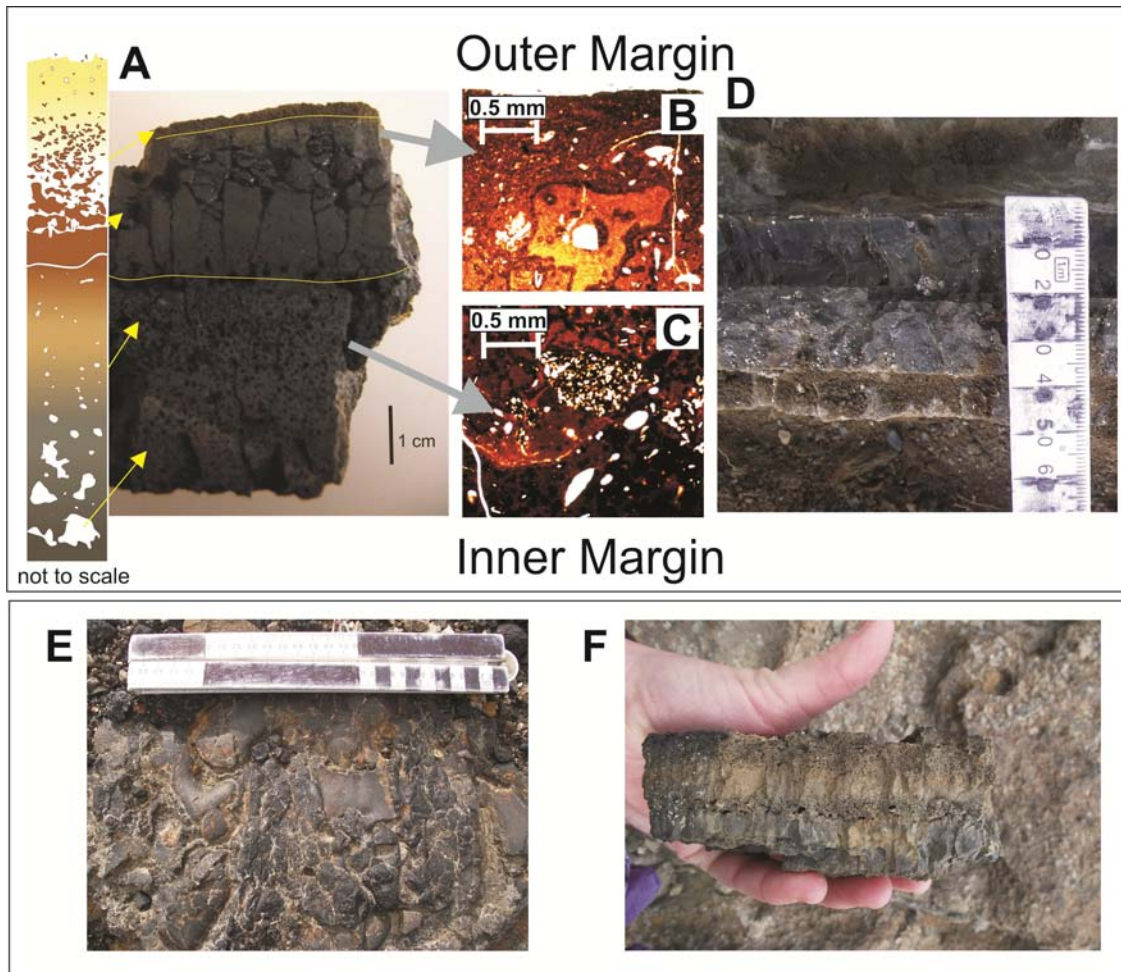


**Figure 7.3 Dike margins in hand sample and thin section. Field scale increments are 1 cm. A) CMVD chill margin hand sample and sketch showing textures. B) Petrographic image of the outer margin of the dike. Note the relict clast, a product of shear. C) Petrographic image of interior of dike margin. D) Hand sample of dike margin revealing multiple chills. E) Hand sample of interior portion of margin displaying complex ropey structures. F) Hand sample of CMVD margin in cross-section the reveals the variations in vesicularity within the margin.**



## 7.2 DIKE INTERIORS

CMVD interiors consist of coarse vitric ash, vitric lapilli, intact pillows (5-35 cm long), pillow fragments (<20 cm) or a mixture of two or more of these components. Pillows may be isolated or connected in a chain (Figure 7.4A and B). In dikes with significant ash-sized particles, sub-parallel banding (Figure 7.4C and D) is present with deformation around outsized clasts (Ross and White, 2005). Convolute banding and clast-rich concentration zones are roughly oriented parallel to the dike (Figure 7.5). Ash and lapilli in CMVD interiors share broadly similar grain shapes, size range and vesicularity with other basaltic glaciovolcanic clastic deposits (Kokelaar, 1986; Robert et al., 2008; White, 1996b). However, the texture of the ash / lapilli in any given CMVD interior is distinct from the texture of ash / lapilli of the surrounding host (Table 7.1). Individual clasts within the dike interiors can display spherical or elongate vesicles, bands of vesicles, or vesicles on clast margins, while the host sediments have a higher occurrence of spherical vesicles. CMVD interiors are dominated by (Figure 7.6) a mixture of vesicular (>40%) and blocky (flat sided, vesicle-free clasts) clasts. Host sediments display equal variability, but overall lower vesicularity within intact clasts. Dike interiors have a wide range of variability in grain size, degree of packing and vesicularity. Contrastingly, the host sediments, ash and lapilli tuffs, show a far less variability between deposits, having a moderate degree of packing (Figure 7.4F), consistent 0.5 mm sized glass fragments and up to 10% free crystals. Free crystals were not observed in CMVD interiors. Given this evidence we argue that the glassy clasts in CMVD interiors are derived from the dike itself and not from the host volcanoclastics.

**Table 7.1 Textural comparison of individual CMVDs with the associated host sediment, chill margins and when available, coherent interior domains of the same CMVD. Statistics were derived from petrographic image analysis. D= Coherent dike, coherent portion of a CMVD.**

Sample (images)		Crystall content (%)	Glass or Ground mass (%)	Porosity (%)	Vesicularity (%)	Grain size (mm)	Sorting
<b>Dike 1</b> (Fig 7.3 A, B, C).	Chill	15.69 <sup>a</sup>	68.52	N.A.	15-45	N.A.	N.A.
	D	63.15 <sup>a</sup>	50.68	N.A.	35	N.A.	N.A.
	Host	0-11 <sup>a,b</sup>	79.49	15-20	4-8	0.1-1.0	moderate
	CMV D	0	40-60	8-10	50	0.01-0.1	Poor
<b>Dike 2</b> (Fig 7.4 A)	Host	0	75	24	2	0.05	moderate
	CMV D	0	72	23	6	0.1-2.0	v. poor
<b>Dike 3</b> (Fig. 7.4 D)	Host	0-5 <sup>c</sup>	73	20	4	0.05-0.1	moderate
	CMV D	0	60-80	20-30	3-8	0.1-0.5	v. poor
<sup>a</sup> Plagioclase <sup>b</sup> N.A. = not applicable <sup>c</sup> Pyroxene							

Four of the CMVDs show a transition along strike from a non-pillowed coherent dike into one with volcanoclastic interiors, but preserve continuous coherent glassy margins across this transition (Figure 7.7). These transitions occur at multiple elevations, with only one corresponding to a lithostratigraphic boundary between a lapilli tuff and overlying ash tuff. One of these transitional dikes displays a structure known locally as the “Rosa”. This cylindrical void in the coherent portion of the dike is 2 m in diameter, has radiating glassy cooling fractures, and does not affect the dike width above or below the structure (Figure 7.8). The void occurs 60 m along strike and 20 m down dip from the transition from coherent dike to CMVD.

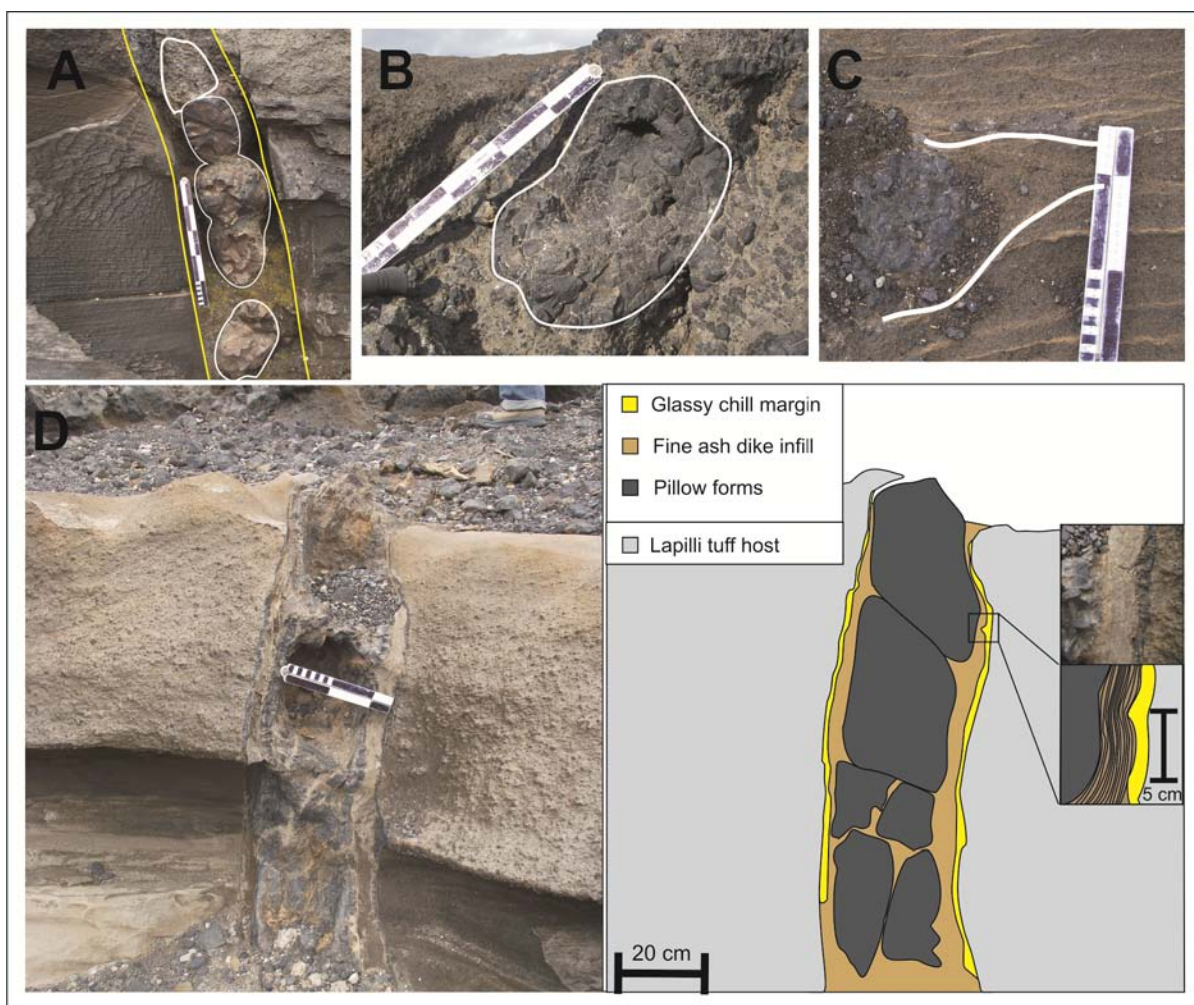


**Figure 7.4 Dike interiors in outcrop and thin section. Yellow lines indicate dike margins; white lines indicate pillows. A) CMVD with pillows and vitric ash interior. B) CMVD with pillow and pillow breccia interior. C) Ash-rich CMVD with deformation of ash banding (parallel to strike) around larger clasts. D) Detailed sketch of the interior of a pillow-dominated CMVD with strike-parallel bands of ash-sized particles between the pillows and the chill margin, as detailed in the inset.**

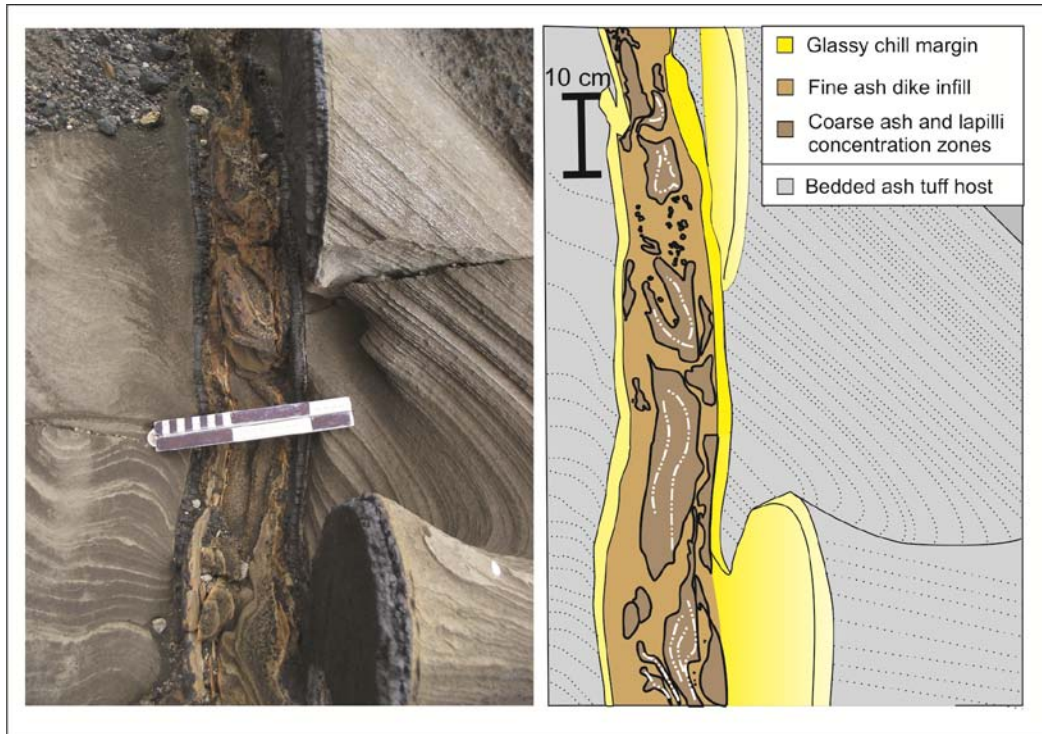


**Figure 7.5 CMVD with ash and lapilli dominated interior. Sketch indicates zones of clast concentration with white lines to indicate the weak structure present within the domains. The sedimentary structure of the host sediment is not disrupted by the dike. Complex margins indicate multiple magma pulses that resulted in the trapping of intact host sediment between an earlier chill margin and a later, final margin which truncates it.**

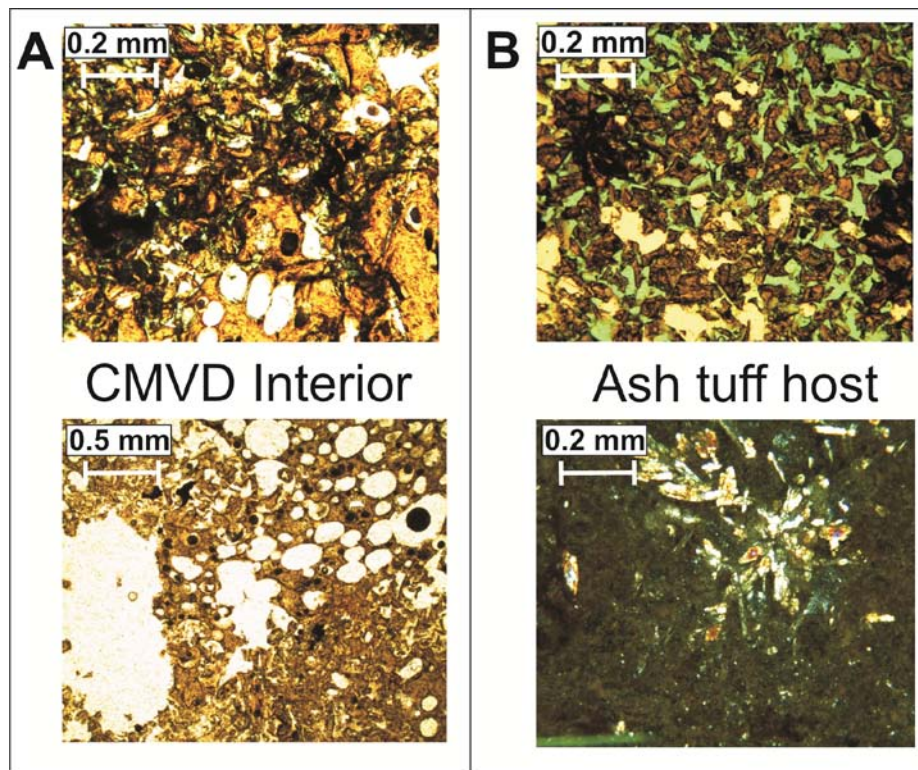


**Figure 7.6** Petrographic image of CMVD ash interior matrix with variable grain shapes and intact vesicular clasts mixed with blocky grain shapes. B) Petrographic image of typical CMVD ash tuff host matrix. Grains are well-sorted and shapes reflect fewer vesicles than CMVD interiors. Free crystals of pyroxene and feldspar, similar in size to the average grain size, are visible in cross-polarized light (xpl) in dike host sediments only.



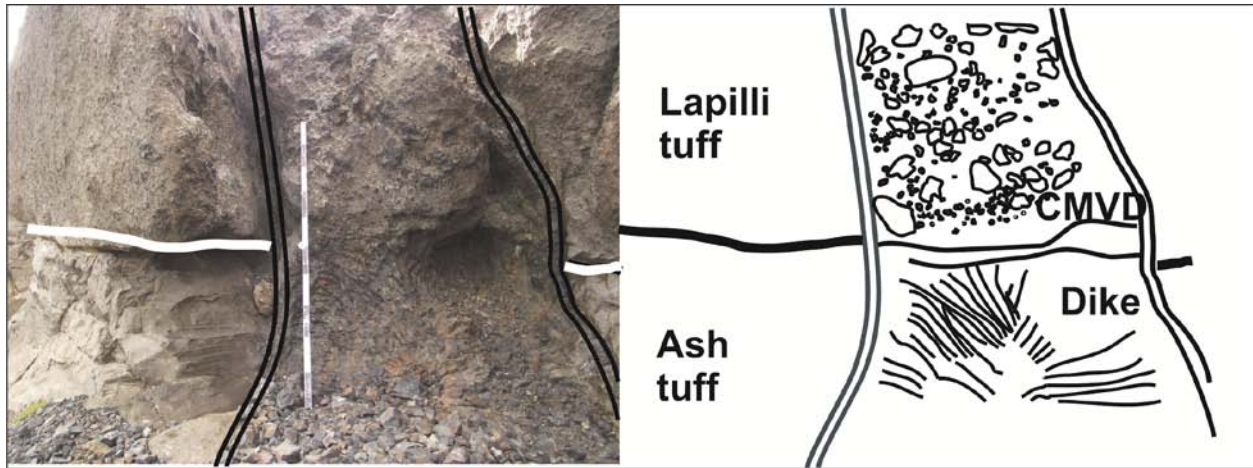


**Figure 7.7** Example of a CMVD transition from coherent basaltic to volcaniclastic dike interior with coherent glassy margins (double lines). Radial cooling cracks are found within the dense dike below the transition. The correlation of a stratigraphic boundary between a massive lapilli tuff and ash tuff with the transition (horizontal line) is limited to this CMVD.

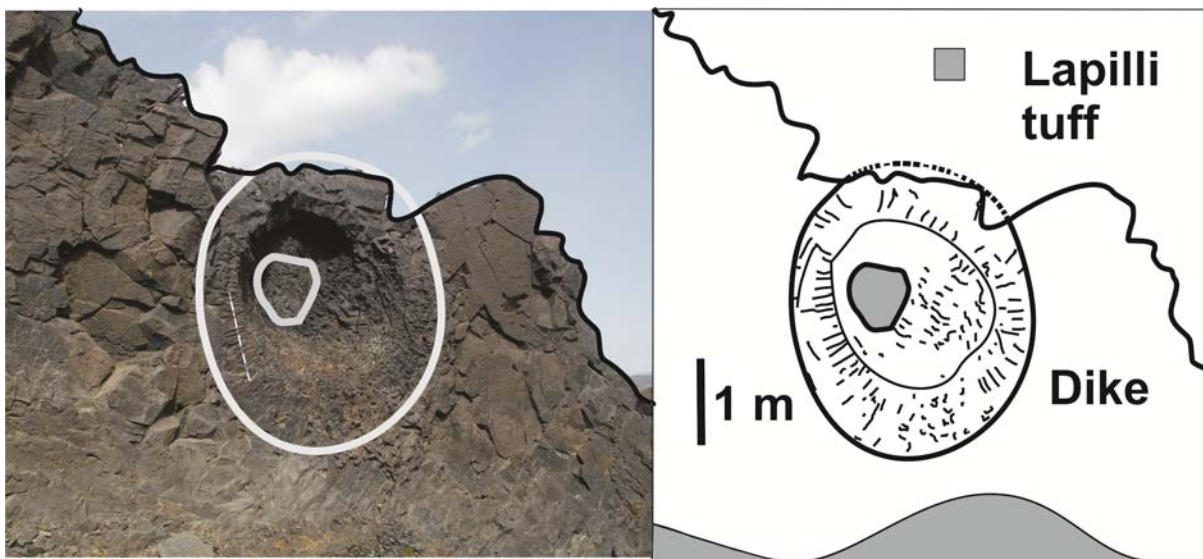


**Figure 7.8 Field image and B) sketch of the Rosa structure, a cylindrical void (outlined) in a 90 cm wide tabular coherent basaltic dike that transitions to a CMVD up dip. View is perpendicular to strike. The void is symmetrical with thick (3 cm) glassy margins and does not disrupt the dike width or the host. This is interpreted as the result of a cryolith (ice-block) that fell into a drained dike after margin formation. Subsequent dike pulses chilled around and thermally eroded the cryolith and associated vapor, creating a round void.**

## **7.3 DISCUSSION**

A model for the formation of CMVDs must address fracture formation, formation and preservation of the coherent glassy margins, the lack of significant interaction with the host and formation of the clastic interiors.

### **7.3.1 Fracture formation**

CMVDs share similarities in diameter, regular planar margins and the lack of alteration and / or deformation of their hosts with typical basaltic dikes emplaced into rock, suggesting that fracture formation for typical basaltic dikes and CMVDs are similar. Peperite generation and localized pillows along the margins imply that the host sediment was wet and not chemically cemented at the time of intrusion. The brittle fracture of rock or sediment is dependent upon the material's tensile strength and the strain rate. The tensile strength of volcanoclastic deposits in glaciovolcanic settings is derived from the overburden pressure of ice-confined lakes, glacial ice and the volcanoclastic pile. Hydrofractures are an important mechanism in clastic dike formation, where fluidized sediments quickly fill the propagating crack. However, for CMVDs, we argue that fracture formation is driven by rising gas at the head of the

dike (Baer, 1995; Carrigan et al., 1992; Taisne et al., 2011). As the pulse nears the sediment / ice interface, magmatic gas escapes and results in localized contraction and drawdown of the dike interior. Drainage could be accomplished through lateral transport of magma along the dike, or back into the feeder system (Agnon and Lyakhovsky, 1995). In both clastic and CMVD formation, high rates of dike propagation would aid fracture formation in unconsolidated sediment (Ross and White, 2005). Fractures in unconsolidated sediments will only remain open while the interior pressure exceeds that of the overburden (Jolly and Lonergan, 2002; Rijdsdijk et al., 1999). In order to form a dike in such a fracture, the space must be held open long enough for the invading material to fill the fracture. In clastic dikes the space is filled with fluidized sediment. In the case of CMVDs the rising dike must preserve the space. However, in the event of volume contraction through degassing or drainage, the fracture in unconsolidated sediments will be preserved only by pore water surface tension, friction (a product of grain size and angularity) and the glassy chill margins. A more efficient mechanism of fracture preservation for Askja CMVD's, given the glaciovolcanic setting (Sigvaldason, 1968), is ice-cementation of the host. Additionally ice-cementation would reduce the pressure variations caused by preexisting discontinuities in the host, such as bedding, grain size variations and palagonitization, explaining the dominant tabular morphology of the dikes (Baer, 1991; Jolly and Lonergan, 2002).

### **7.3.2 Dike Margin Formation**

CMVD margins formed rapidly (Huppert and Sparks, 1989; Lister, 1995; Platten, 1995; Taisne and Jaupart, 2010), as indicated by their glassy nature and the lack of thermal alteration of the surrounding host. The apparent relict clasts, zones of variable vesicularity and slickenline structures in the margin suggest that the total thickness of the margins need not have quenched simultaneously, but rather increased in thickness as the dike remained near the glass transition temperature (600-980<sup>0</sup> C, (Ryan and Sammis, 1981)), or were subject to post-formation ductile shear (Huppert and Sparks, 1989). These textures, and the exceptional thickness of the chills, suggest multiple magma pulses. Two examples of



CMVDs from Askja clearly show the repetition of the less vesicular glassy exterior and more vesicular interior of the margin (Figure 7.3D). These multiple pulses may have been separated by periods of dike drainage.

The thin (<3 mm wide) peperitic zone along the dike margins formed as a result of the minor fragmentation of the outermost glassy chill and mingling within a thin zone of locally granular host material. We suggest this peperite formed in an unusually thin meltwater zone, similar to wider melt zones predicted in dike-cryosphere interactions on Mars, (Head and Wilson, 2002). This meltwater zone is produced along the dike margins by melting of an ice-cemented host.

### **7.3.3 Evidence for ice-cementation of the host**

Investigations of glaciovolcanic edifices have revealed a variety of dike morphologies that are indicative of the environment into which the dikes were emplaced (Table 7.2). Askja has three major categories of dike morphology, revealing a range of host conditions including lithified and competent host rock (non-pillowed coherent dikes), saturated sediments (pillowed dikes) and ice-cemented sediments (CMVDs). The morphologies, interactions between CMVDs and their host sediment and chill margins are environmental indicators that suggest ice-cementation of the host. The host material was unconsolidated volcanoclastic sediments, and not competent rock, as indicated by local undulations in the dike morphology, such as mini-pillows, and the thin peperite on the dike margin. While the presence of a peperite suggests that the host was still unconsolidated, and capable of mixing with fragments of the dike margin, its dimensions (3 mm) are significantly less than that of a typical peperite (cm to m) (Skilling et al., 2002). If the host were simply saturated, as during the formation of pillowed dikes (Edwards et al., 2009; Mercurio, 2011; Schopka et al., 2006) dike morphology would be highly convoluted and would likely have a wider peperite. This is further supported by the distinct lack of chemical (alteration) or mechanical (drag or convolutions) disruption of the volcanoclastic host as seen at other basaltic glaciovolcanic centers in Iceland (Mercurio, 2011). The thin nature of the peperite is suggestive of a more

complicated thermal interaction with the host sediment than modeled here, or for Mars (Wilson and Head, 2002). Instead CMVD chill margins incorporate portions of the host with intact sedimentary structures (Figure 7.3 and 7.4).

Ultimately, ice-cemented host sediments would 1) allow for the constant thermal contrast required to form the continuous thick margins, 2) enable restricted mixing of fragments of the chill with the host sediment in a thin melt zone 3) prevent hydrothermal alteration of the host and 4) maintain an open fracture lined with continuous intact glassy chill margins following dike drainage.

**Table 7.2 Conditions of dike formation in Askja glaciovolcanic sediments and lavas.**

<b>Dike type</b>	<b>Non- Pillowed coherent</b>	<b>Pillowed</b>	<b>Coherent margined volcaniclastic dikes (CMVD)</b>
<b>Morphology</b>	Tabular	Irregular shape to broad zone of intrusion	Tabular (high angle)
<b>Dike width (cm)</b>	10-200	100-400	75-210
<b>Margin (width)</b>	Chill (0.5 -3 cm)	Pillow rinds (0.5- 1 cm)	Complex Chill (3-5 cm)
<b>Host-conditions</b>	Competent / lithified	Wet	Frozen
<b>Host</b>	Any	Unconsolidated (tuff, breccia)	Unconsolidated (tuff, breccia)
<b>Depth</b>	Any	Near surface	Subglacial, near surface
<b>% of occurrence</b>	55	27	18
<b>Distribution (elev. m asl)</b>	Ubiquitous: (up to 1415)	Low elevation: Common (below 1035 )	Confined: clusters (all below 1035)

### 7.3.4 Melting of ice-cemented host

The thin peperite along CMVD margins indicate a ca. 3 mm ice melt zone on either side of the dike. The time required to melt this depth into ice-cemented sediments can be calculated using the standard thermal boundary relationship (Wilson and Head, 2007)

#### Equation 7.1

$$d^2 \approx k * t \quad (1)$$

where  $d$  is distance (m),  $k$  is the thermal diffusivity ( $m^2/s$ ) and  $t$  is time (s)

By using the standard thermal diffusivities of ice ( $4.21 \times 10^{-6} m^2/s$ ) and glass ( $3.42 \times 10^{-7} m^2/s$ ) in an ice-filled host with 20% pore space, the time required to melt 3 mm would be 8 s.

The heat lost by the dike as it equilibrates with the ice-cemented host sediment can be estimated:

#### Equation 7.2

$$H_m = 2X(H_i + H_s) \quad (2)$$

where  $H_m$  is the heat lost by the magma,  $H_i$  is the heat lost to the ice,  $H_s$  is the heat lost to the sediment and  $x$  is the depth of heat transfer into the host on one side of the dike (m).

#### Equation 7.3

$$H_m = W \rho_m [L_m + C_m (T_m - T_i)] \quad (3)$$

#### Equation 7.4

$$H_i = \rho_i L_i P \quad (4) \text{ and}$$

**Equation 7.5**

$$H_s = \rho_s [L_s + C_s(T_m - T_s)] * P \quad (5)$$

where  $\underline{W}$  is the dike width (CMVD average is 1 m),  $\underline{L}_m$  is the latent heat of magma ( $2.09 \times 10^5$  J/kg),  $\underline{\rho}_m$  is the density of the intrusion ( $2480 \text{ kg/m}^3$ ),  $\underline{T}_m$  is the magma temperature (1473 K),  $\underline{T}_i$  is the melting point of ice (273.15 K),  $\underline{C}_m$  is the heat capacity of magma (900 J/kgK),  $\underline{P}$  is the volume percent contribution to the host (20% porosity),  $\underline{\rho}_i$  is the density of ice ( $917 \text{ kg/m}^3$ ),  $\underline{L}_i$  is the latent heat of ice ( $3.33 \times 10^5$  J/kg),  $\underline{T}_s$  is equal to  $\underline{T}_i$ ,  $\underline{\rho}_s$  is the host density ( $2700 \text{ kg/m}^3$ ),  $\underline{L}_s$  is equal to  $\underline{L}_m$  and  $\underline{C}_s$  is equal to  $\underline{C}_m$  (Wilson and Head, 2007).

The resulting value for the depth of melting ( $x$ ) is 54 cm, three orders of magnitude greater than indicated by the peperite. This suggests that heat transfer is more complicated than the simple conductive model above. The amount of heat transferred from the dike to the host is limited by a combination of several factors including the formation of the chills, dike drainage and the infiltration of external water into the dike. We suggest that dike drainage is the principle reason that heat transfer was reduced within 8 s and why a thin melt zone resulted. This limited melting has important implications for heat transfer models in glaciovolcanic systems and the rate at which basaltic chill margins form.

**7.3.5 Dike Interior Formation**

All CMVD interiors have high percentages of vitric ash and lapilli, very limited mixing with the host, domains of sub-parallel banding of ash sized particles and convolute lenses of lapilli (Figure 7.4). The combination of a high proportion of blocky ash particles and vesiculated ash (5-50% vesicularity) suggests that magma fragmentation may have been accomplished through a combination of quenching (Honnorez and Kirst, 1975; Martin and Nemeth, 2007), magmatic or external gas expansion. Textural differences between dike interiors and their host sediment imply that this fragmentation took place within the dike fracture, forming an autoclastic peperite (Skilling et al., 2002). Progressive formation of a

fragmental interior would occur through the repeated interaction of new magma pulses (Lister, 1995) with water and volcanoclastics (Figure 7.9). The mingling, banding and clast sorting in the dike would be aided by the expansion and movement of steam and liquid water (Heiken et al., 1988; Ross and White, 2005) and gravitational settling, leading to a structurally complex, glassy slurry-filled dike. The fragmentation mechanisms involved are non-explosive, as the narrow dimensions and intact glassy margins of the dikes would not be preserved in the presence of significant explosions. We suggest meltwater flooded downward into an open fissure following dike drainage. Lateral infiltration of external water is considered unlikely, as it would be highly difficult to develop, and preserve, such regular chill margins after flooding.

The Rosa structure is interpreted as resulting from the dike chilling around a trapped ice-block (Skilling, 2009), here termed cryolith, that collapsed from overlying ice into the open dike fissure after chilling of the dike margins and drainage. When later pulses of magma interacted with the cryolith, thermal erosion of the block creates a nearly circular space through direct melting and localized vapor pressures. This model is dependent on the rapid formation of chills within the dike, trapping the cryolith or meltwater within the void, despite the relative lower density of water. In near-surface conditions, a small volume of water will expand exponentially upon conversion to vapor; such that the volume of trapped ice and liquid water required to form this void is not significant.

## **7.4 CONCLUSION**

CMVD formation is interpreted to represent near surface, non-explosive mingling of basaltic magma and meltwater within a dike emplaced into ice-cemented volcanoclastics. The ice-cemented nature of the host prevents the deformation and thermal alteration of the host sediments by the dike, limiting the mingling of the dike margins and host sediment and prevents the collapse of the dike fracture during dike drainage. As an individual dike pulse nears the sediment / ice interface, degassing results in contraction and drawdown of the dike interior with potential for significant drainage. The retraction of the interior allows the

downward infiltration of meltwater into an open fracture and the collapse of overlying ice into the opening. The Rosa feature is interpreted as chilling around a cryolith lodged in the drained dike. Interaction of the magma with the meltwater results in dominantly quench and mechanical fragmentation of the magma and the development of a dike-derived vitric ash and lapilli slurry. Subsequent pulses of magma interact with the slurry, creating a range of structurally complex interiors. CMVDs should be expected in other near-surface subglacial or ice-cemented environments, including areas of permafrost on Earth and in the Martian cryosphere. We argue that the presence of a CMVD is therefore an important environmental indicator of ice-cemented sediments in volcanic terrains.

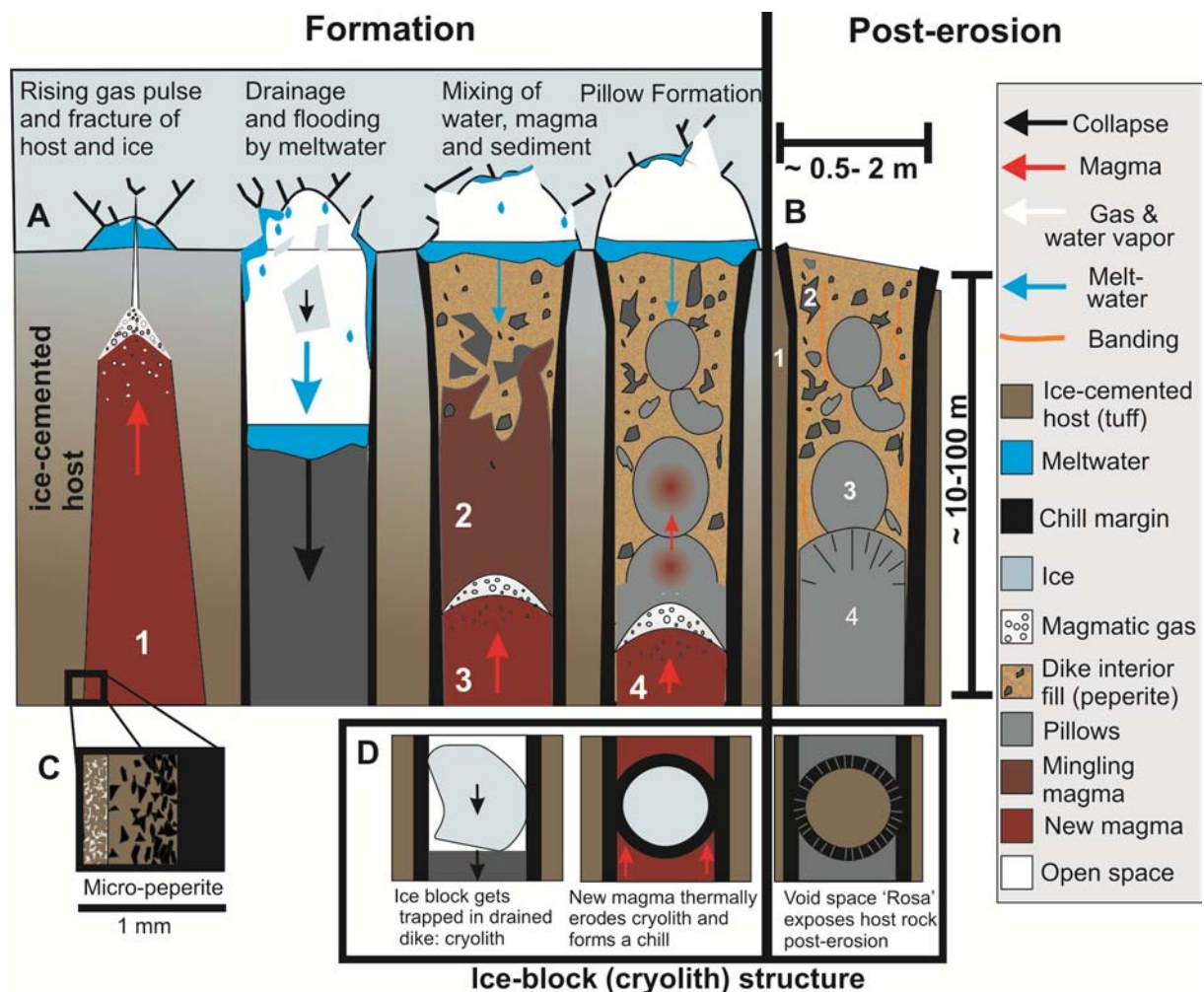


**Figure 7.9 Model of CMVD formation in ice-cemented host (ash / lapilli). A-1) Chill margins form along a rising basaltic dike. The ice-cemented host and overlying ice fracture. The gas driven pulses of magma depressurize near the host / ice / meltwater interface. A-2) Dike drainage creates space, allowing downward flooding of the dike. A-3) Meltwater and magma interact non-explosively, forming a slurry. A-4) Later pulses interact with the slurry; mingling continues. B) Motion of magmatic gas, steam and clasts develop near-vertical flow banding. A final pulse is chilled against the interior, resulting in radial cooling cracks. Evidence of the preceding steps may be preserved in the CMVD (labels). C) Formation of a very thin peperite between chill margin and ice-cemented host. D) Dike behavior when cryolith becomes trapped in the drained dike, forming a Rosa structure.**

## **8.0 PALEO-ICE RECONSTRUCTIONS OF THE REGION AROUND ASKJA VOLCANO USING AUSTURFJÖLL MASSIF**

The construction of Iceland has been dominated by periods of volcanic activity and the remobilization of volcanic deposits by ice, water, and wind. In order to reconstruct Pleistocene paleo-ice conditions, direct evidence and proxies can be measured from basaltic polygenetic formerly ice-confined volcanoes in central Iceland. The study of glaciovolcanic constructs is a growing field, relying heavily on a number of disciplines from petrology, isotope geochemistry, sedimentology, geochronology, glaciology, and hydrology. By unraveling and dating an eruptive sequence that occurred under an ice sheet, the volume of ice at the time of the eruption and the impact of the eruption (melting and landscape alteration) can be quantified. The position of Iceland in the North Atlantic is valuable to climactic studies as it reflects both European and North American climate patterns. The Polar Front currently lies just north of the Icelandic shelf. The climatic history of Iceland reflects not only the advance and retreat of nearly 20 glacial periods (Bourgeois et al., 2000; Geirsdóttir and Eiriksson, 1994), but also the fluctuating position of the Polar Front and the relative strength of the North Atlantic Current and the Eastern Greenland Current.

The limited lithological variation, highly active tectonic setting, frequent volcanic eruptions, small land area, and lack of soil development make climate studies in Iceland unique. In conjunction with a high proportion of deposit recycling these conditions result in limited preservation of traditional climate proxies. Climate reconstruction tools such as paleosol identification, provenance studies of glacial erratics, and lake sediment cores cannot easily be applied to Iceland. Iceland does have a large number of datable tephras, ice-confined and formerly ice-confined volcanic deposits, and extensive sequences of marine shelf sediments that are useful paleoclimate indicators. Glaciovolcanic formations dated



geomagnetically between 0.78 and 0.01 Ma cover about 11,200 km<sup>2</sup> of Iceland (Jakobsson and Gudmundsson, 2008), this corresponds to just under 11% of the land surface. Sedimentation rates on the northern Iceland shelf have been estimated to be around 0.2 to 2 m/ka (Knudsen and Eiriksson, 2002) and 1 million tons/annum to the south (Syvitski et al., 1999). High sedimentation rates preserve fairly rapid environmental variations on the Icelandic shelf. Additionally, stranded beaches and displaced fossils can be found along the coasts and record the complex interaction of fluctuating sea level and isostatic rebound (Hubbard et al., 2006).

As glaciovolcanology has matured as a field, a feedback relationship between eruptive activity and deglaciation has become apparent, though the details remain debated. The rapid deglaciation of an active volcanic region can increase intrusive and eruptive activity through lithostatic unloading with ice removal (Hooper et al., 2011; Hubbard et al., 2006; Jull and McKenzie, 1996; Larsen and Eiriksson, 2008; Sigvaldason et al., 1992; Slater et al., 1998). However, volcanic activity under an ice sheet, and the associated meltwater will increase the rate of ablation of the ice over very short time scales (Bourgeois et al., 2000) and can increase ice sheet mobility by lubricating the ice / bedrock contact (Hubbard et al., 2006). The overburden pressure of LGM extent ice sheet, with proposed thicknesses on the order of 1-2 km in Iceland, subdued the volume of erupted material by 32% relative to modern values (MacLennan et al., 2002; Sigvaldason et al., 1992). Though the production rates were lower, these eruptions under the LGM ice sheet would have had significant impacts on the morphology and thickness of the ice in that region. Historical observations of volcanic and geothermal activity have revealed the establishment of 300 m deep englacial lakes within the Vatnajökull icecap e.g. Grímsvötn, Gjálp (Gudmundsson et al., 1997). The impact of increased meltwater on the hydrology of the ice would increase the mobility along the base (Hubbard et al., 2006) and increase melting along fractures, especially under conditions of high hydrostatic pressure (Bourgeois et al., 2000). This hydrology is in turn controlled by the thickness and morphology of the ice sheet, more than the underlying topography. Further investigation of the thermal budget, meltwater volumes, and processes of meltwater drainage related to ice-confined eruptions to further understand the causality and response of these systems. Furthermore, the significant volumes of

water released from geothermal/volcanically disturbed ice sheets not only represent a significant hazard to Icelanders, the input of significant volumes of cold fresh water to the North Atlantic and Arctic can have significant climate ramifications (Hubbard et al., 2006).

Iceland's glacial history and paleoenvironmental conditions during the Pleistocene have been partially reconstructed through a combination of terrigenous glacial deposits, marine sea level high stands, pollen records, marine sediment cores, and glaciovolcanic deposits (Abbott et al., 2012; Bergh and Sigvaldason, 1991; Bourgeois et al., 1998; Brendryen et al., 2010; Eiríksson, 2008; Geirsdóttir and Eiríksson, 1994). Tephra collected in marine cores of Iceland, Northern Europe and in Greenland ice cores have been used to create a record of Pleistocene volcanic activity from Iceland (Abbott et al., 2012; Brendryen et al., 2010). The following is a discussion of the paleoenvironmental evidence that can be reconstructed from the basaltic glaciovolcanic deposits of Austurfjöll, Askja volcano, Iceland. The reconstruction is based on the evidence for magma-ice interactions, subaqueously emplaced volcanic deposits, glacial deposits, glacio-fluvial deposits, volatile saturation pressures, geomorphology, and regional glacial indicators such as trim lines and glacial scour.

## **8.1 METHODOLOGY**

The reconstruction of paleoclimate conditions from volcanic deposits is a multi-disciplinary technique that relies on the corroboration of multiple data sets to compensate for the lack of traditional glacial deposits and proxies. The glaciovolcanic deposits of Austurfjöll are used to reconstruct the local ice-presence and thicknesses using a combination of field work, quench rind volatile analysis, regional geomorphologic evidence, and radiogenic dating of volcanic deposits.

Regional evidence of glaciation is compiled from the literature (Bourgeois et al., 1998) was compared with ASTER global DEMs of the area immediately surrounding Askja. Regional evidence includes trim lines, striations, coastal shelf deposits, and regional marine cores. Field work to elucidate

past ice presence and thickness focused on the identification of volcanic and sedimentary features that are indicative of the environment of deposition. This includes subaqueous, subaerial, and ice-contact environments. Erosional surfaces, especially where glacial scour was obvious, were measured. The location of glacial erratics was documented. The distribution of lithofacies was mapped (Chapter 2) and correlated with geochemical eruptive units to produce a chemostratigraphy map (Chapter 4). Radiogenic dating was accomplished using unspiked K/Ar isotopes as described in Chapter 3.

Quench rind volatile analysis is based on the assumption of closed-system equilibrium degassing of effusive subaqueous lavas. The confining pressure of the eruptive environment (beneath ice, water, volcanoclastic deposits, or a combination of these) will control the solubility of dissolved volatiles in the magma. Rapid quenching of the melt will form glassy quench rinds containing the pressure soluble volatiles. Sampling of pillow lava and subaqueous sheet flow glassy rinds requires fresh unaltered and in situ stratigraphically constrained deposits. Two glass chips were prepared for each sample, except when limited by sample volume. The glass chips were doubly polished and with an average thickness of 95  $\mu\text{m}$ . The chips were then analyzed using Fourier Transform Infrared (FTIR) spectroscopy at the University of Wisconsin-Madison using a Nicolet Nexus 470 FTIR with a Continuum Analytical-IR microscope attachment using KBr beam splitter and a liquid nitrogen-cooled MCT-A detector. The molar absorptivity coefficient for the  $\text{H}_2\text{O}$  vibration band is 63  $\text{l mol/cm}$ . Each spectrum consisted of 512 scans between 650 and 4000  $\text{cm}^{-1}$  taken at 4  $\text{cm}^{-1}$  resolution. The density of basaltic glass was estimated to be 2800  $\text{kg/m}^3$ . The thickness of the glass chips was calculated using FTIR interference fringes in reflectance mode. The results include  $\text{H}_2\text{O}$  and where sufficiently available,  $\text{CO}_2$ . The detection limit of  $\text{CO}_2$  is 30 ppm. The abundance of these volatiles are used to compute the confining pressure under which the lava was erupted based on the saturation pressure of the volatile species (Edwards et al., 2009; Owen et al., 2012). The solubility calculator VolatileCalc was used for these calculations (Newman and Lowenstern, 2002).

## **8.2 CLIMATE FACTORS INFLUENCING ICELAND**

The geographic position of Iceland in the North Atlantic subjects it to a combination of diverse oceanic currents. It sits astride the boundary between the North Atlantic current and the Polar Front. Along the northern Icelandic shelf the Polar Front is represented by the East Icelandic Current (EIC), which is derived the Eastern Greenland Current (EGC) (Figure 8.1). The EIC runs clockwise along the northern shelf and turns south along the eastern coast where it interacts with the counter-clockwise Icelandic gyre in the north Atlantic (NE of Iceland). The EIC is associated with low plankton productivity and cold water (Eiriksson et al., 2000).

The North Atlantic Current, between eastern Iceland and England is warmer in contrast. The Irminger Current runs south and west of Iceland. This clockwise current is associated with high plankton productivity and warm temperatures (Eiriksson et al., 2000). The interaction of the EIC and the Irminger Current along the northwest coast creates a seasonal water mass, which is subject to the relative strength of the two currents and level of stratification (Eiriksson et al., 2000). Throughout the Quaternary as these currents have fluctuated so too has the position of the Polar Front, having a dramatic impact on the climate of Iceland. The modern climate of Iceland displays a significant north / south temperature gradient across Iceland (Axford et al., 2007), resulting from the contrasting currents.

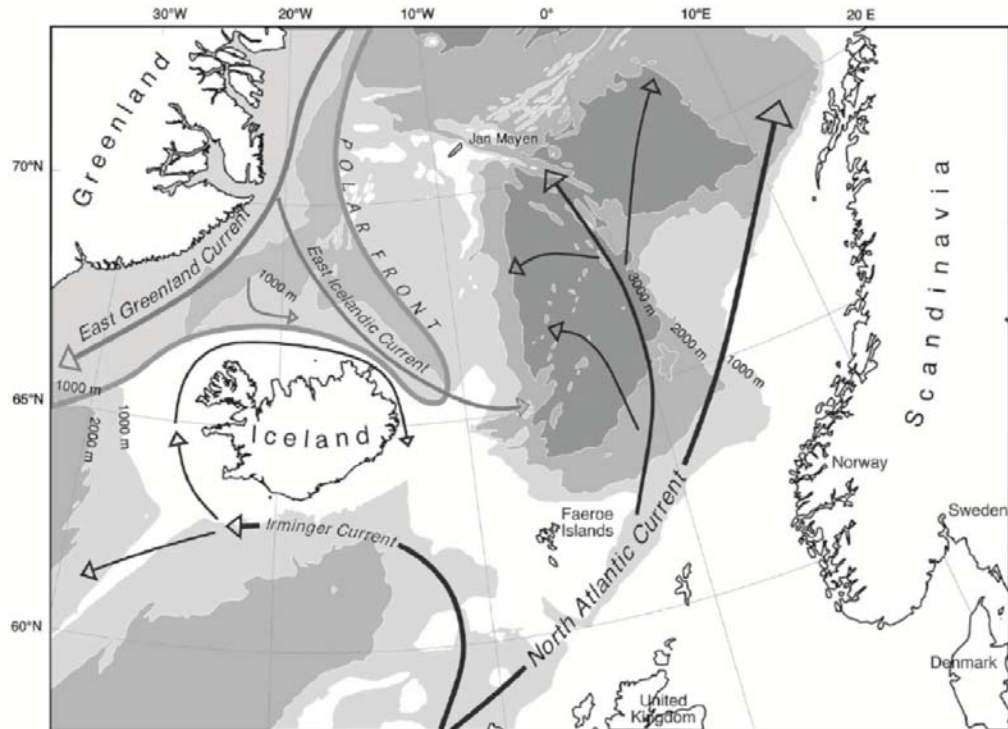


**Figure 8.1 Oceanographic climatic influences on Iceland, adapted from Knudsen and Eriksson, 2002.**

### **8.3 RECONSTRUCTION OF ICELAND'S GLACIAL HISTORY**

As the number and variety of paleoclimate studies in Iceland increases, so too does the detail of the reconstruction of the glacial history over the last 3 mya. Estimates of between 15 and 23 (Bourgeois et al., 2000; Werner and Schmincke, 1999) glacial periods have impacted Iceland between 3 and 0.10 mya in Iceland. The points of continued contention are the thickness of the ice during these periods, their continuity (number of nucleation points/ice centers), and the bounding ages.

### **8.3.1 First glaciation**

The first evidence of a significant glacial presence across Iceland is dated to approximately 3.8 mya, with the earliest glacial deposits in NE Iceland (Geirsdóttir and Eiriksson, 1994). By 2.0 mya the entire country was predominantly glaciated (Geirsdóttir and Eiriksson, 1994) with the first noted foreign drop stones appearing along the northern coastal shelf of Iceland (Einarsson and Albertsson, 1988) suggesting significant contemporaneous ice bodies in Greenland. Marine sediment cores reveal there are somewhere between 3-9 tillite horizons from 3 mya to 2 mya (Einarsson and Albertsson, 1988). The only example of glaciovolcanic studies of deposits from this period of glaciation is at Skaftafell in southeastern Iceland with glaciovolcanic ridges paleomagnetically and K/Ar dated to between 0.8 -3 mya (Helgason and Duncan, 2001).

Subsequent glaciations are more difficult to constrain due to the overprinting of each subsequent glacial period. Marine deposits along the northern shelf reveal eight glacial periods between 2 mya and 0.7 mya, with an additional four glaciations in the last 700,000 yr bp (Einarsson and Albertsson, 1988). The frequency of glacial periods and the large proposed ice extent preclude the preservation of geographically significant non-glaciated surfaces older than about 11 ka. Confirmed ice-free areas predating the LGM occur predominantly around the northwestern Fjordlands in the form of nunataks (Bourgeois et al., 2000; Norðdahl et al., 2008).

### **8.3.2 Interstadials**

The most recent full interglacial period is estimated to have peaked between 70-90 ka (Norðdahl and Petursson, 2005) roughly corresponding to Marine Isotope Stage 5 (Brendryen et al., 2010). In the southwestern Icelandic marine record a significant retreat of ice on the shelf was indicated around 28 ka <sup>14</sup>C (Eiriksson et al., 1997). Other ice-limited periods are recorded around 12.4-12.3 ka to 12.2 ka, 11.2-10.8 ka and 10.3- 9.8 ka (Eiriksson et al., 1996; Norðdahl and Petursson, 2005).

### **8.3.3 Weichselian (Last Glacial Maximum) (100-70 ka to 11 ka)**

The Last Glacial Maximum in Scandinavia is referred to as the Weichselian glacial period. The earliest Weichselian strata in Iceland are glacial sediments bedded with subaerial lava horizons in the Krafla central volcano complex (Norðdahl and Petursson, 2005) (Figure 1.2). These sediments are aged from around 100-70 ka (Bourgeois et al., 2000; Slater et al., 1998) and correspond to Marine Isotope Stage 4 (Abbott et al., 2012; Brendryen et al., 2010). Estimated ice thickness estimates range from 1000 m (Jakobsson and Gudmundsson, 2008) to 2000 m (Bourgeois et al., 2000; Norðdahl et al., 2008). Coastal ice thicknesses were significantly less, likely around 500 m along the northern coast (Bourgeois et al., 2000).

Ice extended to the continental shelf during the Weichselian maximum (Figure 8.2) (Geirsdóttir and Eiriksson, 1994; Hubbard et al., 2006), although localized ice-free areas remained, particularly close to the coast (Bourgeois et al., 2000; Einarsson and Albertsson, 1988). The aspect ratio of the ice sheet would be highly dependent on basal boundary conditions. Strong topographic control and interaction with marine environment relates to flow velocities and margin stability (Hubbard, 2006). Glacially streamlined landforms revealed that the LGM ice sheet was drained through a number of narrow channels of parallel flow fed by convergent onset zones, suggesting ice stream activity (Bourgeois et al., 2000) and highly localized variation in ice thickness. Many of these variations may have been a result of existing topography, including glaciovolcanic ridges (Jakobsson and Gudmundsson, 2008) along the active volcanic zones. A highly active wet based ice system is compatible with a high heat flux along the MAR (Bourgeois et al., 2000).

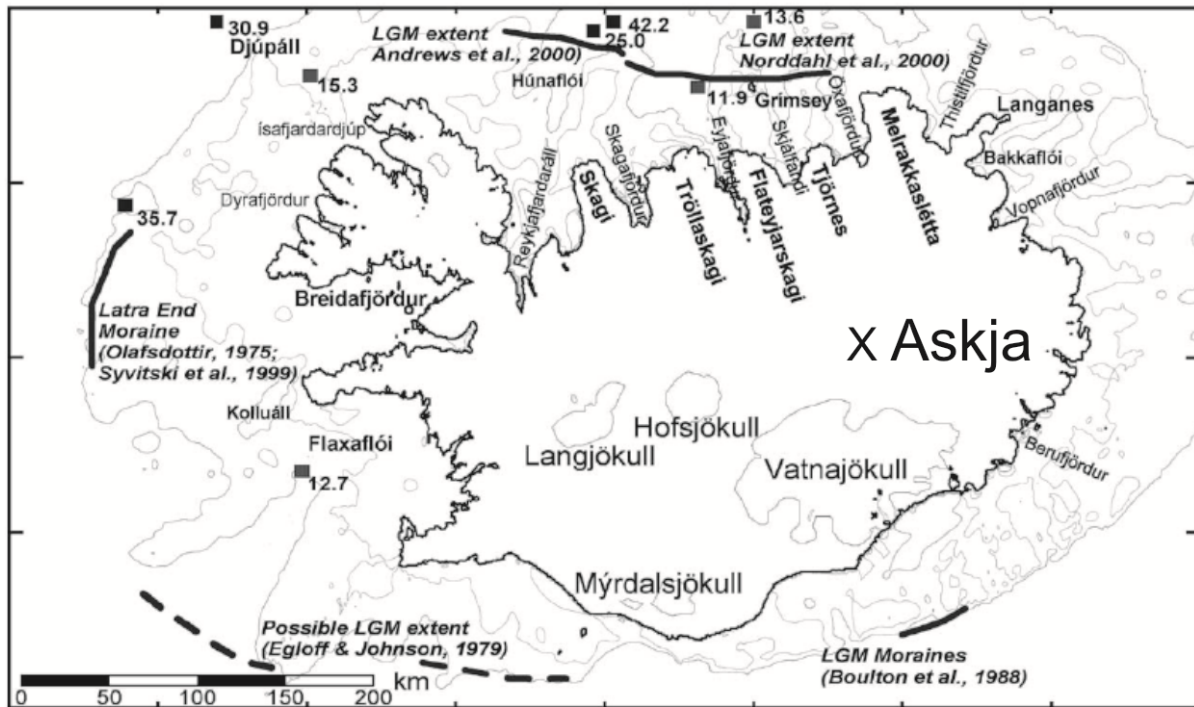


**Figure 8.2** Modeled extent of the Last Glacial Maximum ice sheet in Iceland adapted from Hubbard et al. (2006). Numbers indicate feature ages in thousands of years, and references are noted. The location of offshore end-moraines is illustrated. The position of Askja was fairly central to this large ice sheet.

#### 8.3.4 Deglaciation

Warming, as indicated by Greenland ice cores, began around 14 ka, that was interrupted by the colder Younger Dryas at 12 ka, followed by more rapid warming (Slater et al., 1998). Marine fossils associated with the initial phase of deglaciation of the Icelandic shelf correlate well with deglaciation beginning around 13.6 ka (Norðdahl and Petursson, 2005). The north coast line of Iceland was ice free by 12 ka (Knudsen and Eiriksson, 2002), exposing the shelf rapidly. The last identified temperature minimum occurred 10.5 ka (Sigmundsson, 1991). However, peak Holocene temperatures did not occur until around



5 ka (Axford et al., 2007). Local studies of ice retreat reveal the complex nature of deglaciation in Iceland and the piecemeal nature of the retreat. Localized ice bodies may have remained throughout the highlands up to around 7 ka (Annertz et al., 1985; Larsen, 2002; Thorarinsson, 1968).

Following the retreat of the glacial margin the unloaded areas of coast line experienced rapid isostatic rebound, with estimates for a return to equilibrium in only 1 ka (Sigmundsson, 1991). During rebound the sea level would be fluctuating due to significant volumetric inputs from the melting ice sheets. Initially, glacial loaded coast lines were submerged, creating inland shorelines with their associated fossil assemblages dated to 12.8 ka  $\pm$  200 yr, that are now located 20-60 m above modern sea level (Norðdahl and Petursson, 2005). Rapid retreat of the LGM is supported by the conformable contact between glacial deposits and overlying marine sediments where minimal sedimentation and / or disruption of the deposits occurred following the retreat of the ice sheet until the marine sequence was reestablished (Norðdahl et al., 2008). Marine cores on the northern Icelandic shelf indicate that there was a stable vertically stratified oceanographic system around 9 kya (Eiriksson et al., 2000).

The crustal thickness under Iceland is 20 km (Slater et al., 1998) to 30 km (Eiriksson et al., 1996) with the highest current elevations on the order of 2100 m asl, on the Vatnajökull glacier. The central highlands occupying the region north of Vatnajökull, including Askja, has elevations between 600 and 1900 m. Geothermal flux under Iceland is particularly high, currently concentrated under the Neovolcanic zone. This high geothermal flux results in a responsive lithosphere that deforms rapidly to isostatic loading and unloading (Eiriksson et al., 1996; Slater et al., 1998).

### **8.3.5 Minor cooling periods**

Following the onset of deglaciation there were several notable drops in temperature associated with temporary re-advances in the ice sheet. Coastal records during this period are highly complex due to the compound records of fluctuating sea level and rapid isostatic rebound. The Younger Dryas 13 ka cooling observed in changing marine fossil assemblages, was locally tied to a weakening of the Irminger Current

associated with the disruption of thermohaline circulation in the North Atlantic (Norðdahl and Petursson, 2005). Two local shore lines (Younger Dryas and Preboreal 10.24 k a, 9.8 k a) reflect these cooling periods, with minimum postglacial sea level (-40 m asl) occurring around 8.8-9.2 ka (Norðdahl and Petursson, 2005). A rapid 3 -2.5 ka cooling appeared in the pollen records (Knudsen and Eiriksson, 2002). This period may be associated with the establishment of the current ice caps (Einarsson and Albertsson, 1988).

### **8.3.6 Modern ice coverage in Iceland**

Currently, 11% of the surface area of Iceland is still covered by ice. The largest icecap is Vatnajökull (Geirsdóttir and Eiriksson, 1994), the 4<sup>th</sup> largest ice sheet globally following the east and west Antarctic ice sheets and Greenland. Current Vatnajökull ice sheet thickness are 750-1000 m (Werner and Schmincke, 1999). The polar front represents the modern extent (and seasonally and annually variable) of sea ice (Syvitski et al., 1999).

The modern climate of Iceland is cold-temperate and maritime in the lowlands and low arctic in the highlands (Syvitski et al., 1999). Areas above 550-600 m asl can have permafrost (Björnsson and Pálsson, 2008). The most recent trends in glacial ablation were estimated around 300 km<sup>3</sup> of ice lost over the last two centuries (Björnsson and Pálsson, 2008). However, it is also important to appreciate the impact of continued volcanic activity beneath several of the large ice bodies in Iceland on the rate of ablation. The eruption in 1996 Gjalp eruption of Grímsvötn was studied in depth and provided valuable information on the relationship between volcanic features and volcanic eruptions. The occurrence of this large volume of ice in such an active geothermal and volcanic area affects the stability of the remaining ice.

#### **8.4 JUSTIFICATION OF ASKJA AS A RECORD OF PALEO-ICE THICKNESS**

Askja, a central volcano on the mid-Atlantic Rift, in the central highlands of Iceland, sits in the NVZ about 40 km north of the modern margin of the Vatnajökull. Its position is close to the proposed center of the LGM ice sheet. The complex is currently ca. 1500 m asl (with 800 m thick glaciovolcanic deposits) and several hundred kilometers from the modern coast. Unlike studies of the Eastern Volcanic Zone (EVZ) in southern Iceland there is no requirement to distinguish between submarine and glaciovolcanic magma-water interaction. Ice divides modeled for the LGM (Bourgeois et al., 2000) suggest that meltwater produced from ice retreat and volcanic activity likely drained towards Axarfjörður to the north (Figure 8.3). Glacial features on either side of the NVZ diverge away support the position of a former ice divide (Bourgeois et al., 2000). However, the active volcanic zones is lacking significant streamlined glacial features due to the dominance of postglacial lava flows near around the NVZ.

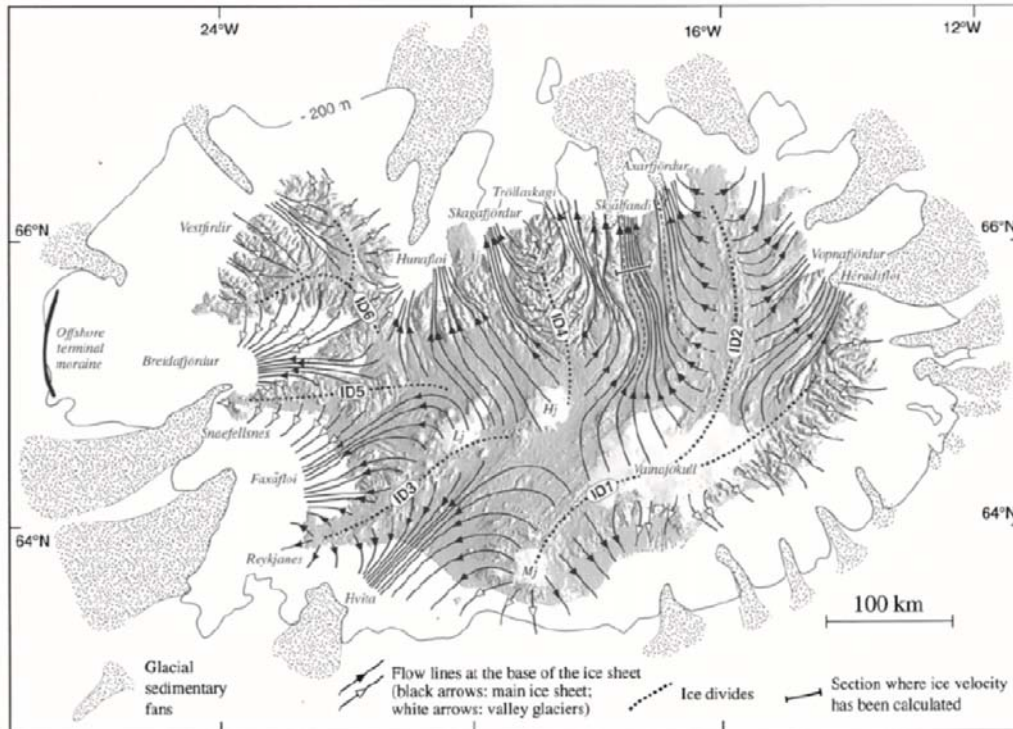


**Figure 8.3 Modeled ice flow models for the LGM ice sheet from Bourgeois et al. (2000).**

The regional topography of Askja is on average 660 m asl, with isolated topographic features such as the table mountain Herðubreið and other small glaciovolcanic features (Chapter 5). Consequently, there is no topographic feature that would be able to pond the large volumes of water indicated by the presence of the subaqueously emplaced deposits of Askja. The first criterion of any glaciovolcanic deposit-based proxy is the absence of contemporaneous topography that would be able to confine a meltwater lake. This indicates the former presence of volumes of ice thick enough to impound meltwater to enable the formation of the 800 m thick sequence of glaciovolcanic deposits. The position of the massif relative to the center of the proposed LGM ice sheet supports ice thicknesses on this order of magnitude. However, the geothermal heat flux in Iceland is highest in the NVZ, which may have affected the thickness of wet-based glaciers in this region (Bourgeois et al., 2000).

The existing knowledge of the presence, distribution, and thickness of ice in this area is limited. The thickness of the Austurfjöll deposits themselves indicates that it was erupted under a minimum of 700 m of water. Transitions from subaqueous to subaerial deposits as a result of the emergence of the massif are here referred to as a paleo-water level. The transition of subaqueous to subaerial deposits as a result of drainage of water from the ice-confined lake is called a drainage event.

Glacial features in the area, such as stream lined landforms and glacial striations are obscured by the large volume of postglacial lava in the region. A 327 m tall interglacial (70-100 ka) shield volcano that sits approximately 10 km to the SW of the complex. This feature, which has not been described in great detail, has a surface of exposed subaerial lava flows and is heavily eroded by a combination of glacial and eolian processes. The morphology of the shield reflects significant erosion along its western margin corresponding to the path of the glacially fed Jökulsá á Fjöllum (see map Chapter 5). This is one of the only regional evidences for pre-LGM conditions.

Additionally, Herðubreið, one of the most famous Icelandic tuyas (a glaciovulcanic to emergent monogenetic eruptive center) is situated about 30 km north of Askja. This feature is approximately 1069 m above the surrounding plain and is reported to preserve a few glacial erratics at its summit (Werner et al., 1996). This then suggests a period, tentatively dated around 10 ka (Licciardi et al., 2007), where the ice thickness was on the order of 1000 m in the vicinity of Askja.

## **8.5 REGIONAL DATA**

Jökulsá á Fjöllum the glacial river fed by Vatnajökull (Figure 1.2) has frequently flooded the area around Askja throughout the Pleistocene, removing unconsolidated glacial deposits (Annertz et al., 1985) and burying striae. The extensive cover of the LGM ice sheet in Iceland has resulted in the preservation of Holocene glacial features. Older features have been overrun and altered by ice and water. Currently the largest topographic features in Iceland are glaciovulcanic edifices like Askja (sitting 800 m above the

surrounding plains). The question of whether these features would be able to divert ice flow, or would rather be overridden and altered (Bourgeois et al., 2000) is still being debated. Glaciovolcanic eruptive deposits have a high glass content and clastic nature, which makes the deposits poor preservers of glacial signature, but evidence at Askja clearly reveals the intrusion of glaciovolcanic basalt into diamictite deposits, local striae, and glacial erratics. Diamictons, putative tillites, have been described in Iceland and Antarctica (Bennett et al., 2006; Bergh and Sigvaldason, 1991; Carrivick et al., 2009; Larsen and Eriksson, 2008; Smellie, 2008), but the identification of glacially overridden glaciovolcanic edifices is still a challenge. It is likely that more glacially altered glaciovolcanic massifs are preserved, than have been reported. Silicic glasses are far more resistant to erosion than basaltic glass (Jakobsson and Gudmundsson, 2008) and are better candidates to preserve such textures, but form fewer and smaller massifs (Tuffen et al., 2010). Nunataks in northwest Fjordland provide important paleo-ice thickness information, and help constrain models of ice distribution. These Nunataks are made up of Tertiary lava piles, and have survived numerous glaciations (Bourgeois et al., 2000; Norðdahl et al., 2008).

### **8.5.1 Offshore evidence**

The small size of Iceland, and its position in the North Atlantic, has resulted in several glacial periods that completely cover the island. A large number of terminal moraines from the LGM occur offshore (Bourgeois et al., 2000; Geirsdottir and Eiriksson, 1994) (Figure 8.2). Látra moraine along SW Iceland is thought to represent the furthest extent of the LMG ice sheet in this region, and is one of the most impressive examples of moraine deposits in Iceland (Syvitski et al., 1999). This feature has been seismically profiled and imaged. The moraine is up to 100 km long and typically 20 m tall with occasional points of 100 m relief above the surrounding sea floor. The moraine is currently under 350 m of water (Syvitski et al., 1999). Dates of deposits on the coastal shelf suggest this period of greatest ice extent range from 13 to 40 ka (Hubbard et al., 2006).

Bathymetry and sonar seismic imagery of the Denmark Strait (western Iceland) revealed large scale glacial scour up to 5-30 m deep and widths of 40-300 m (Syvitski et al., 1999). These features are notably deeper on the shelf sediments and distinctive from structurally controlled troughs present on the shelf (Hubbard et al., 2006). Glacial striae occur at sea level on Grímsey Island, 30 km off the northern coast of Iceland (Bourgeois et al., 2000), reveal a minimum extent of the ice on the northern Icelandic shelf. Models based on the distribution of these offshore features and marine cores suggest that the ice sheet extended some 50-120 km to the shelf edge (Hubbard et al., 2006).

The continental shelf around Iceland has been drilled extensively (Andrews, 2005; Birks et al., 1996; Einarsson and Albertsson, 1988; Eriksson, 2008; Knudsen and Eiriksson, 2002). These cores contain marine sediments, terrestrial derived sediment gravity flow deposits, tillites, dropstones, marine fossils, tephra, and pollen. These cores are ideal for detailed climate reconstructions due to high sedimentation rates that preserve rapid climatic variation, and the large number of recognizable tephra layers. Icelandic ice sheets produced larger volumes of sediment than associated ice sheets in Greenland (Syvitski et al., 1999) likely as a result of volcanic related meltwater flood events. Most fjords in Iceland are <200 m deep due to rapid infill by terrigenous sediments (Syvitski et al., 1999).

Tillites and drop stones in these cores indicate periods of glaciation (Eiriksson et al., 2000; Knudsen and Eiriksson, 2002). Land surface temperatures are preserved in pollen records, e.g. birch (Einarsson and Albertsson, 1988) and marine fossils represent ocean temperatures and the relative strength of local currents (Eiriksson et al., 2000). The high frequency of volcanic tephra enables the dating and correlation of fluctuations in ice extent and sea level. Two of the most important stratigraphic markers, identified in cores and seismic reflection data are the Vedde (10310  $\pm$  50 BP) rhyolitic tephra and the Saksunarvatn (10180  $\pm$  60 cal BP) basaltic tephra. These tephra have a distribution over most of northwest Iceland, but have not yet been documented at Askja. These tephra markers are highly distinctive and occur as layers 2-3 cm in thickness on the Northern Icelandic shelf (Eiriksson et al., 2000). Other important tephra layers are sourced from the frequently active Hekla volcano in SW Iceland (Knudsen and Eiriksson, 2002) which have been used successfully to date postglacial lavas in and around

Askja (Annertz et al. 1985). In marine tephrochronology it is important to distinguish primary ash from the significant volume of ash erupted during the Pleistocene and early Holocene that was deposited on ice and carried as ice rafted debris before deposition (Birks et al., 1996).

### **8.5.2 Onshore evidence**

The terrestrial record of glacial and interglacial periods is far more dislocated than the marine record. Onshore glacial evidence include striae, streamlined landforms (Bourgeois et al., 2000), trim lines (Hubbard et al., 2006), ice confined / marginal deposits, glacial outwash and outburst flood (jökulhlaup) deposits, limited moraine deposits, and transgression / regression sedimentary sequences (Norðdahl and Petursson, 2005). The majority of ice thickness estimates in Iceland have been drawn from saturation pressures calculated from glaciovolcanic volcanic glass (Bourgeois et al., 2000). The applications and limitations of this method are outlined in detail in (Owen et al., 2012; Tuffen et al., 2010). As it currently stands, secondary ice-thickness correlations (e.g. trim lines, paleo-water levels, passage zones) are required for confident estimates, as with any paleoclimate proxy. As the technique improves there will be ample opportunity for precisely dating ice distribution and thickness throughout Iceland.

Other geochemical techniques applied to glaciovolcanic deposits include  $^3\text{He}$  dating (Licciardi et al., 2007). This technique aims to date time which a surface has been exposed to solar radiation and cosmogenic  $^3\text{He}$ . However, it is highly difficult to constrain the exposure age of a surface that is subject to seasonal snow cover, ash cover, and even temporary ice coverage. Askja's neighbor, Herðubreið, that indicates a minimum ice sheet thickness of 1000 m has been dated using this method to 10 ka (Licciardi et al., 2007), however, if the massif were truly impacted by a later glaciation (Werner and Schmincke, 1999), this age would instead reflect the age of glaciation, not the age of eruption. This suggests that ice thicknesses may have reached 1000 m in the region.



Morphological evidence includes streamlined landforms, trim lines, and nunataks (Bourgeois et al., 2000; Norðdahl et al., 2008). Nunataks and intensive periglacial frost shattering of bedrock are indicative of ice-free zones (Einarsson and Albertsson, 1988; Norðdahl and Petursson, 2005) and occur mainly in northwestern and northeastern Iceland. A correlation between the central highlands and coastal ice-free Nunataks suggest that the ice sheet would have been fairly low profile, forming a fairly flat dome extending to the sea (Bourgeois et al., 2000). However, as detailed localized investigations continue there is increasing evidence for far more local ice bodies, covering areas such as the Reykjanes Peninsula (Eiriksson et al., 1996).

## **8.6 FORMER ICE-PRESENCE AT AUSTURFJÖLL**

Deposits which record specific evidence of the interaction of volcanic deposits and the dynamic eruptive environment at Austurfjöll are diverse and widely distributed (Figure 8.4). In conjunction with unspiked K/Ar dating the paleoenvironment of Austurfjöll can be reconstructed.

### **8.6.1 Ages**

Two major glaciovolcanic eruptive units of Austurfjöll were dated at 71 ka +/- 8 ka and 29 ka +/- 7 ka using unspiked K/Ar dating (described in Chapter 3). The dated units make up a significant portion of the 3.62 km<sup>3</sup> massif, where Unit 2 is 2.31 km<sup>3</sup> and Unit 3 is 0.14 km<sup>3</sup>. At least 1 km<sup>3</sup> of glaciovolcanic and emergent deposits within the massif are younger than 29 ka, occurring during the end of the Weichselian, but before significant deglaciation had occurred. These deposits help constrain the geologic evidence of ice presence and inform the paleoclimate reconstruction of Austurfjöll. The preservation of rhyolitic tephras on postglacial lavas in the Askja caldera indicate that the area was ice-free before c. 4 ka (4.030 ka +/- 120 <sup>14</sup>C) (Annertz et al., 1985; Larsen, 2002).

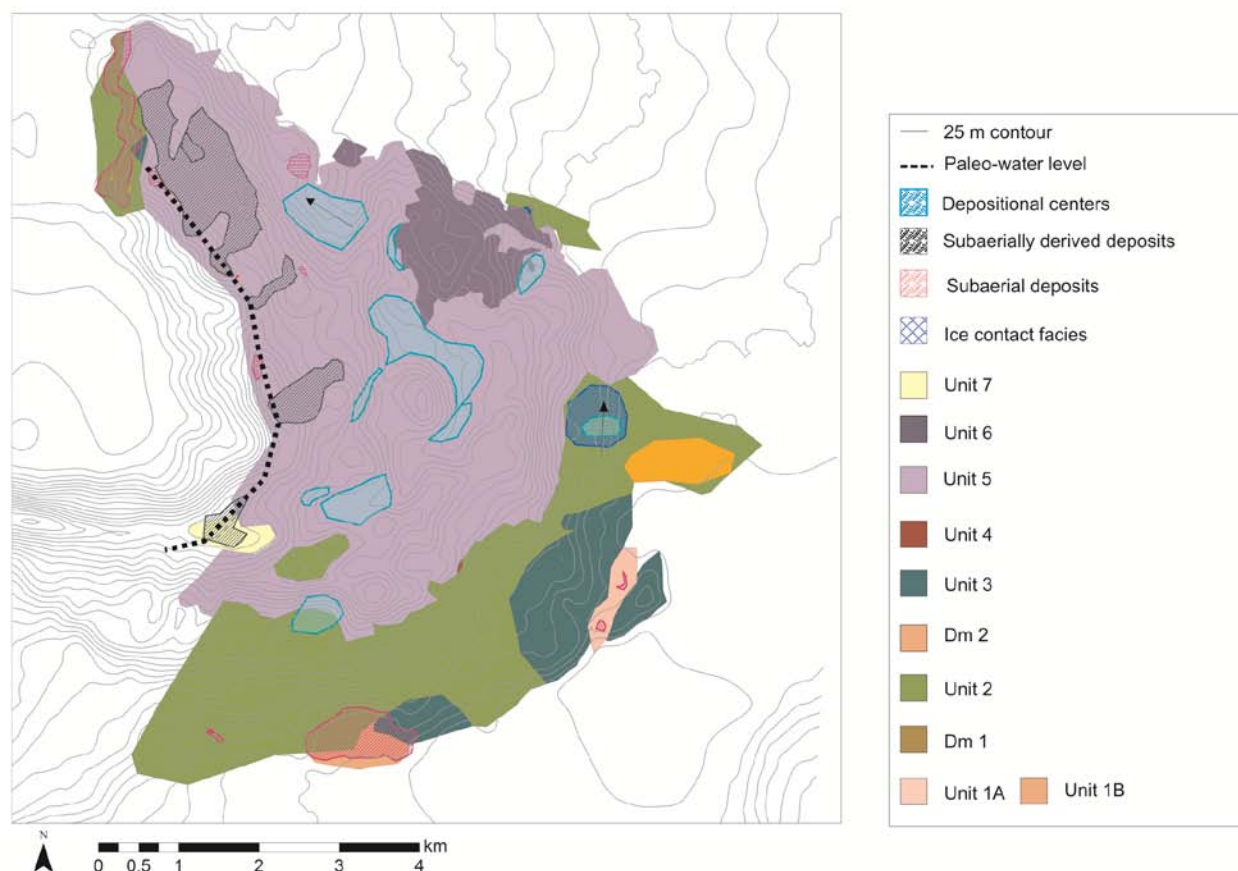


**Figure 8.4** Location of paleoenvironmental indicators overlain on chemostratigraphy map of Austurfjöll. The largest paleo-water level is at 1290 m asl. Arrows indicate the orientation of drainage channels and proposed direction of flow.

### 8.6.2 Deposits

Two major glacial lithofacies were described from Austurfjöll massif and they were documented in two, well-constrained glacio-sedimentary units (Dm1 and Dm2) within the basaltic glaciovolcanic deposits. These deposits were identified by their high matrix content, glacially scoured clasts, and heterolithic

componentry. Full descriptions of the deposits occur in Chapter 2 and Chapter 4. The distribution of diamictite deposits is limited at Austurfjöll to pockets in gullies at the base of the massif and local mantling deposits that range between  $0.3\text{--}0.6 \times 10^5 \text{ m}^2$  in modern distribution. Isolated glacial erratics were observed locally throughout the study area, but were not always associated with diamictite deposits. The identification of glacial erratics was based on the large size of blocks, polish, and position on topographic highs (i.e. not the result of mass wasting).

Glacial scour of subaerial lavas occurs on both Unit 1A and 1B. The most extensive area of glacial scour is in the southeastern corner of the massif on Unit 1B. The orientation of the scour is  $220\text{--}290^\circ$  roughly parallel to the dominant orientation of the rift in this region. This orientation is not unreasonable for the expected flow lines of the LGM ice sheet as proposed by Bourgeois et al. (2000) based on topography and heat flux (Figure 8.3).

#### **8.6.2.1 Evidence of interaction with ice**

Isolated outcrops show evidence of direct interaction of lava or previous deposits with glacial ice. These outcrops are fairly small in extent ( $10 \text{ m}^2$ ). Surfaces interpreted to represent ice-contact surfaces include vertical pillows and radial cooling cracks on over steepened subaqueous lavas (Figure 2.4 and 2.8). These features are produced where the advancement of a lava flow is restricted, or confined by ice, and cooled rapidly. Radial cooling cracks are distinguished from typical columnar joints due to their radial orientation and the increasing spacing of the joints towards the interior of the flow (Figure 8.5). The orientation of the radial cracks can be used to estimate a cooling surface that represents either melt water or potentially direct ice contact. At Austurfjöll the only deposits that exhibit this style of cooling cracks is Unit 6 at approximately 875 m asl. This flow likely defines a cooling surface located at the end of the subaqueous lava flow as it travelled over a dipping paleo-surface of Unit 5. Vertical pillows indicate the presence of a near vertical surface that is overtopped by an advancing pillow flow. The vertical pillows observed in Unit 2 were emplaced over an obscured surface what is likely pillowed lavas. This may indicate confinement of the underlying pillow lava flow during advance of the flow, forming a near

vertical surface in proximity / contact with an ice wall. This stalled flow was later overtopped by the vertical pillow flow. The vertical pillows likely formed in the space formed between the previous flow and the retreating ice.

There is limited discussion in the literature of direct ice-sediment contact surfaces at glaciovolcanic surfaces. Sediments confined by an abutting ice wall are described in Antarctica and Iceland (Mercurio, 2011; Skilling, 2009; Smellie et al., 2008). Askja is the only known location of CMVDs that reveal magma interacting with ice-cemented sediments, (Chapter 7 and Graettinger et al. 2012.). The presence of these deposits in Unit 2 suggests that the ice annealed over portions of the massif after the initial eruption of deposits.

#### **8.6.2.2 Evidence of moving and ponding water**

Large erosion channels are described from three-dimensional exposures in Chapter 2 and Chapter 4. The channels are filled with both sedimentary and volcanic units, such as pillow lavas. At least one channel is filled with sedimentary beds (At2 and At3) that can be relatively dated. The channel was both eroded into and filled with material from eruptive Unit 2. These deposits were then cross-cut by a dike, also of Unit 2 composition. The largest of the drainage channels are oriented parallel to the margin of the massif, rather than radiating away from the high elevations of the massif.

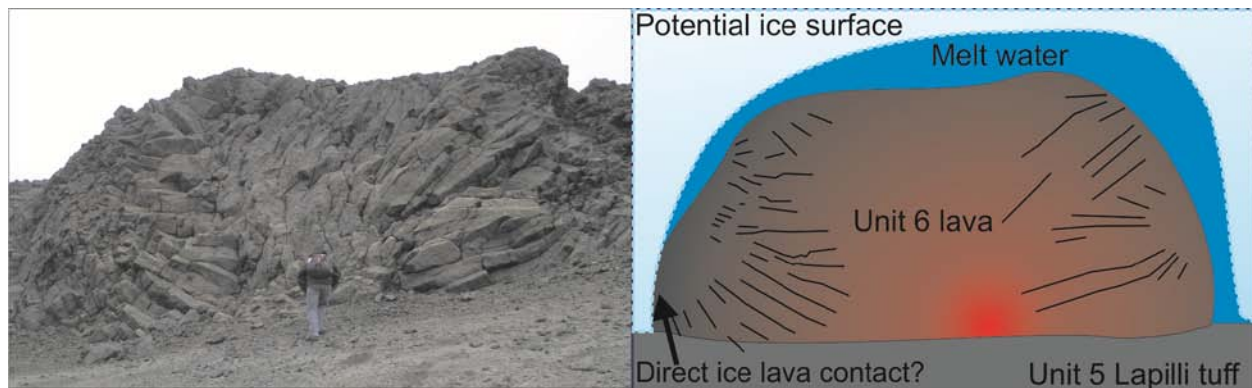


**Figure 8.5 Example of ice confined lava in Unit 6 at an elevation of 850 m asl. The orientation of the radial cooling cracks can be used to estimate a cooling surface that likely reflects the position of ice around the flow.**

**The cooling surface may be a thin water film, or direct ice contact.**

There is some evidence that indicates sediment transport conditions where the massif was not completely submerged. Under these conditions water and sediments likely accumulated in topographic lows between fissure ridges. The topography currently is mantled by 1875 pumice, but accumulation of remobilized pumice illustrates the way the topography of the ridges funnels material into the local lows of the massif (Chapter 5). However, these inter-ridge depositional centers may also be areas of slumping without ponding of water. Calculations presented in Chapter 4 regarding the volume of the massif and the number of constructional features present indicates that there are likely 16 major inter-ridge depositional centers and erosional channel-fills.

Drainage events are common in glaciovolcanic systems (Bennett et al., 2006; Bjornsson, 2002; Carrivick et al., 2004; Gudmundsson et al., 1997; Höskuldsson et al., 2006). However, most of the observed and documented events occurred under modern ice caps that are <10% of the aerial extent of the LGM ice sheet. Significant drainage events can be triggered by lifting the surrounding ice, thermally melting pathways, and collapse of an ice dam (Smellie, 2006). The scale of an LGM ice sheet may somewhat impede the drainage of water from an ice-confined lake central to the ice mass (i.e. Askja),

however, the high geothermal heat flux of the NVZ and local hydrology likely enables the transport of water away from the ice-confined lake. Catastrophic drainage events may be less likely in thick ice scenarios, but nevertheless these large channels indicate periods of erosive water transport parallel to the margin of the massif. This orientation suggests that the water may have been influenced by an overlying ice sheet, or the directed flow of an outburst flood directed by laterally confining ice. Regional evidence of ice position and timing may help constrain the potential for outburst flood drainage or more prolonged englacial water pathways.

### **8.6.2.3 Emergent activity, paleo-water levels, and drainage events**

The Austurfjöll massif is dominated by subaqueously emplaced deposits. Local exposures of subaerial deposits are exposed in the caldera walls at elevations above 1250 m asl. Downhill from these deposits, with dips point away from the caldera are subaerially derived breccias and lapilli tuffs (B3, Lt3, Lt4). These deposits all occur in Unit 5. There are rare examples of bomb sags in deposits within 20 m downhill of the subaerial lithofacies. However, many of these bomb sags occur in slump blocks. As Unit 5 occurs stratigraphically above the radiogenically dated Unit 3, this paleo-water level is younger than 29 ka.

The only other eruptive unit with subaerial deposits is Unit 2, which is radiogenically dated to 71 +/- 7 ka. The exposure of subaerial deposits consists of three isolated exposures of subaerial lava overlying subaqueous deposits. Subaerial lavas are recognized by the presence of scoriaceous tops, lower vesicularity, red oxidation staining, and an abundance of oxide minerals in the groundmass. The largest exposure of subaerial lava occurs along the north western margin of the massif, exposed in the Askja caldera wall. The exposure extends over 1.5 km and is about 25 m thick. The lavas occur in broken exposures covered by talus and slump blocks. Many of the subaerial lavas are micro-porphyritic, but some porphyritic examples occur. Some exposures include local breccia derived from the subaerial lavas. The lavas are fairly low angle and dip slightly toward the north. The lavas occur from 1160 to 1200 m above sea level.

In the southeast corner a 0.01 km<sup>2</sup> exposure of a series of 30 cm thick subaerial lava flows occurs at 800 m above sea level. This exposure is unique for its elevation and lack of similar deposits nearby. The lava sequence is roughly 2 m thick and is covered by 50 cm of bedded ash and lapilli. The bedded deposits are deformed and disrupted by an overlying pillow lava sequence that reached tens of meters in thickness laterally (Figure 8.6). Tracing the subaqueous lavas downhill is difficult due to poor exposure, but the lavas transition into pillowed lavas by 20 m vertically down section). Subaerial tephra is recognized by the occurrence of bedded layers of cored lapilli near an expanding feeder dike (Figure 8.7).

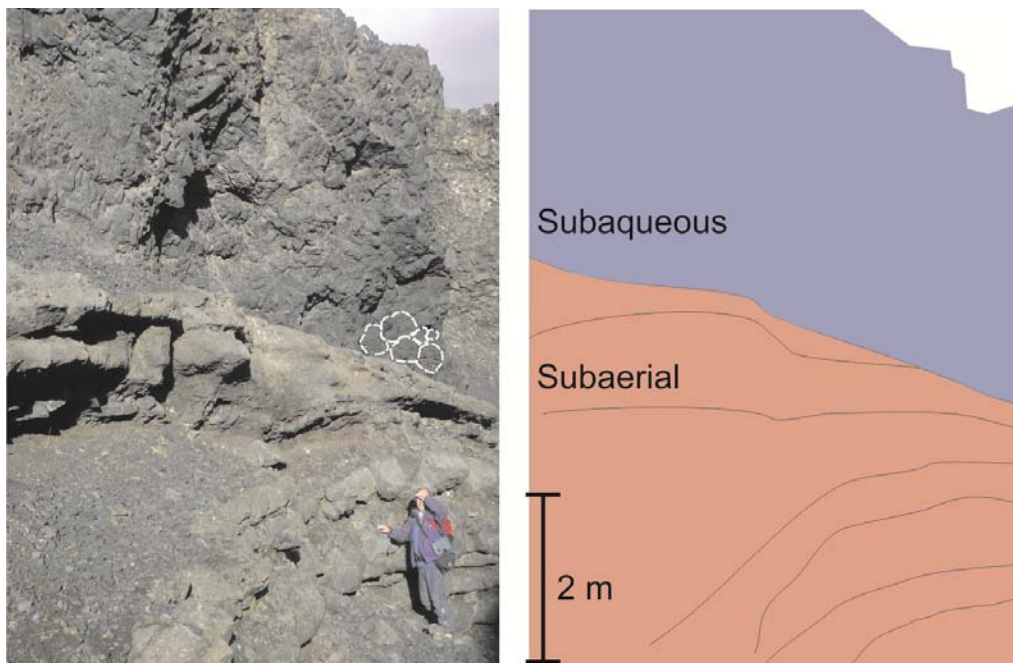


**Figure 8.6 Exposure of subaerial lavas buried by subaqueous pillow lavas at 800 m elevation in eruptive Unit 2. White lines indicate outlines of pillows in the outcrop. The angle of the image does not show the thin (20 cm) of bedded ash between the two deposits.**



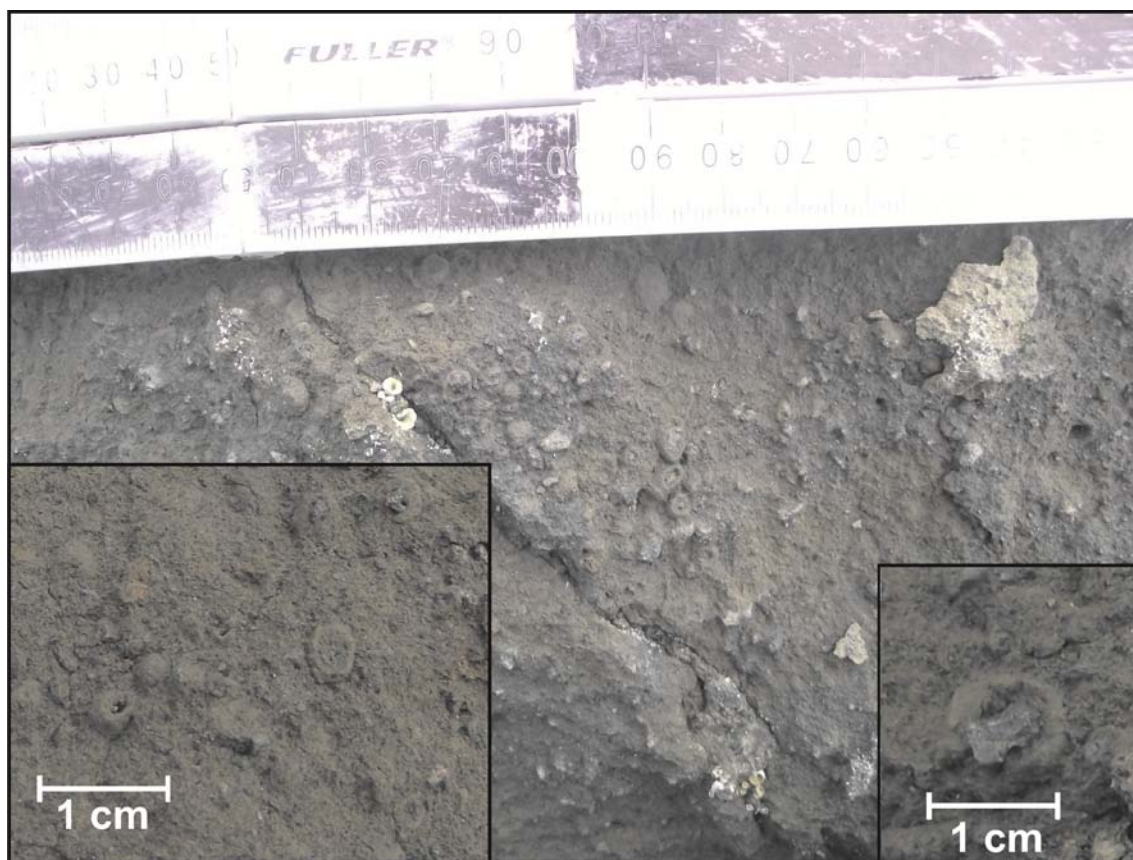


**Figure 8.7 Coated lapilli in subaerial lapilli tuff (Lt3). Divisions on black and white scale are 1 cm.**

#### **8.6.2.4 Interpretation of deposits**

Each eruptive unit contains slight variations in the lithofacies, elevation and distribution of deposits, the combination of which serves as evidence for the environmental conditions at the time of eruption. Each eruptive unit then will be discussed for the evidence of paleoenvironment during the time of that eruptive unit before discussing the implications of Austurfjöll as a whole (Figure 8.8). The estimated scale of ice-confined lakes and ice positions are catered toward the minimum value for any feature at the time in question (lake size, ice thickness etc.). The two largest eruptive units Unit 2 and Unit 5 contain the greatest detail relating to eruptive environment but conservative estimates of the other eruptive units are also possible. The large volume of these eruptive units and the abundance of explosive activity suggest



that the eruption likely rapidly eroded through the ice creating an ice-confined lake. However, each eruptive unit had its own complex interaction with the ice sheet, which is partially preserved in the geomorphic evidence (Table 8.1).

Units 1A and 1B are entirely subaerial and are currently exhibit a fairly planar surface. This surface is locally glacially scoured, but the orientation of lava flows suggests that they were also emplaced over a planar surface. This indicates that Unit 1 was erupted under unconfined subaerial conditions. The lavas are locally over topped with Dm1 diamictite (Dia 1 and Dia 2) of glacial origin. Dia 2 indicates fluvially action of glacially derived clasts, such as in an outwash plain that would suggest the absence of ice, or a voluminous subglacial drainage system. Dia 1 occurs as localized basal or melt out till which is locally eroded and intruded by Unit 2 pillowed dikes. These dikes suggest that the diamictite was not consolidated at the time of dike emplacement, which suggests that Unit 2 eruptive phase occurred not long after the deposition of Dm1.

Diamicton and paleo-outwash plains have been discussed at a variety of glaciovolcanic landforms in Iceland (Bennett et al., 2006; Bergh and Sigvaldason, 1991; Carrivick et al., 2009; Smellie, 2008). But the descriptions are limited due to both the difficulty of distinguishing these deposits in some locations, and the significant erosion and burial of any deposits in low lying areas in Iceland. The diamictite deposits are typically limited in distribution and can have gradational contacts with volcanic breccias or be heavily intruded (as is the case in Austurfjöll). Any descriptions of paleo-outwash acknowledge that they can be easily confused for younger or even modern unconfined fluvial deposits (Carrivick et al., 2009). Scour of underlying bedrock is equally limited in the literature and most common in areas of frequent jökulhlaup activity on bedrock surfaces, e.g. Kverkfjöll (Carrivick et al., 2004). These deposits suggest the presence of ice, but do not indicate the thickness of ice required to create these features.

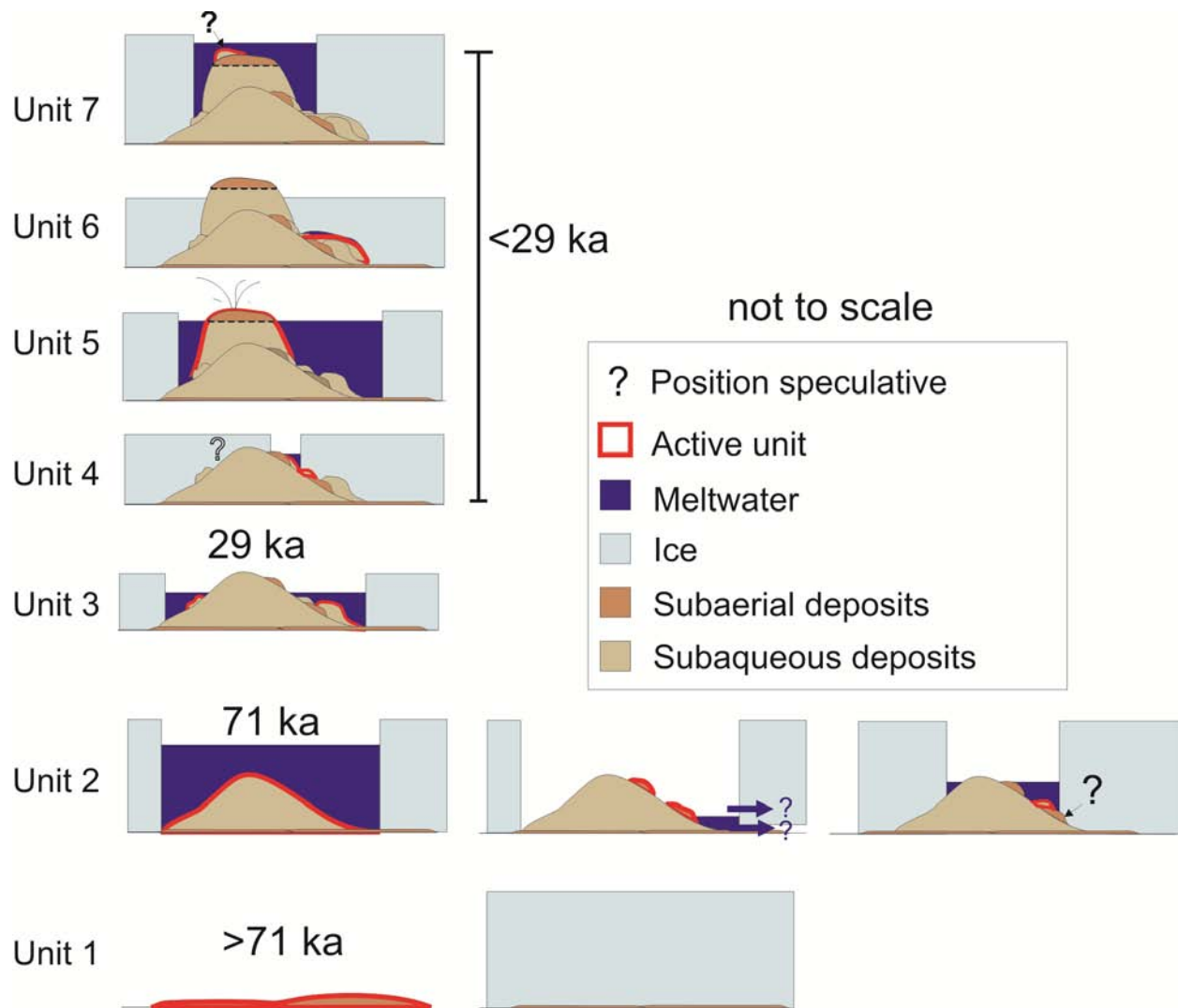


**Figure 8.8** Cartoon of ice thickness and relative position at Austurfjöll massif during construction for each eruptive unit. Elements of greatest speculation are denoted with a question mark in the color or arrow appropriate to the features in question. Lake size is intended to suggest order of magnitude scale only.

**Table 8.1 Summary of environmental indicators by eruptive unit.**

<b>Unit</b>	<b>Deposit types</b>	<b>Ice contact</b>	<b>Depo-centers</b>	<b>Interpretation</b>
<b>7</b>	Pillow breccia		Remobilized	Remobilized subaqueous deposits with a source in what is now the caldera, emplaced <b>after 29 ka</b> .
<b>6</b>	Pillow lavas only	Radially jointed lavas		Subaqueous (subglacial?) effusive eruption at moderate elevations mantling topography. Local interaction with the confining ice.
<b>5</b>	Subaqueous and subaerial deposits		Inter-ridge depositional centers	Predominantly subaqueous eruption <b>after 29 ka</b> that emerged to form a paleo-water level.
<b>4</b>	Pillow lavas only			Subaqueous effusive eruption at high elevations <b>after 29 ka</b> .
<b>3</b>	Pillow lavas and local tuff deposits			Eruption of predominantly subaqueous lavas and local explosive tuffs starting at <b>29 ka</b> .
<b>2</b>	Subaqueous and local subaerial deposits	CMVD's Local diamictite containing eroded clasts of Unit 2.	Large channels and channel fill.	Eruption of subaqueous lavas and tuffs starting <b>71 ka</b> in an englacial lake. Periods of rapid drainage resulting in significant erosion. Followed by further meltwater accumulation and continued subaqueous effusive and explosive activity. Local encroachment of ice onto fresh unconsolidated deposits. Deposition of diamictite.
<b>1 A/B</b>	Subaerial lavas	Glacial scour Local diamictite		Unconfined eruption of lavas from fissures followed by later glacial advance and scour with local deposition of glacial outwash and melt out till. Completed <b>before 71 ka</b> .

The deposits with the highest elevation in Unit 2 are subaqueous, and subaerial deposits confined to isolated pockets at variable elevations. This suggests that Unit 2 did not have a significant emergent component. These isolated subaerial lava exposures in Unit 2 are suggestive of changes in the ice-confined lake level. While subaqueous deposits continue up to 1309 m asl subaerial deposits occur at 1160, 850, and 770 m asl. The 1160 m deposits form the upper contact of the Unit 2 deposits in the area. Their relative position to the maximum elevation of subaqueous Unit 2 deposits indicate either that these lavas may have erupted after partial drainage of the lacustrine system, or that the deposits represent a temporary emergence before the water level within the lake increased. Unit 2 lavas displaying pseudo pillow fractures occur on some of the subaerial lavas and indicate that water or snow was nearby to produce steam during the interaction with the erupting lava (Lodge and Lescinsky, 2009; Mee et al., 2006; Tucker and Scott, 2009). A second paleo-water level occurs at 900 m asl, with coated lapilli and minor scoria near a small point source explosive vent.

The final exposure of subaerial deposits in Unit 2 occurs at 800 m elevation, only 150 m from the base of the sequence, suggesting significant drainage during the Unit 2 constructional phase. These deposits in the southeast corner of Austurfjöll represent a temporary local paleo-water level as they are overlain by thick sequences of subaqueous deposits. Modern and Pleistocene glaciovolcanic centers are associated with frequent large volume drainage events that can produce jökulhlaups, outburst floods which can dramatically alter non-glaciated terrains (Bennett et al., 2006; Carrivick et al., 2004; Gudmundsson et al., 1997; Höskuldsson et al., 2006). Drainage can occur at any point during the eruption exploiting fractures, lifting the confining ice, thermally eroding pathways, or the failure of an ice dam. Meltwater pathways can also be blocked or heal, and once the drainage path is sealed water levels can again rise and enable a return to confined subaqueous deposition (e.g. Gjálp) (Gudmundsson et al., 1997). These isolated deposits may indicate a single drainage event with multiple active vents erupting into the cavity within the ice sheet, or may represent multiple drainage prolonged events. Without further discrimination of timing within Unit 2, however, this drainage can only be described as a minimum of one event, of undetermined rate, that decreased the water level by up to 450 m. This drainage was

subsequently followed by at least one period of local refilling, as indicated by the pillow lavas overtopping the 800 m asl deposits. The volume of meltwater drained during this time may have been as high as 3.08 km<sup>3</sup>.

The drainage of large volumes of water during the eruption of Unit 2 at Austurfjöll is supported by the presence of large gullies up to 50 m deep in Unit 2 deposits through earlier lapilli tuffs. The poorly consolidated tuff would be readily erodible by water or ice. These erosional events can occur while eruptive activity continues, as evidenced by dikes cutting through unconsolidated sediment. Draining water also exploited paleotopography created by earlier eruptive units, which created steep sided gullies that are still active today. Locations where modern drainages accentuate paleotopography are indicated by packets of over-steepened bedded ash along the margins of the gully as discussed in Chapter 2.

The paleoenvironmental history of Unit 2 is further complicated by the presence of CMVDs discussed in Chapter 7. These dikes indicate that there may have been ice-cementation of the lapilli tuff during the intrusion of the Unit 2 CMVDs. This may indicate the healing of ice over the massif during this eruptive period, but may also indicate the presence of permafrost-like conditions under an ice-confined lake. The CMVDs occur from elevations of 750 to 850 m asl. The coincidental elevations of the ca. 800 m asl subaerial lavas and overlying pillow lavas, CMVDs, and the presence of Dm2 deposits at 750 m containing clasts of Unit 2 may reflect that the second filling of the englacial lake was associated with the encroachment of the confining ice back over the Austurfjöll massif as eruptive activity waned.

Unit 3 contains entirely subaqueous deposits at moderate elevations. The presence of effusive and explosive deposits is suggestive of activity within an ice-confined lake, but the minimum ice thickness required to confine this lake is less than Unit 2. The areal extent of the lake was likely on the order of 22 km<sup>2</sup> or greater. There is, however, no evidence against thicker ice.

Unit 4 has a very limited distribution, but is representative of effusive subaqueous activity at moderate elevations suggesting that a local lake may have ponded within a thick ice sheet at the elevation of the vent as a result of the eruption. If the limited distribution of deposits identified in the field is representative of the total distribution of the entire Unit 4 deposits, then the lack of explosive deposits

indicate that the confining ice during this phase of growth may have covered significant portions of the massif where there was no eruptive activity. However, there are no contemporaneously aged glacial surfaces currently identified at Askja.

Unit 5 makes up the bulk of the upper Austurfjöll with deposits occurring at a range of elevations, suggestive of an ice-confined lake, with an aerial extent at least on the order of that of the massif. The eruption of this unit was dominated by effusive and explosive subaqueous behavior which progressively emerged as the massif grew relative to the surface of the lake. This emergence is recorded the paleo-water level established through the presence of in situ subaerial lavas along the caldera wall at a fairly consistent elevation. No subaqueous deposits associated with Unit 5 were observed on Austurfjöll above this elevation. Furthermore, the absence of any subaerial deposits at lower elevations suggests that this lake level was reasonably stable for the duration of the Unit 5 eruption.

The deposits of Unit 6 are unique as they consist of a moderate volume of entirely subaqueous deposits. The pillow lavas of Unit 6 mantle Unit 5 deposits and occur at a range of elevations. The presence of ice-contact / confinement features on the lava flows suggests direct interaction with an ice sheet. This is the best example at Austurfjöll of a potential subglacial eruption, where the lavas thermally excavate the cavity for their emplacement through melting of the ice sheet in the location of the eruption.

As Unit 7 has a very limited distribution and is the product of remobilization, few paleoenvironmental conclusions can be drawn from it. Its elevation and pillow lava fragments are suggestive of subaqueous eruptions occurring at higher elevations than indicated by the Unit 5 paleo-water level, which may indicate an eruption under an ice sheet even thicker than estimated by either of the larger volume Unit 2 and Unit 5 eruptive phases. However, more deposits from eruptive Unit 7 would be necessary to draw any significant conclusions about the thickness of the ice sheet during this phase of the eruption.

### 8.6.3 Volatile saturation pressures

Nine samples of glassy pillow rinds were collected from Austurfjöll massif for volatile content analysis. Most samples were collected from basal pillow lava sheets, but several samples were collected from two dikes of the same eruptive units to see what, if any, variability occurred. These samples represent lavas from two major subaqueous eruptive units, with sample sites located near the base of the massif (Figure 8.9). The samples represent two eruptive units Unit 2 and Unit 5. These units were erupted at least 40 ka apart, and thus the environmental conditions are expected to be different.

Measured H<sub>2</sub>O concentrations for Unit 2 range from 0.350-0.53 wt. % H<sub>2</sub>O. Unit 5 had a range of compositions from 0.44-0.55 wt. % H<sub>2</sub>O (Table 8.2). Internal sample variability was typically on the order of 0.05 wt. % H<sub>2</sub>O. A comparison of water content relative to elevation reveals a linear trend in the Unit 2 data with decreasing water contents with position within the massif. Based on maximum water concentrations of Unit 5 the trend has a significantly shallower slope (Figure 8.10).

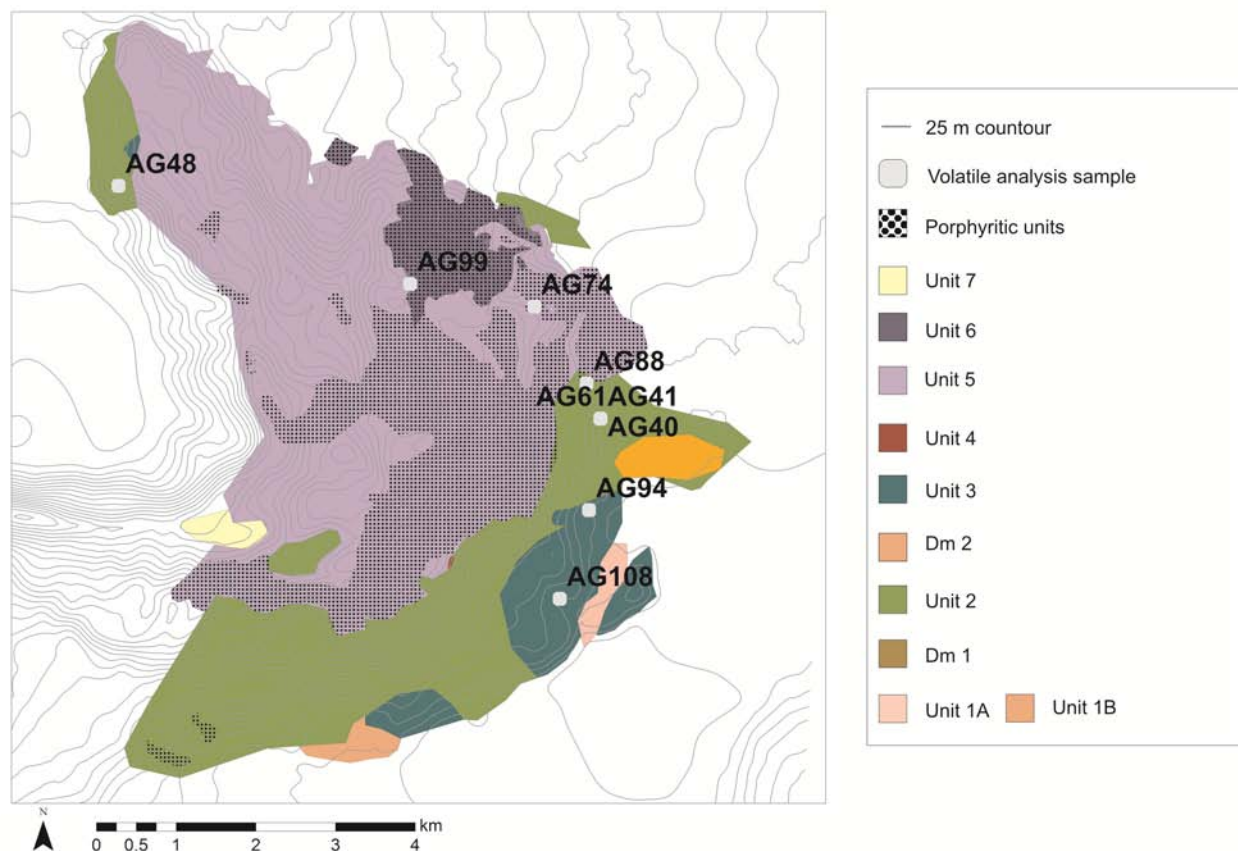


**Figure 8.9** Location of samples for volatile analysis. Samples either occur in Unit 2 or Unit 5. Samples AG 94 and AG 108 both occur in gullies where Unit 2 is exposed beneath Unit 3. Compositions of the samples were confirmed with microprobe analyses (See Chapter 3).



**Table 8.2 Summary of FTIR results and VolatileCalc computed volatile saturation pressures.**

<b>Sample #</b>	<b>Morphology</b>	<b>Unit</b>	<b>Sample elevation (m asl)</b>	<b>wt% H<sub>2</sub>O</b>	<b>wt% CO<sub>2</sub></b>	<b>Pressure MPa</b>	<b>Water depth (m)</b>	<b>Ice thickness (m)</b>	<b>Ice elevation (m asl)</b>
AG 74	Pillow mound	<b>5</b>	930	0.517	25	85	862	939	1869
					0	31	311	339	1269
AG 99	Pillow Mound	<b>5</b>	1000	0.446	25	75	765	833	1833
					0	20	204	222	1222
AG 48	Pseudo pillow	<b>2</b>	1160	0.367	25	67	683	745	1905
					0	13	127	139	1299
AG 94	Pillow sheet	<b>2</b>	710	0.572	25	84	851	928	1638
					0	29	296	322	1032
AG 108	Pillow sheet	<b>2</b>	730	0.455	25	79	802	874	1604
					0	24	245	267	997
AG 88	Pillow in dike*	<b>2</b>	750	0.475	25	80	813	886	1636
					0	25	257	281	1031
AG 41	Pillow in dike*	<b>2</b>	750	0.56	25	84	851	928	1678
					0	30	301	328	1078
AG 40	Chill margin*	<b>2</b>	780	0.208	25	59	602	656	1436
					0	5	51	56	836
AG 61	Chill margin *	<b>2</b>	780	0.257	25	66	673	733	1513
					0	12	117	128	908

As a test of volatile saturation pressure results, the chill margin and internal pillow of a CMVD (see Chapter 7) were sampled to for comparison. The dike is part of Unit 2 and was emplaced in unconsolidated sediments eroded into Unit 2 lapilli tuff deposits. Both the chill margin and the pillows that formed within the CMVD were sampled. The CMVD pillow samples plot well within the field of other Unit 2 lavas that occur proximally to pillow lava sheet rind samples lower in the same gully. The chill margins display the lowest  $H_2O$  concentrations of any of the samples (0.2 wt.%  $H_2O$ ).

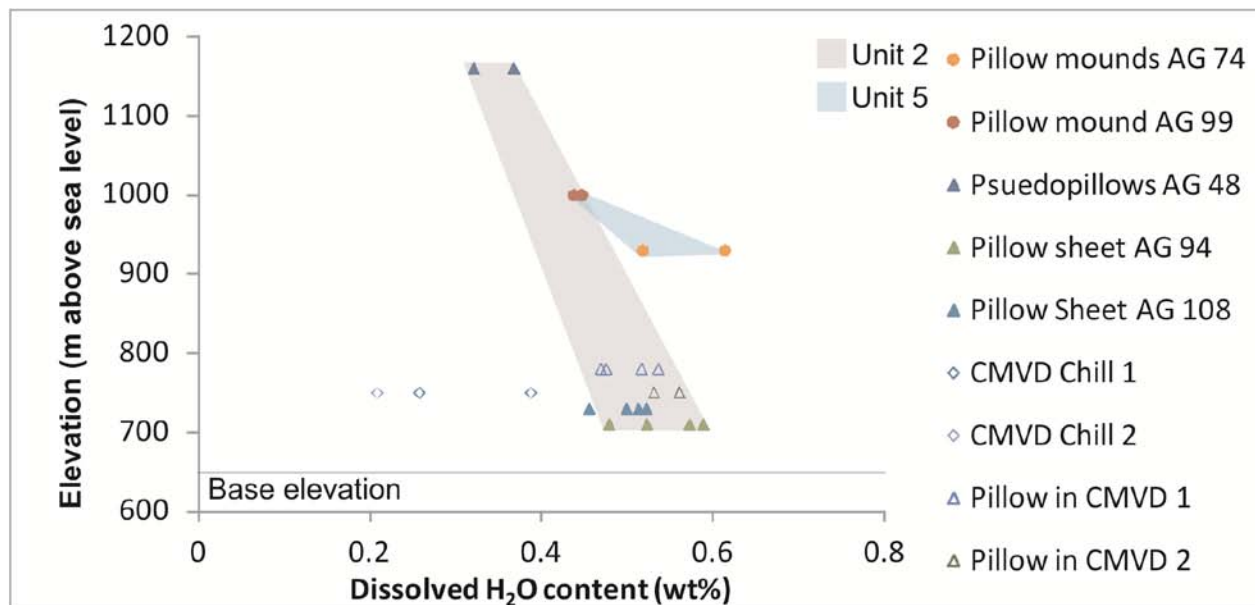


**Figure 8.10 Dissolved water content measured by FTIR compared with elevation of the sample.**

**Compositional unit and morphology of the samples is indicated.**

The CO<sub>2</sub> compositions for all samples were below the detection level (30 ppm), as such the saturation pressure of the glasses was calculated using the measured H<sub>2</sub>O and two values of CO<sub>2</sub> concentration to establish a potential window of values. For a minimum value 0 ppm CO<sub>2</sub> was used and for a maximum value 25 ppm CO<sub>2</sub> was used. The resulting values were then used to calculate the depth of water that would be required to produce these pressures, as well as pure ice. The range of values of water and ice thickness can exceed 530 m of water depth and 600 m of ice. It is important to consider that the saturation pressures may be the result of combinations of ice and water, sediment and water, or ice-cemented sediments.

#### **8.6.4 Interpretation of volatile content of glassy rinds**

The calculations completed using VolatileCalc represent a maximum and minimum estimate of confining pressure due to the lack of CO<sub>2</sub> data. These minimum values can then be interpreted to indicate the depths of water and ice that were likely controlling the volatile saturation pressure of the erupting lavas.

Due to the presence of significant volumes of explosive deposits associated with sampled pillow lavas for both Unit 2 and Unit 5 it is reasonable to assume that the eruptions occurred in an ice-confined lake. Consequently, the pressures recorded by FTIR are assumed to be solely the result of water. The depths of water indicated by the saturation pressures calculated would need to be impounded by thickness of ice that is 10 % greater than the depth of water (Table 8.3) to prevent lifting of the less dense ice, and rapid drainage of the wet based glacier (Smellie et al., 2008). This estimate does not account for any snow or firn cover (permeable) which are typically a few 10's of meters but would be thicker in the interior of large ice sheets (Smellie et al., 2008).

**Table 8.3 Evidence for paleo-ice thicknesses based on volatile analyses and compared with geomorphic evidence.**

<b>Field evidence</b>	<b>Unit 2</b>		<b>Unit 5</b>	
Minimum water depth (m)	591	All subaqueous	666	Paleo-water level
10 % more ice	59		66.6	
Confining Ice thickness (m)	650		732	
Elevation (m asl)	1309		1391	
<b>Volatile data</b>				
	Minimum	Maximum	Minimum	Maximum
Depth (m)	299	822	221	813
10 % more ice	30	82	22	81
Confining Ice thickness (m)	329	904	243	894
Elevation (m asl)	1079	1654	993	1644

Sample AG 48 occurs at an elevation 380 m vertically above the other three samples within Unit 2. However, the estimated difference in the depth of water between the two sample locations is only 139 m. These apparently high saturation pressures are intriguing considering the mechanisms required to increase the confining pressure for higher elevation lavas would require an increase in water depth during the course of the eruption, the downward collapse of the massif, or that the higher deposits were erupted prior to the lower elevation deposits. The consistency of the c. 750 m asl Unit 2 deposits suggests that the values are reasonable, despite the many potential challenges in the method including alteration, the lack of volatile saturation or open system degassing. However, all of these inconsistencies, with the exception of hydration, typically result in an underestimation of saturation pressure and thus are not expected in the 1160 m sample. Hydration, however is still a reasonable candidate for the apparent high saturation pressure despite the high elevation within the Askja center. The sample was collected from an outcrop

displaying pseudo pillow fractures which are considered indicators of shallow water magma interactions, or steam which may have resulted in saturation of the glassy rinds. Consequently, this sample is not included in the final discussion of ice thickness.

This window of ice thicknesses is fairly large, in part due to the challenges still facing saturation pressure models for paleo-ice reconstructions (Owen et al., 2012; Tuffen et al., 2010). However, based on the geologic evidence described above we can determine the minimum elevation of ice that would ensure subaqueous deposits, in the case of Unit 2, or to the level of the paleo-water level in Unit 5. An additional 10 % in thickness can be added to the ice to enable the ponding of water in the englacial lake. This results in minimum ice-thicknesses of 732 m for Unit 2 and 650 m for Unit 5. This value falls in the middle of the estimated values based on saturation pressures. In turn these geomorphologically constrained water level estimates can be used to back calculate a potential concentration of CO<sub>2</sub> in the melt. The range of potential CO<sub>2</sub> concentrations is 14 ppm for Unit 2 and 19 ppm for Unit 5.

The samples collected from the pillowed and CMVD intrusions can be treated independently, as the volatile behavior of intrusions is not well described in the literature. The strikingly low values of the intrusive margins indicate that either the magma had not yet reached volatile saturation, had experienced disequilibrium degassing, or more likely, that the subsequent heating of multiple magma pulses heated the margin above the glass transition temperature to allow further volatile escape (Graettinger et al., 2012). The interior of the dikes have volatile contents similar to that of samples collected from the same eruption from the same elevation. However, there is clearly a delay between the emplacement of the Unit 2 pillow lavas and the Unit 2 CMVDs which cut through bedded ash and lapilli tuffs that fill in a channel cut through Unit 2 lapilli tuff.

Using a combination of geologic and volatile saturation pressures the fluctuation in the LGM ice sheet from 71 ka to some time after 29 ka can be described based on each eruptive unit (Table 8.4). Based on the evolution of Austurfjöll there were between two and five large ice confined lakes at Askja during this period (Figure 8.11). There is only one eruptive unit that can be likely associated with a entirely subglacial eruption, but there may have been incipient periods of growth under the ice before explosive

activity established the lake in any other of the eruptions. Unit 4 is also a likely candidate for ice-contact / confined flows, but the deposit is too small to indicate if they erupted in an isolated cavity or locally established lake.

**Table 8.4 Summary of ice thickness values constructed for each eruption unit. Results indicate that an ice sheet of at least 400 m was present during all of the eruption units of Austurfjöll between 71 and after 29 ka.**

**Ice thicknesses may have been as much at 900 m during largest eruption phases.**

<b>Unit</b>	<b>Eruptive environment</b>	<b>Evidence for ice</b>	<b>Water level m asl</b>	<b>Ice thickness*</b>	<b>Age</b>
<b>7</b>	Subaqueous	Elevation of subaqueous deposits	1369	≥781 m	Between 7 - 29 ka
<b>6</b>	Subglacial	Ice contact, height of subaqueous deposits. No fragmental deposits	1049	≥429 m	Between 7 - 29 ka
<b>5</b>	Subaqueous to emergent	Volatile saturation pressure Paleo-water level	1325	732 -894 m	Between 7 - 29 ka
<b>4</b>	Subaqueous only	Elevation of subaqueous deposits	1030	≥407 m	Between 7 - 29 ka
<b>3</b>	Subaqueous only	Elevation of subaqueous deposits	1225	≥616 m	29 +/- 8 ka
<b>2</b>	Subaqueous dominated, local subaerial	Volatile saturation pressure Elevation of subaqueous deposits, local subaerial lavas	Variable** > 1250- 800 With one return to at least 800	650-904 m	71 +/- 7 ka
<b>1 A/B</b>	Subaerial	Glacial scour after formation	Unconfined subaerial eruptive environment. Over ridden by glacial ice, thickness unknown.		> 71ka
<p>*Calculated assuming a local base elevation of 660 m derived from LMI DEM.</p> <p>** Water levels must have been below 1160, 900 and 800 m asl. But no evidence to indicate if these all events were contemporaneous (continuous) or if the water level fluctuated more than the minimum of two indicated by deposits described in Section 8.5.2.3.</p>					

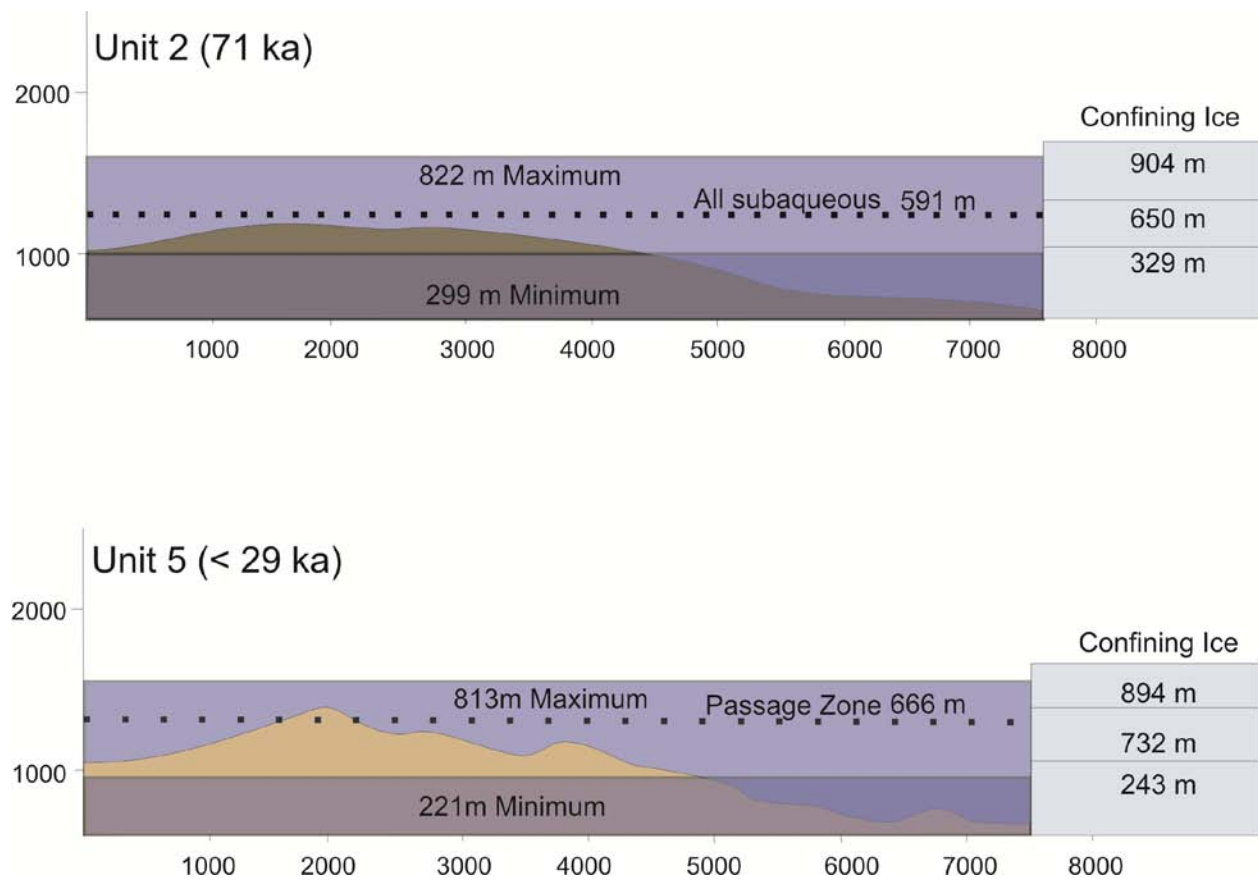


**Figure 8.11 Idealized cross-section of Austurfjöll at two time windows with estimated water levels and confining ice.**

### 8.6.5 Tephra record

Tephrochronology has contributed to paleoclimate studies in the North Atlantic, and is dominated by silicic and basaltic tephras from Iceland (Abbott et al., 2012; Brendryen et al., 2010; Haflidason et al., 2000; Larsen and Eriksen, 2008; Óladóttir et al., 2011). Historic eruptions of basaltic and basaltic andesite systems reveal the frequency of tephra production, and the threshold which controls the preservation of tephra within the marine or ice environment. Activity at Grímsvötn, Iceland's most active basaltic system, in 2004 produced up to 4 km<sup>3</sup> of tephra from a single eruption (Björnsson and Pálsson, 2008). More recent eruptions Eyjafjallajökull 2010 (0.45 km<sup>3</sup>), Grímsvötn 2011 (17 km plume) produced ash plumes that blanketed Europe in ash despite moderate eruption volumes (Icelandic Met Office). The total volume of material preserved at Austurfjöll is 3.62 km<sup>3</sup> with two eruptive phases (Unit 2 and Unit 5) exceeding 0.5 km<sup>3</sup>. Currently no basaltic tephras found in the Greenland ice cores (NGRIP and GRIP) or the Norwegian Sea have been attributed to Askja. However, numerous basaltic tephras and cryptotephras have been described from time periods that overlap with the construction of Austurfjöll, mainly during Marine Isotope Stage (MIS) 4 and MIS 2. There are 18 tephras currently attributed to the Icelandic Rift, of tholeiitic composition that occur within the 71 +/- 7 ka time window of the Unit 2 eruption phase (Abbott et al., 2012; Brendryen et al., 2010; Grönvold et al., 1995). Twelve of these tephras were documented in a core from the Norwegian Sea and have compositions similar to tholeiitic lavas of the central Icelandic rift that span a period of 69 ka to 78 ka (Brendryen et al., 2010). Five cryptotephras, especially GRIP 2532.95, dated at 69.095 +/- 1526 ka and NGRIP 74200 +/- 1652 ka, within the Greenland Ice Core Project and Northern Greenland Ice core project have very similar compositions to Unit 2 lavas (Abbott et al., 2012). Another candidate tephra from GRIP tephras includes GRIP/2608 76.5 ka (<sup>14</sup>C age) tephra that has a tholeiitic composition and no known source (Grönvold et al., 1995). Preliminary comparisons of these tephras and major element concentrations of the whole rock geochemistry of Askja glaciovolcanic lavas suggest that the Austurfjöll Unit 2 is a potential candidate for the tephra layers.



Tephra from ca. 29 ka that might correlate to the emergent eruption of Unit 5 are sparse in the literature. The Greenland ice cores have multiple tephras dated to around 23.5 ka with tholeiitic compositions that seem comparable to Austurfjöll samples, though they tend to share more similarities to more evolved Unit 3 Austurfjöll lavas rather than the more primitive Unit 5 samples (Haflidason et al., 2000). However, the rough spatial sampling of the dated Austurfjöll lavas means that any eruptive from Unit 3 and above are younger than  $29 \pm 8$  ka. The dominance of Unit 5 may hide important information about the Unit 3 eruptions, which are the most evolved of all of the eruptive units, and match well with some proposed GRIP tephras. Additionally, the Unit 5 eruption may be as young as 10 ka, as long as it predates the Askja caldera. Without any reasonable control on the water depth at the time of the Unit 3 eruption (either geologic or volatile) it is possible the eruption had a significant explosive and/or emergent component, the deposits of which were buried by later eruptions (i.e. Unit 5). Although confident identification of these tephra units will not be attempted here, these comparisons suggest that the Austurfjöll geochemical data set should be used in tephrochronology investigations in the future. A more detailed comparison of the compositions of Pleistocene tephras with Austurfjöll data, particularly trace elements would benefit both tephrochronology and paleoclimate studies as the tephras in ice cores have more precise age dating.

## 8.7 CONCLUSIONS

Glaciovolcanic deposits of the Austurfjöll massif represent the bulk of the middle of the Weichselian glacial period, with paleo-ice estimates up to 900 m thick for MIS 4 and MIS 2 in central Iceland (Abbott et al., 2012; Brendryen et al., 2010). Over 40 ka of basaltic glaciovolcanic activity at Askja is preserved in the Austurfjöll massif. The interaction of the eruptions that formed this massif with the confining ice sheet documented in the glaciovolcanic deposits, can serve as a model of poly-genetic basaltic glaciovolcanic centers. The most historically active basaltic central volcano in Iceland, Grímsvötn, is still

covered by the Vatnajökull ice cap and consequently, its architecture is unavailable for study. However, our understanding of such active ice-covered volcanic centers will be improved through comparisons with similar, well exposed edifices like Askja. The Grímsvötn center has erupted repeatedly historically despite its modern 700 m of ice coverage, and it is the most similar active system to the conditions which produced Austurfjöll. Morphological evidence in conjunction with volatile saturation pressure modeled conditions indicates an ice sheet greater than 650 m at both 70 ka and after 29 ka. The saturation pressure models show reasonable agreement with field evidence, consequently, it can be estimated that these ice sheets may have been as thick as 900 m. There is no evidence at Askja for ice thicker than 900 m; however, greater ice thicknesses may have reduced the productivity of Icelandic volcanic systems. The values presented here are lower than published estimates of the maximum thickness of the LGM ice sheet of 1500 m (Bourgeois et al., 2000; Jakobsson and Gudmundsson, 2008; Norðdahl et al., 2008) and estimated values based on neighboring Herðubreið 1000 m (Werner et al., 1996). These minimum values do agree with the minimums established by the glacially scoured Interglacial Valðalða volcano that sits 327 m above the regional base elevation. However, Askja occurs very near the proposed hot spot (Allen et al., 2002), along the high geothermal flux MAR. It is unlikely then the thickest portion of the ice-sheet would occur along the areas of greatest volcanic activity. Nevertheless, these data still suggest that a sustained thick ice sheet occurred in the Askja area despite at least  $3.62 \text{ km}^3$  of material erupted over 40 ka. During large eruptive phases, particularly Unit 2 and Unit 5, the thick ice was likely disrupted enough to form a glacially confined lake that was home to subaqueous eruptions of tholeiitic lava from vents in the Austurfjöll massif. At its greatest extent the lakes were likely on the order of  $50 \text{ km}^2$ . These eruptions consisted of six discrete eruptive units that produced pillow lava sheets, fissure ridges, point sources, and inter-ridge depositional centers in a glaciolacustrine environment. Detailed textural descriptions of Unit 2 and 5 deposits indicate that in deep water glaciolacustrine eruptive environments completely subaqueous effusive to explosive transitions are common as described in Chapter 6.

The presence of 650-900 m of ice at Askja at 71  $\pm$  7 ka helps establish the beginning of the Weichselian in central Iceland. The Austurfjöll deposits provide not only evidence of the minimum thickness of ice during the following 40 ka, but also local variations in the ice presence as a result of the construction of the massif and / or temporal ice thickness variations. Drainage of meltwater lakes during the eruption of Unit 2 are recorded in large drainage channels and small outcrops of subaerial lava (10-100 m<sup>2</sup>). Although unlikely to have been a single catastrophic drainage event, the amount of meltwater drained from the system could have produced a jökulhlaup with a volume on the order of  $3 \times 10^{10}$  m<sup>3</sup> which is comparable to the volume water drained as a result of the Gjalp eruption in 1996 (Gudmundsson et al., 1997). There is evidence of potential exclusively subglacial eruptions at Austurfjöll, with the best evidence occurring in the Unit 6 deposits. The remnants of a never before described paleo-water level are preserved in the Unit 5 deposits in the wall of the Öskjuvatn caldera.

The success of the unspiked K/Ar dating applied to Austurfjöll is promising for further paleoclimate studies of lavas in the Northern Volcanic Zone of Iceland, including further work at Askja. Increased density of dated samples within the massif would likely reveal further complexity about the evolution of the massif and its interaction with a thick ice sheet during the late Pleistocene. Additionally, further sampling of Askja lavas that are not part of the central massif would enable chemostratigraphic relations and expand both the chronological and morphological data set within the paleoclimate investigation. The greatest challenge of glaciovolcanic based climate proxies in Iceland is the challenge of the low resolution database of deposit ages. The introduction of each confident dated deposit description is an important step in the refinement of Icelandic climate reconstruction.

## APPENDIX A

### STRATIGRAPHY AND PETROGRAPHY

**Table A.1 Thin-section description**

AG	Description	Petrography
1	Feldspar rich gabbro	Plagioclase, Cpx (filling in voids between crystals), rare olivine. All minerals are surrounded and surround another mineral type (except the mica) multiphase growth. (Cpx is likely part of a secondary growth phase.)
		EDS indicates the presence of Olivine, Bytownite (An 70-90), Labradorite (An 50), Cpx with a Mg # of 60.
2	Porphyritic tephra	Large Cpx phenocrysts and substantial plagioclase phenocrysts. Some plagioclase phenocrysts have rims of a different glass type (lighter sideromelane). Strange twinning and exsolution patterns in phenocrysts. The matrix is sideromelane glass.
3	Porphyritic lava block within AG2	Convolutd plagioclase crystals occur in multiple sizes. Microcrystalline Cpx is present in the matrix. Vesicle rich (vesicles are smaller than the dominant phenocryst phases). Vesicles are variable in shape, coalesced. Minor opaques in sideromelane dominated groundmass. Crystals in the groundmass show preferential orientations likely due to flow banding or filter pressing.
		EDS indicates the presence of Cpx with Mg # 51, An 83 Bytownite phenocrysts, An 36 Labradorite groundmass, and no olivine.
4	Glassy dike	Sideromelane rimmed tachylite fragments between 0.1-0.5 mm. Rims are up to 0.05 mm thick. Vesicles are common, fairly round in tachylite zone but become more elongate in sideromelane domains (up to 1 mm in radius). Rare (1 %) Cpx crystals with fairly euhedral rectangular grain shapes. Fragments have frequent curves of remnant vesicles, but flat sided breaks are also common. Some vesicles have sideromelane rims as well. All fragment edges are lined with sideromelane. Rind thickness varies across the slide, but is locally similar.

5	Diamictite (putative tillites)	<p>Multi-component groundmass. Including fragments of light tan glass with elongated vesicles (60 %), and minor alteration in bands around cracks with sparse large (0.05 mm) feldspars.</p> <p>Other clast types include: black (tachylite dominated) highly vesicular round clasts (round vesicles) with fairly large (0.1 mm) phenocrysts of plagioclase; light tan glassy blocks with minor vesicularity show cusped and blocky shapes. Some have broken crystals of Cpx and Plagioclase. The crystals vary in size from 0.05 to 1.0 mm; Fragments of tachylite with no crystals or vesicles.</p> <p>The overall slide is poorly sorted.</p>
6	Diamictite (putative tillites)	<p>Multi-component. Fairly well sorted.</p> <p>Clasts dominated by plagioclase laths and minor Cpx crystals, no vesicles. Matrix: free crystals of both plagioclase and Cpx are common. Some of the crystal population is some broken, but most are square in shape. Glass fragments are only slightly larger than the free crystals. Most fragments are composed of sideromelane, but some palagonite and rare tachylite fragments are present.</p> <p>Vesicular fragments composed only of glass are up to 0.5 mm in diameter. Some crystal-rich clasts are surrounded by a corona of glass and microcrysts.</p>
7	Dike (pillowed) with Ag6	<p>Microcline dominated vesicular lava. Vesicles are irregular in shape (coalesced) and compose about 50% of the sample. Vesicle size is mostly consistent and around 0.5 mm in diameter.</p> <p>Microclites are 40% plagioclase feldspar laths with 60% intersertal Cpx. The remainder of the sample (20%) is tachylite glass. Microclites do not exceed 0.5 mm in length.</p>
8	Subaerial lava (date)	<p>Microcrystalline groundmass dominated by Cpx and plagioclase. Magnetite (cubic opaque) is common (~20%). Minor red alteration occurs around the opaques.</p> <p>Vesicles (10%) are coalesced and show some alteration along rims.</p> <p>Larger blades of euhedral plagioclase comprise about 15% of the sample. 3% of the plagioclase is on the order of 1 mm in length displaying carlsbad twins. Of these crystals 0.5% are anhedral.</p>
9	Lt Bedded over AG8 lava	<p>Heterolithic, glass dominated, poorly sorted lapilli tuff matrix.</p> <p>Multiple clast types, each with distinct glassy matrix and percent of phenocrysts.</p> <p>Examples: Black vesicular clasts with round margins. Dominated by parallel plagioclase laths, rather small (0.01 mm), and rare square Cpx (0.01 mm).</p> <p>Light tan glassy fragments with corona texture, altering to clay.</p> <p>Dark grey hypo-crystalline blocks, full of feldspar laths (0.1 mm long). The entire clast is surrounded by a reaction or alteration rim.</p> <p>Large (up to 1 cm) crystal free clasts of vesiculated (spherical) sideromelane glass.</p> <p>Large (up to 1 cm) clasts with scattered feldspars and Cpx with minor alteration.</p> <p>Blocky grain shapes dominate the sample.</p> <p>Total deposit is vesiculated, void space? Filled with blue epoxy. Clast shapes are variable and irregular. General matrix is ash and free crystals of feldspar and &gt; Cpx.</p>
10	Pillow in mound (no glass)	<p>Vesicular sample with two dominant modes of vesicle size (1 mm and 0.3 mm in diameter). Both size ranges are irregular in shape and together compose</p>

		60% of the sample. The remainder of the sample is 75% microlites (plagioclase 40% laths, and 60% intersertal Cpx) and 25% tachylite glass. Glass is concentrated around the margin of vesicles, with crystal free circular aureoles around the vesicles.
<b>11</b>	Pillow fragment	Highly vesicular, with two populations of very large bubbles. Some vesicles (rounded, some coalesced) have and infilling of glass fragments. The sample displays no dominant phenocrysts population (but one unusual crystal, likely plagioclase). The groundmass contains microlites, including some spherulites (oriented glomerocrysts) of plagioclase. Vesicles can be very round and circular. Other vesicles are large and coalesced.
<b>12 A</b>	Sediment (deformed bedded Ac)	20% tachylite glass fragments 2 % reddish glass fragments, 1 % plagioclase crystals, and the remaining 77% is sideromelane. Very fine, well sorted fragments. The grains are well packed and display a range of grain shapes. Vesicles are not common, and bubble wall shards are not distinguishable. All fragments are on the order of 0.1 mm in length. Fluvial emplacement?
<b>12 b</b>	Sediment (deformed bedded Ac)	Poorly sorted, highly diverse crystal-bearing (8%) ash matrix. Clasts are frequently porphyritic with large complicated plagioclase crystals and medium sized anhedral Cpx grains. Clasts are either tachylite dominated and crystal rich, sideromelane and crystal rich, or sideromelane and crystal free. Small crystal free fragments are tachylite are present, but no large clasts. The matrix is moderately sorted with variable grain shapes. Vesicles are rare in smaller clasts (below 0.5 mm). Vesicularity of larger clasts does not exceed 40%. Bubble wall shards are not common.
<b>13</b>	Matrix around pillow	Ash matrix contains various glass shapes: blade shaped, blocky, triangular. The sample contains very few phenocrysts. The overall sample porosity is fairly high (30%). 25% vesicle wall breaks, 25 % blades, 25% blocks, 25% splinters
<b>14</b>	Bedded Ac (Af)	Sideromelane 80% to tachylite 20% dominated sample. Crystals are rare 2% and plagioclase or Cpx. Grains are well packed, but grain shapes are still distinguishable, with lots of curved fragment margins. Intact vesicles are rare. All fragments are below 0.5 mm in diameter. Blocky shapes (including elongate rectangles) compose about 50% of the grain shapes.
<b>15</b>	Massive Lt in bedded sequence	Loosely packed sideromelane (80%) and tachylite (20%) fragments. Individual fragments may reach up to 65% vesicularity. Lots of broken bubble walls. Blocky shapes are common, but do not dominate (40%). Tachylite fragments are typically smaller than sideromelane (0.1 to 0.3 mm in diameter), but larger fragments exists and are also vesicular. Vesicle shapes range from circular to elongate. Free crystals are present as 0.2 mm in diameter plagioclase crystals and compose 1% of the sample.
<b>16</b>	Ltm reverse graded (Log1)	Loosely packed, poorly sorted matrix of glass fragments. Dominantly (70%) sideromelane clasts of 0.1 mm to 1.0 mm in diameter vesicular glass. Tachylite clasts have higher crystal concentrations, and lower preserved vesicularity. Clasts do not exceed 0.5 mm but are all larger than 0.2 mm. Vesicles are predominantly rounded, but can vary in size from 0.1 mm to 0.5 mm in diameter. Individual clast vesicularity does not exceed 50%. Glass fragments may have flat or curved sides in approximately equal

		<p>proportion.</p> <p>Crystals make up 5% of the sample (plagioclase &gt; Cpx). Crystals typically occur as glomerocrysts in the middle of glass fragments. Some free crystals occur.</p>
17	Ltm (Log 1)	<p>Sideromelane dominated (80%) glass fragment matrix. Vesicular clasts with lots of broken bubble wall shards.</p> <p>Vesicle shapes are dominantly smooth-sided, but may be circular or elongate. Crystals occur as glomerocrysts in large sideromelane and tachylite fragments, or as free crystals in the matrix. Plagioclase and Cpx dominate. Some large clasts contain microlites of plagioclase.</p> <p>The smaller fragments contain fewer intact vesicles or definite bubble wall influences.</p> <p>Fragment sizes vary, the deposit is poorly sorted. With clast size ranging from 0.1 to 1.0 mm.</p>
18	Lt1 some bedding (Log 1)	<p>Highly diverse grain types. Dark black tachylite through various colors of sideromelane to the classic light brown. Some orangey alteration clasts are also present. Fragment size varies from a few mm to 0.1 mm in diameter.</p> <p>Vesicularity and crystal content are also highly diverse, but microlites are common. Large plagioclase crystals still display nice twinning structures. Crystal free clasts are also present. Clast shapes are subrounded, but angular shapes become more common in the smaller grain sizes. Fragments less than 0.5 mm in diameter are typically vesicle free and densely packed.</p>
19	Pillow in Lt1	<p>The sample contains less than 10% crystals. Large plagioclase phenocrysts are rare. The largest crystal population is microliths of plagioclase. Vesicles display Lots of coalescence.</p>
20	Lt1 fines at top	<p>Isolated large 0.5 – 0.75 mm in diameter broken feldspar phenocrysts occur in an altered matrix of sideromelane glass. All grains are vesicular, with large round vesicles. The sample shows strong packing.</p>
21	Porphyritic lava	<p>Large (3 mm) phenocrysts of plagioclase with complicated growth histories. All phenocrysts are anhedral with numerous sets of twinning. Some phenocrysts display mechanical breakage, but most are well rounded.</p> <p>The groundmass is predominantly feldspar laths with minor Cpx. All crystals in the groundmass are anhedral. The sample is dominated by tachylite glass with moderate vesicularity. Vesicles are multiple mm in width and highly irregular in shape. Minor alteration of glass to brown palagonite occurs on vesicle margins.</p>
22	Pillows at base	<p>Plagioclase microlith-rich vesicular tachylite glass groundmass. Vesicles are dominantly coalesced. Randomly oriented crystals of plagioclase (laths up to 40% of gm) and stubby crystals of Cpx (20%). Vesicles are irregular and show signs of coalescence.</p>
23	NG dike competent	<p>The groundmass is composed of mostly blade-like phenocrysts of plagioclase and Cpx (0.02mm). Plagioclase crystals show a preferred orientation of 60% of the crystals. Some microcrysts display well formed twins. Crystals are euhedral (rectangular and intact). Between 0.01 and 0.2 mm.</p> <p>Moderate vesiculation (10-15%) with predominantly circular, some elongate, vesicles. Vesicles display only minor coalescence. Vesicles are 0.2 mm to 0.6 mm in diameter. Larger vesicles are irregular in shape. The tachylite groundmass displays minor alteration.</p>
24	Ltm (Log 2)	<p>The sample is almost completely sideromelane glass fragments that are large and have limited vesicularity. Those vesicles present are odd shaped. Glass</p>

		<p>fragments are mostly blocky with rare darkened (altered) rims. Fragment shapes vary from blocky to elongate. Clast size ranges from 0.2 mm to 1.0 mm The sample has significant inter clast pore space.</p> <p>Crystals present (5%) occur as blades and glomerocrysts of plagioclase and minor very small Cpx. Vesicles are predominantly circular.</p>
25	Lt/breccia (Log 2) base	<p>Dominated by sideromelane. Dominantly angular non-vesicle influenced fragments of various sizes. The overall sample is poorly sorted. Glass fragments are frequently elongate in shape and display elongate vesicles, but most are circular.</p> <p>Grain size: 0.25-3.0 mm.</p>
26	Block in Lt	<p>Micro-porphyritic block from a lapilli tuff. Phenocrysts of plagioclase occur as laths in clusters (1 mm long, but 0.25 mm wide). Groups include 4 to 5 crystals. The groundmass is dominated by 0.25 mm long feldspars in glass. Fewer anhedral pyroxenes occur, mostly Cpx. Some display nice 0.25 mm square crystals (largest example of Cpx in sample).</p> <p>Vesicles are large and common (60%). Vesicles coalesce and have irregular margins with little to no apparent alteration. There is some distribution in vesicle size, but all &gt; 0.5 mm.</p> <p>Zones of variable crystal concentration (decreased glass) cross the section.</p>
27	First Ac bedded in NG (Log 2)	<p>Sample is similar to AG 24 (slightly smaller average fragments size). The deposit has a high porosity 45-50% and composed of mostly sideromelane with 5% tachylite. Particularly large grains are vesicular. Some vesicle spaces are filled in with smaller fragments.</p>
28	Ac bedded (Log 2)	<p>Fine ash fragments with up to 30% void space. Fragments are blocky and predominantly sideromelane and fairly uniform in size (0.1 mm). Isolated broken crystals of pyroxene and feldspar (&gt;5%) are distributed throughout the sample.</p>
29	Ac bedded (Log 2)	<p>Large clasts of a variety of sizes and glass types. Some fragments are vesicular, some not. Glass is sideromelane with minor tachylite. Void space (10%) is less than primary vesicle space (20%).</p>
30	Pillows/intrusions NG south	<p>Highly microcrystalline (plagioclase 0.2 mm long with sparse Cpx (0.05 mm) vesicular lava. Large zones of reddish alteration occur in and around vesicles. Rare large crystals up to 0.5 mm in diameter are more equant.</p>
31	Old rhyolite ash (in caldera)	<p>Rhyolitic ash with pipe vesicles. The sample is composed of ash grains, but grain outlines are hard to differentiate.</p> <p>Crystals are mechanically broken and predominantly plagioclase (&lt;0.5 mm). Alteration of glass occurs in patches, highlighting ash fragment shapes, which are elongated and convoluted. Rare OPX displays some twinning.</p>
32	Old glassy rhyolite lava (in caldera)	<p>Glass dominated &gt; 70% sample with phenocrysts of various sizes of plagioclase. Large crystals are mechanically broken, but generally euhedral (0.5 mm long). Typical phenocryst shape is bladed. High birefringence crystal is green in plane polarized light (PPL), no pleochroism, possibly biotite? Inclined extinction.</p> <p>2<sup>nd</sup> phenocryst of high birefringence: less green in PPL. Slightly lower interference colors. , highly altered? Does not go completely extinct (might be parallel) might be OPX.</p>
33	Old rhyolite	<p>Large phenocrysts occur in a glassy groundmass. Phenocrysts include plagioclase (largest &gt; 1mm) and OPX occurs with zoning, which occur in mixed clusters. The growth order appears inconsistent (both species occur inside another). Broken grains are frequent, but euhedral shapes are still</p>



		present. Possibly phlogopite (definitely mica, no pleochroism). Some with bird's eye extinction, but no pleochroism. Some crystals of broken Cpx. Phenocrysts serve as nucleation points for later crystals (particularly plagioclase).
34	Porphyritic Lt	Composed of large blocks of tachylite and microlite-rich lapilli, free crystals and fine sideromelane glass. Microlite-rich, vesicular sideromelane clasts also occur. The fragments range in size from 10's of mm to 0.1 mm in diameter. Crystals tend to occur in clusters, but it is difficult to distinguish glomerocrysts from clusters. Large crystals are 80% plagioclase, with complicated twinning structures. Rare palagonitized porphyritic clasts are also present. Vesicles in clasts are irregular and occur in variable shapes and sizes.
35	Ac weakly bedded	Loosely packed fragments of blocky sideromelane (40%) and subhedral crystals of plagioclase (40%). Tachylite composes about 20% of the sample, and has more irregular grain shapes. Vesicularity of the clasts is particularly low, with occasional preserved vesicle, but rare if present broken bubble walls. Well sorted, all fragments are on the order of 0.4 mm in diameter and equant.
36	Lt porphyritic Glassy and angular	Large, 1-3 mm crystals of plagioclase dominate the sample. The crystals are subhedral and display complicated twinning structures and have some fracturing. Other clasts include vesicular tachylite groundmass surrounding plagioclase crystals, with a total diameter of 2 mm. Vesicular crystal-free tachylite and sideromelane fragments. And microlite rich sideromelane. The sample is poorly sorted but clasts under 0.5 mm in diameter only compose 10% of the total sample. Smaller clasts are typically blocky and vesicle free sideromelane. But may also include fragments of plagioclase grains and microlite-rich sideromelane. Crystals (of any size) make up about 50% of the sample.
		EDS indicates the presence of Cpx with Mg # s of 47 and 85. Phenocrysts of plagioclase, particularly Bytownite (An 85) contain Cpx inclusions with Mg # of 64 and 85.
38	Porphyritic lava, coherent	Highly vesicular with two major populations large (10%): coalesced bubble shapes up to 3 mm in diameter and small (60%) irregular coalesced bubbles with some visible rounded initial shapes up to 0.5 mm. Phenocrysts (up to 1 cm) are large and anhedral, and occur in clusters. Frequent inclusions of plagioclase and Cpx (highly rounded) occur in large plagioclase crystals. Glomerocrysts of Cpx reach similar size of individual plagioclase phenocrysts (5 mm) but are composed of microcrysts (0.5- 1 mm). Diversity in the orientation and size of plagioclase microcrysts, one of the largest ranges yet observed.
39	Pillowed Lt matrix	Sideromelane glass (80%) with tachylite as small fragments or on the margins of larger sideromelane clasts. Packing is inconsistent, but dominantly moderate to poor. 20% macrophenocrysts of plagioclase and glomerocrysts of Cpx and plagioclase are common. The matrix is composed of a diverse range of grain sizes, shapes and vesicularities. Broken bubble walls are common on 2/3 of the grains. Some grains contain intact vesicles in their interiors. However, some clasts do contain only flat sides and dense interiors (1/3). Phenocrysts occur within

		sideromelane glass and independently in the matrix.
40	Chill margin NG dike	Nice transition from dense (10% vesicles) sideromelane to tachylite with increasing vesicle population (30%) and size. Some (5%) crystals occur throughout (plagioclase laths and Cpx, equant, with some fragmented faces). Crystals almost disappear in first vesicle zone, but reappear as dense microcrystalline network by interior of margin.
41	Pillow rind NG dike	Tachylite glass with quench crystals of plagioclase in random orientation. The sample vesicularity is 65% with two modes of bubble size: irregular, coalesced (2-3 mm) and rounded (0.5 mm). Some sideromelane towards outside rim. Section not complete.
42	Lava/sill	Microcrystalline texture with groundmass of opaques (20%), plagioclase (40%) and Cpx (10%) and glass (30%). Rare scattered vesicles with coalesced shapes compose 5 % of the sample. Cracks filled with alteration products like mica and zeolites are 5 cm apart. Some spherulites glass alteration zones, appear as orange glass.
44	Lava/sill chill margin (big slide)	Significant grain plucking? Fluidal voids? Highly altered. The sample is dominated by vesicular tachylite glass. Alteration of plagioclase is common, such as mica: large crystals, with damage (from slide prep?) but shapes are definitively convoluted) up to 3 mm. Smaller crystals (laths) of plagioclase are still preserved in matrix. Some intact larger crystals of plagioclase have preserved twinning, but anhedral crystal shape. Although less visible in thin section, is significant zeolitization.
45	Porphyritic top lava (Log)	Phenocrysts: large plagioclase crystals up to 5 mm. Zoned, anhedral, broken, clustered. Glass: altered to sideromelane from tachylite. Glass alteration tends to occur at the ends of crystals (not complete rings). Opaques: up to .5 mm Groundmass is composed of opaques (10%), plagioclase (40%) microlites and Cpx (50%). The sample is dense (vesicle free). Presence of oxides may indicate a subaerial emplacement.
46	Red dense microcrystalline lava	Dark brown glass (not quite typical tachylite) dominates the slide. With highly deformed vesicles that vary regionally throughout the slide. The section has a preserved red coloration in hand sample, but does not appear in PPL on the slide. Crystals are anhedral plagioclase with twinning and altered margins. Phenocrysts are up to 1mm in diameter and may be clustered. The groundmass is composed of 20% crystals, 20% vesicles, 60% glass. A distinct lack of other crystal species is apparent.
47	Pseudo pillow	Dominated by microcrysts of feldspar. Occasional larger phenocrysts of plagioclase, with twinning and anhedral shapes, are up to 2 mm in length. One particularly notable glomerocryst (xenolith?) of plagioclase crystals with a matrix of broken plagioclase exists. Groundmass is 30% plagioclase, 50% Cpx and 20% tachylite glass. Plagioclase crystals are lath shaped with no preferred orientation, and visible twinning. Cpx are stubby more square shaped grains. Very dense, vesicle free.
49	Red crystals in AG 47	Microlite-rich lava with tachylite groundmass. Spherulitic alteration occurs periodically in the groundmass. Microlites are typically 0.1 mm laths of plagioclase. Larger crystals, up to 0.5 mm occur occasionally, but exhibit cracking and alteration. Cpx is also present in the groundmass between larger plagioclase crystals.

<b>50</b>	Subaerial lava near pt 98	25% opaques 0.05 mm in diameter, equant and evenly distributed through the sample. 45% plagioclase laths, approximately 0.1 mm in length. Twinning occasionally visible. 30% Cpx crystals. Intersertal texture. Occasional 1% larger crystals on the order of 0.3 mm in length of plagioclase. Vesicularity is nil
<b>52</b>	Deformed bedded ash	Variable componentry: sideromelane glass fragments (high to low vesicularity), tachylite glass fragments (low vesicularity), free crystals of plagioclase, microlite rich fragments of tachylite, porphyritic tachylite glass lithics (moderate vesicularity), sideromelane glass porphyritic lithics (high to low vesicularity). Crystal species present include plagioclase (laths, microlites, and glomerocrysts 0.01 to 0.3 mm) and Cpx (equant anhedral crystals, glomerocrysts from 0.01 to 0.1 mm in diameter) Fairly well sorted, clast sizes average 0.3 mm in length.
<b>53</b>	Pillow breccia	Large (>1.0 mm) grains of diverse texture and composition. Vesicle and crystal free sideromelane glass, highly vesicular and crystal-rich tachylite glass, grains with sideromelane and tachylite transitions, dominantly around crystals. Rare palagonitized fragments. Crystal population is dominantly larger (0.2 mm) plagioclase and Cpx crystals, which may occur as glomerocrysts. Some microlite rich fragments occur. Well packed. Total vesicularity is low. Spherulites are common in darker glass.
<b>54</b>	Lt with Ac	Poorly sorted, clast size ranges from 0.2 mm to 1.0 mm. Vesicularity ranges from 0-70% between fragments. All sideromelane glass. Glomerocrysts of plagioclase and Cpx are 20% present in larger fragments. Bubble walls are thin in vesicular fragments. Fine fragments tend to have flat sides and rectangular morphologies. Some bubble wall structures are present, but only on 10% of the total sample.
<b>55</b>	Paleo-water level	Poorly sorted sample. Grain size varies from 2.0 mm. Highly vesicular clasts have convolved, coalesced bubbles with very thin walls. Smaller clasts < 0.1 mm have no vesicles and are densely packed. Fragments have dominantly flat sides, with less than 20% vesicle influenced morphologies. Large crystals of plagioclase occur in groups (not glomerocrysts). Crystals have remnant sideromelane glass, but of less volume than the phenocryst. Hard to tell as the fragment boundaries are difficult to distinguish. Crystals are predominantly plagioclase, some Cpx. Highest variability in grain size yet observed in section.
<b>56</b>	Subaerial lava	25% vesicles which are irregular in shape, coalesced. 10% phenocrysts of highly fractured plagioclase (70%) and Cpx (30%) 65% groundmass. Which is composed of 35% opaques, 35% plagioclase and 30% Cpx. Glomerocrysts of larger phenocrysts are up to 1 mm in diameter, and consist of mostly (70%) Cpx.
<b>57</b>	Pillow in NGD	Two vesicle populations, but both have irregular morphologies (1.0 mm to 0.1 mm) and compose 60% of the sample. Microlite rich. Crystals are fairly uniform in size and randomly oriented. Rare (3%) outsized plagioclase crystals (0.3 mm) occur in glomerocrysts.

		Otherwise the crystal population consists of 60% plagioclase and 40% Cpx. Tachylite glass concentrates around large vesicle walls for 0.01 mm.
<b>58a</b>	Double margin in NGD	<p>Label occurs on inside of margin.</p> <p>Tachylite swirls (approximately 0.5 mm by 0.2 mm wide) inside sideromelane glass.</p> <p>Zones of increased vesiculation have apparent boundaries when viewed in hand, less distinct under microscope. These variations are associated with slight color changes.</p> <p>Overall the slide displays a series of zones. Starting from outermost margin:</p> <p>Zone 1: thin sideromelane glass (0.250 mm).</p> <p>Zone 2 fragments (with blurred edges) of light brown sideromelane containing phenocrysts up to 0.2 mm, surrounded by Tachylite.</p> <p>Zone 3: fragments of sideromelane of variable sizes (0.5 mm to 0.1 mm). Glomerocrysts of plagioclase up to 0.4 mm. Groundmass is predominantly tachylite containing fragments as described in zones 2 and 3.</p> <p>Zone 4: interior vesiculated zone. Heterogeneous patterns of vesiculation. Some vesicles are elongate parallel to the direction of the dike. Others are amorphous and coalesced. Concentration of vesicles also varies.</p>
<b>58b</b>	Second margin (interior)	<p>Tachylite glass with only 15% vesicles and 10% plagioclase crystals.</p> <p>Vesicles that are present are elongated and aligned in swirly domains.</p>
<b>59</b>	Ac deformed in Lt	<p>Large uniform sized loosely packed sideromelane glass fragments, with 2% intact vesicles. Grain shapes have dominantly flat sides, but large curved, potentially vesicle influenced shapes are common (30%). Tachylite grains are common (20%) and are typically vesicle free.</p> <p>Sideromelane fragments may contain crystals in isolation or glomerocrysts (present in ~20% of fragments). Narrow flakes (needle shaped fragments) of sideromelane are present between larger fragments. Splinters.</p> <p>Local areas of elongate fragments with parallel alignment. Not consistent throughout the sample. (30% of fragments show alignment). The alignment however, is parallel throughout the sample.</p>
<b>60</b>	Pillowed intrusion	<p>Some alteration of glass, predominantly in vesicles and along fractures.</p> <p>Highly vesicular (70%) sample with near circular vesicles, some irregularity in thin section, not visible in hand sample.</p> <p>Dominated by microlites, some in radiating structures, but otherwise just displaced by the presence of vesicles. Larger phenocrysts (0.3 mm) are typically plagioclase and present in about 10% of the sample. Microlites are dominantly Cpx (60%) and the remainder are plagioclase crystals. About 35% of the groundmass is tachylite.</p>
<b>61</b>	Chill margin in NGD	<p>Less complete chill margin section. Higher crystallinity of interior than observed elsewhere. No micro-peperite preserved. Some fill attached to interior. Margin fragments in interior.</p>
<b>62</b>	Country rock NGD	<p>Large vesicular fragments, some expanded vesicles filled with finer cusped fragments. Some fragments display large rounded vesicles (0.5 mm) while others show variable sizes and coalescing bubbles. Some fragments are vesicle free sideromelane. Minor tachylite presence on grain margins. Some palagonitization of bubble walls.</p> <p>Radial glomerocrysts of feldspar common (up to 0.5 mm) composed of blades of feldspar. Crystal sizes range from 0.2 mm (feldspar, euhedral) and 0.1 mm (pyroxene, subhedral). Oxides are scattered throughout as rounded crystals of approximately 0.05 mm.</p>

<b>63</b>	Matrix of NGD	<p>Variable fragment sizes up to 1 mm. Larger clasts are highly vesicular. Smaller fragments 0.05. Cuspate shapes are common. Vesicles are highly circular, some show coalescence.</p> <p>Largest clasts are up to 4 mm in diameter (lapilli).</p> <p>Crystal content is confined predominantly to the interior of larger clasts. Cpx (1%) occurs as subhedral and fractured crystals, and plagioclase occurs as intact euhedral grains (&gt;1%). Some larger fragments contain glomerocrysts of feldspar blades (radial distribution) and subhedral to rounded pyroxenes.</p>
<b>64</b>	Upper sill chill NGD	<p>Higher crystal percentages and palagonitization than observed elsewhere. Series of photos taken through section. Increasing vesicularity as observed in other chill examples. Possible micro-peperite of the outermost margin preserved.</p> <p>Possible apparent inner chill.</p>
<b>65</b>	Sediment in sill	<p>Highly angular fragments are packed randomly and occur with 30 % pore space. 95% light brown glass (sideromelane). 4 % black tachylite. Variable fragment sizes and shapes. Predominantly sharp corners. Rare round or cuspate features. Most grains are semi-equi-dimensional. Some elongate blocky fragments are present, up to 0.5 mm.</p> <p>Crystal content is low, but small (0.01 mm) euhedral feldspars are present (1%), small (0.05 mm) fractured pyroxenes are also present (&gt;1%).</p>
<b>66</b>	Coherent porphyritic lava	<p>Highly vesicular sample (up to 75%) with large plagioclase phenocrysts. The groundmass consists of predominantly plagioclase with 30% of Cpx in 15% tachylite glass. Crystals in the groundmass have random orientations. The vesicles have fairly rounded coalesced shapes but do not disrupt the groundmass.</p> <p>Large phenocrysts vary from 0.5 to 2.0 mm in diameter. They show complicated twinning structures and may occur as overgrowths of previous crystals. Some crystals have significant fracturing.</p>
<b>67</b>	Baked sediment in Lt	<p>Fragments of highly angular and irregularly shaped sideromelane (60%), free crystals of plagioclase and rare Cpx (10%) and tachylite (20%) and 10% microlite rich tachylite. The vesicularity of the sideromelane fragments varies from 0 to 40%. Fragment size varies from 0.05 mm to 0.8 mm. Grain shapes are occasionally flat sided, but predominantly irregular in morphology, with some evidence of vesicle wall influence. Occasional alteration (reddening) of sideromelane occurs.</p>
<b>68</b>	Double dipped porphyritic clast	<p>Nice euhedral crystals of plagioclase up to several mm in diameter, with well formed twinning structures. Some multiple growth histories (inclusions of previous plagioclase grains).</p> <p>Color variation is a result of alteration. In thin-section is appears to be slightly green, perhaps chlorite developing from the Cpx.</p> <p>Groundmass of unaltered portion of the sample contains plagioclase and Cpx microlites. The ground mass is oriented relative to the large, multi mm vesicles. The vesicles are fairly circular with smooth sides. More irregular shapes are the result of alteration. Vesicles are about 40% of the sample. Plagioclase crystals are another 35%. The groundmass comprises the remaining 25% of the sample. The glass in the groundmass is tachylite and altered palagonite and sideromelane.</p>
<b>69</b>	Pillow glass porphyritic	<p>Highly altered groundmass, and minor alteration of phenocrysts. Typically expressed around vesicles, but some replacement of microcrysts. The groundmass consists of 70% plagioclase, with 10% Cpx and 20% glass, was</p>

		tachylite. Large rounded vesicles, with minor coalescence take up about 40% of the sample, and larger phenocrysts of plagioclase compose another 30% of the sample. Some crystals are up to 4 mm in diameter.
70	Lt non porphyritic, frothy	Sideromelane dominated sample, fragments are tightly packed and grain boundaries are difficult to distinguish. Most clasts are lapilli sized with some smaller clasts filling in the gaps. Clasts are vesicular up to 40% and vary from circular to deformed near clast boundaries. Palagonitized cement may account for the difficulty distinguishing between grain boundaries. Some grains have minor zones of tachylite. Smaller fragments are poorly vesicular with 1 to no vesicles intact within the grain. Shapes are blocky, but not all sides are flat and vesicle free. Phenocrysts are rare (<1 %), and plagioclase.
71	Mixed porphyritic, non-porphyritic	Significant alteration of glass, particularly on grain margins and along fractures. Fragments are sideromelane glass, both crystal-free and microlite-rich (plagioclase and Cpx). Large isolated plagioclase crystals (some crystals with minor remnant glass on one side). Crystals are broken and anhedral. Fragments are poorly sorted with clast ranging from 0.3 mm to 0.05 mm in diameter. Clasts have some vesicle influence (bubble wall fractures) and flat sides. Internal vesicularity is low (10%).
72	Lt porphyritic	Sideromelane glass fragments with significant 0.05 mm thick alteration rinds. Large phenocrysts of plagioclase, with complicated growth histories (up to 2 mm in diameter) occur predominantly as free crystals with occasional glass rinds. Vesicles in glass fragments are altered, but previous morphologies were elongate or round and only 10% of fragment volume. Some microlite-rich glass fragments are present (10%). Limited number of lithic fragments with microlites and large plagioclase crystals.
73	Mix of porphyritic and micro-porphyritic lapilli	Diverse fragment varieties: sideromelane/tachylite glass, free and broken plagioclase crystals, tachylite microlite-rich fragments, vesicular sideromelane. Most fragments have alteration rims, but previous morphologies are still visible. Clasts have vesicle influenced grain boundaries, but few internal vesicles. But some clasts show blocky shapes, and some show signs of mechanical abrasion.
74	Pillow microcrystalline glass	Tachylite glass dominated by radial spherulites of plagioclase microlites. Vesicular (70%) sample with no phenocryst population. Some Cpx microlites disrupt the spherulitic texture of the rest of the matrix. Vesicles are highly irregular in shape to circular. Toward the margin of the pillow the glass slowly becomes sideromelane through patchy evolution.
75	Lt Massive heterolithic	Clast varieties include holo-crystalline lithics, sideromelane and tachylite holo-hyaline fragments, altered palagonite fragments, micro-porphyritic basalt lithics with tachylite groundmass (varieties with glomerocrysts and without), and red scoria. Matrix fragments are dominantly sideromelane and free plagioclase crystals.
76	Lt mono-lithologic non-porphyritic	Contains large clast of typical micro-porphyritic basalt with macrophenocrysts of feldspar and vesicles (tachylite groundmass). Sideromelane glass fragments of various sizes and vesicularity. Some smaller tachylite fragments are also present. Micro-phenocrysts of plagioclase and Cpx are common in most clasts.

<b>78</b>	Heterolithic bedded Lt	Contains grains of highly altered vesiculated glass, deformed vesicle shapes. Other clasts are less altered and have circular vesicles (70% vesicularity). Free crystals are rare and typically broken. Some broken (jigsaw) tachylite clasts are present.
<b>79</b>	Lt vesiculated non-porphyritic, small lapilli	Fresh clean independent grains of sideromelane. With broken bubble walls, flat sides and variable clast shapes. Some clasts have internal vesicles, but many are dense. Some evidence of vesicle collapse, very fluidal looking structures. Poor packing. Grain size varies from sub mm to 1 cm. Crystals of plagioclase (4%) are rare and typically loose in the matrix. Grains are fractured and do not show zoning. Cpx also present but less common (1%)
<b>80</b>	Altered Lt, heterolithic	Highly altered, grains are reddish brown. Grain boundaries are hard to distinguish in places. Clasts are highly vesicular up to 80%, very round vesicles. Variations in grain size from large cm clasts to sub mm dense matrix fragments. Phenocrysts are rare (5%) Cpx and Plagioclase and are highly disrupted, broken edges, missing cores etc. Variation in color of some clasts. Large red clast is dominant feature at the center of the slide.
<b>81</b>	Altered Ac with micro-porphyritic lapilli	Palagonitized, very orange grains (edges are still distinct). Clasts are vesicular (60%) with frequent breakages along bubble walls. Some jigsaw fragments where grains are still in place after fracture. Minor sideromelane still present, usually at the core of altered grains. Vesicles are round, but vary in size from 0.1-0.5 mm in diameter. Spaces between fragments vary but packing is moderate. Rare crystals of plagioclase 0.5 mm, free crystals in matrix. Bubbles are filling in with zeolites and altered glass and minor mica.
<b>82</b>	Pillow from dike south side NGD Pillow rind (fragmented )	Chill rind of pillow, similar to chill on dikes. Transition from tachylite to sideromelane. Limited crystal presence. Rare glomerocrysts in individual clasts. Some color variation amongst clasts. Elongate flat sided clasts common
<b>83</b>	Lt glassy, non-porphyritic, angular	Tightly packed, angular clasts, low vesicularity. Contains large vesiculated clasts of tachylite, swirly contact (IMG 117). Vesiculated clasts of sideromelane also present, with round margins, elongate vesicles. Some coalesced vesicles. Clast size 0.25-1.5 mm
<b>84</b>	Sediment in CMVD	Bands of alteration and clast concentration. Highly porous. Mostly void space 50%. Some large clasts of broken tachylite. Otherwise predominantly sideromelane. Some coalesced vesicles, some broken. Frequent blocky clasts. Glomerocrysts of feldspar only 5%. Occasional larger individual crystals (euhedral) occur. These occur in larger fragments.
<b>85</b>	Lt country rock	Poorly sorted vesicular sideromelane glass fragments. Fragments range from 0.01 mm to 1.0 mm. Fragments have blocky flat sides with angular corners, and broken vesicle walls (40%). Vesicle shapes vary from circular to angular. Some needle-like splinters of glass are present next to blocky fragment walls.
<b>87</b>	Pillow in unit above dike	Plagioclase 40% and Cpx 40% microlite rich tachylite groundmass with numerous coalescing vesicles (50%). The microlites have a random orientation. Vesicles have 0.2 mm tachylite rims before microlite presence dominates. 1% larger phenocryst population of plagioclase is present.
<b>88</b>	Pillow in dike	Only occasional large crystals of OPX

		<p>Impressive transition between sideromelane and tachylite.</p> <p>Part of a pillow core.</p> <p>Predominantly circular pillows.</p>
89	Country rock	<p>Vesicles are highly coalesced in matrix. Individual clasts have irregular grain shapes. More spherical vesicle shapes, more self-similar sizes.</p> <p>Glomerocrysts of feldspar and pyroxene are more common in clasts than in matrix. Feldspars are well formed, euhedral, pyroxenes are rounded, anhedral.</p> <p>Includes some clasts of highly vesicular tachylite.</p>
90	Peperitic dike matrix (CMVD)	<p>Contains large (1 cm) fragments of light brown sideromelane, vesiculated, some alteration around vesicles.</p> <p>Matrix is highly fragmental, with significant void space.</p> <p>Some highly altered feldspars in matrix. Broken edges.</p> <p>Cusate forms common. Blocky forms more common in fine particles.</p> <p>Blue epoxy used to estimate void space 35-45%.</p> <p>Fractures in large grains filled with fragmental matrix.</p> <p>Shows increased alteration relative to host rock.</p>
91	Porphyritic lava	<p>Large (up to 1 cm) crystals of plagioclase. Contains inclusions of discrete and twinned anhedral plagioclase grains up to 1 mm in diameter. Also anhedral Cpx ca. 1 mm. Isotropic elongate shapes are also included in the plagioclase crystals. (Potentially late stage glass is occupying fractures or 3 dimensional surfaces in the grain that appear to be inclusions in 2 dimensions?). At least one example The sides of the host grain show significant chemical disequilibrium including embayments, anhedral shapes and new growth directions (crystals are used as nucleation points for other crystals).</p> <p>Vesicles are round and up to 5 mm in diameter. The ground mass consists of microcrysts of plagioclase and Cpx.</p> <p>30 % of the groundmass is glass.</p> <p>25% macro-porphyritic crystals.</p> <p>Some larger crystals of Cpx have plagioclase microcrysts nucleating along the margins.</p>
92	Heterolithic LT	<p>Highly altered, glass fragments have alteration rims up to 0.2 mm in diameter. Phenocrysts of plagioclase up to 1.5 cm are present, and usually display broken grain shapes, complex twinning structures, and inclusions of older plagioclase grains.</p> <p>Crystals may have remnant matrices of sideromelane or microlite rich sideromelane glass. Other fragments include vesicle rich sideromelane, poorly vesiculated tachylite, sideromelane with Cpx phenocrysts, and altered tachylite. Grain size is variable, but average clast size is on the order of 0.2 to 0.5 mm in diameter. Crystals of plagioclase are typically 0.5 mm. Crystals and glass fragments display mechanical breakages. Vesicle wall influenced fractures are still visible on 20% of grains.</p>
93	Lt glassy matrix in gully	<p>Large intact lithic (tachylite) grains, lots of interstitial fragments filling spaces between clasts. Most fragments are sideromelane glass, with low vesicularity and lots of blocky grain shapes. Needles are common near flat sided fragments. Some fragments have banding of tachylite and sideromelane.</p> <p>Large grains have larger mechanical fractures. Small fragments of tachylite are more common in the vicinity of the larger fragments that contain tachylite.</p> <p>Micro-phenocrysts of feldspar are common 15% in sideromelane clasts.</p> <p>Packing of grains is variable.</p>



<b>94</b>	Pillow, possible glass	Glomerocrysts of plagioclase and microlites make up 40% of the tachylite groundmass. The sample is highly vesicular with multiple bubble sizes (60%) between 0.1mm to 2.0 mm. Vesicle shapes are irregular and show signs of coalescence.
<b>95</b>	Deformed sediment	Lots of alteration of vesicles and grain margins, palagonite and clay. Phenocrysts include Cpx and plagioclase, some crystals display undulose extinction. Clasts are typically around 0.3 mm in diameter. Grain sizes are variable and well packed (palagonite makes clast margin identification difficult). Vesicularity varies between 0-15%. Tachylite fragments are typically smaller, but can be up to 1.0 mm and are typically crystal-free. Large phenocryst glomerocrysts include large Cpx. Other microcrysts rich clasts contain equal feldspar and Cpx.
<b>96</b>	Glass pillow at base	Microlite rich tachylite lava. With irregularly shaped vesicles up to 70%. Vesicles have tachylite rims up to 0.1 mm in thickness. Minor alteration (oxidation?) at vesicle walls. Groundmass is 20% tachylite, 70% plagioclase and 10% Cpx.
<b>97</b>	Lava flow	Microcrystalline dominated vesicular tachylite basalt. Groundmass is 40% plagioclase, 30% Cpx and 30% tachylite glass, which is concentrated around the vesicle walls. Crystals have random orientation, occasional glomerocrysts, but otherwise even distribution throughout the groundmass. Vesicles are 40% of the total. Bubble shapes are near circular with minor coalesces.
<b>98</b>	Heterolithic Lt	Large rounded clasts dominated by tachylite glass, vesicular and crystal-free with a speckled appearance. Groundmass is dominated by sideromelane glass 60% to 40% tachylite. Some free crystals of plagioclase are present in the groundmass (0.4 mm). Moderate packing. Clasts are variable in color, crystal content, and grain shape. Vesicles are not common in the sideromelane glass, but do occur up to a few percent. Glomerocrysts are present in some of the sideromelane glass fragments. Vesicles are frequently lined with more orangey altered glass. Some reddish altered glass fragments are present as free clasts in the matrix.
<b>99</b>	Pillow core and glass	75% crystals (35% Cpx; 40% plagioclase). Crystals have random orientation and appear to have grown into each other. Remaining 25% is tachylite glass. 60% vesicular. Hand sample appearance is regularly shaped, round vesicles. The shapes are far more coalesced and convoluted in section. Bands of smaller vesicles (sub mm) are present. Glomerocrysts of larger plagioclase grains are rare (1%). The crystal shapes are highly altered.
<b>100</b>	Porphyritic lava	Weak alteration present in the form of orange alteration on the margins of crystals. 30% vesicularity with large 1-5 mm coalesced vesicles. Vesicles are lined with sideromelane, which is altering. Dominated by large 1-10 mm crystals of plagioclase. The crystals are anhedral, cracked and display some inclusions including other plagioclase grains. Plagioclase is frequently twinned (carlsbad and albite). Rare large Cpx grains (0.5 mm) are present. Large crystals are frequently used as a nucleation point for later, smaller crystals.

<b>102</b>	Subaerial lava	Microcrystalline groundmass of plagioclase 35% and 55% opaques and 10% tachylite glass. Phenocrysts are plagioclase isolated crystals (0.2 mm) and glomerocrysts (0.5-1 mm) of plagioclase and Cpx. 25 % vesicularity. Vesicles are irregular in morphology suggesting coalescence. Only minor alteration of glass within vesicle walls.
<b>103</b>	Lava flow (connected to pillows?)	60% vesicular microcrystalline basalt. Groundmass is 60%, 20% tachylite glass, 20% Cpx (smaller crystals). 2% outsized crystals of mostly plagioclase (euhedral crystal laths) and rare Cpx. Vesicles have irregular coalesced morphologies. Vesicles are outlined by crystal-free tachylite.
<b>104</b>	Bedded Lt, micro-porphyrritic vesicular	20% tachylite clasts. They reach up to .5 mm in diameter. Some are vesicle poor, with a maximum vesicularity of 20%. Vesicles are large; up to 2 mm. Crystals are small and have indistinguishable grain shapes. Free crystals of plagioclase and Cpx occur in the matrix 30%. Fragment size in the matrix ranges from 0.01 mm to 1 mm. The void space between individual fragments is discrete. Some clasts of lithified glass shards are present (1%). Some clasts of low vesicularity sideromelane glass lava with high crystal (70%) contents.
<b>105</b>	Diamictite (putative tillite)	15% tachylite clasts in a sideromelane clast matrix. Tachylite clasts have crystal contents between 20-90%. Matrix is sideromelane dominated; rounded grains and some more typical ash shaped (triangular) clasts are present. Mostly crystal free and vesicle free. Multiple glass colors are distributed throughout the matrix. Yellow, orange, brown and black. Some clasts show fresh breakages, others have rounded margins. Particularly the highest crystal content clasts. Clasts of palagonitized ash tuff are common. Vesicular clasts have variable vesicle shapes. Rare isolated clasts are present in the matrix. Clasts reach up to 1 cm.
<b>106</b>	Vesicular lava (sub aerial)	Microcrystalline (micron-scale crystals), large 5 mm long convolute vesicle shapes, lots of coalescence. Glomerocrysts of plagioclase and Cpx, reaching 1 mm in size. Matrix has approximately 35% opaques (magnetite), 20% feldspar, 10% glass, 35% Cpx.
<b>107</b>	Vesicular micro-porphyrritic pillow (irregular unit)	Crystalline groundmass of 0.5 to 1 mm grains of plagioclase (30%), Cpx (50%) and 20 % glass (tachylite). Rare (1%) broken plagioclase grains. Vesicles are coalesced and irregular, cm scale.
<b>108</b>	Pillow core (regular unit ) some glass	Crystal-rich groundmass. Glassy rinds of vesicles are up to 0.5 mm thick. The matrix is otherwise dominated by glomerocrysts of plagioclase and Cpx grains. Plagioclase content is approximately 40%, Cpx is 35% and glass is 30%. Vesicles are approximately 30% of the total sample. They appear fairly round to the naked eye, but display common convolutions at the sub mm scale, indicated possible coalescence.
<b>109</b>	Glassy Lt	Very low vesicularity (0-4%). Although rare vesicles that do occur show signs of coalescence. And are up to 0.5 mm across. Large blocks contain tiny phenocrysts of plagioclase on the order of 0.08 mm. (Possible Cpx on the order of 0.005 mm. Color in PPL of crystals and glass are very similar.) Blocky shapes. Small fragments down to 0.05 mm to large fragments 1.0 cm. No orientation of grains or phenocrysts.

<b>111</b>	Lt Rosagil top	Low vesicularity. Obviously altered in hand sample. Visible palagonitization in thin section. Interstitial space has been filled in with orangey palagonite. Clasts are blocky and range in size from 0.01 mm to 2 mm. Predominantly sideromelane. Some tachylite clasts. Some transitional tachylite to sideromelane clasts up to 0.5 mm. No orientation of grains. Micro-phenocrysts of plagioclase common, but less apparent 20% than AG109.
<b>112</b>	Lt with variable vesicularity clasts	Presence of grain scale rims of palagonite. Some vesicles are also ringed with palagonite. Ca. 40% tachylite, rims weaker on black clasts. < 5% crystal content. Tachylite breaks down (honeycombed).
<b>113</b>	CMVD interior	Sideromelane clasts with rinds of more orange glass (alteration, weak palagonitization). Grain margins are dominated by flat, non curved fractures. Occasional (10%) have vesicular influences on grain shape. Some grains have intact vesicles on fragment interior. Bubbles are circular and also lined with orange glass. On the order of 0.5 mm in diameter. Fragments may occur in zones of similar shapes (elongate vs. equant). Dominantly 60% rectangular. 1% occurrence of tachylite fragments. Occur in clusters, distributed through the matrix. Rare 1% occurrence of broken plagioclase grains.
<b>114</b>	Porphyritic Lt intruded by 113	Macro-porphyritic, crystals are anhedral 1 – 6 mm clasts. Fractured and anhedral plagioclase grains. May display twinning or inclusions of Cpx and other feldspars. Matrix is composed of fragments of 90% sideromelane. Some clasts have tachylite zones. Some grains contain large plagioclase crystals. 50% of the sideromelane clasts have rinds of orange (palagonite) glass. Rare fragments of micro-crystalline lava. Similar to micro-porphyritic lavas described elsewhere. Crystals are broken along fragment edges. Glomerocrysts of feldspar crystals still occur. Some crystals are independent in the matrix.
<b>115</b>	Interior of expanding dike	Vesicles are coalesced and have irregular shapes and boundaries. Some are connected in larger networks (cm scale). Average vesicle dimensions are on the order of 1 to 5 mm. Significant (cm scale) glomerocrysts are preserved despite grain plucking. The groups consist of plagioclase and Cpx, opaques and rare fragments of tachylite. Opaques compose about 50% of the matrix. The remainder is sideromelane glass and micro-crystals of plagioclase 30%.
<b>119</b>	Black dragon Lt non-porphyritic	Sideromelane dominated 99%. Fragments range in size from 0.1 mm to 2 mm across. Fairly tight packing. Grain shapes are variable. Broken vesicles are common for about 60% of the grains. But other margins are dominated by flat sided ‘blocky’ breaks. Some of the larger fragments display elongate vesicles on the order of 1 mm in length. About 1 % crystals are present. They are typically broken and on the order of 0.1 mm. The crystals are plagioclase with about 30% Cpx. Grain shapes are all anhedral and fractured. Red spots of palagonitized glass is rare <1 %.
<b>120</b>	Heterolithic Lt	Fragments are predominantly sideromelane. Occasional vesicular tachylite fragments occur and are ca. 0.5 mm in diameter. Some grains contain feldspar and Cpx phenocrysts. Typically vesicular (irregular, coalesced morphologies). Rare grains of Cpx are loose in the matrix. Fragments may be highly vesicular (50%) some have lower vesicle

		<p>occurrences (5-10%).</p> <p>Clast sides are dominantly flat, but broken vesicles are common. Vesicle shapes within grains are circular, but some elongate bubbles are present. The fragments have high packing in some areas and significant void spaces in other (plucking?). Some of the glass is highly textured.</p>
121	Matrix-rich Lt with altered scoria	<p>Clasts of bright yellow altered glass with high (80%) vesicularity, vesicles are various sizes from 1 mm to 1 cm in diameter. Vesicle shapes are dominantly elongated and fluidal. Clasts of vesicular tachylite dominated glass (60%) have smaller vesicles predominantly 0.5 mm. Some fragments are dense tachylite glass. 5% of clasts have low percentages of 0.5 mm crystals of plagioclase (laths).</p> <p>Matrix fragments are 1 to 3 mm in diameter predominantly sideromelane (70%). Fairly well packed. Clast margins are mostly flat, or with a very weak curvature. Grains are triangular. Rare 1% isolated crystals of plagioclase in the matrix.</p>
140	FG B matrix	<p>Good sample for palagonite measurements and descriptions. Exploitation of cracks and vesicles. Sideromelane glass with microlites of plagioclase (60 %) and Cpx (40%). 30%-60% of total glass. Some color variations are apparent on slide, but the distinction is harder to notice under microscope. Clast shapes are blocky and variably vesicular. Rounded and elongate bubbles dominate (when intact). Broken irregular bubbles are common at grain margins. The beginning of coalescence.</p> <p>Transitions from sideromelane to tachylite. Clasts with this transition compose 15% of the sample. Bubbles of clasts can be deformed around microlites. Isolated phenocrysts of plagioclase up to 0.5 mm in length. Cpx, more equant and smaller. 2 and 1 % of the deposit respectively.</p>
141	FG C clast	<p>Highly convoluted bubble morphologies, coalesced. Some rounded edges, but plain circular cross sections rare.</p> <p>Microlites make up about 20% of the groundmass. Tachylite glass is the remaining 60%. Plagioclase and Cpx. &lt; 0.3 mm</p> <p>Rare larger crystals are present 1%. Obvious remnants of vesicle coalescence. Some large vesicles have sideromelane fragment infill. Palagonite has begun to form in some vesicles.</p>
142	FG C matrix	<p>Multiple clast types. Sideromelane with microlites, sideromelane and tachylite with microlites and tachylite without microlites combined, tachylite. Vesicle patterns are inconsistent and may change over 1 mm or less.</p> <p>Sideromelane fragments dominate and have an alteration coating.</p> <p>Crystals are randomly oriented and have an uneven distribution.</p>
143	FG D clast	<p>Highly convoluted vesicles and some alteration rims (0.0.2 mm) developing. Microlite rich (60%) tachylite groundmass. Plagioclase crystals randomly oriented. Some Cpx (20% of crystals). Crystals can circumscribe vesicles filled with opaques.</p>
144	FG D matrix	<p>Limited matrix attached to large vesicular clast.</p> <p>Matrix is preserved in vesicles of the clast margins. Highly angular sideromelane clasts with 20% opaques.</p> <p>Some broken vesicles in sideromelane fragments.</p>
146	KT C matrix	<p>Sideromelane dominated matrix, broken vesicles and fractures dominate grain edges. Poorly sorted.</p> <p>Variable concentrations of microcrysts.</p> <p>Larger clasts may have transitions into tachylite</p>

		Larger phenocrysts of plagioclase do occur. Vesicles are fairly round, some coalescence.
147	KT C clast	Vesicles are highly rounded, except when filled with palagonite. Very larger irregularly shaped coalesced vesicles are common (20%). Very black tachylite glass. Some microlites (10%) Very red palagonite occurs in largest vesicles. Most crystals are randomly oriented, some are spherulites. Dominated by plagioclase, with likely minor Cpx, in tachylite groundmass. Larger crystals of plagioclase and Cpx consist of <1% of the total sample <0.2 mm in diameter.
148	KT C pillow bit	Highly similar to C clast. Tachylite groundmass with randomly oriented phenocrysts. Greater variability in vesicle shape (occurs in deformed bands). Some phenocrysts protrude into vesicles. Suggesting that the crystals formed before the vesicles. Polymodal vesicle size distribution. Phenocrysts (1%) of Cpx and plagioclase up to 0.5 mm Some palagonite formed on vesicle interiors. Bulbous growths. Glomerocrysts are rare, but include Cpx and plagioclase.
149	KT D clast	Tachylite matrix with microlites randomly oriented. Vesicles of various sizes, some are coalesced and quite large. Smaller vesicles are more rounded. Zones of vesicle populations (some are elongate and grouped) Spectrum of vesicle sizes. Some palagonite formed in vesicles. Groundmass is randomly oriented plagioclase phenocrysts in tachylite matrix. Bubbles are deformed around microlite.
151	KT E matrix	Sideromelane fragment dominated, larger tachylite clasts have vesicles that are intact and rounded, and vesicles on the edge of clasts are filled with sideromelane fragments. Bubble trains and fluidal structures internal to large clasts. Sideromelane clasts have very tiny microlites of plagioclase. Even distribution suggests possibly devitrification. Larger phenocrysts do exist, but are frequently broken. Some clasts have swirls of crystals in cross-polarized light that are associated with darker bands swirled in the PPL. Clasts with transitions between tachylite and sideromelane are still present, only smaller 5% of total. Mild palagonite rim on most clasts.
152	KT E clast	Vesicles are predominantly rounded, but are irregular (not smooth). Some coalescence. Does irregularity result from bubble collapse. Coalesced vesicles reach 2 mm in diameter. Occasional glomerocrysts of plagioclase occur in the groundmass. The groundmass is tachylite glass with two size populations of microlites. The smaller may be devitrification.
153	KT F clast	Bubble train. Vesicles are variable in shape, lots of elongate vesicles and convolute shapes. Aphyric to 1% plagioclase phenocryst (<0.1 mm). One phenocryst up to 0.2 mm of plagioclase. In decent shape. Very dark tachylite.

155	KT G clast	<p>Highly fluidal textures in vesicles. Near margins. Center of the clast have more equi-dimensional, but not circular in shape.</p> <p>Trapped vitric sideromelane particles in some deformed vesicles.</p> <p>Development of sideromelane at the margins of the clast, the contact is highly fluidal and convoluted.</p> <p>1% phenocrysts of plagioclase (broken) and Cpx (broken)</p> <p>Very dark tachylite groundmass.</p>
156	KT G matrix	<p>Large clasts with tachylite to sideromelane transitions</p> <p>Dominantly shards of sideromelane with tiny microlites.</p> <p>Some chunks of crystal-free tachylite</p> <p>Larger phenocrysts are skeletal.</p> <p>Phenocrysts are less than 1% of the total. Plagioclase crystals, broken.</p> <p>Phenocryst distribution is variable. From 10-40% of the sideromelane fragments.</p> <p>Vesicle coalescence is common in sideromelane fragments.</p>
157	KT H clast	<p>Lots of vesicle coalescence, smooth sided, isolated vesicles are more rounded.</p> <p>Some palagonite accumulating on vesicle margins. Multiple vesicle populations.</p> <p>Some crystals protrude into vesicles, others are oriented around them.</p> <p>Crystals formed first.</p> <p>Micro-phenocryst dominated groundmass. Larger crystals are nucleation points for microcrysts.</p> <p>Some dense bands of vesicle and crystal depleted glass are darker.</p> <p>Overall tachylite glass.</p>
158	KT H matrix	<p>Microlite (&lt;30%) bearing sideromelane glass shards with palagonite rims.</p> <p>Tachylite is minor (1%) and contains no microlites.</p> <p>Coalescing bubbles, double bubbles.</p> <p>Vesicle shapes in intact fragments are rounded, some coalescing. Various sizes. Cpx phenocrysts are present and highly fractured.</p> <p>15% of the sample includes clasts that are transitional sideromelane to tachylite.</p> <p>The remainder is sideromelane.</p>
159	DG A matrix	<p>Sideromelane and tachylite glass fragments. Microlites are TINY. Potential devitrification driven crystallization.</p> <p>Elongation of coalesced, irregular margined vesicles.</p> <p>Large phenocrysts of plagioclase, broken edges.</p> <p>Elongate bubbles along transitions between sideromelane and tachylite, fragment boundaries.</p> <p>Large clasts surrounded by smaller highly angular clasts of sideromelane, transition sideromelane to tachylite and tachylite.</p>
160	DG A clast	<p>Fluidal shapes of vesicles and bands of glass.</p> <p>Tachylite and sideromelane/tachylite transitional clasts.</p> <p>Some sideromelane rims may be agglutinative. Especially when crystal contents vary between the two. With irregular boundaries.</p> <p>Vesicle orientations are highly variable. Fluidal patterns and at least two size populations.</p>
161	DG B matrix	<p>Tachylite dominated clast with sideromelane edges and adhered clasts.</p> <p>Lots of fluidal textures of bubbles and glass colors.</p> <p>Lots of alteration textures (darkening around phenocrysts). Sideromelane has lots of microlites</p>

		Long chains of coalesced bubbles. Phenocrysts of plagioclase up to 0.2 mm
162	DG B clast	<p>Microcline rich. Most vesicles are highly rounded, but some convoluted coalesced vesicles are present.</p> <p>Range in vesicle sizes is nearly continuous.</p> <p>Minor sideromelane rim on tachylite dominate clasts.</p> <p>Break down of glass is visible in color variation and tiny crystals</p> <p>Large phenocrysts of Cpx up to 0.2 mm and plagioclase, broken and rounded.</p>
163	DG B pillow	<p>A: Microcline-rich with predominantly ovoid vesicles, some irregularities in vesicle walls.</p> <p>Red alteration (spherical), bubble chains and larger crystals of plagioclase (1%) are up to 0.2 mm.</p> <p>B: Microcline-rich with minor alteration (reddish oxidation). Large vesicles of variable shapes (coalesced). Plagioclase and Cpx microcline up to 40% rare larger crystals are broken plagioclase up to 0.2 mm. Growths inside vesicles of secondary minerals.</p>
164	DG C matrix	<p>Matrix attached to large clast of tachylite with sideromelane rim.</p> <p>Matrix is sideromelane fragments with high angular sides and alteration rims.</p> <p>Microclines up to 0.1 mm are common, predominantly plagioclase.</p> <p>Vesicles are commonly near grain edges, but nearly complete.</p> <p>Matrix also includes clasts which are both sideromelane and tachylite, porphyritic tachylite, and altered sideromelane. Sideromelane vesicles are rounded but some are elongate and coalesced.</p> <p>Clasts of tachylite (crystal-free) and tachylite with crystals make up 2% of the matrix.</p> <p>The big tachylite clast has very few phenocrysts.</p>
166	DG D matrix	<p>Sideromelane clast dominated lapilli tuff with tachylite sideromelane mixed clasts, tachylite clasts and altered glass clasts.</p> <p>Sideromelane is poorly crystalline.</p> <p>Lots of fluidal textures in larger sideromelane grains, highlighted by tachylite, alteration and or vesicles.</p> <p>Circular and oblate vesicles common.</p> <p>Complicated clast shapes not uncommon.</p> <p>Free crystals of plagioclase occur near tachylite clasts.</p> <p>Some apparent included clasts in the sideromelane of a darker glass type, contacts appear fairly sharp.</p>
167	DG D clast	<p>Tachylite clast with complicated sideromelane transition to thick (mm) margin</p> <p>Phenocrysts of twinned plagioclase up to 0.2 mm in length scattered throughout clast. Devitrification crystallization. Alteration around microcrysts and cracks expressed as a darkening of the glass (oxidation). Fibrous.</p> <p>Palagonite developed along cracks and inside vesicles.</p> <p>Vesicles are mostly rounded with irregular margins and some evidence of coalescence.</p> <p>Bubble trains and elongate vesicles occur together.</p> <p>Vesicles on margin show evidence of bubble destruction.</p>
168	DG E matrix	<p>Large sideromelane fragments with convoluted bubble shapes, some collapsed, some elongate and rounded. Smooth sides of vesicles dominate.</p> <p>Very limited alteration especially compared to previous samples. Alteration focused mainly around smaller clasts.</p> <p>Very low crystal content. Glassy dominated.</p>

		<p>Some clasts have high microlite content (up to 70%) in smaller fragments about 10% of total.</p> <p>Phenocrysts that are present are plagioclase (twinned) up to 0.2 mm long. &lt;1% of total. Some sideromelane clasts have dark edges (tachylite or oxidation? Too minor to distinguish).</p> <p>Poorly sorted sample. Large elongate vesicles distort surrounding vesicles. Good bubble coalescence</p>
169	DG E clast	<p>Some matrix attached to outside. Might be part of the clast's sideromelane rim.</p> <p>Limited crystal content. Large phenocrysts present are up to 0.2mm and are plagioclase.</p> <p>Alteration concentrates along fractures at grain edges (affecting predominantly sideromelane).</p> <p>Ductile and brittle deformation, high shear rate on the clasts.</p> <p>Potential agglutination at clast margins of other clasts, tachylite with concentrated alteration (oxidation).</p> <p>Larger elongate (parallel to clast margin) vesicles near clast rim, more circular and smaller vesicles toward clast center. Vesicle coalescence common. Irregularly shaped vesicles at center of clast, caused by bubble collapse.</p> <p>Some phenocrysts present of plagioclase up to 0.2 mm, broken edges (twinned). Some devitrification crystallization.</p> <p>B: lots of swirly textures and convoluted vesicles.</p> <p>Same crystal population. Increasing microlite population to center of clast.</p>
170	DG F porphyritic xenoliths	<p>Large 1-4 mm phenocrysts of plagioclase with well established twins, overgrowth structures and broken edges. The ground mass is 50% Cpx, 40% plagioclase laths and 10% tachylite glass.</p> <p>Vesicles are large and round with two distinct size populations. Larger phenocrysts of Cpx reach up to 0.5 mm.</p> <p>Some vesicle coalescence in the small to moderate size vesicles.</p> <p>Oxidation of 40% of vesicle interiors. Appears in PPL as a darkened rim.</p>
171	DG F matrix	<p>Sideromelane fragment dominated. Some clasts have lots of microcrysts and altered margins. Others have large crystals that are broken (up to 0.5 mm) plagioclase.</p> <p>Sideromelane that is crystal free.</p> <p>All fragment types have vesicular clasts, but the smaller they are the lower the vesicularity.</p> <p>Irregular vesicles with lots of coalescence, fairly small. Large r bubbles are rounder.</p> <p>Clast void spaces (vesicles and cracks) can be filled in with sideromelane clasts and smaller fragments.</p>
172	DG G matrix	<p>Dominated by light colored sideromelane fragments with 5-8 % fragments with tachylite zones and transitions, or darker brown sideromelane.</p> <p>The lighter clasts have alteration rims that are visible in x polar.</p> <p>Vesicles present are elongate and round. Many are partially broken by clast margins, but not dominated the margin shape. Vesicle shapes are similar in all clast types. Clast shapes are variable but flat sides dominate.</p> <p>Very low crystal content. Approximately 10% of smaller clasts are microlite rich. Some rare free crystals. Poorly sorted, lots of fines between larger grains.</p>



173	DG G clast	<p>Lots of convoluted vesicles, some elongated, others with irregular margins. Groundmass is full of plagioclase microlites randomly oriented in tachylite. Large (0.2mm) phenocrysts of plagioclase are rectangular and occasionally broken, commonly twinned. Some vesicles have fragmental sideromelane infill.</p> <p>Complicated networks of vesicles are in close proximity to fairly round coalesced vesicles, lots of zoning in within individual clasts.</p>
175	DG H clast	<p>Sideromelane rim of clast has rounded circular vesicles. Swirly glass banding. Limited microliths, nearly crystal free. Rounded vesicles pervasive, some smaller vesicles concentrate in zones. Some elongate vesicles cluster. Subject to ductile deformation.</p> <p>Zeolites filling some vesicles.</p>
176	NG B 1 <sup>st</sup> pillow in breccia	<p>Variable vesicle shapes, lots of coalescence. Groundmass is tachylite with microlites of plagioclase and Cpx. Glomerocrysts of microlites up to 0.3 mm. Transition from rim to core from sideromelane with 15% microlites to core of tachylite with up to 40%.</p> <p>Very round vesicles dominate. Large coalesced vesicles are common. Vesicles are disrupted by the surrounding crystals.</p> <p>Larger phenocrysts are used as nucleation points for microcrysts. Larger crystals are broken.</p> <p>Minor palagonite in vesicles.</p>
177	NG A pillow	<p>Irregular circular vesicles with some coalescence.</p> <p>Glomerocrysts of plagioclase (up to 0.5 mm) and Cpx in a matrix of randomly oriented plagioclase and Cpx microlites. , some bubbles are disrupted by crystals suggesting crystals formed first. Lots of crystals are broken. Larger phenocrysts are all broken (plagioclase up to 0.4 mm; Cpx up to 0.2 mm).</p> <p>Minor palagonite on vesicle interiors.</p>
179	NG C clast with minor matrix	<p>Lots of clasts with sideromelane tachylite transition.</p> <p>Some sideromelane can incorporate pieces of dense tachylite (with phenocrysts 2%).</p> <p>The sideromelane contains microlites &lt;0.05 mm.</p> <p>Large vesicles in tachylite clasts contain broken shards of sideromelane.</p> <p>Some fluidal trains of vesicles in larger clast. Parallel to margins.</p> <p>Larger clast of tachylite is fairly crystal free (&lt;2%).</p> <p>With a rim of sideromelane including elongate vesicles. Up to 0.75 mm long.</p> <p>Between sideromelane fragments palagonite veining has developed.</p> <p>Phenocrysts present include plagioclase and Cpx. In small rectangular grains.</p> <p>Sideromelane clasts are full (30-40%) of microlites.</p> <p>Transitional glass types have fluidal textures that are bisected by and deformed by vesicles.</p>
180	NG D matrix	<p>Coalescing bubbles in progress. Preservation of very fragile features.</p> <p>Some palagonite on vesicle walls</p> <p>Microlites in a tachylite groundmass.</p> <p>Vesicle spaces are occasionally filled with tachylite glass fragments (result of thin section process?).</p> <p>Vesicles are very rounded when not obviously being coalesced.</p> <p>Radial glomerocrysts (spherulites) are present in about 5% of the sample</p> <p>Margins of clasts transitions into sideromelane.</p> <p>No variation in microcrysts at the transition.</p> <p>Smaller vesicles not present in the sideromelane rim.</p>

182	NG E clast	<p>Sideromelane glass infilling some vesicles.</p> <p>Highly microlite rich tachylite groundmass with lots of coalesced vesicles. Predominantly blades of plagioclase that are randomly oriented.</p> <p>Vesicles are highly deformed, perhaps collapsing.</p> <p>Glomerocrysts of feldspar up to 0.5 mm</p> <p>Increasing sideromelane to clast margins. No decrease in phenocrysts, but tachylite persists around crystals. Vesicles in sideromelane zone still larger and convoluted.</p> <p>Rare Cpx phenocrysts (microlite) are present about 5% of total.</p>
183	NG E matrix	<p>Complicated clasts with sideromelane and tachylite. Some with transitions and some with sharp contacts.</p> <p>Microlites of about 10% are scattered throughout (random).</p> <p>Contains larger sideromelane fragments with elongate rounded bubbles. All clasts have angular margins, some with more vesicle influence than others.</p> <p>Glomerocrysts up to 0.4 mm of plagioclase and Cpx are present about 5% of the time.</p> <p>Sideromelane fragments have developed a thin palagonite rim (0.01mm)</p> <p>Some dense tachylite (5%) has limited crystals.</p> <p>Includes larger clast margin with sideromelane to tachylite transition, with lots of fluidal textures.</p> <p>Some textures are deformed around vesicles, other cut by vesicles.</p>
184	NG F matrix	<p>Clasts are made of sideromelane and tachylite sideromelane transitional clasts</p> <p>The lighter sideromelane has some alteration along fracture plans and contacts.</p> <p>Both glass types have available crystals and glomerocrysts of dominantly feldspar, some Cpx.</p> <p>Phenocrysts are about 10% of the total groundmass</p> <p>Vesicles have smooth sides, but elongate rounded shapes. Grain outlines are easier to see in cross-polarized light.</p> <p>Preserved bubble coalescence wall.</p> <p>Vesicles in tachylite bearing grains are frequently filled in with sideromelane fragments</p> <p>Fluidal vesicle textures common in tachylite bearing grains.</p>
185	NG F clast	<p>Lots of preserved sideromelane rim</p> <p>Limited phenocrysts present in either glass type. Typically plagioclase, isolated.</p> <p>Vesicle margins are disrupted, but overall shape is fairly circular.</p> <p>Crystals have darker glass surrounding them. Fibrous growth? See pictures at 40x</p> <p>Large phenocryst of plagioclase in sideromelane rime.</p> <p>Vesicles with partial fill (cusped) of dark glass, does not look fragmental.</p> <p>Darker glass without crystal in the middle is still fibrous in nature. Tachylite or oxidation. Undulose extinction, no isotropic. Mineral! Break down of glass. Turning into clay.</p>
187	NG H clast and matrix	<p>A and B clast:</p> <p>B: Some circular vesicles some collapsed. Some elongate.</p> <p>Multiple vesicle size populations Highly irregular vesicle walls, overall shape is rounded. Lower crystal content than has been observed &lt;10% some spherulites in the glass.</p>

		<p>Cracks filled with sideromelane fragments.</p> <p>Sideromelane margins of clasts with a higher crystal content (plagioclase)</p> <p>A: Highly crystalline up to 60%, 30% vesicles 10% groundmass</p> <p>Highly coalesced vesicles- starting to form convoluted pipes.</p> <p>Areas of crystal concentration up to 70%, surrounded by slightly less dense crystal population</p> <p>Crystals radiate from multiple points, spherulites?</p> <p>Alteration concentrated along vesicle walls.</p>
189	NG I matrix	<p>Vesicular crystal-free tachylite is enclosed in a fluidal clast of glomerocryst-rich tachylite clasts. Microlites are tiny. Phenocrysts of plagioclase do not exceed 0.2 mm and are only present in 1% of the sample.</p> <p>Highly diverse shapes of vesicles from small and round to large and elongate, irregular and coalesced. Deformation of glass structures occur around the largest bubbles.</p>
190	Pillow (non-porphyritic)	<p>Microcrystalline vesicular lava. Long laths of plagioclase are oriented randomly dominating the groundmass. Cpx grains are shorter and stubby and make up 15% of the groundmass.</p> <p>Domains without crystals remain vesicular, and are composed of tachylite glass. Secondary melt infill or Tachylite. Vesicular. Crystals are distributed around vesicles, parallel to vesicle walls.</p>
201	Clast and matrix	<p>Three major clast types: sideromelane glass with microcrystalline randomly oriented feldspar (30%) and rare Cpx (5%). The vesicularity of these clasts varies; Dark brown, vesicular glass with microcrystalline feldspar laths, randomly oriented, composing 25% of the sample. Large (0.2 mm) isolated phenocrysts of feldspar, subhedral, and twinned (2%). Groundmass also contains 5% Cpx, small. Subhedral to anhedral crystals tends to form clusters; Dense black glass with 15% feldspar laths.</p> <p>Clast margins are fairly rounded and coated in alteration products. Rare angular clasts do occur, and some spaces between grains are filled with smaller particles. Dominated by type one clasts.</p>
202	Pillow	<p>Fairly dense crystalline groundmass full of randomly oriented, slightly spherulites feldspars. Rare larger (0.2 mm) feldspars make up approximately 3%. Vesicles that are present are in roughly formed coalesced chain.</p> <p>Groundmass is ~50% plagioclase laths, and 50% dark glass.</p> <p>Rare subhedral Cpx crystals up to 2 mm occur (&lt;2%).</p>
203	Ac and Lt	<p>Well developed cement (light yellow). Larger, most common sideromelane fragments, with rounded margins have well developed alteration rims.</p> <p>Multiple clast types are present (up to 4). Micro-phenocrysts occur free in matrix and in high concentration in some of the clasts. Some clasts are highly vesicular, and/or crystalline. Cpx are present up to 5% in some fragments. Some glass fragments have a reddish hue.</p> <p>Alteration rims occur in vesicles of some particles. Poorly sorted grain size.</p>
204	Top of pillowed intrusion	<p>Glomerocryst rich dark glassy matrix. Micro-phenocrysts are laths of feldspar and small round crystals of Cpx. Crystals are deformed around vesicles indicating relative order of formation. Laths are very thin, but can be up to 0.5 mm in length. Vesicle morphology indicates coalescence. Sample is highly vesicular (up to 40%) and microcrystalline content is up to 40%</p>
205	Pillows at top	<p>Dominated by fantail crystal structures suggesting rapid crystallization.</p> <p>Overprinting a crystalline matrix of glomerocrysts. Vesicles are deformed and suggest coalescence. Crystals appear to be deformed around vesicles, but</p>

		devitrification textures do not. Phenocrysts present are predominantly 90% plagioclase. Cpx is common only in the core of glomerocrysts.
206	Lt 1	Sideromelane fragment dominated. Grains are fractured and sizes are variable. Angular clasts dominate. Glomerocrysts are common (15%). Glomerocrysts are large, up to 1 mm, and dominated by rounded grains of Cpx. Crystals have undulatory extinction, and apparent zoning (possible alteration rim?). Individual crystals are between 0.2 and 1.0 mm. Isolated broken clasts of feldspar are also common. Vesicle shapes are deformed (uni-directional). Some phenocrysts are associated with spherulites in a sideromelane background.
207	Pillow	Polylobate vesicles dominate. Some are filled with sideromelane fragments. Glomerocrysts are common. Glomerocrysts are composed of stubby Cpx grains with elongate spindles of feldspar. Vesicles appear to be deformed around the crystals (not the other way around). Crystals compose approximately 20% of the groundmass.
208	Bedded Ac	Large clasts of finer sediment, up to 2 cm long. Orange and palagonitized fine ash. Bedding is preserved in thin section. Images are taken with horizontal axis parallel to apparent bedding. Clasts occur in a fine matrix of multiple grain types including crystals, tachylite glass, and sideromelane glass. Some are vesicular, some are dense. Some alteration at margins of clasts is visible. Matrix is poorly sorted, with zones of similar clast concentrations. Free crystals include Cpx and Feldspar up to 0.2 mm. A gross structure appears at the scale of slide, but at the scale of the FOV the grains appear to be randomly oriented. Slide scale banding is due to concentrations in grain sizes. May contain olivine bearing tachylite glass.
209	Pillow breccia	Ashy matrix with multiple clast types. Dominated by sideromelane glass with glomerocrysts of Cpx and feldspar. Second clast type is sideromelane glass and may have devitrified (blackened) margins. Most clasts are vesicular, with random vesicle distribution, and variable sizes, shapes of vesicles. Feldspar crystals are long thin blades with round stubby Cpx at the center of the glomerocrysts. Larger clasts have devitrification textures around feldspars (spherulites).
210	Pillow	Microcrystalline ground mass up to 90% crystals. Small rounded Cpx (40%) and long bladed feldspar (50%). Even distribution throughout sample. Vesicles have rims of higher glass concentration. Rounded, coalescing shapes of vesicles.
211	Matrix	Clast margin fragments, some devitrification textures with sideromelane rim. Crystals in the sideromelane are tiny and do not exceed 15%. Phenocrysts appear to be predominantly feldspar. Alteration rims are common. Dominated by sideromelane fragments of various sizes. Some clasts have fragmented particles at their rims. Dominated by fairly intact pieces of glass. Large rounded vesicles with some coalescence and weakly deformed morphologies. Other clast types include more tachylite, higher crystal contents and reddish colors. Clast margins are subrounded.
212	Matrix	Contains sideromelane only clasts, obvious lapilli margins (partial chills) and dark tachylite dominated clasts. Alteration rims are common. Clasts are predominantly angular. Crystal content is generally low. Rare fragments with

		20% macrophenocrysts are present. Reddish altered fragments are present. Vesicles are present, but overall vesicularity is low. Vesicle are rounded and minimally deformed.
213	Pillow (non-porphyritic)	Highly convolute vesicle shapes and multiple size ranges. Phenocrysts are common, but occur in domains. Phenocrysts are predominantly feldspar, with random orientations.
214	Pillow (non-porphyritic)	Vesicular microcrystalline lava. Crystals are predominantly feldspar laths, up to 0.2 mm in length. Crystals make up approximately 60% of the groundmass, with 40% being feldspar. Vesicles dominate the sample volumetrically and are predominantly rounded, with irregular edges. Some coalescence is visible. Some glomerocrysts occur in the groundmass. Feldspar with supporting Cpx (stubby grains). Vesicles appear undisturbed by vesicle formation.
215	Pillow (non-porphyritic)	Vesicular microcrystalline lava. Vesicles have multiple size populations. Crystals are more dominant in groundmass than previous sample (larger crystals, up to 70% of groundmass). Crystals have radiating structures, but random orientation. Some vesicles are polylobate due to infilling. Some create chains. Devitrification likely. Crystal free rims of vesicles. Some vesicles have fine ash infill (sideromelane and tachylite fragments and plagioclase crystals).
216	Pillow (non-porphyritic)	Vesicular microcrystalline lava. Two major modes of vesicle sizes are present. Large and round and fine and convolute. Large round vesicles show evidence of coalescence at margins. Crystals are shorter, with more abundant Cpx in the groundmass. Only 15% glass. Vesicles appear to be late stage and fill in spaces between crystals, not influencing fabric, but exploiting.
217	Pillow (non-porphyritic)	Cpx are more euhedral, making up 30% of the groundmass. And laths of feldspar compose 40% of the groundmass. Vesicles are of various sizes and appear to influence the geometry of crystals only locally. Otherwise they are radial. Concentration of black glass, or infill on vesicle walls.
218	Pillow (non-porphyritic)	Vesicular microcrystalline lava. Two modes of vesicles, small deformed vesicles and large coalesced vesicles and vesicle chains. The groundmass is predominantly crystals of plagioclase 50% and Cpx 40%. The Cpx are small and stubby. The plagioclase crystals are long and radial. Some glomerocrysts are apparent, but others are spherulites in structure.
219	Clast	Microcrystalline, vesicular lava. Vesicles are deformed and show signs of coalescence. Two major size ranges. Crystals are disrupted randomly in radiating patterns throughout the groundmass. Cpx make up approximately 20% of the groundmass. Some crystals are well formed, others are more stubby and anhedral. Crystals make up 90% of the groundmass. Vesicles have concentration of black glass at vesicle walls. Vesicles on the margin of sample are filled with fine ash.
220	Matrix	Sideromelane fragment dominated poorly sorted matrix sample. Clast sizes are variable. Large intact clasts have large deformed round sided vesicles. Vesicles make up approximately 10% of the fragments. Small randomly orientated crystals (except along the margins of large vesicles). Cpx forms nice euhedral grains, but show some fractures. Plagioclase forms thin blades, poorly formed. Some fragments have alteration rims around crystals (darkening of glass). Dominantly clasts are dense. Vesicles have dark black lining visible in tachylite dominated samples.

		Very fragile shapes are preserved.
222	Mix till and breccia	Very heterolithic mix of clast types. Vesicular larger clasts have vesicles filled with fine ash. Clast types include microcrystalline vesicular basalt, sideromelane (light brown to dark brown), lapilli quench margin fragments, Altered crystalline fragments hyper crystalline oxide bearing fragments and free crystals of plagioclase and Olivine up to 0.2 mm, vesicular porphyritic clasts. Clusters of phenocrysts of plagioclase with thin remnants of glass around the margins of the fragment. Fragment margins can be angular or rounded. The degree of alteration varies throughout the sample.
223	Tillite	Granular sample, clastic. Rounded clasts dominated. Some angular fragments are preserved (20%). Size range is more constrained than typically tuff deposits. Some clasts contain crystals in the middle (plagioclase). Predominantly sideromelane, but tachylite and mixed fragments are common. Crystals appear mechanically broken. Some alteration of clasts is observed.
228	Matrix	Dominated by fragments of sideromelane. Some alteration, discoloration of the glass occurs. Very low crystal content. Vesicles are large and round, slightly elongated. Clast sizes vary. Fine ash concentrated between larger lapilli clasts. Fracture and vesicle infill by dark opaque glass.
229	Pillow	Microcrystalline vesicular lava. Vesicles are rounded with irregular walls. Showing signs of coalescence. Walls are lined with opaque black. Groundmass is dominated by plagioclase laths and Cpx micro-phenocrysts. Rare (1%) larger phenocrysts are present. Phenocrysts are randomly oriented and show only local disruption by vesicles. Cpx composes about 15% of the groundmass.
230	Pillow	Microcrystalline vesicular basalt. The vesicles are rounded but have irregular walls and smaller vesicles are convolute. Glomerocrysts are common. Cpx is usually anhedral, plagioclase can be bladed or lathlike. Other groundmass is randomly oriented. Rare large phenocrysts of plagioclase occur (up to 0.5 mm long).
234	Valðalða lava	Large Cpx crystals with intersertal and variably sized plagioclase. Significant alteration of Cpx leads to a reddening of the sample. Plagioclase has radiating growth patterns. Seed crystals of plagioclase in altered olivine crystals.
235	Porphyritic Lapilli tuff	Sideromelane dominated sample. Some fragments are highly frothy. Small fragments fill in gaps between larger fragments. Vesicles are deformed, but have smooth rounded margins. Larger free crystals of Cpx and Plagioclase occur with incomplete glassy rims. Small clusters of plagioclase crystals occur in some grains. Possible olivine very fractured. Clasts of microcrystalline vesicular lava also present. Limited crystal content of the sideromelane itself.
236	Crystal rich Breccia	Glomerocryst-rich crystalline block in crystalline block dominated breccia. Glomerocrysts consist of plagioclase crystals around 0.5 mm and Cpx crystals up to 0.25 mm. Cpx crystals have undulose extinction and anhedral shapes. Broken crystal shapes are common. The glomerocrysts reach up to 1 cm in diameter. Isolated large phenocrysts of plagioclase reach up to 1 cm in diameter. Vesicles are rounded, but irregular in shape, forming after the crystals did. Boundaries of tachylite dominated glass indicate the clast boundaries.

		Vesicularity reaches ca. 20%
237	Pillow	Contains olivine, plagioclase and Cpx macrophenocrysts up to 0.5 mm in length (up to 10% of the sample). Smaller plagioclase laths make up 15% of the sample. The vesicularity of the sample isolates glomerocrysts, large phenocrysts and laths. Vesicle shapes are convolute and show signs of coalescence. The plagioclase macrophenocrysts have fractured habits and swallowtail shapes.
238	Pillow fragment	Large phenocrysts of plagioclase and Cpx occur in clusters. Glomerocrysts are common. Cpx at the center with spines of plagioclase radiating outwards. Groundmass contains blades of plagioclase and rare small Cpx. Vesicles are convoluted and coalesced and disrupted amongst crystals suggesting formation after the glomerocrysts.
239	Pillow	Vesicular microcrystalline lava. Groundmass is holo-crystalline, with only 5% glass. Phenocrysts up to 0.2 mm of plagioclase are common, but significantly outnumbered by smaller laths and blades of feldspar. Cpx grains are stubby and smaller, but make up to 50% of the groundmass. Vesicles are convoluted with no apparent disruption of crystals. Crystal orientations are predominantly random, except on the largest of vesicles, where they parallel vesicle walls. Altered glassy fills of some vesicles. Larger crystals have undulose extinction and complex twinning. Some phenocrysts are up to 1 cm in length (twinned plagioclase, with complicated growth histories).
244	Lapilli tuff matrix	Sideromelane glass fragments with significant crystal components may have alteration rims around crystals and glomerocrysts (devitrification). Microphenocrysts are predominantly plagioclase, with 15% Cpx. Coloration is mainly a result of devitrification. But the coloration occurs along bands, following fractures. Path of oxidization. Some fragments show a concentration of crystals along the walls of broken vesicles. Some clasts show weak alteration of rims, but most do not.
245	Vesicular lapilli tuff	Matrix is loose with lots of free crystals and small broken pieces of microcrystalline and holo-hyaline materials. Also contains larger particles of vesicular tachylite glass and sideromelane glass. Grain margins are rounded or angular (frequently showing vesicle influence). Fragments of vesicular lava common.
247	Lt	Dark brown sideromelane with rounded elongate vesicles. Grain shapes are angular and may intersect vesicles and are rarely vesicle influenced. Vesicles can be connected in chains. Crystal content of the glass is low <30%, with glomerocrysts common. Plagioclase and Cpx dominate, with elongate blades and laths. A finer ash matrix is disturbed loosely between larger grains. Some grains have alteration rims.
249	Lt with pillow fragments	Crystals are large and isolated, frequently up to 0.5 mm. Plagioclase and olivine and Cpx. Vesicles are rounded and deformed in one direction (elongate). Ash sized particles infill vesicles near grain boundaries. Most particles are angular and may show some vesicle influence, but are predominantly flat sided. Some glomerocrysts occur of Cpx and Plagioclase. The largest crystals present are phenocrysts of plagioclase up to 1 mm in diameter in a sideromelane clast.

250	A'a on lapilli tuff	Oxide rich cryptocrystalline vesicular lava. The phenocrysts large enough to identify make up 15% of the groundmass and include 0.5 mm plagioclase clusters, and Cpx grains that are clinging to their sides or oxides. Twinning is a common feature of the plagioclase. Vesicles are convoluted and show signs of coalescence. Minor alteration rims surround oxides.
251	Coated lapilli tuff	Highly deformed lapilli, with elongate frothy vesicles. No regular orientation of particles. Highly altered. Low crystal content. Isolated crystals of plagioclase and Cpx. Some are isolated in the matrix, and others occur in glass fragments.
253	At	Sideromelane fragments dominate the sample, up to 95%. Other clasts include crystal rich tachylite (microcrystalline lava) and crystal bearing sideromelane fragments. Vesicles are present in large clasts and broken on the side of smaller clasts. Typically round and occasionally elongate. Isolated crystals are rare, but typically plagioclase laths. Some sideromelane fragments contain glomerocrysts of plagioclase and Cpx. Grains are loosely packed and fairly well sorted.
254	Pillow	Dominated by large round vesicles that disrupt the microcrystalline groundmass, enough to align crystals in proximity to the vesicles. Crystal population consists of plagioclase laths and subhedral blocks of Cpx. Larger phenocrysts (<1%) serve as nucleation point for groundmass crystals. Crystals in the groundmass have a random orientation. Some evidence of vesicle coalescence.
256	Lt	Altered sideromelane glass with loose crystals of Cpx and Plagioclase. Fragments are vesicular with large coalesced vesicles and small convolute vesicles. Some vesicles have a fine ash infill Phenocrysts in glass fragments can be oriented around vesicles or occur in clusters. The matrix is well packed.
257	Bedded lapilli tuff	Sideromelane clasts with limited phenocryst population (<5%). Some crystals of plagioclase occur freely within the matrix. Typically below 0.2 mm. Vesicular clasts contain large rounded and frequently interconnected vesicles. Particles have flat sides and angular shapes. Influence of vesicles is observed in particle shape, but do not dominate fracture planes. Most particles are equant in shape, but some elongate particles also occur. Tachylite dominated particles make up 5% of the total.
258	Mega pillow	Large deformed vesicles are filled with ash particles. Vesicular microcrystalline lava. Some large phenocrysts are present of clustered Cpx and Plagioclase, up to 0.5 mm in diameter. Vesicle morphology is convolute with irregular edges. . Ground mass is dominated by phenocrysts of plagioclase and Cpx in radiating random textures. The glass component of the groundmass is approximately 5%
259	Lt above pillows	Large clasts of a weakly microcrystalline vesicular lava in a sideromelane dominated matrix. Some particles are frothy, others have isolated rare vesicles. Vesicles are predominantly rounded, or have elongation. The tachylite gm lava has glomerocrysts of Cpx and Plagioclase and irregular convoluted vesicles at various scales. Sideromelane particles have a low crystal content < 5%. Crystals present are Cpx and Plagioclase. Crystals typically occur in glomerocrysts, with some glass holding the cluster together.
260	Fine ash up section of	Well sorted fine ash with minor alteration of sideromelane particles to clay/palagonite. Rare isolated crystals of plagioclase and Cpx occur. Glass



	previous point	fragments are sideromelane and rarely tachylite. Particle shapes are predominantly flat sided, with some evidence of vesicles preserved along fracture surfaces. Lots of elongate shapes, and fragile shapes that suggest there was little to no remobilization. Particle sizes are all too small to preserve intact vesicles.
261	Porphyritic pillows	Low phenocryst end member of porphyritic pillows (<10%). Vesicle shapes are highly amorphous. Vesicularity is 30%. Possible crystals of Olivine displaying a straight extinction angle. (1% of crystals, in groundmass) The groundmass is fine, composed of Cpx, Plagioclase and Opaques. Opaques concentrate at grain and vesicle boundaries. Other crystals are all inter-grown, with poor crystal forms. Some spherulites, radial glomerocrysts are common. Larger phenocrysts of plagioclase are lathlike, with complicated twins.
262	Porphyritic pillows	Phenocrysts (plagioclase) are more common (5-10 %) than 261. With large irregular crystal morphologies, with detectable crystal boundaries. Twinning is frequently interrupted along the length of the crystal. Some seed crystals display undulose extinction. Crystal boundaries are rounder (anhedral shapes). Groundmass is composed of glass (15%), plagioclase (80%), Cpx (1-3%) and some opaques (1-3%). The crystals are intersertal, and may include some devitrification influence.
267	Porphyritic dike	Micro-porphyritic dominated. Groundmass crystals are deformed around vesicles. Discrete clear margined crystals of plagioclase (35 %), Cpx (35%) and tachylite glass (30%). Crystal groupings are spherulites and radial. Plagioclase laths are elongate with rough edges. Cpx is predominantly intersertal with some anhedral equi-dimensional crystals. Vesicles have dark rims and smooth but irregular shapes. 20% vesicularity.
269	Matrix at pillow base	Loosely packed sideromelane glass fragments dominate. Tachylite glass makes up 10% of the sample. Some sideromelane. Glass fragments contain crystals of plagioclase and Cpx. Grain shapes are predominantly blocky or elongate needle shapes. Some evidence of vesicle influence, but <10 %. Some free crystals of plagioclase are present up to 0.2 mm in diameter. Particles show no sign of remobilization.
271	Lt 1	Clast of micro-phenocryst rich vesicular lava. Vesicle sizes vary and shapes are predominantly irregular, showing some signs of coalescence. Phenocrysts are oriented randomly and (70%) plagioclase and (30%) Cpx. All crystals are small and poorly formed (rapid quenching). Vesicles range from 2 mm to 0.2 mm in diameter. Vesicles are ringed with black 'glass'. Limited affixed sideromelane glass preserved in the vesicles of the clast margin.
272	Chill of porphyritic dike	Very nice transition from sideromelane to tachylite. Crystals do not appear until the tachylite is fully established. Microlites have a consistent increase toward the center of the rind. Far more competent margin.
273	Host (heterolithic lt)	Clast of microcrystalline vesicular lava. Some sideromelane glass preserved at the margin. Sideromelane glass is vesicular and predominantly crystal free. Some alteration of particle margins. Clast contains phenocrysts of plagioclase with some weak orientation, but zones of randomly oriented grains are common. Spherulites are common between vesicles. Radiating crystals of plagioclase. Some zones of larger

		plagioclase (up to 0.2 mm) occur, but otherwise the groundmass is dominated (75%) by laths of plagioclase, with irregular ends. Vesicles are predominantly rounded, with mild irregularities. Coalescence is common. Vesicles are frequently filled with particles of fine sideromelane ash.
274	Dike feeding pillows	Slide crosses vesicle bands. Plagioclase microcrysts are all radial, with frequent spherulites texture. Cpx occurs (15%) as stubby crystals. Rare (<1%) plagioclase crystals up to 0.2 mm in clusters. Vesicle infill of layered isotropic alteration products. Vesicles are polylobate and convoluted in morphology. With smooth sides and concentrations in bands. Concentrations also include variations in Cpx.
275	Pillow fed by dike	Microcrystalline vesicular lava. Vesicles are large rounded and show some coalescence. Groundmass contains 60% plagioclase laths and 25% Cpx with 15% tachylite glass. Skeletal plagioclase indicative of rapid growth. Other grains are randomly oriented or form spherulites with radial orientations of plagioclase. Some vesicles are lined with orange alteration products.
277	Subaerial lava	Fine microlites of plagioclase make up approximately 60% of the groundmass. With 30% tachylite glass. Larger crystals of plagioclase and Cpx make up 10% of the sample. The grain shapes are suggestive of rapid crystallization, or regrowth. Skeletal grains, swallowtail shapes. Vesicle shapes are convoluted and have irregular sides. Sizes vary from
279	Pillow clast in breccia	Clast of microcrystalline lava. Crystals are irregularly distributed throughout the sample. Vesicles have black glass lining. Shapes are polylobate and convoluted. Coalescence is common with multiple size modes. Plagioclase crystals dominate the ground mass. Some crystals are incredibly long and thin. With no apparent orientation. Some spherulites are present. No Cpx population. Rare sideromelane fragments in the marginal vesicles.
281	Dike	Microcrystalline lava with spherulites of plagioclase and isolated stubby crystals of Cpx (10%). Some crystals of Cpx are surrounded by overgrowths of plagioclase. Spherulite textures dominate. Vesicles are irregular in morphology with evidence of coalescence. Some alteration is present along vesicles. Bands of larger vesicles are associated with fewer microlites.
282	Dike	Groundmass is dominated by plagioclase (60%), Cpx (10%) and possible olivine (10%). Multiple crystals sizes, but spherulites are common in the 0.5 mm range. Long lathlike crystals of plagioclase occur in groups of parallel oriented crystals, but not in particular preference to vesicles, flow banding, or other groups of crystals. Others form radiating spherules of well formed crystals. Though crystal margins are rough. Vesicles have irregular morphologies and show significant coalescence. Their edges are ragged. And have irregular distribution. Some vesicles have orange alteration infill.
283	Porphyritic pillow sample	Crystallization occurred before vesiculation. Plagioclase phenocrysts in a matrix of Cpx, plagioclase and opaque microlites. Plagioclase makes up 45% of the groundmass, Cpx makes up 30% and opaques make up the remaining 15%. Vesicularity is on the order of 30%. With large irregularly shaped, but smooth sided vesicles. Opaques tend to concentrate at vesicle walls. Some

		<p>vesicles have very fine ash infill.</p> <p>Patchwork plagioclase crystals are the dominant phenocryst, up to 25% of the total. Crystals have complicated boundaries with evidence of both physical and chemical alteration of grain shape.</p>
		<p>EDS indicates that the sample has Cpx with Mg # of 74 in its groundmass and no phenocryst population. Plagioclase crystals have Bytownite (An 86) and Labradorite (An 52) compositions, with inclusions of Cpx with Mg # of 70. With Bytownite (An 72) and Labradorite crystals in the groundmass (An 49).</p>
284	Porphyritic tuff	<p>Sideromelane glass dominated fragmental slide. Large (1 cm) crystals of plagioclase are common, up to 15% of the total. Vesicularity is high, up to 40%. Vesicles are round, and only show minor deformation due to clustering. Cpx grains are smaller, up to 0.5 mm. Some crystals display undulatory extinction. Some (&lt;1%) OPX grains may be present as well. All crystals display physical fracturing, and chemical disequilibrium. Pore space exists between crystals and matrix glass.</p>
		<p>EDS indicates the presence of phenocrysts of Bytownite (An 87 and An 75), with inclusions of Cpx (Mg # 50).</p>
285	Porphyritic dike or lava	<p>Porphyritic Tuff:</p> <p>Highly glassy, orangey altered, very vesicular. Vesicles are distributed in an irregular fashion, with cracking common along bubble walls (product of thin sectioning?). Vesicularity can reach 80% locally and is locally more dense (30% vesicularity).</p> <p>Contains crystals and glomerocrysts of plagioclase and Cpx up to 0.5 mm. No groundmass. The largest crystals are plagioclase (10%) crystals up to 1 cm in diameter. Cpx crystals are smaller and less common (5%) not exceeding 0.5 mm.</p> <p>Secondary alteration minerals occupy vesicles and void spaces, low birefringence. Some clays are present in cracks.</p>
286	Porphyritic dike	<p>Large phenocrysts of Cpx (15 %) along with less abundant (than observed elsewhere) phenocrysts of plagioclase (20 %). Cpx crystals reach 1 mm. May display fantails of plagioclase at the ends of crystals. Morphologies of phenocrysts vary, but they all display anhedral rough outlines. Most are reasonably equi-dimensional, some more rectangular shapes are present. Some Cpx displays undulatory extinction. Glomerocrysts of plagioclase and Cpx can be up to 1 mm in diameter.</p> <p>Vesicle shapes can be highly convoluted and are lined with black (alteration or opaques?)</p> <p>Crystallization occurred before vesiculation; 15% vesicularity</p> <p>Plagioclase phenocrysts are irregular in morphology, with multiple growth stages visible. Crystals are up to 1 cm in diameter, but are predominantly on the order of 1 to 2 mm.</p> <p>The groundmass has approximately 20% opaques, 35% plagioclase and 45% Cpx.</p> <p>Plagioclase laths can be up to 1 mm long, but average 0.5mm. Some Cpx show clear interactions (growth relationships) with larger plagioclase laths.</p>
287	Non porphyritic lava from breccia	<p>Glassy (50%) groundmass containing plagioclase crystals and Cpx and olivine. Olivine crystals are skeletal and broken (2%). Crystal orientations are random. Cpx grains are elongate and broken.</p> <p>Vesicles are irregular in shape, with rough edges but overall rounded shapes. Fairly uniform size range.</p>

289	Gabbro nodules	Large, cm sized, phenocrysts of plagioclase with intersertal Cpx of equal size. Plagioclase grains have significant intergrowth. Complicated twinning is common. Most grain shapes are anhedral. Some crystals of smaller (<5 mm) plagioclase are isolated within Cpx.
290	Porphyritic Pillow breccia	Lathlike crystals of plagioclase dominate the groundmass. Crystals have well formed crystals shapes (flat edges and occasionally show parallel orientation of clusters of crystals, with no apparent preference for vesicles or flow banding. Additional stubby crystals of Cpx make up (5%) part of the groundmass. Larger crystals of plagioclase and Cpx occur in clusters with resorption rims and broken margins. Crystals over 0.5 mm have obvious recrystallization histories. Large rounded vesicles with red to orange alteration growths.
291	Lt	Large crystals in the matrix have signs of physical alteration, and chemical disequilibrium. Some crystals occur in sideromelane fragments, but stills how the physical and chemical alteration. Clasts have variable vesicularity from dense to frothy with rounded vesicles. Lots of sideromelane glass, with rare tachylite. Vesicles can also be highly deformed or regular. Most large clasts are crystal poor to crystal free. Clasts are of a variety of sizes, poorly sorted, with variable levels of alteration.
292	Lt clasts	Porphyritic (5%) phenocrysts of plagioclase. Patchwork clusters of crystals. Groundmass is tachylite parallel to the length of the slide. Vesicles and large phenocrysts share the same orientation. Groundmass includes glomerocrysts of plagioclase laths surrounded by anhedral Cpx crystals. Individual components are 0.3 mm to 1 mm in diameter, but the construct is up to 5 mm in diameter. Groundmass is composed of tachylite glass (45%), plagioclase (35 %) laths and less Cpx (20%). Plagioclase forms in laths (2 size ranges 0.1 mm to 0.5 mm), Cpx are anhedral (0.5 mm).
293	Lt	Sideromelane fragments with rare tachylite (5%) of better sorting than most, range of clast sizes and vesicularity is still high. Tight packing. Most clasts are microcrystal poor, but larger crystals (<0.5 mm) of plagioclase may have glass residuals attached. Some minor alteration along grain boundaries results in the difficulty to distinguish grain boundaries.
294	Subaerial lava breccia	Very dense clast of microcrystalline lava with alteration. All crystals are stubby and similar sizes. Plagioclase (20%), opaques (20%) and minor Cpx (20%).
295	Matrix of AG 294	Altered poorly sorted and heterolithic matrix. Smaller particles (0.5 mm) have significant alteration, and are composed of sideromelane glass, crystals and some microcrystalline lava fragments. Lager fragments of lava can be microcrystal rich, or poor. The particles have variable vesicle contents as well from dense to frothy. Some large crystals are present (1.0 mm) and have remnants of sideromelane glass attached. Free crystals are predominantly plagioclase, with some Cpx. All large crystals have anhedral shapes and signs of chemical disequilibrium.
296	Matrix of hLt	Sideromelane glassy matrix between clasts of microcrystalline and devitrified lava. Free crystals are rare and of plagioclase only. And the crystal content of most particles is very fine grained. Large clasts frequently have vesicles fills of alteration products.
297	Subaerial lava	Microcrystalline dense (<30% vesicularity) lava. Groundmass is composed of plagioclase (65%) and opaques (35%). Opaques display alteration; reddish discoloration surrounded 10% of grains. Grains are fairly uniform in size for

		both compositions.
298	Porphyritic pillow	<p>Groundmass is finer than sample 299. Crystals consist of Cpx, Plagioclase and Opaques. Cpx dominates the groundmass 50%. Plagioclase composes 35%, with 15% opaques. The laths are below 0.4 mm. More equant Cpx are around 0.3 mm.</p> <p>Vesicles are large, with evidence that the vesicles formed after crystallization took place. Large crystals protrude slightly into vesicles, but smaller crystals are arranged around vesicles. Alteration in vesicles is the same distinctive color observed in other samples. Can just line a portion of the vesicle interior, but also appears as chunks that may have been previously attached to vesicle walls. Some evidence of mobilization of ferrous components from opaques, including cracks through nonferrous minerals that are lined with red.</p> <p>Spherical shaped alteration growth in vesicles.</p> <p>Large phenocrysts compose 20% of the sample, with 15% vesicularity. Phenocrysts range in size from 0.5mm to 4 mm. Some mechanical breakage, chemical disequilibrium, multiple growth stages, twinning. Some crystals now have complicated morphologies, including large, mm to cm size L shapes. Some crystals have Cpx growth in void spaces. Exsolution lamellae of Cpx are rare, but present in phenocrysts.</p>
		EDS indicates the presence of titanium bearing oxides. Plagioclase phenocrysts are Bytownite (An 84). Cpx with Mg# 70 are present.
299	Porphyritic subaerial lava	<p>Plagioclase dominated: Phenocrysts and ground mass. Intersertal Cpx (rounded anhedral grains). Phenocrysts exceed 2 mm, highly disrupted grains. Broken grain margins, multiple growth phases, zoning, twinning, and some chemical resorption of margins. Compose 55% of the sample. The groundmass is 55% plagioclase laths (twinned) with 40% Cpx and 5% opaques. The laths are up to 1 mm in length, but average 0.5 mm. Cpx are more equi-dimensional up to 0.5 mm. Opaques can display deep red alteration. Some alteration focused on vesicles. Opaques are consistently &lt;0.5 mm. Vesicles make up &lt;10% of the sample. Alteration growths in vesicles appear banded and are up to 0.5 mm thick.</p>
300	Inclusion in lava	<p>Microcrystalline bordering on cryptocrystalline. Equi-dimensional, anhedral crystals of plagioclase (60%) and oxides (40%) compose this dense (&lt;5% vesicularity) sample.</p> <p>Occasional larger crystals (laths and larger blocks up to 0.5 mm) of plagioclase are rare.</p>
302	Lava in hLt breccia	<p>Very dense microcrystalline lava. Isolated large phenocrysts of plagioclase and Cpx occur up to 1 mm in length. Phenocrysts display physical and chemical alteration.</p> <p>The groundmass is composed of predominantly plagioclase and opaques (20%). Some Cpx (20%) is visible.</p> <p>The sample shows banding resulting from alteration of oxides.</p>
304	Dike	<p>Porphyritic dike with large chemical and physically altered phenocrysts of plagioclase up to 1 cm. Moderately vesicular sample. Phenocrysts occur in clusters, or isolated. Plagioclase displays complicated zoning and twinning. Groundmass is composed of plagioclase laths (60%) and stubby Cpx crystals (15%) with opaques and tachylite glass. Localized parallel orientation of crystals in groundmass is not continuous.</p>
305	Matrix (Peperitic)	<p>Fragmental grains of sideromelane glass. Variable vesicularity fragments with a wide range of clast sizes. The glass has very low crystal content. Alteration</p>

		is limited, but concentrated in glass fragments. Cpx that are present are small and occur as free crystals or on the margins of large plagioclase crystals. Large (up to 1 cm) plagioclase crystals have physical and chemical alteration, including fracturing. The plagioclase crystals make up 20% of the sample. Some crystals occur as independent grains, others have remnants of vesicular sideromelane glass or microcrystalline lava.
306	Matrix away from dike	Large plagioclase crystals have less indication of mechanical alteration (but some examples are still present), and make up 10% of the sample. Crystals occur with more sideromelane attached. Fragments of tachylite glass are present and have strong alteration rims. The particles display finer packing and vesicle presence is muted by a finer grain size and pore space infill. Frothy clasts contain vesicles of various shapes, closely packed and mostly rounded. Sideromelane glass is crystal poor. Dark lining of vesicles.
308	Non porphyritic Lt	Dominated by sideromelane glass, well packed and mostly vesicular. Crystal-free sideromelane. Vesicularity is variable. Vesicles are deformed and rounded.
309	Subaerial lava breccia	Microcrystalline dense lava. Some bands of alteration result in a change in color from black to brown. Crystals show mostly random orientation, but have a roughly lengthwise orientation across the sample. This pattern is not visible in hand sample. Crystals are predominantly well formed laths of plagioclase (70%) and stubby crystals of Cpx (30%). Alteration concentrates around the Cpx crystals.
310	Porphyritic subaerial lava	Large plagioclase phenocrysts (up to 1 cm) in a fairly dense (Vesicularity is <20%) microcrystalline groundmass. Phenocrysts display physical alteration and have complicated twins. Coronas of disequilibrium textures appear on the plagioclase grains. The groundmass is composed of plagioclase (30%), Cpx (40%) and oxides (30%). The crystals are all fairly equi-dimensional, excepting the lathlike tendency of the plagioclase. Vesicles have alteration infill. Some are concentric, spherical structures, others merely line the wall. Cracks are filled in more than isolated vesicles.
314	Pillow core and rind	Crystal rich vesicular lava. Groundmass is dominated by plagioclase (35%) and Cpx (45%). Olivine makes up 5% of the sample, with the remaining 15% tachylite glass. Glomerocrysts dominated by plagioclase crystals radiating are common. But less common than randomly oriented grains. Vesicles are irregular in shape and controlled by the presence and orientation of crystals.
316	Lt	Sideromelane glass fragments that have variable vesicularity in a well packed matrix. Crystal content of fragments and matrix is much higher than typical. Plagioclase makes up about 10% of the crystals occurring in isolation or in glomerocrysts with olivine (20%) and lesser Cpx (10%). Clasts are vesicular with influence on finer particles. Lots of sharp needle shapes occur, with typical ash shapes dominating. Intact vesicles are typically elongate in shape.
317	Lt above pillows	Sideromelane glass fragments with vesicles and crystals of olivine and plagioclase. Total crystal content is up to 40%. Vesicles are large and frequently elongated and control the distribution of crystals with the exception of glomerocrysts which influence vesicle location. Alteration of glass occurs along margins of olivine. Particles are moderately packed, with

		smaller particles filling in the larger broken vesicles on the margins of other grains. Grain shapes are blocky and some vesicle influenced fragment sides.
318	Pillow mound	Vesicular microcrystalline lava. Crystals frequently occur in glomerocrysts. Spherulites and devitrification textures are common. Crystals are plagioclase and Cpx. Vesicles are irregularly shaped and show signs of coalescence.
319	Porphyritic pillow	Highly vesicular, up to 70%. Large (up to 1 cm) plagioclase crystals with convoluted grain morphologies, growth histories and twins. The large plagioclase (15%) phenocrysts occur in a vitric groundmass with strong spherulites (devitrification textures). Crystals of plagioclase have fantails and undulose extinction. Tachylite glass and minor opaque crystals occur between plagioclase grains.
321	Pillows fed from dike	Highly abused crystals of plagioclase, with complicated twining and growth structures, in a plagioclase (40%), tachylite (50%), Cpx (10%) groundmass. Significant alteration of vesicles by orange infill. Original vesicularity on the order of 30%. Plagioclase is altering to clay.
322	Dike cutting pillows	Glassy dense sample with rare (5%) phenocrysts and some glomerocrysts of smaller plagioclase crystals. The groundmass is 70% tachylite glass, with randomly oriented plagioclase crystals.
323	host	Dominated by sideromelane glass with tachylite fragments making up 5% of the samples. Some fragments of quench rind are also present. Vesicles are common and typically elongate, but vesicularity is typically below 50%. Microcrystal content is low in most clasts, up to 40% in approximately 10% of the sample.
324	Bedded sediment	Contains a variety of clasts from fresh and altered sideromelane glass to crystal rich, to gabbroic samples. Plagioclase and Cpx crystals dominate all grain sizes. Large clasts are vesicular, with large rounded vesicles. The matrix is fine grained and well packed, and equally variable. Large vesicular tachylite fragments have the highest crystal content. Some crystals occur free in the matrix, but may also have a thin coating of glass. Some large crystals have complicated growth histories including melt inclusions, zoning, and multiple growth stages.
327	Subaqueous lava pile	Crystal-poor vesicular lava with elongate parallel trending vesicles suggestive of flow banding. Vesicles are convoluted, reflecting a history of coalescence. Zones of plagioclase crystals are indicative of devitrification crystallization. Weak shapes, random orientations. Isolated well formed crystals represent less than 1% of the sample. Zonation of vesicle concentration and resulting coloration of the sample. Rare bands of more crystal rich glass.
328	Peperite at the edge of the pillowed dike	Large fragments of vesicular porphyritic lava can be black in PPL, or slightly darker brown. Some clasts have gradational or transitional zones of sideromelane to tachylite. Margins of clasts are fluidal, with stringy shapes of glass and deformed vesicles, or fractured. Vesiculated margins of fragments may be filled with fine ash matrix. Crystals up to 1 cm are present in the lava blocks, in the matrix, and in glassy fragments. Crystals in the matrix appear to be mechanically broken fragments of larger plagioclase crystals. Larger crystals on the edge of lava and glass particles are mechanically broken, ragged edges. Large clasts also contain crystals and glomerocrysts of Cpx up to 1 mm. Large particles are vesicular with rounded occasionally coalesced clasts. Vesicularity ranges and vesicle size is from 0.1 mm to 5.0 mm.

		The matrix is well packed and made of small ash particles, glass, crystals and tachylite. Grain shapes are difficult to distinguish in the fine ash due to packing. Minor alteration of the glass is observed. Fracture planes suggest that breakage is not limited to preexisting planes of weakness and might be indicative of high strain rates.
330	Lt 1 at pillow mound	Sideromelane glass fragments with vesicle influence on fracture planes and larger clasts have preserved vesicles. Vesicle shapes are rounded and coalesced. Crystals (up to 25%) in the glass occur as glomerocrysts and isolated grains of Cpx (50%), Plagioclase (35%) and Olivine (15%). Crystal shapes are poorly formed and show signs of mechanical breakage.
331	Pillow	Microcrystalline vesicular lava. Phenocryst population makes up 85% of the groundmass. Plagioclase crystals occur as laths (65%). Cpx occurs as stubby grains (35%). All crystals are randomly oriented. Larger crystals (1%) of plagioclase have broken margins or anhedral shapes. Vesicles are irregular in shape and sizes, showing signs of coalescence. Vesicles display black rims.
332	Pillow clast in sediment blob	Microcrystalline vesicular lava. Vesicles are large and irregular with obvious coalescence. Black lining of vesicles appears to separate, possibly as a result of the slide making process. Crystals make up 80% of the groundmass, with the remainder tachylite glass. Crystals are randomly oriented plagioclase laths (80%) and stubby Cpx (20%). Larger phenocrysts of plagioclase, up to 0.5 mm, display twinning and subhedral shapes.



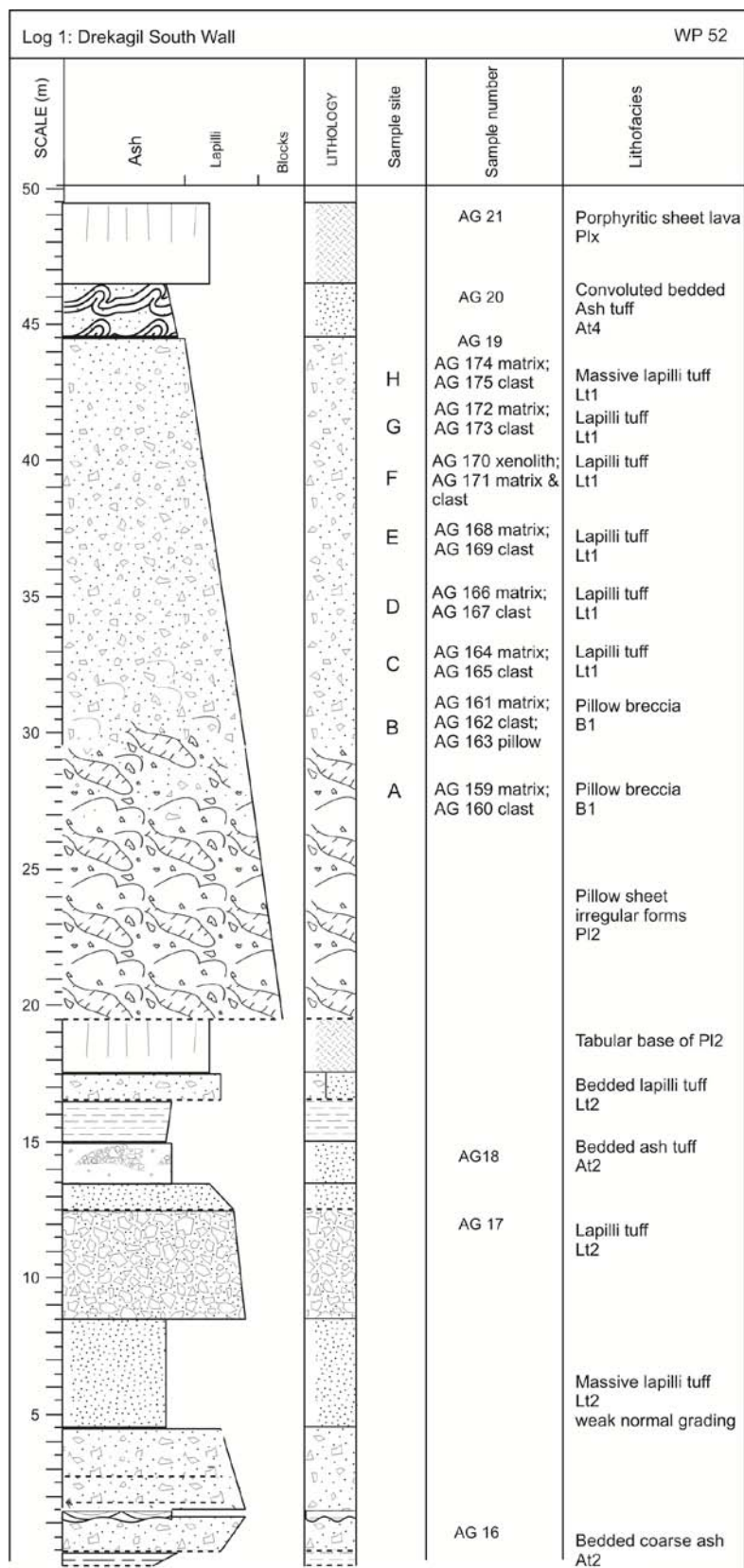


Figure A.1 Log 1

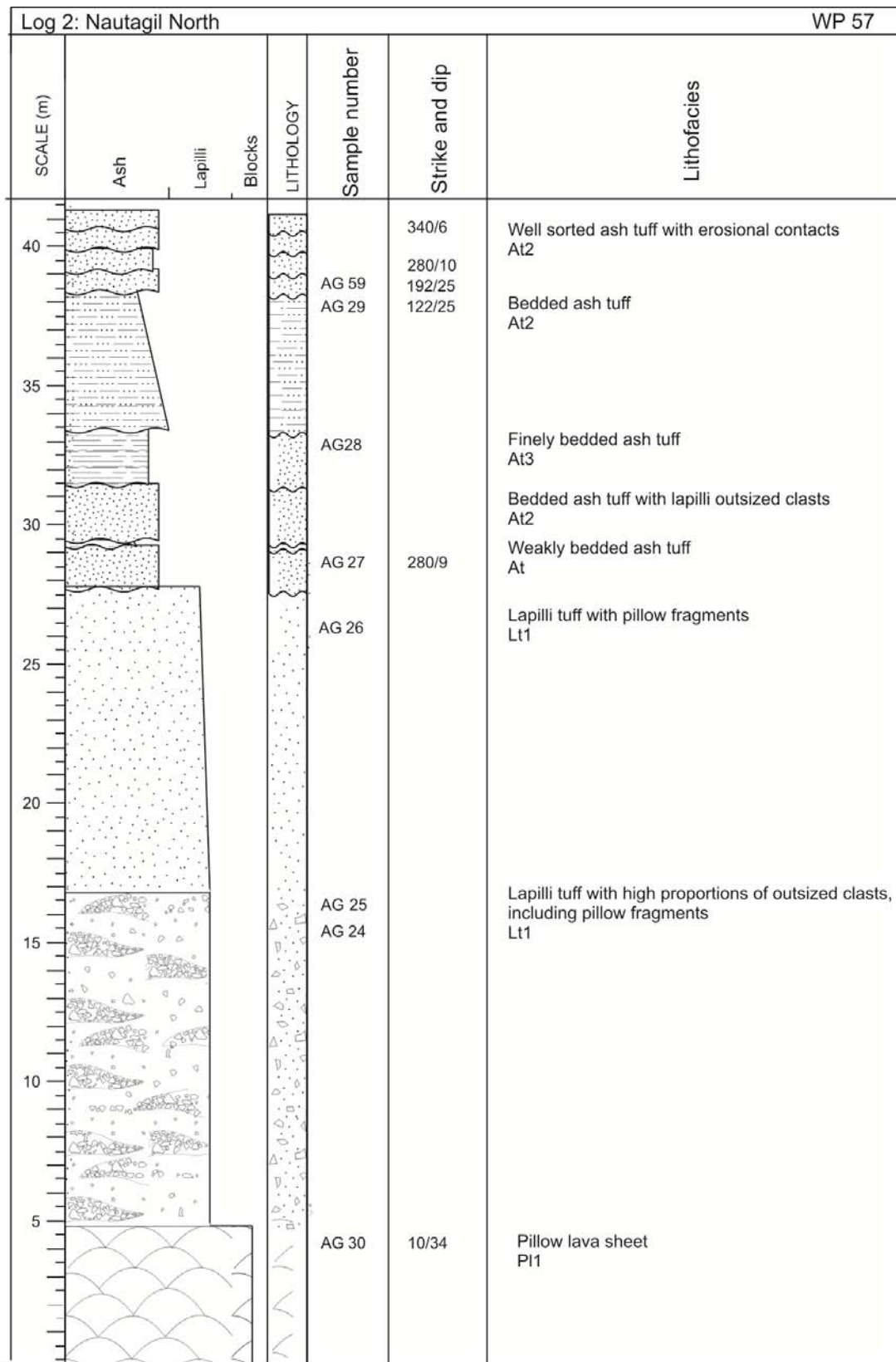


Figure A.2 Log 2

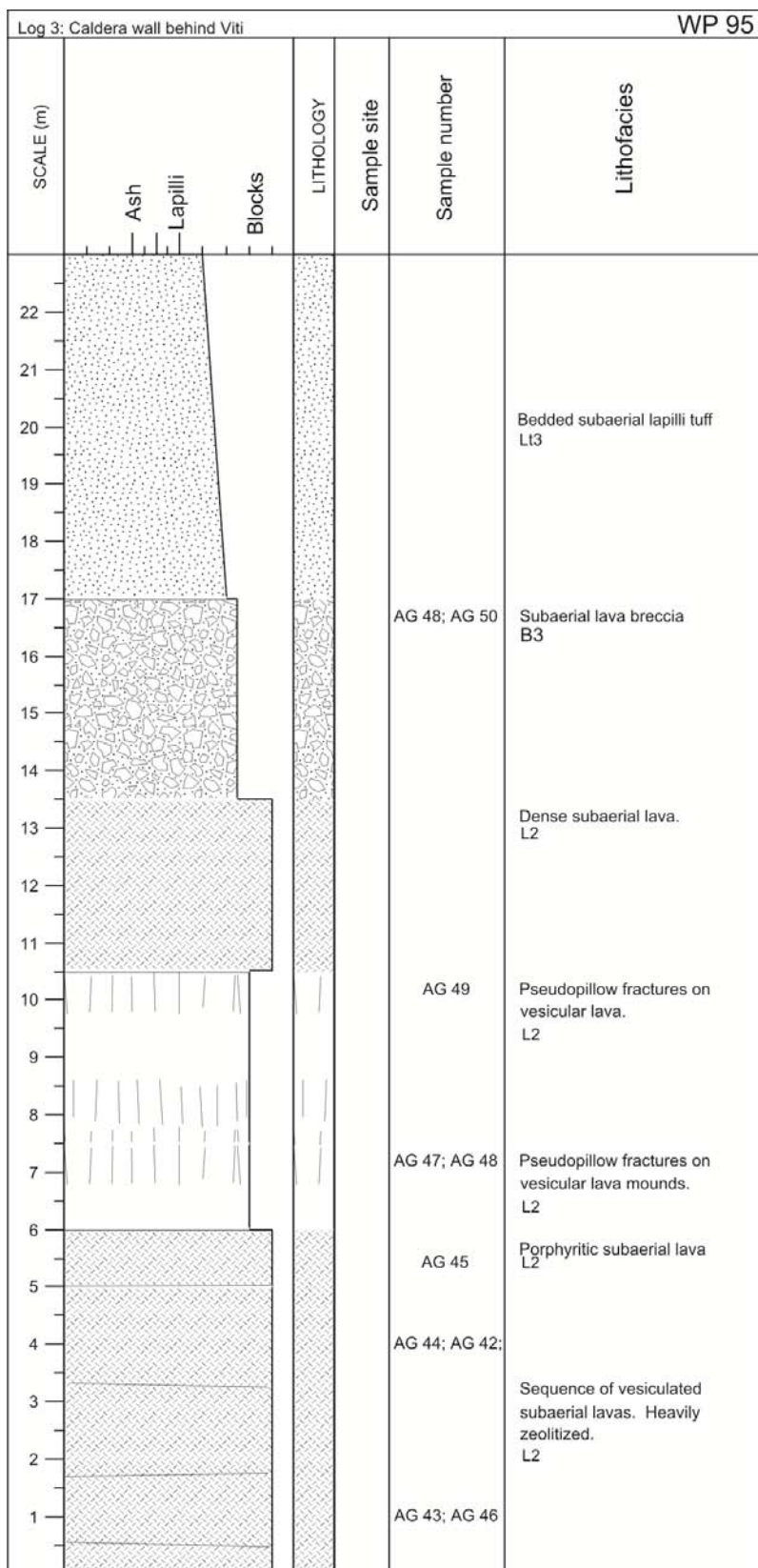


Figure A.3 Log 3

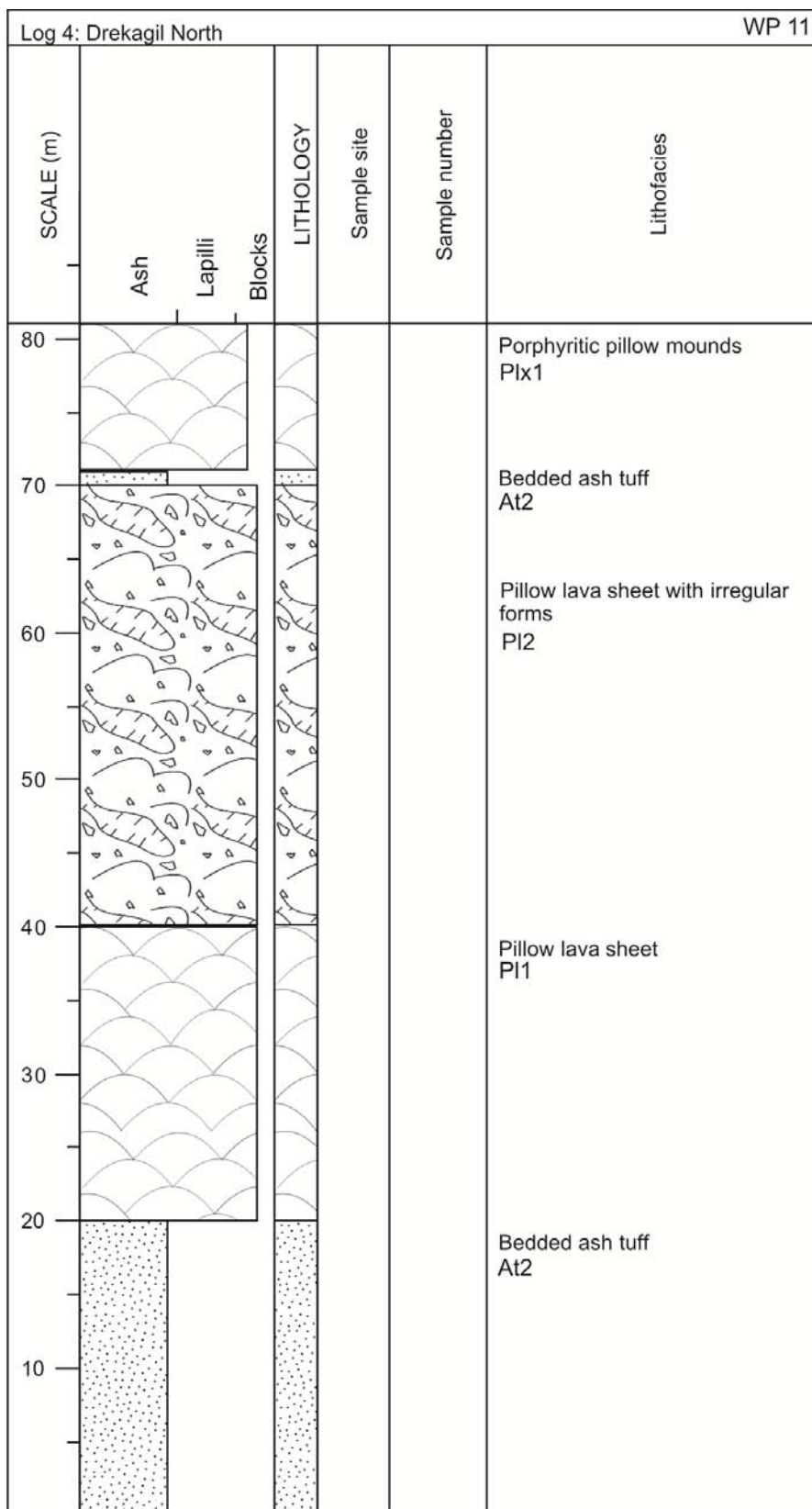


Figure A.4 Log 4

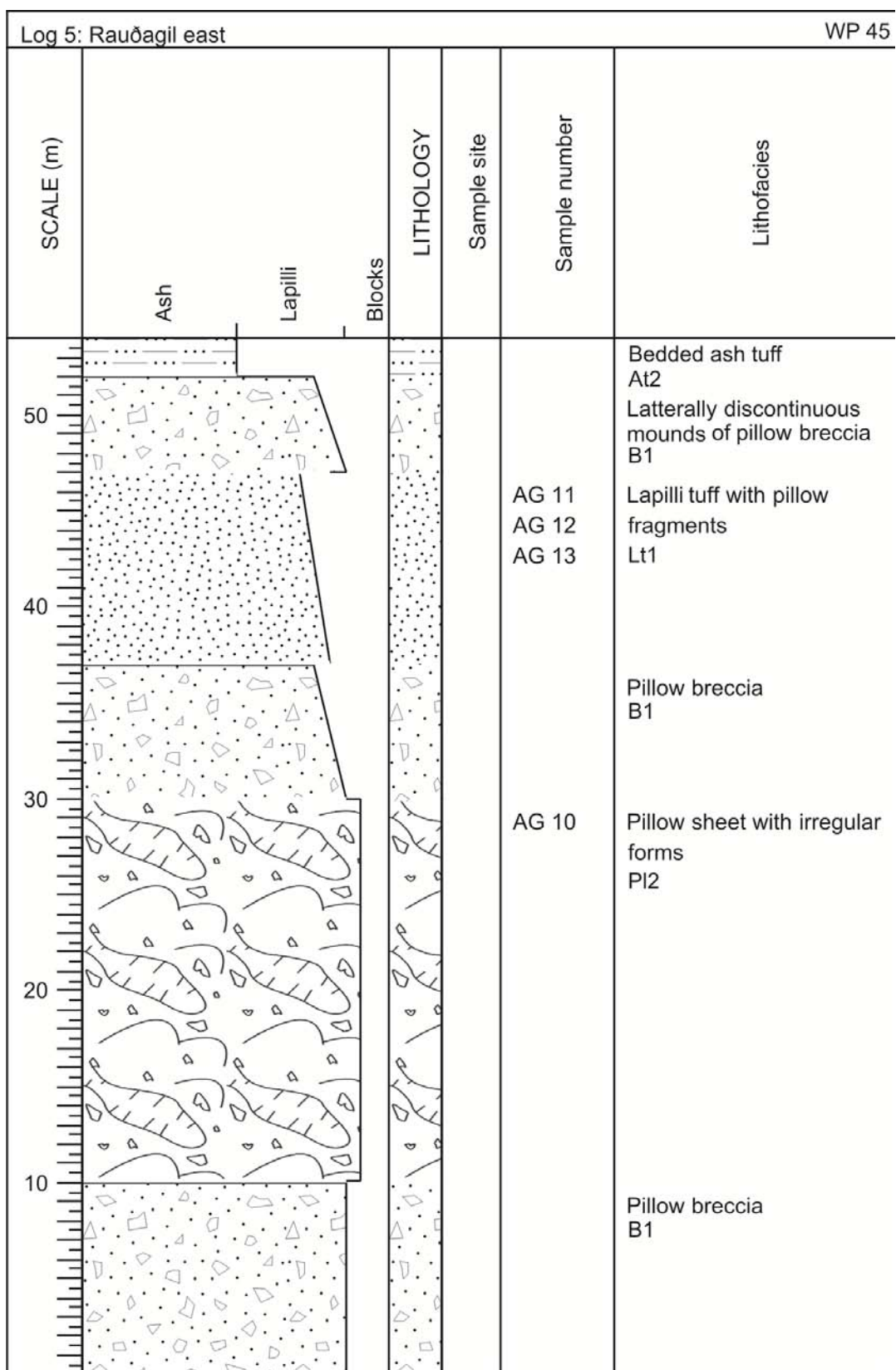
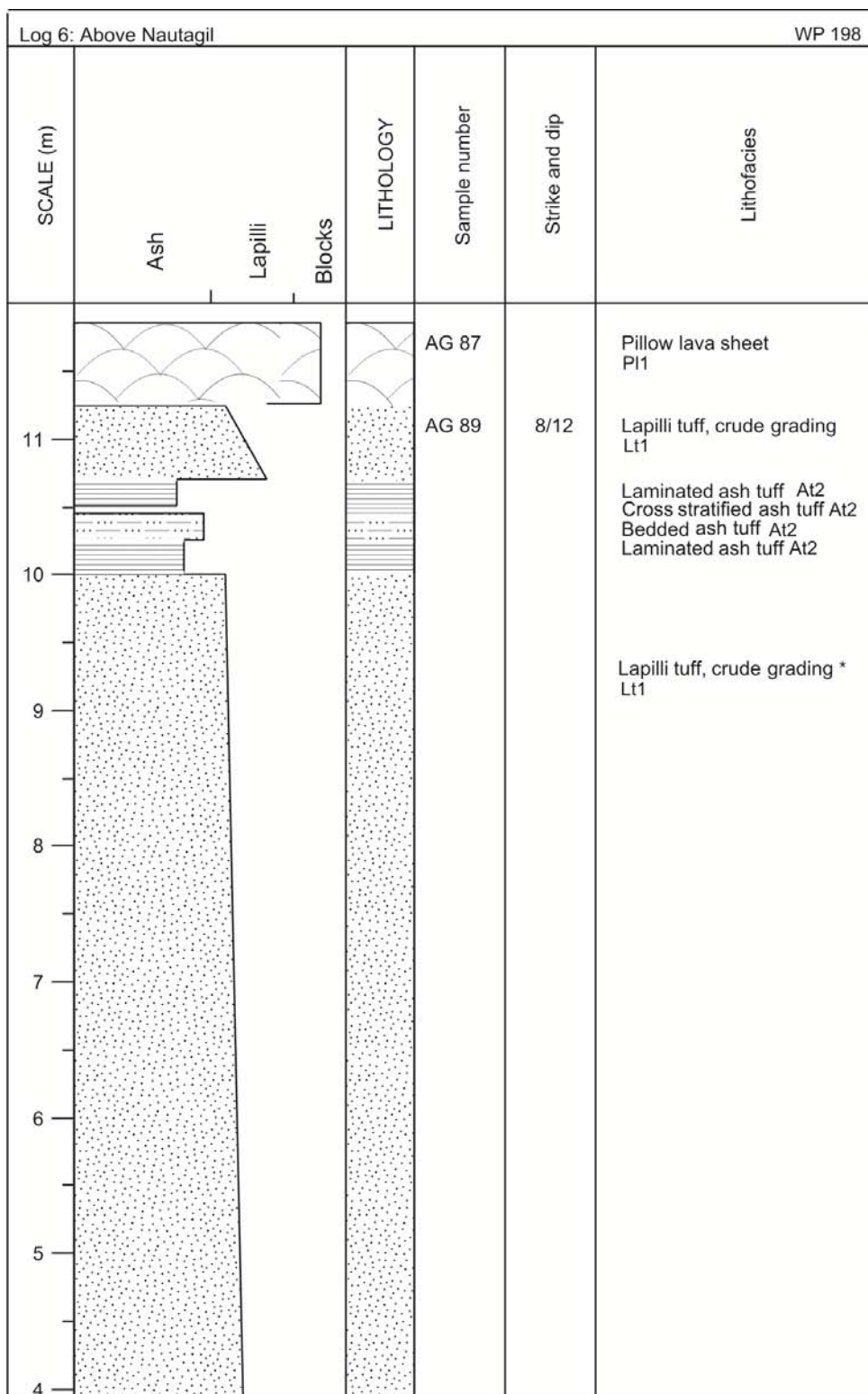


Figure A.5 Log 5





\*Thickness depicted is only a minimum

Figure A.6 Log 6

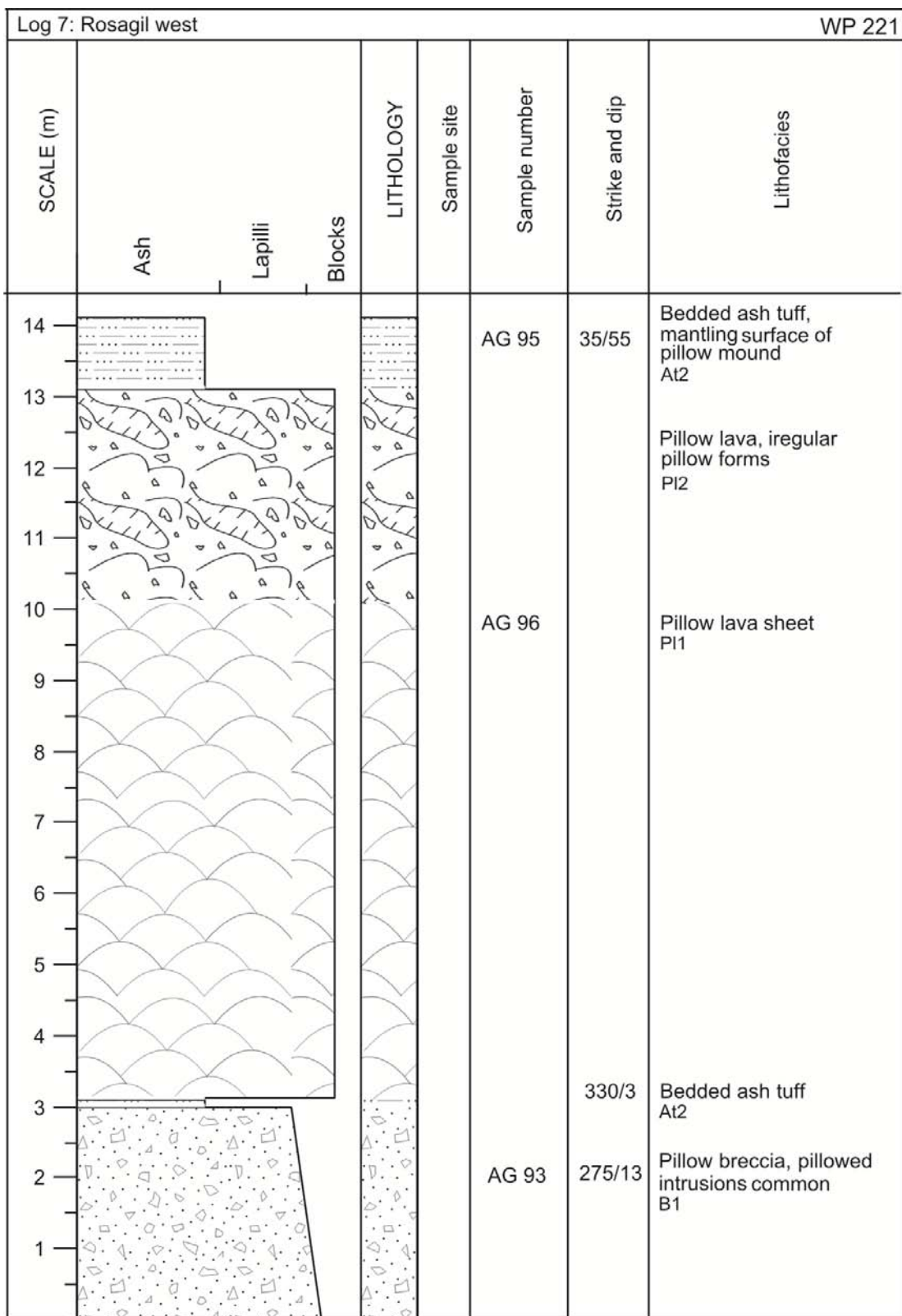


Figure A.7 Log 7

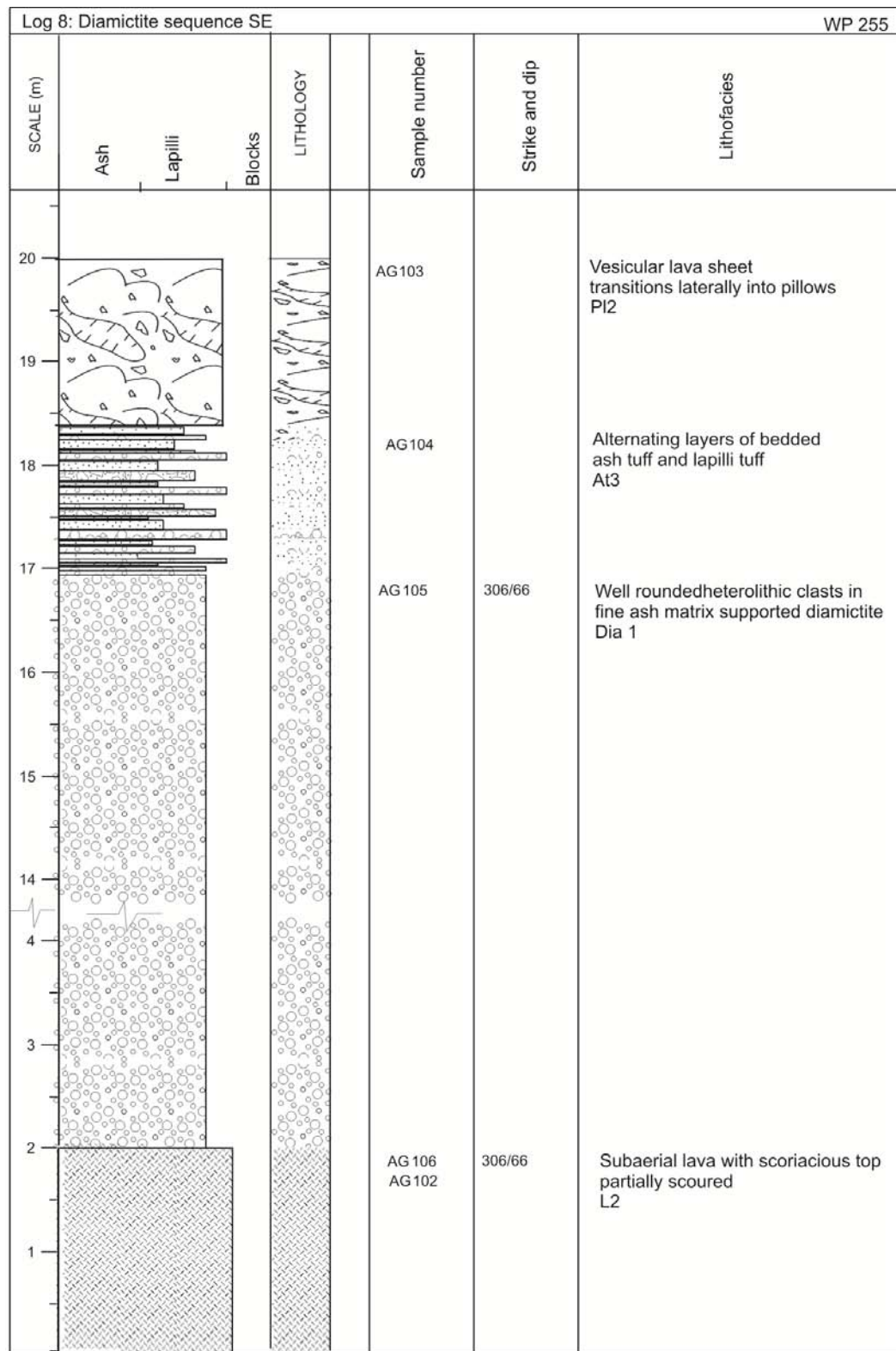


Figure A.8 Log 8



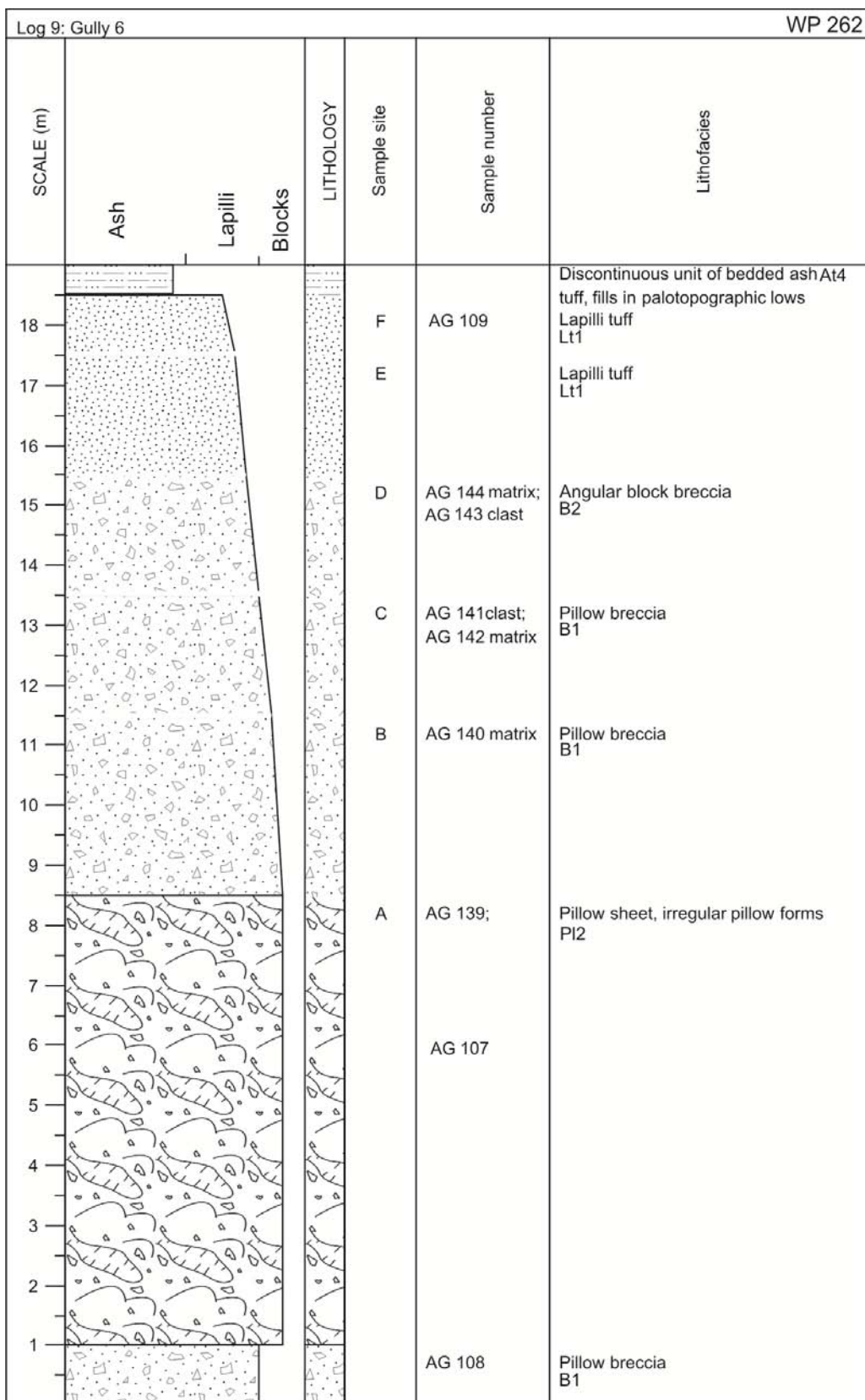


Figure A.9 Log 9

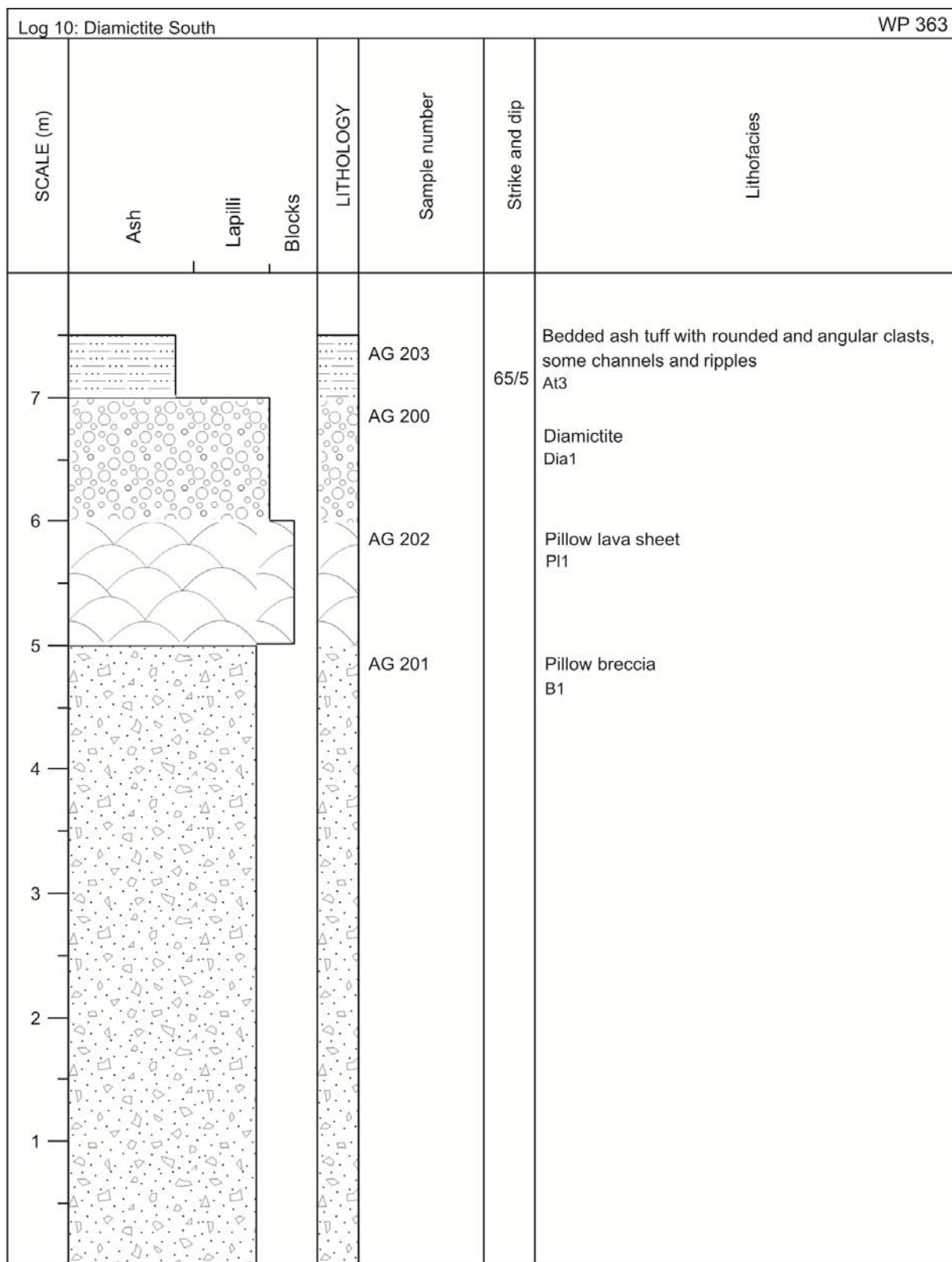


Figure A.10 Log 10

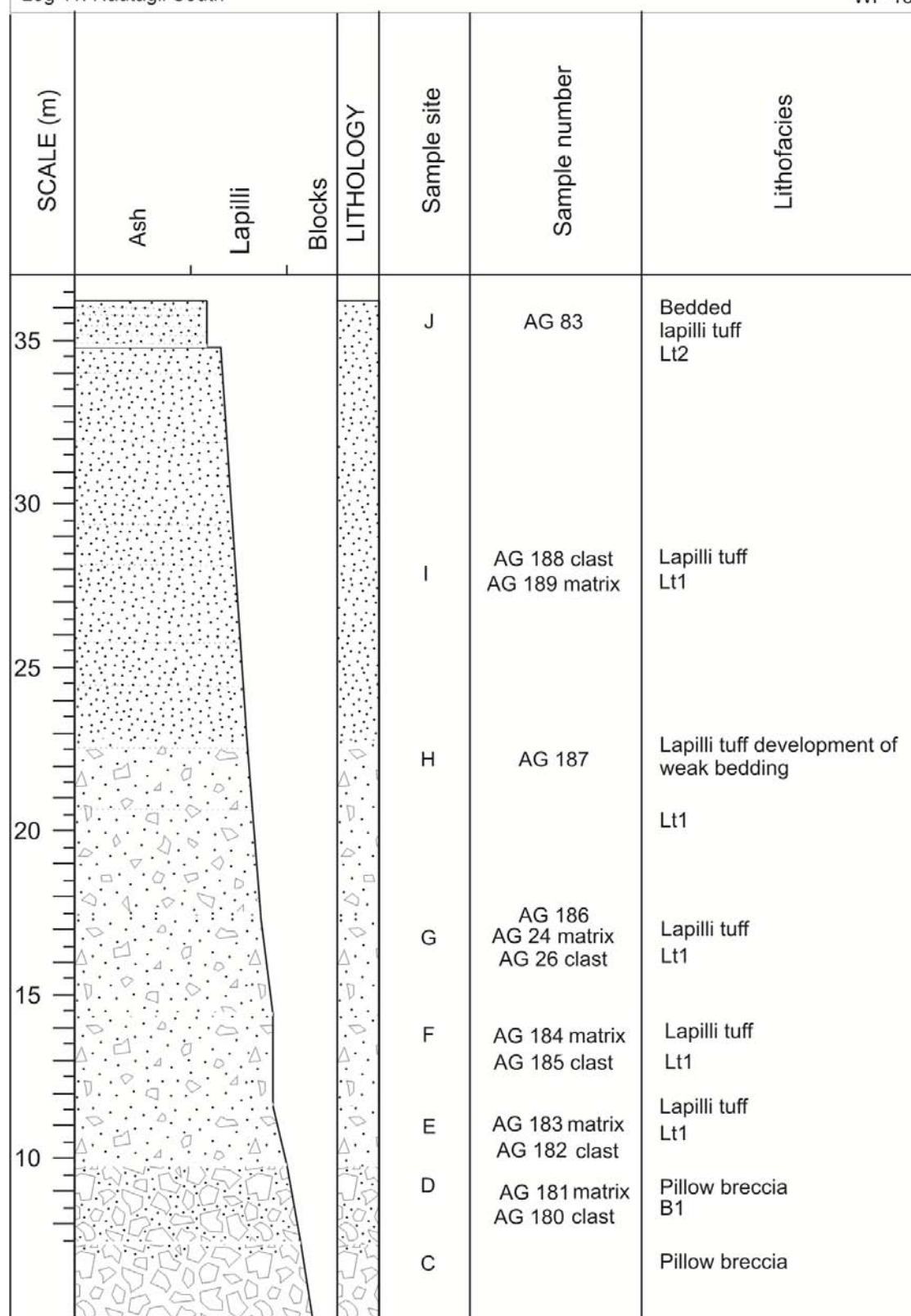


Figure A.11 Log 11

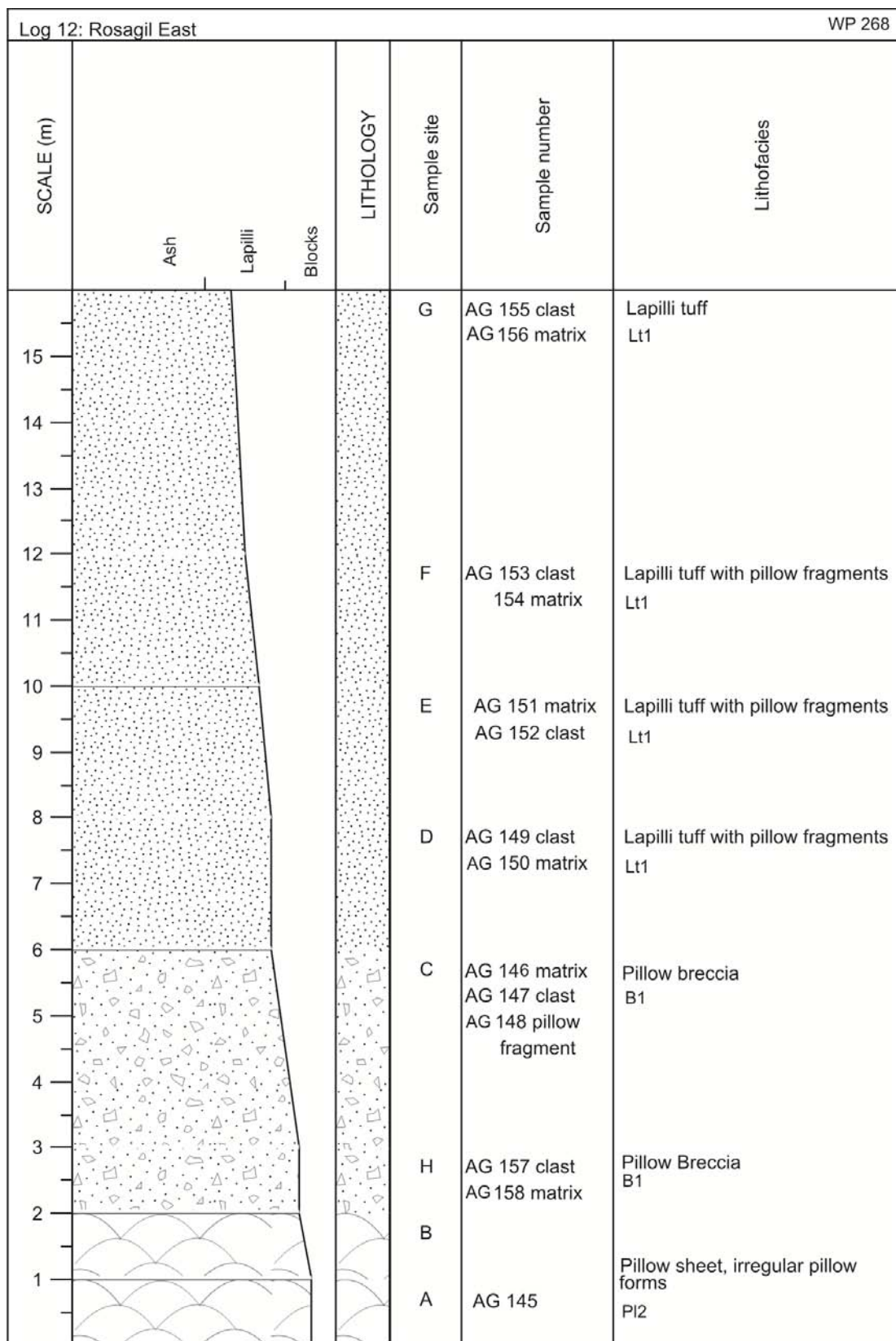


Figure A.12 Log 12

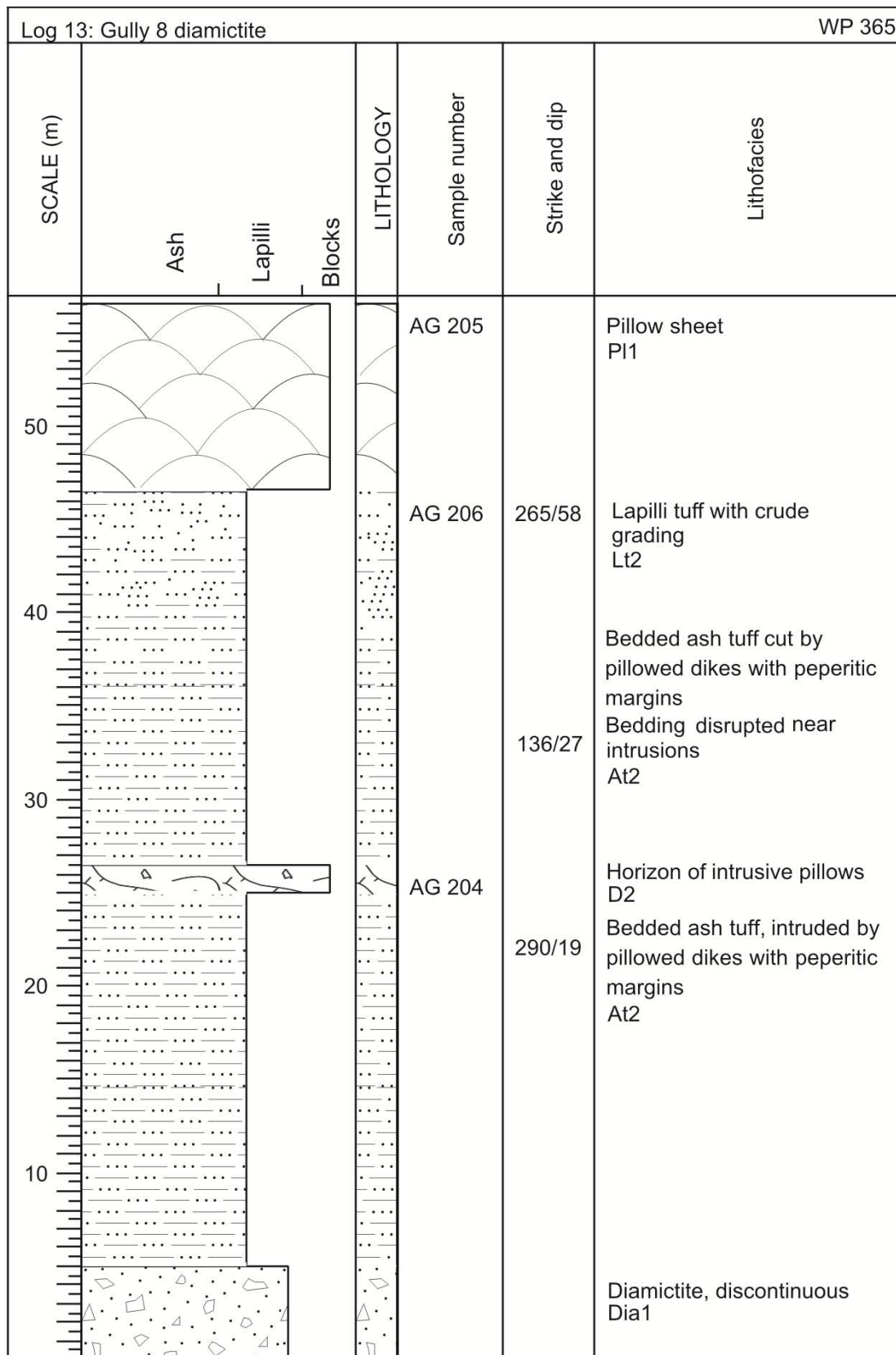


Figure A.13 Log 13



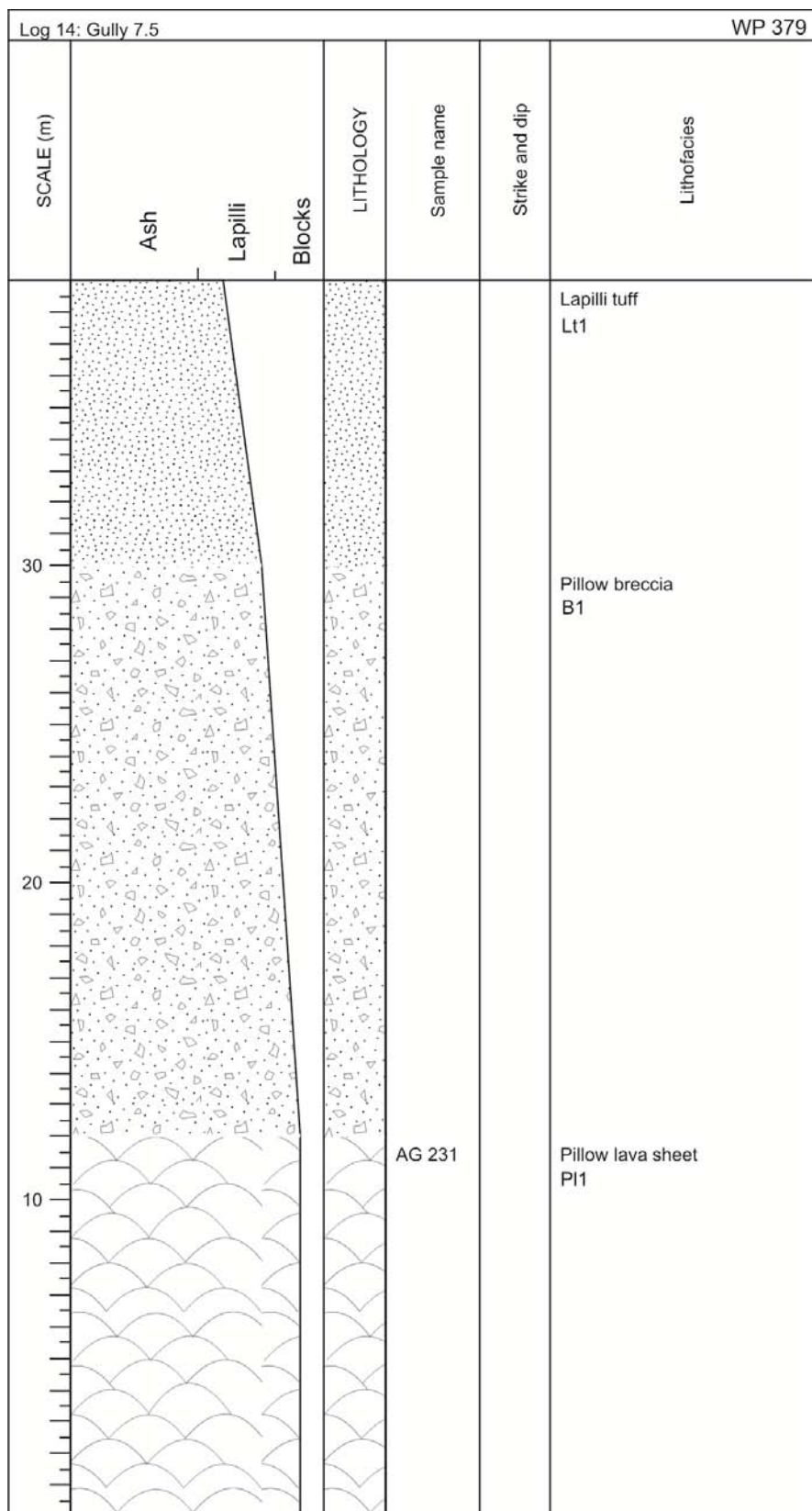


Figure A.14 Log 14

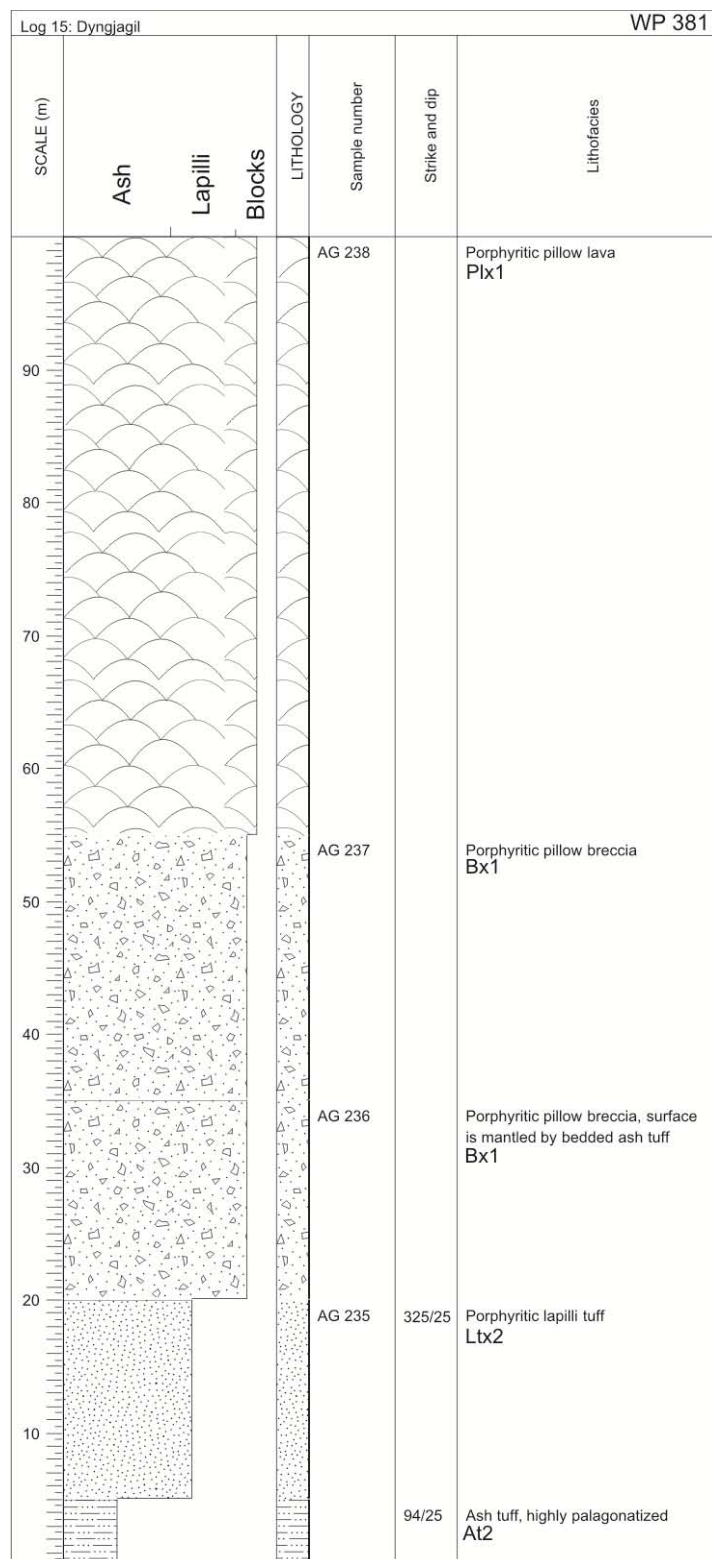


Figure A.15 Log 15

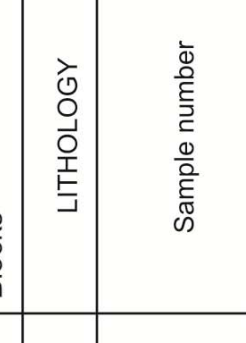
Log 16: Southern edge					WP 464
SCALE (m)	Ash  Lapilli  Blocks	LITHOLOGY	Sample number	Strike and dip	Lithofacies
8		AG 265		Porphyritic blocky and pillowed transitional lava sheet Plx2	
7					
6			AG 266		Porphyritic lapili tuff Ltx1
5					
4			AG 263		Porphyritic lapilli tuff, fines upward Ltx1
3					
2					
1		AG 264		Poorly exposed porphyritic pillow lava Plx1	

Figure A.16 Log 16



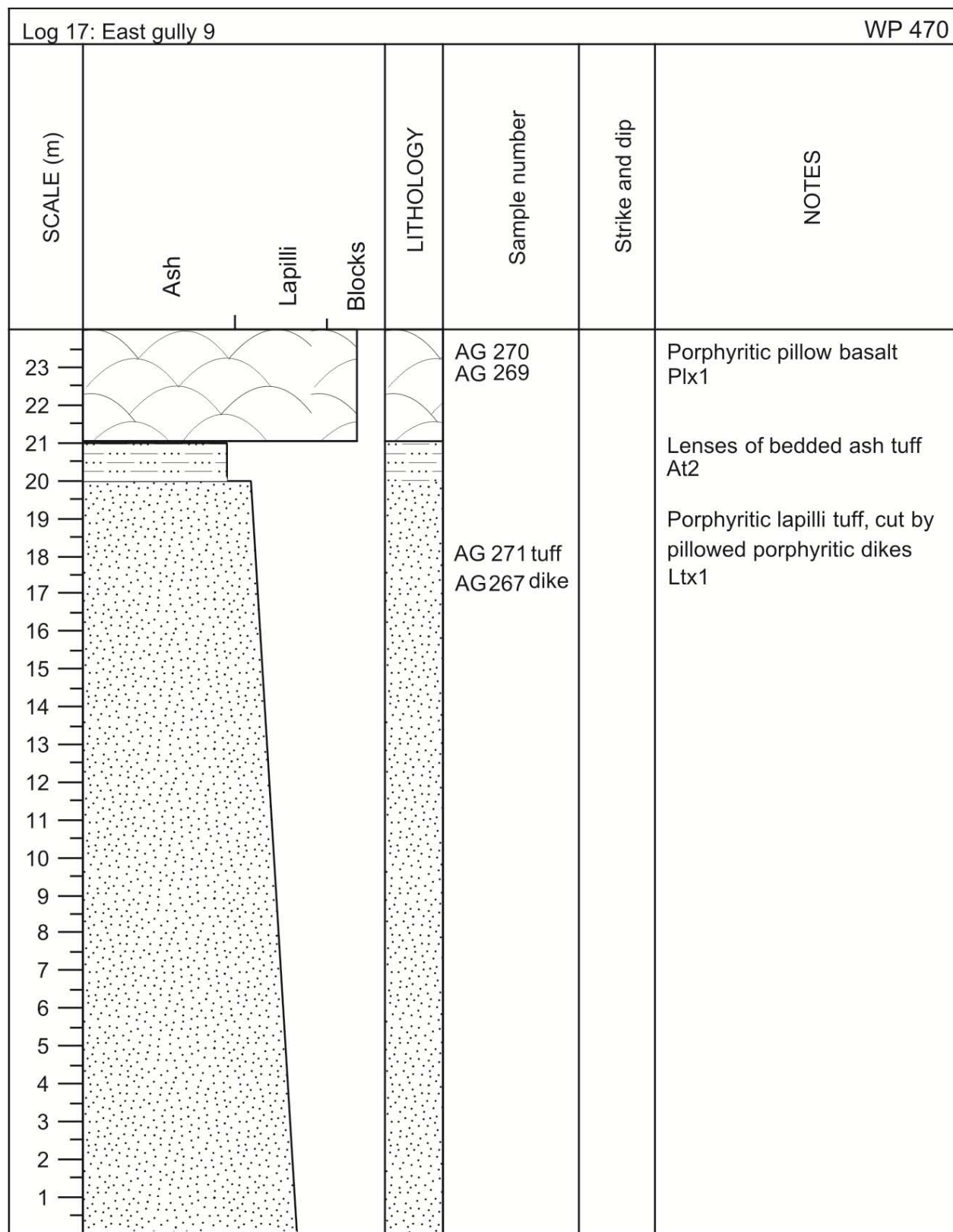
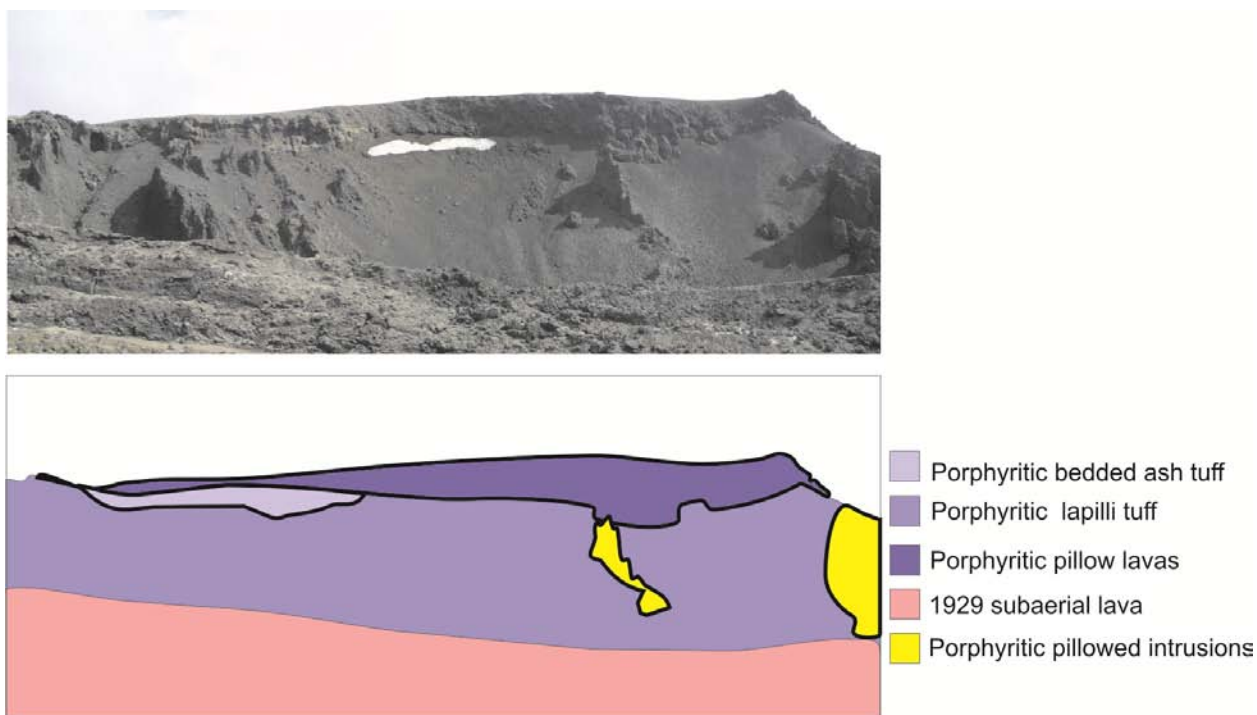


Figure A.17 Log 17



**Figure A.18** Field image and mosaic accompanying Log 17

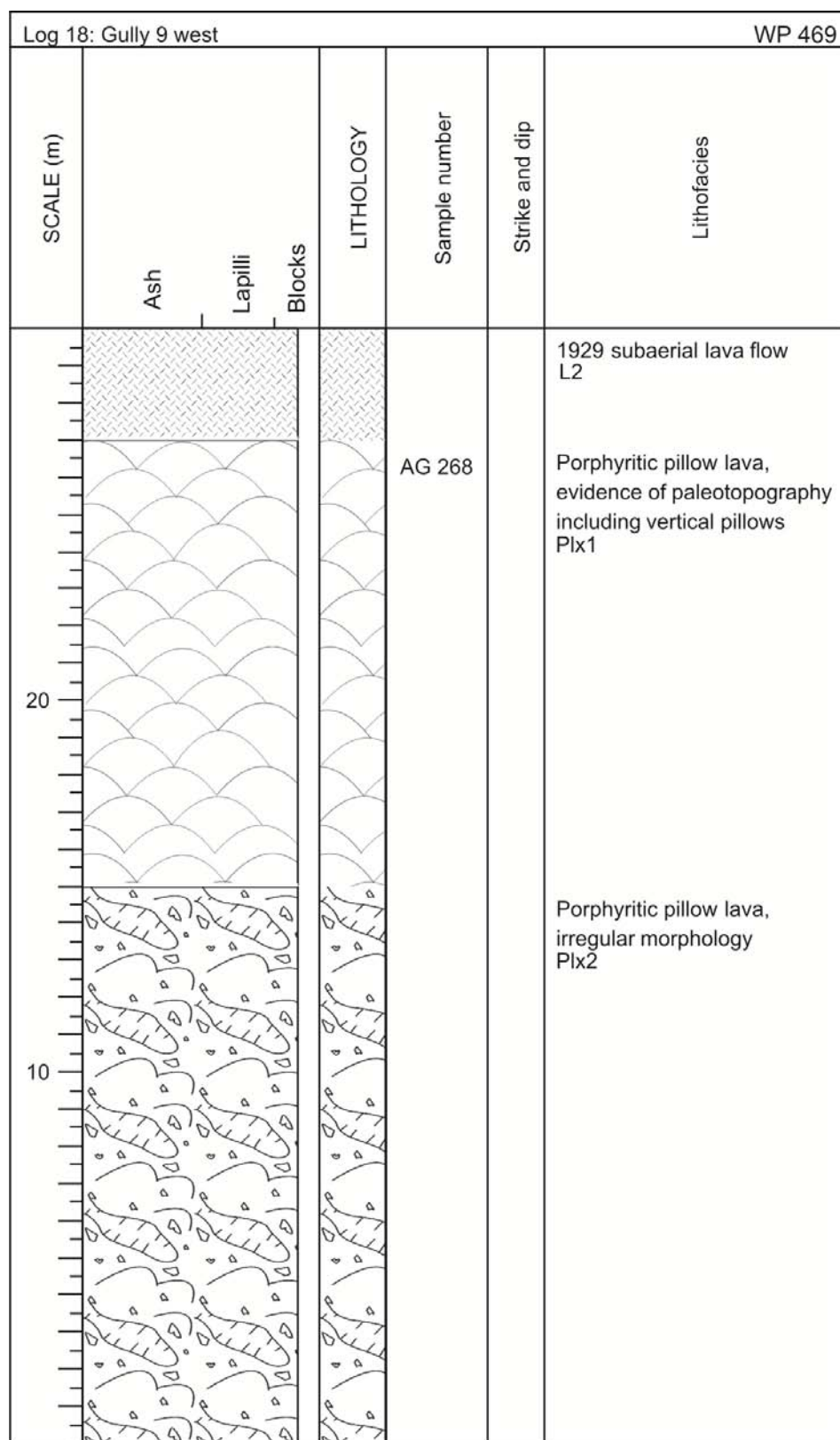


Figure A.19 Log 18

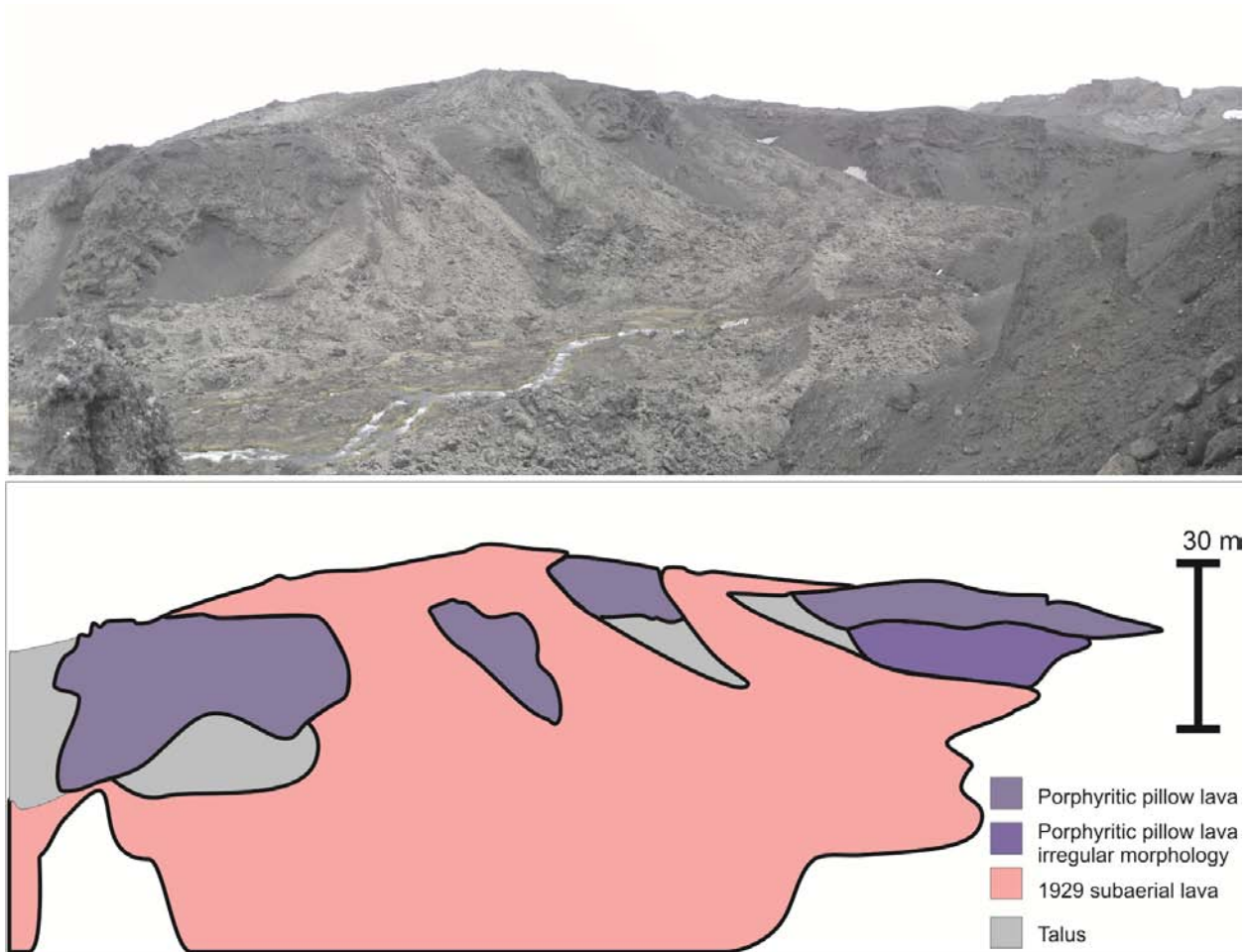


Figure A.20 Field image and mosaic for log 18

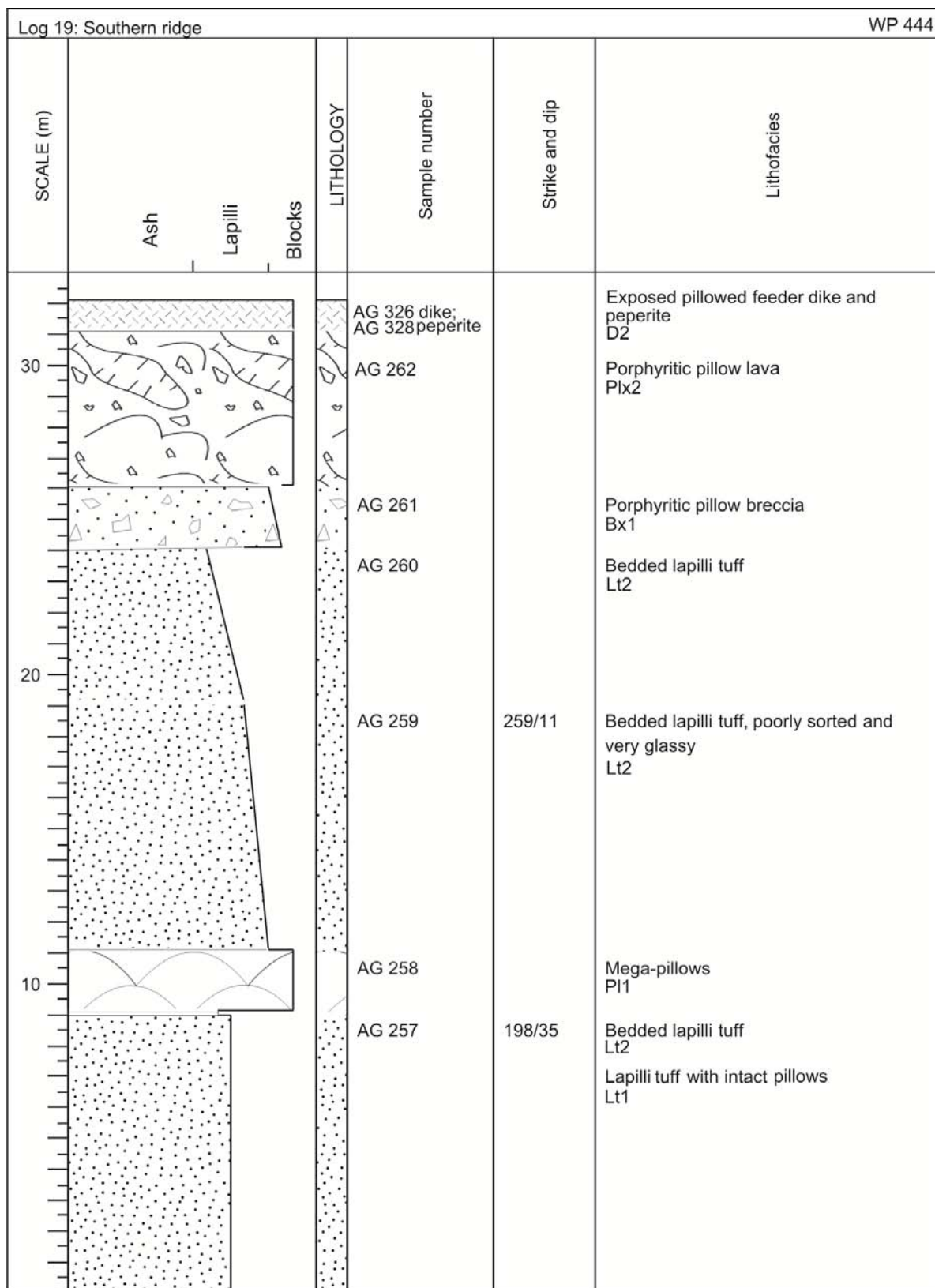


Figure A.21 Log 19



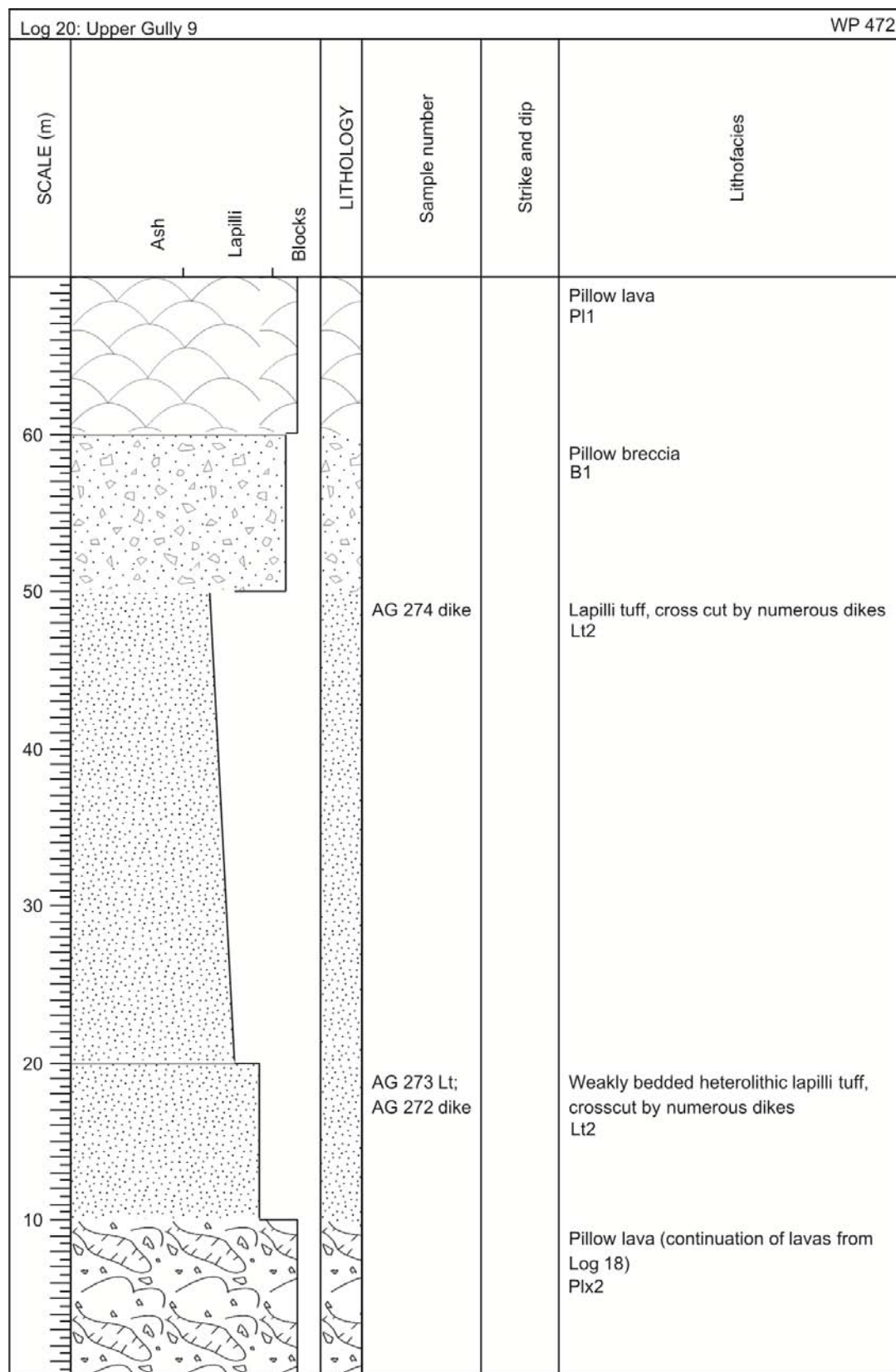


Figure A.22 Log 20

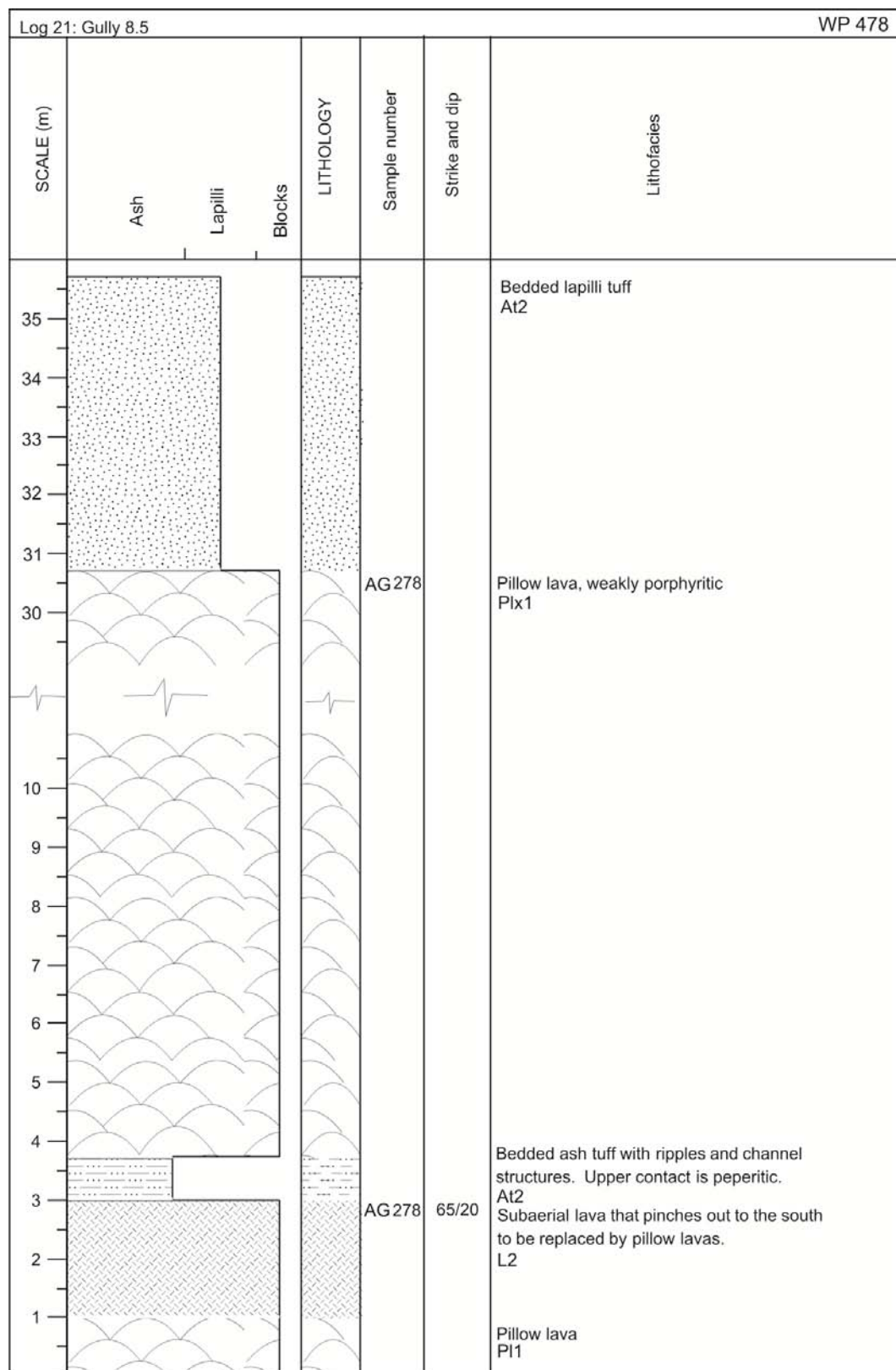


Figure A.23 Log 21





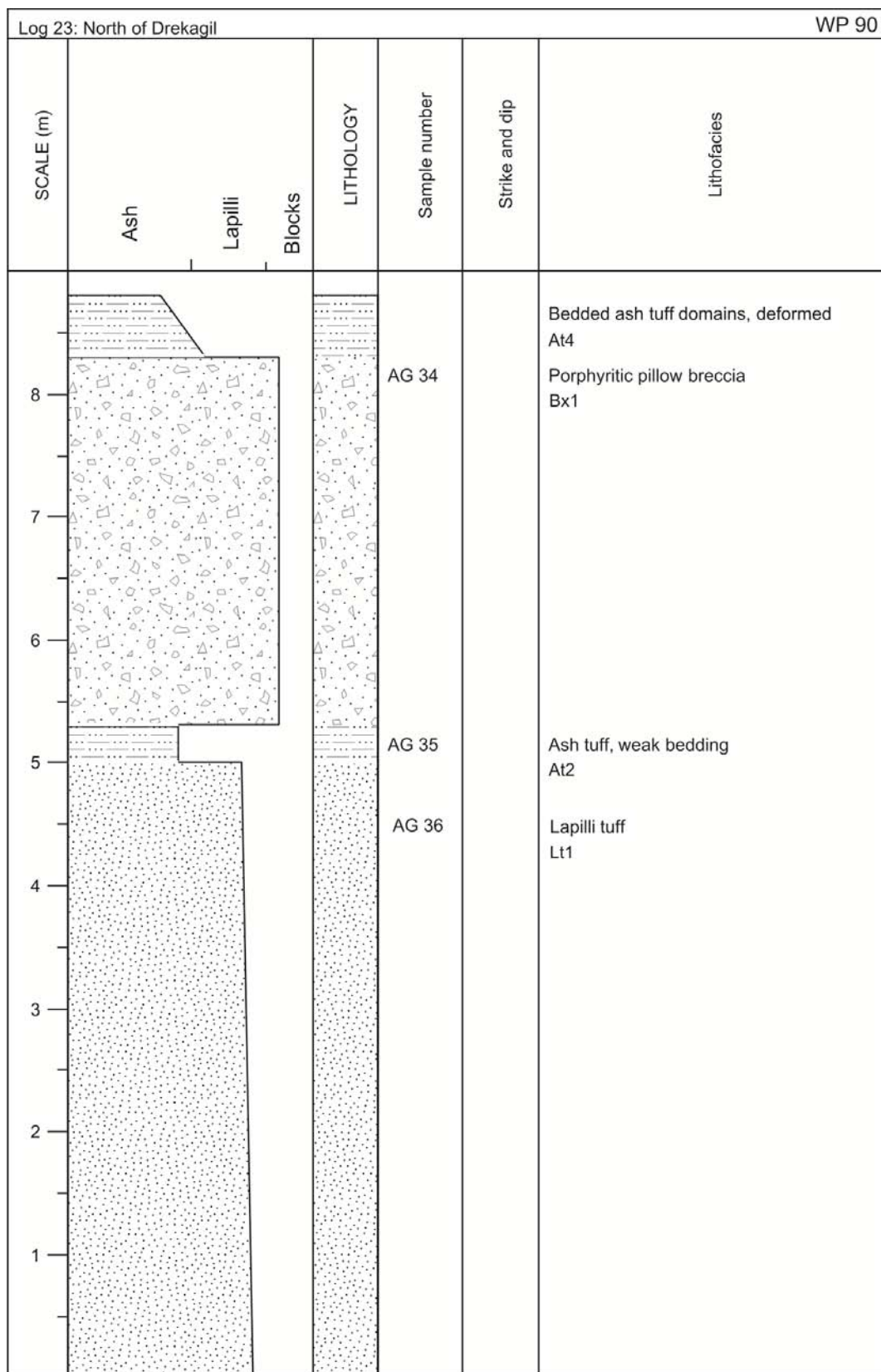


Figure A.25 Log 23

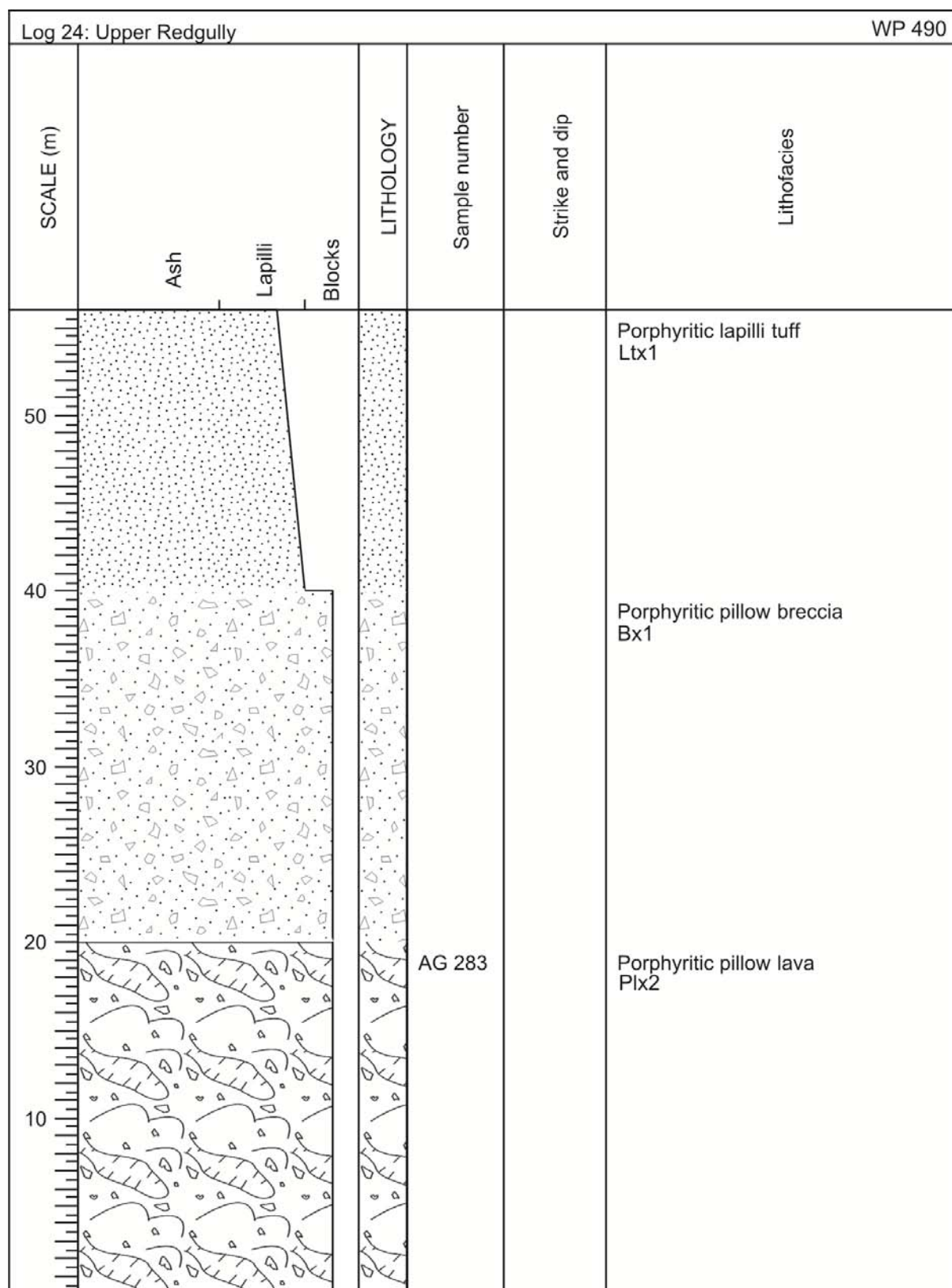


Figure A.26 Log 24



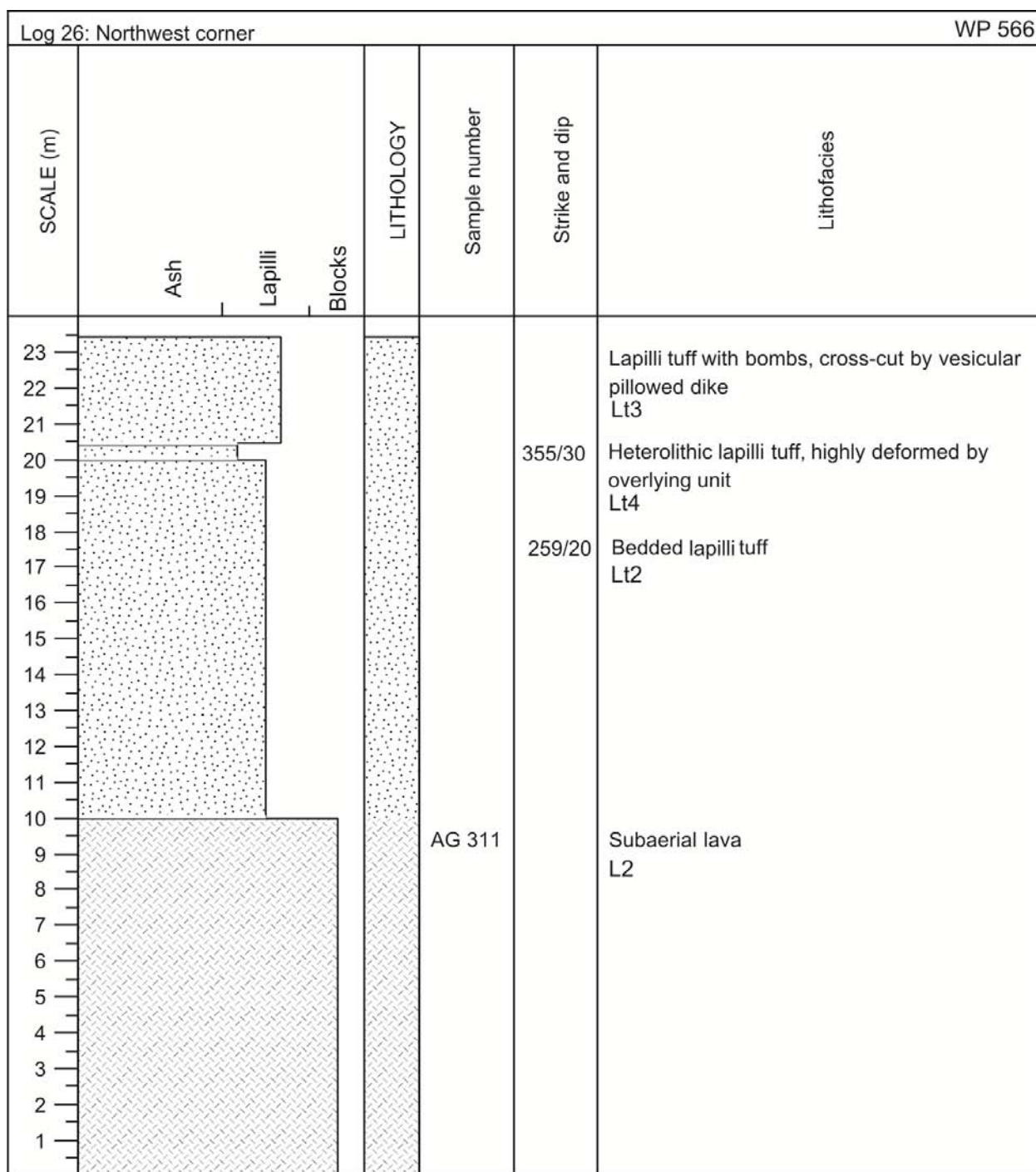


Figure A.28 Log 26

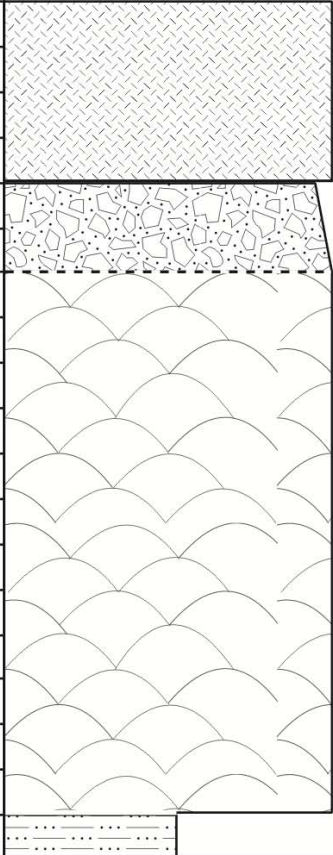


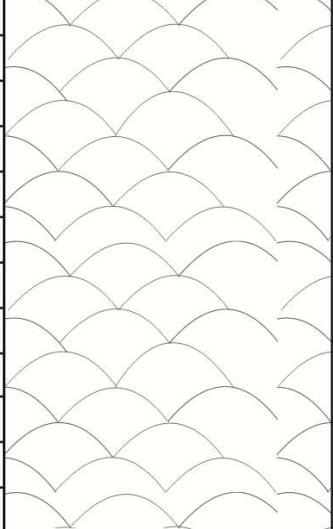


Log 27: South of Dyngjagil					WP 583
SCALE (m)	Ash Lapilli Blocks	LITHOLOGY	Sample number	Strike and dip	Lithofacies
9			AG 319		Subaerial a'a lava L2
8					Porphyritic pillow breccia Bx1
7					Porphyritic pillow lava, transitions laterally into a breccia, followed by a lapilli tuff Plx1
6					Bedded ash and lapilli tuff At2

Figure A.29 Log 27

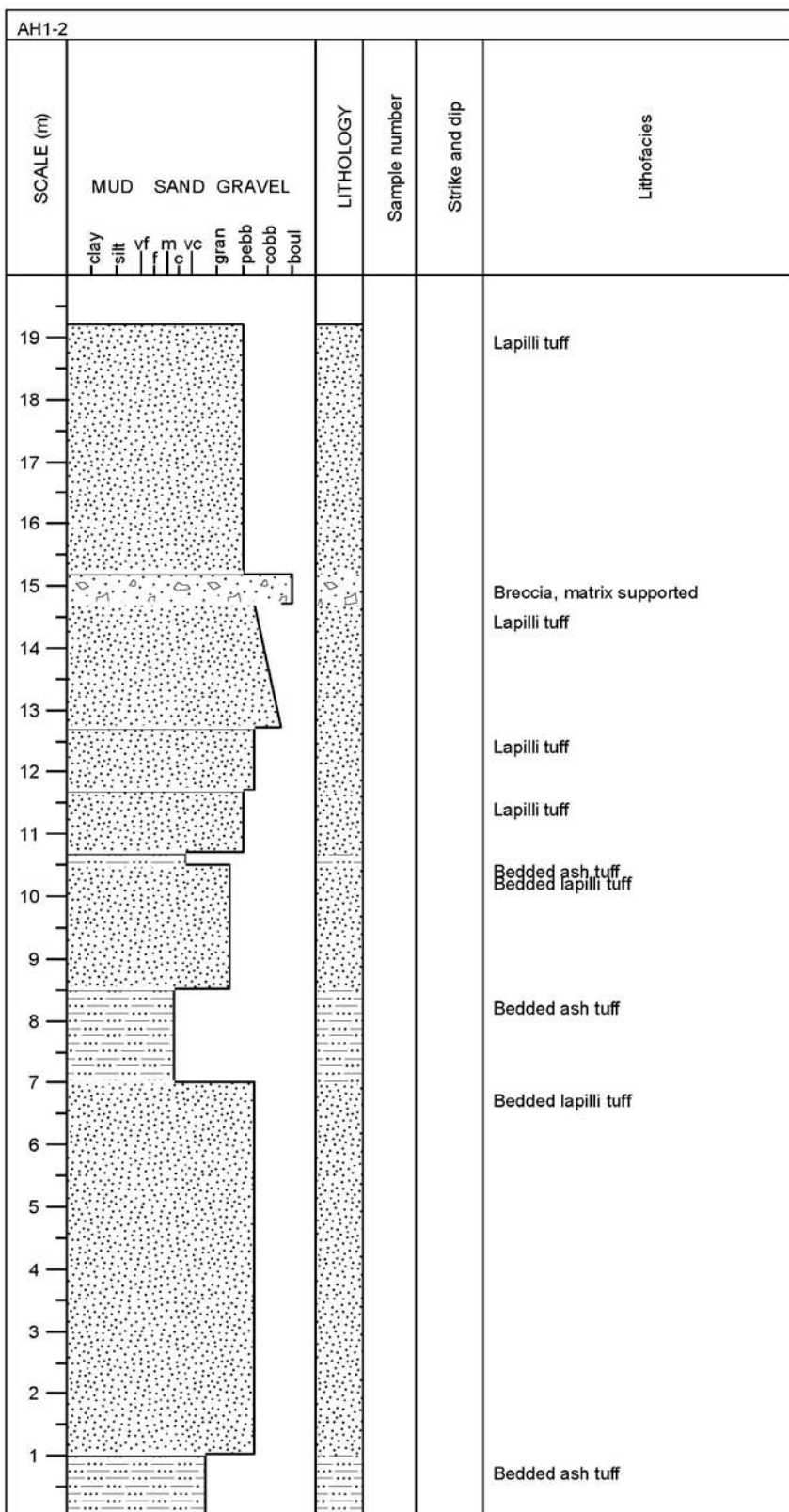


Figure A.30 Log AH1-2



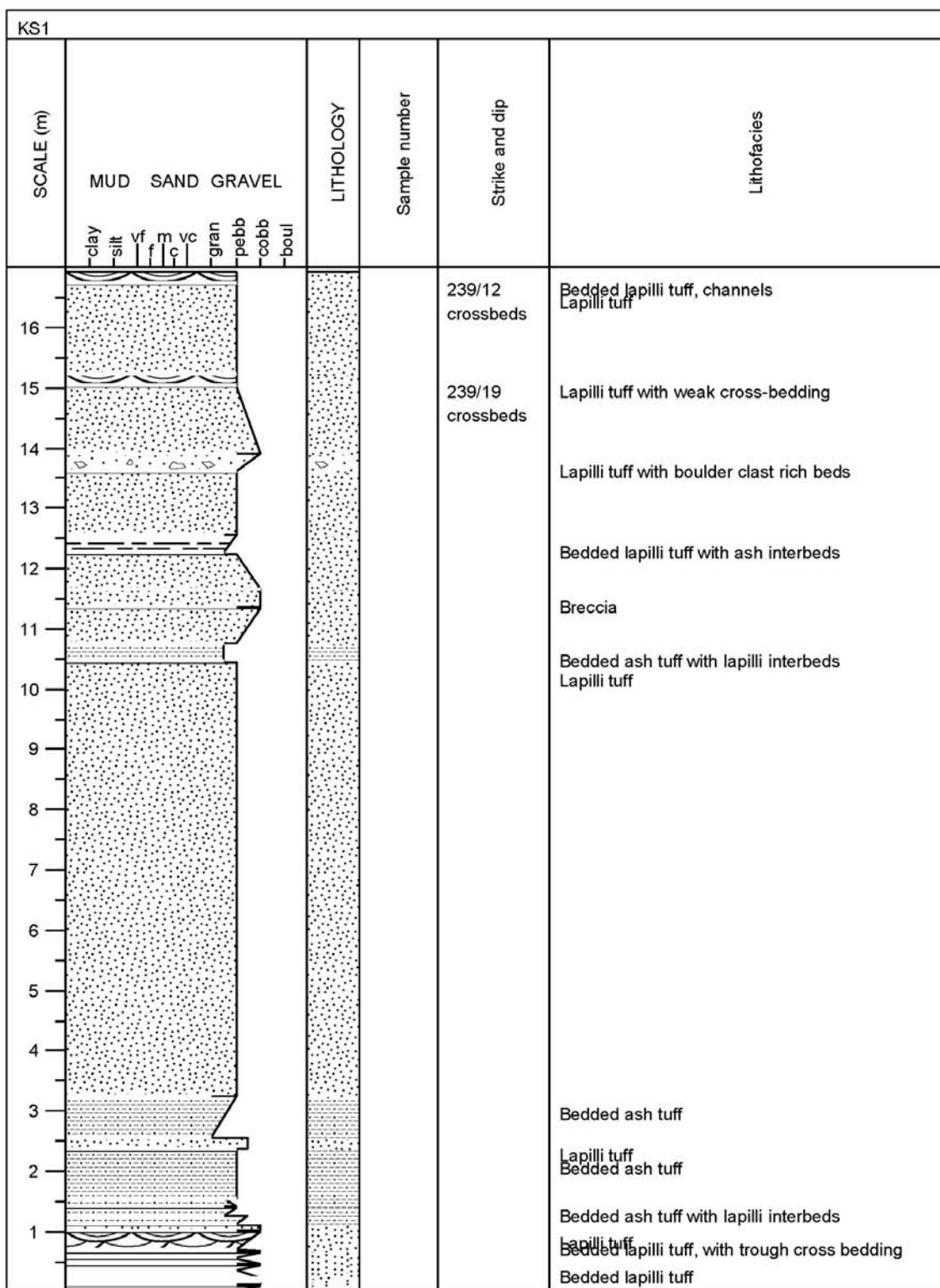


Figure A.31 Log KS1

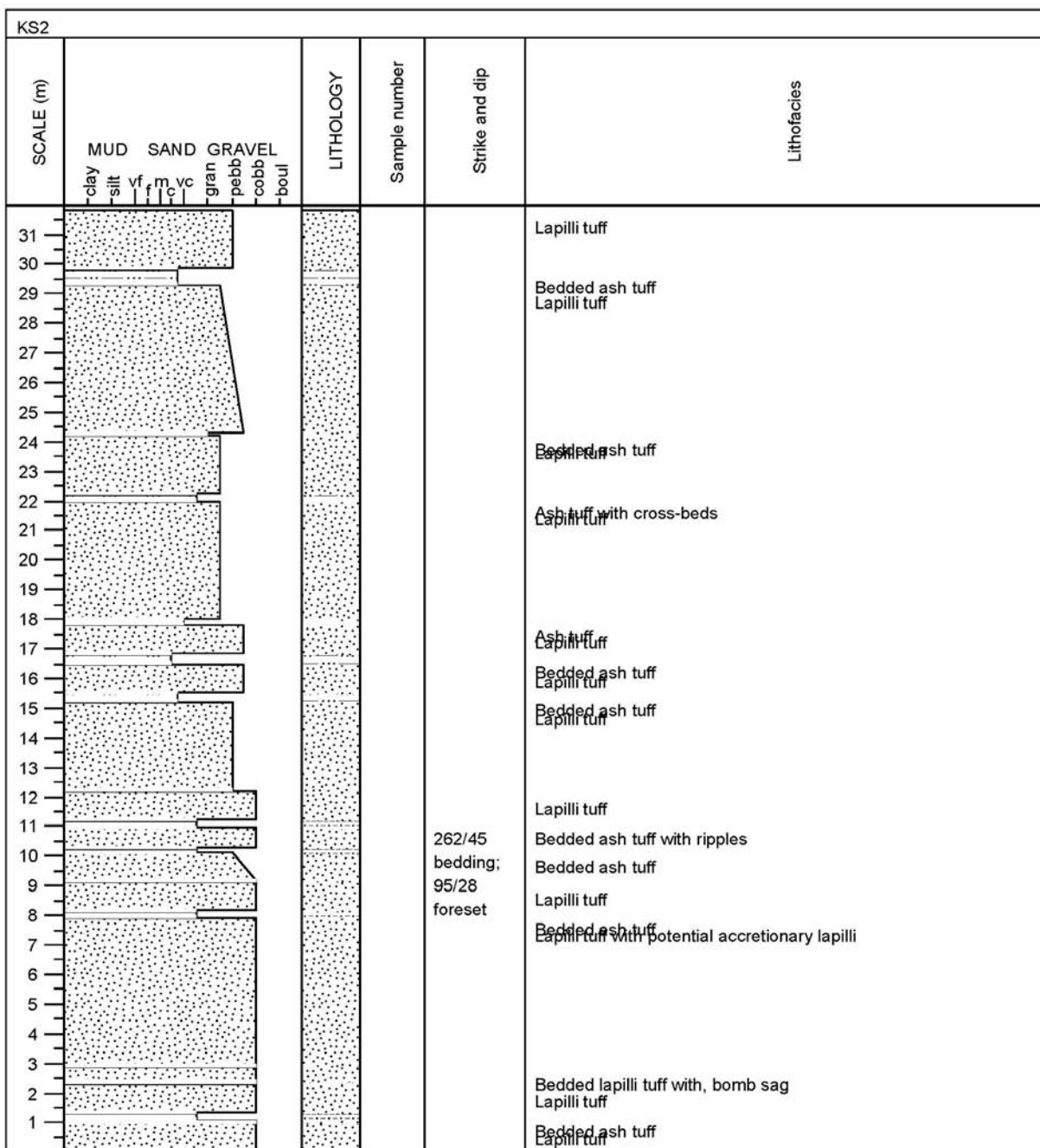


Figure A.32 Log KS2



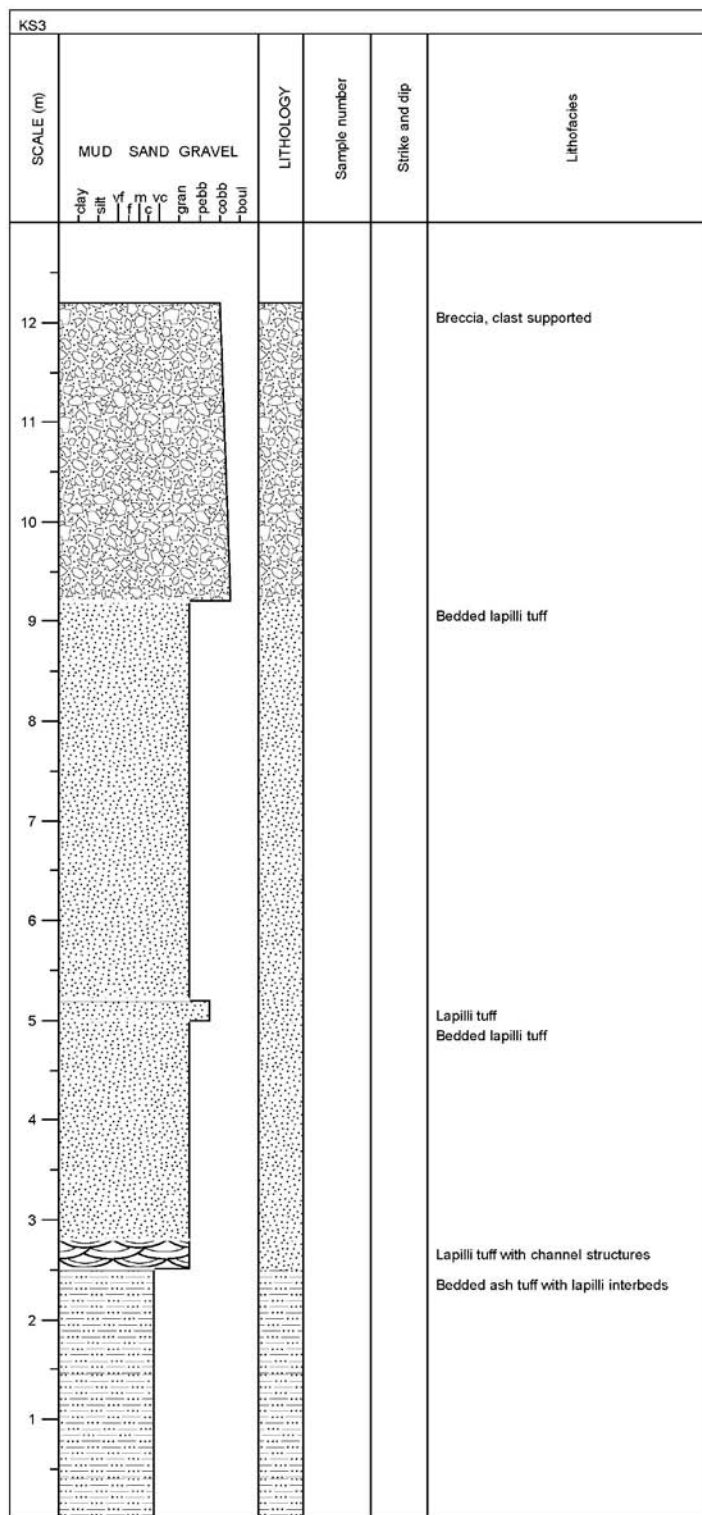


Figure A.33 Log KS3

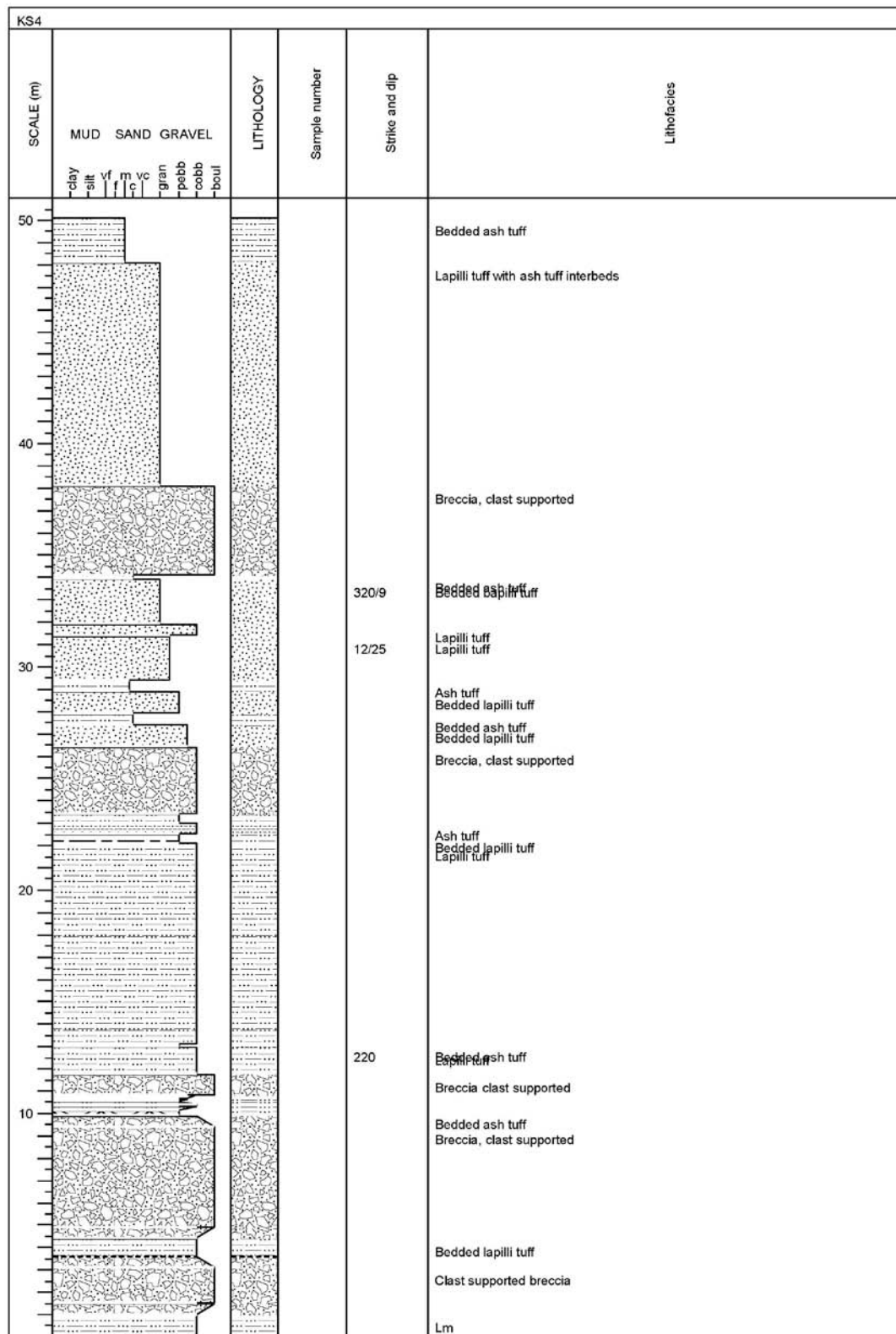


Figure A.34 Log KS4

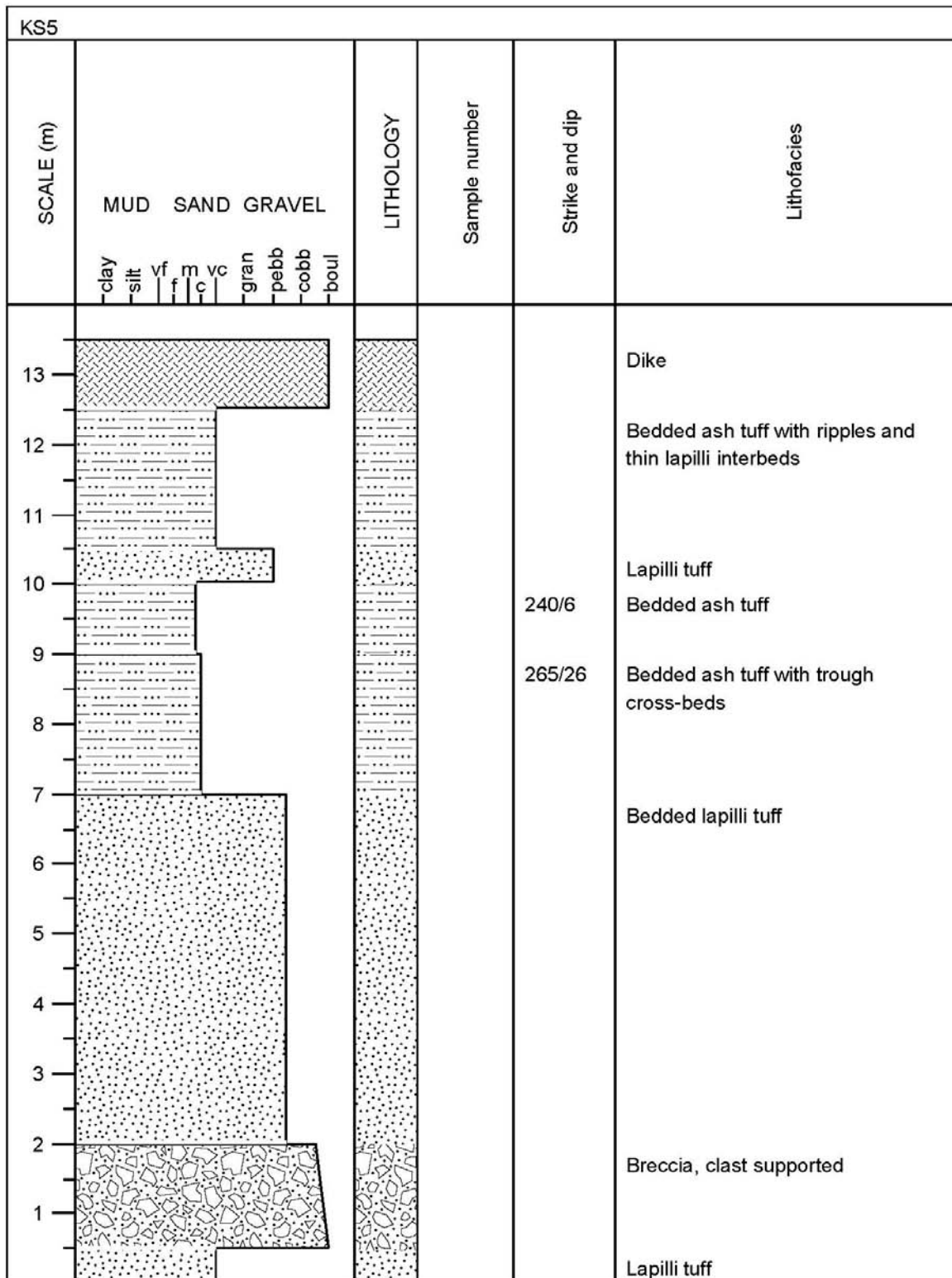


Figure A.35 KS5

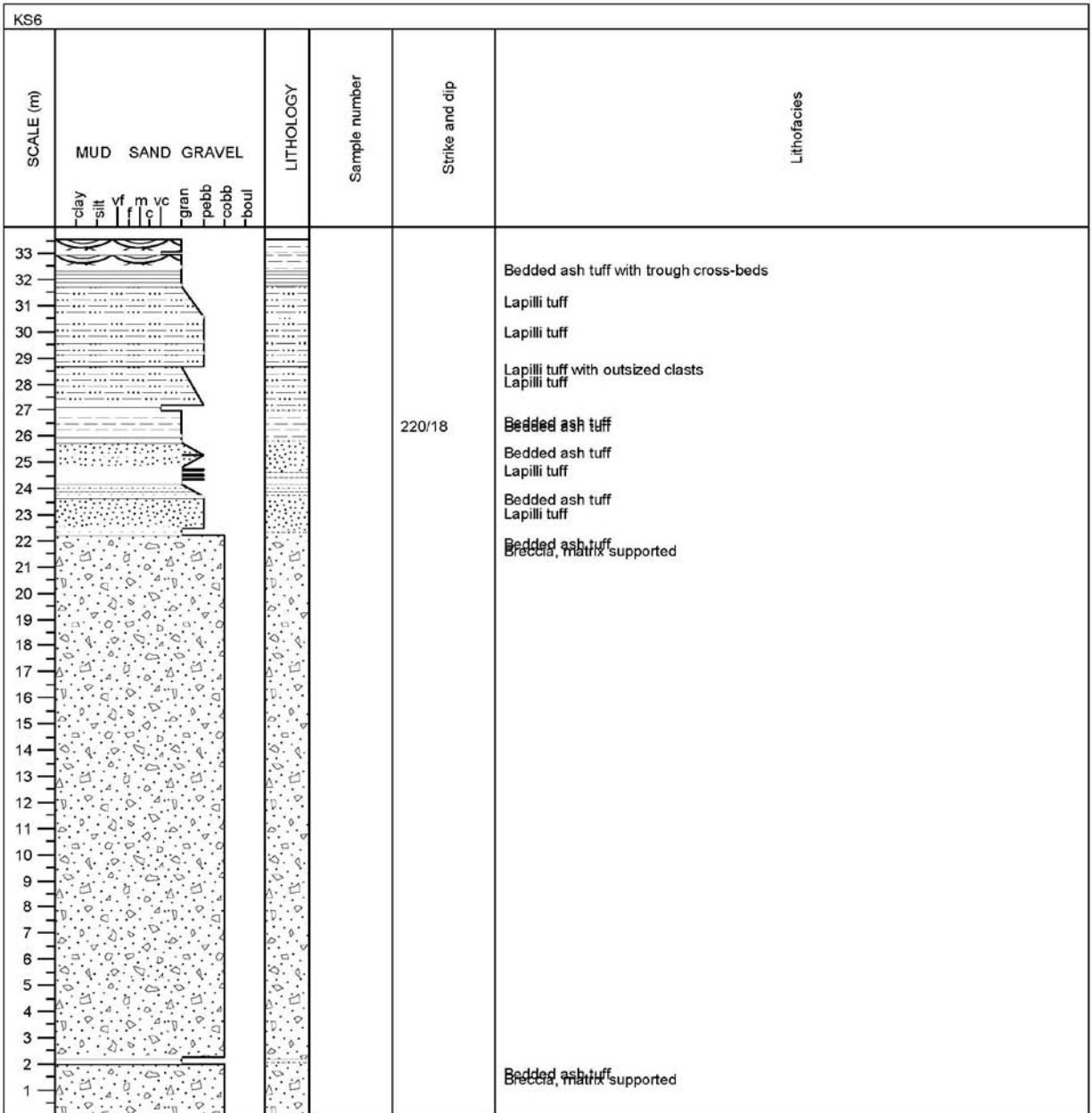


Figure A.36 KS6



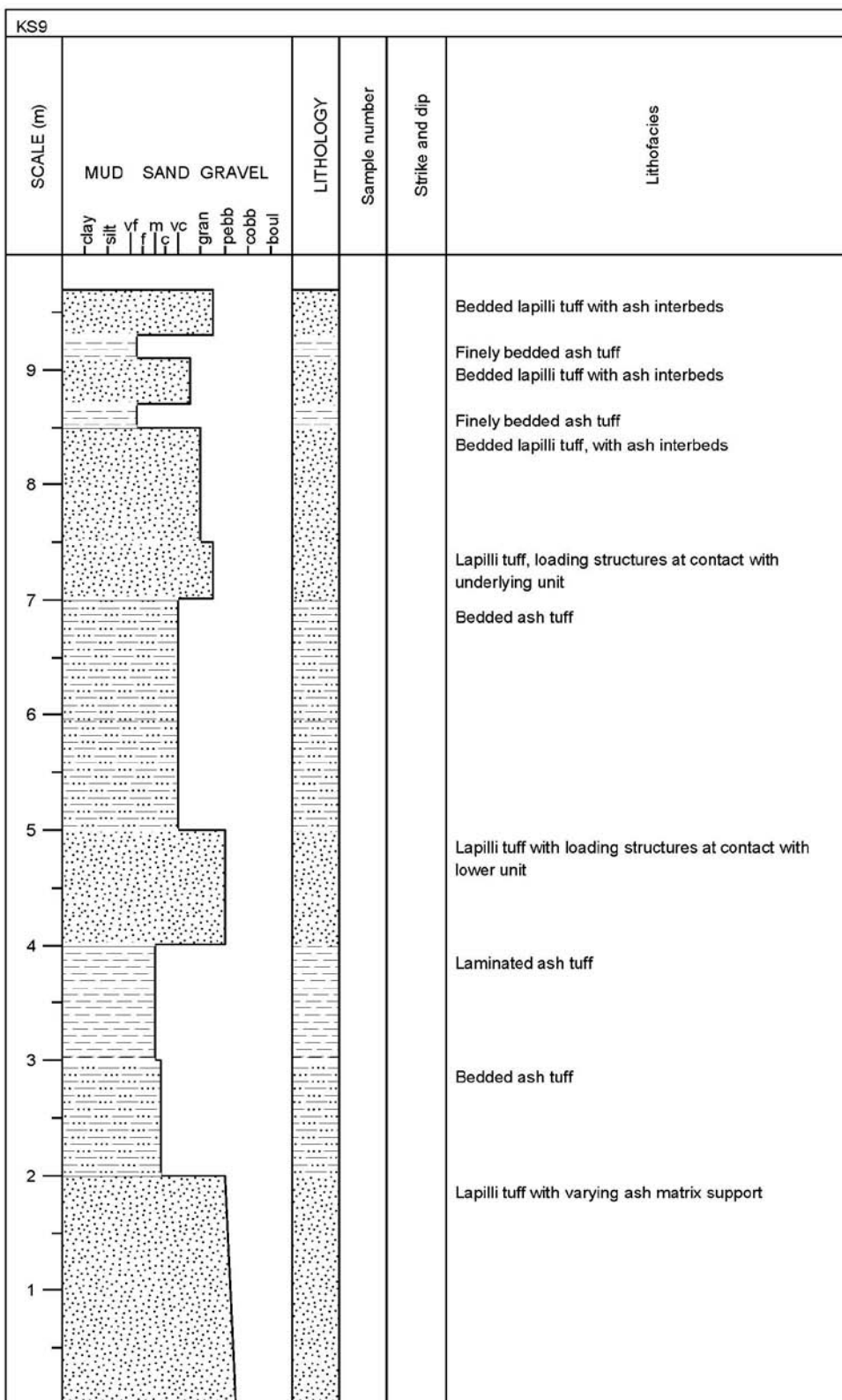


Figure A.38 KS9

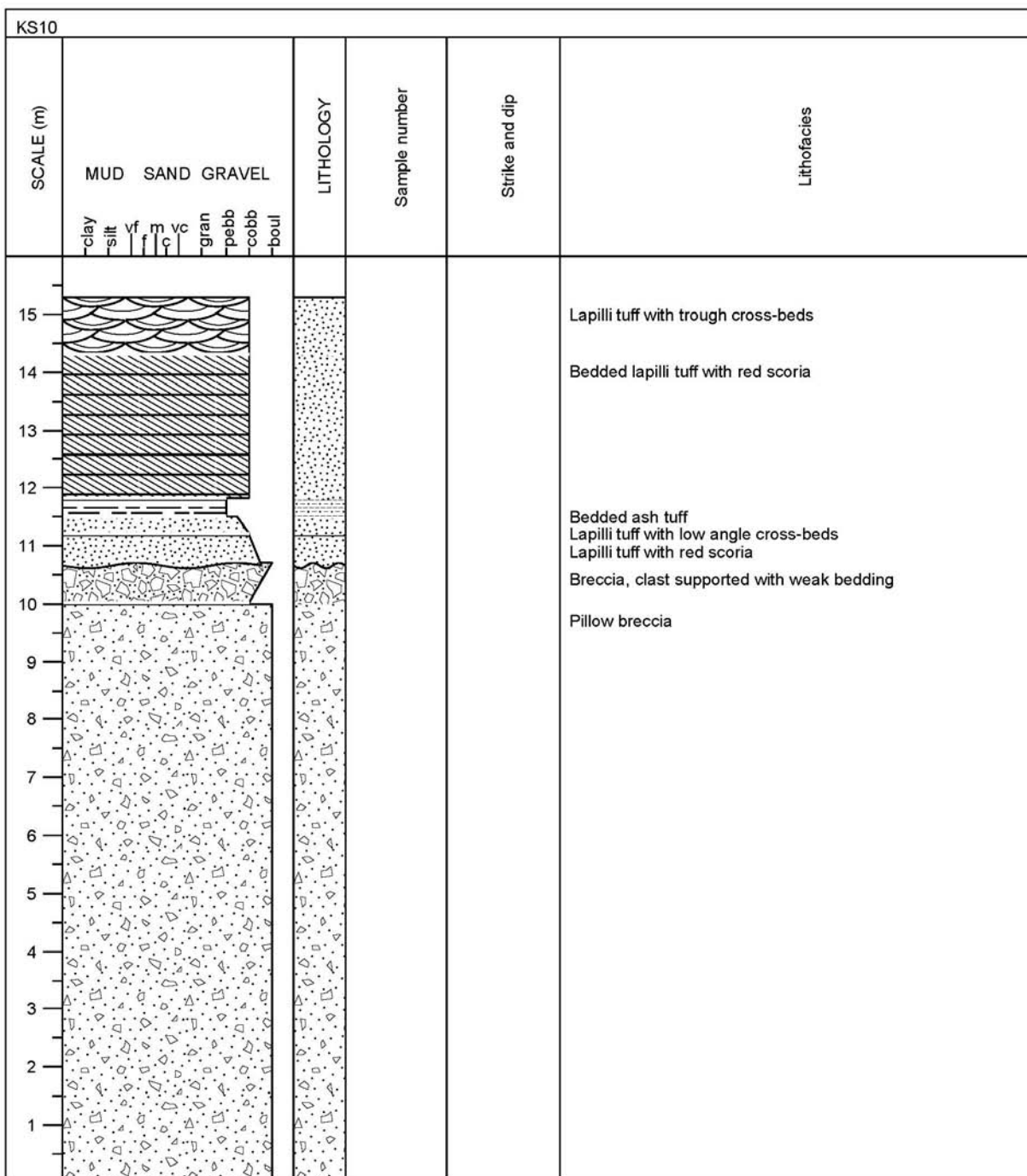


Figure A.39 KS10

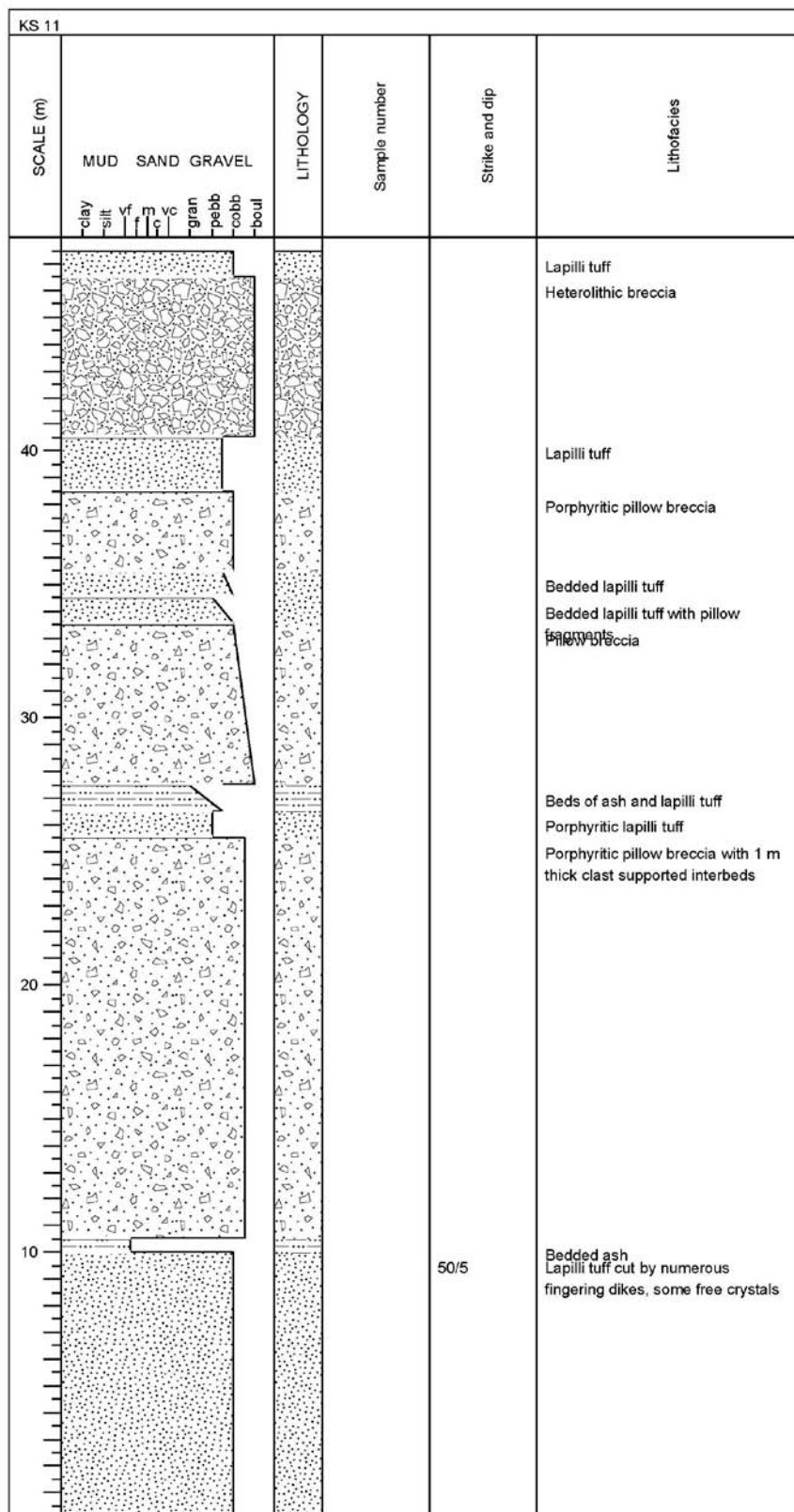


Figure A.40 KS11



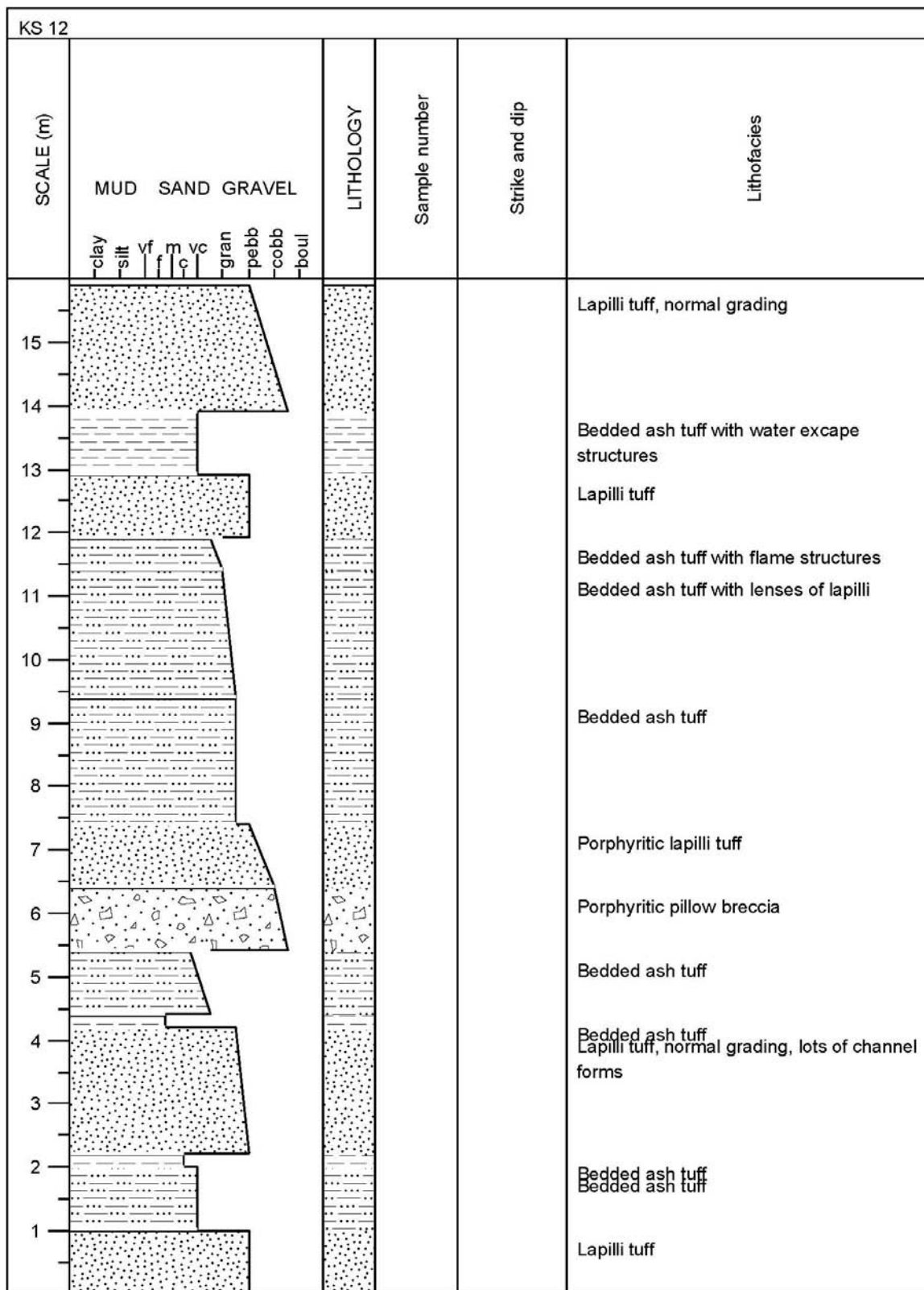


Figure A.41 KS12

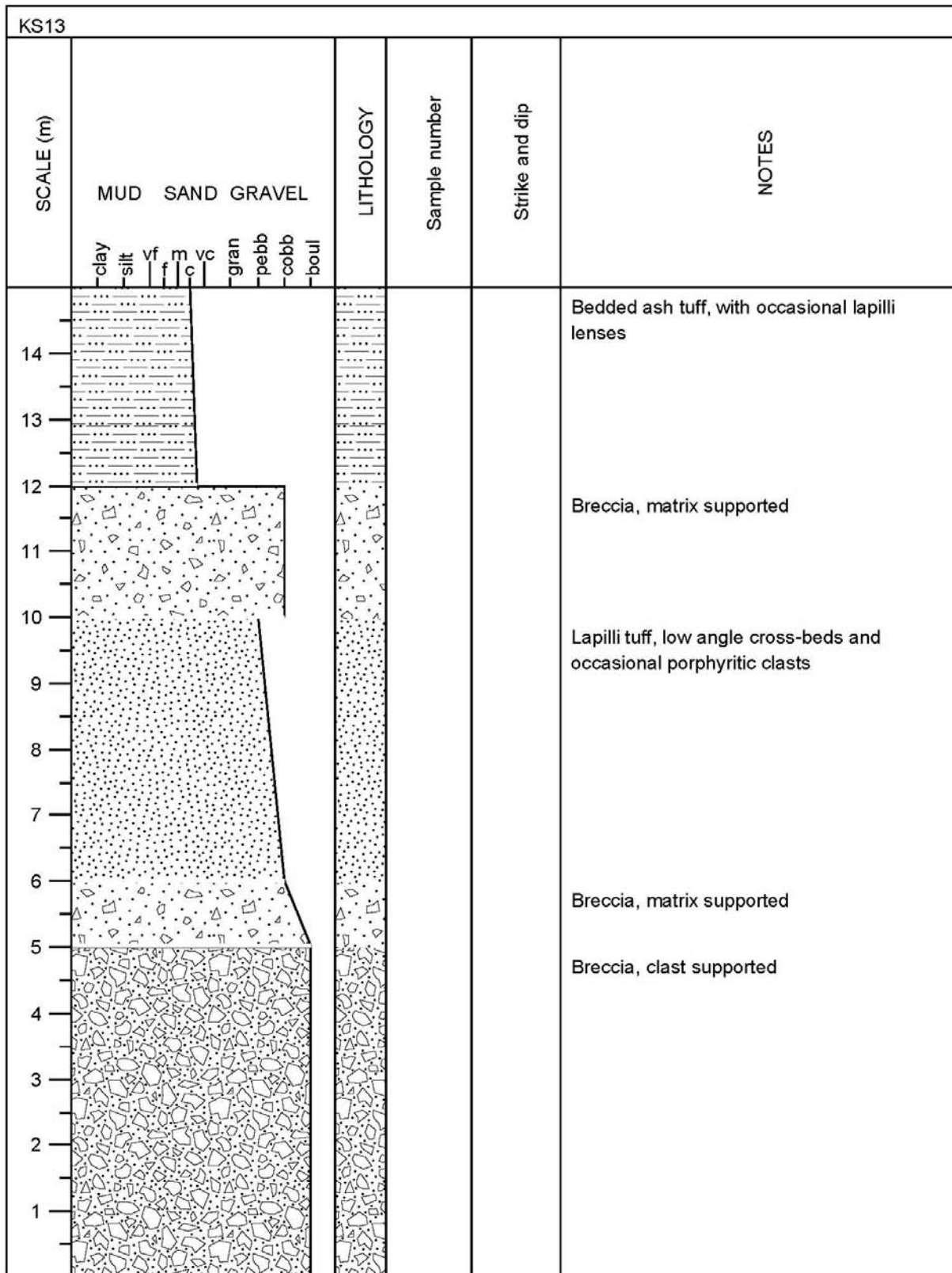


Figure A.42 KS13

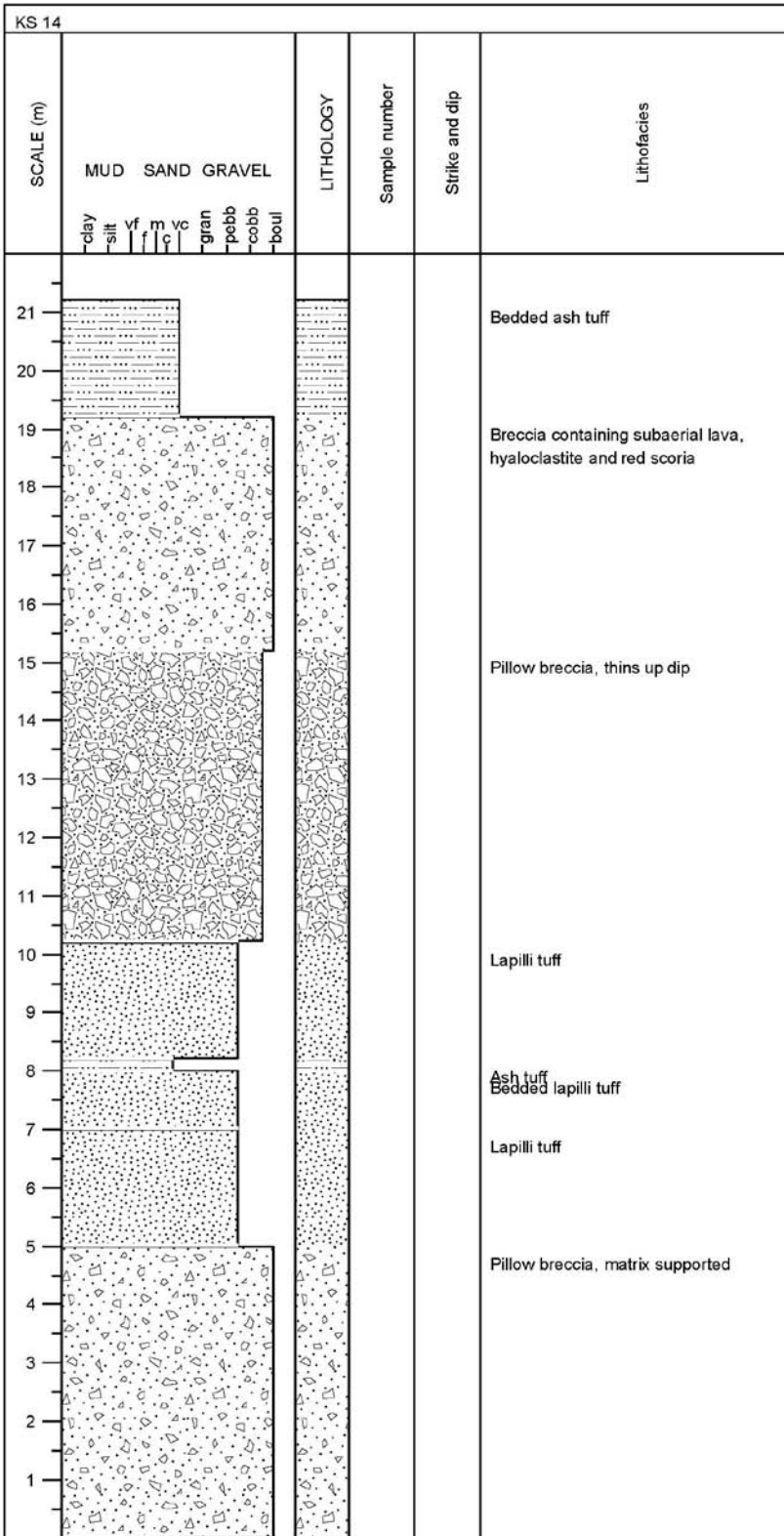


Figure A.43 KS14



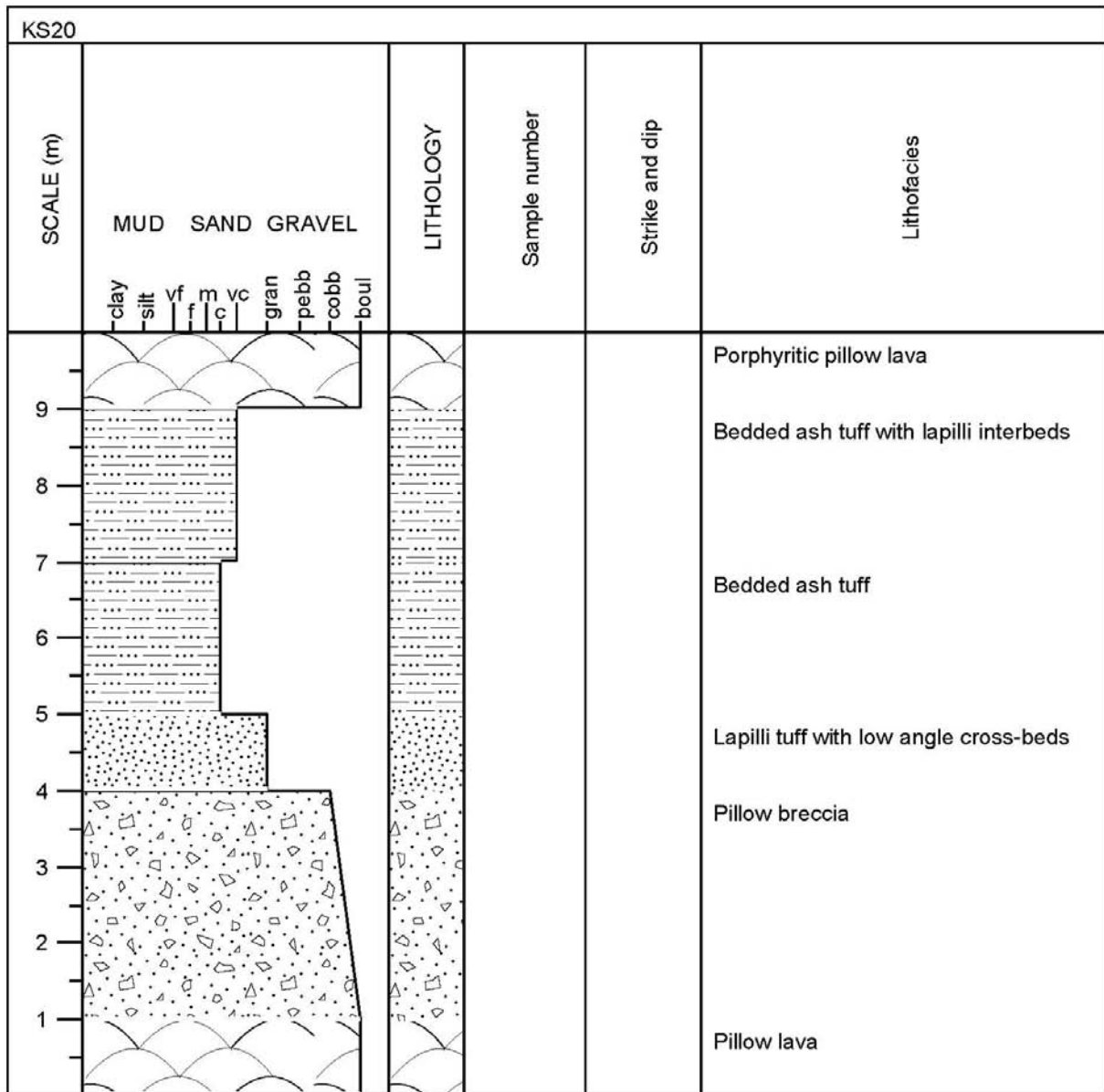


Figure A.45 KS20



## **APPENDIX B**

### **GEOCHEMISTRY**

**Table B.1 Complete XRF results split by eruptive unit**

<b>Grade</b>	**		***	***	***	***	*	*	
<b>Unit</b>	Unassigned		<b>Unit 1A</b>				<b>1B</b>	<b>Dm1</b>	
<b>Sample</b>	<b>AG301</b>		<b>AG56</b>	<b>AG106</b>	AG56 <sup>1</sup>	AG 06 <sup>1</sup>	AG8 <sup>1</sup>	<b>AG222</b>	
<b>Facies</b>	Plx2		L2	L2	L2	L2	L2	Dm1	
<b>SiO<sub>2</sub></b>	51.72		50.91	51.04	50.84	50.52	50.75	50.14	
<b>TiO<sub>2</sub></b>	2.626		2.304	2.133	2.27	2.10	1.96	3.064	
<b>Al<sub>2</sub>O<sub>3</sub></b>	13.24		13.72	13.72	13.65	13.68	13.80	13.21	
<b>FeO <sup>2</sup></b>	14.84		13.41	13.58	14.91	15.02	14.59	13.81	
<b>MnO</b>	0.253		0.227	0.232	0.23	0.24	0.23	0.221	
<b>MgO</b>	4.78		5.61	5.64	5.64	5.68	6.09	4.48	
<b>CaO</b>	9.36		10.27	10.25	10.26	10.29	10.80	9.58	
<b>Na<sub>2</sub>O</b>	2.87		2.62	2.62	2.63	2.63	2.50	2.90	
<b>K<sub>2</sub>O</b>	0.54		0.42	0.44	0.46	0.46	0.42	0.65	
<b>P<sub>2</sub>O<sub>5</sub></b>	0.286		0.240	0.225	0.25	0.23	0.21	0.372	
<b>Total</b>	100.52		99.73	99.89	101.25	100.93	101.45	98.44	
<b>Nb</b>	18		16	16	17	16	14	24	
<b>Rb</b>	12		9	9	10	9	8	12	
<b>Sr</b>	192		194	197	189	192	190	235	
<b>Y</b>	44		38	37	36	34	30	41	
<b>Zr</b>	180		156	147	153	142	127	224	
<b>Ce</b>	40		36	34	53	20	46	56	
<b>Cu</b>	72		118	129	206	208	239	142	
<b>Ni</b>	21		37	30	39	31	37	25	
<b>Sc</b>	43		43	43	41	42	47	38	
<b>V</b>	415		405	393	406	386	370	418	
<b>Zn</b>	138		119	119	88	86	82	129	
<p>Grade reflects the confidence of the fit of a sample with its group. * Low confidence, but best fit, ** moderate confidence, *** high confidence.</p> <p>Samples processed at the WSU geoanalysis laboratory, WA, USA.</p> <p><sup>1</sup>Indicates samples processed in a second laboratory at McGill University, Montreal Canada.</p> <p><sup>2</sup>Fe is presented as FeO except for samples from McGill where they were calculated to be Fe<sub>2</sub>O<sub>3</sub>, resulting in higher values.</p>									



Table B.1 continued									
Grade	***	***	***	***	***	***	***	***	***
Unit	2								
Sample	AG274	AG331	AG58	AG182	AG22	AG314	AG176	AG207	AG327
Facies	D1	P11	CMVD	Lt1	P11	P11	B1	P11	L1
SiO <sub>2</sub>	50.63	50.77	51.13	50.70	50.51	50.64	50.43	51.04	50.43
TiO <sub>2</sub>	2.519	2.499	2.515	2.509	2.492	2.472	2.506	2.281	2.288
Al <sub>2</sub> O <sub>3</sub>	13.27	13.22	13.33	13.24	13.22	13.19	13.23	13.76	13.84
FeO <sup>2</sup>	14.13	13.87	14.17	14.04	13.79	14.26	14.09	13.50	13.59
MnO	0.246	0.233	0.241	0.237	0.239	0.236	0.241	0.229	0.235
MgO	5.22	5.29	5.43	5.37	5.42	5.47	5.00	5.72	5.53
CaO	10.00	9.92	9.83	9.84	9.95	9.99	9.89	10.40	10.28
Na <sub>2</sub> O	2.52	2.61	2.55	2.59	2.56	2.62	2.58	2.57	2.75
K <sub>2</sub> O	0.48	0.50	0.51	0.49	0.48	0.48	0.48	0.43	0.48
P <sub>2</sub> O <sub>5</sub>	0.276	0.269	0.278	0.273	0.270	0.261	0.276	0.236	0.264
Total	99.28	99.18	99.98	99.28	98.92	99.62	98.73	100.16	99.68
Nb	19	19	19	19	19	19	19	17	17
Rb	9	11	11	10	11	12	10	9	10
Sr	189	187	186	186	187	183	188	193	214
Y	41	41	42	41	41	41	41	38	33
Zr	172	170	174	172	169	165	172	152	150
Ce	38	39	42	37	39	38	40	32	34
Cu	130	114	119	111	121	127	123	126	131
Ni	36	32	32	31	34	35	32	39	34
Sc	43	43	42	42	41	43	42	43	43
V	424	421	420	417	422	412	424	401	374
Zn	127	128	129	130	125	125	127	118	116
Grade reflects the confidence of the fit of a sample with its group. * Low confidence, but best fit, ** moderate confidence, *** high confidence. Samples processed at the WSU Geoanalysis laboratory, WA, USA. <sup>1</sup> Indicates samples processed in a second laboratory at McGill University, Montreal Canada. <sup>2</sup> Fe is presented as FeO except for samples from McGill where they were calculated to be Fe <sub>2</sub> O <sub>3</sub> , resulting in higher values.									

Table B.1 continued									
Grade	***	***	***	***	***	***	***	***	**
Unit	2A (continued)								
Sample	AG213	AG30 <sup>1</sup>	AG58a <sup>1</sup>	AG58b <sup>1</sup>	AG87 <sup>1</sup>	AG88 <sup>1</sup>	AG115 <sup>1</sup>	AG23 <sup>1</sup>	AG267
Facies	Pillows	Pl1	CMVD	CMVD	Pl1	CMVD	D1	D1	Dx1
SiO <sub>2</sub>	46.83	50.57	50.13	50.04	51.39	50.23	50.50	50.33	50.46
TiO <sub>2</sub>	2.326	2.48	2.46	2.45	2.50	2.49	2.47	2.51	2.229
Al <sub>2</sub> O <sub>3</sub>	13.99	13.31	13.19	13.18	13.37	13.28	13.19	13.25	13.68
FeO <sup>2</sup>	13.66	15.79	16.25	16.07	14.83	15.88	15.89	16.06	14.13
MnO	0.291	0.25	0.25	0.24	0.25	0.25	0.24	0.25	0.243
MgO	5.21	5.22	5.38	5.39	5.40	5.43	5.46	5.20	5.58
CaO	10.44	9.95	9.75	9.76	10.03	9.85	9.86	9.92	10.24
Na <sub>2</sub> O	2.56	2.60	2.47	2.52	2.61	2.47	2.54	2.57	2.63
K <sub>2</sub> O	0.19	0.52	0.51	0.53	0.51	0.49	0.54	0.50	0.44
P <sub>2</sub> O <sub>5</sub>	0.271	0.28	0.28	0.28	0.28	0.28	0.27	0.28	0.250
Total	95.78	101.06	100.77	100.58	101.28	100.75	101.06	100.98	99.88
Nb	18	20	20	20	20	20	19	20	17
Rb	2	11	11	11	11	10	10	10	8
Sr	195	182	178	179	188	181	181	183	201
Y	34	38	38	38	38	38	37	39	35
Zr	153	170	170	169	170	169	169	170	150
Ce	39	56	32	31	36	34	32	57	37
Cu	128	196	214	202	195	208	169	198	127
Ni	31	32	49	45	39	35	33	32	33
Sc	43	42	43	44	45	42	43	41	45
V	390	418	411	409	423	422	418	416	374
Zn	118	98	98	102	115	100	96	100	119
Grade reflects the confidence of the fit of a sample with its group. * Low confidence, but best fit, ** moderate confidence, *** high confidence. Samples processed at the WSU Geoanalysis laboratory, WA, USA. <sup>1</sup> Indicates samples processed in a second laboratory at McGill University, Montreal Canada. <sup>2</sup> Fe is presented as FeO except for samples from McGill where they were calculated to be Fe <sub>2</sub> O <sub>3</sub> , resulting in higher values.									

Table B.1 continued									
Grade	**	*	*	*	*	***	***	***	
Unit	2A (continued)					Dm2	3		
Sample	AG 322	AG 277	AG 265	AG 310	AG 271	AG 332	AG 219	AG 196	
Facies	D1	L2	Plx1	Lx2	Lt 1	Dm1	Lt 1	Pl1	
SiO <sub>2</sub>	48.06	52.32	50.33	51.01	50.95	50.71	50.51	49.93	
TiO <sub>2</sub>	2.311	1.861	2.342	2.219	2.359	2.499	2.916	2.932	
Al <sub>2</sub> O <sub>3</sub>	14.36	13.94	13.62	14.25	13.69	13.18	12.91	13.08	
FeO <sup>2</sup>	13.80	12.14	13.90	12.44	14.20	14.33	15.16	15.52	
MnO	0.224	0.202	0.237	0.256	0.247	0.242	0.252	0.253	
MgO	5.18	5.56	5.36	5.45	4.94	5.45	5.08	5.10	
CaO	10.31	9.87	10.02	10.44	9.46	9.90	9.48	9.58	
Na <sub>2</sub> O	2.41	2.54	2.70	2.51	2.82	2.60	2.68	2.63	
K <sub>2</sub> O	0.37	0.60	0.52	0.38	0.54	0.50	0.52	0.45	
P <sub>2</sub> O <sub>5</sub>	0.270	0.207	0.268	0.260	0.290	0.272	0.324	0.323	
Total	97.29	99.23	99.30	99.23	99.48	99.68	99.82	99.80	
Nb	18	15	19	19	19	19	22	22	
Rb	6	14	12	10	12	11	11	10	
Sr	203	186	214	212	203	186	191	197	
Y	34	37	35	37	39	41	45	46	
Zr	153	158	157	157	177	170	192	193	
Ce	32	34	37	40	36	36	40	40	
Cu	129	134	140	130	94	116	118	117	
Ni	33	38	31	30	26	32	28	29	
Sc	43	38	43	43	41	43	43	44	
V	378	332	391	367	345	417	463	471	
Zn	114	105	116	118	125	127	141	141	
Grade reflects the confidence of the fit of a sample with its group. * Low confidence, but best fit, ** moderate confidence, *** high confidence. Samples processed at the WSU geoanalysis laboratory, WA, USA. <sup>1</sup> Indicates samples processed in a second laboratory at McGill University, Montreal Canada. <sup>2</sup> Fe is presented as FeO except for samples from McGill where they were calculated to be Fe <sub>2</sub> O <sub>3</sub> , resulting in higher values.									

Table B.1 continued									
Grade	**	*	*	*	*	***	***	***	
Unit	2A (continued)					Dm2	3		
Sample	AG 322	AG 277	AG 265	AG 310	AG 271	AG 332	AG 219	AG 196	
Facies	D1	L2	Plx1	Lx2	Lt 1	Dm1	Lt 1	Pl1	
SiO <sub>2</sub>	48.06	52.32	50.33	51.01	50.95	50.71	50.51	49.93	
TiO <sub>2</sub>	2.311	1.861	2.342	2.219	2.359	2.499	2.916	2.932	
Al <sub>2</sub> O <sub>3</sub>	14.36	13.94	13.62	14.25	13.69	13.18	12.91	13.08	
FeO <sup>2</sup>	13.80	12.14	13.90	12.44	14.20	14.33	15.16	15.52	
MnO	0.224	0.202	0.237	0.256	0.247	0.242	0.252	0.253	
MgO	5.18	5.56	5.36	5.45	4.94	5.45	5.08	5.10	
CaO	10.31	9.87	10.02	10.44	9.46	9.90	9.48	9.58	
Na <sub>2</sub> O	2.41	2.54	2.70	2.51	2.82	2.60	2.68	2.63	
K <sub>2</sub> O	0.37	0.60	0.52	0.38	0.54	0.50	0.52	0.45	
P <sub>2</sub> O <sub>5</sub>	0.270	0.207	0.268	0.260	0.290	0.272	0.324	0.323	
Total	97.29	99.23	99.30	99.23	99.48	99.68	99.82	99.80	
Nb	18	15	19	19	19	19	22	22	
Rb	6	14	12	10	12	11	11	10	
Sr	203	186	214	212	203	186	191	197	
Y	34	37	35	37	39	41	45	46	
Zr	153	158	157	157	177	170	192	193	
Ce	32	34	37	40	36	36	40	40	
Cu	129	134	140	130	94	116	118	117	
Ni	33	38	31	30	26	32	28	29	
Sc	43	38	43	43	41	43	43	44	
V	378	332	391	367	345	417	463	471	
Zn	114	105	116	118	125	127	141	141	
Grade reflects the confidence of the fit of a sample with its group. * Low confidence, but best fit, ** moderate confidence, *** high confidence. Samples processed at the WSU Geoanalysis laboratory, WA, USA. <sup>1</sup> Indicates samples processed in a second laboratory at McGill University, Montreal Canada. <sup>2</sup> Fe is presented as FeO except for samples from McGill where they were calculated to be Fe <sub>2</sub> O <sub>3</sub> , resulting in higher values.									

Table B.1 continued									
Grade	***	***	***	***	***	*		**	***
Unit	3 (continued)							4	5
Sample	AG190	AG11	AG10 <sup>1</sup>	AG107 <sup>1</sup>	AG97 <sup>1</sup>	AG309		AG258	AG163
Facies	P11	B1	P11	P11	P11	B3		P12	P12
SiO <sub>2</sub>	50.61	50.46	49.88	50.33	50.35	50.37		49.60	50.28
TiO <sub>2</sub>	2.873	2.873	2.8569	2.84	2.80	2.720		2.152	1.939
Al <sub>2</sub> O <sub>3</sub>	12.80	12.88	12.87	12.99	13.09	13.38		13.60	14.35
FeO <sup>2</sup>	15.12	14.83	16.8652	16.52	16.36	14.53		13.94	12.10
MnO	0.250	0.247	0.2576	0.25	0.25	0.256		0.241	0.211
MgO	4.97	4.83	4.98	5.04	5.07	4.73		5.92	6.36
CaO	9.34	9.32	9.48	9.51	9.49	9.15		10.79	11.81
Na <sub>2</sub> O	2.66	2.67	2.6529	2.67	2.70	2.78		2.47	2.33
K <sub>2</sub> O	0.54	0.53	0.53	0.55	0.56	0.39		0.35	0.31
P <sub>2</sub> O <sub>5</sub>	0.325	0.324	0.327	0.33	0.33	0.323		0.230	0.212
Total	99.49	98.97	100.81	101.13	101.10	98.63		99.30	99.90
Nb	22	22	23	23	23	22		16	14
Rb	12	12	11	12	12	9		7	6
Sr	189	189	187	186	186	207		195	202
Y	46	47	41	42	42	41		34	31
Zr	196	199	188	191	191	191		139	125
Ce	39	45	49	42	41	47		31	32
Cu	117	105	190	163	164	130		137	163
Ni	27	29	30	28	32	26		32	46
Sc	43	43	42	38	39	42		45	47
V	455	458	461	459	454	423		387	338
Zn	141	137	108	107	108	132		115	99
Grade reflects the confidence of the fit of a sample with its group. * Low confidence, but best fit, ** moderate confidence, *** high confidence. Samples processed at the WSU geoanalysis laboratory, WA, USA. <sup>1</sup> Indicates samples processed in a second laboratory at McGill University, Montreal Canada. <sup>2</sup> Fe is presented as FeO except for samples from McGill where they were calculated to be Fe <sub>2</sub> O <sub>3</sub> , resulting in higher values.									

Table B.1 continued									
Grade	***	***	***	***	***	***	***	**	**
Unit	5 (continued)								
Sample	AG302	AG304	AG19	AG294	AG297	AG169	AG99 <sup>1</sup>	AG38	AG261
Facies	B3	D2	Lt1	B3	L2	Lt1	Pl1	LX1	Plx1
Wt%									
SiO <sub>2</sub>	49.89	49.95	50.10	49.81	49.16	50.16	50.69	50.76	49.75
TiO <sub>2</sub>	1.953	1.940	1.903	1.847	1.842	1.911	1.78	1.649	1.829
Al <sub>2</sub> O <sub>3</sub>	14.12	16.44	14.04	14.23	14.05	14.06	14.40	15.46	14.14
FeO <sup>2</sup>	12.58	10.90	12.44	11.78	12.59	12.59	12.49	10.90	12.06
MnO	0.215	0.185	0.220	0.255	0.250	0.214	0.21	0.195	0.211
MgO	6.48	4.55	6.57	5.79	5.90	6.58	6.69	6.14	7.08
CaO	11.45	11.93	11.65	11.88	11.69	11.38	11.96	11.82	11.87
Na <sub>2</sub> O	2.39	2.42	2.36	2.42	2.41	2.23	2.37	2.32	2.23
K <sub>2</sub> O	0.32	0.28	0.33	0.31	0.31	0.30	0.37	0.36	0.27
P <sub>2</sub> O <sub>5</sub>	0.205	0.191	0.212	0.193	0.194	0.207	0.22	0.192	0.179
Total	99.61	98.78	99.83	98.52	98.40	99.63	101.27	99.80	99.60
ppm									
Nb	13	13	15	12	12	14	15	14	13
Rb	7	6	6	6	7	7	7	8	5
Sr	207	221	199	206	204	197	192	204	200
Y	28	31	30	28	27	30	29	31	27
Zr	113	115	123	106	107	124	126	133	109
Ce	24	23	26	24	27	30	21	25	26
Cu	160	144	186	138	124	179	212	143	154
Ni	49	27	51	48	52	49	59	49	56
Sc	48	43	48	47	45	46	39	42	47
V	353	358	336	356	355	324	289	290	332
Zn	99	94	100	101	107	101	78	92	93
Grade reflects the confidence of the fit of a sample with its group. * Low confidence, but best fit, ** moderate confidence, *** high confidence. Samples processed at the WSU Geoanalysis laboratory, WA, USA. <sup>1</sup> Indicates samples processed in a second laboratory at McGill University, Montreal Canada. <sup>2</sup> Fe is presented as FeO except for samples from McGill where they were calculated to be Fe <sub>2</sub> O <sub>3</sub> , resulting in higher values.									

Table B.1 continued						
Grade	*	***	***	***	***	**
Unit	5 (continued)	6				7
Sample	AG255	AG299	AG298	AG21	AG66	AG290
Facies	Dx1	Lx2	Plx2	Plx2	LX1	B2
Wt %						
SiO <sub>2</sub>	49.70	48.18	49.83	49.16	48.67	51.72
TiO <sub>2</sub>	1.892	1.072	1.452	1.313	1.515	2.453
Al <sub>2</sub> O <sub>3</sub>	16.88	20.61	18.14	19.72	17.83	14.13
FeO <sup>2</sup>	10.47	8.42	9.21	8.13	9.90	13.26
MnO	0.183	0.172	0.171	0.145	0.172	0.234
MgO	4.38	3.74	4.64	5.00	5.72	3.70
CaO	12.11	14.14	13.33	13.54	13.05	8.67
Na <sub>2</sub> O	2.39	1.90	2.07	2.03	2.00	2.99
K <sub>2</sub> O	0.27	0.14	0.23	0.21	0.17	0.70
P <sub>2</sub> O <sub>5</sub>	0.185	0.105	0.152	0.134	0.136	0.339
Total	98.46	98.47	99.23	99.38	99.17	98.19
ppm						
Nb	13	8	10	9	10	23
Rb	5	3	5	4	3	14
Sr	224	213	227	227	216	215
Y	31	19	23	20	23	47
Zr	109	63	87	77	88	202
Ce	28	17	20	18	20	49
Cu	129	87	135	119	133	107
Ni	25	37	40	38	48	20
Sc	42	32	39	36	40	41
V	350	217	263	247	278	335
Zn	93	59	77	63	79	167
Grade reflects the confidence of the fit of a sample with its group. * Low confidence, but best fit, ** moderate confidence, *** high confidence.						
Samples processed at the WSU geoanalysis laboratory, WA, USA.						
<sup>1</sup> Indicates samples processed in a second laboratory at McGill University, Montreal Canada.						
<sup>2</sup> Fe is presented as FeO except for samples from McGill where they were calculated to be Fe <sub>2</sub> O <sub>3</sub> , resulting in higher values.						

Table B.1 continued				
Grade	***	***	***	***
Unit	Gabbro		Holocene lava	
Sample	AG1	AG289	AG241	AG250
Facies	G1	G1	Spatter	A'a
Wt%				
SiO <sub>2</sub>	48.37	48.10	48.86	49.24
TiO <sub>2</sub>	1.347	0.276	1.647	1.629
Al <sub>2</sub> O <sub>3</sub>	23.03	25.09	14.41	14.48
FeO <sup>2</sup>	7.77	2.91	11.66	11.74
MnO	0.129	0.056	0.205	0.201
MgO	2.94	3.86	7.18	7.36
CaO	13.32	16.75	11.92	12.13
Na <sub>2</sub> O	2.60	1.36	2.09	2.08
K <sub>2</sub> O	0.12	0.03	0.25	0.24
P <sub>2</sub> O <sub>5</sub>	0.049	0.013	0.159	0.155
Total	99.66	98.46	98.37	99.25
ppm				
Nb	3.7	0.9	10.0	9.3
Rb	2	1	4	5
Sr	284	250	185	184
Y	11	6	26	25
Zr	29	9	93	89
Ce	10	0	20	19
Cu				
Ni	35	19	164	160
Sc	13	29	68	71
V	26	29	45	45
Zn	233	95	328	327
<p>Grade reflects the confidence of the fit of a sample with its group.  * Low confidence, but best fit, ** moderate confidence, *** high confidence.  Samples processed at the WSU Geoanalysis laboratory, WA, USA.  <sup>1</sup>Indicates samples processed in a second laboratory at McGill University, Montreal Canada.  <sup>2</sup>Fe is presented as FeO except for samples from McGill where they were calculated to be Fe<sub>2</sub>O<sub>3</sub>, resulting in higher values.</p>				



**Table 5 Microprobe results for selected samples of glassy pillow dike rind. Collected at the University  
of Wisconsin Madison, WI, USA.**

<b>Unit</b>	<b>2</b>						
<b>Sample</b>	<b>AG108</b>	<b>AG4</b>	<b>AG40</b>	<b>AG41</b>	<b>AG51</b>	<b>AG61</b>	<b>AG7</b>
<b>Facies</b>	Pl1	D1	CMVD	PL1	D1	CMVD	D2
<b>Wt%</b>							
<b>SiO2</b>	49.3357	48.7560	49.7143	50.2265	49.4980	49.9915	50.1423
<b>TiO2</b>	2.5003	2.4963	2.5243	2.4665	2.4140	2.5040	2.4767
<b>Al2O3</b>	12.8747	13.1277	12.9117	13.1245	13.0095	13.2035	13.0803
<b>FeO</b>	13.9177	14.2770	14.3347	13.5625	13.3110	13.5645	13.9373
<b>MnO</b>	0.2263	0.2513	0.2583	0.2250	0.2425	0.2595	0.2230
<b>MgO</b>	5.2227	5.5843	4.9627	4.9545	5.3670	4.9295	5.4187
<b>CaO</b>	9.4510	9.9397	9.2283	9.2550	9.8455	9.5000	9.8843
<b>Na2O</b>	2.6577	2.5453	2.6047	2.5835	2.5085	2.5655	2.2990
<b>K2O</b>	0.4833	0.3960	0.5347	0.5380	0.4990	0.5045	0.4697
<b>P2O5</b>	0.2957	0.2720	0.3467	0.3005	0.3060	0.3240	0.2773
<b>SO3</b>	0.2303	0.2440	0.1467	0.2310	0.2960	0.2370	0.2507
<b>Cl</b>	0.0197	0.0203	0.0217	0.0200	0.0200	0.0195	0.0163
<b>F</b>	0.0563	0.0737	0.0223	0.0405	0.0515	0.0585	0.0223
<b>Total</b>	97.2717	97.9830	97.6110	97.5275	97.3690	97.6625	98.4983

Table B.2 continued.			
<b>Unit</b>	<b>2</b>		<b>5</b>
<b>Sample</b>	<b>AG88</b>	<b>AG94</b>	<b>AG74</b>
<b>Facies</b>	D2	Pl1	Pl2
<b>Wt%</b>			
<b>SiO2</b>	49.6780	49.4777	48.9993
<b>TiO2</b>	2.4287	2.5327	1.8367
<b>Al2O3</b>	13.1413	13.0490	14.1350
<b>FeO</b>	13.5350	13.9877	11.9563
<b>MnO</b>	0.2637	0.2400	0.2367
<b>MgO</b>	5.2770	4.9527	6.4693
<b>CaO</b>	9.4287	9.3823	11.2870
<b>Na2O</b>	2.4303	2.3057	2.3247
<b>K2O</b>	0.4963	0.5560	0.2997
<b>P2O5</b>	0.3083	0.3003	0.2360
<b>SO3</b>	0.2317	0.2373	0.2037
<b>Cl</b>	0.0213	0.0163	0.0210
<b>F</b>	0.0460	0.0507	0.0497
<b>Total</b>	97.2863	97.0873	98.0560

**Table B.3 Bulk rock geochemistry of greater Askja historic and Holocene lavas.**

Unit	<b>Bátshraun (1921)</b>							
<b>Sample</b>	<b>BAT1</b>	<b>BAT2</b>	<b>BAT3</b>	<b>BAT4</b>	<b>BAT5</b>	<b>BAT6</b>	<b>BAT7</b>	<b>BAT8</b>
<b>Wt %</b>								
<b>SiO<sub>2</sub></b>	51	50.2	51.1	50.8	50.8	50.3	49.8	50.3
<b>TiO<sub>2</sub></b>	2.72	2.73	2.72	2.74	2.73	2.72	2.68	2.7
<b>Al<sub>2</sub>O<sub>3</sub></b>	13.14	13.1	13.28	13.44	13.58	13.48	13.4	13.52
<b>Fe Total</b>	16.64	16.77	16.66	16.67	16.57	16.63	16.7	16.5
<b>MnO</b>	0.28	0.28	0.28	0.28	0.28	0.28	0.28	0.28
<b>MgO</b>	4.89	5.19	4.89	5.08	4.96	5.17	5.2	4.98
<b>CaO</b>	8.68	8.94	8.67	8.83	8.74	8.93	9.01	8.75
<b>Na<sub>2</sub>O</b>	2.86	2.76	2.87	2.77	2.86	2.78	2.74	2.81
<b>K<sub>2</sub>O</b>	0.64	0.57	0.64	0.59	0.62	0.57	0.54	0.6
<b>P<sub>2</sub>O<sub>5</sub></b>	0.32	0.31	0.32	0.32	0.32	0.32	0.32	0.31
<b>SUM</b>	100.7	100.3	100.8	101	100.9	100.6	100.2	100.2
<b>ppm</b>								
<b>Rb</b>	14.3	12.1	14.7	13.3	14.3	12.4	12.7	13.3
<b>Sr</b>	185	184	184	185	186	186	186	185
<b>Y</b>	49.5	49.1	49.4	49.3	49.8	49	46.9	48.8
<b>Zr</b>	212	201	211	205	214	202	196	206
<b>Nb</b>	20.4	19.4	20.1	20.2	20.6	19.3	19.8	20.4
<b>Ga</b>	21	22	22	21	21	21	22	21
<b>Pb</b>	3	2	2	1	1	1	2	1
<b>Th</b>	3.5	2.5	3.2	3.6	4.6	3.8	4.2	3
<b>Zn</b>	148	46	142	147	142	139	142	138
<b>Ni</b>	21	27	20	25	22	26	29	22
<b>Cu</b>	90	114	91	105	98	115	117	99
<b>Cr</b>	29	35	52	29	30	33	35	24
<b>V</b>	484	504	480	501	476	500	505	485
<b>Ba</b>	136	141	157	144	147	148	133	133
<b>La</b>	15	21	21	15	21	15	20	16
<b>Ce</b>	57	52	50	52	49	42	46	57
<b>Mn</b>	2446	2500	2482	2486	2473	2485	2490	2461
<b>Ti</b>	27612	28268	28321	28276	27777	27804	28183	27764

Table B.3 continued								
Unit	Mývatnsveitahraun (1922)							
Sample	MYV1	MYV2	MYV3	MYV4	MYV5	MYV6	MYV7	MYV8
Wt%								
SiO <sub>2</sub>	50	50	56.5	57.1	56.1	57.8	57.9	57.1
TiO <sub>2</sub>	2.8	2.77	2.26	2.29	2.25	2.2	2.21	2.23
Al <sub>2</sub> O <sub>3</sub>	13.79	13.88	14.3	14.42	14.35	14.69	14.31	14.43
Fe Total	15.33	15.18	11.48	11.27	11.17	15.13	10.89	11.04
MnO	0.28	0.28	0.24	0.24	0.24	0.24	0.24	0.24
MgO	5.03	5.08	3.2	2.94	3.12	2.88	2.84	2.89
CaO	8.81	8.8	6.77	6.57	6.69	6.45	6.37	6.46
Na <sub>2</sub> O	2.83	2.72	3.43	3.48	3.39	3.56	3.54	3.56
K <sub>2</sub> O	0.61	0.59	1.11	0.15	1.11	1.21	1.21	1.2
P <sub>2</sub> O <sub>5</sub>	0.32	0.31	0.37	0.4	0.38	0.38	0.39	0.4
SUM	101	100.8	100.8	100.8	99.7	101	100.8	100.5
<i>ppm</i>								
Rb	12.8	12	26.4	27	26	29.3	29.4	28.4
Sr	184	180	180	183	179	179	180	181
Y	49.1	48.4	31.4	64.2	62.1	63.5	64.8	64.5
Zr	204	201	298	311	305	316	321	319
Nb	20.1	19.5	27.6	29.3	28.1	29.2	30	29.4
Ga	22	23	22	21	21	22	21	21
Pb	2	1	1	3	3	3	2	3
Th	3.8	1.8	4.6	6.2	5.7	7.7	5.5	6.2
Zn	144	143	140	145	140	141	143	142
Ni	22	23	6	5	7	4	4	3
Cu	93	95	40	27	30	29	24	25
Cr	22	23	5	5	2	0	0	3
V	527	513	213	154	166	160	135	136
Ba	144	144	219	224	218	239	223	223
La	18	21	29	33	30	33	28	31
Ce	47	42	65	64	61	58	69	66
Mn	2510	2452	2256	2310	2282	2221	2249	2267
Ti	29163	28460	23704	23758	23738	22851	22991	23364

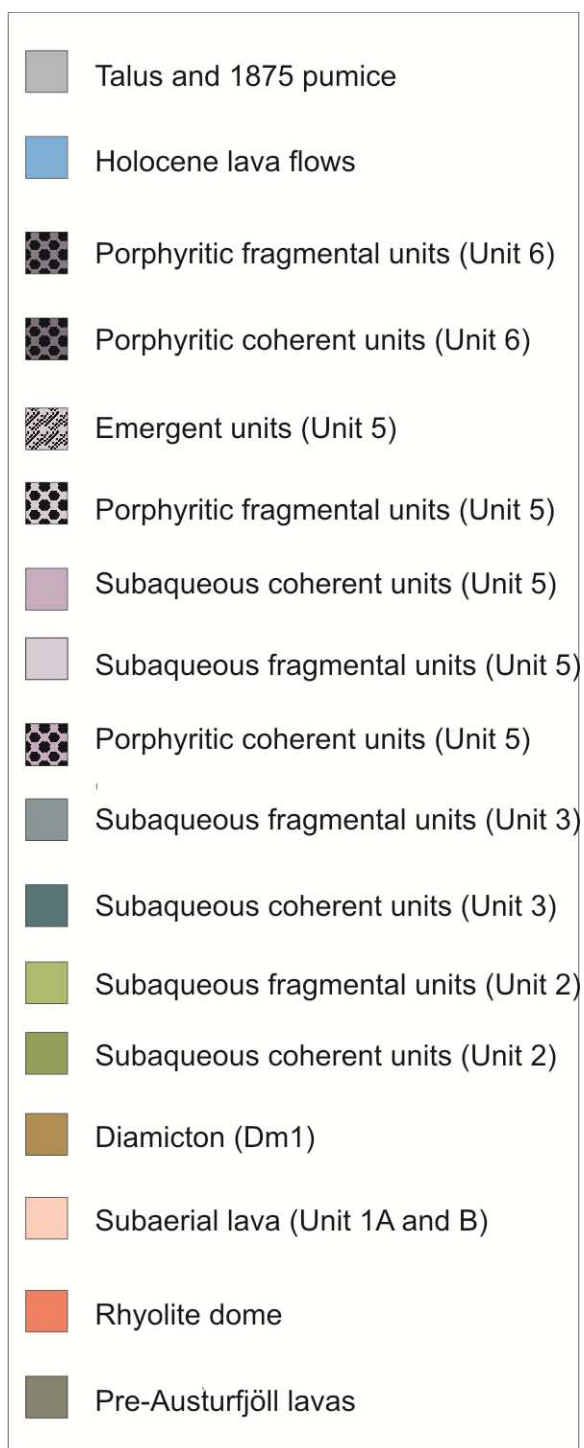
Table B.3 continued									
Unit	Kvíslahraun (1922/23)						Suðurbotnahraun (1922/23)		
Sample	KVI1	KVI2	KVI3	KVI3A	KVI4	KVI7	SBOT1	SBOT2	SBOT3
SiO <sub>2</sub>	49.9	49.4	49.5	50	49.7	49.9	50.1	49.4	49.7
TiO <sub>2</sub>	2.64	2.65	2.64	2.64	2.69	2.67	2.76	2.79	2.79
Al <sub>2</sub> O <sub>3</sub>	13.71	13.76	14.1	14.2	14.12	14.05	13.88	13.93	14.06
Fe Total	14.76	14.75	14.86	14.84	14.96	14.82	15.21	15.22	15.3
MnO	0.27	0.27	0.27	0.27	0.28	0.28	0.28	0.28	0.28
MgO	5.3	5.24	5.22	5.32	5.34	5.31	4.98	4.99	5.01
CaO	8.69	8.81	9.06	9.06	9.4	9.11	8.61	8.67	8.73
Na <sub>2</sub> O	2.14	2.62	2.58	2.59	2.65	2.75	2.79	2.83	2.84
K <sub>2</sub> O	0.52	0.53	0.52	0.52	0.54	0.54	0.6	0.6	0.31
P <sub>2</sub> O <sub>5</sub>	0.3	0.31	0.31	0.3	0.31	0.31	0.31	0.32	0.32
SUM	99.3	99.5	100.2	100.8	100.8	100.8	100.7	100.2	100.8
<i>ppm</i>									
Rb	12	12	12	12	11.3	12.5	13.5	13.2	14.3
Sr	176	182	183	183	185	185	179	180	183
Y	47.1	46.2	45.9	45.9	47.8	46	47.9	47.9	47
Zr	194	195	191	191	194	195	203	200	202
Nb	19	19.8	18.5	18.5	18.7	18.5	19.6	19.2	20.1
Ga	22	22	21	21	20	22	22	21	22
Pb	0	2	1	1	1	1	0	2	2
Th	2	3.6	2	2.1	2.6	4.5	2.3	4.8	5
Zn	140	141	140	141	142	138	144	142	139
Ni	27	30	31	29	28	28	23	20	20
Cu	109	112	121	120	120	118	91	91	86
Cr	36	45	44	40	41	36	17	13	15
V	499	513	495	501	504	503	519	514	513
Ba	132	132	129	130	138	143	152	147	141
La	14	16	16	15	16	21	19	18	16
Ce	48	50	38	50	37	47	48	51	45
Mn	2444	2463	2445	2484	2495	2500	2484	2460	2494
Ti	27718	27840	27335	27900	27869	28157	28884	28401	28517

Table B.3 continued								
Unit	Southeastern Flank (1924 and 1929)							
Sample	SUD1	SUD2	SUD3	SUD4	SUD6	SUD7	SUD8	SUD9
SiO <sub>2</sub>	49.0	49.0	48.2	49	49.3	49.1	49.1	49.4
TiO <sub>2</sub>	2.76	2.83	1.48	2.72	2.67	2.72	2.74	2.71
Al <sub>2</sub> O <sub>3</sub>	13.89	13.68	18.23	14.17	14.04	14.3	14.1	14.12
Fe Total	17.85	18.02	11.3	16.76	16.46	16.76	16.8	16.66
MnO	0.29	0.29	0.19	0.28	0.27	0.28	0.28	0.28
MgO	5.24	5.24	6.74	5.32	5.29	5.36	5.36	5.33
CaO	9.07	8.98	12.79	9.14	8.99	9.18	9.2	9.12
Na <sub>2</sub> O	2.64	2.72	2.1	2.74	2.73	2.83	2.78	2.76
K <sub>2</sub> O	0.44	0.44	0.24	0.54	0.54	0.54	0.54	0.53
P <sub>2</sub> O <sub>5</sub>	0.29	0.29	0.15	0.31	0.31	0.31	0.31	0.31
SUM	100.9	101	100.8	100.4	100.8	100.7	100.7	100.6
<i>ppm</i>								
Rb	9.9	9.2	5.3	11.7	12.3	11.5	12.6	11.7
Sr	175	178	203	187	184	186	187	185
Y	45.6	46.9	24	46.9	45.9	46.3	46.9	46.3
Zr	174	180	89	193	190	194	193	192
Nb	16.5	17.1	8.4	19	18.6	19.5	18.8	19.3
Ga	22	23	20	20	22	22	21	22
Pb	0	0	2	1	2	1	2	2
Th	2.3	3.9	2.3	3	4.9	3.1	5.5	4
Zn	145	143	79	140	141	141	139	141
Ni	23	24	52	27	28	29	28	26
Cu	132	113	129	118	119	118	124	117
Cr	26	24	128	42	46	49	47	34
V	554	542	313	495	500	503	496	514
Ba	127	123	54	142	142	133	134	147
La	11	15	8	18	16	16	18	18
Ce	34	34	25	35	47	37	49	39
Mn	2627	2694	1758	2437	2475	2445	2465	2509
Ti	28607	28573	14857	27569	27979	27505	27414	28290

Table B.3 continued								
Unit	Southeastern Flank (continued)					1961		
Sample	SUD10	SUD11	SUD12	SUD13		VIK1	VIK2	VIK3
SiO <sub>2</sub>	57	57	48.4	49.2		49.9	48.9	49.9
TiO <sub>2</sub>	1.62	1.66	1.43	1.53		2.75	2.75	2.75
Al <sub>2</sub> O <sub>3</sub>	15.16	15.19	18.86	15.42		13.75	13.92	13.83
Fe Total	10.86	10.88	10.92	12.69		16.5	16.83	16.76
MnO	0.19	0.19	0.19	0.22		0.28	0.28	0.28
MgO	4.37	4.28	6.44	8.12		5	5.18	5.16
CaO	7.69	7.64	12.75	12.12		8.63	8.9	8.88
Na <sub>2</sub> O	3.03	3.17	2.1	2.15		2.73	2.76	2.76
K <sub>2</sub> O	1.06	1.12	0.23	0.25		0.6	0.55	0.55
P <sub>2</sub> O <sub>5</sub>	0.22	0.23	0.14	0.14		0.31	0.31	0.32
SUM	100.7	100.9	100.8	101		99.9	100.8	100.6
<i>ppm</i>								
Rb	25.6	25.3	5.9	5.6		13.4	12.1	13.1
Sr	164	163	204	175		180	182	186
Y	48	49.8	23.2	26.2		48.6	46.9	47.5
Zr	250	258	88	93		203	196	199
Nb	20.5	20.9	8.5	7.8		19.6	18.8	20.2
Ga	19	20	19	19		22	21	22
Pb	1	1	1	1		3	1	2
Th	4.2	7.2	1.2	1.7		3.5	2.4	3.6
Zn	100	102	78	91		143	141	141
Ni	27	25	57	64		22	26	26
Cu	74	72	128	153		100	113	114
Cr	43	43	123	192		14	28	28
V	288	274	313	354		479	504	516
Ba	196	194	60	62		149	143	150
La	28	24	10	10		20	18	18
Ce	58	56	22	27		48	38	43
Mn	1750	1712	1747	2023		2483	2498	2504
Ti	16803	16274	14845	15797		29071	28716	28884

## **APPENDIX C**

### **CHEMOSTRATIGRAPHY**



**Figure C.1 Key for cross-sections. For locations see Chapter 4 Figure 4.5**



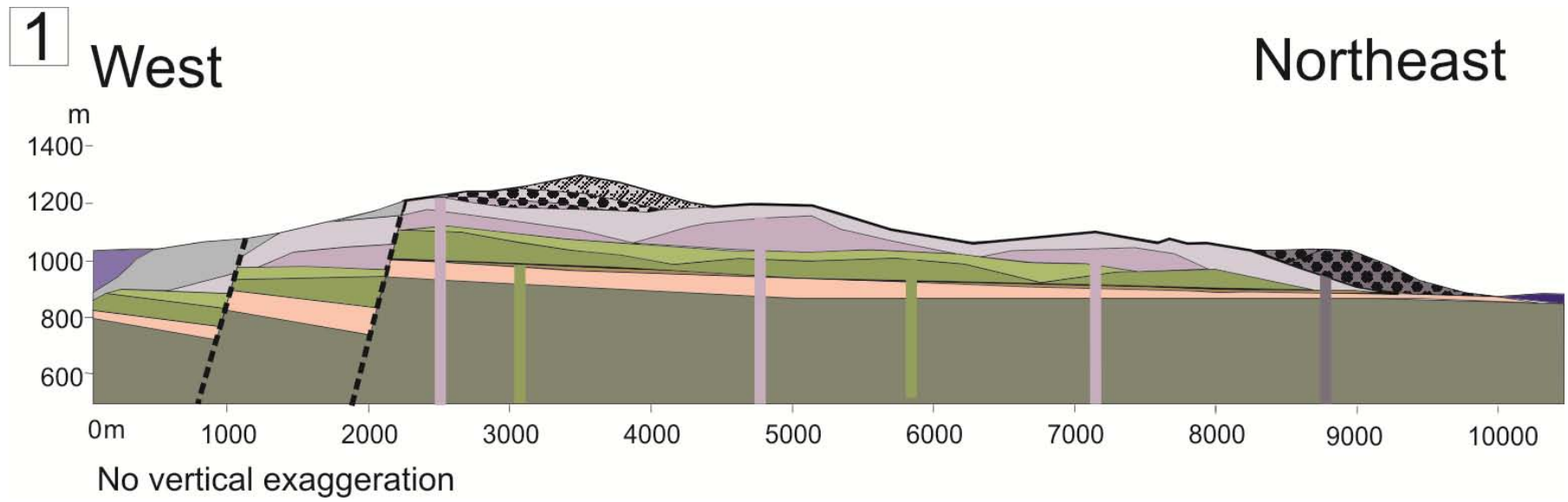


**Figure C.2 Cross-section 1**

2 West

East

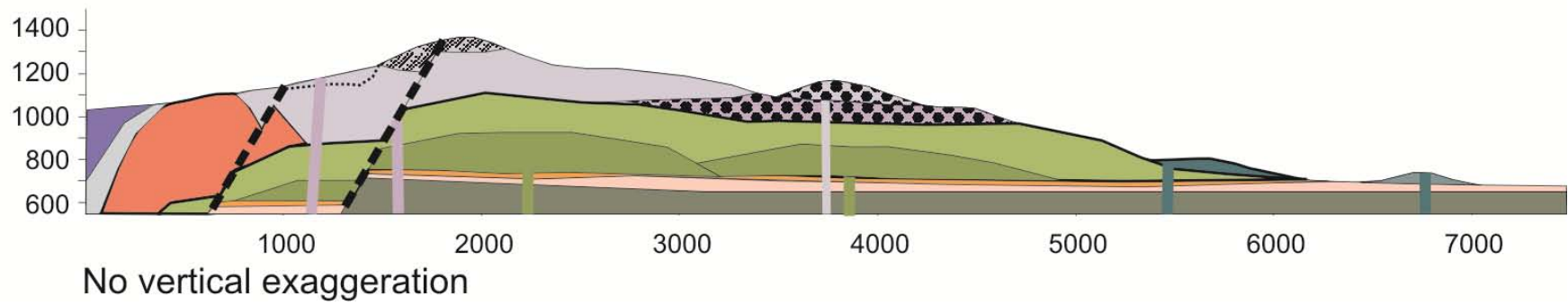


Figure C.3 Cross-section 2

3 West

Southeast

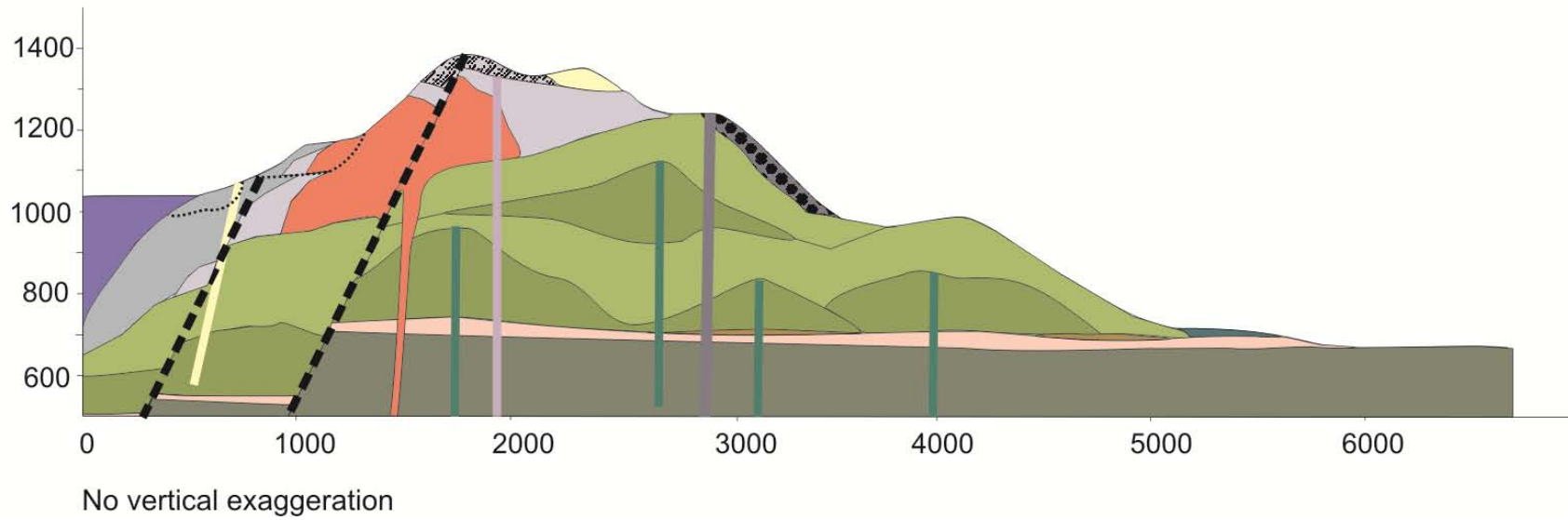
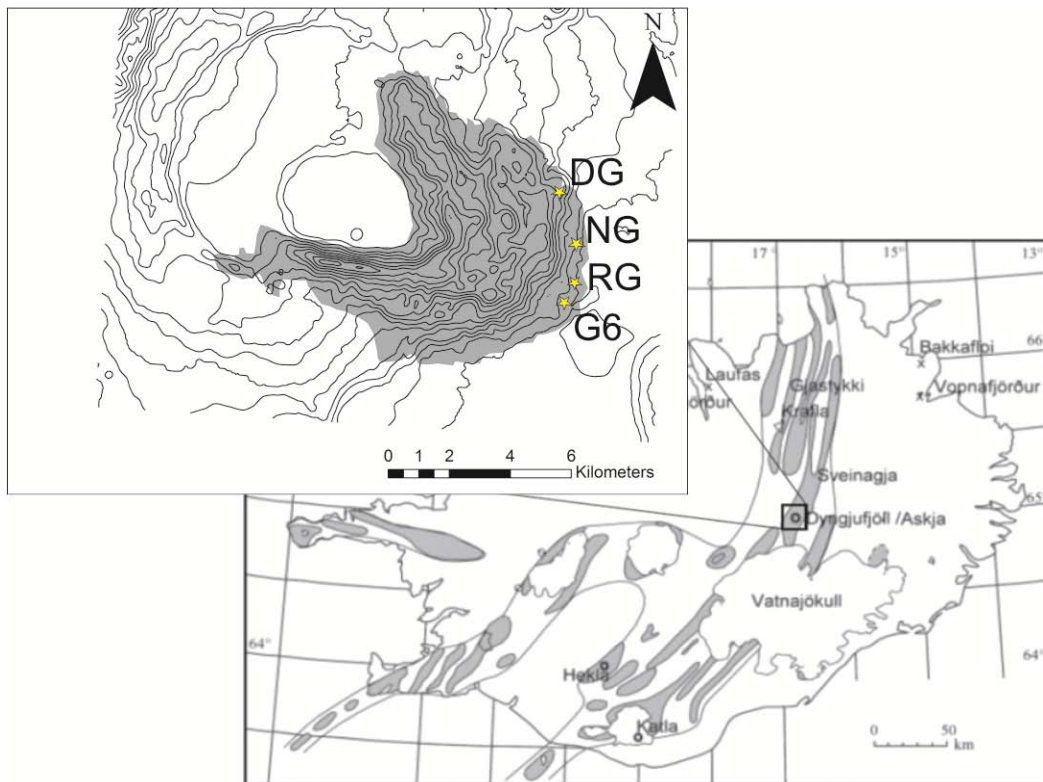


Figure C.4 Cross-section 3

## APPENDIX D

### TEXTURAL DESCRIPTIONS

One additional sequence was studied in the comparison of pillow lavas, breccias and lapilli tuffs in Gully 6 (Figure D.1) presented in Chapter 6. This sequence bears some gross similarities to the ones in DK, NG and RG, but has a distinctive absence of fluidal bombs.



**Figure D.1 Location of deposits in Chapter 6 and including Gully 6 (G6).**

Gully 6 has exposures of extensive pillow lavas and a variety of breccias. The sequence of interest begins with a pillow lava unit that is at least 8 m thick that locally overlies a pillow breccia with a convolute contact. Laterally the pillow lavas grade into pillow breccias and are locally overtopped by pillow lavas (Figure D.2). The pillow forms are irregular and contain local lobate morphologies. The pillow lavas are overlain by seven meters of clast-supported pillow breccia that contains angular bombs in the upper two meters of the exposure. This dominance of pillow fragments throughout the breccia is distinctive in comparison with the sequences discussed in Chapter 6. The breccia grades into three meters of angular bomb-bearing vitric lapilli tuff. Unlike the previous three sample locations the lapilli tuff exposure is limited (2 m), and preferentially eroded relative to the breccia units. Gully 6 shows a marginal increase in block size in the breccia and no significant change in block size within the lapilli tuff. Overall, the Gully 6 deposit has much less pronounced decrease in grain size up-section, with a high abundance of blocks >20 %, throughout. The vesicularity of blocks in Gully 6 varies and shows no distinguishable trend up section. The sequence is mantled by a thin (50 cm) well-bedded ash tuff.

Gully 6 shares large scale similarity in lithofacies architecture to the three other sequences, but had limited lapilli tuff deposits and does not share hand sample and fine scale similarities. Additionally, fluidal bombs were absent from the breccia and lapilli tuff of Gully 6. The breccia of Gully 6 is interpreted as a collapse breccia as it is dominated by pillows, pillow fragments and angular blocks and no ductile deformed bombs were observed.

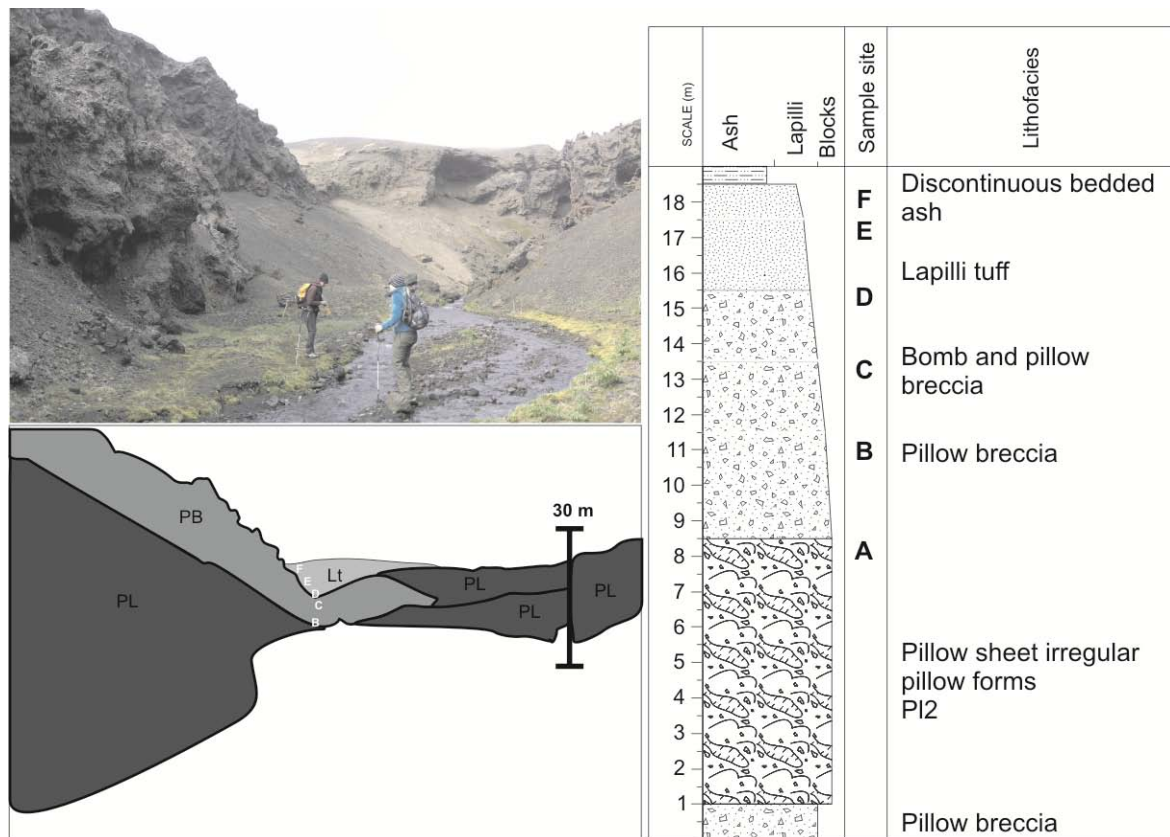


**Figure D.2 Image of sample locations and stratigraphic column for Gully 6.**

The Gully 6 sequence is interpreted as a collapse breccia overlain by local lapilli dominated units that likely were sourced from an eruption nearby. Large sequences of fragmental basaltic glass can be produced by debris flows and surges, slumps and edifice collapse (Carlisle, 1963; Corcoran, 2000; Jones, 1970; Sohn et al., 2008), all the direct result of remobilization, and potentially concentration or thickening away from source. The higher occurrence of angular blocks and more erratic trends in vesicularity and grain size suggest mechanical disruption of the deposit, but the high angularity and glassy content suggest that transport only occurred over short distances, such as within a slump or the collapse margins of a flow. The regional stratigraphy of Gully 6 is dominated by repeating sequences of PI2 lavas and breccias with limited lapilli tuff, supporting this interpretation.

## APPENDIX E

### COMPLETE FTIR RESULTS

**Table E.1 Complete FTIR results from the University of Wisconsin, Madison.**

Sample #	Morphology	Unit	Sample elevation (m asl)	wt% H <sub>2</sub> O	wt % CO <sub>2</sub>	Pressure (MPa)	Water depth (m)	Ice thickness (m)	Ice elevation (m asl)	Ice elevation (m asl)
AG 74	Pillow Mound	5	930	0.517	25	81	830	904	1228	1834
					0	27	273	298		
				0.613	25	88	899	890		
					0	34	343	374		
AG 99	Pillow Mound	5	1000	0.446	25	75	765	834	1228	1834
					0	20	208	228		
				0.437	25	75	757	824		
					0	20	204	222		
AG 48	Pseudopillow	2	1160	0.367	25	69	699	762	1281	1922
					0	14	143	156		
				0.320	25	65	667	727		
					0	11	111	121		
AG 94	Pillow sheet	2	710	0.572	25	86	881	960	967	1694
					0	32	324	354		
				0.478	25	78	792	863		
					0	23	236	257		
				0.588	25	89	902	984		
					0	34	346	377		
				0.522	25	81	830	905		
					0	27	273	298		
AG 108	Pillow sheet	2	730	0.455	25	75	765	833	952	1635
					0	20	204	222		
				0.498	25	80	810	884		
					0	25	254	277		
				0.512	25	81	830	905		
					0	27	273	298		
AG 88	Pillow in dike	2	750	0.475	25	78	792	863	997	1676
					0	23	236	257		

				0.469	25	77	783	853		
					0	22	226	247		
				0.516	25	81	830	905		
					0	27	273	298		
				0.535	25	83	850	926		
					0	29	293	320		
AG 41	Pillow in dike	2	750	0.560	25	85	871	949	1059	1699
					0	31	314	342		
				0.530	25	82	840	916		
					0	28	283	309		
AG 40	Chill margin	2	780	0.208	25	59	606	661	834	1441
					0	5	50	54		
AG 61	Chill margin	2	780	0.257	25	62	632	689	855	1561
					0	7	82	75		
				0.387	25	70	716	781		
					0	16	174	160		



## BIBLIOGRAPHY

- Abbott, P.M., Davies, S.M., Steffensen, J.P., Pearce, N.J.G., Bigler, M., Johnsen, S., Seierstad, I.K., Svensson, A., and Wastergard, S., 2012. A detailed framework of Marine Isotop Stages 4 and 5 volcanic events recorded in two Greenland ice-cores. *Quaternary Science Reviews*, 36, 59-77.
- Adams, J.B., Smith, M.O., and Gillespie, A.R., 1989. Simple models for complex natural surfaces: A strategy for the hyperspectral era of remote sensing IGARSS Canadian Symposium of Remote Sensing Volume 12, IGARSS Canadian Symposium of Remote Sensing pp. 16-21.
- Agnon, A., and Lyakhovsky, V., 1995. Damage distribution and localization during dyke intrusion. Baer, G., and Heimann, A., eds., *Physics and Chemistry of Dykes*: Balkema, Geological Survey of Israel (IGCP), pp. 65-78.
- Allen, C.C., 1980. Icelandic subglacial volcanism: thermal and physical studies *The Journal of Geology*, 88, 108-117.
- Allen, C.C., Jercinovic, M.J., and Allen, J.S.B., 1982. Subglacial volcanism in North-Central British Columbia and Iceland *The Journal of Geology* 90, 699-715.
- Allen, R.M., Nolet, G., Morgan, W.J., Vogfjord, K., Nettles, M., Ekstrom, G., Bergsson, B.H., Erlendsson, P., Foulger, G.R., Jakobsdóttir, S.S., Julian, B.R., Pritchard, M., Ragnarsson, S., and Stefansson, R., 2002. Plume-driven plumbing and crustal formation in Iceland *Journal of Geophysical Research*, 107, B8, 2163.
- Anders, E., and Grevesse, N., 1989. Abundances of the elements: Meteoritic and solar. *Geochemica et Cosmochimica Acta*, 53, 197-214.
- Andrew, R.E.B., and Gudmundsson, A., 2007. Distribution, structure, and formation of Holocene lava shields in Iceland. *Journal of Volcanology and Geothermal Research*, 168, 137-154.
- Andrews, J.T., 2005. Late Quaternary marine sediment studies of the Iceland shelf-palaeoceanography, land/ice sheet/ ocean interactions, and deglaciation: a review. Caseldin, C., Russel, A., and Hardardottir, J., eds., *Iceland- Modern Processes and Past Environments*, Volume 5: Amsterdam, Elsevier, pp. 5-24.

- Annertz, K., Nilsson, M., and Sigvaldason, G.E., 1985. The postglacial history of Dyngjufjöll NORVULK, Volume 8503: Reykjavik Nordic Volcanological Institute, pp. 22.
- Árnadóttir, T., Lund, B., Jiang, W., Geirsson, H., Björnsson, H., Einarsson, P., and Sigurdsson, T., 2009. Glacial rebound and plate spreading: results from the first country wide GPS observations in Iceland. *Geophysics Journal International*, 177, 691-716.
- Axford, Y., Miller, G.H., Geirsdóttir, Á., and Langdon, P.G., 2007. Holocene temperature history of northern Iceland inferred from subfossil midges. *Quaternary Science Reviews*, 26, 3344-3358.
- Baer, G., 1991. Mechanisms of dike propagation in layered rocks and in massive, porous sedimentary rocks. *Journal of Geophysical Research*, 96, 11911-11929.
- Baer, G., 1995. Fracture propagation and magma flow in segmented dykes: Field evidence and fabric analyses, Makhtesh Ramon, Israel. Baer, G., and Heimann, A., eds., *Physics and Chemistry of Dykes*: Balkema Geological Survey of Israel, pp. 125-140.
- Ball, G., and Hall, D., 1965. Isodata, a novel method of data analysis and pattern classification. . Stanford Research Institute Technical Report, 79.
- Bear, A.N., and Cas, R.A.F., 2007. The complex facies architecture and emplacement sequence of a Miocene submarine mega-pillow lava flow system, Muriwai, North Island, New Zealand. *Journal of Volcanology and Geothermal Research*, 160, 1-22.
- Befus, K.S., Hanson, R.E., Miggins, D.P., Breyer, J.A., and Busbey, A.B., 2009. Nonexplosive and explosive magma/wet-sediment interaction during emplacement of Eocene intrusions into Cretaceous to Eocene strata, Trans-Pecos igneous province, West Texas. *Journal of Volcanology and Geothermal Research*, 181, 155-172.
- Bemmelen, R.W.v., and Rutten, M.G., 1955. Tablemountains of northern Iceland: (and related geological notes). Leiden, E.J. Brill.
- Bennett, M.R., Huddart, D., and Waller, R.I., 2006. Diamict fans in subglacial water-filled cavities- a new glacial environment. *Quaternary Science Reviews*, 25, 3050-3069.
- Bergh, S.G., and Sigvaldason, G.E., 1991. Pleistocene mass-flow deposits of basaltic hyaloclastite on a shallow submarine shelf, South Iceland *Bulletin of Volcanology*, 53, 597-611.
- Bevins, R.E., and Roach, R.A., 1979. Pillow lava and isolated-pillow breccia of rhyodacite composition from the Fishguard Volcanic Group, Lower Ordovician, S.W. Wales, United Kingdom. *The Journal of Geology*, 87, 193-201.
- Birks, H., Gulliksen, S., Haflidason, H., Mangerud, J., and Possnert, G., 1996. New Radiocarbon dates for the Vedde Ash and the Saksunarvatn Ash from Western Norway. *Quaternary Research*, 45, 119-127.
- Björnsson, A., 1985. Dynamics of crustal rifting in NE Iceland. *Journal of Geophysical Research*, 90, 10151-10162.
- Björnsson, H., 2002. Subglacial lakes and jokulhlaups in Iceland. *Global and Planetary Change*, 35, 255-271.

- Björnsson, H., and Pálsson, F., 2008. Icelandic glaciers. *Jökull*, 58, 365-386.
- Boulton, G.S., and Caban, P., 1995. Groundwater flow beneath icesheets, Part II. Its impact on glacier tectonic structures and moraine formation. *Quaternary Science Reviews*, 14, 563-587.
- Bourgeois, O., Dacuteuil, O., and Van Vliet-Lanoë, B., 2000. Geothermal control on flow patterns in the Last Glacial Maximum Ice Sheet of Iceland. *Earth Surface Processes and Landforms*, 25, 59-76.
- Bourgeois, O., Dauteuil, O., and Van Vliet-Lanoë, B., 1998. Pleistocene subglacial volcanism in Iceland: tectonic implications. *Earth and Planetary Science Letters*, 64, 165-178.
- Breddam, K., 2002. Kistufell: Primitive melt from the Iceland Mantle Plume. *Journal of Petrology*, 43, 345-373.
- Brendryen, J., Haflidason, H., and Sejrup, H.P., 2010. Norwegian Sea tephrostratigraphy of marine isotope stages 4 and 5: Prospects and problems for tephrochronology in the North Atlantic region. *Quaternary Science Reviews*, 29, 847-864.
- Brown, G.C., Everett, S.P., Rymer, H., McGarvie, D.W., and Fester, I., 1991. New light on caldera evolution- Askja, Iceland *Geology*, 19, 352-355.
- Brown, S.J.A., Smith, R.T., Cole, J.W., and Houghton, B.F., 1994. Compositional and textural characteristics of the strombolian and surtsey K-Trig basalts, Taupo Volcanic Centre, New Zealand: Implications for eruption dynamics. *New Zealand Journal of Geology and Geophysics*, 37, 113-126.
- Büttner, R., Dellino, P., La Volpe, L., Lorenz, V., and Zimanowski, B., 2002. Thermohydraulic explosions in phreatomagmatic eruptions as evidenced by the comparison between pyroclasts and products from Molten Fuel Coolant Interaction experiments. *Journal of Geophysical Research*, 107, 2277.
- Büttner, R., Dellino, P., and Zimanowski, B., 1999. Identifying magma-water interaction from the surface features of ash particles. *Nature*, 401, 688-690.
- Byrnes, J.M., Ramsey, M.S., and Crown, D.A., 2004. Surface unit characterization of the Mauna Ulu flow field, Kilauea Volcano, Hawai'i, using integrated field and remote sensing analyses. *Journal of Volcanology and Geothermal Research*, 135, 169-193.
- Carey, R.J., Houghton, B.F., and Thordarson, T., 2009. Abrupt shifts between wet and dry phases of the 1875 eruption of Askja Volcano: microscopic evidence for macroscopic dynamics. *Journal of Volcanology and Geothermal Research*, 184, 256-270.
- Carey, R.J., Houghton, B.F., and Thordarson, T., 2010. Tephra dispersal and eruption dynamics of wet and dry phases of the 1875 eruption of Askja Volcano, Iceland. *Bulletin of Volcanology*.
- Carlisle, D., 1963. Pillow breccias and their aquagene tuffs, Quadra Island, British Columbia. *The Journal of Geology*, 71, 48-71.
- Carrigan, C.R., Schubert, G., and Eichelberger, J.C., 1992. Thermal and dynamical regimes of single- and two-phase magmatic flow in dikes *Journal of Geophysical Research*, 97, 17377-17392.

- Carrivick, J.L., Russell, A.J., Rushmer, E.L., Tweed, F.S., Marren, P.M., Deeming, H., and Lowe, O.J., 2009. Geomorphological evidence towards a de-glacial control on volcanism. *Earth Surface Processes and Landforms*, 34, 1164-1178.
- Carrivick, J.L., Russell, A.J., and Tweed, F.S., 2004. Geomorphological evidence for jokulhlaups from Kverkfjoll volcano, Iceland. *Geomorphology*, 63, 81-102.
- Carter, A.J., Girina, O., Ramsey, M.S., and Demyanchuk, Y.V., 2008. ASTER and field observations of the 24 December 2006 eruption of Bezymianny Volcano, Russia. *Remote Sensing of the Environment*, 112, 2569-2577.
- Cas, R.A.F., Yamagishi, H., Moore, L., and Scutler, C., 2003. Miocene submarine fire fountain deposits, Ryugasaki Headland, Oshoro Peninsula, Hokkaido, Japan: implications for submarine fountain dynamics and fragmentation processes. White, J.D.L., Smellie, J.L., and Clague, D.A., eds., *Subaqueous Explosive Volcanism Volume 140*: Washington DC, AGU pp. 299-316.
- Charbit, S., Guillo, H., and Turpin, L., 1998. Cross-calibration of K-Ar standard minerals using an unspiked Ar measurement technique. *Chemical Geology* 150, 147-159.
- Clague, D.A., Batiza, R., Head, J.W., and Davis, A.S., 2003. Pyroclastic and hydroclastic deposits on Loihi Seamount, Hawaii. White, J.D.L., Smellie, J.L., and Clague, D.A., eds., *Explosive subaqueous volcanism, Volume 140*: Washington DC, AGU pp. 73-95.
- Clague, D.A., and Davis, A.S., 2003. Submarine Strombolian eruptions on the Gorda Mid-Ocean Ridge. White, J.D.L., Smellie, J.L., and Clague, D.A., eds., *Explosive subaqueous volcanism, Volume 140*: Washington DC, AGU pp. 111-128.
- Clague, D.A., Paduan, J.B., and Davis, A.S., 2009. Widespread strombolian eruptions of mid-ocean ridge basalt. *Journal of Volcanology and Geothermal Research*, 180, 171-188.
- Corcoran, P.L., 2000. Recognizing distinct portions of seamounts using volcanic facies analysis: examples from the Archean Slave Province NWT, Canada. *Precambrian Research*, 101, 237-261.
- De Zeeuw-van Dalfsen, E., Pedersen, R., Hooper, A., and Sigmundsson, F., 2012. Subsidence of Askja caldera 2000-2009: Modelling of deformation processes at an extensional plate boundary, constrained by the time series InSAR analysis. *Journal of Volcanology and Geothermal Research*, 213-214, 72-80.
- de Zeeuw-van Dalfsen, E., Rymer, H., Sigmundsson, F., and Sturkell, E., 2005. Net gravity decrease at Askja volcano, Iceland: constraints on processes responsible for the continuous caldera deflation, 1988-2003. *Journal of Volcanology and Geothermal Research*, 139, 227-239.
- Dimroth, E., Pierre, C., Leduc, M., and Sanshagrin, Y., 1978. Structure and organization of Archean subaqueous basalt flows, Rouyn-Noranda area, Quebec, Canada. *Canadian Journal of Earth Science* 15, 902-918.
- Doyle, M.G., 2000. Crystal shape and textural associations in peperite as a guide to hydromagmatic interactions: Upper Permian basaltic and basaltic andesite examples from Kiama, Australia. *Australian Journal of Earth Sciences*, 47, 167-177.

- Edwards, B.R., I.P., S., Cameron, B., Haynes, C., Lloyd, A., and Hungerford, J.H.D., 2009. Evolution of an englacial volcanic ridge: Pillow Ridge tindar, Mount Edziza volcanic complex, NCVP, British Columbia, Canada. *Journal of Volcanology and Geothermal Research*, 185, 251-275.
- Edwards, B.R., Russel, J.K., and Simpson, K., 2011. Volcanology and petrology of Mathews Tuya, northern British Columbia, Canada: glaciovolcanic constraints on interpretations of the 0.730 Ma Cordilleran paleoclimate. *Bulletin of Volcanology*, 73, 479-496.
- Einarsson, P., 2008. Plate boundaries, rifts and transforms in Iceland *Jökull* 58, 35-58.
- Einarsson, T., and Albertsson, K.J., 1988. The glacial history of Iceland during the past three million years. *Philosophical Transactions of the Royal Society of London*, 318, 637-644.
- Eiríksson, J., 2008. Glaciation events in the Pleistocene volcanic succession of Iceland. *Jökull*, 58.
- Eiríksson, J., Knudsen, K.L., Halfidason, H., and Henriksen, P., 2000. Late-glacial and Holocene palaeoceanography of the North Icelandic shelf. *Journal of Quaternary Science*, 15, 23-42.
- Eiríksson, J., Simonarson, L.A., Knudsen, K.A., and Kristensen, P., 1996. Fluctuations of the Weichslian ice sheet in SW Iceland: A glaciomarine sequence from sudurnes, Seltjarnarnes. *Quaternary Science Reviews*, 16, 221-240.
- Eiríksson, J., Simonarson, L.A., Knudsen, K.A., and Kristensen, P., 1997. Fluctuations of the Weichslian ice sheet in SW Iceland: A glaciomarine sequence from sudurnes, Seltjarnarnes. *Quaternary Science Reviews*, 16, 221-240.
- Eissen, J.-P., Fouquet, Y., Hardy, D., and Ondreas, H., 2003. Recent MORB volcanoclastic explosive deposits formed between 500 and 1750 m.b.s.l. on the axis of the Mid-Atlantic Ridge, South of the Azores. White, J.D.L., Smellie, J.L., and Clague, D.A., eds., *Explosive Subaqueous Volcanism Volume 140*: Washington DC, AGU, pp. 143- 166.
- Eiríksson, J., 2008. Glaciation events in the Pleistocene volcanic succession of Iceland. *Jökull*, 58.
- Fowler, A.D., Berger, B., Shore, M., Jones, M.I., and Ropchan, J., 2002. Supercooled rocks: development and significance of varioles, spherulites, dendrites and spinifex in Archean volcanic rocks, Abitibi Greenstone belt, Canada. *Precambrian Research* 115, 311-328.
- Fujibayashi, N., and Sakai, U., 2003. Vesiculation and eruption processes of submarine effusive and explosive rocks from the middle Miocene Ogi Basalt, Sado Island, Japan. White, J.D.L., Smellie, J.L., and Clague, D.A., eds., *Explosive submarine volcanism, Volume 140* Washington DC, AGU pp. 259-272.
- Furman, T., Meyer, P.S., and Frey, F., 1992. Evolution of Iceland central volcanoes: evidence from the Austurhorn intrusion, southeastern Iceland. *Bulletin of Volcanology*, 55, 45-62.
- Gee, M.A.M., Thirlwall, M.F., Taylor, R.N., Lowry, D., and Murton, B.J., 1998. Crustal processes: Major controls on Reykjanes Peninsula Lava Chemistry, SW Iceland. *Journal of Petrology*, 39, 819-839.
- Geirsdóttir, A., and Eiríksson, J., 1994. Growth of an intermittent ice sheet in Iceland during the Late Pliocene and Early Pleistocene. *Quaternary Research*, 42, 115-130.

- Geirsdóttir, Á., and Eiriksson, J., 1994. Growth of an intermittent ice sheet in Iceland during the Late Pliocene and Early Pleistocene. *Quaternary Research*, 42, 115-130.
- Gorny, C., F., White, J.D.L., and Gudmundsson, M., 2012. Contortoclasts and shoaling subglacial intrusions, Volcano Ice Interactions III: Anchorage, Alaska.
- Goto, Y., and McPhie, J., 2004. Morphology and propagation styles of Miocene submarine basanite lavas at Stanley, northwestern Tasmania, Australia. *Journal of Volcanology and Geothermal Research*, 130, 307-328.
- Graettinger, A.H., Skilling, I.P., McGarvie, D.W., and Hoskuldsson, A., 2012. Intrusion of basalt into frozen sediments and generation of Coherent-Margined Volcaniclastic Dikes (CMVD's). *Journal of Volcanology and Geothermal Research*, 217-218, 30-38.
- Gregg, T.K.P., and Fink, J.H., 1995. Quantification of submarine lava-flow morphology through analog experiments. *Geology*, 23, 73-76.
- Gregg, T.K.P., and Smith, D., 2003. Volcanic investigations of the Puna Ridge, Hawai'i: relations of lava flow morphologies and underlying slopes. *Journal of Volcanology and Geothermal Research*, 126, 63-77.
- Griffiths, R.W., and Fink, J., 1992. Solidification and morphology of submarine lavas: A dependence on extrusion rate. *Journal of Geophysical Research*, 97, 19729-19737.
- Grönvold, K., Oskarsson, N., Johnsen, S., Clausen, H.B., Hammer, C., Bond, G., and Bard, E., 1995. Ash layers from Iceland in the Greenland GRIP ice core correlated with oceanic and land sediments. *Earth and Planetary Science Letters*, 135, 149-155.
- Gudmundsson, A., 2002. Emplacement and arrest of sheets and dykes in central volcanoes. *Journal of Volcanology and Geothermal Research*, 116, 279-298.
- Gudmundsson, M.T., 2003. Melting of Ice by magma-ice-water interactions during subglacial eruptions an indicator of heat transfer in subaqueous eruptions. White, J.S., JL; Clague, DA, ed., *Explosive Subaqueous Volcanism Volume Geophysical Monograph 140: Washington DC, American Geophysical Union*, pp. 61-72.
- Gudmundsson, M.T., Sigmundsson, F., and Björnsson, H., 1997. Ice-volcano interaction of the 1996 Gjálp subglacial eruption, Vatnajökull, Iceland. *Nature*, 389, 954-957.
- Guillou, H., Van Vilet-Lanoe, B., Gudmundsson, A., and Nomade, S., 2010. New unspiked K-Ar ages of Quaternary sub-glacial and sub-aerial volcanic activity in Iceland. *Quaternary Geochronology*, 5, 10-19.
- Haflidason, H., Eiriksson, J., and van Kreveld, S., 2000. The tephrochronology of Iceland and the North Atlantic region during the Middle and Late Quaternary: a review *Journal of Quaternary Science*, 15, 3-22.
- Hansen, H., and Grönvöld, K., 2000. Plagioclase ultraphyric basalts in Iceland: the mush of the rift. *Journal of Volcanology and Geothermal Research*, 98, 1-32.

- Harðarson, B.S., Fitton, J.G., and Hjartarson, Á., 2008. Tertiary volcanism in Iceland. *Jökull*, 58, 161-178.
- Harpel, C.J., Kyle, P.R., and Dunbar, N.W., 2008. Englacial tephrostratigraphy of Erebus volcano, Antarctica. *Journal of Volcanology and Geothermal Research*, 177, 549-568.
- Hartley, M.E., and Thordarson, T., 2012. Formation of Oskjuvatn caldera at Askja, North Iceland: Mechanism of caldera collapse and implications for the lateral flow hypothesis. *Journal of Volcanology and Geothermal Research*, 227-228, 85-101.
- Head, J.W., and Wilson, L., 2002. Mars: a review and synthesis of general environments and geological settings of magma-H<sub>2</sub>O interactions. Smellie, J.L., and Chapman, M.G., eds., *Volcano-Ice Interactions on Earth and Mars*, Volume 202: London, Geological Society, pp. 27-57.
- Head, J.W., and Wilson, L., 2003. Deep submarine pyroclastic eruptions: theory and predicted landforms and deposits. *Journal of Volcanology and Geothermal Research*, 121, 155-193.
- Heiken, G., Wohletz, K.H., and Eichelberger, J.C., 1988. Fracture fillings and intrusive pyroclasts Inyo Domes, California. *Journal of Geophysical Research*, 93, 4335-4350.
- Helgason, J., and Duncan, R.A., 2001. Glacial-interglacial history of the Skaftafell region, southeast Iceland, 0-5 Ma. *Geology*, 29, 179-182.
- Helo, C., Longpre, M.-A., Shimizu, N., Clague, D.A., and Stix, J., 2011. Explosive eruptions at mid-ocean ridges driven by CO<sub>2</sub>-rich magmas. *Nature Geoscience*, 4, 260-263.
- Hjartardóttir, A.R., Einarsson, P., and Sigurdsson, H., 2009. The fissure swarm of the Askja volcanic system along the divergent plate boundary of N Iceland. *Bulletin of Volcanology*, 71, 961-971.
- Honnorez, J., and Kirst, P., 1975. Submarine basaltic volcanism: morphometric parameters for discriminating hyaloclastites from hyalotuffs. *Bulletin of Volcanology*, 39, 1-25.
- Hooper, A., Ofeigsson, B., Sigmundsson, F., Lund, B., Einarsson, P., Geirsson, H., and Sturkell, E., 2011. Increased capture of magma in the crust promoted by ice-cap retreat in Iceland. *Nature Geoscience*, 1269.
- Höskuldsson, Á., 1987. Some chemical properties of the Askja volcanic center Reykjavík, Nordic Volcanological Institute, University of Iceland
- Höskuldsson, A., Sparks, R.S.J., and Carroll, M.R., 2006. Constraints on the dynamics of subglacial basalt eruptions from geological and geochemical observations at Kverkfjöll, NE-Iceland. *Bulletin of Volcanology*, 68, 689-701.
- Houghton, B.F., and Gonnermann, H., 2008. Basaltic explosive volcanism: Constraints from deposits and models *Chemie der Erde* 68, 117-140.
- Houghton, B.F., and Nairn, I.A., 1991. The 1976-1982 Strombolian and phreatomagmatic eruptions of White Island, New Zealand: eruptive and depositional mechanisms at a 'wet' volcano. *Bulletin of Volcanology*, 54, 25-49.
- Houghton, B.F., and Schmincke, H.-U., 1989. Rotenberg scoria cone, East Eifel: a complex Strombolian and phreatomagmatic volcano. *Bulletin of Volcanology*, 52, 28-48.

- Hubbard, A., 2006. The validation and sensitivity of a model of the Icelandic ice sheet. *Quaternary Science Reviews*, 25, 2297-2313.
- Hubbard, A., Sugden, D., Dugmore, A., Norddahl, H., and Petursson, H., 2006. A modelling insight into the Icelandic Last Glacial Maximum ice sheet. *Quaternary Science Reviews*, 25, 2283-2296.
- Huppert, H.E., and Sparks, R.S.J., 1989. Chilled margins in igneous rocks Earth and Planetary Science Letters, 92, 397-405.
- Jakobsson, S.P., and Gudmundsson, M.T., 2008. Subglacial and intraglacial volcanic formations in Iceland. *Jökull*, 58, 179-196.
- Jakobsson, S.P., Jónasson, K., and Sigurdsson, I.A., 2008. The three igneous rock series of Iceland. *Jökull*.
- Jónhneðsson, H., and Sæmundsson, K., 1998. Jarðfræðikort af Íslandi 1:500000 Bergrunner (Geological map of Iceland, Bedrock Geology): Reykjavik Icelandic Institute of Natural History pp. 1:500000.
- Jolly, R.J.H., and Lonergan, L., 2002. Mechanisms and control on the formation of sand intrusions. *Journal of the Geological Society*, 159, 605-617.
- Jones, J.G., 1970. Intraglacial volcanoes of the Laugarvatn region, Southwest Iceland II. *The Journal of Geology*, 78, 127-140.
- Jull, M., and McKenzie, D., 1996. The effect of deglaciation on mantle melting beneath Iceland. *Journal of Geophysical Research*, 101, 21815-21828.
- Kagy, H., 2011. Interaction of basaltic dikes and wet sediment at glaciovolcanic centers: examples from Iceland and Mars: Pittsburgh, University of Pittsburgh.
- Kano, K.-i., 1989. Interactions between andesitic magma and poorly consolidated sediments: examples in the Neogene Shirahama Group, South Izu Japan. *Journal of Volcanology and Geothermal Research*, 37, 59-75.
- Kelsey, C.H., 1965. Calculation of the C.I.P.W. norm. *Mineralogical Magazine*, 34, 276-282.
- Kennish, M.J., and Lutz, R.L., 1998. Morphology and distribution of lava flows on mid-ocean ridges: a review. *Earth-Science Reviews*, 43, 63-90.
- King, P.L., Ramsey, M.S., McMillian, P.F., and Swayze, G.A., 2004. Laboratory Fourier transform infrared spectroscopy methods for geologic samples King, P.L., ed., *Infrared Spectroscopy in Geochemistry, Exploration Geochemistry, and Remote Sensing Volume 33*, Mineralogical Association of Canada pp. 57-911.
- Kinvig, H.S., Geyer, A., and Gottsmann, J., 2009. On the effect of crustal layering on ring-fault initiation and the formation of collapse calderas. *Journal of Volcanology and Geothermal Research*, 186, 293-304.



- Knudsen, K.L., and Eiriksson, J., 2002. Application of tephrochronology to the timing and correlation of palaeoceanographic events recorded in Holocene and Late Glacial shelf sediments off North Iceland. *Marine Geology*, 191, 165-188.
- Kokelaar, P., 1986. Magma-water interactions in subaqueous and emergent basaltic volcanism. *Bulletin of Volcanology*, 48, 275-289.
- Kuritani, T., Yokoyama, T., Kitagawa, H., Kobayashi, K., and Nakamura, E., 2011. Geochemical evolution of historical lavas from Askja Volcano, Iceland: Implications for mechanisms and timescales of magmatic differentiation. *Geochemica et Cosmochimica Acta*, 75, 570-587.
- Larsen, G., 2002. A brief overview of eruptions from ice-covered and ice-capped volcanic systems in Iceland during the past 11 centuries: frequency, periodicity and implications. Smellie, J.L.C., M. G., ed., *Volcano-Ice Interaction on Earth and Mars*, Volume 202: London, Geological Society, pp. 81-90.
- Larsen, G., and Eiriksson, J., 2008. Late Quaternary terrestrial tephrochronology of Iceland--frequency of explosive eruptions, type and volume of tephra deposits. *Journal of Quaternary Science* 23, 109-120.
- Licciardi, J.M., Kurz, M.D., and Curtice, J.M., 2007. Glacial and volcanic history of Icelandic table mountains from cosmogenic  $^3\text{He}$  exposure ages. *Quaternary Science Reviews*, 26, 1529-1546.
- Liss, D., Hutton, D.H.W., and Owens, W., 2002. Ropy flow structures: A neglected indicator of magma-flow direction in sills and dikes. *Geology*, 30, 715-718.
- Lister, J.R., 1995. Fluid-mechanical models of the interaction between solidification and flow in dykes. Baer, G., and Heimann, A., eds., *Physics and Chemistry of Dykes*: Balkema, Geological Survey of Israel, pp. 115-124.
- Lloyd, S.P., 1982. Least squares quantization in PCM *IEEE Transactions on Information Theory* 28, 129-137.
- Lodge, R.W.D., and Lescinsky, D.T., 2009. Fracture patterns at lava-ice contacts on Kokostick Butte, OR, and Mazama Ridge, Mount Rainier, WA: Implications for flow emplacement and cooling histories. *Journal of Volcanology and Geothermal Research*, 185, 298-310.
- Loughlin, S.C., 2002. Facies analysis of proximal subglacial and proglacial volcanoclastic successions at the Eyjafjallajökull. Smellie, J.L.C., M.G., ed., *Volcano-Ice Interaction on Earth and Mars*, Volume 202: London, The Geological Society of London, pp. 149-178.
- Lyubetskaya, T., and Korenaga, J., 2007. Chemical composition of Earth's primitive mantle and its variance: 1 Method and results. *Journal of Geophysical Research*, 112, B03211.
- MacLennan, J., Jull, M., McKenzie, D., Slater, L., and Grönvold, K., 2002. The link between volcanism and deglaciation in Iceland. *Geochemistry, Geophysics, Geosystems*, 3.
- Maicher, D., White, J.D.L., and Batiza, R., 2000. Sheet hyaloclastite: density-current deposits of quench and bubble-burst fragments from thin, glassy sheet lava flows, Seamount Six, Eastern Pacific Ocean. *Marine Geology*, 171, 75-94.

- Martin, U., and Nemeth, K., 2007. Blocky versus fluidal peperite textures developed in volcanic conduits, vents and crater lakes of phreatomagmatic volcanoes in Mio/Pliocene volcanic fields of Western Hungary. *Journal of Volcanology and Geothermal Research*, 159, 164-178.
- Mastin, L.G., Spieler, O., and Downey, W.S., 2009. An experimental study of hydromagmatic fragmentation through energetic, non-explosive magma-water mixing. *Journal of Volcanology and Geothermal Research*, 180, 161-170.
- Mattox, T., and Mangan, M., 1997. Littoral hydrovolcanic explosions: a case study of lava-seawater interaction at Kilauea volcano *Journal of Volcanology and Geothermal Research*, 75, 1-17.
- McGarvie, D.W., 2009. Rhyolitic volcano-ice interactions Iceland. *Journal of Volcanology and Geothermal Research*, 185, 367-389.
- McPhie, J., Doyle, M.G., and Allen, C.C., 1993. *Volcanic Textures: A guide to the interpretation of textures in volcanic rocks*: Hobart, CODES Key Centre, University of Tasmania
- Mee, K., Tuffen, H., and Gilbert, J.S., 2006. Snow-contact volcanic facies and their use in determining past eruptive environments at Nevados de Chillán volcano, Chile. *Bulletin of Volcanology*, 68, 363-376.
- Mercurio, E., 2011. Processes, products and depositional environments of ice-confined basaltic fissure eruptions: a case study of the Sveifluhals volcanic complex, SW Iceland. [Dissertation thesis]: Pittsburgh, University of Pittsburgh.
- Meyer, P.S., Sigurdsson, H., and Schilling, J.-G., 1985. Petrological and geochemical variations along Iceland's Neovolcanic Zones. *Journal of Geophysical Research*, 90, 10034-10072.
- Moore, J.G., 1975. Mechanism of formation of pillow lava. *American Scientist*, 63, 269-277.
- Moore, J.G., and Calk, L.C., 1991. Degassing and differentiation in subglacial volcanoes, Iceland *Journal of Volcanology and Geothermal Research*, 46, 157-180.
- Moore, J.G., Hickson, C.J., and Calk, L.C., 1995. Tholeiitic-alkalic transition at subglacial volcanoes, Tuya region, British Columbia, Canada. *Journal of Geophysical Research*, 100, 24577-24592.
- Murtagh, R.M., White, J.D.L., and Sohn, Y.K., 2011. Pyroclast textures of the Ilchulbong 'wet' tuff cone, Jeju Island *Journal of Volcanology and Geothermal Research*, 201, 385-396.
- Nemeth, K., and Cronin, S.J., 2011. Drivers of explosivity and elevated hazard in basaltic fissure eruptions: The 1913 eruption of Ambrym Volcano, Vanuatu (SW-Pacific). *Journal of Volcanology and Geothermal Research*, 201, 194-209.
- Newman, S., and Lowenstern, J., 2002. VolatileCalc: a silicate melt -H<sub>2</sub>O-CO<sub>2</sub> solution model written in Visual Basic for excel.
- Norðdahl, H., Ingólfsson, Ó., Pétursson, H.G., and Hallsdóttir, M., 2008. Late Weichselian and Holocene environmental history of Iceland. *Jökull*, 58, 343-364.
- Norðdahl, H., and Pétursson, H., 2005. Relative sea-level changes in Iceland: new aspects of the Weichselian deglaciation of Iceland Caseldine, C.R., A.; Hardardottir, J.; Knudsen, O, ed.,

- Iceland- Modern Processes and Past Environments, Volume 5: Developments in Quaternary Science: Amsterdam, Elsevier, pp. 25-78.
- Óladóttir, B.A., Larsen, G., and Sigmarsson, O., 2011. Holocene volcanic activity at Grímsvötn, Bárðunga and Kverkfjöll subglacial centres beneath Vatnajökull, Iceland. *Bulletin of Volcanology*, 73, 1187-1208.
- Owen, J., Tuffen, H., and McGarvie, D.W., 2012. Using dissolved H<sub>2</sub>O in rhyolitic glasses to estimate palaeo-ice thickness during a subglacial eruption at Blahnukur (Torfajökull, Iceland). *Bulletin of Volcanology*.
- Pagli, C., Sigmundsson, F., Árnadóttir, T., Einarsson, P., and Sturkell, E., 2006. Deflation of the Akja volcanic system: Constraints on the deformation source from combined inversion of satellite radar interferograms and GPS measurements. *Journal of Volcanology and Geothermal Research*, 152, 97-108.
- Parfitt, E., A., Gregg, T.K.P., and Smith, D., 2002. A comparison between subaerial and submarine eruptions at Kilauea Volcano, Hawaii: implications for the thermal viability of lateral feeder dikes. *Journal of Volcanology and Geothermal Research*, 113, 213-242.
- Parfitt, E., A., and Wilson, L., 2009. *Fundamentals of Physical Volcanology* Malden, MA, Blackwell Publishing pp. 230.
- Pedersen, R., Sigmundsson, F., and Masterlark, T., 2009. Rheologic controls on inter-rifting deformation of the Northern Volcanic Zone, Iceland. *Earth and Planetary Science Letters*, 281, 14-26.
- Platten, I.M., 1995. The significance of phenocryst distributions in chilled margins of dykes and sills for the interpretation of tip processes. Baer, G., and Heimann, A., eds., *Physics and Chemistry of Dykes*: Balkema Geological Society of Israel, pp. 141- 150.
- Portner, R.A., Daczko, N.R., and Dickinson, J.A., 2010. Vitriclastic lithofacies from Macquarie Island (Southern Ocean): compositional influence on abyssal eruption explosivity in a dying Miocene spreading ridge. *Bulletin of Volcanology*, 72, 165-183.
- Ramsey, M.S., and Christensen, P.R., 1998. Mineral abundance determination: Quantitative deconvolution of thermal emission spectra. *Journal of Geophysical Research*, 103, 577-596.
- Ramsey, M.S., and Dehn, J., 2004 Spaceborne observations of the 2000 Bezymianny, Kamchatka eruption: The integration of high-resolution ASTER data into near real-time monitoring using AVHRR. *Journal of Volcanology and Geothermal Research*, 135, 127-146.
- Ramsey, M.S., and Fink, J., 1997. Mapping vesicularity of Hawaiian lava flows via thermal infrared remote sensing, AGU, Volume 78:46, EOS pp. F777.
- Ramsey, M.S., and Fink, J., 1999. Estimating silicic lava vesicularity with thermal remote sensing: A new technique for volcanic mapping and monitoring. *Bulletin of Volcanology*, 61, 32-39.
- Rijsdijk, K.F., Owen, G., Warren, W.P., McCarroll, D., and van der Meer, J.J.M., 1999. Clastic dykes in over-consolidated tills: evidence for subglacial hydrofracturing at Killiney Bay, eastern Ireland *Sedimentary Geology*, 129, 111-126.

- Rivalta, E., and Dahm, T., 2006. Acceleration of buoyancy-driven fractures and magmatic dikes beneath the free surface. *Geophysical Journal International*, 166, 1424-1439.
- Robert, G., Russel, J.K., Giordano, D., and Romano, C., 2008. High-temperature deformation of volcanic materials in the presence of water. *American Mineralogist*, 93, 74-80.
- Ross, P.S., and White, J.D.L., 2005. Unusually large clastic dykes forms by the elutriation of a poorly sorted, coarse grained source. *Journal of the Geological Society*, 162, 579-582.
- Ross, P.S., and White, J.D.L., 2006. Debris jets in continental phreatomagmatic volcanoes: A field study of their subterranean deposits in the Coombs Hills vent complex, Antarctica *Journal of Volcanology and Geothermal Research*, 149, 62-84.
- Ruff, S., Christensen, P.R., Barbera, P.W., and Anderson, D.L., 1997. Quantitative thermal emission spectroscopy of minerals: a laboratory technique for measurement and calibration. *Journal of Geophysical Research* 102, 14899-14913.
- Russell, J.K., Nichols, J., Stansley, C.R., and Pearce, T.H., 1990. Pearce element ratios. *EOS*, 71, 234-236.
- Ryan, M.P., and Sammis, C.G., 1981. The glass transition in basalt. *Journal of Geophysical Research*, 86, 9519-9535.
- Rymer, H., and Tryggvason, E., 1993. Gravity and elevation changes at Askja, Iceland. *Bulletin of Volcanology*, 55, 362-371.
- Saemundsson, K., 1991. The geology of the Krafla system. Gardarsson, A.E., A., ed., *Natura Myvatns: Reykjavik, Hid islenska natturufraedifelag*, pp. 25-95.
- Sansone, F.J., and Smith, J.R., 2006. Rapid mass wasting following nearshore submarine volcanism on Kilauea volcano, Hawaii. *Journal of Volcanology and Geothermal Research*, 151, 133-139.
- Scheidt, S., Ramsey, M.S., and Lancaster, N., 2010. Determining soil moisture and sediment availability at White Sands DUNE Field, NM from apparent thermal inertia (ATI) data. *Journal of Geophysical Research*, 115, F0204109.
- Schilling, J.-G., Zajac, M., Evans, R., Johnston, T., White, W.M., Devine, J.D., and Kingsley, R., 1983. Petrologic and geochemical variations along the Mid-Atlantic Ridge from 29°N to 73°N. *American Journal of Science*, 283, 510-586.
- Schipper, C.I., and White, J.D.L., 2010. No depth limit to hydrovolcanic limo o Pele: analysis of limo from Lō'ihi Seamount, Hawai'i *Bulletin of Volcanology*, 72, 149-164.
- Schipper, C.I., White, J.D.L., and Houghton, B.F., 2010a. Syn- and post-fragmentation textures in submarine pyroclasts from Lo'ihi Seamount, Hawai'i. *Journal of Volcanology and Geothermal Research*, 191, 93-106.
- Schipper, C.I., White, J.D.L., and Houghton, B.F., 2011a. Textural, geochemical, and volatile evidence for a Strombolian-like eruption sequence at Lo'ihi Seamount Hawai'i *Journal of Volcanology and Geothermal Research*, 207, 16-32.

- Schipper, C.I., White, J.D.L., Houghton, B.F., Shimizu, N., and Stewart, R.B., 2010b. Explosive submarine eruptions driven by volatile-coupled degassing at Lo'ihi Seamount, Hawai'i. *Earth and Planetary Science Letters*, 295, 497-510.
- Schipper, C.I., White, J.D.L., Houghton, B.F., Shimizu, N., and Stewart, R.B., 2010c. "Poseidic" explosive eruptions at Loihi Seamount, Hawaii. *Geology*, 38, 291-294.
- Schipper, C.I., White, J.D.L., Zimanowski, B., Büttner, R., Sonder, I., and Schmid, A., 2011b. Experimental interaction of magma and "dirty" coolants. *Earth and Planetary Science Letters*, 203, 323-336.
- Schmid, A., Sonder, I., Seegelken, R., Zimanowski, B., Büttner, R., Gudmundsson, M.T., and Oddsson, B., 2010. Experiments on the head discharge at the dynamic magma-water-interface. *Geophysical Research Letters*, 37, L20311.
- Schopka, H.H., Gudmundsson, M.T., and Tuffen, H., 2006. The formation of Helgafell, southwest Iceland, a monogenetic subglacial hyaloclastite ridge: Sedimentology, hydrology and volcano-ice interaction. *Journal of Volcanology and Geothermal Research*, 152, 359-377.
- Scott, C.R., Richard, D., and Fowler, A.D., 2003. An Archean submarine pyroclastic flow due to submarine dome collapse: The Hurd Deposit, Harker Township, Ontario, Canada. White, J.D.L., Smellie, J.L., and Clague, D.A., eds., *Subaqueous Explosive Volcanism Volume 140*: Washington DC, AGU pp. 317-327.
- Sigmarsson, O., MacLennan, J., and Carpentier, M., 2008. Geochemistry of igneous rocks in Iceland: a review. *Jökull*, 58, 139-160.
- Sigmarsson, O., and Steinthórsson, S., 2007. Origin of Icelandic basalts: a review of their petrology and geochemistry. *Journal of Geodynamics*, 43, 87-100.
- Sigmundsson, F., 1991. Post-glacial rebound and asthenosphere viscosity in Iceland. *Geophysical Research Letters*, 18, 1131-1134.
- Sigurdsson, H., and Sparks, R., 1978. Rifting episode in North Iceland in 1874-1875 and the eruptions of Askja and Sveinagja. *Bulletin of Volcanology*, 41, 149-167.
- Sigvaldason, G.E., 1964. Some geochemical and hydrothermal aspects of the 1961 Askja eruption. *Contributions to Mineralogy and Petrology*, 10, 263-274.
- Sigvaldason, G.E., 1968. Structure and products of subaquatic volcanoes in Iceland. *Contributions to Mineralogy and Petrology*, 18, 1-16.
- Sigvaldason, G.E., 1979. Rifting, magmatic activity and interaction between acid and base liquids., Volume 79: Reykjavik, Nordic Volcanologic Institute, pp. p. 31.
- Sigvaldason, G.E., 1992. Recent hydrothermal explosion craters in an old hyaloclastite flow, central Iceland. *Journal of Volcanology and Geothermal Research*, 54, 53-63.
- Sigvaldason, G.E., 2002. Volcanic and tectonic processes coinciding with glaciation and crustal rebound: an early Holocene rhyolitic eruption in the Dyngjufjöll volcanic centre and the formation of the Askja caldera, north Iceland. *Bulletin of Volcanology*, 64, 192-205.

- Sigvaldason, G.E., Annertz, K., and Nilsson, M., 1992. Effect of glacier loading/deloading on volcanism: postglacial volcanic production rate of the Dyngjujökull. *Bulletin of Volcanology*, 54, 385-392.
- Sigvaldason, G.E., Steinthorsson, S., Oskarsson, H., and Imsland, P., 1974. Compositional variation in recent Icelandic tholeiites and the Kverkfjöll hot spot. *Nature*, 251, 579-582.
- Simpson, K., and McPhie, J., 2001. Fluidal-clast breccia generated by submarine fire fountaining, Trooper Creek Formation, Queensland, Australia. *Journal of Volcanology and Geothermal Research*, 109, 339-355.
- Sinton, J., Gronvöld, K., and Saemundsson, K., 2005. Postglacial eruptive history of the Western Volcanic Zone, Iceland. *Geochemistry, Geophysics, Geosystems*, 6, 1-34.
- Skilling, I.P., 2009. Subglacial to emergent basaltic volcanism at Hlöðufell, south-west Iceland: A history of ice-confinement. *Journal of Volcanology and Geothermal Research*, 185, 276-289.
- Skilling, I.P., Mercurio, E., and Cameron, B., 2009. Ice-confined basaltic eruptive fissure complexes in Iceland: Accessible analogs for understanding shallow submarine ridge construction, AGU: San Fransico, AGU.
- Skilling, I.P., White, J.D.L., and McPhie, J., 2002. Peperite: a review of magma-sediment mingling. *Journal of Volcanology and Geothermal Research*, 114, 1-17.
- Slater, L., Jull, M., McKenzie, D., and Gronvöld, K., 1998. Deglaciation effects on mantle melting under Iceland: results from the norther volcanic zone. *Earth and Planetary Science Letters*, 164, 151-164.
- Smellie, J.L., 2001. Lithofacies architecture and construction of volcanoes erupted in englacial lakes: Icefall Nunatak, Mount Murphy, Eastern Marie Byrd Land, Antarctica White, J.D.L., and Riggs, N.R., eds., *Volcaniclastic Sedimentation in Lacustrine Settings*, Volume 30: London, Blackwell Science Ltd, pp. 309.
- Smellie, J.L., 2006. The relative importance of supraglacial versus subglacial meltwater escape in basaltic subglacial tuya eruptions: An important unresolved conundrum. *Earth-Science Reviews*, 74, 241-268.
- Smellie, J.L., 2007. Quaternary volcanism: subglacial landforms.
- Smellie, J.L., 2008. Basaltic subglacial sheet-like sequences: Evidence for two types with different implications for the inferred thickness of associated ice. *Earth-Science Reviews*, 88, 60-88.
- Smellie, J.L., and Hole, M.J., 1997. Products and processes in Pliocene-Recent, subaqueous to emergent volcanism in the Antarctic Peninsula: examples of englacial Surtseyan volcano construction. *Bulletin of Volcanology*, 58, 628-646.
- Smellie, J.L., Johnson, J.S., McIntosh, W.C., Esser, R., Gudmundsson, M.T., Hambrey, M.J., and van Wyk de Vries, B., 2008. Six million years of glacial history recorded in volcanic lithofacies of the James Ross Island Volcanic Group, Antarctic Peninsula. *Palaeogeography, Palaeoclimatology, Palaeoecology*, 260, 122-148.

- Sohn, R.A., Willis, C., Humphris, S., Shank, T.M., Singh, H., Edmonds, H.N., Kunz, C., Hedman, U., Helmke, E., Jakuba, M., Liljebladh, B., Linder, J., Murphy, C., Nakamura, K.-i., Sato, T., Schlindwein, V., Stranne, C., Tausenfruen, M., Upchurch, L., Winsor, P., Jakobsson, M., and Soule, A.A., 2008. Explosive volcanism on the ultraslow-spreading Gakkel ridge, Arctic Ocean. *Nature*, 453, 1236-1238.
- Sohn, Y.K., 1995. Geology of Tok Island, Korea: eruptive and depositional processes of a shoaling to emergent island volcano. *Bulletin of Volcanology*, 56, 660-674.
- Solgevik, H., Mattson, H.B., and Hermelin, O., 2007. Growth of an emergent tuff cone: Fragmentation and depositional processes recorded in the Capelas tuff cone, Sao Miguel, Azores. *Journal of Volcanology and Geothermal Research*, 159, 246-266.
- Soosalu, H., Key, J., White, R.S., Knox, C., Einarsson, P., and Jakobsdóttir, S.S., 2010. Lower-crustal earthquakes caused by magma movement beneath Askja volcano on the north Iceland rift. *Bulletin of Volcanology*, 72, 55-62.
- Soosalu, H.K., Janet; White, Robert S.; Knox, Clare; Einarsson, Páll; Jakobsdóttir, Steinunn S., 2009. Lower-crustal earthquakes caused by magma movement beneath Askja volcano on the north Iceland rift. *Bulletin of Volcanology*.
- Sorrentino, L., Cas, R.A.F., and Stilwell, J.D., 2011. Evolution and facies architecture of Paleogene Surtseyan volcanoes on Chatham Islands, New Zealand, Southwest Pacific Ocean *Journal of Volcanology and Geothermal Research*, 202, 1-21.
- Stanely, C.R., and Russel, J.K., 1989. Petrologic hypothesis testing with Pearce element ratio diagrams: derivation of diagram axes. *Contributions to Mineralogy and Petrology*, 103, 78-89.
- Staudigel, H., and Schmincke, H.-U., 1984. The Pliocene Seamount Series of La Palma/Canary Islands. *Journal of Geophysical Research*, 89, 11195-11215.
- Steiger, R.H., and Jaeger, E., 1977. Subcommittee on geochronology: convention on the use of decay constants in geo- and cosmochemistry. *Earth and Planetary Science Letters*, 36, 359-362.
- Stevenson, J.A., Smellie, J.L., McGarvie, D.W., Gilbert, J.S., and Cameron, B.I., 2009. Subglacial intermediate volcanism at Kerlingarfjöll, Iceland: magma-water interactions beneath thick ice. *Journal of Volcanology and Geothermal Research*, 15.
- Stovall, W.K., Houghton, B.F., Gonnermann, H., Fagents, S., and Swanson, D.A., 2011. Eruption dynamics of Hawaiian-style fountains: the case study of episode 1 of the Kilauea Iki 1959 eruption. *Bulletin of Volcanology*, 73, 511-529.
- Strand, K., 1987. Models for the deposition and the role of external water in explosive volcanism of the Dyngjufjöll Late Pleistocene-Holocene central volcano complex in North Iceland, Volume Preliminary Report Reykjavik Nordic Volcanological Institute, University of Iceland
- Stroncik, N., and Schmincke, H.-U., 2002. Palagonite- a review. *International Journal of Earth Science (Geol Rundsch)*, 91, 680-697.
- Sturkell, E., Sigmundsson, F., Geirsson, H., Ólafsson, H., and Theodórsson, T., 2008. Multiple volcano deformation sources in a post-rifting period: 1989-2005 behaviour of Frafla, Iceland constrained

- by levelling, tilt and GPS observations *Journal of Volcanology and Geothermal Research*, 177, 405-417.
- Sturkell, E., Sigmundsson, F., and Slunga, R., 2006. 1983-2003 decaying rate of deflation at Askja caldera: Pressure decrease in an extensive magma plumbing system at a spreading plate boundary. *Bulletin of Volcanology*, 2006, 727-735.
- Syvitski, J.P., Jennings, J.T., and Andrews, J.T., 1999. High- resolution seismic evidence for multiple glaciation across the southwest Iceland shelf. . *Artic, Antarctic, and Alpine Research* 31, 50-57.
- Taisne, B., and Jaupart, C., 2010. Magma expansion and fragmentation in a propagating dyke. *Earth and Planetary Science Letters*, 301, 146-152.
- Taisne, B., Tait, S., and Jaupart, C., 2011. Conditions for the arrest of a vertical propagating dyke. Moran, S.N., CG; Roman, DC (eds) ed., *Failed eruptions: Late -stage cessation of magma ascent.* , Volume 73, *Bull Volcanology* pp. 191-204.
- Þorarinsson, S., 1963. *Eldur í Öskju*. Reykjavik, Almenna Bókafélagið.
- Thorarinsson, S., 1968. On the rate of lava- and tephra production and the upward migration of magma in four Icelandic eruptions. *Geologische Rundschau*, 57, 705-718.
- Thorarinsson, S., and Sigvaldason, G., 1962. The eruption in Askja, 1961 a preliminary report. *American Journal of Science* 260, 641-651.
- Thoroddsen, T., 1925. *Die Geschichte der Islandischen Vulkane*. Copenhagen.
- Tryggvason, E., 1989. Ground deformation in Askja, Iceland: its source and possible relation to flow of the mantle plume *Journal of Volcanology and Geothermal Research*, 39, 61-71.
- Tucker, D.S., and Scott, K.M., 2009. Structures and facies associated with the flow of subaerial basaltic lava into a deep freshwater lake: the Sulphur Creek lava flow, North Cascades, Washington. *Journal of Volcanology and Geothermal Research*, 185, 311-322.
- Tuffen, H., and Castro, J.M., 2009. The emplacement of an obsidian dyke through thin ice: Hrafninnuhryggur, Krafla Iceland. *Journal of Volcanology and Geothermal Research*, 185, 352-366.
- Tuffen, H., Owen, J., and Denton, J., 2010. Magma degassing during subglacial eruptions and its use to reconstruct palaeo-ice thicknesses. *Earth-Science Reviews*, 99, 1-18.
- Vezzoli, L.M., Hauser, N., Omarini, R., Mazzuoli, R., and Acocella, V., 2008. Non-explosive magma-water interaction in a continental setting: Miocene examples from the Eastern Cordillera. *Bulletin of Volcanology*.
- Walker, G.P.L., 1992. Morphometric study of pillow-size spectrum among pillow lavas. *Bulletin of Volcanology*, 54, 459-474.
- Walker, G.P.L., and Croasdale, R., 1971. Characteristics of some basaltic pyroclasts. *Bulletin of Volcanology*, 35, 303-317.



- Werner, R., and Schmincke, H.-U., 1999. Englacial vs lacustrine origin of volcanic table mountains: evidence from Iceland. *Bulletin of Volcanology*, 60, 335-354.
- Werner, R., Schmincke, H.-U., and Sigvaldason, G.E., 1996. A new model for the evolution of table mountains: volcanological and petrological evidence from Herdubreid and Herdubreidartögl volcanoes (Iceland) *Geol Rundsch*, 85, 390-397.
- White, J.D.L., 1996a. Impure coolants and interaction dynamics of phreatomagmatic eruptions. *Journal of Volcanology and Geothermal Research*, 74, 155-170.
- White, J.D.L., 1996b. Pre-emergent construction of a lacustrine basaltic volcano, Pahvant Butte, Utah (USA). *Bulletin of Volcanology*, 58, 249-262.
- White, J.D.L., 2000. Subaqueous eruption-fed density currents and their deposits. *Precambrian Research*, 101, 87-109.
- White, J.D.L., McPhie, J., and Skilling, I.P., 2000. P eperite: a useful genetic term. *Bulletin of Volcanology*, 62, 65-66.
- Wilson, L., and Head, J.W., 2002. Heat transfer and melting in subglacial basaltic volcanic eruptions: implications for volcanic deposit morphology and meltwater volumes Smellie, J.L., and Chapman, M.G., eds., *Volcano-Ice Interaction on Earth and Mars*, Volume 202: London, Geological Society, pp. 5-26.
- Wilson, L., and Head, J.W., 2007. Heat transfer in volcano-ice interactions on Earth. *Annals of Glaciology*, 45.
- Wohletz, K.H., 1986. Explosive magma-water interactions: Thermodynamics, explosions mechanisms, and field studies. *Bulletin of Volcanology*, 48, 245-264.
- Wohletz, K.H., 2002. Water/magma interaction: some theory and experiments on pe perite formation. *Journal of Volcanology and Geothermal Research*, 114, 19-35.
- Wohletz, K.H., 2003. Water/magma interaction: physical considerations for the deep submarine environment. White, J.D.L., Smellie, J.L., and Clague, D.A., eds., *Explosive Subaqueous Volcanism Volume 140*: Washington DC, AGU pp. 25-49.
- Zervas, D., Nichols, G.J., Hall, R., Smyth, H.R., Luthje, C., and Murtagh, F., 2009. SedLog: a shareware program for drawing graphics and log data manipulation. *Computers & Geosciences*, 35, 2151-2159.
- Zimanowski, B., and Büttner, R., 2002. Dynamic mingling of magma and liquefied sediments *Journal of Volcanology and Geothermal Research*, 114, 37-44.
- Zimanowski, B., and Büttner, R., 2003. Phreatomagmatic explosions in subaqueous volcanism. White, J.D.L., Smellie, J.L., and Clague, D.A., eds., *Explosive Subaqueous Volcanism*, Volume 140: Washington DC, AGU, pp. 51-60.
- Zimanowski, B., and Wohletz, K.H., 2000. Physics of Phreatomagmatism-1. *Terra Nostra*, 6, 515-523.

Zimanowski, B., Wohletz, K.H., Dellino, P., and Büttner, R., 2003. The volcanic ash problem. *Journal of Volcanology and Geothermal Research*, 122, 1-5.